Università degli Studi di Ferrara

DOCTORAL COURSE IN

BIOMEDICAL SCIENCES AND BIOTECHNOLOGY

CYCLE XXXV

COORDINATOR Prof. Pinton Paolo

# MITOCHONDRIAL PERMEABILITY TRANSITION PORE (mPTP) OPENING INHIBITORS AS POTENTIAL DRUGS FOR THE TREATMENT OF ISCHEMIA REPERFUSION INJURY (IRI): DESIGN, SYNTHESIS AND BIOLOGICAL EVALUATION OF DIFFERENT CLASSES OF SMALL MOLECULES.

Scientific/Disciplinary Sector (SDS) CHIM/06


**Candidate**
Dott. Turrin Giulia

*(signature)*

**Supervisor**
Prof. Rizzo Roberta

*(signature)*

**Co-Supervisor**
Prof. Trapella Claudio

*(signature)*


Year 2019/2022

# TABLE OF CONTENTS

# 1. INTRODUCTION

## 1.1 MITOCHONDRION: THE "POWERHOUSE" OF THE CELL.

Mitochondrion (from Greek μίτος, "wire" e χόνδρος, "granule") is an intracellular organelle with a generally elongated shape present in the cytoplasm of all eukaryotic cells and it is considered the "powerhouse" of the cell: in fact, it is used for the production of ATP, through the process of oxidative phosphorylation. In this way it provides the energy to the cells to work. The mitochondrion is the only cellular organelle that has its own DNA, defined as mtDNA: it is matrilineally inherited and the genes contained in it encode mostly for proteins that participate in the system of oxidative phosphorylation. Structurally, the mitochondrion has two membranes, one external and one internal, which delimit an intermembrane space. The former is readily permeable to small molecules (size up to 5000 Da) and ions that can permeate through integral membrane proteins, called porins. The latter, on the other hand, is impermeable to small molecules and almost all ions, including protons. The passage through this membrane is selective for those molecules that possess a specific transporter: these conditions, therefore, define a highly selective permeability and consequently a clear separation between the metabolic processes that take place in the mitochondrion compared to those that take place in the cytosol. The inner membrane shows some invaginations, called mitochondrial cristae, which contribute to increase considerably the area of its surface: in this way the efficiency of ATP production is considerably greater, and so the energy production growths a lot. The innermost part of the organelle, delimited by the inner membrane, is called matrix: it has fluid consistency and contains enzymatic complexes, mtDNA, ribosomes and many metabolic intermediates. In addition to supplying cellular energy, mitochondria are involved in other tasks, such as, cellular differentiation, and as well as maintaining control of the cell cycle and cell growth. Consequently, mitochondria have been implicated in several human disorders and conditions, such as for example mitochondrial diseases, cardiac dysfunction and heart failure.

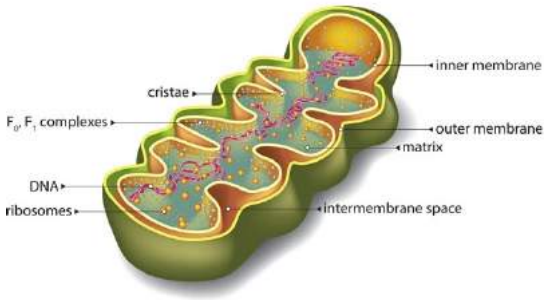


**Figure 1**. Mitochondrion structure

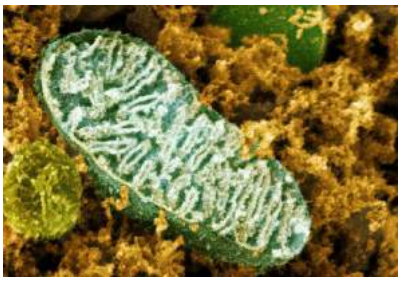

**Figure 2**. Mitochondrion (SEM)

## 1.2 OXIDATIVE PHOSPORYLATION AND ELECTRON TRANSPORT CHAIN

Oxidative phosphorylation (OXPHOS) is the biochemical process of producing and storing energy in the form of ATP molecules. It consists of two steps: the first is called the electron transport chain, which creates a proton gradient in the intermembrane space; the second is the actual synthesis of ATP molecules from ADP and $P_i$ by the enzyme ATP synthase. During the oxidation of fuel molecules, $FADH_2$ and NADH play a central role as the major electron carriers taking the electrons to the ultimate acceptor, oxygen ($O_2$). The transfer of electrons from NADH and $FADH_2$ to $O_2$ takes place in the inner membrane of the mitochondria. During this transfer, a number of protons are pumped out of the mitochondrial matrix, forming a proton gradient. Finally, with the help of the ATP synthase enzyme, the protons flow back into the matrix generating the necessary energy to generate ATP. In eukaryotes, these redox reactions are catalyzed by a series of protein complexes within the inner membrane of the cell's mitochondria. During this process, electrons carried by NADH and $FADH_2$ (obtained from glycolysis and the Krebs cycle) are transferred from one complex to another until they reach the final acceptor, molecular oxygen, which is reduced to $H_2O$. Electron transport consists of a series of highly exergonic reactions ($\Delta G^0$ = -81 KJ $mol^{-1}$): much of the energy released is used to pump protons out of the mitochondrial matrix, thus contributing to create a charge separation and a gradient, also known as the proton motive force. This one, described in the chemiosmotic model by Peter Mitchell in 1961, is defined as electrochemical energy contained in the proton concentration difference and charge separation across the inner mitochondrial membrane, leading to ATP synthesis when the proton flow reverses its direction and protons return to the matrix through a proton channel associated with ATP synthase.[1]

In this system, protons are pumped from the matrix across the mitochondrial inner membrane through respiratory complexes: I, III, and IV. The protons return to the mitochondrial matrix following their electrochemical gradient through ATP synthase; ATP is synthesized via complex V converting ADP and phosphate using this potential energy (figure 3). Thus, the mitochondrion converts energy derived from chemical fuels by an OXPHOS process that is more efficient than anaerobic glycolysis. In the mitochondrion, indeed, the metabolism of one molecule of glucose produces about 30 molecules of ATP, while only two molecules of ATP are produced by glycolysis in the cytoplasm.

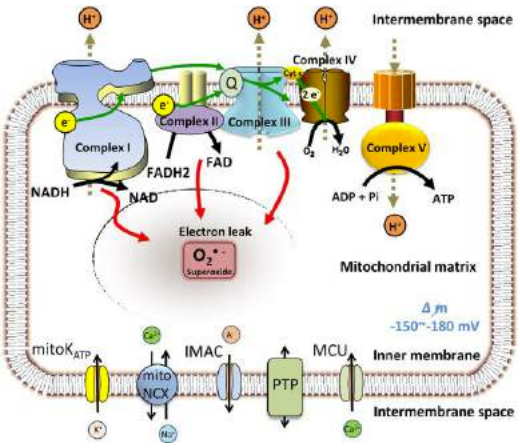


**Figure 3**. Oxidative phosphorylation and reactive oxygen species (ROS) production in mitochondria. Here are also highlighted other proteins and complexes involved in the ion's equilibrium maintenance, such as PTP and MCU.

Figure 3 (above) shows key components of the electron transport chain (ETC, upper side) and channels and transporters (lower side). The electrons flow through the ETC with the following sequence: two electrons are removed from NADH and transferred to ubiquinone, obtaining ubiquinol, that diffuses within the membrane, while complex I transfers the four protons across the membrane. Then, complex II transports electrons from succinate, that is been oxidized, to coenzyme Q. Then the electrons pass through complex III to cytochrome C (Cyt C). Finally, complex IV (cytochrome oxidase) transports electrons from Cyt C to $O_2$, reducing it in $H_2O$, during which coupled redox reactions drive $H^+$ across the inner membrane, forming the proton gradient and the negative mitochondrial membrane potential ($\Delta\Psi_m$ =−150 to −180 mV). The free energy stored in the proton gradient and $\Delta\Psi_m$, then, drive $H^+$ through the mitochondrial ATP synthase (complex V), converting ADP to ATP. An estimated 0.1% to 1% of the electrons leak prematurely to O at complexes I, II, or III, resulting in the formation of superoxide ($O^{\bullet -}$). Multiple important mitochondrial channels located on the inner membrane including mitochondrial K channels (mito-K), the mitochondrial $Na^+$ /$Ca^{2+}$ exchanger (mito-NCX), the inner membrane anion channel (IMAC), the permeability transition pore (PTP) and the mitochondrial calcium uniporter (MCU) also contribute to the regulation of mitochondrial function, myocardial ROS, and cellular cation homeostasis.[2] Below, Figure 4 graphically summarizes the events of the ETC.

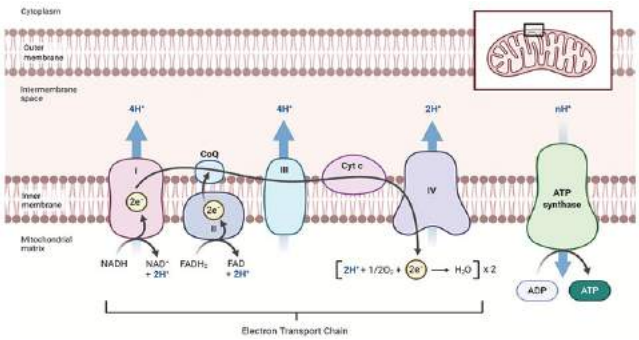


**Figure 4**. Electron transport chain

## 1.3 ATP SYNTHASE: MAKING THE FUEL OF LIFE.

### 1.3.1 ATP: THE MOLECULAR CURRENCY

Often referred as “molecular currency” for intracellular energy transfer, Adenosine Triphosphate (ATP) functions as a chemical fuel by powering many organic processes of life. ATP generation is the principal energy generating procedure found in all forms of life. ATP is the fuel for the operation of almost all metabolic pathways of the cell. In an ATP molecule, two high-energy phosphate bonds, called phosphoanhydride bonds, are responsible for high energy content. Hydrolysis of the third phosphate group produces adenosine diphosphate (ADP) and inorganic phosphate ($P_i$), along with considerable release of energy. ADP can absorb energy and regain the group to regenerate an ATP molecule to maintain constant ATP concentration. Estimates show that the normal body uses 40 kg of ATP on a daily basis; hence ATP production is one of the most frequent processes occurring in the body.[3] The aggregate amount of ATP in the human body is about 0.1 Mole. The energy utilized every day by an adult requires the hydrolysis of 100

to 150 Moles of ATP. This implies every ATP molecule must be reused 1000 or more multiple times in a day.[4] ATP cannot be stored and so its synthesis is closely linked to its consumption. ATP is produced under aerobic conditions through glycolysis, citric acid cycle/oxidative phosphorylation and beta-oxidation and under anaerobic condition through fermentation, photophosphorylation and replenishment reactions catalyzed by nucleoside diphosphate kinase.[5]

### 1.3.2 ATP SYNTHASE

ATP synthesis is the most widespread chemical reaction inside the biological world. ATP synthase is the very last enzyme in oxidative phosphorylation pathway that makes use of electrochemical energy to power ATP synthesis. The mitochondrial ATP synthase is a multi-subunit protein complex having an approximate molecular weight of 550 kDa. The human mitochondrial ATP synthase or $F_1/F_O$ ATPase or complex V is the fifth component of oxidative phosphorylation chain. This enzyme is the smallest known biological nanomotor and plays a crucial role in ATP generation.[6] It is constituted by two subunits: $F_O$, an integral membrane protein that acts as a channel for the protons flow (the letter O indicates that this portion gives the complex sensitivity to Oligomycin) and $F_1$, a peripheral membrane protein consisting of nine subunits of five different types, with the composition $\alpha_3\beta_3\gamma\delta\varepsilon$; each of the β subunits has a catalytic site for ATP synthesis. The γ subunit forms a kind of central axis which, as it rotates, causes conformational changes. These conformational changes are the basis of the enzyme's ability to synthesize ATP.

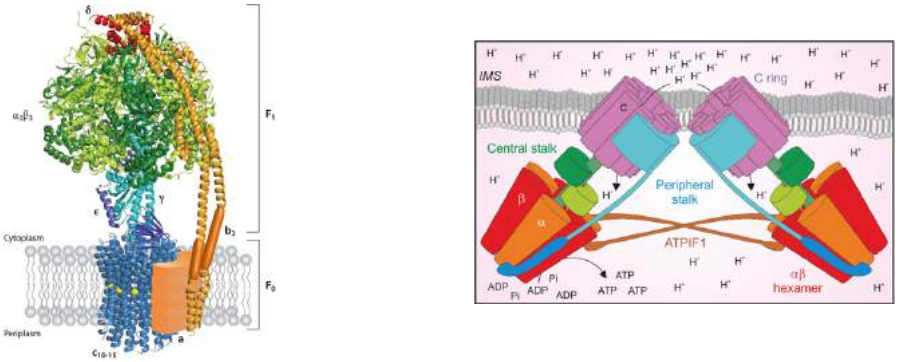


**Figure 5**. On the left, ATP synthase structure; on the right, molecular and supramolecular organization of the mammalian ATP synthase. Notably, the ATP synthase forms dimers and high-order oligomer *in cellula*.

The mechanism proposed to comprehend how the ATP synthase works is that of rotational catalysis in which the three active $F_O$ sites take turns catalyzing ATP synthesis. One of the β subunit begins the cycle of catalysis in its β-ADP conformation, binding ADP and $P_i$; at this point the β subunit changes conformation, assuming the β-ATP form, which firmly binds and stabilizes ATP, generating a state of equilibrium between ADP + $P_i$ and ATP on the enzyme surface. Finally, the β subunit further changes its conformation, assuming the β-empty form, which has very little affinity for ATP, which is then released.

The conformational changes that enable this mechanism are due to the passage of protons through $F_O$, which causes the γ subunit to rotate.[1]

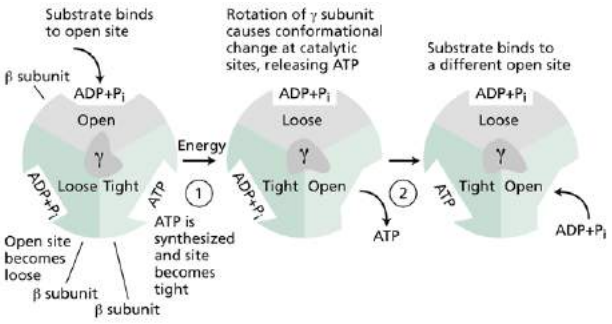


**Figure 6**. Rotational catalysis for the synthesis of ATP.

Notably, the $F_0F_1$ ATP synthase complex associates to form dimers, which are considered to be the "building blocks" of long rows of oligomers that promote cristae formation and may optimize the enzyme's catalytic performance. The angle formed by the dimers seems to display a large variability, and dimers are believed to represent the physiological unit of complex V in the inner membrane. [7]

### 1.3.3 THE C-RING

As described above, ATP synthase is constituted by two distinct sections: the extrinsic sector or $F_1$, which protrudes outside of the membrane and catalyzes the synthesis/hydrolysis of ATP, and the transmembrane sector or $F_O$, which channels ions across the membrane. The two opposite functions of ATP synthesis and hydrolysis are based on the capability of the membrane-embedded rotor to rotate in two directions. In the presence of transmembrane proton motive force (Δp), protons flow downhill across the membrane. This proton translocation makes the central stalk, which connects $F_O$ to $F_1$, rotate counterclockwise (viewed from $F_1$). Such rotation is promptly transmitted to the catalytic sector $F_1$ that undergoes conformational changes which allow the synthesis of ATP from ADP and $P_i$. Conversely, if the membrane is not enough energized, in other words if Δp is poor, the same $F_1F_O$ complex acts as ATPase, namely it hydrolyzes ATP to ADP and $P_i$. In this case, the energy obtained from ATP hydrolysis is exploited to move protons uphill across the membrane through a clockwise rotation (viewed from $F_1$) of $F_O$, leading to Δp re-building.[8,9]

In this system, it appears to have consistence importance the c-ring, an essential component of the $F_O$ rotor. In all organisms, it is constituted by monomers (c subunits) arranged in a circle as a cylindrical palisade which form and contain an internal phospholipid-containing hydrophobic cavity. Through this small ring protons flow and ATP synthase or hydrolysis are promoted.

In particular, the c-ring has aroused our interest because it appears to be involved in the formation and regulation of mPTP, a pore forming in the inner mitochondrial membrane (IMM), that is involved in a series of precise events concerning in particular in the regulation of necrosis and apoptosis of the cells and whose structure is still not precisely defined. The controversies that still swirl around what the actual structure of the mPTP will be discussed in more detail below. However, the newly proposed mechanisms involving the c subunits reconstituted in membranes in the formation of a pore refractory to CyP-D are still unclear. Other findings support the hypothesis that the c-ring may associate with other membrane proteins such as ANT and $P_i$C, at first considered as mPTP components, to form the ATP synthasome complex. In such complex, ANT and $P_i$C could modulate the pore-forming capability of the c-ring.[7]

More details will be described in Chapter 1.5.2.5. To sum up, the whole matter is still controversial, but what is clear is that c-ring is somehow involved in the mPTP formation and/or regulation.

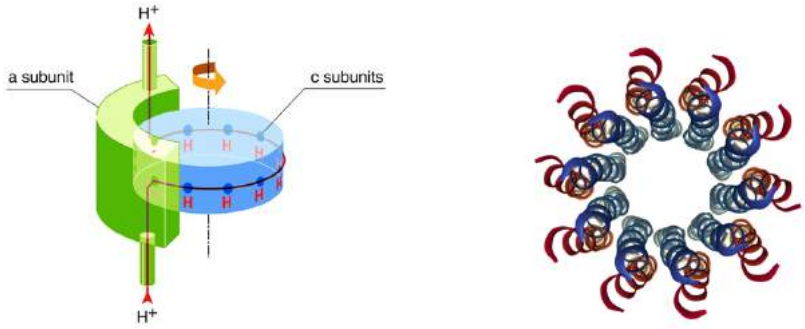


**Figure 7**. On the left, detail of the $F_1F_O$ complex, focused on the c- and the a- subunits. On the right, crystal structure (PDB 4F4S) of the c-ring. Notably, the c-ring is constituted of several c-subunits.

What particularly caught our attention was the interaction of the c-ring with a particular macrolide, produced by Streptomyces, called Oligomycin A, [10] which we will discuss in detail later because on these facts our research projects have begun.

## 1.4 MITOCHONDRIA: THE CORE OF THE APOPTOTIC PATHWAY

The mitochondrion also has another fundamental role within the cell: it is, in fact, involved in regulating the mechanisms of apoptosis, i.e., programmed cell death. Specifically, apoptosis is a cellular self-destruction mechanism involved in a variety of biological events. It is programmed and involves use of energy: mainly due to these aspects it is very different from necrosis, that is a traumatic, degradative and unprogrammed cell death. Excessive or insufficient apoptosis contributes to various diseases related to ischemia, neurodegeneration, autoimmunity, and viral infections, and it is involved in the growth and regression of tumors. There are multiple cellular pathways triggering apoptosis, two of which, the extrinsic and intrinsic pathways, are better characterized: intrinsic, for which mitochondrion is the central organelle governed by pro- and anti- apoptotic Bcl-2 family members, and extrinsic, consisting of cell surface TNF-related family of receptors (TNF receptor, CD95/Fas, and TRAIL death receptors, etc.), their inhibitory counterparts and cytoplasmic adapter or death inhibitory molecules (e.g., FADD or FLIP). [11] The apoptotic process is executed by a family of cysteine proteases which specifically cleave their substrates at aspartic acid residues. These proteases, known as caspases, are activated through extrinsic and/or intrinsic pathways. The extrinsic pathway is activated by cell surface death receptors, while the intrinsic pathway is initiated by formation of the cytosolic apoptosome composed of Apaf-1, procaspase 9, and the cytochrome c released from mitochondria.[12] The mechanisms of apoptosis are highly complex and sophisticated, involving an energy dependent cascade of molecular events. So, as mentioned above, to date research indicates that there are two main apoptotic pathways: the extrinsic or death receptor pathway and the intrinsic or mitochondrial pathway. Both of them converge on the same terminal, or execution pathway. This pathway is initiated by the cleavage of caspase-3 and results in DNA fragmentation, degradation of

cytoskeletal and nuclear proteins, cross linking of proteins, formation of apoptotic bodies, expression of ligands for phagocytic cell receptors and finally uptake by phagocytic cells.

Caspases have proteolytic activity and are able to cleave proteins at aspartic acid residues, although different caspases have different specificities involving recognition of neighboring amino acids. Once caspases are initially activated, there seems to be an irreversible commitment towards cell death. To date, ten major caspases have been identified and broadly categorized into initiators (caspase -2,-8,-9,-10), effectors or executioners (caspase -3,-6,-7) and inflammatory caspases (caspase -1,-4,-5). The other caspases that have been identified include caspase-11, which is reported to regulate apoptosis and cytokine maturation during septic shock, caspase-12, which mediates endoplasmic-specific apoptosis and cytotoxicity by amyloid-β, caspase-13, which is suggested to be a bovine gene, and caspase-14, which is highly expressed in embryonic tissues but not in adult tissues.

The extrinsic signaling pathways that initiate apoptosis involve transmembrane receptor-mediated interactions. These involve death receptors that are members of the tumor necrosis factor (TNF) receptor gene superfamily. The sequence of events that define the extrinsic phase of apoptosis are best characterized with the FasL/FasR and TNF-α/TNFR1 models (i.e. the death receptors). In these models, there is clustering of receptors and binding with the homologous trimeric ligand. Upon ligand binding, cytoplasmic adapter proteins are recruited and exhibit corresponding death domains that bind with the receptors. The binding of Fas ligand to Fas receptor results in the binding of the adapter protein FADD and the binding of TNF ligand to TNF receptor results in the binding of the adapter protein TRADD with recruitment of FADD and RIP. FADD then associates with procaspase-8 via dimerization of the death effector domain. At this point, a death-inducing signaling complex (DISC) is formed, resulting in the auto-catalytic activation of procaspase-8. Once caspase-8 is activated, the execution phase of apoptosis is triggered. [13]

On the other hand, the intrinsic pathway is quite different and the mitochondria represent the core of this one, because all of the events concerning this way are mitochondrial-initiated events. The intrinsic signaling pathways that initiate apoptosis involve a diverse array of non-receptor-mediated stimuli that produce intracellular signals that act directly on targets within the cell and are mitochondrial-initiated events. The stimuli that initiate the intrinsic pathway produce intracellular signals that may act in either a positive or negative fashion, causing loss of apoptotic suppression and subsequent activation of apoptosis. All of these stimuli cause changes in the inner mitochondrial membrane that results in an opening of the mitochondrial permeability transition pore, loss of the mitochondrial transmembrane potential and release of two main groups of normally sequestered pro-apoptotic proteins from the intermembrane space into the cytosol. The first group consists of cytochrome c, Smac/DIABLO, and the serine protease HtrA2/Omi. These proteins activate the caspase dependent mitochondrial pathway. Cytochrome c binds and activates Apaf-1 as well as procaspase-9, forming an “apoptosome”. [13] At this point, caspase 3 is activated and the “execution pathway” follows.

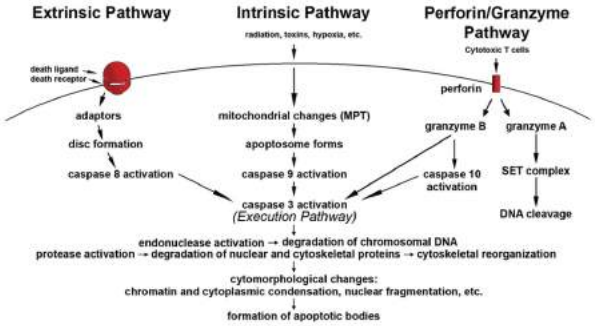


**Figure 8**. Schematic representation of apoptotic events.

## 1.5 mPTP: STORY OF AN IMPORTANT AS CONTROVERSIAL SYSTEM

In the previous paragraph, reference was made to mPTP, defined as a mitochondrial permeability transition pore. Mitochondrial permeability transition (mPT) is a phenomenon of sudden increase of the permeability of the mitochondrial inner membrane in response to excessive accumulation of calcium and/or oxidative stress. It is generally agreed that mPT is caused by the opening of a large channel (mitochondrial permeability transition pore or mPTP) that allows flux of ions and small molecules up to 1.5 kDa across the inner membrane.[14] As mentioned above, in physiological conditions the flow of molecules through the mitochondrion is very controlled, due to the very strict selectivity of the IMM.

The opening of the mPTP makes the IMM non-selectively permeable to molecules less than 1.5 kDa, collapsing the mitochondrial membrane potential, uncoupling oxidative phosphorylation, leading to ATP depletion and cell death. Another important effect of mPTP opening is mitochondrial matrix swelling and the outer mitochondrial membrane (OMM) rupture resulting in the deposition of pro-apoptotic factors such as cytochrome c from the inter-membranous space into the cytosol, thereby initiating apoptotic cell death. Thus, given these premises, a sudden change in membrane permeability can cause various damages at both cellular and systemic levels. So, it is believed that mPT is a central event leading to the mitochondrial dysfunction and is the major cause of cell damage in a wide range of pathologies from acute conditions related to stroke and heart attack to neurodegenerative diseases. Moreover, genetics studies in 2005 confirmed the role of the mPTP as a mediator of IRI, in three independent laboratories who have found that mice deficient in CypD (regulatory component of mPTP) sustained smaller MI size compared to the wild type.[15] More on what IRI is will be addressed in Chapter 1.7.

### 1.5.1 mPTP AND CALCIUM HOMEOSTASIS

The term 'permeability transition' was coined by Haworth and Hunter in 1979 to define a process of altering the permeability of the IMM. They suggested that this process depended on the opening of a channel (the Permeability Transition Pore, PTP) and was regulated and potentially reversible. [16] The presence of PTP is now recognized, and it is widely accepted that its opening leads to depolarization, cessation of ATP synthesis (in favor of ATP hydrolysis) and mitochondrial swelling with release of pro-apoptotic proteins from the intermembrane space. These events are linked to others, such as ischemia, organ reperfusion damage, muscular dystrophy and neurodegenerative diseases.[17] Definitively, the scientific community has therefore

recognized the existence of mPTP, and that its opening is linked, among other things, to mitochondrial calcium concentration. In fact, the concentration of calcium in the mitochondrion under physiological conditions is 10 μM. Calcium is a universal carrier of biological information, so any alteration in its homeostasis is a drastic signal. Under physiological conditions, most calcium is stored in the endoplasmic reticulum (at a concentration of 300-600 μM) and in the Golgi apparatus (200-500 μM), while only a modest amount is present in the cytoplasm (the measured concentration is 100 nM). When this cytoplasmic threshold is exceeded, there is a massive accumulation of $Ca^{2+}$ in the mitochondrial matrix. This event leads to the opening of a non-selective pore in the inner mitochondrial membrane, mPTP: thanks to the free and non-selective passage of ions, the potential difference between the two membranes decreases and the inner membrane swells. This results in the rupture of the outer mitochondrial membrane and the release of proteins from the intermembrane space into the cytoplasm.[7]
The mPTP is therefore the pore responsible for this event whereby the inner mitochondrial membrane, which is highly impermeable under physiological conditions, becomes extremely permeable.

### 1.5.2 Structure of mPTP: an actual debate

Since its discovery, the mPTP structure has been the object of various controversies. It was first characterized in seminal experimental studies from the late 1970s by Haworth and Hunter. [16] It refers to the mitochondrial channel which mediates the abrupt change, or transition, in inner mitochondrial membrane permeability which occurs under certain conditions.
Although several years have passed since its discovery and its importance in cardio protection is understood with certainty, the precise molecular identity of mPTP remains uncertain to this day. Summarized below are the major components of mPTP that have been supposed over the years, most of which have now been confirmed as modulators of it.

- Adenine nucleotide translocase (ANT)

Initially this protein was considered to be involved in the molecular identity of mPTP. This because mPTP opening is inhibited by ATP and ADP, but not by their complexes with $Mg^{2+}$ or by other nucleotides such as AMP, GDP or GTP, none of which are transported by the ANT.[18] However, in 2004, Kokoszka et al. demonstrated that murine liver mitochondria deficient in ANT-1 or ANT-2 still exhibited CsA-sensitive MPTP opening,[19] suggesting that the ANT was unlikely to be the obligatory pore component of the MPTP, and was more likely to act as a modulator of mPTP opening.

- Cyclophilin-D (CypD)

The finding in 1988 by Crompton's research group that mPTP opening could be inhibited by the immunosuppressant Cyclosporine A (CsA) provided initial evidence that the mitochondrial target of CsA may be mitochondrial cyclophilin-D (CypD), a peptidylprolyl cis–trans isomerase.[20] However, Halestrap *et al.* confirmed the hypothesis that mPTP opening involves a conformational change in a membrane protein that is triggered by calcium and facilitated by CypD, but can occur in the absence of CypD if sufficient stimulus is given. So, to date, also CypD is considered a modulator of the pore.[18]

- Voltage-dependent anion channel (VDAC)

The voltage-dependent anion channel (VDAC) of the OMM had long been considered to be a component of the mPTP, with the suggestion that the mPTP formed at contact sites between the VDAC of OMM and the ANT of the IMM. However, to date several experiments have demonstrated that it does not represent the molecular identity of mPTP. To mention one, in 2007, Baines *et al.* found that murine liver mitochondria deficient in VDAC-1, VDAC-2 or VDAC-3 still displayed CsA-sensitive mPTP opening, suggesting that VDAC may not be an obligatory component of the mPTP.[18]

- Mitochondrial phosphate carrier (PiC)

The mitochondrial phosphate carrier (PiC) mediates the import of inorganic phosphate across the IMM and into the matrix, making it critical for ATP synthesis. Several lines of experimental evidence had implicated the PiC as the potential pore-forming components of the mPTP: (1) from its initial characterization the mPTP has been known to be sensitive to phosphate; (2) the PiC has been shown to form non-specific channels in lipid membranes; [21] (3) there appears to be a direct interaction between PiC and CypD. [22] However, experimental studies involving genetic over-expression of cardiac specific PiC failed to affect mPTP opening in isolated mitochondria and genetic deletion of PiC did not abolish mPTP opening, although it did reduce the sensitivity to mPTP opening and protect hearts from acute IRI, suggesting that although the PiC may not be the obligatory pore-forming component of the mPTP, it appears to modulate its function.[15]

- Mitochondrial ATP-synthase (or ATPase)

As mentioned above, in the 1.3.3 paragraph, through the years ATP synthase elicit interest to be the site of mPTP formation. ATP synthase is commonly isolated as a functional monomer, but this appears not to be the physiological state in the membrane. Indeed, electron microscopy demonstrated that ATP synthase is organized in dimers associated to form long rows of oligomers. [23] From the first decade of 2000, this enzyme has been studied as a potential site of mPTP opening. In 2009, Giorgio *et al.* demonstrated that CypD is able to interact with the stalk of the ATP synthase, decreasing its enzymatic activity and favoring the enzymatic hydrolysis of ATP. [24] From here, attention began to shift to the c-subunit of the $F_O$ portion of the ATP synthase, since the discovery that agents targeting or gene-silencing the c-subunits protect against mPTP opening. Moreover, the phosphorylation status of c-subunits might modulate the mPTP kinetics and cation selectivity. Consistently, the c-ring was shown to generate a non-specific current ascribable to the mPTP. Interestingly, Bonora *et al.* in 2013 have described experiments that allow us to think that $F_1F_0$ ATP synthase and in particular the c-ring are involved in the formation pf the PTP. [25]

Going into more detail, two partially reconcilable models have been put forward to explain the contribution of the $F_1F_O$ ATP synthase to MPT in molecular terms. On the one hand, it has been proposed that the $F_1F_O$ ATP synthase would dimerize in the course of MPT and that such dimers would allow for the generation of a poorly selective channel with PTPC-like activity. [26] On the other hand, it has been suggested not only that the c-subunit of the $F_O$ complex has a key role in the regulation of the mPT, but also that c-rings (homo-oligomeric, preassembled IMM channels composed of c-subunits) *de facto* constitute the long-sought PTPC pore-forming subunit. They, stabilizing $F_1F_O$ ATP synthase dimers (by two genetically distinct approaches) observed that PTP opening was limited and that the dissociation of $F_1F_O$ ATP synthase dimers is a cause, not

a consequence, of mPT. In addition, they demonstrated that depleting the c-subunit with specific bacterial small RNAs (sRNAs) is sufficient to inhibit mPT. In conclusion, they claim that PTPC opening is a multistep process that involves disassembly of $F_1F_O$ ATP synthase dimers and rearrangement of c-rings and that the c-subunit of the $F_1F_O$ ATP synthase may constitute a promising target for the development of novel cardio-, neuro-, or nephroprotective agents.[27]

The same research group performed studies to demonstrate that the c-subunit of the ATP synthase was involved in the mPTP opening, showing that the depletion of the $F_O$ c-subunit, but not that of the $F_1$ a-subunit, inhibited mPT as efficiently as did the pre-administration of CsA. [25] Other studies support the involvement of the c-ring in mPTP opening: in 2014, Alavian *et al.* demonstrated that depletion of the c-subunit attenuates $Ca^{2+}$ induced IMM depolarization and inhibits $Ca^{2+}$ and reactive oxygen species-induced cell death, whereas increasing the expression or single-channel conductance of the c-subunit sensitizes to death. So, they hypothesized that the c-ring could be the site of the mPTP formation, after a rearrangement of it and dissociation between $F_1$ and $F_O$. [28] Another finding about the involvement of the c-ring in mPTP opening was proposed by Morciano *et al.*, who have noticed a complete block of the $Ca^{2+}$ MPT induction by silencing c-subunit expression. Furthermore, silencing the c-subunit does not affect ATP synthesis, suggesting that mPT inhibition is not due to the accumulation of ADP in the mitochondrial matrix. Furthermore, silencing α subunit expression does not lead to any significant alteration in MPT activity, suggesting that the c-subunit of the mitochondrial ATP synthase is a central component of the mPTP. In support of these results, it has been recently reported that the isolated c-subunit induces the MPT in isolated mitochondria and forms ion channels in artificial bilayer membranes. Furthermore, this activity is stimulated by $Ca^{2+}$, inhibited by CsA and dependent on the phosphorylation state of the c-subunit.[17] All these information taken together provide evidence of the strong involvement of c-ring to form the mPTP.

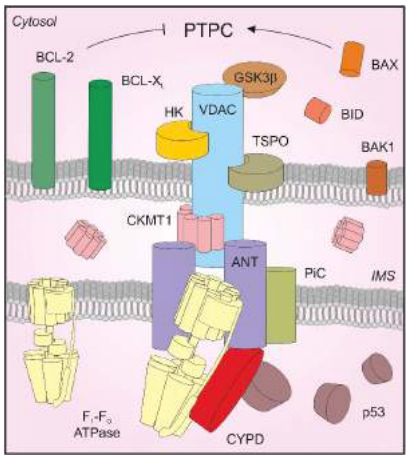


**Figure 9**. Possible configuration of PTPC. Here is described as a large multiprotein complex. It's worth noting that here is proposed a model in which, for the opening pf the mPTP, the ATP synthase are organized as monomers and it rearranges with other proteins (demonstrated to act as regulators of the complex) to locate the PTPC. A number of modulators are depicted around the complex: they favor the opening of the pore, but are not strictly part of it.

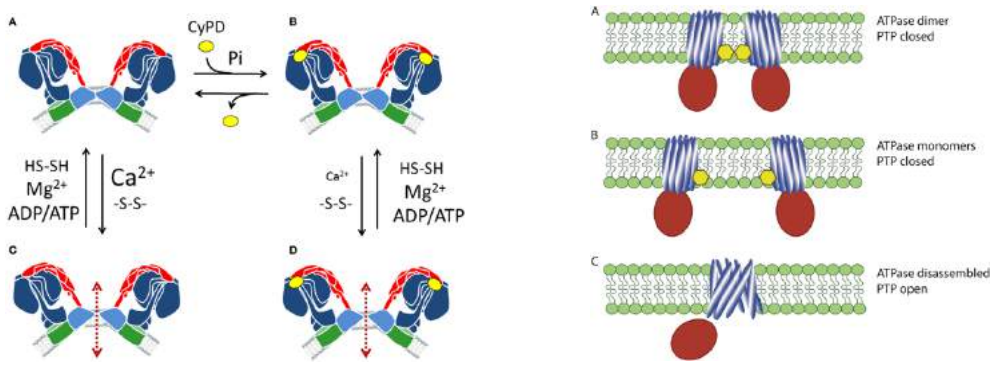


**Figure 10**. Two different hypotheses proposed regarding the dissociation and the rearrangement of the ATP synthase to form the mitochondrial permeability transition pore. On the left, Bernardi *et al.*, 2013; on the right Amodeo *et al.*, 2017.

## 1.6 OLIGOMYCIN A: A NATURAL INSPIRATION

Oligomycin A is a macrolide produced by Streptomyces and has been considered a potent ATP synthase inhibitor since 1958. [10] Today, several types of oligomycin are known, which differ in the side chains between the sugar part and the macrolide ring, but the most active towards the $F_OF_1$ complex is Oligomycin A.[29]

This molecule caught our interest because of its ability to bind and inhibit ATP-synthase. In particular, Oligomycin is a specific inhibitor of transmembrane $F_O$ domain (which takes the O subscript from Oligomycin): it inhibits the $H^+$ translocation required for the enzyme rotation. Structurally, Oligomycin belongs to the polyketide class of macrolide antibiotics whose basic structure consists of polyketide units arranged to build a large lactone ring covalently bound to one or more deoxy sugars. The macrolide ring confers the inhibition power, while the deoxy sugar moiety is not crucial for the ATPase inhibition. The oligomycin-binding site on the c-subunits has been defined at high-resolution (1.9 A°) crystal structure. Oligomycin binds to the amino acid side chains of two adjacent c-subunits of $F_O$, *c*1 and *c*2, and covers the $H^+$-binding site (E59) on *c*1. By shielding the carboxyl access to the aqueous environment of the proton half channel of *a* subunit, oligomycin blocks the proton flux within $F_O$ without affecting the c-ring backbone conformation. On the contrary, on the C-terminal $\alpha$-helices the side chains of L63 of *c*1 subunit and F64 of *c*2 subunit would rotate to allow the propanol residue linked to the spiropyranose sugar rings of Oligomycin to penetrate between the two c monomers so as to establish non-covalent interactions with the $\alpha$-helical N terminus of the *c*1 subunit. The macrocyclic lactone ring is involved in both hydrophilic and hydrophobic interactions with 7 amino acids of the C-terminal $\alpha$-helices of *c*1 subunit and 5 amino acids of the C-terminal $\alpha$-helix of *c*2 subunit. The proton-binding site (E59 of *c*1 subunit) is also involved in Oligomycin binding via a bridging water molecule.[8]

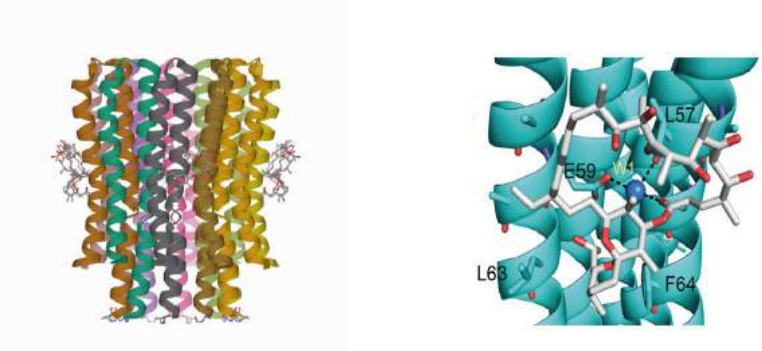


**Figure 11**. Crystal structure of Oligomycin bound to c-ring (PDB 4F4S, on the left); particular of the interaction of Oligomycin with the amino acids of the c-ring (on the right).

Hence, although this molecule is interesting from a biological point of view, its structure is very complicated, as it's depicted in Figure 12. So, we simplified the structure, dividing it in two portions, the northern (in blue) and the southern (in red); the two portions of the molecule were tested separately to precisely understand which one was active on the ATP-synthase. These studies showed that the spirocenter, which gives the molecule a certain structural rigidity, is of fundamental importance.

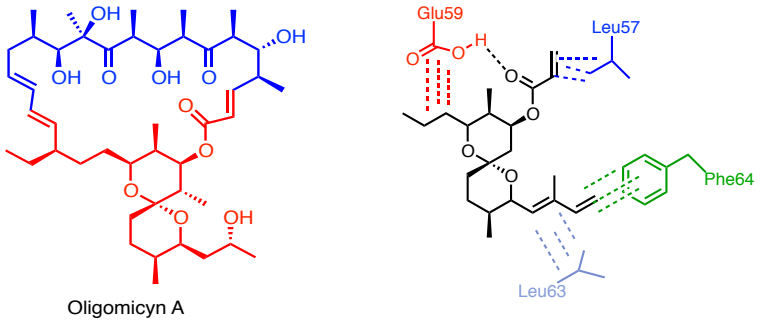


**Figure 12**. Chemical structure of the Oligomycin A (on the left); detail of the spiroketalic structure interactions with interesting amino acids of the c-ring (on the right).

### 1.6.1 KNOWN MPTP OPENING MODULATORS

The interest about mPTP arises when in 1988 Crompton *et al*. found that the immunosuppressant cyclosporin-A (CsA) could inhibit the pore opening: these data developed the idea that the mPTP could be an interesting target of cardioprotection. [20] Approximately 40 years have passed since the first biochemical description of the mitochondrial permeability transition in isolated mitochondria by Haworth and Hunter and 30 years since the discovery that CsA inhibits opening of the mPTP *in vitro*. Since then, mitochondrial dysfunction and persistent mPTP opening has emerged as a final common pathway to cell death underlying many disease states.

In this chapter, with the help of a summary table (Table 1), the main modulators known as mPTP inhibitors are described. The molecules are divided in different classes, depending on their structure and their action pathways, in macrocyclic CypD inhibitors, small molecule CypD inhibitors and small molecules working by Non-CypD mechanism inhibitors. [30] All the structures depicted below in Table 1 will not be commented on in detail, as this is beyond the scope of this thesis, but it is interesting to note that all the development

studies about mPTP modulators are inspired by nature, as commonly happens. Indeed, macrocyclic molecules as Cyclosporin A, Sangliferhin A and Oligomycin A are the complex structures from which studies has been developed in order to find simpler small molecules active in a more efficient and more specific way.

Cyclosporin A (CsA). It is known to bind Cyclophilin D, that is a peptidylprolyl isomerase D also known as PPID. As a member of the peptidyl-prolyl cis-trans isomerase (PPIase) family, this protein catalyzes the isomerization of proline amidic peptide bonds, which allows it to facilitate folding or repair of proteins. In addition, CypD participates in many biological processes, including mitochondrial metabolism, apoptosis, redox, and inflammation, as well as in related diseases and conditions, such as ischemic reperfusion injury. As a cyclophilin, PPID binds the immunosuppressive drug CsA to form a CsA-cyclophilin complex, which then targets calcineurin to inhibit the signaling pathway for T-cell activation. In cardiac myogenic cells, cyclophilins have been observed to be activated by heat shock and hypoxia-reoxygenation as well as complex with heat shock proteins. Thus, cyclophilins may function in cardioprotection during ischemia-reperfusion injury. Although CypD has been regarded as a structural component of the pore, it has now been confirmed to be a regulator of it. The bind with CsA, however, remains interesting because it is capable of decreasing pore opening. For this reason different research groups developed structurally similar molecules.[31]

Sanglifehrin A (SfA). It is a large molecular weight natural product, isolated from Streptomyces sp., and is also a nonselective inhibitor of cyclophilins and has significant immunosuppressive activity. SfA is structurally unrelated to CsA and also binds to the PPIase domain. SfA, CsA, and analogues are limited by poor physicochemical properties (aqueous solubility, high molecular weight), polypharmacology, and cytotoxicity (most notably nephrotoxicity). To note, all are large molecules (CsA = 1200 Da), with poor blood– brain barrier (BBB) permeability, restricting their utility as neuroprotective agents.

The latter class of molecules work on the most different pathways: for example, TRO-40303 interacts with TSPO and compound GNX-4975 relates with PiC and ANT. Notably, all these proteins are regulators of the mPTP. [30]

| Compound name | Chemical class | Structure | Target | Comment |
|---|---|---|---|---|
| Cyclosporin A (CsA) | Natural product (macrocyclic) | 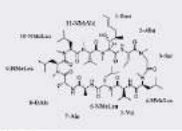 | CypD | Failed Phase II clinical trial in cardiac reperfusion injury |
| NIM-811 | CsA-derivative (macrocyclic) | 4-NMeIleCsA | CypD | Equipotent to CsA |
| Debio025 | CsA-derivative (macrocyclic) | 3-NMeDAla,4-NEtValCsA | CypD | Greater potency than CsA in mitochondrial swelling assay (10-fold) |
| Sanglifehrin A (SfA) | Natural product (macrocyclic) | 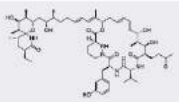 | CypD | PPIase inhibition $K_i$ = 2.2, equipotent to CsA |
| C-9 | 4-amino benzenesulfonamide | 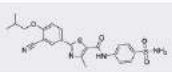 | CypD | Cyclophilin inhibition demonstrated using PPIase activity and binding assays |
| Compound 19 | Urea-based | 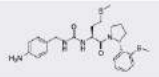 | CypD | $K_d$ CypD = 410 nM<br>$K_i$ CypD = 99 nM |
| Compound 7<br>Chem Div ID: 8017-0165<br>(http://www.chemdiv.com/) | Thiadiazole | 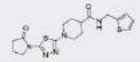 | CypD | Very low Rmax reported for SPR binding data |

| Compound name | Chemical class | Structure | Target | Comment |
|---|---|---|---|---|
| Compound 20<br>Chem Div ID: F965-0666<br>(http://www.chemdiv.com/) | Imidazole | 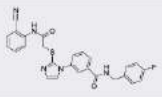 | CypD | Very low Rmax reported for SPR binding data |
| TRO-40303 | Steroid analogue | 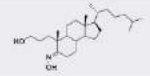 | TSPO | Failed to limit myocardial injury following reperfusion in Phase II study |
| Compound 22 | Cinnamic anilide | 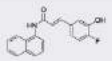 | ND | Protective in rabbit model of acute myocardial infarction (5 mg/kg) |
| (1) GNX-4975<br>and (2) GNX-4728 | Cinnamic anilide | Structure unclear from publication but belongs to same class as compound 22 above (maybe identical). | Stabilisation of PiC and c-ANT interaction | (1) $K_i$ for mPTP inhibition of ~2 nM<br>(2) 2-fold increase in lifespan G3/R-human mSOD-1 mouse |
| Compound 60 | Isoxazole | 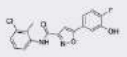 | ND | Improved muscle function and structure in mutant collagen VI zebrafish |
| ML404 | Isoxazole | 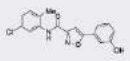 | ND | Similar to compounds disclosed in [9] |
| Compound 4 | *N*-phenyl-benzamide | 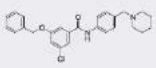 | ND | $EC_{50}$ = 0.280 μM in $Ca^{2+}$-induced mitochondrial swelling assay |
| ER-000444793 | Quinolone |  | ND | $IC_{50}$ = ~2.8 μM in $Ca^{2+}$-induced mitochondrial depolarisation (CsA = 72 nM)<br>$IC_{50}$ = ~1.2 μM in $Ca^{2+}$ retention assay (CsA = 34 nM) |

| Compound name | Chemical class | Structure | Target | Comment |
|---|---|---|---|---|
| Compound 10 (PP11 analogue) | 1,3,8-triazaspiro[4.5] decane |  | ATP synthase c subunit | Protective in an *ex vivo* model of myocardial infarction |
| Edaravone (Radicut™) | Dihydropyrazol-3-one |  | Antioxidant | Enol form linked to activity, approved for ALS |
| AntiOxBEN$_6$ | TPP-linked antioxidant | 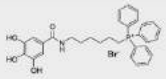 | Antioxidant | |
| DS44170716 | Tetrahydroquinoline | 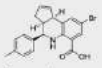 Plus enantiomer | ETC inhibitor | |
| DS16570611 | Substituted 1H-indol-1-yl butanoic acid | 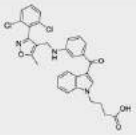 | MCU inhibitor | |
| Ro-68-3400 | Dihydrospiro [cyclopentane-1,5'-dibenzo[a,d][7] annulen]-2-one |  | VDAC1 | $EC_{50}$ = 0.19 μM in $Ca^{2+}$-induced mitochondrial swelling assay |

| Compound name | Chemical class | Structure | Target | Comment |
|---|---|---|---|---|
| mtCsA | Mitochondrially targeted CsA. 3-Sar substituted | 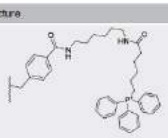 | CypD | Binding affinity to CypD ~ 30-fold lower than for CsA ($K_i$ = 93 nM) |
| JW47 | Mitochondrially targeted CsA, 1-Bmt substituted | 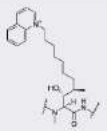 | CypD | $K_i$ CypD = 202 nM<br>$IC_{50}$ = ~10 nM in $Ca^{2+}$ retention assay (CsA = ~40 nM)<br>Protective in relapsing-progressive EAE model of MS |

**Table 1**. Table listing the different mPTP inhibitors, including macrocyclic CyPD inhibitors, small molecules CypD inhibitors and small molecules mPTP opening inhibitors working by non CyPD mechanism.

## 1.7 CHEMICAL BACKGROUND: FROM OLIGOMYCIN A TO 1,3,8-TRIAZASPIROOXINDOLES

As described in paragraph 1.5, the Oligomycin A, and in particular its spiro-ketal moiety, is an inhibitor of ATP synthase. It was a good starting point for our research, but this molecule possesses several critical issues. In fact, in addition to being very complex structurally (this also confers some no-specificity toward the target and thus the occurrence of various side effects), the spiro-ketalic portion is susceptible to hydrolysis in the physiological environment. Hence, given this background, as it is described in the paper by Morciano *et al.*, our research group decided to synthesize structurally more stable small molecules. It has been selected a series of compounds, which are based on a 1,3,8-triazaspiro[4.5]decane scaffold. These preliminary investigations resulted in the identification of 1-phenyl-1,3,8-triaza-spiro-[4,5]decan-4-one derivative PP11. The demonstration that PP11 is effective in inhibiting $Ca^{2+}$-mediated mPTP opening has been provided by measuring its biological activity in HeLa cells by calcein−cobalt assay. mPTP opening was stimulated by the addition of the ionophore ionomycin, and the resulting kinetics were compared. As shown in Figure 13, the addition of 1 μM ionomycin to cells pretreated with 1 μM PP11 resulted in desensitization of mPTP opening by approximately 50% as assessed by the slope of the curve after stimulation, which was significantly less than that observed in vehicle treated cells.

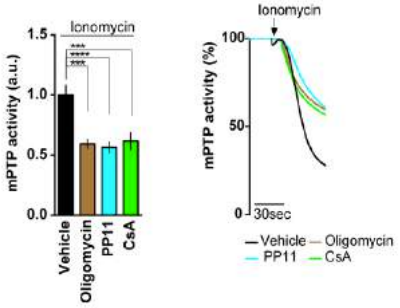


**Figure 13**. Calcein–cobalt assay in living cells pretreated with vehicle, oligomycin A, PP11, and CsA. mPTP opening was stimulated by ionomycin administration, and representative kinetics data are reported.

Moreover, PP11 was able to inhibit the mPTP opening in a manner very similar to that of Oligomycin A as a direct derivative but at a 10-fold lower concentration. These data demonstrated that the small-molecule inhibitor derived from the known compound Oligomycin A was able to efficiently inhibit mPTP opening. In particular, to monitor and better characterize PP11's biological activity in cells, we investigated its subcellular localization, focusing on the amount localized within mitochondria, the hypothetical site of action: fractionation of living cells treated with vehicle or PP11 resulted in successful isolation of pure mitochondrial, cytosolic, and endoplasmic reticulum (ER) fractions. Samples from each subcellular compartment were analyzed by HPLC-HRMS to detect the compound. As shown in Figure 14a, PP11 selectively accumulated in the mitochondria without detectable traces in the other subcellular fractions (Figure 14b and 14c); the same investigation performed after administration of Oligomycin A revealed a less selective distribution of the compound with significant amounts detected in all of the isolated subcellular compartments. Therefore, PP11 was selected as the starting point for further studies.

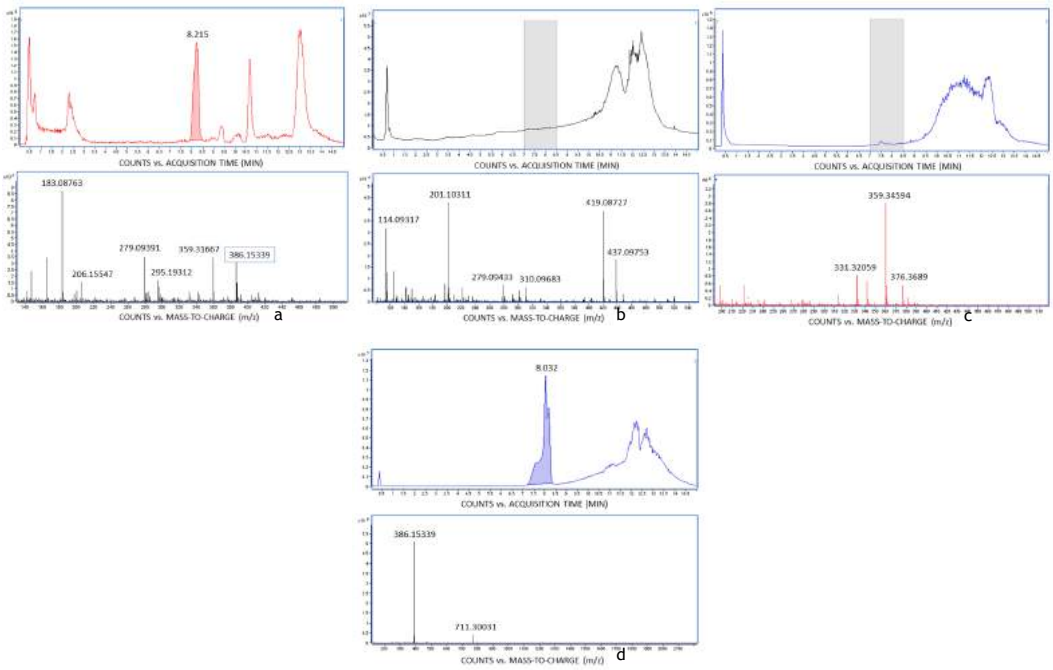


**Figure 14**. Subcellular localization of PP11 was investigated via HPLC-HRMS analysis of samples from different cellular compartments before and after treatment with the compound. PP11 $[M + H]^+$ m/z of 386.15339 ($[M + H]^+$ calculated for PP11 386.1533); a) isolated mitochondria; b) cytosolic fraction; c) ER fraction; d) HPLC-HMRS of PP11 in physiological solution.

The use of compound PP11 as a reference compound allowed us to synthesize a series of analogues, which are described specifically in the paper by Morciano *et al*. In particular, three of them showed activity on mPTP opening modulation: hence, to investigate the effectiveness of the new synthesized PP11 analogues against mPTP opening, it has been used the mitochondrial swelling assay; in conclusion, PP11 significantly inhibited mPTP opening and most of the small molecules showed good inhibitory potential compared to the control mitochondrial sample and also compounds **5c**, **6g**, and **10** (as they are referred in the paper) have demonstrated to be active, even significantly more potent than PP11 in inhibiting mPTP opening. [32]

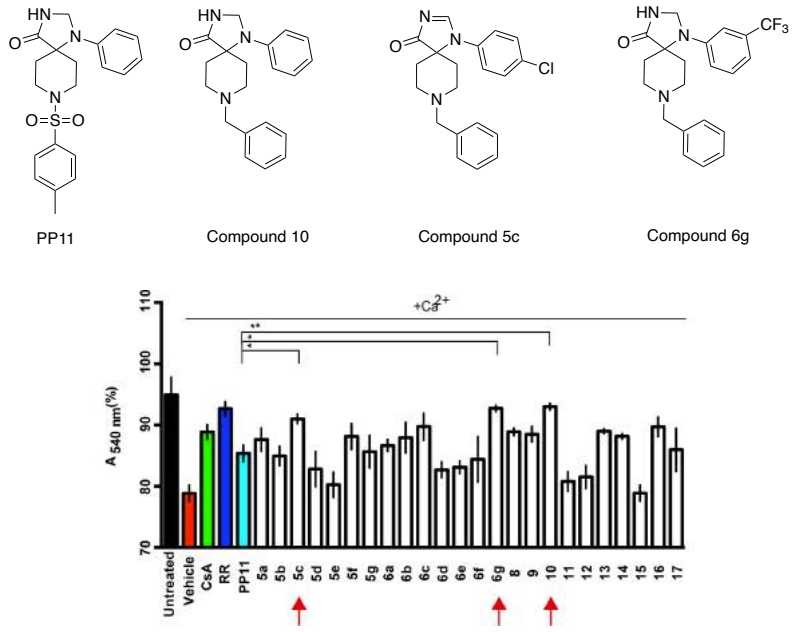


**Figure 15**. Structure of compounds of interest (above); inhibitory activity against mPTP opening (mitochondrial swelling assay, below). Data were obtained by recording changes in absorbance (540 nm), and then the data were converted into percentages: (black bar) untreated and unstimulated mitochondria; (red bar) untreated mitochondria stimulated with 500 μM $Ca^{2+}$; (green bar) pretreatment with 1 μM CsA and stimulation with 500 μM $Ca^{2+}$; (blue bar) pretreatment with 5 μM RR and stimulation with 500 μM $Ca^{2+}$; (cyan bar) pretreatment with 1 μM PP11 and stimulation with 500 μM $Ca^{2+}$; (white bars) pretreatment with 1 μM PP11 analogs and stimulation with 500 μM $Ca^{2+}$.

Starting from these considerations, we decided to synthesize a small library of molecules, hoping to comprehend and improve the effectiveness of these molecules as mPTP modulators to find a therapy for different types of diseases, like, one among all, the reperfusion injury damage.

## 1.8 Hints on ischemic reperfusion injury (IRI)

According to a study by Timmis *et al*. (2020), in which are described statistics among cardiovascular diseases in the European Society of Cardiology (ESC) members referring to 2019, in 54 ESC member countries there were 19.9 million new cases of cardiovascular disease (CVD) and 108.6 million people living with CVD in 2017. Ischemic heart disease (IHD) was the most common manifestation of CVD with 3.6 million new cases and 34.9 million people living with IHD. CVD is the most common cause of death in Europe accounting for

4.1 million deaths (2.2 mio in females, 1,9 mio in males) each year; corresponding to 47% of all deaths among women and 39% among men. IHD and cerebrovascular disease are the most common causes of cardiovascular death and IHD accounts for 1.67 million deaths corresponding to 17% and 18% of all deaths in men and women, respectively.[33] Hence, all these data are certainly representative of the fact that cardiovascular disease is a very significant problem in our society.

Ischemia is a condition in which, in a given district of the body, there is an absence of blood supply, which causes an inadequate supply of oxygen and glucose to the tissues. It can occur in various district of the body and among these is the myocardium. The current standard therapies for the acute myocardial infarction (AMI) are reperfusion techniques. They may, however, result in paradoxical cardiomyocyte dysfunction and worsen tissue damage, in a process known as "reperfusion injury". Ischemic reperfusion injury (IRI) typically arises in patients presenting with an acute ST-segment elevation myocardial infarction (STEMI), in whom the most effective therapeutic intervention is timely and effective myocardial reperfusion. Reperfusion itself is known as a "double-edged sword" due to the spectrum of reperfusion-associated pathologies.[34] In fact, since this technique could be life-saving for the patient, it has been demonstrated that in some cases it does not work.[35] This fact happens because of a number of changes at the cellular metabolism level: during an ischemia, for example, anaerobic glycolysis is activated, which leads to the production of significantly less ATP than under aerobic conditions (2 molecules of ATP instead of 30) and in addition there is a buildup of $H^+$ due to the fact that oxidative phosphorylation is disrupted. To raise the pH, the cell reacts by activating $Na^+/H^+$ exchangers and a $Na^+/Ca^{2+}$ antiport system: these events, therefore, result in an increase in mitochondrial $Ca^{2+}$. This fact, as specified earlier, is an inducer of apoptosis as well as of the opening of the mPTP complex.[36]

The comprehension of the exact pathophysiological mechanisms of IRI remains a challenge for clinicians, and the existence of reperfusion injury is still a matter of debate in the scientific community, essentially due to a lack of a definitive clinical documentation. Many gaps still exist between experimental animal models and human clinical experience, with subsequent difficulties in translating experimental results on cardioprotection to clinical practice. Despite the difficulties that still exist in fully comprehending myocardial IRI, early and aggressive reperfusion strategies remain the most important intervention and are strongly advocated.

The development of ischemic conditioning strategies to limit the extent of infarcted tissue caused by ischemia/reperfusion injury markedly enhances the ability of the heart to withstand an ischemic insult.[34] This technique, developed over the past decades, consists in an exposure of tissues to brief periods of ischaemia to protect them from the harmful effects of subsequent, prolonged ischaemia. This process, termed *ischaemic preconditioning*, was first described in the heart, but has subsequently been demonstrated in many other organs as well as in patients with cardiovascular disease. Preconditioning blunts the impaired endothelial-dependent relaxation to acetylcholine, capillary plugging, leukocyte adhesion, and emigration, as well as venular protein leakage effects of prolonged ischaemia. Thus, ischaemic preconditioning preserves endothelial function in the arteriolar, capillary, and venous segments of the vascular tree. Recent evidence suggests that there are actually two temporally and mechanistically distinct types of protection afforded by preconditioning. *Acute or classical preconditioning* is effective as long as the interval between the initial, brief, preconditioning ischaemia and the later, prolonged insult is less than

approximately 2 h. However, a second window of protection, termed *delayed preconditioning* or ischaemic tolerance, becomes apparent in tissues subjected to the prolonged ischaemia 24 h after the initial insult.[36] In summary, tissue exposure to an ischemic condition can enable cells to adapt rather than suffer damage. Therefore, cells under those conditions are able to manage further challeng-ing situations more effectively.

As mentioned above, through reperfusion techniques, blood flow can be restored and thus oxygen supply to the cells can return to normal. However, this intervention also leads to tissue necrosis: hence, we speak of reperfusion injury. In fact, when blood flow is restored, a large amount of oxygen arrives at the cell, which in the meantime had adjusted to hypoxic conditions; in the period of time, therefore, between the arrival of oxygen to the cell and its readjustment to aerobic conditions, it is observed that the ETC is still inactive, but the large amount of oxygen to which the cell is exposed lead to the formation of ROS, which are also inducers of mPTP opening and apoptosis.[35]

Together these events result in what is called ischemia-reperfusion injury, which is mainly related to microvascular dysfunction in most organs and it is a potentially serious problem during a number of standard medical and surgical procedures, such as thrombolytic therapy, organ transplantation, coronary angioplasty, and cardiopulmonary bypass.

For example, one of the most important types of ischemia is cardiac ischemia (IHD). Normally, percutaneous coronary intervention (PCI) is used for the resolution of this clinical case. It has been shown that a number of consequences result from this type of mechanical reperfusion, leading to left ventricular remodeling and myocardial infarction: this seems to be because both apoptosis and necrosis of cardiomyocytes and endothelial cells are evident after reperfusion surgery. The opening of mPTP seems to play a key role in these occurrences, so understanding the dynamics of mPTP formation and opening could be of fundamental importance in cardioprotection.[17]

### 1.8.1 IRI AND MITOCHONDRIA

Since this thesis report is focused on finding molecules that are involved in mitochondrial metabolism, it is appropriate to investigate further the role of the mitochondria in myocardial IRI.
Mitochondria play a critical role in the pathogenesis of myocardial IRI. They occupy 30–50% of the cardiomyocyte cytoplasmic volume and are critical in cardiac energy balance since energy supply for cardiomyocytes is mostly derived from mitochondrial oxidative phosphorylation (OXPHOS).
Mitochondrial dysfunction, reflected in the structure, function, and number of mitochondria within the cardiomyocyte, leads to diminished energy production, loss of myocyte contractility, altered electrical properties, and eventual cardiomyocyte cell death. In this context, the mitochondrial permeability transition pore (mPTP) is thought to play a critical role in myocardial IRI.[34]
Only from the mid to late 1980s in pioneering experimental studies by Crompton's group, mPTP was the first investigated as a potential mediator of acute myocardial IRI. In these early studies it was demonstrated that mPTP opening in isolated liver and cardiac mitochondria was regulated by factors such as $Ca^{2+}$, inorganic phosphate, oxidative stress, and ADP; crucially, all these factors are modulated during acute IRI and act to induce mPTP opening.[15]

It is fundamental to note that all the pathological events described in the previous paragraphs could be resumed here to comprehend how mitochondria are effectively involved in the myocardial ischemic injury. In fact, after ischemia, hypoxia condition occurs. Consequently, hypoxia results in reduction of ATP production and ion pump disfunction, increase of ROS production, that are responsible to induce cell dysfunction and death via other mechanisms, including mitochondrial permeability transition pore opening which contributes to swelling and lysis of cells. This may elicit the release of proapoptotic factors in the cytosol, thus contributing to cell death.[34]

During ischemia/reperfusion, intertwined biochemical events occur leading to mPTP opening. In the ischemic period, following factors such as $Ca^{2+}$, long-chain fatty acids, and ROS accumulation, the possibility that mPTP will occur upon reperfusion gradually increases.[37] During ischemia, due to increased glycolysis, an accumulation of lactic acid and a pH reduction occur. To restore the pH, the $Na^+/H^+$ antiporter is activated, but it acts inefficiently because $Na^+$ cannot be pumped out of the cell, as the $Na^+/K^+$ ATPase is inhibited by the absence of intracellular ATP. Consequently, the cytosolic $Ca^{2+}$ concentration increases. Moreover, the existing decrease in the adenine nucleotide concentration, which is associated with an increased phosphate concentration, is likely to sensitize mPTP opening in response to $Ca^{2+}$; however, low pH inhibits the opening. When reperfusion occurs, the mitochondria recover their ability to respire and rescue the sustained mitochondrial membrane potential, which is required for ATP synthesis. In addition, strong production of ROS occurs when the inhibited respiratory chain is re-exposed to oxygen. Thus, the following resulting conditions are nearly optimal for mPTP opening: high $Ca^{2+}$ levels within the mitochondrial matrix, increased levels of phosphate and oxidative stress, depletion of adenine nucleotide concentration, and rapid restoration of physiological value of pH.[17]

Hence, summarizing all these notions, it is important to cite Griffiths and Halestrap, who, in their milestone paper, have demonstrated that mPTP are closed during ischemia and open the first few (2-3) minutes of reperfusion.[38] Subsequent data has confirmed that the pore opening occurs during reperfusion of the heart after ischemia, but not in the ischemic period.[15] For all these reasons, mPTP is an important new target for cardio protection during reperfusion.

### 1.8.2 IRI IN KIDNEY

Like the heart, the kidney is also subject to ischemic reperfusion damage. Renal IR induced acute kidney injury (AKI) contributes to high morbidity and mortality rate in a wide range of injuries. In ischemic kidney and subsequent re-oxygenation, generation of reactive oxygen species (ROS) at reperfusion phase initiates a cascade of deleterious cellular responses leading to inflammation, cell death, and acute kidney failure.

IRI first attacks endothelial cells and tubular epithelial cells. The lesions may be so severe that they lead to acute kidney injury (AKI) and delayed graft function (DGF), which can impair the graft survival. The unfavourable impact of DGF is worse when DGF is associated with acute rejection.[39]

Most of the data on mechanisms of ischemic injury in eukaryotic cells are derived from cardiomyocyte studies. The heart can reveal many stages of ischemia-reperfusion injury, including stunning, hibernation, arrhythmias, and infarction. These stages are not as well defined in other tissues and organs. Ischemia of a transplant is somehow unique as complete cessation of the blood supply as is observed in a removed organ

and hardly ever occurs in ischemic tissues—heart, kidneys, brain, liver, skeletal muscle—which are left in situ after arterial/portal flow occlusion. Herein, we discuss cellular mechanisms of ischemia-reperfusion injury of transplanted organs and methods to prevent this injury with available organ preservation methods.[40]

Reperfusion injury, as an effector phase of ischemic injury, develops during hours or days after the initial insult. Repair and regeneration processes occur together with cellular apoptosis, autophagy, and necrosis; in fact, the fate of an organ depends on whether cell death or regeneration prevails. As apoptosis needs energy and protein synthesis, it occurs mostly upon reperfusion. Cytochrome c release and caspase activation has been noted as early as 5 minutes after reperfusion. The rapid burst of free radicals shortly following reperfusion is a well-documented phenomenon. Most likely, discordant respiratory chain enzymes are the main source of radicals on reperfusion. Free radicals probably trigger endothelial injury, since only after reperfusion do endothelial cells, which seem fairly well preserved after the ischemic phase, become edematous and leaky to proteins and small particles. As a source of both free radicals and potent radical-scavenging potential via cytochrome c, mitochondria seem to be a gatekeeper to cellular injury during reperfusion. The mitochondrial permeability transition pore which remains closed during ischemia due to inhibition by acidosis, opens upon reperfusion and contributes actively to worsening the condition of the organ, promoting the phenomena described above.[40]

Therefore, it is important to find a therapy to avoid this irreparable damage which compromises the usage of the organ.

# 2. AIM OF THE PROJECT

The aim of this project was to synthesize compounds which are modulators of mitochondrial permeability transition pore (mPTP).

Initially, we focused our attention on small molecules, drawing inspiration from a simple organic compound, dicylohexylcarbodiimide, DCC (in a physiological environment hydrolyzed to dicylohexylurea, DCU): it is known to bind the c-ring of ATP synthase and to inhibit calcium-induced mPTP opening. Starting from this point, a small library of molecules with three different but similar functionalities have been developed (urea, thiourea and carbamate scaffold based). Our purpose was to see if slightly modified molecules (but retaining their structural simplicity of DCC) were able to exhibit an improved aptitude for interaction with the target and thus a decreased pore opening.


**Figure 16**. General structures about urea (green structure, X=O), thiourea (green structure, X=S) and carbamate (yellow structure).

Another main part of the project was based on a known natural molecule that is able to bind the c-ring and inhibit mPTP opening. In this case we are referring to the previously widely discussed Oligomycin A (see introduction). In particular, for the development of our new molecules, we were inspired by its spiroketalic portion. We synthesized various classes of different substituted monospiranic compounds. The main core of the natural reference compound has been slightly modified, making it more stable upon metabolic inactivation, obtaining an 1,3,8-triazaspiro[4.5]decan-4-one core. The foundation of this part of the project is solid and well proven by previous studies conducted by our research group, which had developed other derivatives with a similar structure. Since a selection of these showed a good inhibitory potential, it stimulated us to continue studying modifications on the same core with the intention of improving the interaction with the target and thus the activity of the molecule itself. The syntheses in the laboratory were combined with computational studies (conducted by dr. Ettore Lo Cascio of the Università Cattolica del Sacro Cuore, Rome) thanks to which it was possible to predict the interactions of the molecules with the aminoacidic residues of the c-ring. Moreover, thanks to an HTVS, we had the possibility to hypothesize structures with a potentially high binding affinity to the c-ring. By combining the knowledge previously obtained with these new insights, several molecules were obtained, all of which have the same basic core and to which gradual and rational modifications were made: in this way, with a sort of SAR study approach, we will be able to understand exactly which functionality exhibits the best biological activity.

Another part of the project has been dedicated to synthesize a further class of small molecules. Inspired still by the spiranic structure of Oligomycin A, we tried to increase the structural rigidity of the molecules by adding another spirocentre: we thus obtained dispiranic derivatives with both piperidine and pyrrolidine scaffolds, functionalized with sterically encumbered and hydrophobic elements.

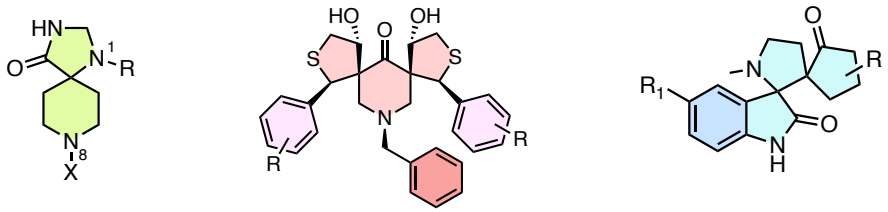


**Figure 17**. General structures for the three classes of spiro compounds synthesized. The1,3,8-triazaspiro[4.5]decan-4-one monispiranic core is highlighted in light green; the spiropiperidone-tetrahydrothiophene core is shown in pale red and finally the isatin based dispiropyrrolidine scaffold is depicted in light blue.

The final part of the project involved biological evaluations, thanks to which we have been able (and will be able) to find confirmation of our assumptions. The tests were conducted in two different laboratories. On one hand, we collaborated with professor Paolo Pinton's team of the department of Medical Sciences, University of Ferrara. Specifically, the tests involved evaluations *in vitro* on HeLa and AC16 cells, in order to assess modulatory activity on mPTP, once its opening was induced. In this case we were focusing on the cardiac model of IRI. Further investigations were planned on a selection of the most interesting compounds in order to evaluate their cardioprotective activity *ex vivo* and *in vivo*, specifically on pig hearts subjected to ischemia and then perfused. More details will be discussed in the dedicated sections.

On the other hand, we evaluated the activity of the compounds in a renal model of IRI, in collaboration with professor Alessandro Arcovito's team (section of Biochemistry of the Catholic University of the Sacred Heart, based in Rome). With their aid, a series of compound has been tested, firstly on HeLa cells and then on proximal tubular epithelial cells (PTEC).

Our purpose was to compare the results, to have multiple points of view to help us find a molecule suitable for this issue, that is ischemia reperfusion injury.

# 3. DISCUSSION

## 3.1 UREA-BASED COMPOUNDS

Dicyclohexylcarbodiimide (DCC) is known to interact with ATP synthase since 1979. In particular, it has been demonstrated that DCC can bind covalently the glutamyl residue 59 of the ATP synthase, forming a ureic function. [41,42,43] Going into more detail, DCC induces an irreversible inhibition according to the formation of a dicyclohexyl-*N*-acylisourea (DCU)-modified c-monomer. In 2017, Bonora *et al*. performed a test to demonstrate if treatment of living cells with DCC (inhibitor of ATP synthase) would affect the sensitivity to mPT induction by ionomycin plus $Ca^{2+}$ in cobalt-calcein assay. They also determined that, in an *ex vivo* cardiac reperfusion injury model, treatment with DCC can significantly improve the condition of the heart after reperfusion (data were obtained by measuring tissue damage levels, considering the left ventricular diastolic pressure, LVEDP): in other words, after DCC administration, LVEDP levels returned close to the baseline, confirming cardioprotection.[27] Despite this recognized mechanism, we considered that DCC in aqueous solution is partially hydrated to the corresponding dicyclohexylurea (DCU), that was tested for its activity as PTPC opening inhibitor. In addition, DCU is more soluble in water than DCC and it is more active in PTPC inhibition, according to the calcein-cobalt assay performed in human ventricular cardiomyocytes (AC16) under conditions of mitochondrial calcium overload: in fact, DCU works at a 15-fold lower concentration (1 μM) than DCC (15 μM) to exert the same extend of PTPC inhibition. To note, DCC administration has been demonstrated to be more potent than CsA administration in limiting the changes of LVEDP imposed by ischemia/reperfusion *ex vivo*. [27]

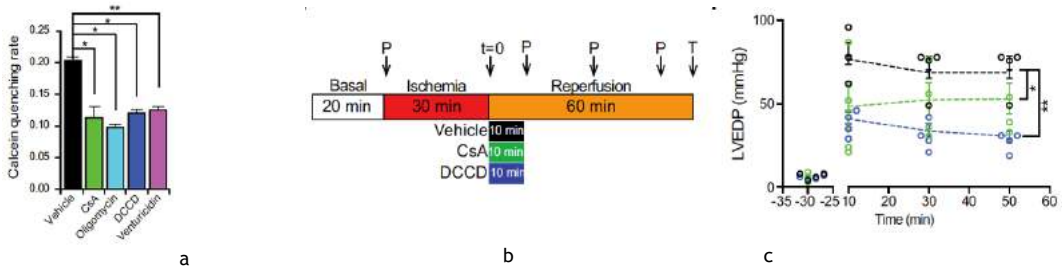


**Figure 18**. *a*: quenching rate quantification in HEK239T cells pre-treated with 15 μM DCC and then exposed to 1mM ionomicine: DCC (blue) reduces mPTP opening compared to the vehicle (black); *b*: design of the experimental approach to study cardiac ischemia/reperfusion injury *ex vivo*; *c*: quantification of the LVEDP inischemia *ex vivo* and then reperfused DCC (blue dashed line). Basal LVEDP level are close to zero.

Based on these considerations, we decided to develop a library of urea scaffold- based molecules, to test their activity on mPTP opening. We also consider the fact that in our previous paper, among the molecules that have demonstrated the most activity is one with ureidic functionality (IB16).[32]

Following this approach, five classes of DCU derivatives have been synthesized. Firstly, the intact urea moiety has been maintained and a number of symmetric (compounds **1**–**7**) or asymmetric (**8**,**9**) N/N' -

modifications were introduced by combination of different alkyl/ cycloalkyl/ (substituted)aryl/ benzyl groups. Secondly, the urea function has been substituted with a thiourea group to evaluate the effect of the removal of a potential hydrogen bond acceptor. Even in this case, symmetric (**10, 11**) and asymmetric (**12**) compounds have been prepared. Lastly, two carbamate derivatives were synthesized (**13**,**14**), in order to understand how a hydrogen bond acceptor instead of a donor one influences the activity. The synthesis of DCU derivatives have been carried out following different straightforward approaches, through which the target molecules were easily produced, purified and almost all of the reactions led to high yields. Symmetric ureas **1-7** have been prepared by the typical reaction between carbonyldiimidazole (CDI) and two equivalents of aromatic or aliphatic primary amines. Since the reaction between CDI and primary amines rearranges into an isocyanate intermediate, this approach can conceivably be used for the synthesis of asymmetric ureas, by adding a different amine. However, because of its rather high reactivity, the isocyanate intermediate is not easy to isolate for the further reaction with amines. For this reason, asymmetric ureas, as well as thioureas (**8**–**12**) have been prepared by the direct reaction between aromatic or aliphatic primary amines and commercially available isocyanates or isothiocyanates. Carbamates **13** and **14** were prepared by reacting either aryl- or cyclohexyl-amine with ditertbutyl-dicarbonate. In producing urea derivatives, five classes of structural modifications have been introduced (Table 1), in order to investigate which parts of DCU are involved in the PTPC inhibition, to figure out which improvements can be undertaken for the biological activity optimization.

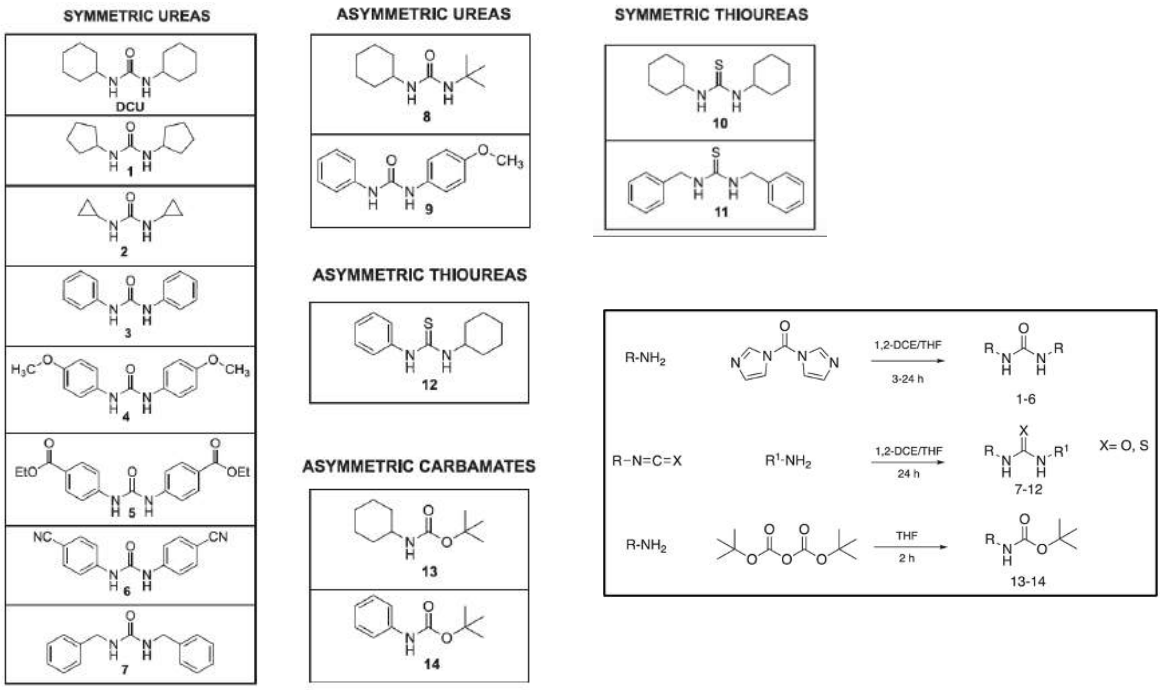


**Table 2**. List of the urea compound synthesized and general synthetic procedure.

To test the biological activity of urea derivatives, human cardiomyocytes cell line AC16 has been chosen as cell model to study PTPC inhibition under mitochondrial calcium overload conditions induced by the ionophore ionomycin. All the molecules have been demonstrated to have an inhibitory or a stimulating

activity in mPTP opening. In particular, among symmetric urea derivatives, we observed that aliphatic cyclic substituents with less than six carbon atoms demonstrated to have less inhibition potency if compared to DCU. Moreover, in the case of *N,N*-diphenyl substitution, the presence of electron-withdrawing groups showed to be detrimental for the inhibitory activity contrarily to the electron-donor ones that, inducing the enolic or thioenolic form, lose the inhibition function in favor of an activation of PTPC.

Summarizing our biological results, we developed a theory concerning the interaction of the different functional groups tested (urea, thiourea and carbamate) comparing them to the interaction with the Glu[59] residue, which has been proven to interact with DCC, as mentioned above. We assume, however, that ureas interact non-covalently with the supposed target protein: this is an interesting aspect in drug develop, because it could be avoided the typical side effects of the covalent bound (for example, ATP synthase activity could be compromise irreversibly). In particular, we supposed, concerning the interaction of the urea moiety with the carboxylate of Glu[59] residue through H-bond, that:

a) Interaction between urea derivatives and Glu[59] through interposition of a water molecule which behaves as a "bridge-molecule" thanks to the capability of the urea –NH group and the carboxylate of glutamate to form H-bonds: this translates in an inhibitory potential;

b) In the case of thiourea derivatives, the more stable thioenolic form subtracts the water molecule from the interaction with the carboxylate. This could be translated into an activating behavior as observed.

c) In the case of carbamate derivatives, both the two oxygen atoms work as H-bond acceptors with water, which in turn is not able to prevent carboxylate of the glutamate from proceeding in the physiological way: also in this case, an activator potency is observed.[42]

These aspects are depicted more clearly in Scheme 1 below.

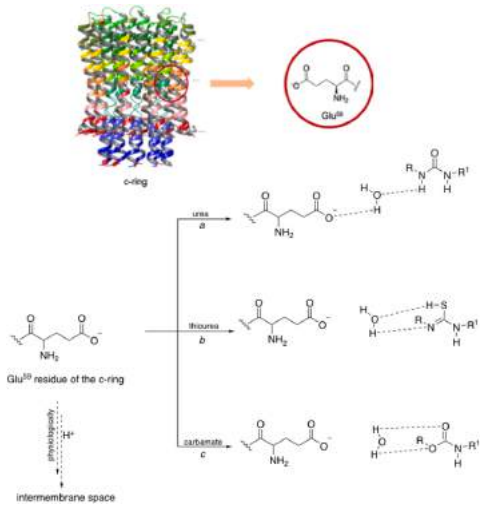


**Scheme 1**. Supposed interaction mechanism of urea or thiourea compounds with Glu[59]. The c-ring crystal (PDB 4F4S) is shown on the top of the Scheme and some amino acid residues, involved in the proton translocation, are put in evidence. In particular, as mentioned above, residue Glu[59] (circled in red) plays a crucial role in the mechanism.

## BIOLOGICAL EVALUATIONS

Here are depicted and described the biological results regarding the effectiveness of the derivatives **1-14**, in terms of PTP activity. The typical procedure for the cobalt$^{2+}$-calcein assay is described in detail in the paper by Bonora *et al*.[44] Briefly, the cells are pre-treated with the inhibitors (1μM) and then calcein is added. It can passively diffuse into the cells and collect in cytosolic compartments including the mitochondria. Once the dye is inside cells, esterases cleave the acetoxymethyl esters, trapping the dye in intracellular compartments. At this point, the living cells become fluorescently labeled, with fluorescence spread throughout all subcellular compartments. The utility of the method originates from the ability of cobalt to quench calcein fluorescence in the cytosol but not in mitochondria. Thus, in the case of healthy cells, calcein is able to reveal the mitochondrial matrix network with good localization. Opening of the mPTP (in this case induced by ionomycin) leads to both the exit of calcein from the mitochondrial matrix and entry of $Co^{2+}$ into the mitochondrial matrix, resulting in quenching of calcein stored in the mitochondria. This event manifests as a reduction of calcein fluorescence intensity and is easily measurable by fluorescence microscopy. Thus, once ionomycin is administered, the PTP are totally opened, so we express in all the graphs presented in this thesis the inhibitors capability to prevent the mPTP opening as PTP activity: as control we used cells not treated with any inhibitors, so in this case the PTP activity is 100%. Therefore, to comprehend to the best the graph, the more PTP activity is low, the more our compounds possess good inhibitory activity; as is shown in the histogram, it seems that a couple of compounds are better inhibitors than the reference compound DCU and the others seems to favor the PTP opening, due to the motivations discussed before.

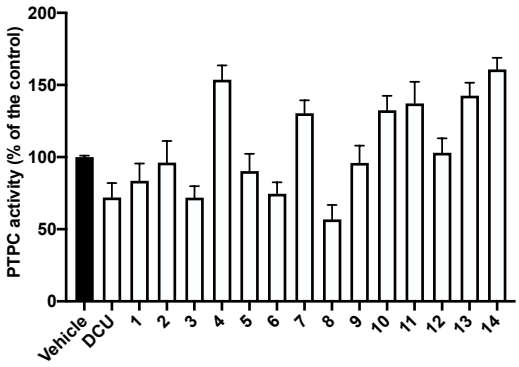


**Graph 1**. In this histogram are shown the results of the $Co^{2+}$-calcein assay using AC16 cells. The control represents cell not treated with any inhibitors, so the PTP, after administration of ionomycin, are opened (thus here we assume an activity of 100%); dicyclohexylurea (DCU) is our reference compound, that can reduce the opening of mPTP for 28%. Compounds **3** and **8** demonstrate respectively very similar or better activity as inhibitors and the others seem to promote the mPTP opening. Cells are pre-treated with inhibitors at 1μM concentration.

# 3.2 MONOSPIRANIC COMPOUNDS

## 3.2.1 PIPERIDINE SCAFFOLD-BASED MONOSPIRANIC COMPOUNDS

As we mentioned previously, we obtained very good results from preliminary biological evaluations on piperidine scaffold based monospiranic compounds (in particular compounds 5g, 6g, 10).[32]

We therefore decided to investigate further to better understand which portion of the molecule is essential for interaction with the target and which is not. To do this, we worked on the piperidine core: initially, we made modifications to $N_1$, trying to understand if and how the steric bulk affects the activity of the molecule. In the second analysis, we functionalized $N_8$ differently; finally, we combined the modifications. We thus obtained three series of compounds modified in a gradual and rational manner, which will allow us to refine the study and understand more about the action of these molecules in modulating pore opening. In order to approach the study in a precise manner, we have also made use of a small computational study, which will be detailed later.

### 3.2.1.1 FIRST STEP: $N_1$ MODIFICATIONS TO THE 1,3,8-TRIAZASPIRO[4.5]DECAN-4-ONE CORE

Given these premises, a large part of the project has been focused on the synthesis of further compounds with a common spiropiperidine structure, maintaining tosylic or benzylic substituents in position 8, because we reported them among the most interesting derivatives. This common scaffold was then functionalized on the nitrogen at position 1, using differently substituted aromatic amines, in order to subsequently investigate *in vitro* how the steric size affects the inhibitory activity of the mPTP opening. We hypothesized that in order to improve the binding system, the hydrophobicity and the steric size of the group at position 1 could be increased.

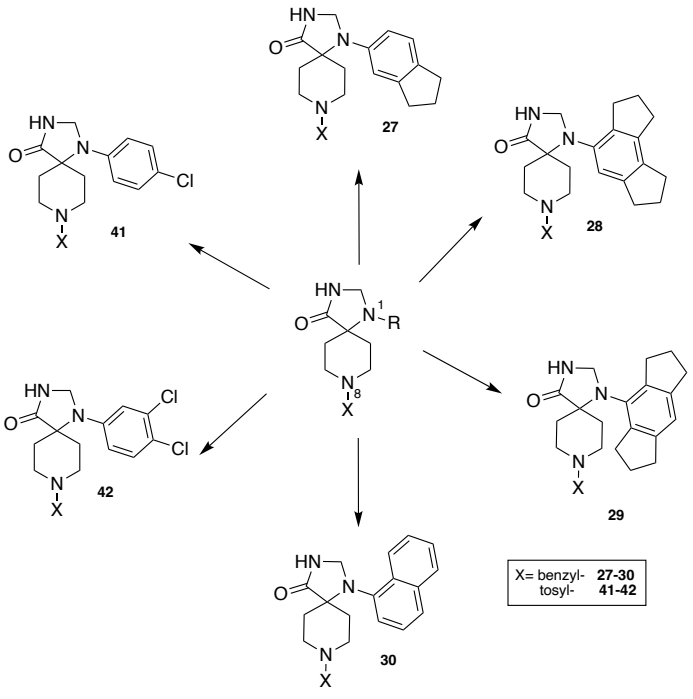


**Scheme 2.** Various substitutions to the $N_1$ position of the main monospiranic core.

The designed structures (Scheme 2) have variously substituted hydrophobic both aromatic and aliphatic functional groups in position 1, while, for position 8, we chose the benzyl- and tosyl- groups as substituents, since, as evidenced by the previously published study, they proved to be useful for inhibitory activity (also with 5-chlorothiophen-sulphonyl moiety).[32]

All these final products were provided by the classic synthetic route proposed in the paper by Morciano *et al.*[32] Briefly, the first reaction that takes place is the Strecker reaction: N-benzyl-piperidone reacts with a differently substituted aromatic amine and a source of cyanide ion (in this case trimethylsilyl cyanide, TMSCN) in mild acidic conditions to provide an aminonitrile intermediate (a). Then, nitrile was hydrolyzed to amide in a strong acidic environment by concentrated sulfuric acid for 18h (b). The resulting amide was cyclized by DMF/DMA (c); finally, the C=N double bond was reduced with $NaBH_4$.

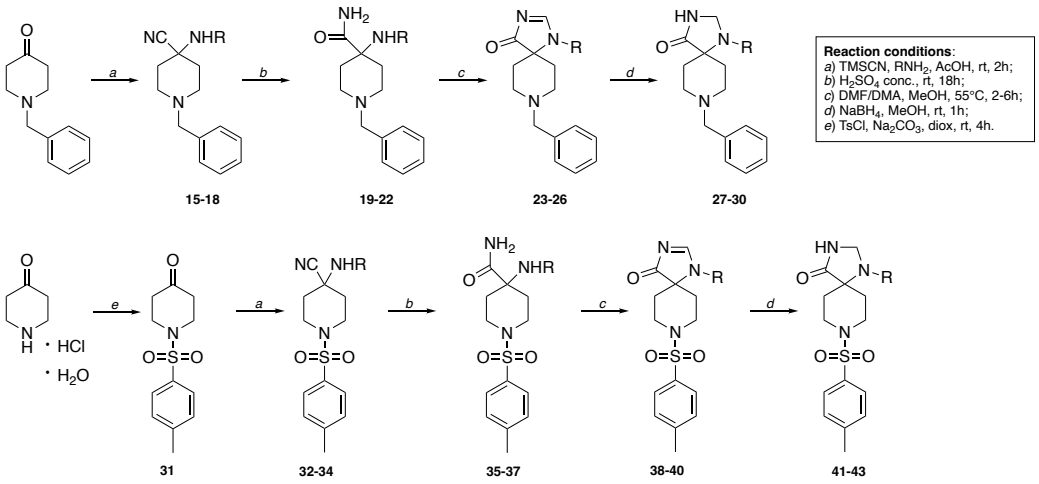


**Scheme 3**. General procedures for the synthesis of $N_1$-modified 1,3,8-triazaspiro[4.5]decan-4-one derivatives; above is shown the protocol followed for the synthesis of $N_8$-benzyl compounds **27-30**, while below that for the $N_8$-tosyl products **41-43** is depicted. Structure **43** presents R as benzylic substituent and it is elucidated in Scheme 4 below.

## PRELIMINARY BIOLOGICAL EVALUATIONS

To evaluate their activity, all the derivatives were tested using $Co^{2+}$-calcein assay. The method is based on the response given by the cells in terms of fluorescent emission (described above in paragraph 3.1) and was carried out at the Department Medical Sciences of the University of Ferrara, in the laboratories of Professor Paolo Pinton. The preliminary data proposed show that compounds **41** and **29** are very promising as inhibitors of PTP; they inhibit the opening of the complex by 92% and 51% respectively. Compound **27**, on the other hand, shows a fair inhibition of 30%. Three others, however, **42**, **28** and **30** show a little or no activity; the first two in particular appear to be detrimental for the cells and the latter is active, but not with a significant value. Further tests will be carried out later to validate the results obtained. Below the histogram summarizing the conclusions drawn from the processing of the data acquired during the tests.

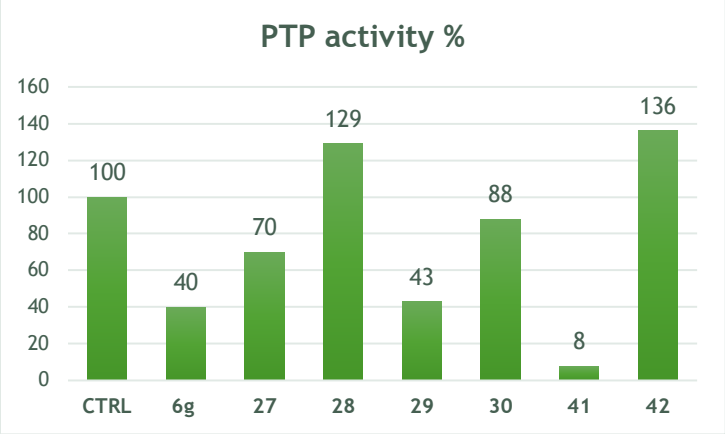


**Graph 2**. Histogram depicting inhibitory activity as a percentage. Results are obtained by the cobalt-calcein test on HeLa cells.

These data were also compared with the computational evaluations previously conducted. From the table below, it can be seen that for compound **27**, the computational model fully predicted the compound activity, while for compounds **29** and **30**, although the two values differed slightly, the predicted inhibition% fell within the uncertainty of the actual data. For the tosylic derivatives, **41-42**, however, prediction was not possible since no tosyl- derivatives were present in the training set.

| Compound | % pred. inhib. | % actual inhib. |
|---|---|---|
| **27** | 29.99 | 30 |
| **28** | 27 | -29 |
| **29** | 53.5 | 57 |
| **30** | 20 | 15.7 |

**Table 3**. Comparison of inhibitory activities predicted by QSAR model and actual activities obtained by cobalt-calcein assay.

For compound **28**, to which the QSAR model had assigned a certain activity, this turned out to be completely incorrect. However, through a molecular dynamics study, it was found that after only 100 ps of simulation, the ligands move away from the binding site.

So, in conclusion, we can affirm that CADD (Computer Aided Drug Design) methods are very useful in directing synthesis towards active compounds, and that a single type of CADD experiment (QSAR, docking, molecular dynamics) is not sufficient to explore all the variables in the system that may influence the binding phenomenon. It can be concluded by saying that the steric hindrance in the ortho- and meta-position does not bring about significant improvements in activity quality; the B-pocket, therefore, is disinclined to bind large groups, and the increased steric hindrance brings, indeed, a disadvantage in binding, not allowing ligands to get close enough to the C-pocket to find the interaction with the water molecule.

### 3.2.1.2 SECOND STEP: $N_8$ MODIFICATIONS TO THE 1,3,8-TRIAZASPIRO[4.5]DECAN-4-ONE CORE

The substitutions in position $N_1$ were followed by those in position $N_8$, in order to see how the different functionalization affected inhibitory activity. In this case, we decided to keep either a phenyl or a benzyl as a fixed reference at position 1, to have both an aromatic and an aliphatic substituent as reference molecules. The structures were developed starting from 4-piperidone monohydrate hydrochloride for the $N_1$-benzyl derivatives and from 1-phenyl-1,3,8-triazaspiro[4.5]decan-4-one for $N_1$-phenyl derivatives. We obtained two series of compounds differently functionalized, with both aromatic and aliphatic moieties; we chose substituents by combining together information on the most active derivatives from previous studies and data from *in silico* evaluations (to be mentioned later).

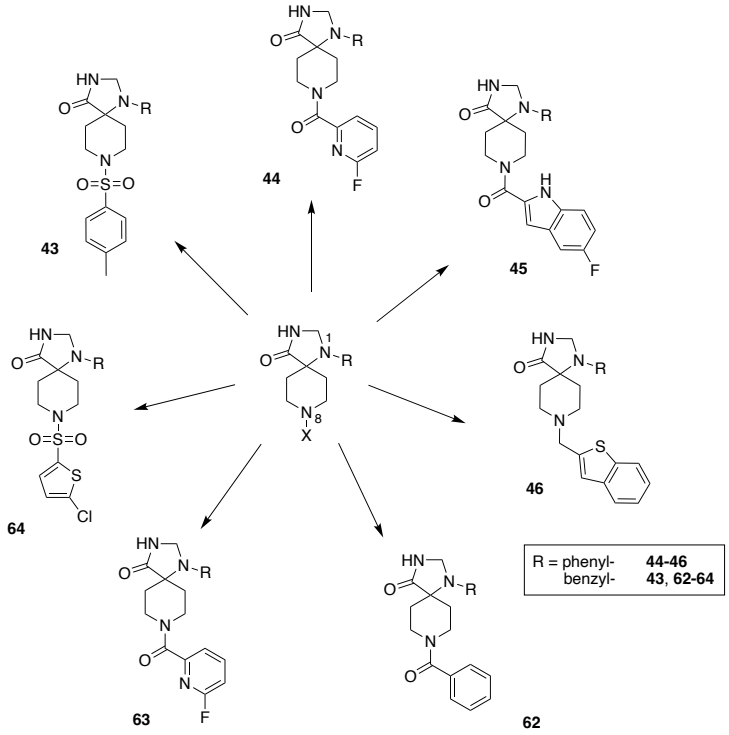


**Scheme 4**. Various substitutions at $N_8$ position to the main monospiranic core, maintaining phenyl (**44-46**) or benzyl (**43**, **62-64**) groups at $N_1$ position.

Compound **43**.

It is synthesized with the route described in the previous paragraph and depicted in Scheme 4, with no particular synthetic issues and in good yields (see experimental data).

Compounds **44-46**.

As shown in the Scheme 5 below, the synthesis of these compounds was conducted in only one step, i.e., the functionalization of the piperidinic nitrogen $N_8$. For derivatives **44** and **45** an amide was obtained from the corresponding carboxylic acid after activation with oxalyl chloride; instead, for compound **46**, we performed the alkylation of the nitrogen using a bromide derivative **47**, previously obtained from the corresponding alcohol, through an Appel reaction, that involves the formation of an alkyl halide from an alcohol via phosphonium salt as an intermediate.

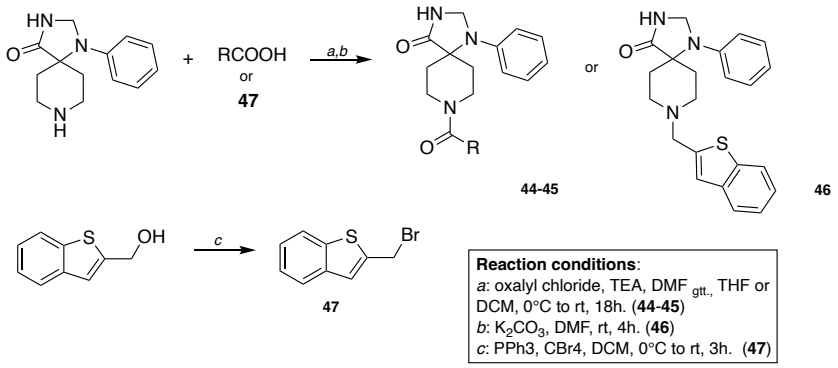


**Scheme 5**. General procedure for the synthesis of the $N_1$ phenyl derivatives, differently substituted in $N_8$ position.

Compounds **62-64**.

The structures of this series were developed starting from 4-piperidone monohydrate hydrochloride. Nitrogen was then appropriately functionalized, using different synthetic routes, depending on the substituent to be inserted.

In particular, for compound **62**, the amide was obtained by the alkylation of benzoyl chloride; for compound **63**, instead, the amide was obtained using WSC and HOBt as classical coupling agents. Finally, for compound **64**, 5-chlorothiophene-2-sulfonyl chloride has been employed.

After functionalizing the nitrogen of piperidone, the next step involved the Strecker reaction, in which the differently substituted piperidone derivatives reacted with benzylamine and trimethylsilyl cyanide (TMSCN), in an acidic environment, to give an aminonitrile intermediate. However, this reaction often gave problems of poor reactivity, low yields or obtaining cyanohydrin as the main product. To overcome this problem, various attempts were made, such as increasing the number of benzylamine equivalents, isolating imine, and transforming cyanohydrin into its corresponding mesylated derivative, in the hope of obtaining a good leaving group, but with little or no results; then, as an alternative to Strecker, the reaction with indium tribromide ($InBr_3$), a Lewis acid, was carried out to activate the piperidinonic carbonyl, resulting in a mixture of cyanohydrin and its silyl derivative, easily isolable and hydrolysable to the desired intermediate (**51-52**), as reported in the scheme 6.

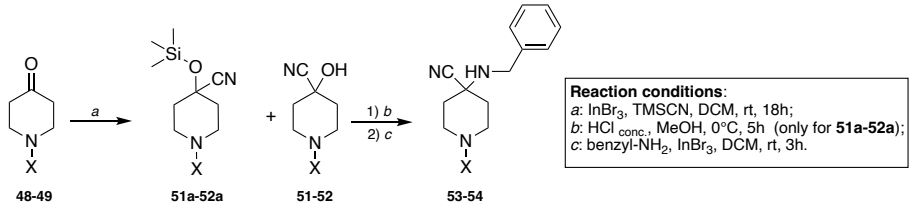


**Scheme 6**. General procedure for the synthesis of aminonitrile derivatives **53-54**. To note, after the first reaction (a), mixtures of protected and non-protected species were obtained. Therefore, as described by route *b*), the silyl derivatives (**51a**-**52a**) were purified and hydrolyzed with concentrated HCl in order to isolate the corresponding cyanohydrin (**51-52**). Then the two batches were combined and submitted together to the following step (*c*).

Once obtained the aminonitrile derivatives, the following steps are the same as those proposed previously for compounds **27-30** and **41-43** (see Scheme 3 steps *b*, *c*, *d*). It is worth emphasizing that the corresponding

benzyl analogues of compound **45** ($N_8$-5-fluoro-1H-indole-2-carboxamidic derivative) and compound **46** ($N_8$-benzothiophenic derivative) are not present in this series; in fact, as far as the former is concerned, we could not proceed with the synthesis due to compound solubility problems; as far as the latter is concerned, on the other hand, during the hydrolysis step of nitrile to amide with concentrated $H_2SO_4$, we obtained the sulfonation of the benzene ring. Alternative attempts were therefore made to complete the hydrolysis of the nitro group, such as the use of an $H_2O_2$ solution in a basic environment for $Na_2CO_3$, NaOH and KOH, but without satisfactory results.

### 3.2.1.3 Combined $N_1$ and $N_8$ modifications to the 1,3,8-triazaspiro[4.5]decan-4-one core

As the last step, we combined the modifications at the imidazoline nitrogen $N_1$ and those at the piperidinyl nitrogen $N_8$ to afford the final series of compounds. With this type of approach, therefore, we have introduced changes gradually and rationally, so we will be able to identify exactly which structural change leads to an increase or decrease in biological activity, once the experimental results have been obtained.

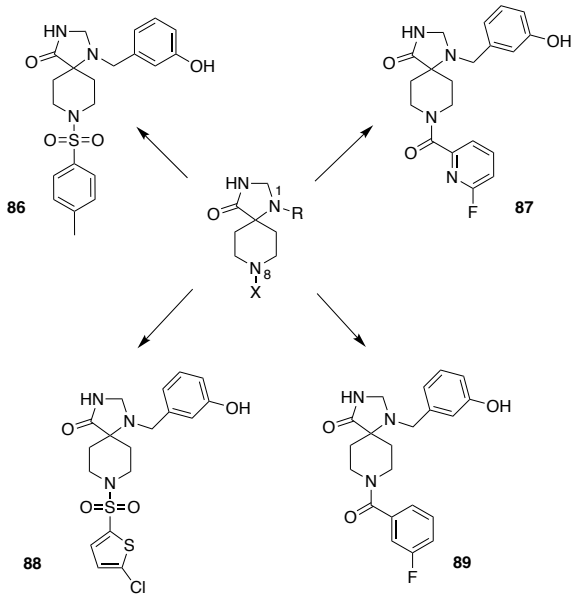


**Scheme 7**. Combined $N_1$ and $N_8$ modifications to obtain desired final products **86-89**.

Compounds **86-89**.

These compounds are $N_1$-benzyl derivatives, which additionally have a hydroxyl function in position 3 of the aromatic ring. This feature was introduced in order to add a polar element, perhaps capable of effecting hydrogen bonds with the amino acid residues of the binding pockets.

In this case, we synthesized it as a $N_8$ tosyl- derivative, because, as cited above, a similar structure has been known to have a high inhibitory activity; we also wanted to introduce the modifications to the main core one at a time, with a gradual approach.

In this case, we performed a Strecker variation than the one we have used so far: here, N-tosyl-piperidone reacted with TMSCN and a solution of $NH_4^+Cl^-$ in $NH_4^+OH^-$ to obtain primary amine (*a*).

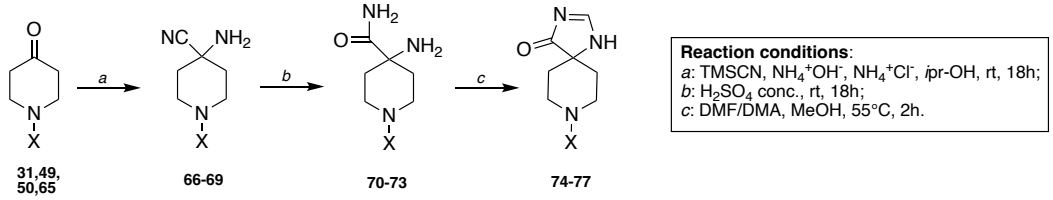


**Scheme 8**. General procedure to obtain intermediates **74-77**, useful to achieve the final products **86-89**.

In parallel, the alkylating agent for the $N_1$ position of the monospiranic compound was prepared. Initially, 3-hydroxybenzaldehyde was reacted with imidazole and terbutyl-dimethyl-silylchloride (TBDMSCl) in DCM to give rise to the phenol protected as terbutyldimethyl-silyl ether. Afterwards, the aldehyde was reduced to alcohol with $NaBH_4$ in MeOH and finally an Appel reaction was conducted with $PPh_3$ and $CBr_4$ to convert the alcohol to a brominated derivative, similarly to as described above.

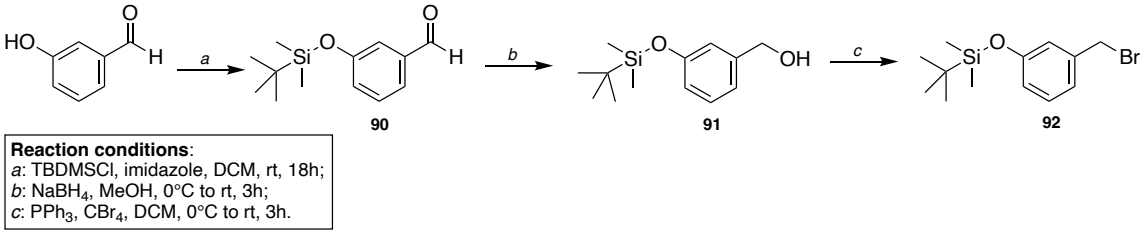


**Scheme 9**. General procedure for the synthesis of the alkylating agent (3-(bromomethyl)phenoxy)(*tert*-butyl)dimethylsilane **92**.

Once afforded the two types of "building blocks" (**74-77**) and **60**, they were submitted together to the next step with $K_2CO_3$ in DMF for 18 hours to obtain the alkylated compounds **86-89**. This strategy, however, led to an overalkylation by-product, which was difficult to separate from the desired product even in the chromatographic column; another approach with acetonitrile and using the bromide derivative in slight defect (0.9 eq) in a more diluted environment allowed us to obtain exclusively the monoalkylation products (**86-89**).

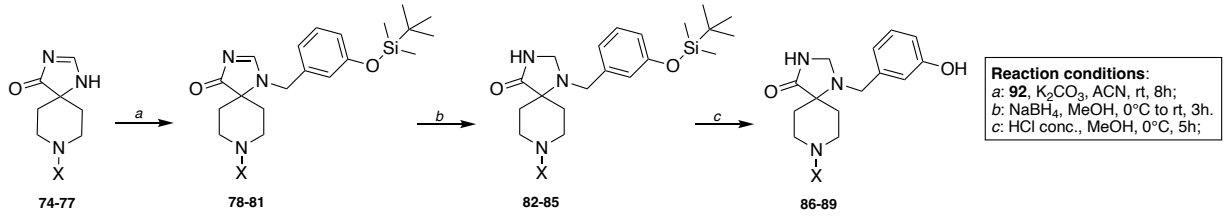


**Scheme 10**. General procedure for the synthesis of $N_1$- 3-hydroxybenzyl derivatives **86-89**.

We have combined information from previous biological studies and others extrapolated from a computational study (to be discussed later, in section 3.2.2), which highlighted compound **87** as a structure capable of interacting with the binding site in a very stable manner ($\Delta G$ = -46.71). In contrast, compound **88** has 5-chloro thiophen sulfonamide in $N_8$, which is present in derivative Compound 10 [32] (inhibitory activity of 66,8%). Two other promising structures also emerged from the study, but, as specified above, were not synthesized due to problems that occurred during the optimization of the synthesis (solubility and side reactions).

The Table 4 below summarizes all the monospiranic structures developed during this study. It fucuses the attention on the various modifications made to the 1,3,8-triazaspiro[4.5]decan-4-one main core. In this summary scheme, the derivatives have been divided into reference molecules (line 2, highlighted in the article cited), $N_1$-phenyl substitution molecules (line 3), benzyl substitution molecules (line 4), 3-OH-benzyl

substitution molecules (line 5) and molecules with a combination of modifications (line 6). In this way, the work of gradually and rationally adding modifications to the reference structure is well evident.

| | |
|---|---|
| **MAIN CORE** | 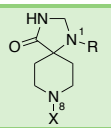 |
| **REFERENCE COMPOUNDS** | 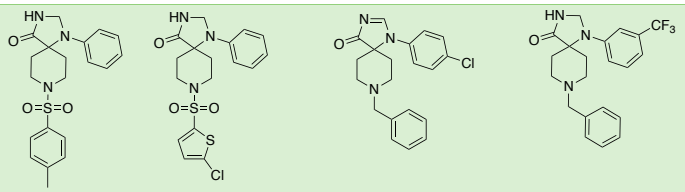 PP11 Compound 10 Compound 5c Compound 6g |
| **$N_1$-PHENYL DERIVATIVES** | 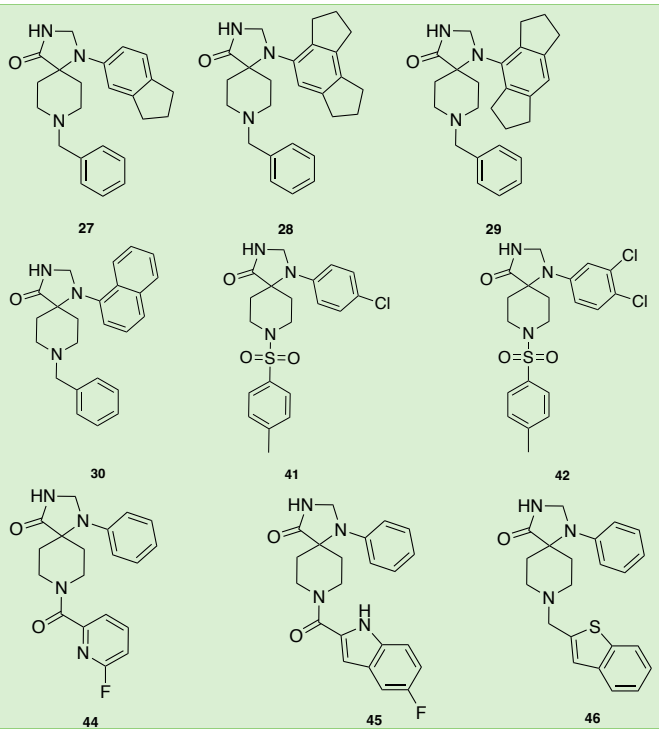 27 28 29 30 41 42 44 45 46 |
| **$N_1$-BENZYL DERIVATIVES** | 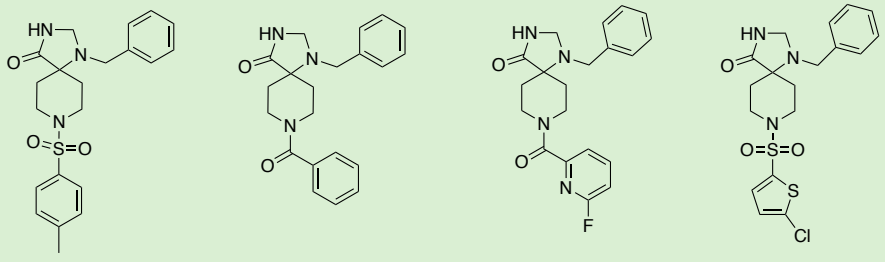 43 62 63 64 |
| **$N_1$-3-OH-BENZYL DERIVATIVES** | 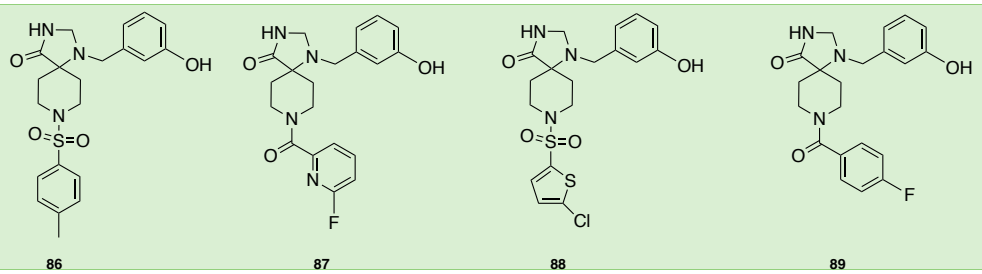 86 87 88 89 |

**Table 4**. Table that resumes together all the modifications applied to the main core.

### 3.2.2 COMPUTATIONAL ANALYSES

As previously mentioned, for a selection of monospiranic compounds, a computational study has been conducted. All the analyses have been developed in the laboratories of Professor Alessandro Arcovito of Catholic University of the Sacred Heart, based in Rome.
Among the CADD techniques used are: molecular docking to study the protein-ligand binding mode; the QSAR study (based on biological activity data of a training set of molecules already tested and described in the literature) which can predict the biological activities of the designed compounds based on their three-dimensional structure and finally molecular dynamics to test whether the designed molecules form a long-lasting complex with the protein. From these CADD studies, spiropiperidinic derivatives **27**-**30** were designed, inspired by 8-benzyl-1-(3-(trifluoromethyl)phenyl)-1,3,8-triazaspiro[4.5]decan-4-one, the best of the inhibitors tested so far. [32] As described in more detail previously, the data collected were then compared with those actually obtained.

On the other hand, this was followed by studies in which the common spiropiperidinic scaffold was combinatorial functionalized on $N_1$ and $N_8$, resulting in a database of more than 4 million molecules: after subjecting all of these to a computational study, six structures emerged with valid conformational and pharmacophoric characteristics for a biological interaction with the target to take place. In particular, the 1,3,8-triazaspiro[4.5]decan-4-one (or "spiropiperidine") was used; as building blocks for the first reaction alkyl, sulfonyl and acyl halides with aromatic moiety (phenyl, benzofuranyl, indolyl, imidazolyl, etc...) were selected (the aromatic ring is needed to establish the π-π interaction with the two Phenylalanines in the pocket A) and as reactants for the Strecker reaction anilines and benzylamines were used. Combining these fragments to our spiropiperidine scaffold, 4660950 compounds were generated. From here, as summarized in Scheme 11 below, a series of analyses were carried out with the aim of identifying structures with a high affinity to this specific binding site. Once approximately 4 million molecules were obtained, they were docked to the c-ring via two docking procedures: *a)* High Throughput Virtual Screening (HTVS, fast and less accurate, used to skim the database) and *b)* Standard Precision Docking (SPD, slower but more accurate). The successful compounds were selected according to their pose, measuring the distance between the ligand and two Phenylalanines (F124 and F130), H-bond length (between carbonyl group and E119 water) and H-bond angles. This procedure reduced the database to a handy pool made up of 9000 compounds. At this point, other analyses were conducted, to further reduce the list of possible structures by calculating the binding affinity between the molecule and the potential target, in Kcal/mol. In order to have compounds with a certain activity a cut-off of –25 kcal/mol was set and approximately 4000 compounds were extracted from the pool. Then, the molecules were ranked according to a linear consensus between ΔG and Glide Energy and the first 100 compounds were selected and submitted to a 5 ns long Molecular Dynamic Simulation, in order to study the stability and behavior of ligands when interacting with the c-ring. The simulations were analyzed and Simulation Interaction Contact results of every ligand were compared with 5 ns long simulation of Oligomycin A as reference, selecting those compounds which contacts were higher than reference, mainly with E119, F130, F124 and L123. At the end of all these procedures, the selected molecules were only six.


**Scheme 11**. Flowchart showing all the steps of the drug design process, from filters to docking and Molecular Dynamic Simulation.

### 3.2.3 Observations on Strecker reaction mechanism

The Strecker reaction is defined as a simple atom economic multicomponent one pot reaction. By a simple mixing of the easily available acetaldehyde, ammonia, and hydrogen cyanide for a fixed period of time, the resulting amino nitrile adduct was formed in high yield. It was first documented by the German chemist Adolph Strecker in 1850.[45]

The mechanism described to afford the amino nitrile final product is divided into two steps: firstly, the carbonyl oxygen of an aldehyde is protonated, followed by a nucleophilic attack of ammonia to the carbonyl carbon. Then, after subsequent proton exchange, water is cleaved from the iminium ion intermediate. A cyanide ion then attacks the iminium carbon yielding an aminonitrile.

During the syntheses we noticed something interesting about the Strecker reaction. In fact, in some cases, particularly when we performed the reaction with an aliphatic amine, we observed that the main product in most cases was the cyanohydrin; so, to circumvent this problem, the alternative synthetic routes described above were used (see Schemes 6 and 8).

But what is interesting is that what we observed goes against what stated earlier: in fact, if we appreciate the cyanohydrin formation, it may mean that no reaction with the amine was carried out and so, consequently, the first step of the Strecker reaction was not occurred.

At this point, to ascertain what we assumed, we conducted several small-scale tests, changing one variable at a time, so we could formulate a theory based on our empirical observations, and these attempts are summarized in the Table 5 below.

| Entry | Ketone | Amine | TMSCN | Lewis acid | Solvent | Product |
|---|---|---|---|---|---|---|
| **1** | 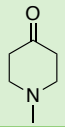 | 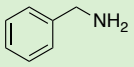 | yes | no | MeOH | Yes via Cyanohydrin |
| **2** | "" | 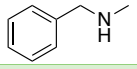 | yes | no | MeOH | No prod |
| **3** | "" |  | yes | no | MeOH | No prod (even after addition of $InBr_3$) |
| **4** | "" |  | yes | no | MeOH | Yes via cyanohydrin (but very very slow) |
| **5** | "" |  | yes | $InBr_3$ | MeOH | Yes via cyanohydrin |
| **6 (two steps)** | "" | 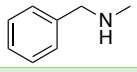 | yes | $InBr_3$ (0.1eq in the first step) | MeOH | Yes via cyanohydrin |
| **7 (two steps)** | "" | "" | yes | Yes (0.1eq in the first step) | DCM | Yes via cyanohydrin |
| **8** | "" | "" | yes | $InBr_3$ (0.1eq) | MeOH | Yes via protected cyanohydrin |
| **9** | "" | "" | yes | $InBr_3$ (0.1eq) | DCM | Yes via protected cyanohydrin |
| **10** | "" | "" | yes | $InBr_3$ (0.1eq) | DCM dry | No prod |
| **11 (two steps)** | "" | "" | yes | $InBr_3$ (0.5eq in the first step) | MeOH | Yes via cyanohydrin |
| **12** | "" | "" | yes | $InBr_3$ (0.1eq + 0.1eq) | MeOH | Yes via cyanohydrin |
| **13** | "" | "" | yes | no | DCM | Protected cyanohydrin |
| **14** | "" | "" | yes | no | DCM dry | Traces |
| **15** | 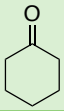 |  | yes | no | MeOH | Via iminium ion |
| **16** | 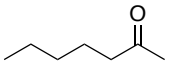 | 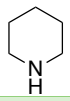 | yes | no | MeOH | Via iminium ion |
| **17** | 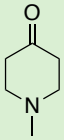 | no | yes | no | DCM | Protected cyanohydrin |
| **18** | 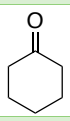 | no | yes | no | MeOH | No prod |
| **19** | 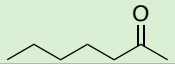 | no | yes | no | MeOH | No prod |
| **20** | 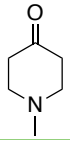 | 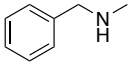 | yes | $BF_3$ etherate | MeOH | Yes via cyanohydrin |

| | | | | | | |
|---|---|---|---|---|---|---|
| **21** | 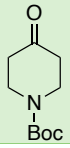 |  | yes | no | MeOH | Slow via iminium ion |
| **22** | 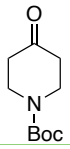 |  | yes | $InBr_3$ (0.1eq) | MeOH | Slow via iminium ion |

**Table 5**. Set of reactions conducted to investigate how ketones, amines, Lewis' acids and solvents affect the Strecker reaction.

In Table 5 it is briefly resumed the aim of these experiments. We set all the reactions in the same manner: in a tube, ketones were solubilized in the appropriate solvent; subsequently, the amine and the TMSCN were added dropwise. The reactions were monitored via MS-ESI for three days, with a check after 30 min and 3, 8, 24, 30, 36, 48, 60 and 72 hours (or until the reaction was completed). We performed all the reactions in a one pot way, except for three cases (line 6,7,11), where we wanted to investigate how the reaction proceeded step by step. In these specific cases, the first step involved the ketone dissolution in the appropriate solvent only with the TMSCN; in a second step, after 5 hours, the amine was added.

Initially, we tried to perform the Strecker reaction with primary, secondary and tertiary amines (respectively lines 1 to 4). The reaction with the primary benzyl amine provided the aminonitrile very fast. After 30 minutes, we detected a major peak corresponding to the cyanohydrin and a minor peak of the product. After 3 hours, the cyanohydrin peak disappeared in favor of a rising aminonitrile product peak. For secondary and tertiary amines no product or only traces were evident after three days.

Secondly, we decided to add in the reaction environment a Lewis acid ($InBr_3$), because it could help to increase the speed of the reaction and push it due to its capability of make the carbonyl carbon more electrophilic. In this case (line 6) the reaction took place faster and we obtained the aminonitrile, again observing the initial formation of the cyanohydrin peak, which, as time went on, diminished in favor of that of the product.

At this point, we analyzed how the Lewis acid affected the reaction (lines 5 to 12): we have conducted several tests, adding it in both catalytic and semi-stoichiometric quantities, with both one-step and two-step reactions. We have observed that Lewis's acid is not essential for forming the cyanohydrin (its appearance is indeed very fast), but it is essential for the reaction to proceed quickly after the addition of the amine. We also tried to change the Lewis acid from $InBr_3$ to $BF_3$ etherate (line 20), and it did not affect the course of the reaction.

Then we evaluated the role of the solvent: we changed it from methanol (a polar and protic solvent) to dichloromethane (which has less polar strength, lines 7 and 9). The reaction proceeded in the same way via cyanohydrin, but, in this case, we obtained it as trimethylsilyl derivative. Contrary, using dry DCM with an anhydrous environment the reaction did not occur (lines 10 and 14). So, we have assumed that maybe the humidity in the environment and in the solvent can help to deprotect the silyl ether and allow the reaction to proceed.

Finally, we considered also how the type of ketone affected the occurrence of the reaction. We used cyclohexanone and 2-heptanone in the same conditions as described above: the reactions led to the formation of the product via iminium ion (lines 15 and 16). In fact, by mass, it was easy to detect the initial presence of the iminium ion peak, which then decreased in favor of that of the aminonitrile. To be sure of this claim, we conducted a further test, reacting these ketones only with TMSCN, with the intention of monitoring the possible formation of cyanohydrin: as expected, the reaction failed (lines 18 and 19).

Once collected all these data, with the aid of quantomechanical analyses, we analyzed the shape of the atom orbitals involved in the reactions; in particular, we chose as reference compounds 1-methylpiperidin-4-one (or N-methyl piperidone) and *tert*-butyl 4-oxopiperidine-1-carboxylate (or N-boc-piperidone), because of their antithetic behavior during our tests (see Table 5). As it can be easily appreciated from the Figure 19 below, we analyzed the HOMO of the nitrogen atom and the LUMO of the carbonyl group and, in the two cases, their shapes are quite different. In particular, in *a)* and *b)*, referring to the N-methyl piperidone, the stereo electronic effect of the HOMO of the nitrogen atom (blue and red) makes it capable to interact with the LUMO of the carbonyl (green and yellow): the orbitals are close enough to interact to each other. Instead, *c)* shows the asset of the N-boc piperidone orbitals: in this case is evident that the HOMO of the nitrogen is engaged in resonance with the carbonyl of urethane and is therefore much further away from the LUMO of carbonyl ketones.

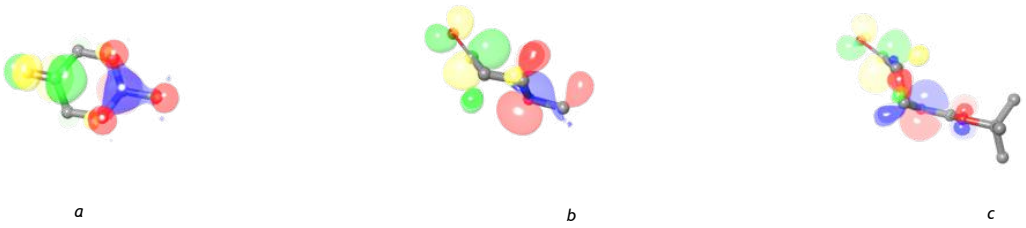

*a* *b* *c*

**Figure 19**. Representation of the HOMO and LUMO orbitals to better comprehend the interactions between atoms. *a)* and *b*) refers to N-methyl piperidone and c) refers to N-boc piperidone. In blue and red are shown the HOMO and in green and yellow the LUMO.

What we could conclude from all these synthetic attempts is that the reactivity of all these species is different because of the position and shape of the orbitals in the space: depending on their chemical surroundings, they have different reactivity. In particular, N-boc piperidone (as well as cyclohexanone or 2-heptanone) are harder electrophiles, because they have HOMO of the atom in position 4 uncapable to interact with the LUMO of the carbonyl; therefore, the interaction preferred is the HARD-HARD one (with the harder nucleophile amine) and the product of the reaction is preferentially the amino-nitrile; in the other case, the stereo electronic effect of the nitrogen on the carbonyl makes the N-methyl piperidone softer electrophile: therefore, the interaction preferred is SOFT-SOFT (so the one with the cyanide, a nucleophile softer than the amine).

## PRELIMINARY BIOLOGICAL EVALUATIONS.

The derivatives of these series were tested firstly on HeLa cells and then on Proximal Tubular Epithelial Cells (PTECs) in the laboratories of professor Alessandro Arcovito, section of Biochemistry of the Catholic University of the Sacred Heart based in Rome. Here, the test used for the evaluation of the inhibition

potential is a measurement of the mPTP-dependent alteration of the mitochondrial membrane potential, using carbonyl cyanide 4-(trifluoromethoxy)phenylhydrazone (FCCP) as stimulating agent for the mPTP opening. FCCP is an uncupling agent that causes depolarization of the mitochondrial membrane and one of the consequences of this is the mPTP opening (in fact mPTP opening leads to the loss of the proton gradient across membranes). Pre-treating cells with an inhibitor can diminish or avoid the entity of the depolarization. Briefly, this assay measures this gradient using the Nernstian dye tetramethylrhodamine methyl ester (TMRM). TMRM is a cell-permeable, cationic, red-orange fluorescent dye. TMRM freely passes through cellular and mitochondrial membranes and, because of the large electrochemical $H^+$ gradient across the mitochondrial inner membrane, accumulates in the mitochondrial matrix according to Δψm. Opening of mPTP causes an efflux of TMRM from the mitochondria that manifests as a reduction of fluorescence intensity that is easily measurable by fluorescence microscopy. Here are described the experiments using a series of monospiranic compounds; as reference, Oligomycin A was used (inhibition of 58%).

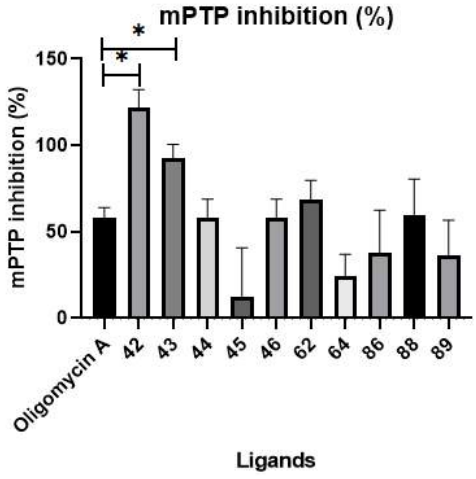


**Graph 3**. Measurement of the mPTP-dependent alteration of the membrane potential using FCCP on RPTEC cells. As reference Oligomycin A was used. Compound **42** and **43** show an interesting activity in avoiding the depolarization of the IMM.

From Graph 3, we can appreciate that a couple of compounds, in particular **42** and **43** are very interesting as inhibitory agents: compound **43** inhibits the mPTP opening for 92% and compound **42** seems to induce a hyperpolarization of the membranes. It is worth to note that these two compounds have in common the tosyl- moiety, which has confirmed to be fundamental for a good interaction with the target. Other compounds have an inhibitory potential very similar or slightly higher than the reference, but not in a significant way. Other test will be conducted to confirm all the data. To note, in this graph, results are expressed as mPTP inhibition percentage.

# 3.3 DISPIRANIC COMPOUNDS

Since we have developed monospiro compounds with promising results, we decided also to evaluate how the steric hindrance and the structural rigidity could affect the activity of the molecules to inhibit mPTP opening. We synthesized two small libraries of dispiro molecules, the former piperidine scaffold- based and the latter isatine scaffold- based. The syntheses were conducted following the "one pot reactions" or "tandem reactions" approach, minimizing the reaction steps. In the following paragraphs, it will be discussed the synthetic approach and the biological results concerning the testing of these compounds as modulators of mPTP opening.

## 3.3.1 PIPERIDINE SCAFFOLD-BASED DISPIRANIC COMPOUNDS

The first class of dispiranic compounds considered is that of the piperidine scaffold compounds. It seemed natural to us to use the same main core, as it has led to some remarkable results in monospiranic compounds. We therefore decided to combine this scaffold with tetrahydrothiophene, that is present in many natural and synthetic compounds with biological activity: antibacterial, antioxidant, enzyme activity and others; we assemble them in the hope of obtaining heterocycles with relevant biological activity.[46] These molecules have been obtained with a "domino reaction", that consists in a series of cascade reactions that constitute a relevant tool for the construction of complex organic molecules from simple substrates. A remarkable feature of this type of reaction is that it takes place with a mechanism such that all the atoms of the reactants are incorporated into the final product. This peculiarity avoids the need to isolate and purify waste products: bonds are thus formed in a stereoselective manner, in a single operation and with an 'eco-friendly' approach.

The library of dispiropiperidone - tetrahydrothiophene heterocyclic compounds was synthesized with two steps: initially, N-benzyl piperidone is alkylated in position 3 and 5 through a double aldolic reaction, followed by dehydration, with different aromatic aldehydes; then the intermediate reacts with 1,4-dithiane-2,5-diol, in presence of triethylamine (TEA), obtaining a double cyclization through a tandem reaction, which is Michael reaction.

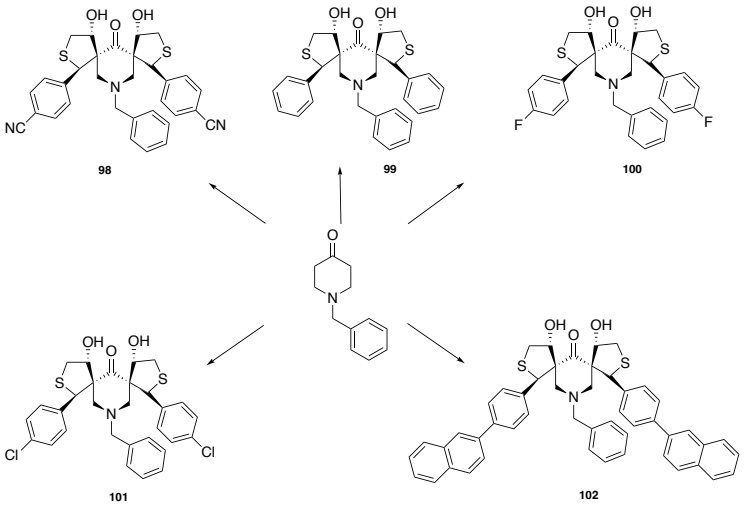


**Scheme 12**. Dyspiropiperidone - tetrahydrothiophene heterocyclic compounds' library.

### 3.3.1.1 REACTION MECHANISM TO SYNTHESIZE DYSPIROPIPERIDONE - TETRAHYDROTHIOPHENE HETEROCYCLIC COMPOUNDS

The first reaction is the alkylation of N-benzyl piperidone in position 3 and 5 with different aromatic aldehydes, through a double Knoevenagel-like reaction. N-benzyl piperidone in its enolic form, which works as nucleophile, attacks the aromatic aldehyde. Intermediates **93**-**97** are achieved after the dehydration of the aldol.

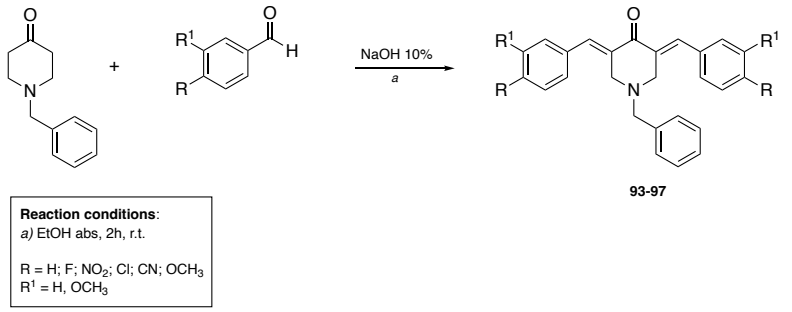


**Scheme 13**. Schematic procedure to obtain intermediates **93**-**97** through a double Knoevenagel reaction.

Once the intermediate is obtained, in these cases with yields between 32% and 73%, the cycles are closed to form the final dispiranic compound. The reagent used for this purpose is 1,4-dithiane,2,5-diol, which releases two molecules of 2-mercaptoacetaldehyde, which, once deprotonated by the TEA, acts as a nucleophile, attacking the carbon in beta of intermediate, through a Michael addition. A monospiranic intermediate product is thus obtained. Through another Michael addition, the final products (**98**-**102**) are then achieved, with yields between 30% and 92%.

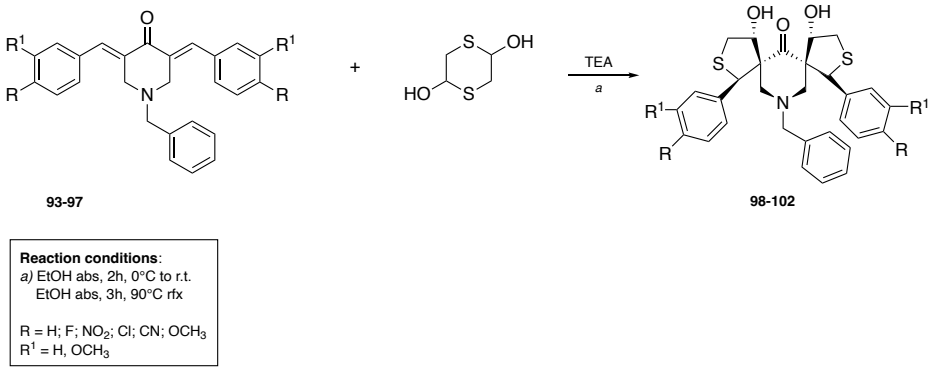


**Scheme 14**. Schematic procedure to obtain final dispiropiperidonic compounds **98**-**102**.

It is interesting to know that the second annulation involving the reaction of another anion of 2-mercaptoacetaldehyde to the monospiranic intermediate again occurs on the same side as the initial Micheal addition presumably in a bid to obviate its steric interaction with the initially generated benzylic carbon. [47]

## 3.3.2 ISATIN SCAFFOLD-BASED DISPIRANIC COMPOUNDS

Two series of compounds have been synthesized from isatin. This has been reacted with sarcosine and various cyclic ketones leading to the synthesis of several similarly structured dyspiropyrrolidinic compounds. The reactions were conducted using the one pot reactions technique: the final product, although molecularly rather complex, was obtained in a single step. Isatin has been used because of its interesting activity in the biological field, as it is present as a precursor in many natural compounds. In particular, some spiropyrrolidines have been shown to be potential anticonvulsants and antileukaemics and possess local anesthetic activity.[46] 5-Fluoro isatin, on the other hand, was chosen as it appears to have interesting pharmacodynamic properties concerning drug metabolism and elimination processes.

Below is an overview of compounds derived from isatin:

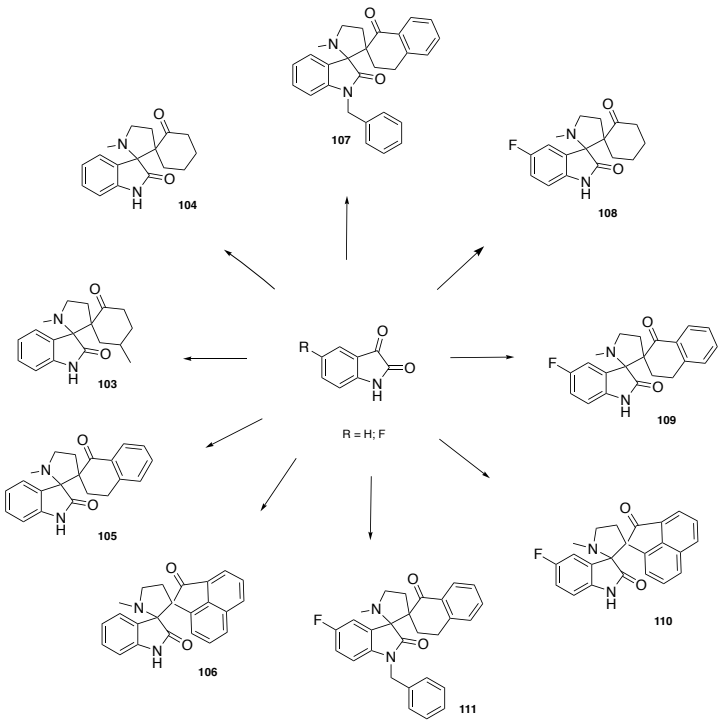


**Scheme 15**. Isatin and F-isatin scaffold- based compounds library.

Initially, monocyclic ketones were used (for compounds **103**, **104**, **108**). Subsequently, α-tetralone and acenaphthenone were chosen, in an attempt to insert additional aromatic elements into the molecule (**105**, **106**,**109**, **110**), with the aim of increasing the hydrophobic interactions of the drug with the enzyme.

Another route was also tried, using an amino acid other than sarcosine. It was therefore decided to perform a reductive amination on ß-alanine, using benzaldehyde as the alkylating agent, in order to obtain a secondary amine. The resulting dispiropyrrolidine-forming reaction, however, did not yield the desired results: it was rather difficult to isolate the product, which was moreover obtained in very low quantities and therefore with an unsatisfactory yield; furthermore, what we obtained was probably a diasteroisomeric mixture, since the TLC conducted shows two very close spots. This assumption is also confirmed by the fact that the analytical HPLC of the product shows two close peaks that are difficult to separate even by

preparative HPLC. The NMR of the product is very complex as frequent doubling is shown, which supports our hypothesis. Since this variation proved unpromising, it was decided to continue using sarcosine.

Scheme 16 below describes the general procedure for the synthesis of the dispiropyrrolidinic compounds.

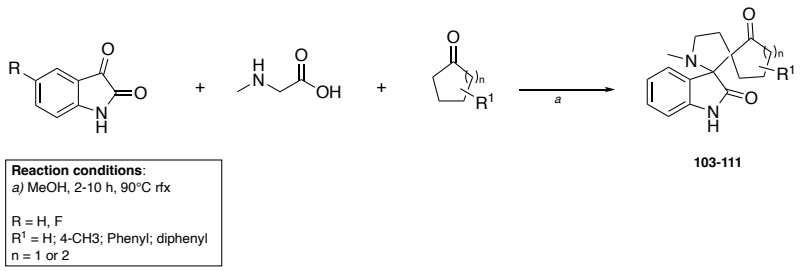


**Scheme 16**. General procedure for the synthesis of the isatin scaffold -based compounds **103**-**111**.

In two cases, we decided also to further increase the steric hindrance of the molecule, so we added a benzylic functionality. To do this, we have alkylated the amidic nitrogen of the isatin with benzyl bromide, after deprotonation with NaH, thus obtaining the products **107** and **111**, which are not only very bulky but also more hydrophobic.

These tandem reactions are of paramount importance in the context of green chemistry as they offer a convenient strategy for the rapid, elegant and convergent construction of complex organic molecules without isolating and purifying the intermediates resulting in substantial minimization of waste, labor, time and cost. Although the synthesis process is rather simple, the reaction mechanism of the molecules is not. It is, as described below (see section 3.3.2.2), rather complicated; yields are therefore modest (ranging between 32% and 70%). Hence, once the preliminary results were obtained, and as they were interesting, we decided to try to improve the reaction yields by better studying the reactivity of product and by-product formation and it will be discussed in the paragraph below.

### 3.3.2.1 Proposed mechanism and Observations on stereochemistry

The products described above were obtained in a single reaction step. The proposed mechanism to achieve these structurally very complex molecules is as follows:

a) in a first phase, isatin reacts on the carbonyl group with the amine moiety of sarcosine, to obtain the iminium salt **113**, which undergoes a nucleophilic attack by a water molecule, providing the imine **115** and a molecule of 2-hydroxyacetic acid **114**.

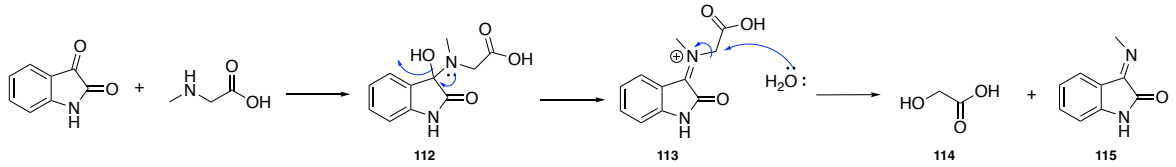


**Scheme 17**. Reaction between isatin and sarcosine, to obtain intermediates **114** and **115**.

b) then, the intermediate **114** reacts with another isatin molecule to obtain the addition product **116**, which, after decarboxylation, provides 3-hydroxyindolin-2-one **117** and a molecule of formaldehyde **118**.

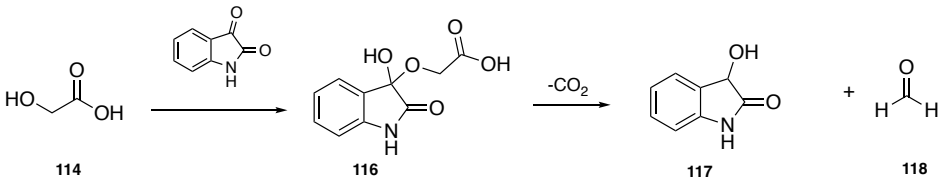


**Scheme 18**. Reaction between hydroxyacetic acid **114** and isatin to obtain 3-hydroxyindolin-2-one **117** (crucial for the by-product formation discussed below) and a molecule of formhaldeyde **118**, useful to provide the final desired compound.

c) As a last step, the previously obtained intermediate **113**, upon decarboxylation, leads to the formation of ilide **119**, which reacts with formaldehyde **118** to obtain the iminium alcohol **120**. The latter will then react with the ketone (in its enolic form) to obtain an addition product **122a-d**. Following rearrangement with the loss of a water molecule, the desired final product is thus obtained (specifically **103**-**111**).

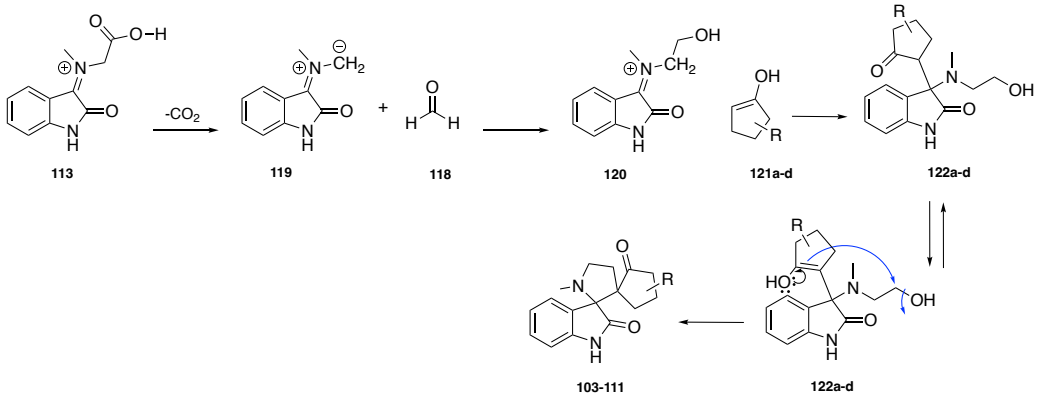


**Scheme 19**. Last steps to the formation of the desired final dispiropyrrolidinic compounds **103**-**111**.

This mechanism has been proposed by Kumar et al.[48] To summarize, the key step is the formation of azomethine ylide **119**, which reacts with enol to form adduct **122**; this rearranges and, subsequently, after cyclization and the loss of a water molecule, the dispiropyrrolidine is afforded.

During the synthesis we also observed something about the stereoselectivity of these reactions. Kumar et al reported that these types of reactions were diastereoselective. [49] This evidence was also confirmed by our small-scale syntheses. However, when we tried to scale up the synthesis in order to obtain the products in larger quantities, we observed two phenomena:

1) on the medium scale, two diasteroisomeric species of the product of interest are evident (clearly distinguishable by NMR analysis and confirmed by heterocorrelation, see Figure X below);

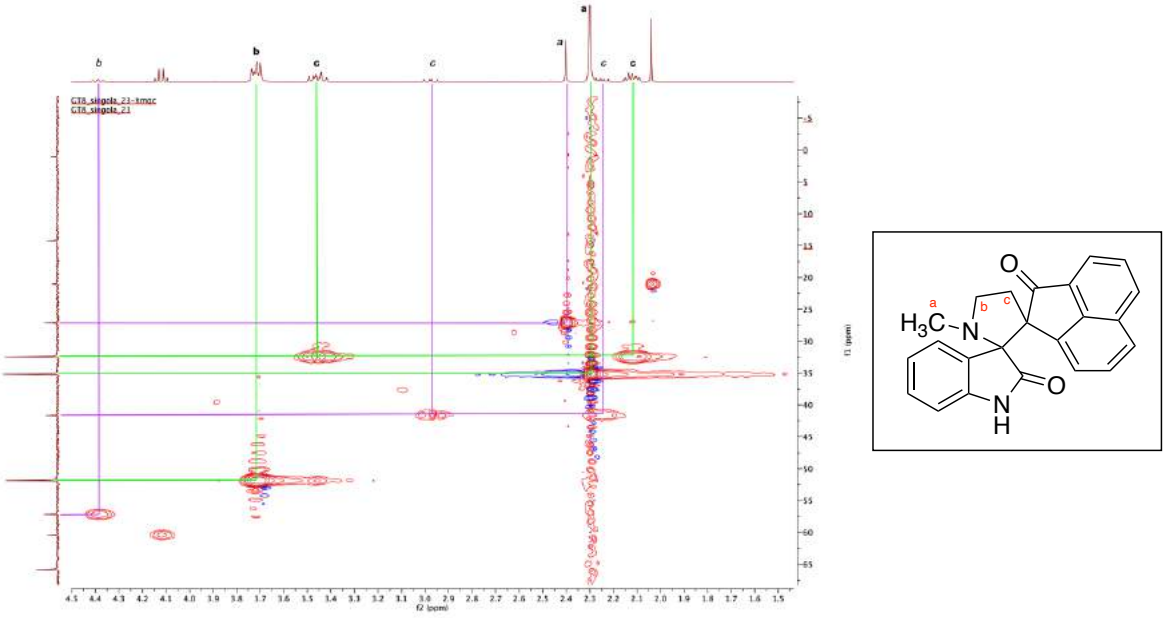


**Figure 20**. On the right, detail of HMQC analysis of compound 79. Matches relating to the majority diastereoisomer are highlighted in green; matches relating to the minority diastereoisomer are highlighted in pink. We assume that the majority compound is the one with the carbonyls in anti (letters in bold) and the trace compound is the one with the carbonyls in sin (letters in italics).

The fact that the reaction is stereoselective is evident on a small scale, as it gives rise to the enantiomeric mixture of compounds with carbonyls on opposite sides; on the medium scale, however, we also notice the formation of small but appreciable amounts of another species, presumably the diasteroisomer with the carbonyls on the same side. The figure below shows these structures (on the left the enantiomers with the 'anti' carbonyls and on the right the corresponding 'sin' carbonyls).

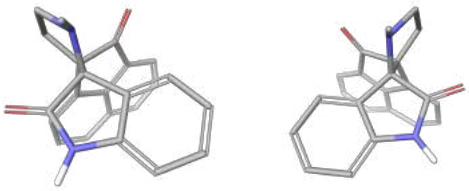

**Figure 21**. Favored enantiomeric couples of compound **106**. Here the structures with “anti” carbonyl groups are shown (in red).

To support our theories, computational studies on stability of intermediate **122** reveals that the preferential arrangement to obtain the final product is the one with the two carbonyl groups in anti, even though the syn conformation still occurs (and it is consistent with the NMR evidence discussed above).

2) the presence of a by-product is evident, which is favored on a large scale and whose formation is supported by the reaction mechanism proposed for the one-pot synthesis described above. The structure below represents the isolated impurity. NMR analysis (Figure 22) has been helpful to deduce the exact structure of the side product. Two diasteroisomeric species were also isolated for

this impurity in a 1:9.5 ratio, which can be clearly observed by the comparative NMR analysis shown below.

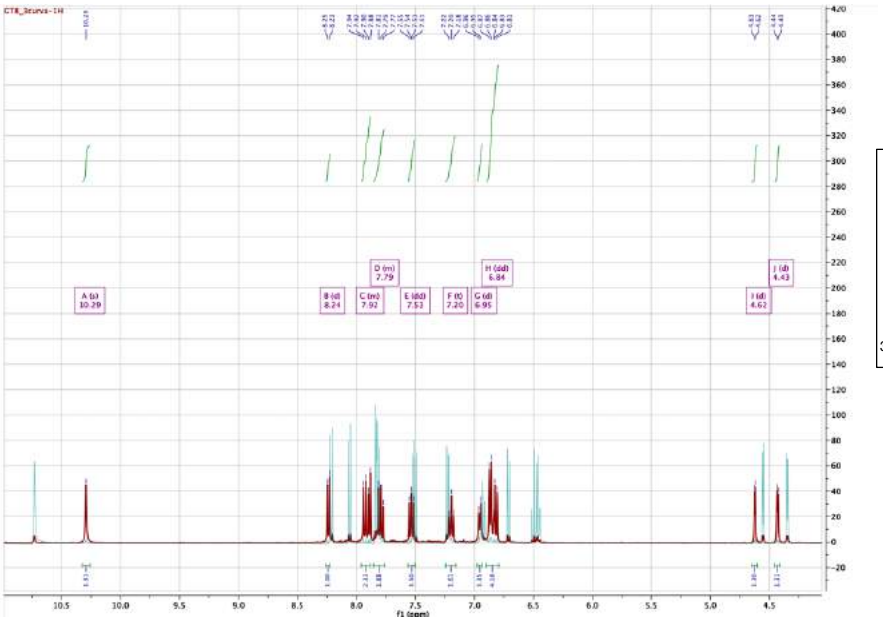

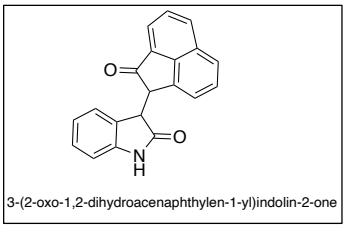


**Figure 22**. $^{1}H$ NMR spectra of the impurity. The two species refer to two diasteroisomers of the same compound. Two distinguishable species were appreciable only in larger scale synthesis. The structure of the compound is depicted on the right.

From the NMR shown above, the structure of the compound is clearly deducible. Its formation is probably due to the fact that, as described above in Schemes 17-19, the intermediate 3-hydroxyindolin-2-one **117** competes with iminium **120** in the reaction with acenaphthenone and thus gives rise to the substitution by-product, which appears to be the most favored one. Furthermore, the formation of this product is likely to be more noticeable on a medium scale, as the quantity of solvent used has not been scaled up in proportion to the reactants, and the reaction environment is therefore much more concentrated, so that the probability of side reactions occurring is greatly increased. This event also explains the rather low yield of this reaction (15-25%).

Given this assumption, therefore, we tried to analyze the reaction mechanism to improve the yield. As is evident from Schemes 18-19 (above), the crucial step in the formation of the dispiranic compound is the reaction of iminium **120** with the ketone (in its enolic form); intermediate **120** in turn derives from the reaction of ilide **119** with a molecule of formaldehyde **118** (obtained *in situ* from previous steps, and that maybe could evaporate from the environment, since the reaction is set to 90°C). We therefore tried to push the reaction forward by directly adding an equivalent of formaldehyde to the reaction medium: this approach yielded the desired results as the reaction proceeded much faster, the presence of impurity was minimized and the desired product was obtained in much better yield (65-77%).

## BIOLOGICAL EVALUATIONS.

Even for dispiranic compounds, $Co^{2+}$-calcein assay was performed, in order to evaluate the potential inhibitory activity on mPTP opening.

From the data proposed, which take the PP41 molecule as a term of comparison, it is demonstrated that compound **106** and **109** are very promising as mPTP opening inhibitors; in fact, as it can be appreciated from the Graph 4 below, compound **109** is active with an inhibition of mPTP opening for 45% and compound **106** even for 70%.

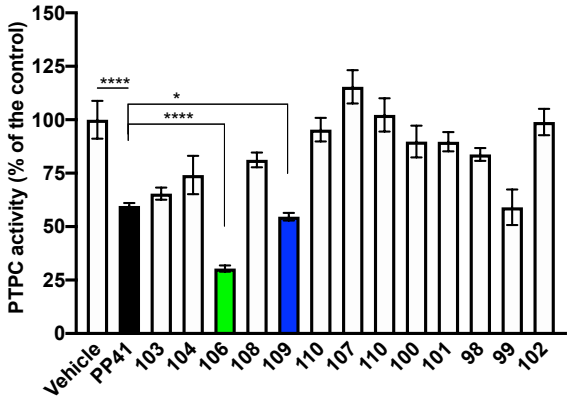


**Graph 4**. Histogram depicting the results obtained from the $Co^{2+}$-calcein test on AC16 treated with dispianic derivatives.

It appears that the presence of fluorine and aromatic elements (which increase both the possible hydrophobic interactions with the enzyme and the molecule's steric size) are crucial to the structure-activity relationship of these dispiranic derivatives.

The two most promising compounds (**106** and **109**) were chosen to investigate deeply their activity.

A wide number of *in vitro* tests have been performed to better analyze the biological profile of the most promising compounds. All the data has been obtained in collaboration with Professor Paolo Pinton's team of the department of Medical Sciences of the University of Ferrara. Here there is described a selection of those are more interesting for understanding the implications of mPTP opening inhibition in cardio protection.

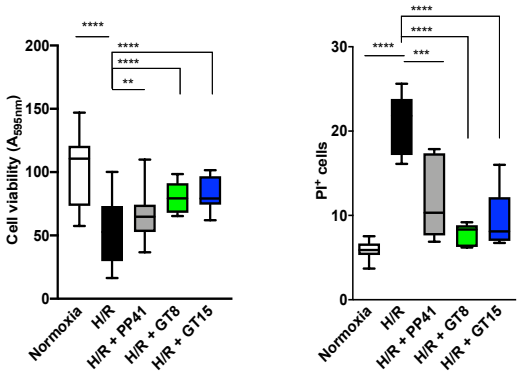


**Graph 5**. Cell viability upon H/R in vitro protocol quantified with crystal violet staining (on the left); cell death upon H/R protocol quantified with incorporated fluorescent PI (on the right).

AC16 cells were subjected to hypoxia/reoxygenation (H/R) conditions, being exposed to 1% $O_2$ at 37°C for 12 hours to simulate ischemia. At the time of reperfusion, cells were cultured with complete fresh medium (with or without the mPTP inhibitor) and measured 6 hours later.[44,50] As it can be appreciated from Graph 5, treatment with **106** and **109** highlights impressive results in cell viability, considering that the number of living cells is significantly close to that of control conditions (normoxia). Moreover, the data is consistent with the fact that the number of dead cells is significantly lower after the cells have undergone H/R treatment, as shown by the number of $PI^+$ cells. The biological meaning of these data is that compounds **106** and **109** are very promising as mPTP opening inhibitors and that they are cardioprotective agents, useful for recovering cell function after ischaemic reperfusion injury.

# 4. CONCLUSIONS AND FUTURE PERSPECTIVES

## 4.1 CONCLUSIONS.

The main purpose of this thesis project was the synthesis of small molecules as modulators of mPTP opening. Basing our assumptions on what is known about mPTP identity, formation and modulation, we developed different classes of molecules, which have in common structural elements able to interact with our supposed target (as widely discussed in Chapter 1 and 3). The main three different classes of synthesized compounds are urea-scaffold based compounds, monospiranic and dispiranic compounds.

The first class consists of structurally simple molecules, whose formation mechanism did not pose any particular synthetic problem and allowed us to isolate the desired products in good yields and pure enough to be tested *in vitro*. The library presents differently substituted compounds with different functionalities (urea, thiourea, carbamate). Although the biological results are not particularly exciting, this study has allowed us to understand how H-bond acceptor or donor moieties can affect the interaction with the target and the activity of the molecules, providing an interesting speculation, discussed widely in our published paper (and in paragraph 3.1).

With regard to monospiranic compounds, some considerations are in order. For the first class ($N_1$ modifications, paragraph 3.2.1.1) any particular synthetic issue was identified. We were able to provide the derivatives using a previously refined pathway, with good yields. Even if, also in this case, the biological results are not particularly interesting, we had the opportunity to develop a computational model to predict, trough CADD methods, the behavior of our compounds: the tests, in fact, have been demonstrated useful to confirm the reliability of our model and to comprehend deeply the data obtained (with particular regards to molecular dynamic studies).

As regard the second and the third classes of 1,3,8-triazaspiro[4.5]decan-4-one derivatives ($N_8$ and combined $N_1$ and $N_8$ modifications), the syntheses have demonstrated to be more challenging. Although we experienced several problems with the various steps in the synthesis, we were able to develop alternatives that allowed us to circumvent the inconveniences and achieve the desired products. Also in this case, the results have demonstrated to be consistent with *in silico* processed data, and they are also very promising, from a biological point of view, and worthful to be more investigated.

The latter part of this project has been focused on the synthesis of dispiranic compounds. This project was initially based on our curiosity to know how an increase of spirocentres (that make the molecule more rigid) could affect the ability to interact with the target. It seemed natural to speculate on this in the light of the very interesting results obtained with the monospiro compounds, and thanks to this resourcefulness we had the opportunity to obtain compounds with very interesting behavior. We therefore designed compounds with the same elements useful for interaction (aromatic element, carbonyl group, five-atoms cycle, nitrogen

as H-bonds acceptor), but with increased rigidity and steric size. We were able to obtain all the products in good yield and the opportunity to study the scale up of the reaction, that challenged us a lot, but gave us important information about the mechanistic dynamics of product formation. The biological evaluations were very impressive, so much so that several functionality assays were carried out on a couple of compounds to further investigate their behavior and properties.

Overall, this study, which combined computational, synthetic and biochemical skills, has enabled us to further develop our knowledge in this area, although there is still much to be ascertained. The chemical background was a fundamental starting point for the development of our project, as well as the know-how and collaborations with other research groups: this has enabled the development of a multidisciplinary study, with the ultimate aim of obtaining as much information as possible on this topic, as well as opening up hopes for a possible therapy for organ reperfusion damage, which currently represents a serious health problem.

## 4.2 FUTURE PERSPECTIVES.

Future perspectives will be focused on further investigations of the compounds behaviour *in vivo*: we have developed a protocol for the solubilization of three compounds in pig serum and, in collaboration with professor Fabio Anastasio Recchia, Sant'Anna School of Advanced Studies (Pisa, Italy), we are approaching the test on pig subjected to a heart ischemia and then perfused and treated with our most promising inhibitors.
On the other hand, the biological evaluations of all the synthesized compounds will be confirmed and deepened, in order to better understand and compare their functionality both in the kidney and in the heart models of IRI, using respectively renal proximal tubular epithelial cells and cardiomyocytes. In this way we will be able to compare the functionality of the compounds in two models, which are different but similarly affected by the problems arising from the IRI.
From a chemical point of view, our intention is to more investigate the formation of the dispiropyrrolidinic compounds, aided by molecular dynamics that can help us to comprehend how precisely the intermediates are arranged in space in order to obtain the desired product.

With this multidisciplinary project, regarding the development of valid mPTP inhibitors, our hope is to have contributed and will contribute pragmatically to find a possible therapy for this critical medical condition that is IRI, making considerable progress in the field of research about how the opening of the mitochondrial permeability transition pore interferes with the life expectancy of patients.

# 5. EXPERIMENTAL SECTION

Analytical thin-layer chromatography (TLC) was carried out using precoated silica gel plates Macherey-Nagel poligram SIL G/UV254 with thickness of the layer of 0,25 mm and further monitoring with 254/365 nm UV lamp. Column chromatography was performed using Isolera One (Biotage Sweden) or traditional column chromatography with silica gel 60 (40-63 um). Melting point was measured with a Reichert Termovar (Austria). 1H, 13C, DEPT, bidimensional (gCOSY) and heterocorrelated (gHMQC, gHMBC) NMR spectra were recorded on a VARIAN 400 MHz instrument. Chemical shifts (¤) are reported in parts per million (ppm), using 7.256 ppm peak of deuterated chloroform as an internal standard and coupling constants (J) are reported in Hertz. Following abbreviations have been used for multiplicity: s=singlet, d=doublet, t=triplet, q=quartet, m=multiplet, bs=broad signal, dd=doublet of doublets, dt=doublet of triplets, td=triplet of doublets. Mass spectral analysis were performed by ESI MICROMASS ZMD 2000 electrospray mass spectrometer, after dissolution of compounds in a solution composed by 40:60:0,1 of H2O:CH3CN:TFA. High resolution mass spectrometry data were achieved using a ESI-QTOF 6520 instrument coupled with a nano HPLC with Chip Cube® technology (Agilent Tecnologies, USA) For analytical controls Beckmann System Gold 168 HPLC have been used with LC column Kinetex 5µm EVO C18 100 A (250 X 4.6 mm) and a variable wavelength UV detector fixed to 220 nm. Analysis were conducted using two solution A and B containing, respectively, 100:0,1 H2O:TFA and 40:60:0,1 of H2O:CH3CN:TFA with different gradients for the products. For purification Water Delta Prep 4000 HPLC have been used with column Jupiter 10 µm C18 AXIA (100x 30,00 mm). For the hydrogenation reactions we used a continuous flow reactor H-Cube® (Thales-Nano, Hungary).

## 5.1 UREA- BASED COMPOUNDS.

### 5.1.1 GENERAL PROCEDURE FOR THE SYNTHESIS OF SYMMETRIC UREAS **1-6.**

To a solution of primary amine (2 eq, 7.54 mmol) in $CH_2Cl_2$ or THF (10 mL) was added carbodiimidazole (CDI) (1 eq, 3.77 mmol). The solution was then stirred at room temperature or under reflux for 3-18 h. After the reaction was complete, as indicated by TLC, the precipitate was filtered and washed with $Et_2O$ to afford the product as a white solid.

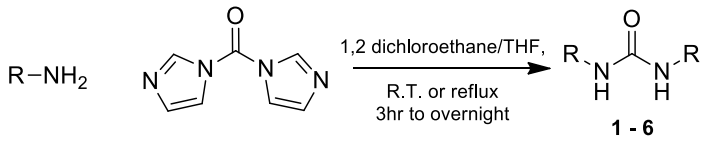


**Compound 1**. Synthesis of *1,3 dicyclopentyl-urea*
*Reaction solvent:* $CH_2Cl_2$;
MS (ESI): m/z $[M+H]^+$ 196.29 g/mol;
*Yield:* 80%;
*mp:* 235-240 °C;

**$^1$H NMR** *(400 MHz, DMSO-$d_6$)* $\delta$ 5.60 (d, $J$ = 7.3 Hz, 1H), 3.87 – 3.72 (m, 1H), 1.72 (m, 2H), 1.68 – 1.51 (m, 2H), 1.45 (m, 2H), 1.22 (m, $J$ =, 2H).

**$^{13}$C NMR** *(101 MHz, DMSO-$d_6$)* $\delta$ 157.30, 50.82, 33.01, 23.12.

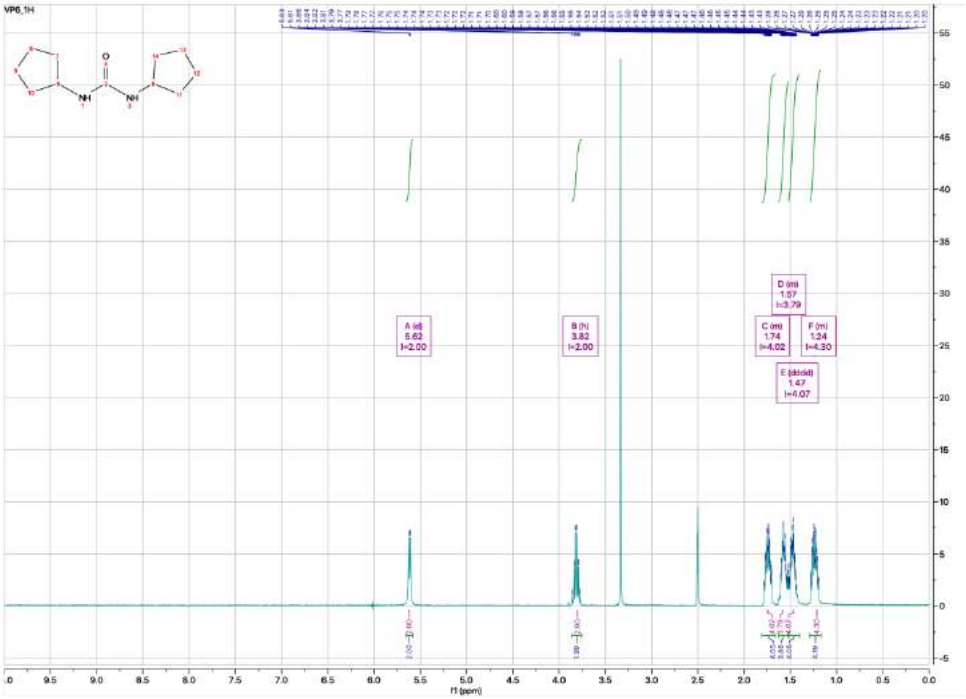

$^1$H NMR spectrum of compound **1**.

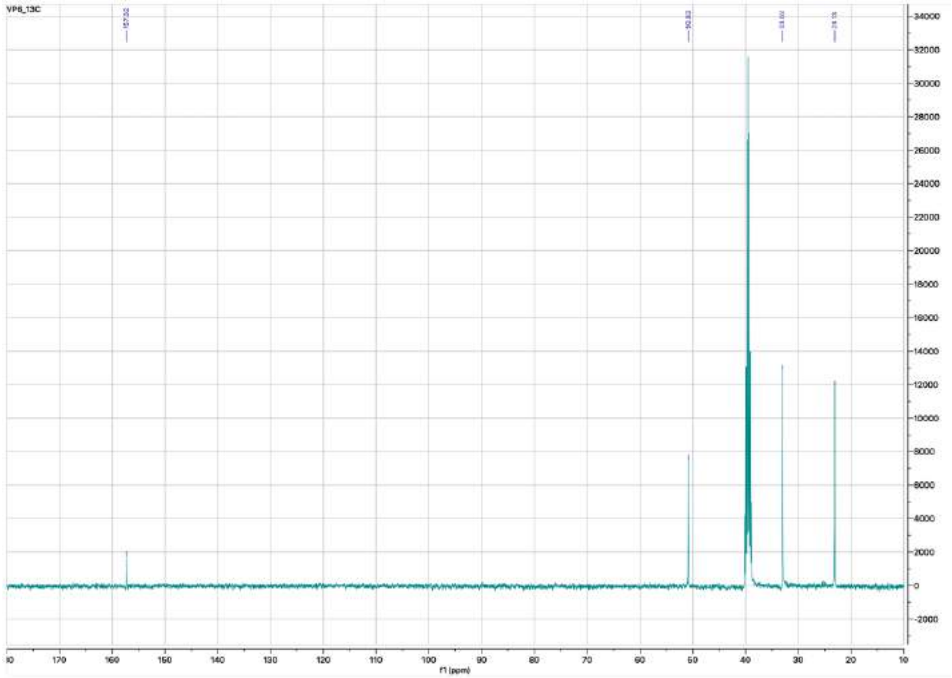

$^{13}$C NMR spectrum of compound **1.**

**Compound 2.** Synthesis of *1,3-dicyclopropyl-urea*

*Reaction solvent:* $CH_2Cl_2$;

MS (ESI): m/z $[M+H]^+$ 140.18 g/mol;

*Yield:* 61%;

*mp:* 168-173 °C;

**$^1$H NMR** *(400 MHz, DMSO-$d_6$)* $\delta$ 6.01 (s, 1H), 2.36 (m, 1H), 0.60 – 0.45 (m, 2H), 0.38 – 0.23 (m, 2H).

**$^{13}$C NMR** *(101 MHz, DMSO-$d_6$)* $\delta$ 159.41, 22.46, 6.46.

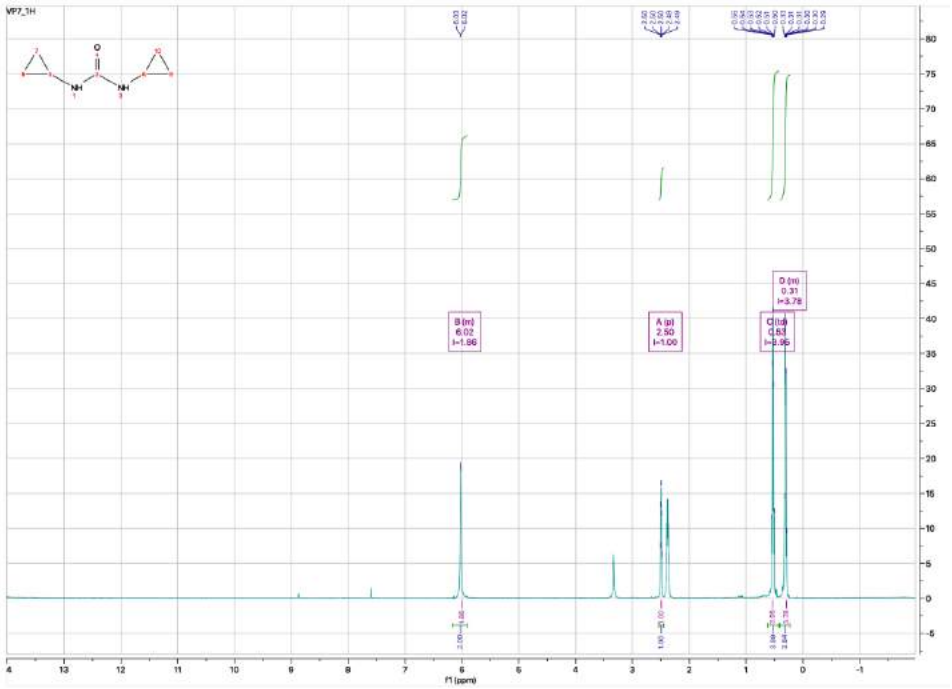

$^1$H NMR spectrum of compound **2**.

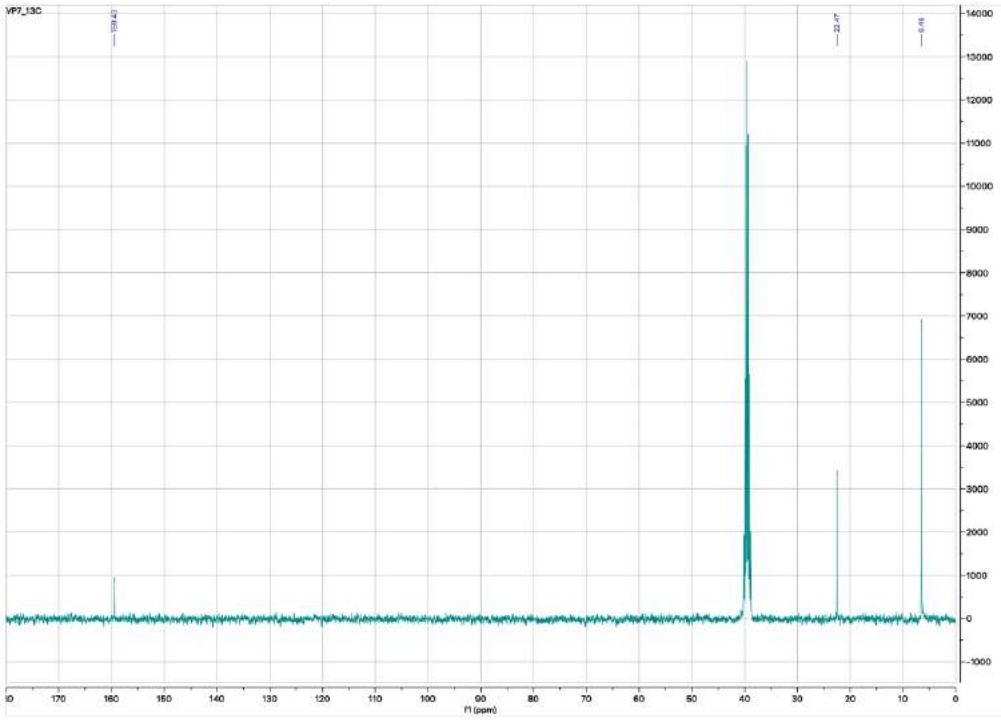

$^{13}$C NMR spectrum of **2.**

**Compound 3.** Synthesis of *1,3-diphenyl-urea*

*Reaction solvent:* $CH_2Cl_2$;

MS (ESI): m/z $[M+H]^+$ 212.25 g/mol;

*Yield:* 88%;

*mp*: 257-261 °C;

**$^1$H NMR** *(400 MHz, DMSO-$d_6$)* $\delta$ 8.64 (s, 1H), 7.43 (dd, $J$ = 8.6, 1.0 Hz, 2H), 7.26 (m, 2H), 6.99 – 6.90 (m, 1H).

**$^{13}$C NMR** *(101 MHz, DMSO-$d_6$)* $\delta$ 152.50, 139.69, 128.78, 121.79, 118.14.

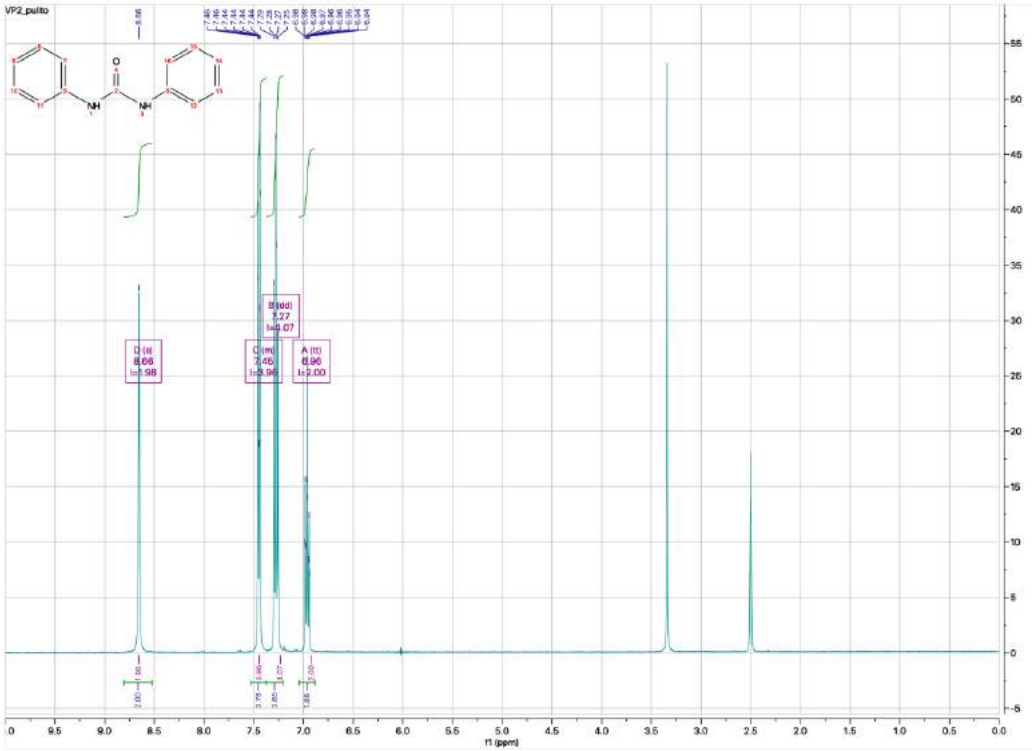

$^1$H NMR spectrum of compound **3**.

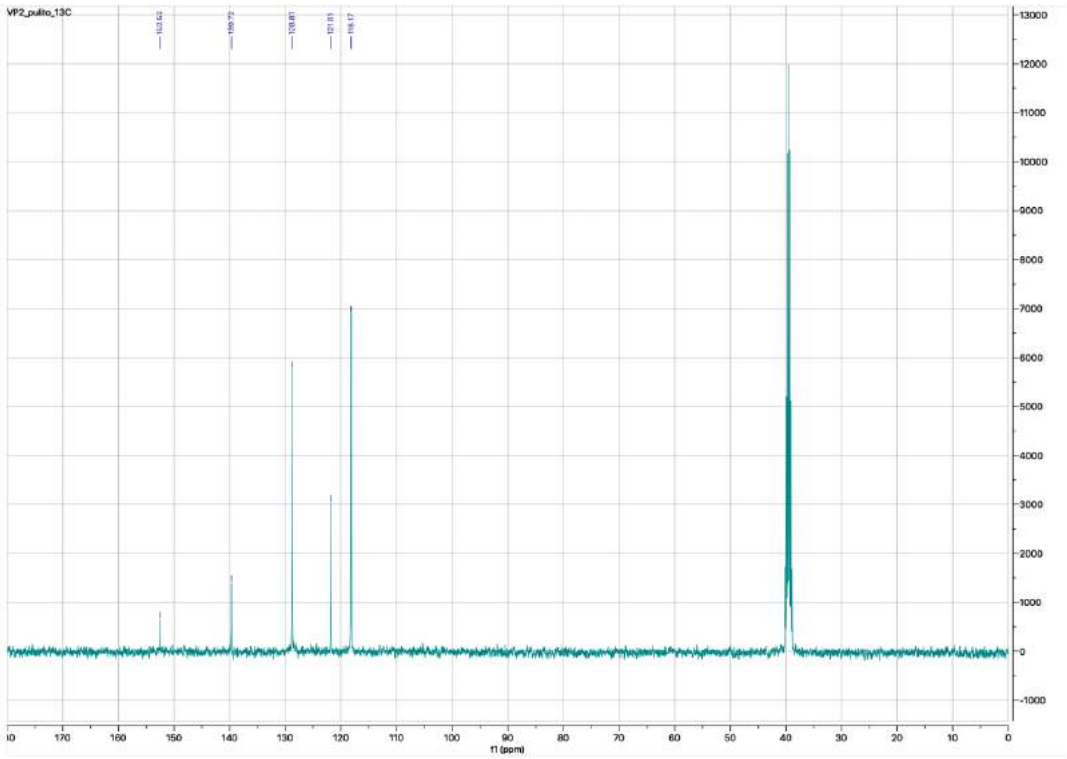

$^{13}$C NMR spectrum of compound **3**.

**Compound 4.** Synthesis of *1,3-bis(4-methoxyphenyl)urea*

*Reaction solvent:* $CH_2Cl_2$;

MS (ESI): m/z $[M+H]^+$ 272.30 g/mol;

*Yield:* 85%;

*mp:* 250 – 253 °C;

**$^{1}$H NMR** *(400 MHz, DMSO-$d_6$)* $\delta$ 8.36 (s, 1H), 7.36 – 7.27 (d, *J* = 8.0 Hz, 2H), 6.83 (d, *J* = 9.0 Hz, 2H), 3.69 (s, 3H).

**$^{13}$C NMR** *(101 MHz, DMSO-$d_6$)* $\delta$ 154.29, 132.94, 119.86, 113.94, 55.15.


$^{1}$H NMR spectrum of compound **4**.

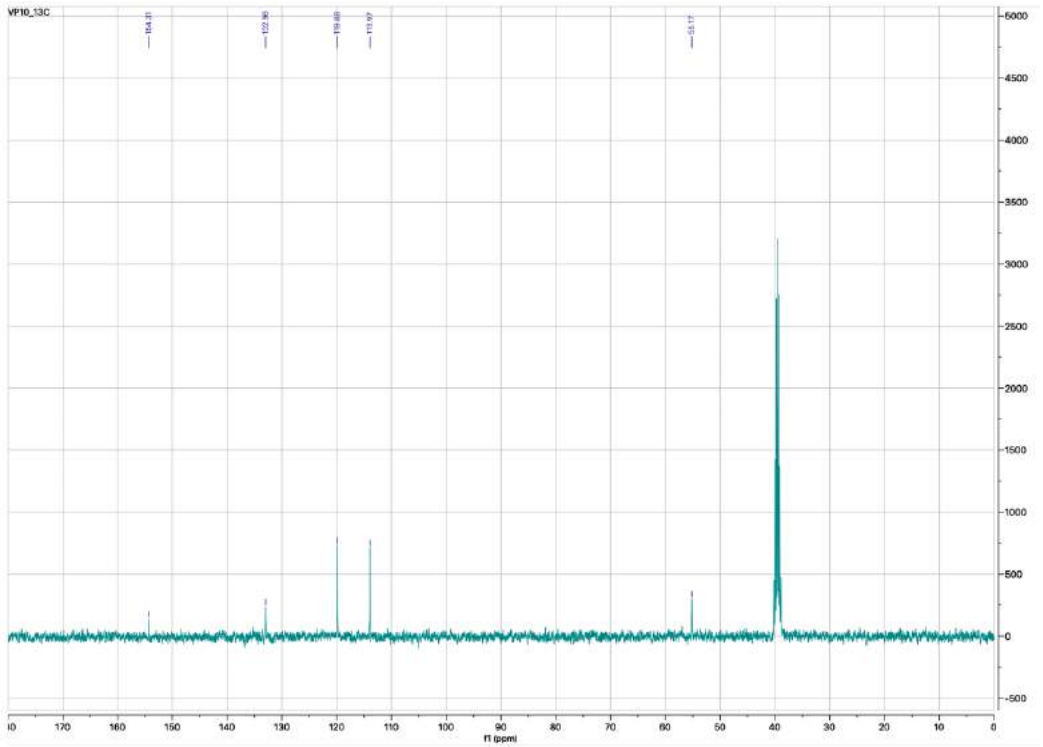


$^{13}$C NMR spectrum of compound **4**.

**Compound 5.** Synthesis of *Diethyl 4,4'- (carbonylbis(azanediyl)) dibenzoate*

*Reaction solvent:* $CH_2Cl_2$;

MS (ESI): m/z $[M+H]^+$ 356.37 g/mol;

*Yield:* 80%;

*mp:* 225 – 228 °C;

**$^1$H NMR** *(400 MHz, DMSO-$d_6$)* $\delta$ 9.28 (s, 1H), 7.88 (d, *J* = 8.8 Hz, 2H), 7.58 (d, *J* = 8.9 Hz, 2H), 4.26 (q, *J* = 7.1 Hz, 2H), 1.29 (t, *J* = 7.1 Hz, 3H).

**$^{13}$C NMR** *(101 MHz, DMSO-$d_6$)* $\delta$ 165.38, 151.89, 143.94, 130.38, 123.05, 117.48, 60.34, 14.26.

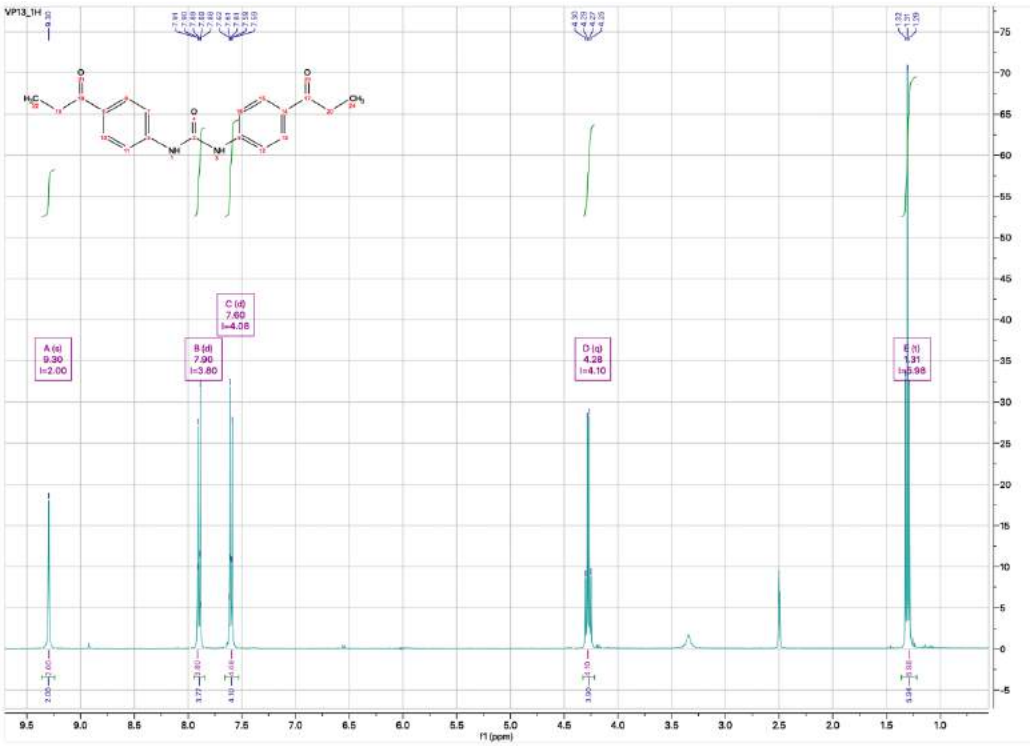

$^1$H NMR spectrum of compound **5.**

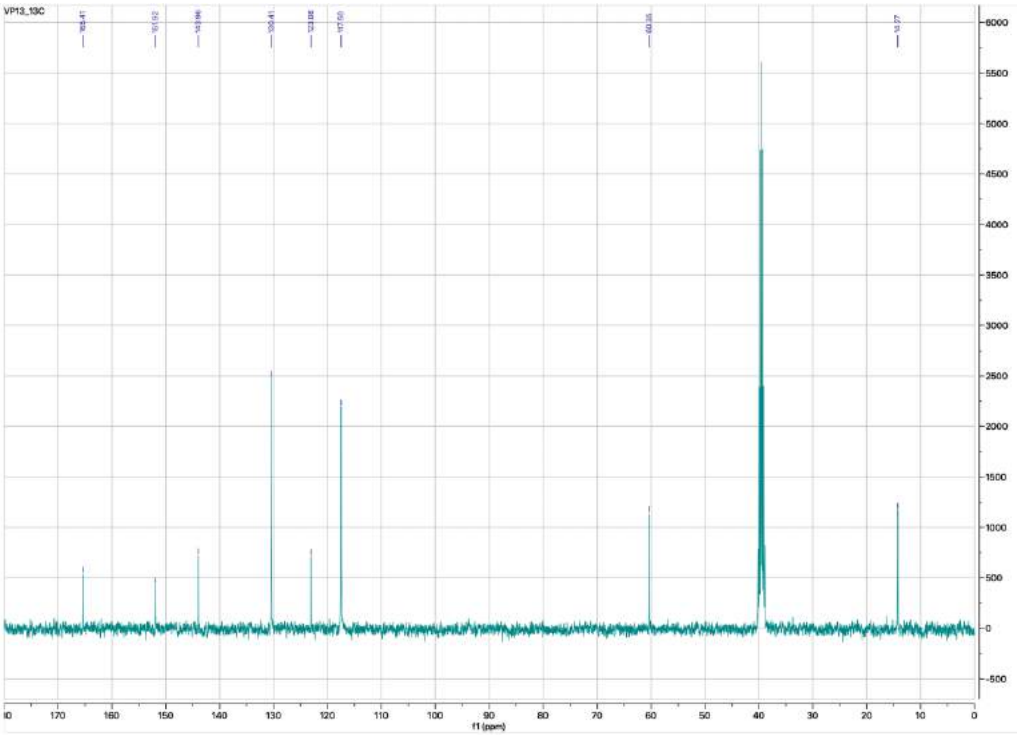


$^{13}$C NMR spectrum of compound **5.**

**Compound 6.** Synthesis of *1,3-bis(4-cyanophenyl)urea*

*Reaction solvent:* THF;

MS (ESI): m/z $[M+H]^+$ 262.27 g/mol;

*Yield:* 25%;

*mp:* 266 – 269 °C;

**$^1$H NMR** *(400 MHz, DMSO-$d_6$)* $\delta$ 9.43 (s, 1H), 7.73 (d, *J* = 8.5 Hz, 2H), 7.63 (d, *J* = 8.8 Hz, 2H).

**$^{13}$C NMR** *(101 MHz, DMSO-$d_6$)* $\delta$ 151.80, 143.70, 133.34, 119.22, 118.37, 103.79.

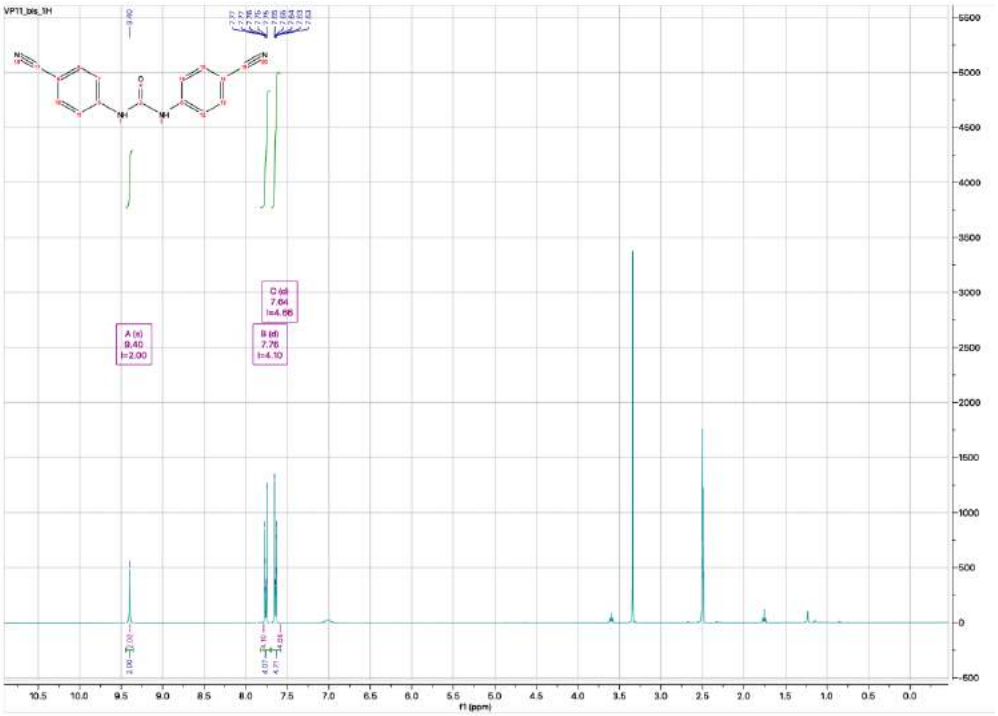

$^{1}$H NMR spectrum of compound **6.**

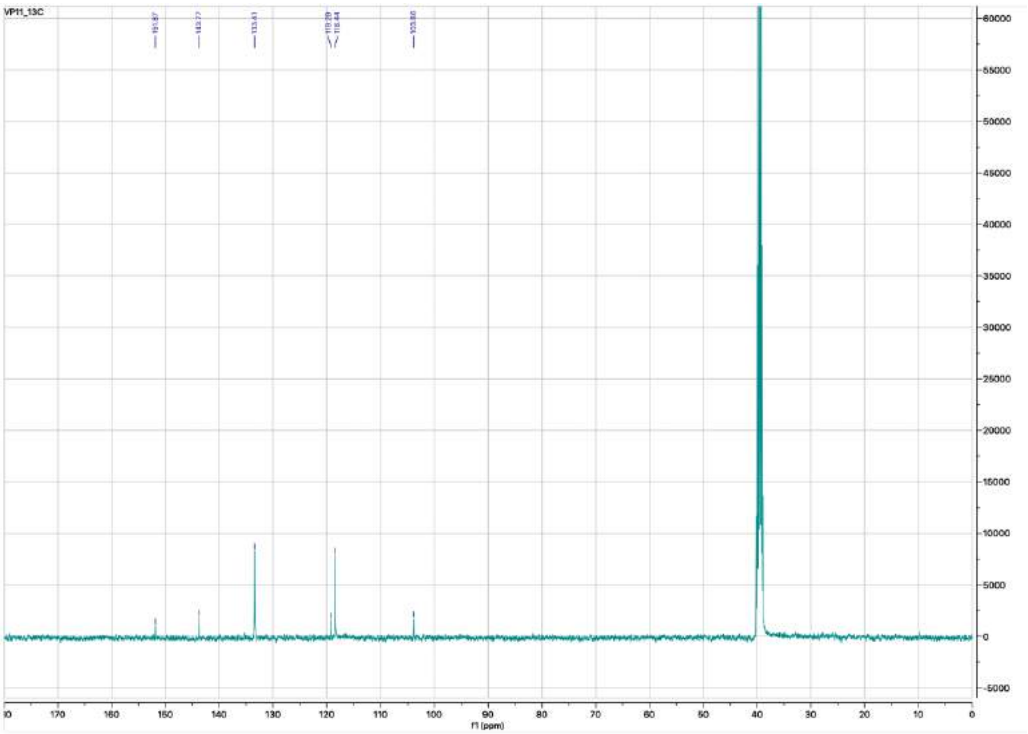

$^{13}$C NMR spectrum of compound **6.**

## 5.1.2 General procedure for the synthesis of 1, 3 dibenzylurea, asymmetric ureas and thioureas **7-12.**

To solution of amine (1 eq, 4.8 mmol) in 1,2 dichlorethane or THF (30 mL) was added isocyanate/isothiocyanate (1 eq, 4.8 mmol). The solution was then stirred at room temperature for 18 h. After the reaction was complete as indicated by TLC, the solution was evaporated and washed two times with $Et_2O$ to afford the product as a white solid.

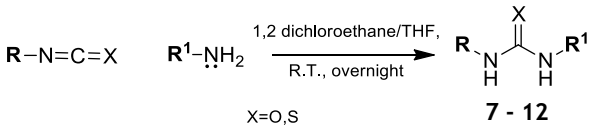


**Compound 7.** Synthesis of *1, 3-dibenzylurea*

*Reaction solvent:* 1,2 dichlorethane;

MS (ESI): m/z $[M+H]^+$ 240.30 g/mol;

*Yield:* 89%;

*mp:* 169 – 173 °C;

**$^1$H NMR** *(400 MHz, DMSO-$d_6$)* δ 7.34 – 7.15 (m, 5H), 6.42 (t, *J* = 6.0 Hz, 1H), 4.21 (d, *J* = 6.0 Hz, 2H).

**$^{13}$C NMR** *(101 MHz, DMSO-$d_6$)* δ 158.08, 140.93, 128.21, 126.98, 126.56, 67.03, 42.96, 25.14.

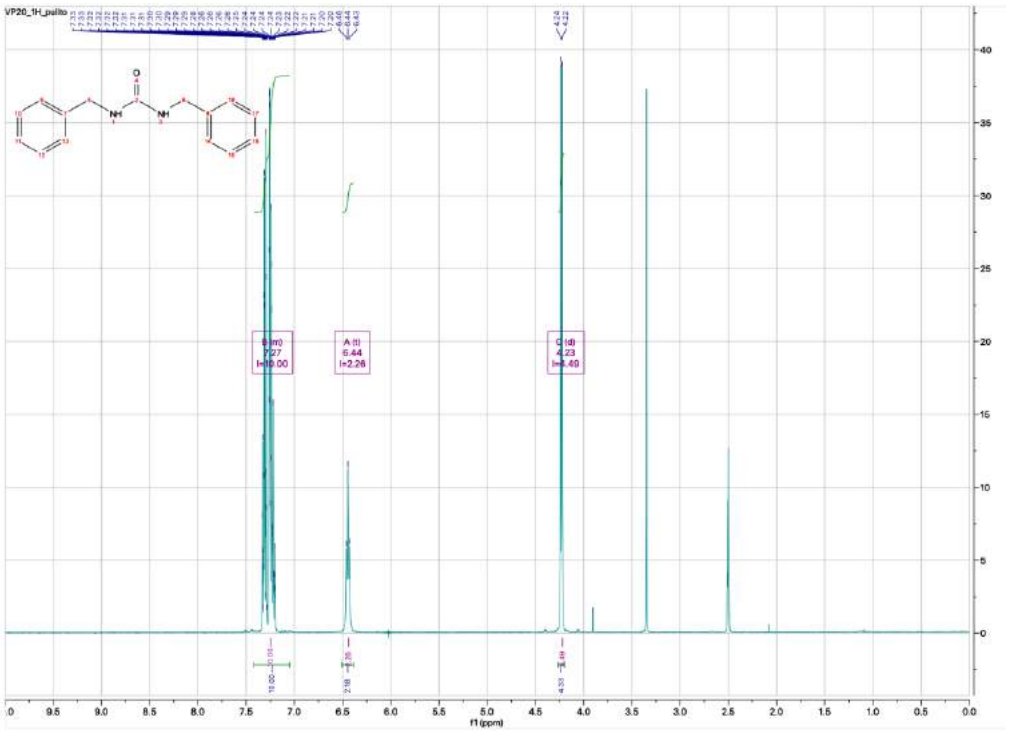

$^1$H NMR spectrum of compound **7**.

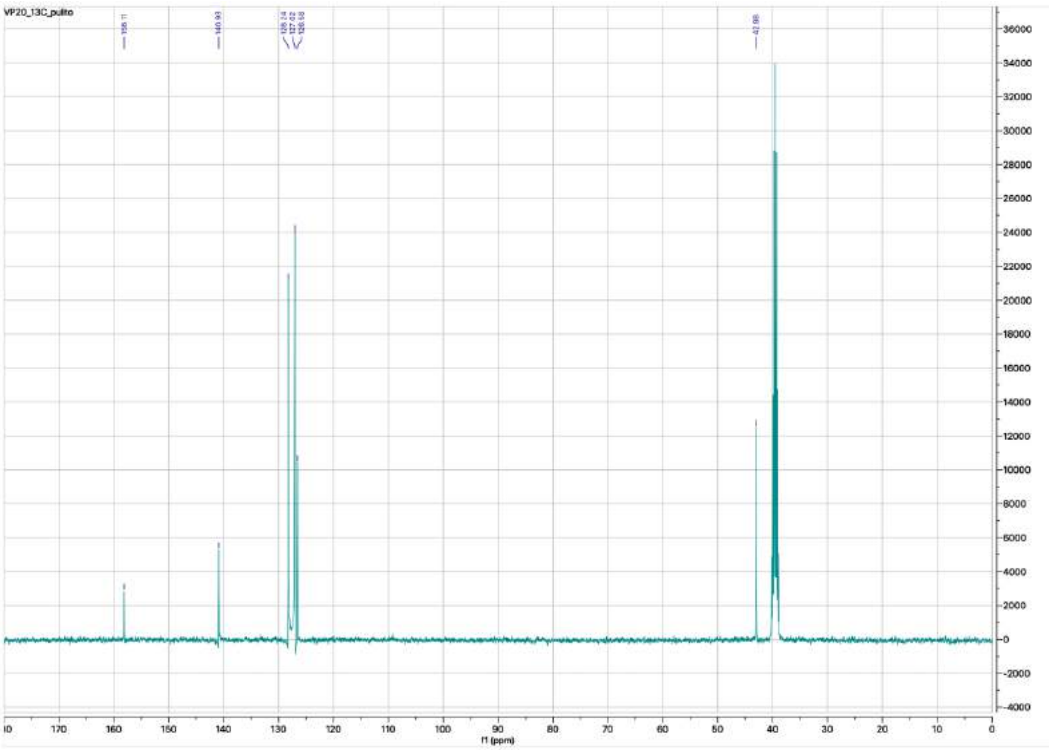


$^{13}$C NMR spectrum of compound **7**.

**Compound 8.** Synthesis of *1-(tert-butyl)-3-cyclohexylurea*

*Reaction solvent:* THF;

MS (ESI): m/z $[M+H]^+$ 198.31 g/mol;

*Yield:* 84%;

*mp:* 225 °C;

**$^1$H NMR** *(400 MHz, DMSO-$d_6$) δ* 5.53 – 5.43 (m, 2H), 3.31 (s, 6H), 1.69 (m, 2H), 1.59 (m, 2H), 1.46 (s, 1H), 1.29 – 0.91 (m, 9H).

**$^{13}$C NMR** *(101 MHz, DMSO-$d_6$) δ* 156.69, 48.88, 47.19, 33.40, 29.36, 25.34, 24.47.

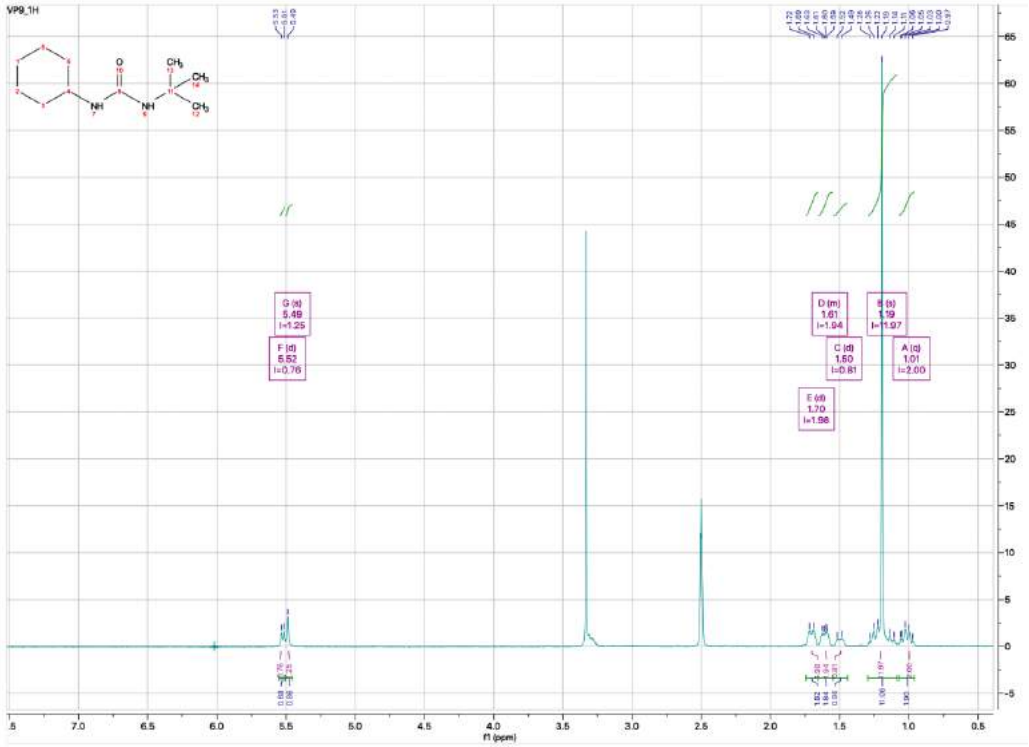

$^{1}$H NMR spectrum of compound **8**.

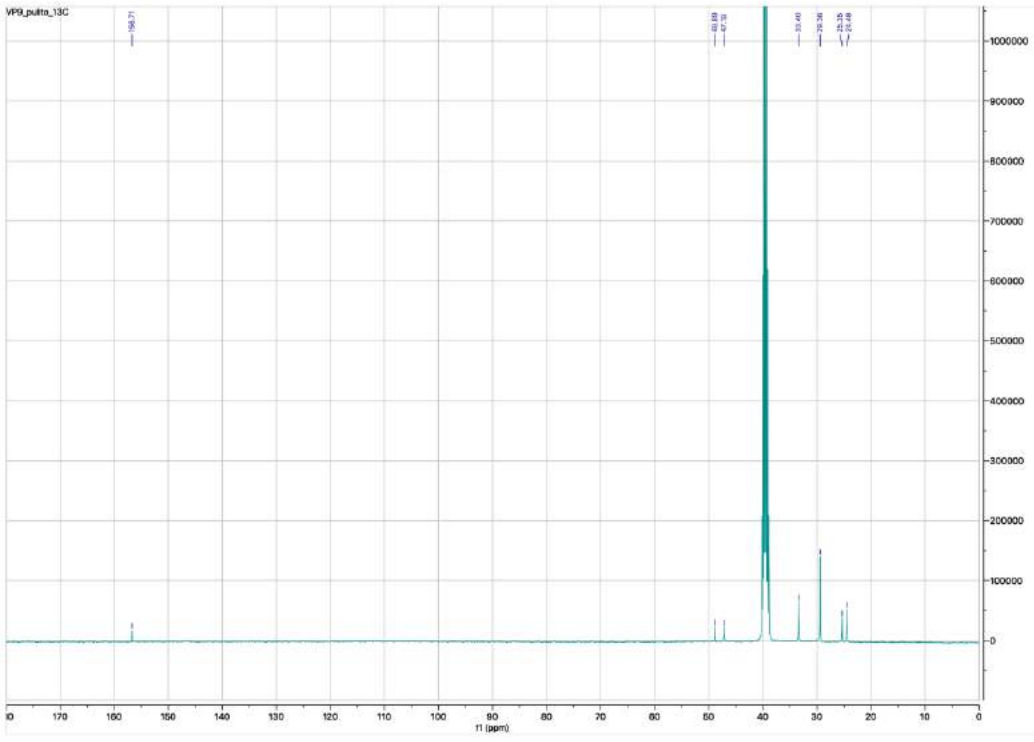

$^{13}$C NMR spectrum of compound **8**.

**Compound 9.** Synthesis of *1-(4-methoxyphenyl)-3-phenylurea*

*Reaction solvent:* 1,2 dichlorethane.

MS (ESI): m/z $[M+H]^+$ 242.27 g/mol;

*Yield:* 86.73%;

*mp:* 194 – 199 °C;

**$^1$H NMR** *(400 MHz, DMSO-$d_6$)* $\delta$ 8.55 (s, 1H), 8.44 (s, 1H), 7.49 – 7.11 (m, 6H), 6.99 – 6.66 (m, 3H), 3.69 (s, 3H).

**$^{13}$C NMR** *(101 MHz, DMSO-$d_6$)* $\delta$ 154.42, 152.71, 139.90, 132.71, 128.75, 121.59, 119.98, 118.04, 113.98, 55.17.

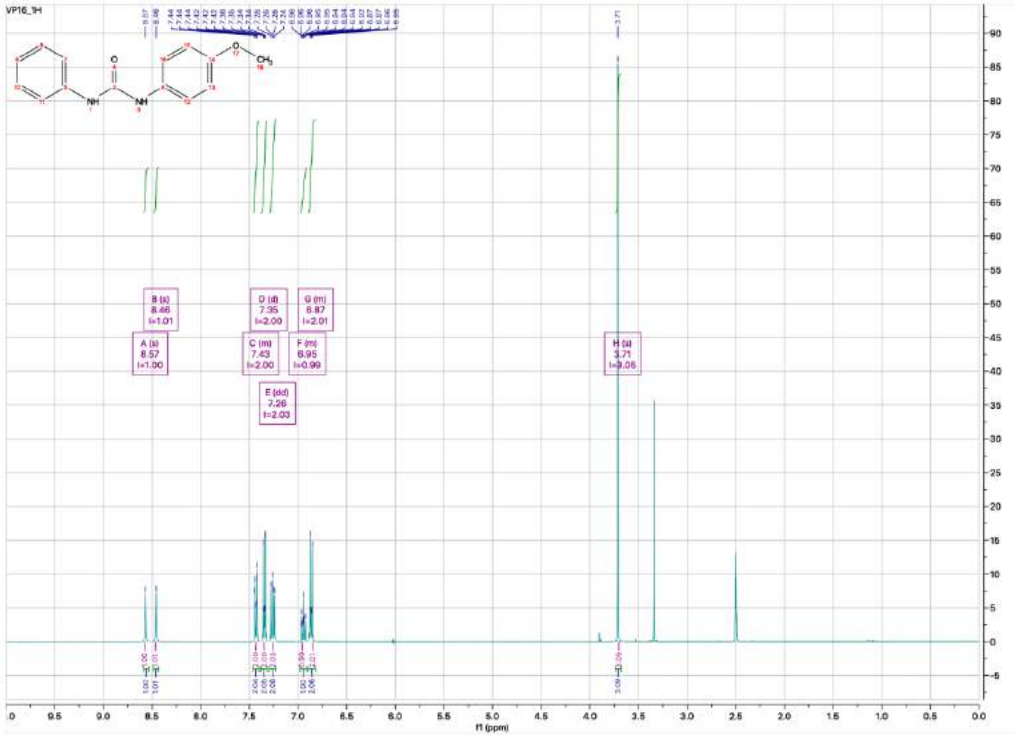


$^1$H NMR spectrum of compound **9.**

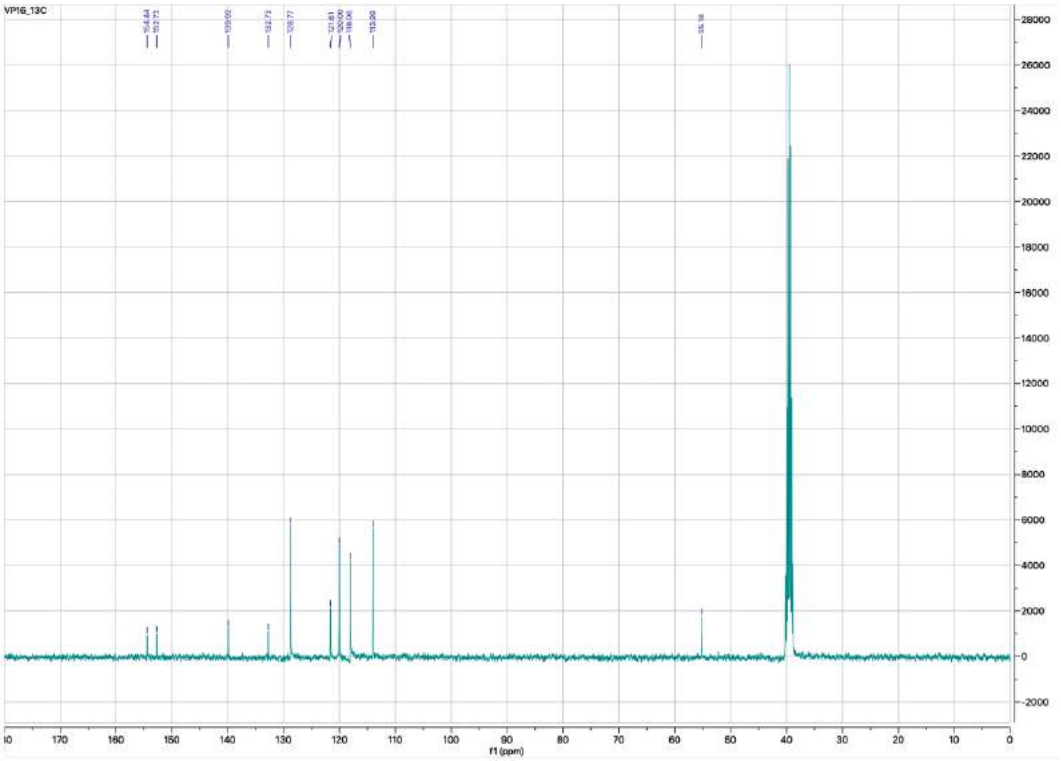


$^{13}$C NMR spectrum of compound **9**.

**Compound 10.** Synthesis of *1,3 Dicyclohexylthiourea*

*Reaction solvent:* 1,2 dichlorethane;

MS (ESI): m/z $[M+H]^+$ 240.41 g/mol;

*Yield:* 88.12 %;

*mp:* 184-187 °C;

**$^1$H NMR** *(400 MHz, DMSO-$d_6$)* *δ* 7.07 (d, *J* = 7.9 Hz, 1H), 3.93 (s, 1H), 1.81 (m, 2H), 1.68 – 1.40 (m, 3H), 1.36 – 0.96 (m, 5H);

**$^{13}$C NMR** *(101 MHz, DMSO-$d_6$)* δ 179.93, 51.47, 32.37, 25.22, 24.51.

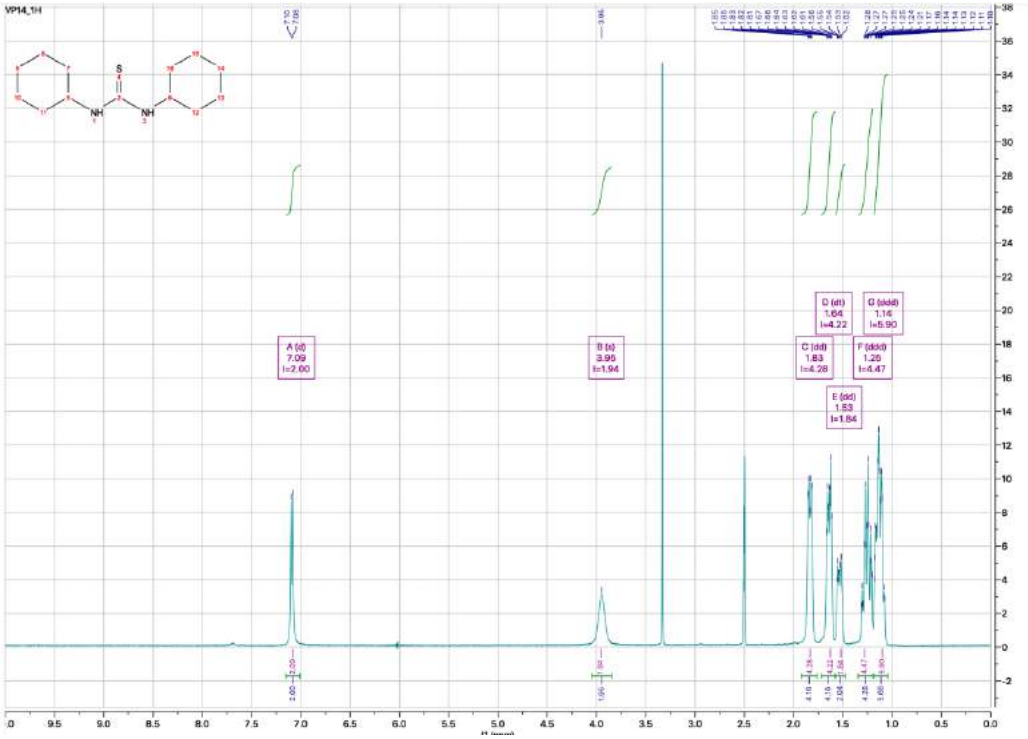


$^1$H NMR spectrum of compound **10**.

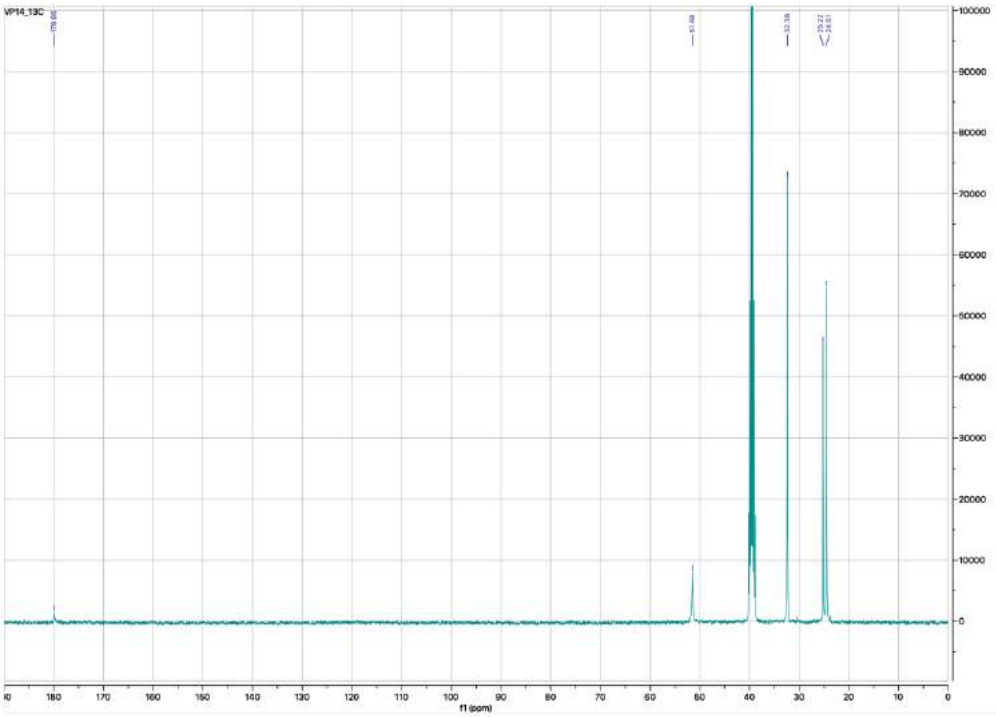

$^{13}$C NMR spectrum of compound **10**.

**Compound 11.** Synthesis of *1, 3-dibenzyl-thiourea*

*Reaction solvent:* 1,2 dichlorethane;

MS (ESI): m/z $[M+H]^+$ 256.37 g/mol;

*Yield:* 88.66 %;

*mp:* 169 - 173 °C;

**$^1$H NMR** *(400 MHz, DMSO-$d_6$)* δ 7.96 (s, 1H), 7.44 -7.04 (m, 5H), 4.68 (s, 2H);

**$^{13}$C NMR** *(101 MHz, DMSO-$d_6$)* δ 139.15, 128.15, 127.10, 126.72, 46.95.

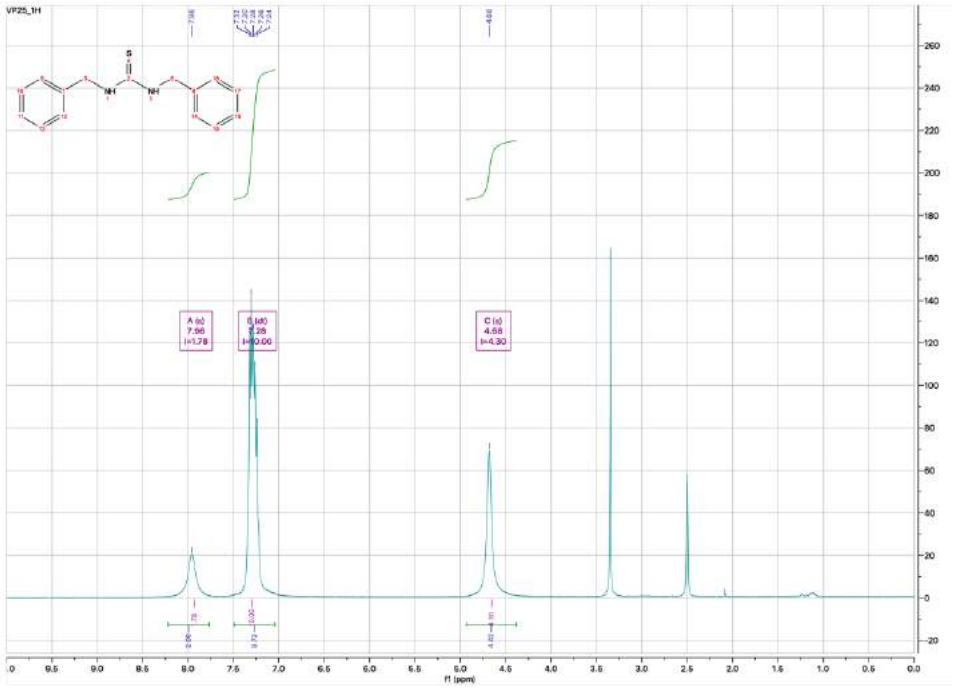

$^1$H NMR spectrum of compound **11**.

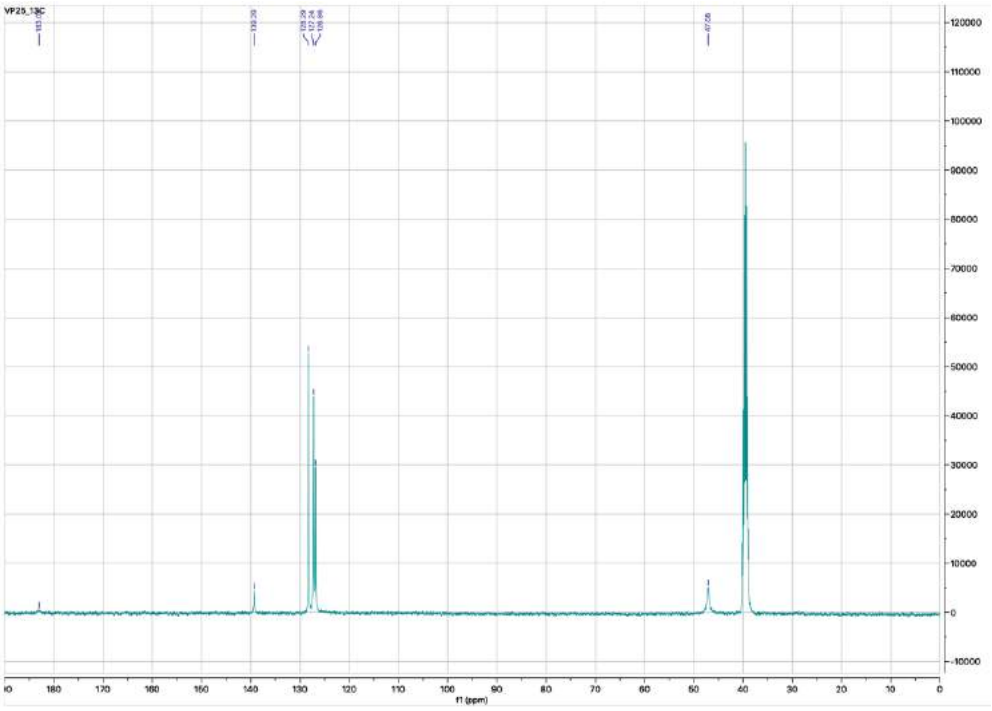

$^{13}$C NMR spectrum of compound **11**.

**Compound 12.** Synthesis of *1-cyclohexyl-3-phenyl-thiourea*

*Reaction solvent:* 1,2 dichlorethane;

MS (ESI): m/z $[M+H]^+$ 234.36 g/mol;

*Yield:* 14.48 %;

*mp:* 143-148 °C;

**$^1$H NMR** *(400 MHz, DMSO-$d_6$)* $\delta$ 9.36 (s, 1H), 7.78-6.83 (m, 5H), 4.06 (s, 1H), 3.56 (s, 1H), 2.01-1.38 (m, 5H), 1.38 – 0.98 (m, 5H).

**$^{13}$C NMR** *(101 MHz, DMSO-$d_6$)* $\delta$ 179.15, 139.59, 128.42, 123.73, 122.61, 52.09, 31.86, 25.17, 24.53.

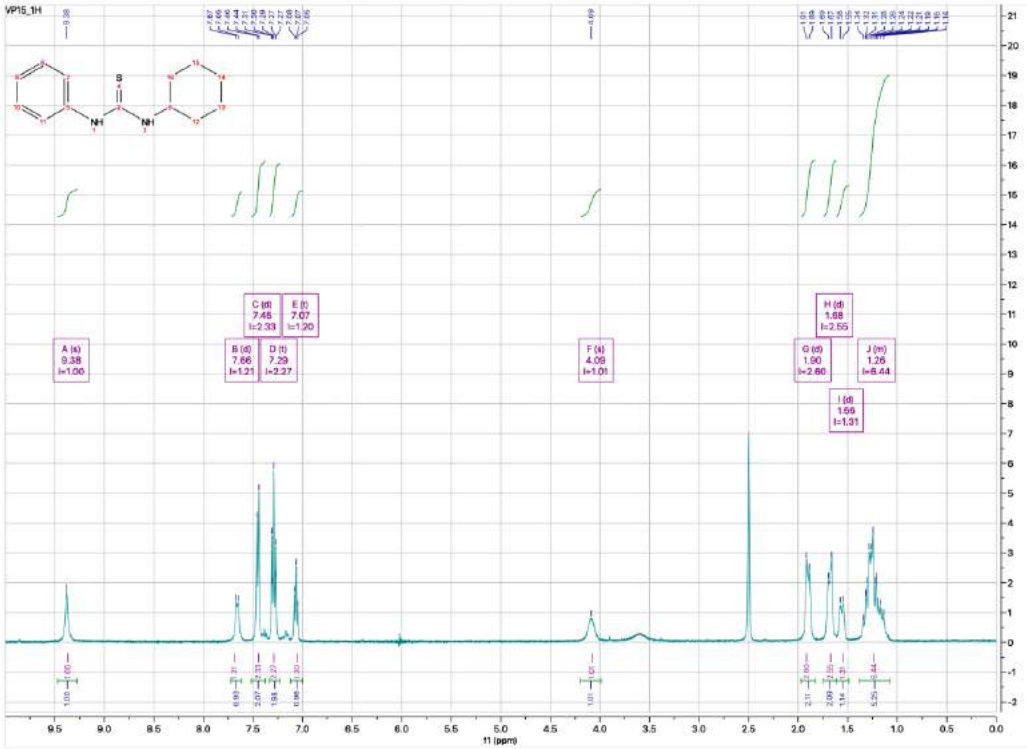


$^{1}$H NMR spectrum of compound **12.**

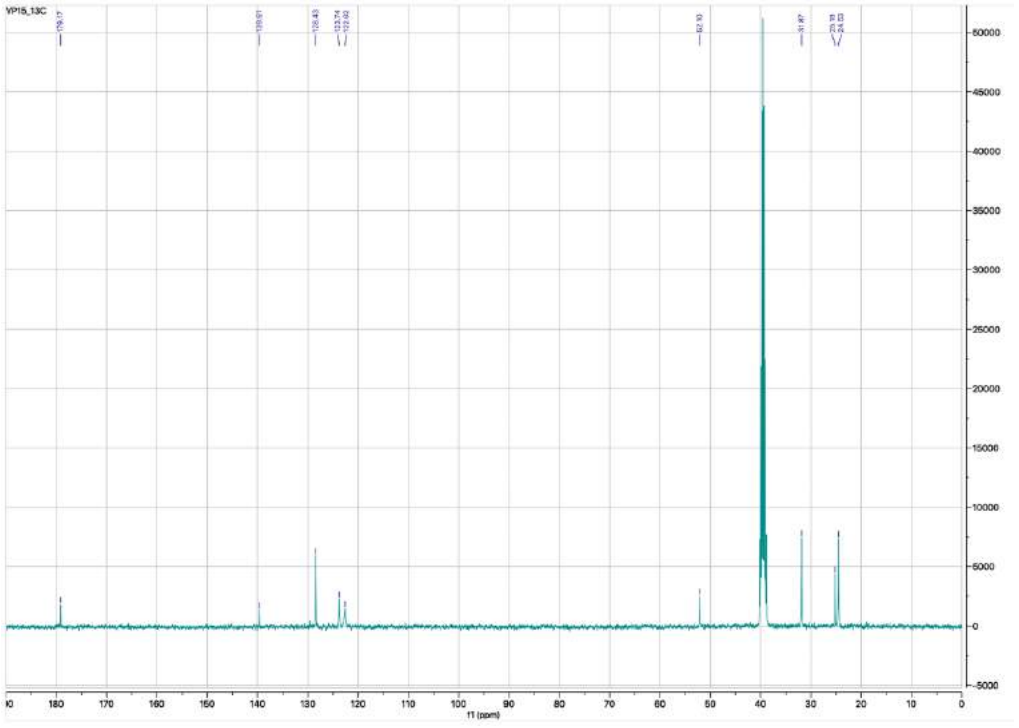


$^{13}$C NMR spectrum of compound **12.**

## 5.1.3 General procedure for the synthesis of carbamates **13-14.**

To solution of amine (1 eq, 2.62 mmol) in THF (10 mL) was added ditertbutyldicarbonate (1 eq, 2.62 mmol). The solution was then stirred at room temperature for 2 h. After the reaction was complete as indicated by TLC, the solution was evaporated to afford the product as a white solid.

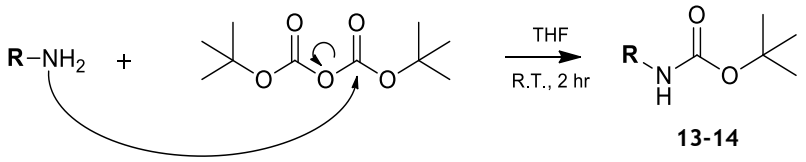


**13-14**

**Compound 13.** Synthesis of *Tert-butyl cyclohexylcarbamate*

MS (ESI): m/z $[M+H]^+$ 199.29 g/mol;

*Yield:* 87%;

*mp:* 78-80 °C;

**$^1$H NMR** *(400 MHz, $CDCl_3$)* δ 4.45 (s, 1H), 3.37 (s, 1H), 1.90 – 1.85 (m, 2H), 1.68 – 1.61 (m, 2H), 1.57 – 1.51 (m, 1H), 1.39 (s, 9H), 1.32 – 1.20 (m, 2H), 1.15 – 1.00 (m, 3H);

**$^{13}$C NMR** *(101 MHz, $CDCl_3$)* δ 155.14, 78.84, 49.36, 33.49, 28.38, 25.49, 24.87.

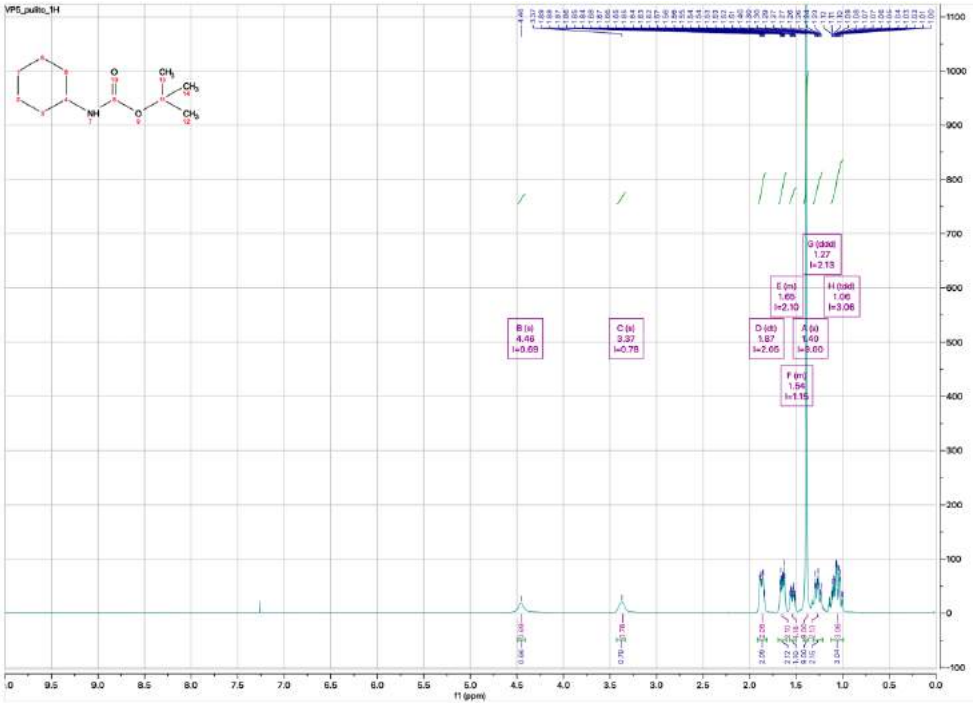

$^1$H NMR spectrum of compound **13.**

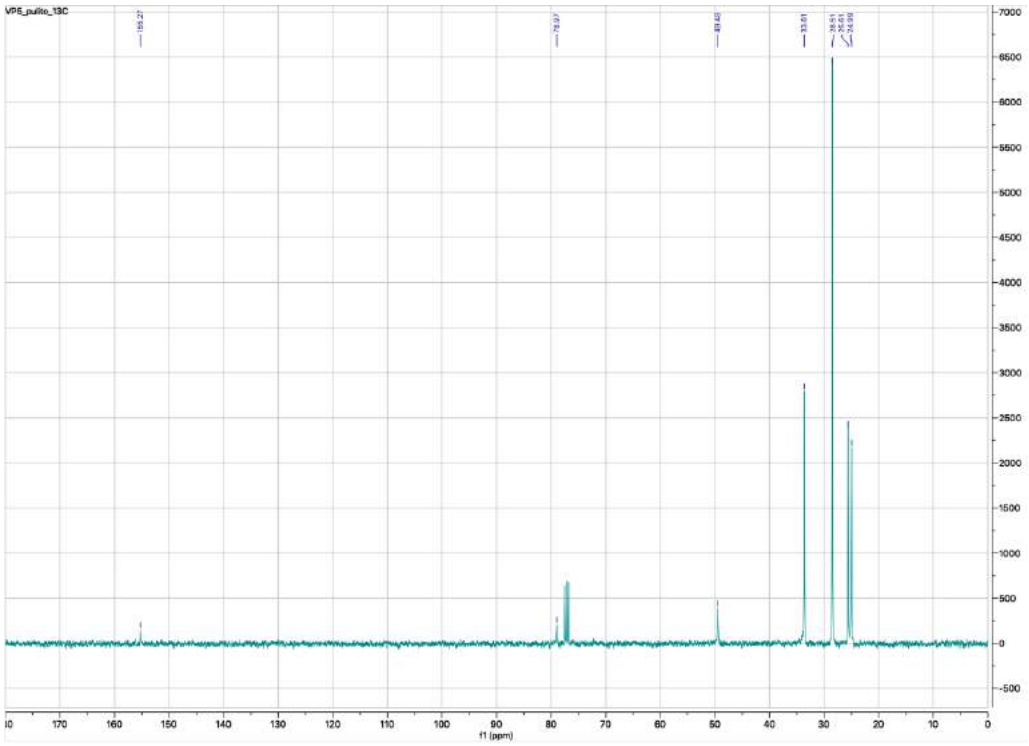

$^{13}$C NMR spectrum of compound **13**.

**Compound 14.** Synthesis of *Tert-butyl phenylcarbamate*

MS (ESI): m/z $[M+H]^+$ 193.24 g/mol;

Yield: 81%;

mp: 135-137 °C;

**$^1$H NMR** *(400 MHz, DMSO-$d_6$)* δ 9.32 (s, 1H), 7.63- 6.52 (m, 5H), 1.82- 0.98 (s, 9H);

**$^{13}$C NMR** *(101 MHz, DMSO-$d_6$)* δ 152.64, 139.39, 128.49, 128.20, 121.87, 121.56, 117.94, 78.84, 28.02.

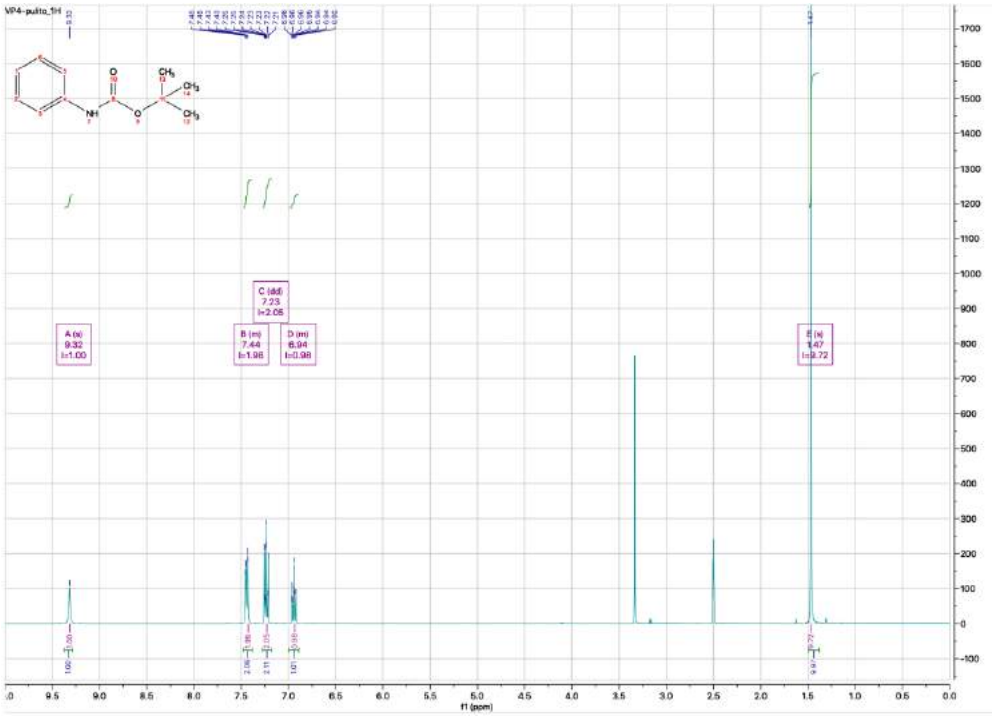

$^1$H NMR spectrum of compound **14**.

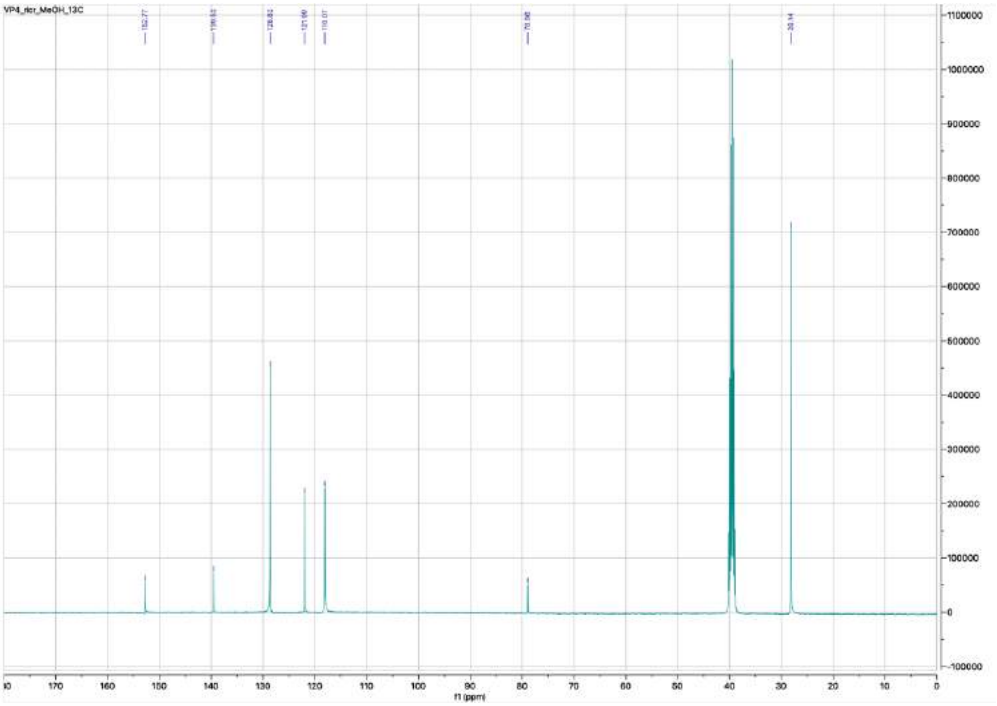

$^{13}C$ NMR spectrum of compound **14**.

## 5.2 PIPERIDINE SCAFFOLD-BASED MONOSPIRANIC COMPOUNDS.

### 5.2.1 GENERAL PROCEDURE FOR THE SYNTHESIS OF MONOSPIRANIC COMPOUNDS **27-30.**

Intermediates 15-18.

To a solution of commercially available N-benzyl piperidone (500mg, 2.24mmol) in AcOH (5ml) at 0°C, the appropriate aniline is added dropwise (1eq). Then, 3eq of TMSCN are added. The mixture is stirred at room temperature, until the completion of the reaction. The progress of the reaction is monitored via TLC and MS-ESI. The mixture is then basified with NaOH 20% until the pH=10; after that, an extraction of the water phase is performed with DCM (3x30ml). The reaction is then dried and the organic solvent is evaporated: an amorphous solid is obtained, which is titrated with EtOH, to provide a yellowish/orange powder.

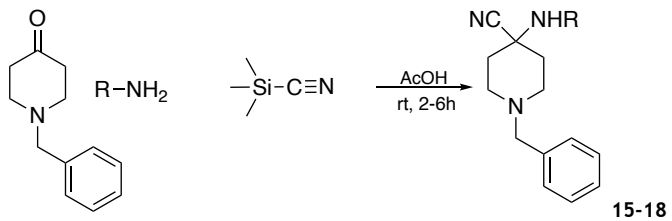


**15-18**

**Compound 15**. Synthesis of *1-benzyl-4-((2,3-dihydro-1H-inden-5-yl)amino)piperidine-4-carbonitrile*

MS (ESI): m/z $[M+H]^+$ 332.59;

*Yield:* 55%;

**$^1$H NMR** *(400 MHz, $CDCl_3$)* δ 7.28 (s, 5H), 7.12 (dt, J = 7.2, 1.0 Hz, 1H), 6.81 (dd, J = 7.4, 1.5 Hz, 1H), 6.61 (q, J = 1.1 Hz, 1H), 5.98 (s, 1H), 3.52 (s, 2H), 3.07 – 2.72 (m, 6H), 2.71 – 2.50 (m, 2H), 2.28 – 1.96 (m, 6H).

**Compound 16**. Synthesis of *1-benzyl-4-((1,2,3,6,7,8-hexahydro-as-indacen-4-yl)amino)piperidine-4-carbonitrile*
MS (ESI): m/z $[M+H]^+$ 372.41;
*Yield:* 84%;
**$^1$H NMR** *(400 MHz, $CDCl_3$)* δ 7.29 (s, 5H), 6.64 (s, 1H), 6.53 (s, 1H), 3.49 (s, 2H), 2.93 – 2.50 (m, 12H), 2.27 – 1.91 (m, 7H).

**Compound 17**. Synthesis of *1-benzyl-4-((1,2,3,5,6,7-hexahydro-s-indacen-4-yl)amino)piperidine-4-carbonitrile*
MS (ESI): m/z $[M+H]^+$ 372.41;
*Yield:* 65%;
**$^1$H NMR** *(400 MHz, $CDCl_3$)* δ 7.29 (s, 5H), 6.59 (s, 1H), 6.58 (s, 1H), 3.49 (s, 1H), 3.13 – 2.39 (m, 12H), 2.37 – 1.90 (m, 8H).

**Compound 18**. Synthesis of *1-benzyl-4-(naphthalen-1-ylamino)piperidine-4-carbonitrile*
MS (ESI): m/z $[M+H]^+$ 342.30;
*Yield:* 60%;
**$^1$H NMR** *(400 MHz, $CDCl_3$)* δ 8.11 – 7.87 (m, 1H), 7.85 – 6.96 (m, 11H), 6.58 (s, 1H), 3.67 – 3.36 (m, 2H), 2.82 (dt, J = 12.7, 7.4 Hz, 2H), 2.59 (ddd, J = 12.3, 7.2, 6.8 Hz, 2H), 2.21 – 1.91 (m, 4H).

Intermediates 19-22.

Amino-nitrile intermediates **15-18** (1eq) are solubilized in $H_2SO_4$ conc. 96% at room temperature for 18 hours. The proceeding of the reaction is monitored by TLC and MS-ESI. After the completion of the reaction, the mixture is put at -10°C and basified with $NH_4^+OH^-$ 28% until pH=10-11. At this point, a white suspension is obtained. The ammonium salts are filtered through Celite with methanol and the filtrate is concentrated to obtain an amorphous. Then, an extraction with DCM (3x30ml) and water is performed. The desired products **19-22** are white powders.

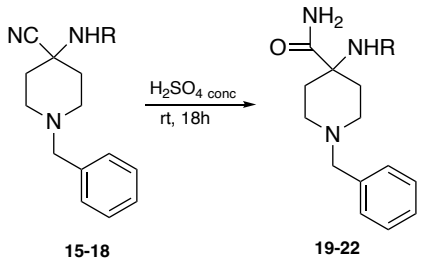

**15-18** **19-22**

**Compound 19**. Synthesis of *1-benzyl-4-((2,3-dihydro-1H-inden-5-yl)amino)piperidine-4-carboxamide*
MS (ESI): m/z $[M+H]^+$ 350.33;
*Yield:* 98%;

**Compound 20**. Synthesis of *1-benzyl-4-((1,2,3,6,7,8-hexahydro-as-indacen-4-yl)amino)piperidine-4 carboxamide*
MS (ESI): m/z $[M+H]^+$ 390.24;
*Yield:* 98%.

**Compound 21**. Synthesis of *1-benzyl-4-((1,2,3,5,6,7-hexahydro-s-indacen-4-yl)amino)piperidine-4-carboxamide*
MS (ESI): m/z $[M+H]^+$ 390.24;
*Yield:* 98%.

**Compound 22**. Synthesis of *1-benzyl-4-(naphthalen-1-ylamino)piperidine-4-carboxamide*
MS (ESI): m/z $[M+H]^+$ 360.35;
*Yield:* 95%.

Intermediates 23-26.

To a solution of intermediates **19-22** (1eq) in methanol (10ml), DMF/DMA (3eq) is added dropwise. The mixture is reacted at 55°C for 6/10 hours and is monitored by MS-ESI. At the completion of the reaction, the solvent is evaporated and a yellow solid is obtained. The desired product, checked by TLC and MS-ESI, is used as such for the next step.

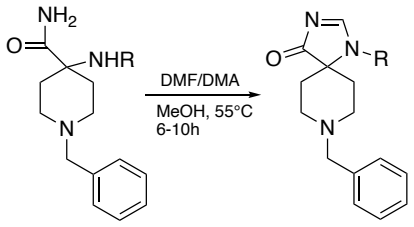


**19-22** **23-26**

**Compound 23**. Synthesis of *8-benzyl-1-(2,3-dihydro-1H-inden-5-yl)-1,3,8-triazaspiro[4.5]dec-2-en-4-one*
MS (ESI): m/z $[M+H]^+$ 360.34;
*Yield:* 88%;
$^1$**H NMR** *(400 MHz, $CDCl_3$)* δ 8.01 (s, 1H), 7.34 – 7.24 (m, 5H), 7.22 – 7.09 (m, 3H), 3.53 (s, 2H), 2.97 (dd, *J* = 8.6, 5.8 Hz, 2H), 2.92 – 2.80 (m, 6H), 2.58 (dd, *J* = 8.6, 5.9 Hz, 2H), 2.16 – 2.01 (m, 4H).

**Compound 24**. Synthesis of *8-benzyl-1-(1,2,3,6,7,8-hexahydro-as-indacen-4-yl)-1,3,8 triazaspiro[4.5]dec-2-en-4-one*
MS (ESI): m/z $[M+H]^+$ 400.43;
*Yield:* 84%;

**$^1$H NMR** *(400 MHz, $CDCl_3$)* δ 8.06 (s, 1H), 7.29 – 7.26 (m, 5H), 7.18 (s, 1H), 3.55 (s, 2H), 3.02 – 2.95 (m, 2H), 2.93 – 2.87 (m, 4H), 2.77 – 2.71 (m, 4H), 2.67 (d, *J* = 11.8 Hz, 2H), 2.11 (dddd, *J* = 12.2, 7.5, 4.7, 2.9 Hz, 2H), 2.03 – 1.93 (m, 4H), 1.92 – 1.87 (m, 2H).

**Compound 25**. Synthesis of *8-benzyl-1-(1,2,3,5,6,7-hexahydro-s-indacen-4-yl)-1,3,8-triazaspiro[4.5]dec-2-en-4-one*

MS (ESI): m/z $[M+H]^+$ 400.43;

*Yield:* 89%;

**$^1$H NMR** *(400 MHz, $CDCl_3$)* δ 8.05 (s, 1H), 7.35 – 7.21 (m, 5H), 6.87 (p, *J* = 1.0 Hz, 1H), 3.52 (s, 2H), 3.27 (tdd, *J* = 8.8, 6.2, 3.2 Hz, 4H), 2.97 (dd, *J* = 8.5, 5.8 Hz, 2H), 2.87 (dd, *J* = 8.6, 5.9 Hz, 2H), 2.76 (dddd, *J* = 11.3, 9.2, 2.4, 1.2 Hz, 4H), 2.61 (dd, *J* = 8.6, 5.9 Hz, 2H), 2.27 – 2.04 (m, 6H).

**Compound 26**. Synthesis of *8-benzyl-1-(naphthalen-1-yl)-1,3,8-triazaspiro[4.5]dec-2-en-4-one*

MS (ESI): m/z $[M+H]^+$ 370.42;

*Yield:* 93%;

**$^1$H NMR** *(400 MHz, $CDCl_3$)* δ 8.03 (s, 1H), 7.95 – 7.78 (m, 3H), 7.56 – 7.48 (m, 2H), 7.48 – 7.34 (m, 2H), 7.34 – 7.25 (m, 5H), 3.53 (s, 2H), 2.97 (dd, J = 8.6, 5.9 Hz, 2H), 2.87 (dd, J = 8.6, 5.9 Hz, 2H), 2.59 (dd, J = 8.6, 5.9 Hz, 2H), 2.09 (dd, J = 8.6, 5.9 Hz, 2H).

Final compounds **27-30**.

The intermediates **23-26** (1eq) are suspended in methanol (10ml) and the mixture is cooled at 0°C with an ice bath. Then, $NaBH_4$ (1.2eq) is added slowly and bubbling is observed. The reaction is monitored with MS-ESI upon completion. Then, the reaction is quenched with deionized water, the methanol is evaporated and the resulting aqueous phase is extracted three times with DCM (3x30ml). The combined organic phases are dried and the solvent is evaporated. The resulting amorphous solid is titrated with $Et_2O$ to obtain the desired products **27-30** as white or yellow solid.

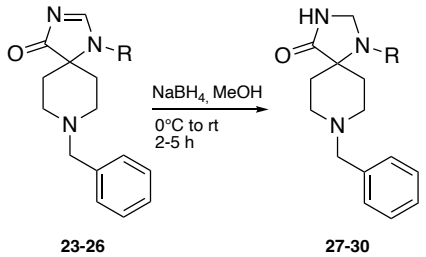


**Compound 27.** Synthesis of *8-benzyl-1-(2,3-dihydro-1H-inden-5-yl)-1,3,8-triazaspiro[4.5]decan-4-one*

MS (ESI): m/z $[M+H]^+$ 362.40;

*Yield:* 95%;

**$^1$H NMR** *(400 MHz, $CDCl_3$)* δ 7.40 – 7.28 (m, 3H), 7.24 (d, J = 7.2 Hz, 1H), 7.16 (d, J = 8.2 Hz,1H), 6.89 (s, 1H), 6.82 (dd, J = 8.2, 2.4 Hz, 1H), 6.75 (s, 1H), 4.70 (d, J = 0.8 Hz, 2H), 2.88 (dt, J = 21.4, 7.4 Hz, 6H), 2.79 (s, 2H), 2.44 (s, 2H), 2.18 – 1.94 (m, 2H), 1.75 (d, J = 14.0 Hz, 2H).

**$^{13}$C NMR** *(101 MHz, $CDCl_3$)* δ 178.28, 145.42, 141.80, 139.01, 136.60, 129.01, 128.20, 126.89, 124.69, 116.84, 114.91, 62.82, 59.89, 49.66, 33.28, 32.06, 29.57, 25.68.

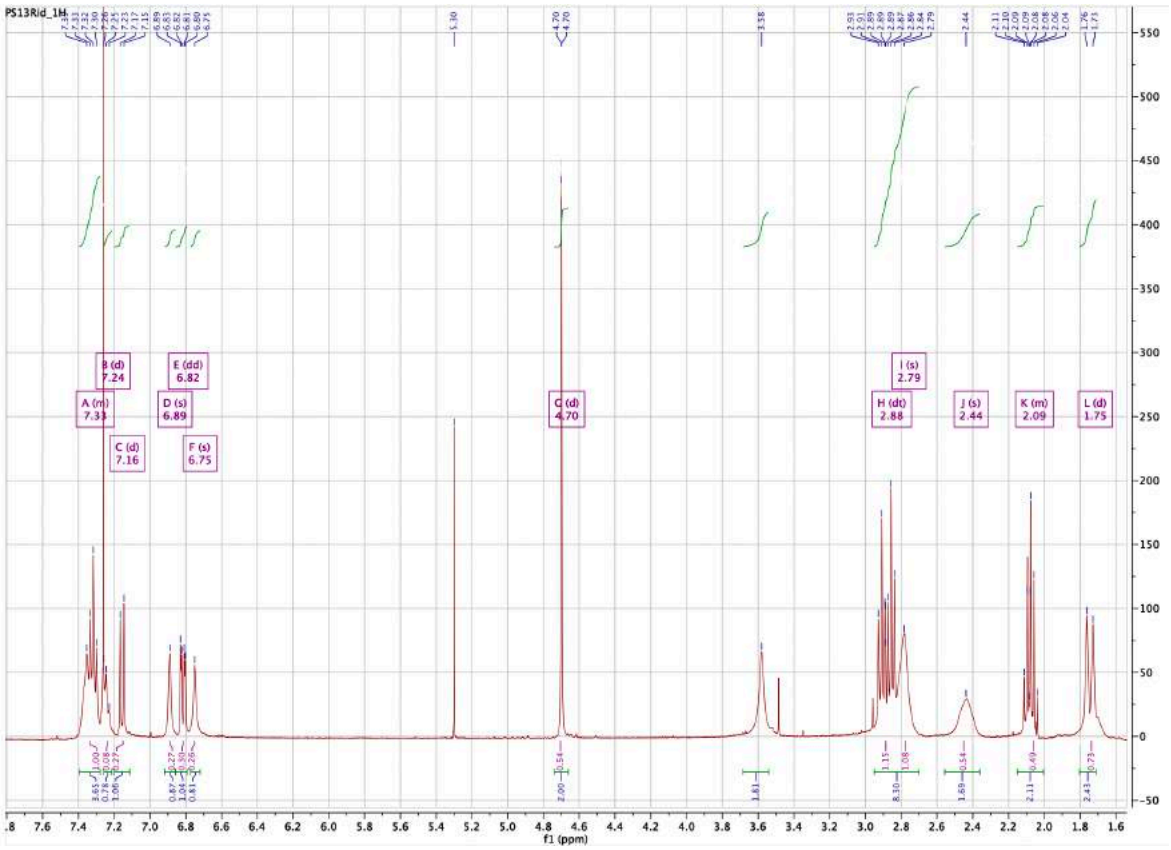


$^{1}$H NMR spectrum of compound **27**.

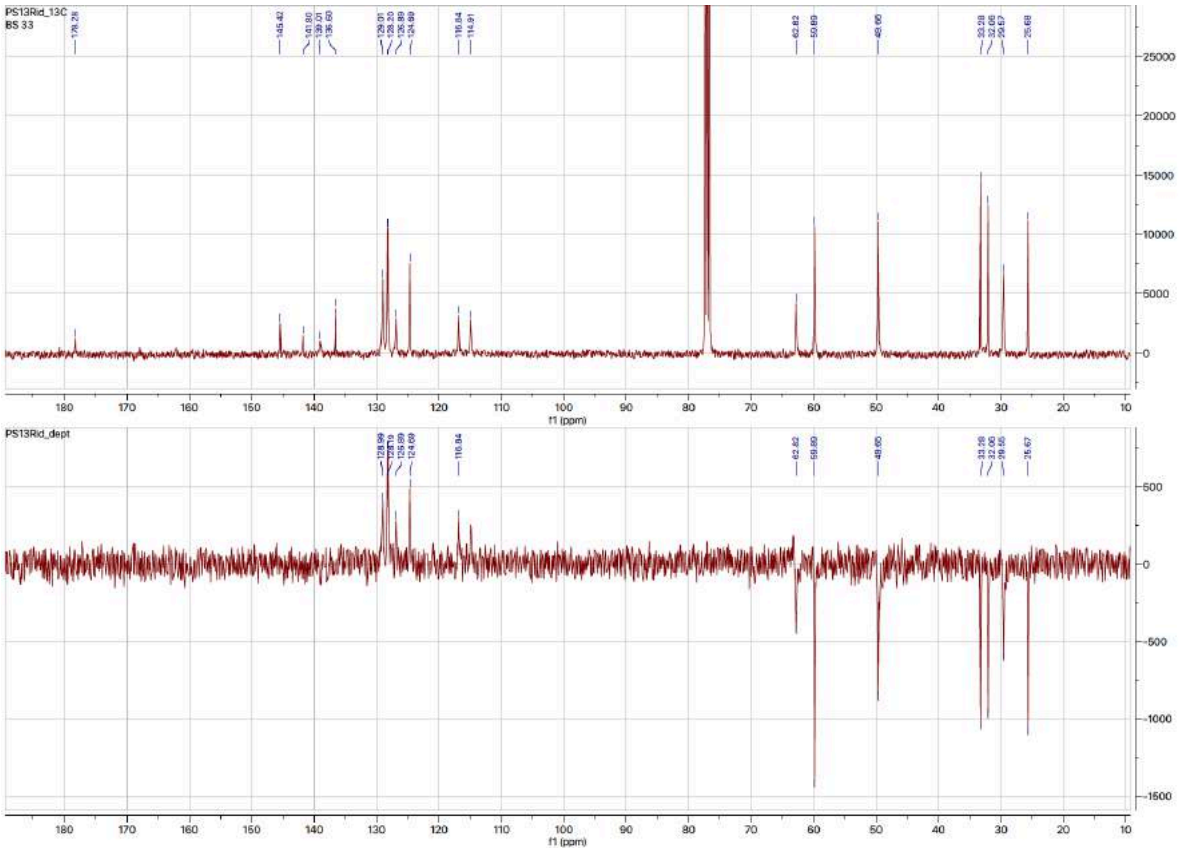


$^{13}$C NMR and DEPT spectra of compound **27**.

**Compound 28**. Synthesis of *8-benzyl-1-(1,2,3,6,7,8-hexahydro-as-indacen-4-yl)-1,3,8-triazaspiro[4.5]decan-4-one*

MS (ESI): m/z $[M+H]^+$ 402.43;

*Yield*: 55%;

**$^1$H NMR** *(400 MHz, $CDCl_3$)* δ 7.36 – 7.16 (m, 5H), 6.93 (s, 1H), 6.45 (s, 1H), 4.57 (s, 2H), 3.52 (s, 2H), 3.06 – 2.67 (m, 10H), 2.58 (s, 2H), 2.05 (dp, J = 24.9, 7.4 Hz, 4H), 1.96 – 1.84 (m, 2H), 1.73 (s, 2H).

**$^{13}$C NMR** *(101 MHz, $CDCl_3$)* δ 179.36, 143.22, 142.56, 141.01, 138.52, 129.40, 128.21, 127.01, 122.33, 63.02, 62.80, 61.77, 49.33, 32.69, 32.18, 31.93, 31.15, 31.02, 29.78, 25.65, 25.56.


$^{1}$H NMR spectrum of compound **28**.

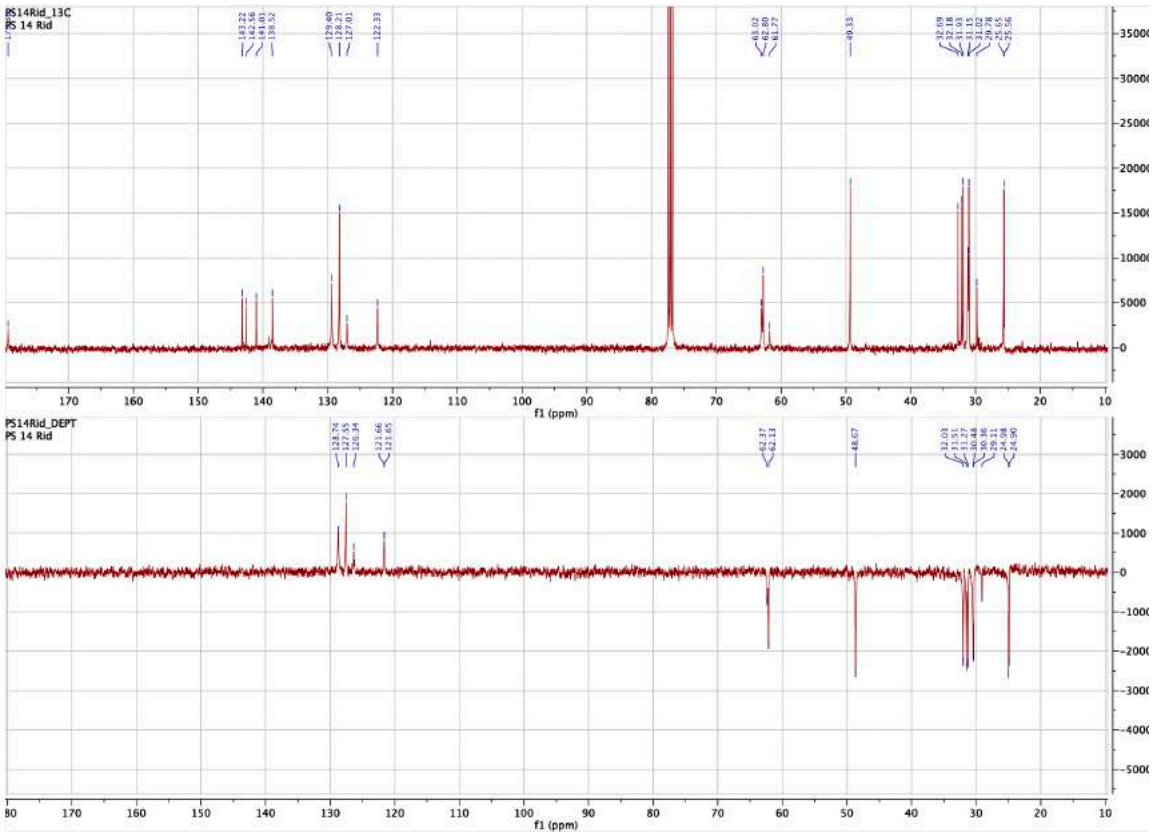


$^{13}$C NMR and DEPT spectra of compound **28**.

**Compound 29**. Synthesis of *8-benzyl-1-(1,2,3,5,6,7-hexahydro-s-indacen-4-yl)-1,3,8-triazaspiro[4.5]decan-4-one*

MS (ESI): m/z $[M+H]^+$ 402.43;

*Yield:* 70%;

**$^1$H NMR** *(400 MHz, $CDCl_3$* δ 7.28 (s, 5H), 7.24 (d, J = 4.2 Hz, 1H), 7.00 (s, 1H), 6.33 (s, 1H), 4.60 (s, 2H), 3.53 (s, 2H), 2.96 – 2.77 (m, 8H), 2.71 (s, 2H), 2.50 (s, 2H), 2.01 (s, 4H), 1.89 (dt, J = 13.5, 4.3 Hz, 2H), 1.71 (s, 2H).

**$^{13}$C NMR** *(101 MHz, $CDCl_3$)* δ 179.57, 144.44, 142.45, 129.20, 128.11, 126.87, 119.25, 62.86, 61.72, 49.14, 32.94, 32.50, 31.96, 29.69, 26.00.

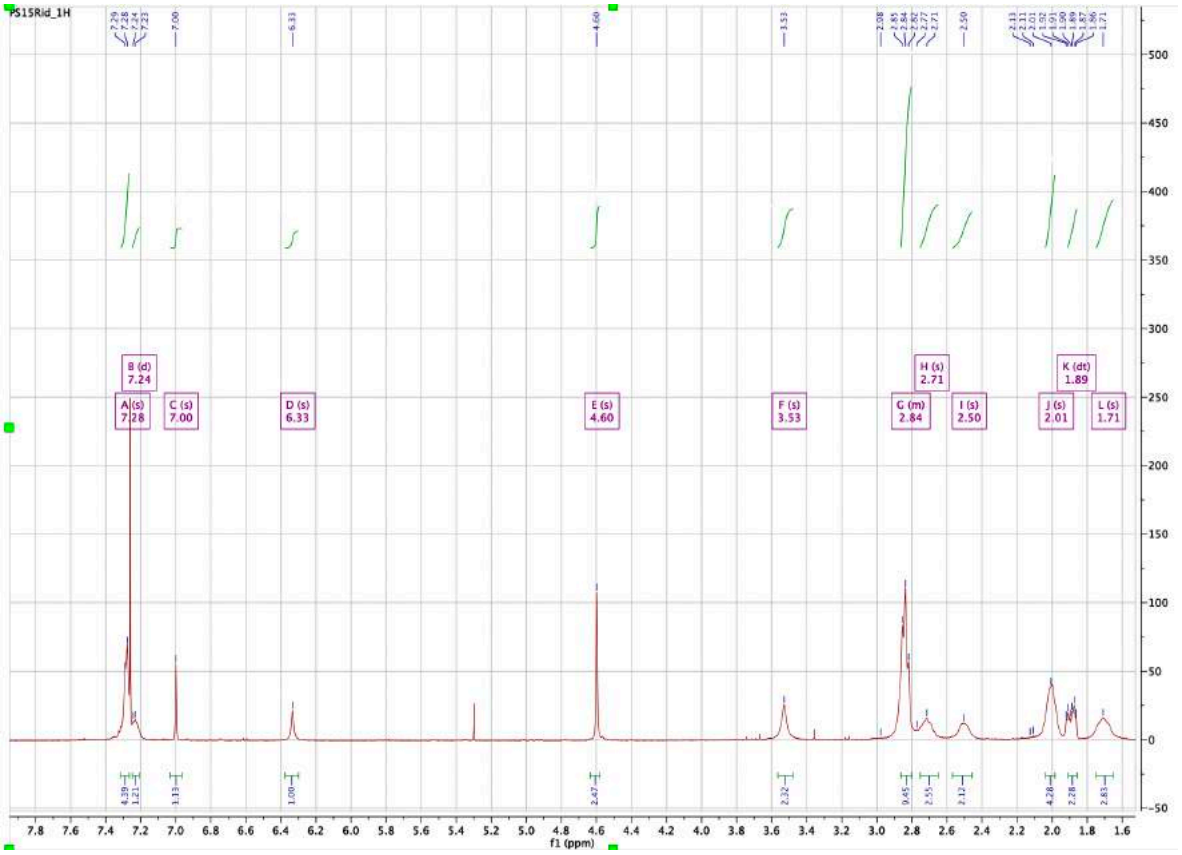


$^1$H NMR spectrum of compound **29**.

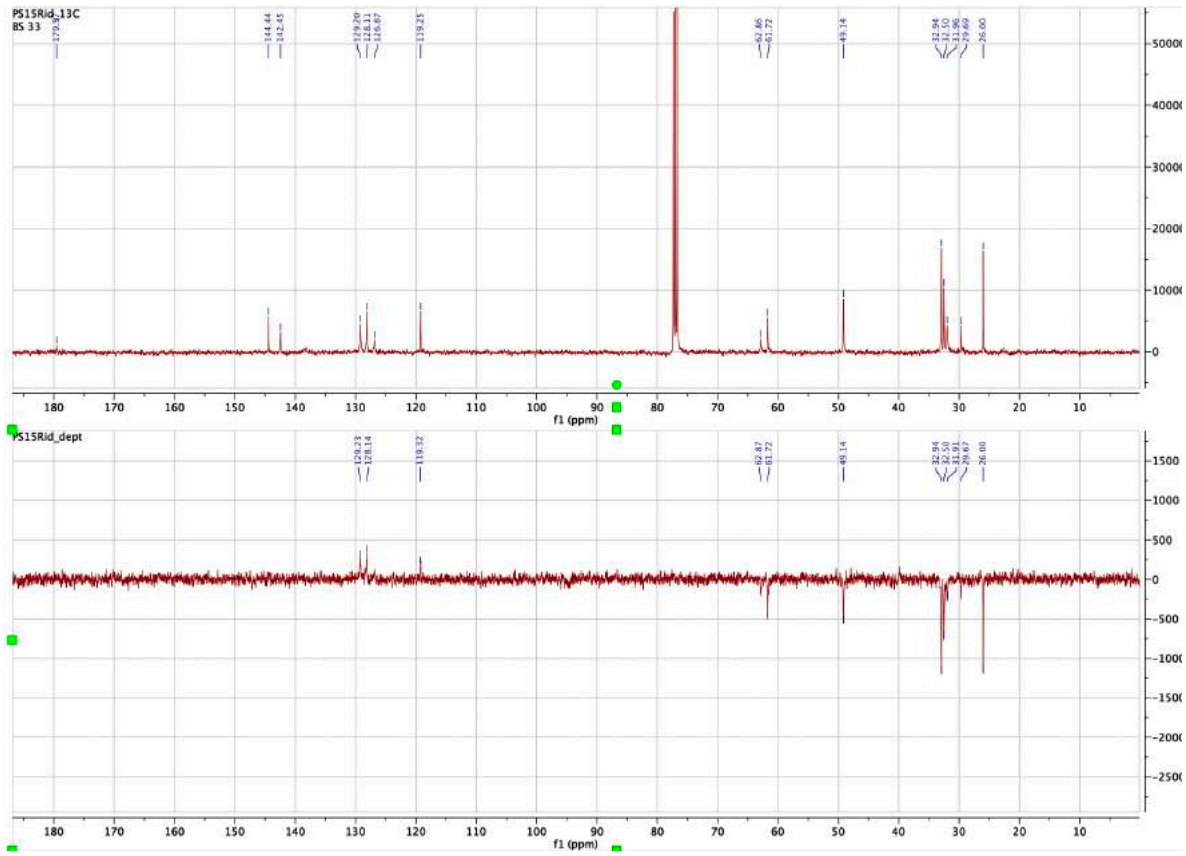


$^{13}$C NMR and DEPT spectra of compound **29**.

**Compound 30**. Synthesis of *8-benzyl-1-(naphthalen-1-yl)-1,3,8-triazaspiro[4.5]decan-4-one*

MS (ESI): m/z $[M+H]^+$ 371.20;

*Yield:* 54%;

**$^1$H NMR** *(400 MHz, $CDCl_3$* δ 8.58 – 8.44 (m, 1H), 7.88 – 7.81 (m, 1H), 7.80 – 7.73 (m, 1H), 7.56 – 7.40 (m, 4H), 7.26 – 7.11 (m, 5H), 6.71 (s, 1H), 4.79 – 4.61 (m, 2H), 3.49 (d, J = 12.3 Hz, 2H), 2.77 (s, 2H), 2.57 (s, 2H), 2.11 – 1.94 (m, 2H), 1.80 (s, 2H).

**$^{13}$C NMR** *(101 MHz, $CDCl_3$)* δ 179.09, 134.72, 134.30, 129.34, 129.11, 128.22, 128.04, 127.29, 127.10, 126.30, 126.18, 126.00, 125.35, 124.52, 63.55, 62.79, 62.00, 49.29, 48.96, 31.18, 29.78.

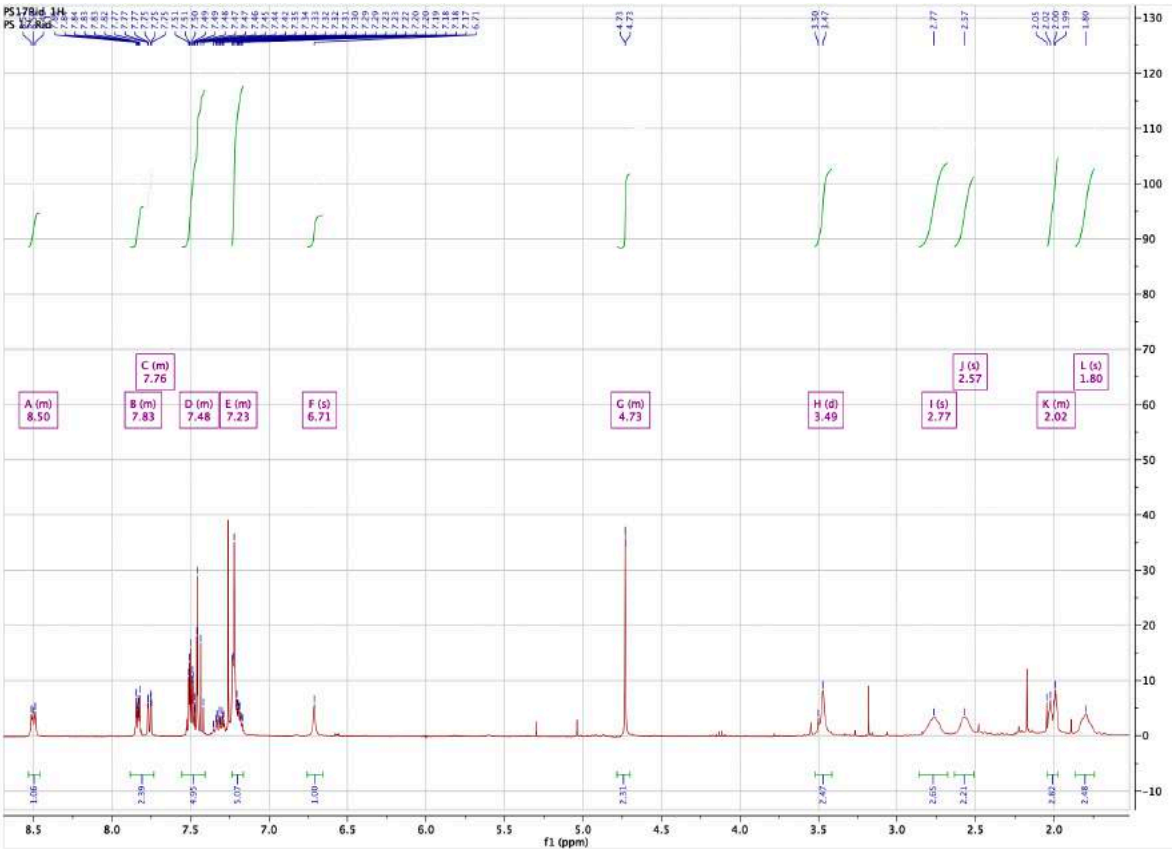


$^{1}$H NMR spectrum of compound **30**.

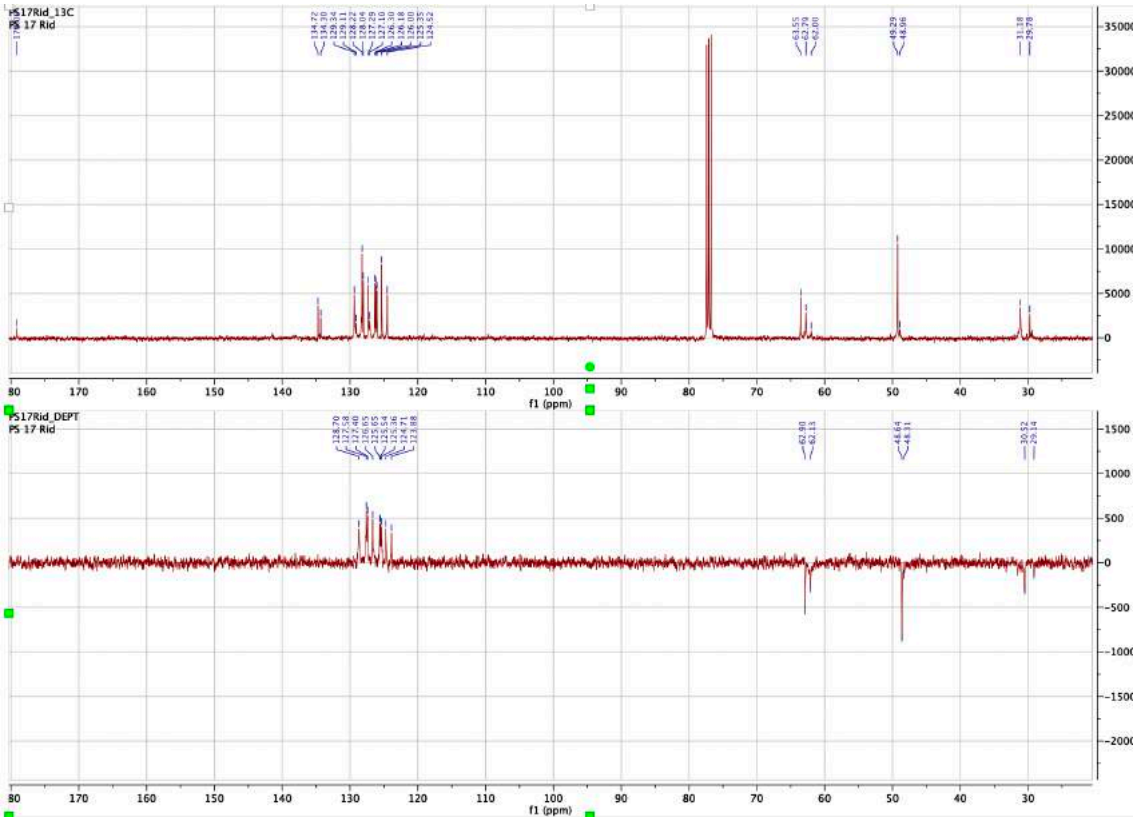


$^{13}$C NMR and DEPT spectra of compound **30**.

Intermediate 31.

Commercially available 4-piperidone monohydrate hydrochloride (1eq) is suspended in a solution of $H_2O$ and dioxane (1:2, 20ml) and then Na2CO3 (2eq) is added. After 15 minutes, p-toluen sulphonyl chloride (1.1eq) is slowly put in the mixture. The reaction is stirred at room temperature for 8-18 hours and monitored by TLC (A1P1) and MS-ESI. When complete, the dioxane is evaporated and the aqueous phase is extracted with AcOEt (3x30ml). The resulting solid is ground with $Et_20$ and then filtered, to isolate the desired compound **107**.

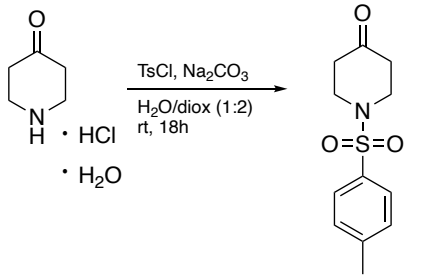


**31**

**Compound 31**. Synthesis of *1-tosylpiperidin-4-one*
MS (ESI): m/z $[M+H]^+$ 254.30;
Yield: 92%
**$^1$H NMR** (400 MHz, Chloroform-*d*) δ 7.70 – 7.65 (m, 2H), 7.36 – 7.32 (m, 2H), 3.38 (t, *J* = 6.2 Hz, 4H), 2.53 (t, *J* = 6.3 Hz, 4H), 2.44 (s, 3H).
**$^{13}$C NMR** (101 MHz, Chloroform-*d*) δ 206.08, 144.60, 133.83, 130.39, 128.01, 46.35, 41.12, 22.00.

Intermediates **32-34**.

A solution of compound **31** (1eq) in AcOH (5ml) is cooled at 0°C and the appropriate aniline or benzylamine is added dropwise (1eq). Then, 3eq of TMSCN are added. The mixture is stirred at room temperature, until the completion of the reaction. The progress of the reaction is monitored via TLC and MS-ESI. The mixture is then basified with NaOH 20% until the pH=10; after that, an extraction of the water phase is performed with DCM (3x30ml). The reaction is then dried and the organic solvent is evaporated: an amorphous solid is obtained, which is titrated with EtOH, to provide a yellowish/orange powder.

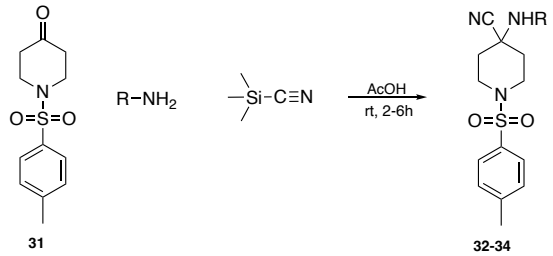


**31** **32-34**

**Compound 32**. Synthesis of *4-((4-chlorophenyl)amino)-1-tosylpiperidine-4-carbonitrile*
MS (ESI): m/z $[M+H]^+$ 390.49; 392.24
*Yield:* 66%;

**$^1$H NMR** *(400 MHz, $CDCl_3$)* δ 7.73 – 7.59 (m, 2H), 7.32 (ddt, J = 6.9, 1.3, 0.7 Hz, 2H), 7.25 – 7.12 (m, 2H), 6.76 – 6.66 (m, 2H), 6.01 (s, 1H), 3.37 (t, J = 7.1 Hz, 4H), 2.43 (s, 3H), 2.25 (t, J = 6.9 Hz, 3H).

**Compound 33**. Synthesis of *4-((3,4-dichlorophenyl)amino)-1-tosylpiperidine-4-carbonitrile*
MS (ESI): m/z $[M+H]^+$ 424.39; 426.39
*Yield:* 91%
**$^1$H NMR** *(400 MHz, $CDCl_3$)* δ 7.88 – 7.56 (m, 2H), 7.32 (m, 3H), 6.99 (dd, J = 7.2, 1.7 Hz, 1H), 6.50 (dd, J = 7.6, 1.5 Hz, 1H), 5.73 (s, 1H), 3.37 (t, J = 6.9 Hz, 4H), 2.43 (s, 3H), 2.25 (t, J = 7.1 Hz, 4H).

**Compound 34**. Synthesis of *4-(benzylamino)-1-tosylpiperidine-4-carbonitrile*
MS (ESI): m/z $[M+H]^+$
*Yield: 57%*
*MS (ESI) $[M+H]^+$: 369.15*
***$^1$H NMR** (400 MHz, $CDCl_3$)* δ 7.68 – 7.61 (m, 2H), 7.37 – 7.33 (m, 2H), 7.32 – 7.24 (m, 5H), 3.86 (s, 2H), 3.59 (dt, J = 12.6, 4.6 Hz, 2H), 2.83 (ddd, J = 12.7, 10.1, 2.9 Hz, 2H), 2.46 (d, J = 0.8 Hz, 3H), 2.16 – 2.06 (m, 2H), 1.89 (ddd, J = 13.7, 10.1, 3.9 Hz, 2H).
***$^{13}$C NMR** (100 MHz, $CDCl_3$)* δ 142.51, 139.53, 137.00, 129.62, 128.61, 128.43, 127.42, 127.26, 120.41, 53.49, 48.90, 43.23, 34.71, 21.53.

Intermediates **35-37**.

Amino-nitrile intermediates **32-34** (1eq) are solubilized in $H_2SO_{4\ conc.}$ 96% at room temperature for 18 hours. The proceeding of the reaction is monitored by TLC and MS-ESI. After the completion of the reaction, the mixture is put at -10°C and basified with $NH_4^+OH^-$ 28% until pH=10-11. At this point, a white suspension is obtained. The ammonium salts are filtered through Celite with methanol and the filtrate is concentrated to obtain an amorphous. Then, an extraction with DCM (3x30ml) and water is performed. The desired products **35-37** are isolated as white powders.

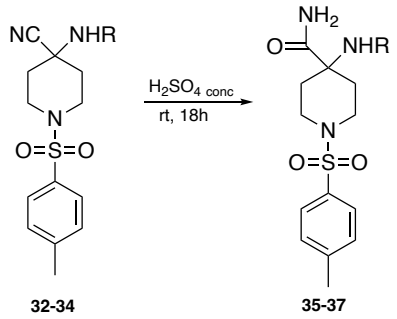

**32-34** **35-37**

**Compound 35**. Synthesis of *4-((4-chlorophenyl)amino)-1-tosylpiperidine-4-carboxamide*
MS (ESI): m/z $[M+H]^+$ 408,31 ; 410,31
*Yield:* 94%

**Compound 36**. Synthesis of *4-((3,4-dichlorophenyl)amino)-1-tosylpiperidine-4-carboxamide*
MS (ESI): m/z $[M+H]^+$ 442.34 ; 444,34

*Yield:* 84%

**Compound 37**. Synthesis of *4-(benzylamino)-1-tosylpiperidine-4-carboxamide*
MS (ESI): m/z $[M+H]^+$ 388.17
*Yield:* 94%
**$^1$H NMR** (401 MHz, Chloroform-*d*) δ 7.71 – 7.60 (m, 2H), 7.41 – 7.20 (m, 7H), 4.54 – 4.39 (m, 1H), 3.93 (dd, J = 8.6, 0.9 Hz, 2H), 3.35 (t, J = 7.1 Hz, 3H), 2.43 (t, J = 0.8 Hz, 4H), 2.17 – 1.90 (m, 4H).
**$^{13}$C NMR** (100 MHz, Chloroform-*d*) δ 174.14, 142.79, 138.81, 136.80, 129.72, 128.61, 128.44, 127.42, 127.20, 60.79, 48.96, 43.16, 30.56, 21.53.

Intermediates **38-40**.

To a solution of intermediates **35-37** (1eq) in methanol (10ml), DMF/DMA (3eq) is added dropwise. The mixture is reacted at 55°C for 6/10 hours and is monitored by MS-ESI. At the completion of the reaction, the solvent is evaporated and a yellow solid is obtained. The desired products **38-40**, checked by TLC and MS-ESI, is used as such for the next step.

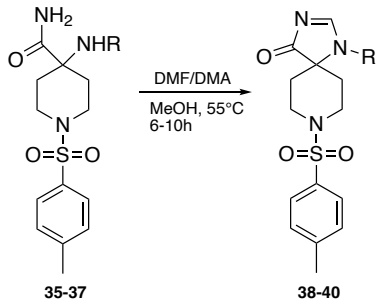

35-37 38-40

**Compound 38**. Synthesis of *1-(4-chlorophenyl)-8-tosyl-1,3,8-triazaspiro[4.5]dec-2-en-4-one*
MS (ESI): m/z $[M+H]^+$ 418,56; 420,31
*Yield:* 87%
**$^1$H NMR** *(400 MHz, $CDCl_3$)* δ 8.23 (s, 1H), 7.65 – 7.60 (m, 2H), 7.51 – 7.45 (m, 2H), 7.35 – 7.29 (m, 2H), 7.13 – 7.07 (m, 2H), 3.70 (ddt, *J* = 12.2, 4.6, 1.9 Hz, 2H), 3.34 (dd, *J* = 12.3, 2.7 Hz, 2H), 2.44 (s, 3H), 2.10 – 2.00 (m, 2H), 1.84 – 1.77 (m, 2H).

**Compound 39**. Synthesis of *1-(3,4-dichlorophenyl)-8-tosyl-1,3,8-triazaspiro[4.5]dec-2-en-4-one*
MS (ESI): m/z $[M+H]^+$ 452.35; 454.28
*Yield:* 79%
**$^1$H NMR** *(400 MHz, $CDCl_3$)* δ 8.01 (s, 1H), 7.72 – 7.64 (m, 2H), 7.44 – 7.34 (m, 2H), 7.34 – 7.26 (m, 2H), 3.47 (dd, *J* = 9.6, 7.1 Hz, 4H), 2.51 – 2.40 (m, 7H).

**Compound 40**. Synthesis of *1-benzyl-8-tosyl-1,3,8-triazaspiro[4.5]dec-2-en-4-one*
MS (ESI): m/z $[M+H]^+$ 398.15
*Yield:* 87%
**$^1$H NMR** *(400 MHz, $CDCl_3$)* δ 7.75 (s, 1H), 7.68 (d, J = 7.5 Hz, 2H), 7.38 – 7.20 (m, 7H), 4.60 (d, J = 0.9 Hz, 2H), 3.39 (td, J = 7.2, 0.8 Hz, 4H), 2.43 (d, J = 1.0 Hz, 3H), 2.27 – 1.91 (m, 4H).

**$^{13}$C NMR** (100 MHz, Chloroform-*d*) δ 181.17, 159.58, 142.79, 136.90, 129.53, 128.78, 127.66, 127.44, 127.23, 58.55, 49.78, 42.19, 28.70, 21.52.

Final compounds **41-43**.

The intermediates **38-40** (1eq) are suspended in methanol (10ml) and the mixture is cooled at 0°C with an ice bath. Then, $NaBH_4$ (1.2eq) is added slowly and bubbling is observed. The reaction is monitored with MS-ESI upon completion. Then, the reaction is quenched with deionized water, the methanol is evaporated and the resulting aqueous phase is extracted three times with DCM (3x30ml). The combined organic phases are dried and the solvent is evaporated. The resulting amorphous solid is titrated with $Et_2O$ to obtain the desired products **41-43** as white or yellow solid.

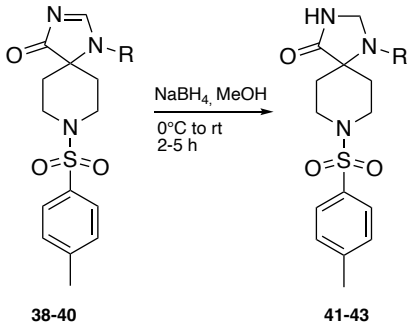


**38-40** **41-43**

**Compound 41**. Synthesis of *1-(4-chlorophenyl)-8-tosyl-1,3,8-triazaspiro[4.5]decan-4-one*
MS (ESI): m/z $[M+H]^+$ 420,56; 422,31
*Yield:* 57%
**$^1$H NMR** *(400 MHz, DMSO-d6)* δ 8.78 (s, 1H), 7.66 (d, J = 8.3 Hz, 2H), 7.53 – 7.43 (m, 2H), 7.25 (d, J = 9.1 Hz, 1H), 6.71 (d, J = 9.1 Hz, 2H), 4.54 (s, 2H), 3.64 (dd, J = 11.7, 5.0 Hz, 2H),
3.02 (d, J = 3.2 Hz, 1H), 2.47-2.39 (m, 5H), 1.67 (d, J = 13.7 Hz, 2H).
**$^{13}$C NMR** (*101 MHz, DMSO-d6*) δ 174.73, 143.27, 141.67, 133.09, 129.72, 128.65, 127.22, 121.63, 115.36, 58.59, 57.45, 42.45, 27.80, 20.83.

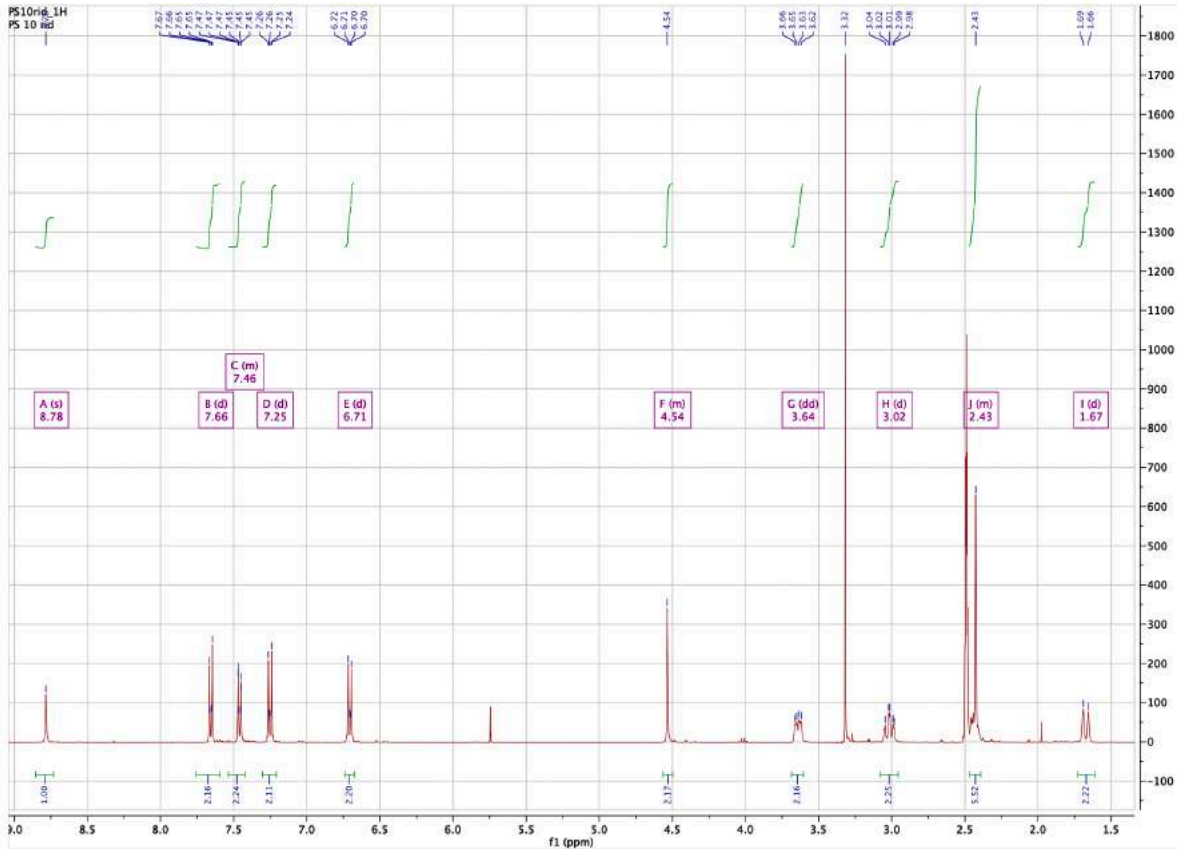


$^{1}$H NMR spectrum of compound **41**.

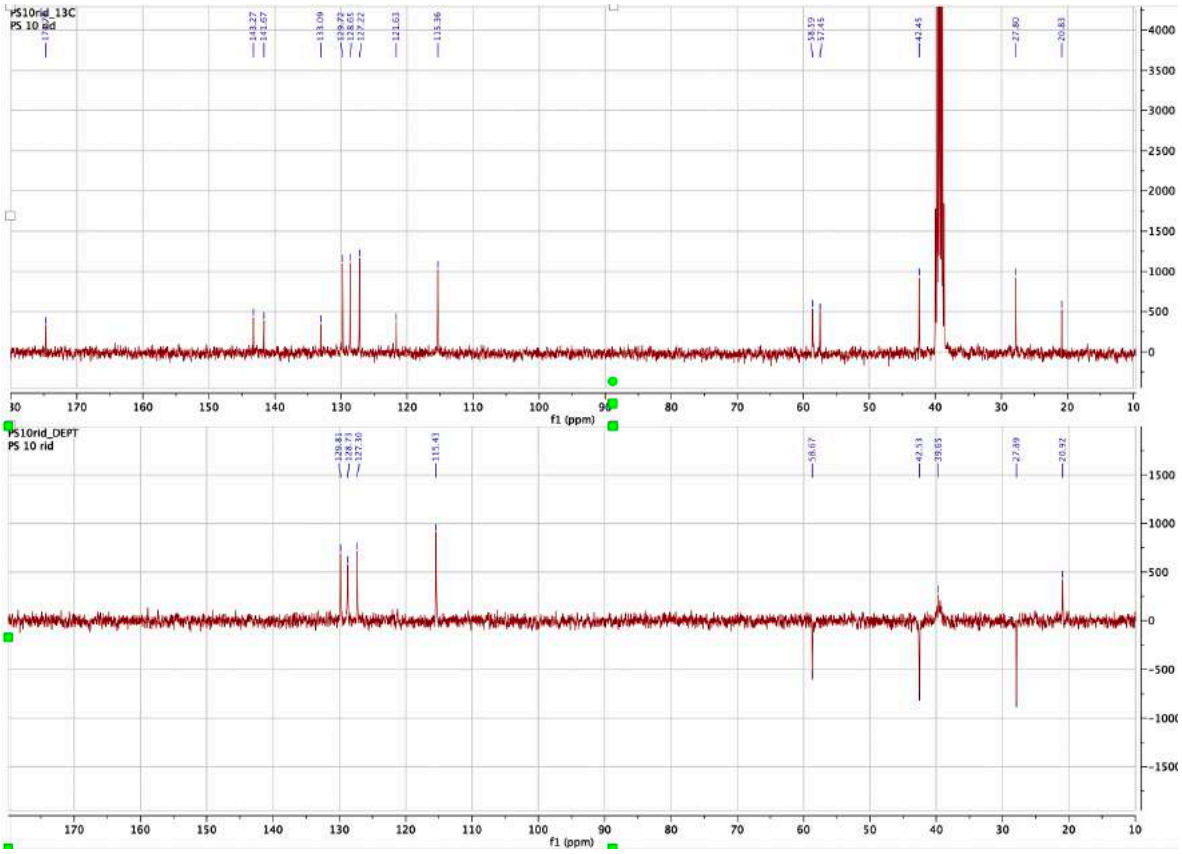


$^{13}$C NMR and DEPT spectra of compound **41**.

**Compound 43**. Synthesis of 1-*benzyl-8-tosyl-1,3,8-triazaspiro[4.5]decan-4-one*

MS (ESI): m/z $[M+H]^+$

*Yield:* 66%

**$^1$H NMR** (400 MHz, Chloroform-*d*) δ 7.70 – 7.65 (m, 2H), 7.36 – 7.32 (m, 2H), 3.38 (t, *J* = 6.2 Hz, 4H), 2.53 (t, *J* = 6.3 Hz, 4H), 2.44 (s, 3H).

**$^{13}$C NMR** (101 MHz, Chloroform-*d*) δ 206.08, 144.60, 133.83, 130.39, 128.01, 46.35, 41.12, 22.00.

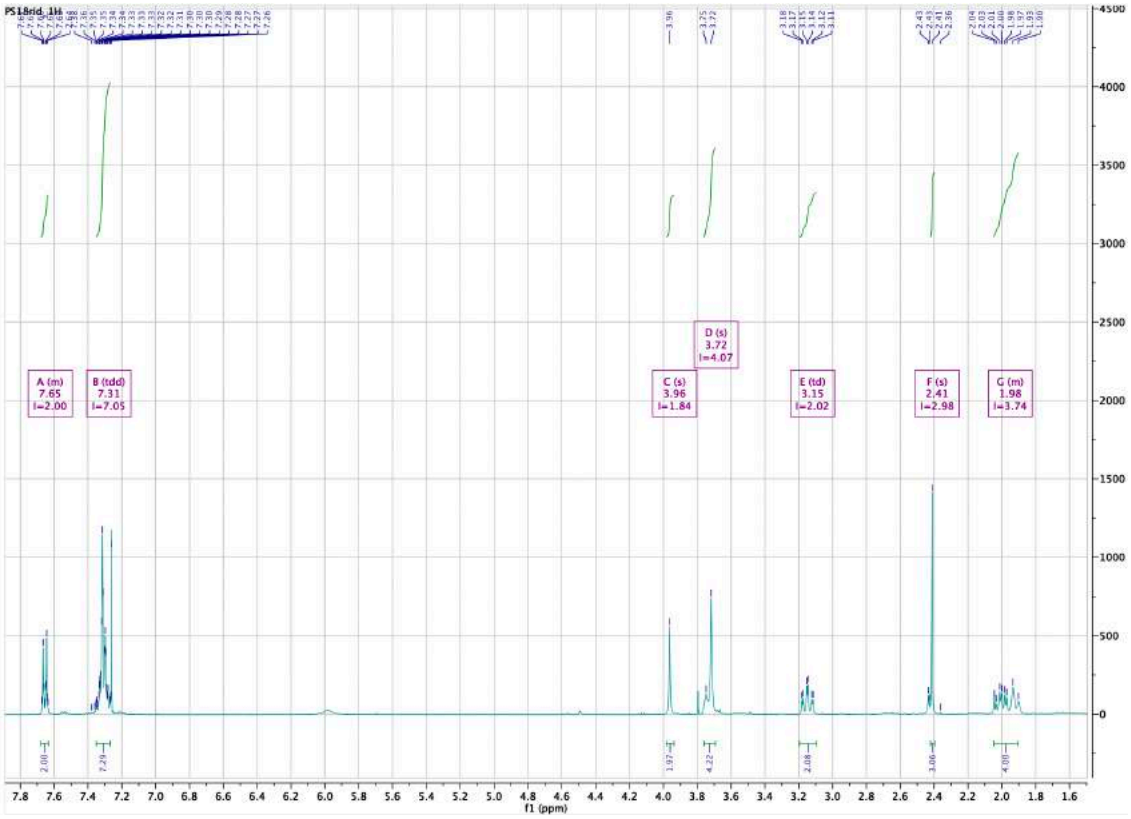


$^1$H NMR spectrum of compound **43**.

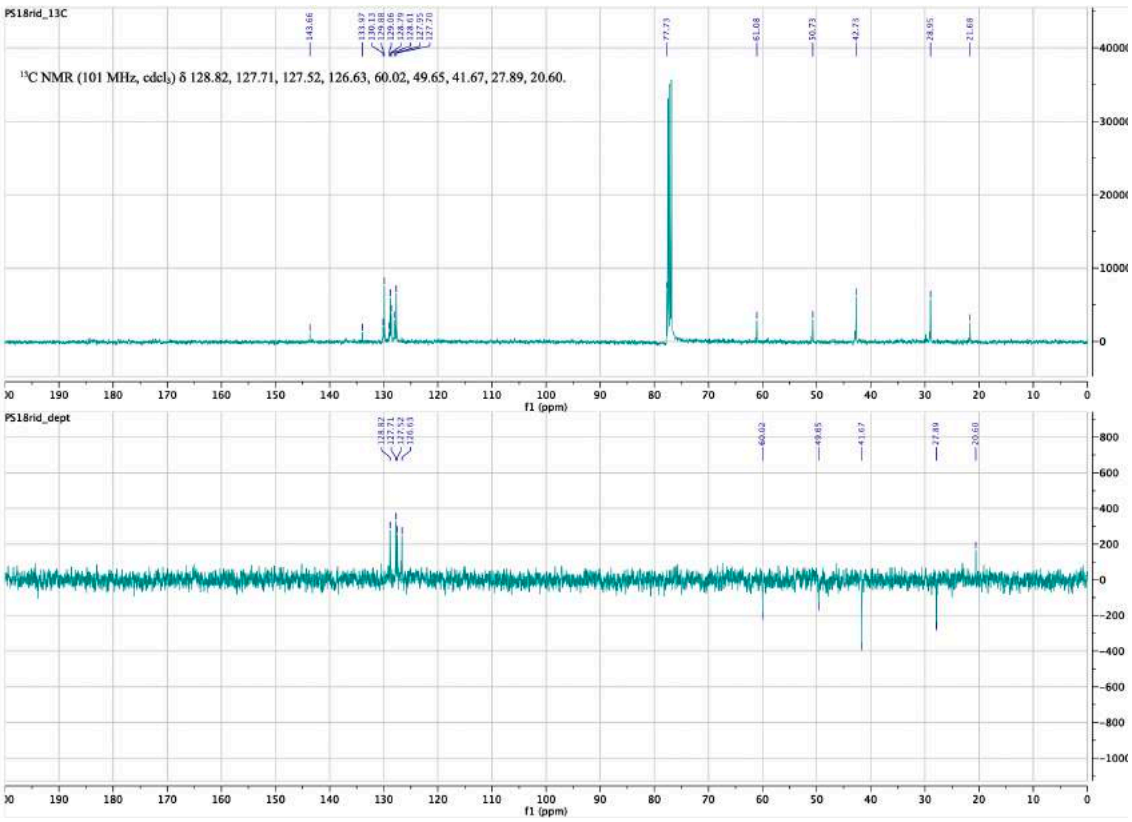


$^{13}$C NMR and DEPT spectra of compound **43**.

**Compound 42**. Synthesis of *1-(3,4-dichlorophenyl)-8-tosyl-1,3,8-triazaspiro[4.5]decan-4-one*

MS (ESI): m/z $[M+H]^+$ 454.35; 456.41

*Yield:* 47%

**$^1$H NMR** *(400 MHz, DMSO-d6)* δ 8.84 (s, 1H), 7.70 – 7.64 (m, 2H), 7.46 (dd, J = 10.5, 8.6 Hz, 3H), 6.87 (d, J = 2.8 Hz, 1H), 6.74 (dd, J = 9.1, 2.9 Hz, 1H), 4.58 (s, 2H), 3.66 (dd, J = 11.7, 5.0 Hz, 2H), 3.00 (td, J = 12.1, 3.1 Hz, 2H), 2.47-2.38 (m, 5H), 1.71 (d, J = 13.8 Hz, 2H).

**$^{13}$C NMR** (*101 MHz, DMSO-d6*) δ 175.07, 144.00, 143.39, 133.51, 132.28, 130.99, 130.37, 127.93, 119.60, 115.29, 114.20, 59.27, 58.14, 43.12, 28.41, 21.49.

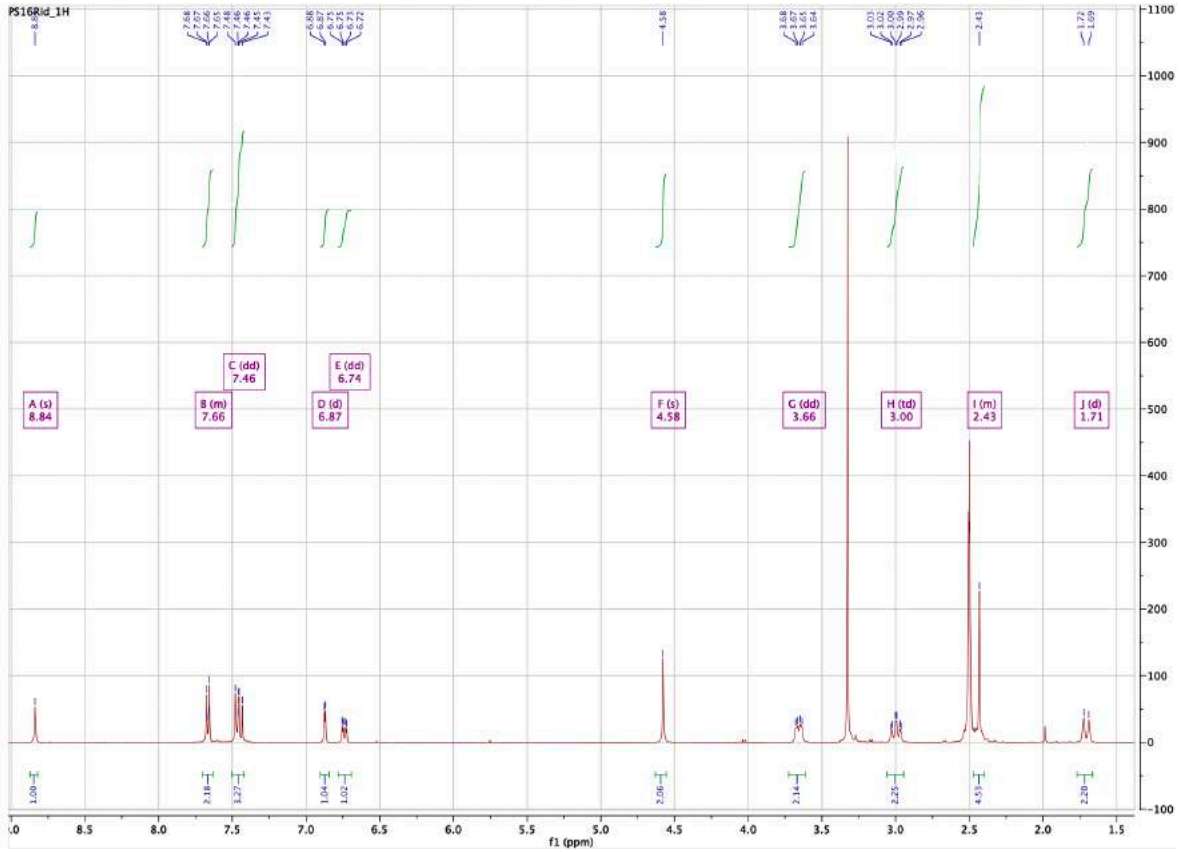


$^{1}$H NMR spectrum of compound **42**.

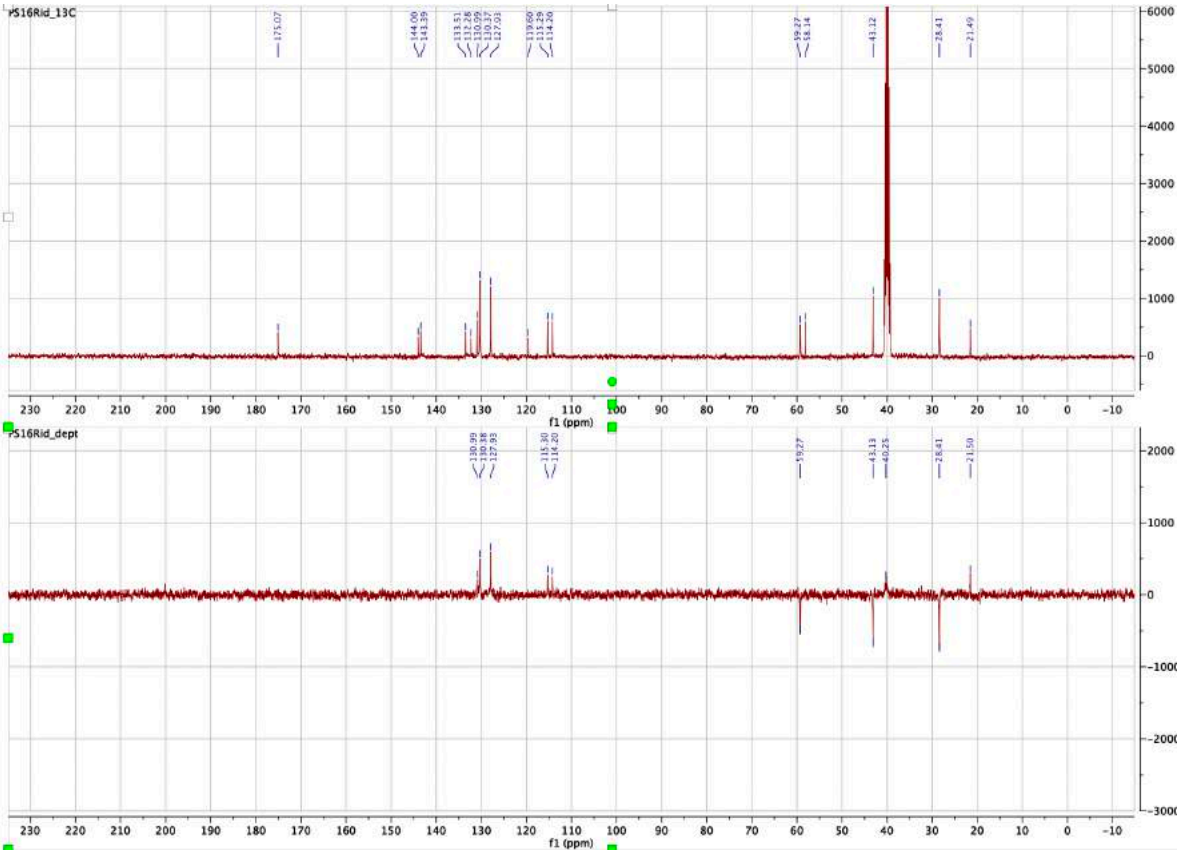


$^{13}$C NMR and DEPT spectra of compound **42**.

## 5.2.2 General procedure for the synthesis of monospiranic compounds **44-46.**

Final compounds **44-47**.

**Compound 44.** Synthesis of *8-(6-fluoropicolinoyl)-1-phenyl-1,3,8-triazaspiro[4.5]decan-4-one*

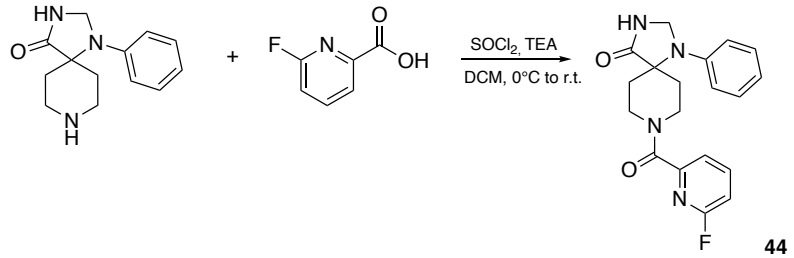


**44**

To a solution of 6-fluoropicolinic acid (1 eq, 2.16 mmol) in DCM at 0°C, oxalyl chloride (1.2 eq, 2.6 mmol) was added dropwise. Catalytic amount of DMF was added and bubbling was observed. After 15 minutes, triethylamine (TEA, 1 eq, 2.16 mmol) was added, followed by a solution of the commercially available 1-phenyl-1,3,8-triazaspiro[4.5]decan-4-one (1 eq, 2.16 mmol), previously dissolved in DCM. The reaction was warmed to room temperature and stirred for 18 hours. After the reaction was complete, as indicated by TLC and mass (ESI), the solvent was removed under vacuum and the residue was redissolved in DCM. The organic layer was washed three times with water, dried over $Na_2SO_4$, filtered and concentrated in vacuum. The crude yellowish oil was purified by flash chromatography (9:1 AcOEt/petroleum ether) obtaining the compound **44** as a white solid (235 mg).

MS (ESI): m/z $[M+H]^+$ 354,15

Yield: 47%

**$^1$H NMR** (400 MHz, Chloroform-*d*) δ 7.91 (q, J = 7.8 Hz, 1H), 7.59 (ddd, J = 7.3, 2.2, 0.8 Hz, 1H), 7.34 – 7.27 (m,2H), 7.04 – 6.99 (m, 1H), 6.93 – 6.86 (m, 2H), 6.80 (s, 1H), 4.78 (t, J = 4.2 Hz, 2H), 4.70 – 4.65 (m, 1H), 3.93 – 3.89 (m, 2H), 3.70 – 3.63 (m, 1H), 2.89 – 2.81 (m, 1H), 2.72 – 2.65 (m, 1H), 1.88 (d, J = 14.1 Hz, 1H), 1.76 (dd, J = 14.0, 3.5 Hz, 1H).

**$^{13}$C NMR** (101 MHz, Chloroform-*d*) δ 177.44, 166.11, 163.28, 160.86, 152.71, 152.59, 142.73, 142.23, 129.67, 121.29, 119.86, 115.67, 111.13, 110.77, 59.70, 59.48, 43.89, 39.53, 29.84, 29.17.

**$^{19}$F NMR** (376 MHz, Chloroform-*d*) δ -66.01, -66.60.

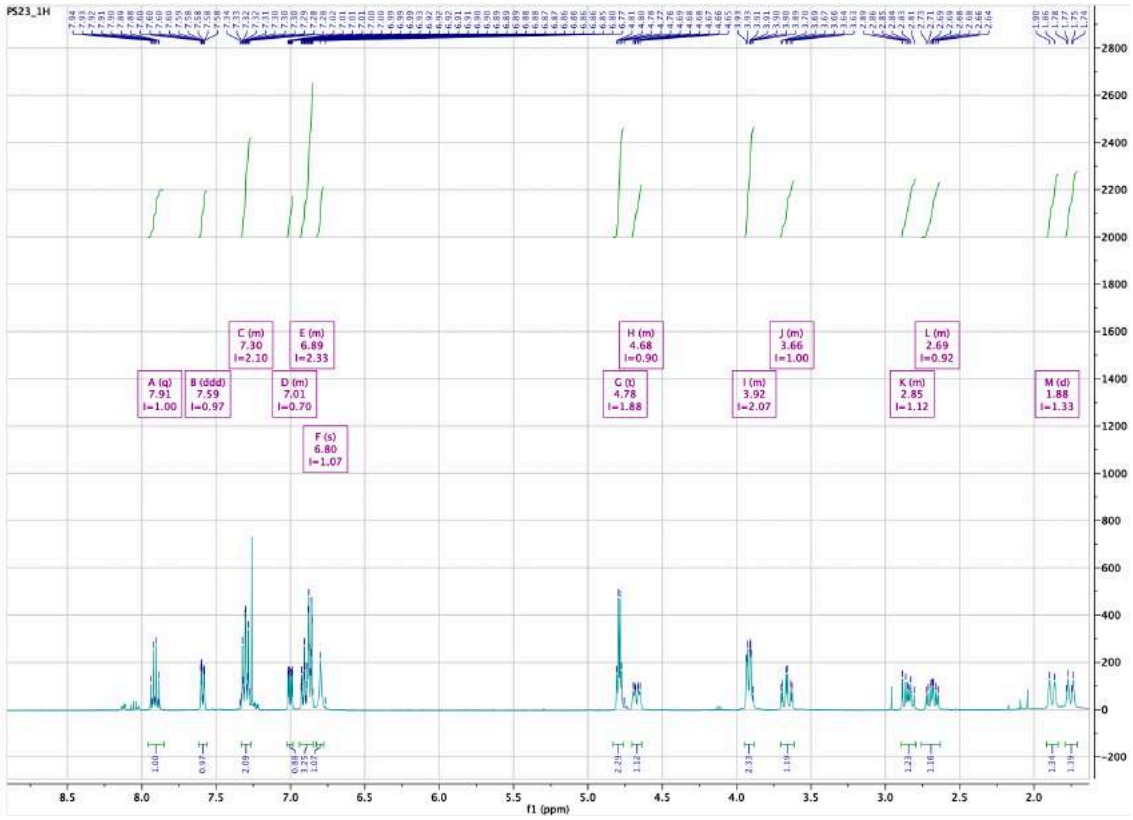


$^{1}$H NMR spectrum of compound **44**.

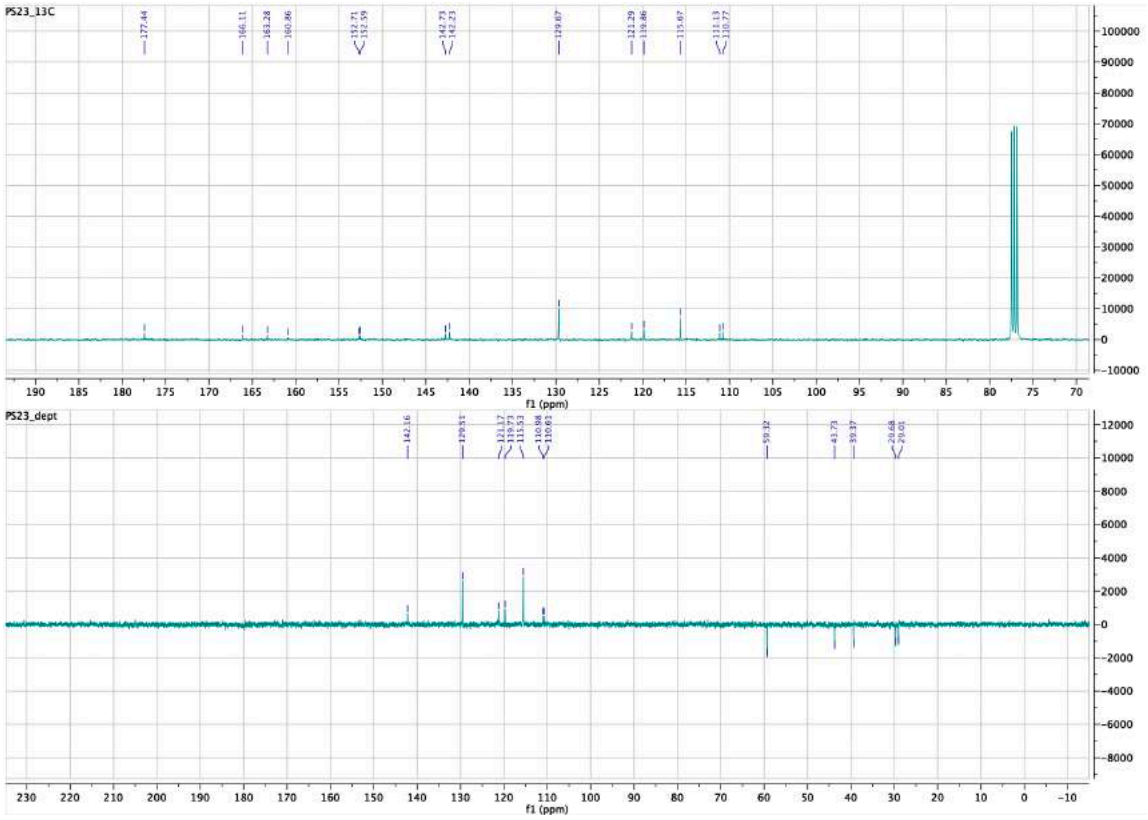


$^{13}$C NMR and DEPT spectra of compound **44**.

**Compound 45**. Synthesis of *8-(5-fluoro-1H-indole-2-carbonyl)-1-phenyl-1,3,8-triazaspiro[4.5]decan-4-one*

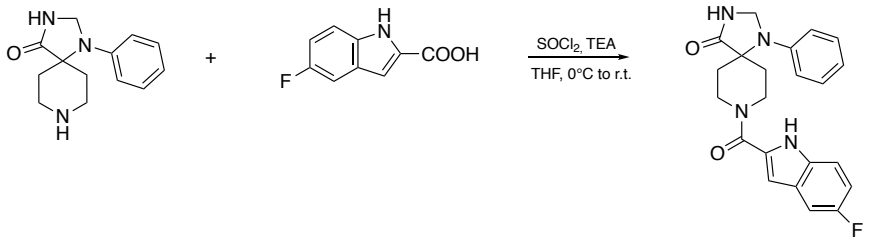


**45**

To a solution of 5-fluoro-1*H*-indole-2-carboxylic acid (1eq, 2.16 mmol) in THF at 0°C, oxalyl chloride (1.2 eq, 2.6 mmol) was added dropwise. Catalytic amount of DMF was added and bubbling was observed. After 15 minutes, triethylamine (TEA, 1 eq, 2.16 mmol) was added, followed by a solution of the commercially available 1-phenyl-1,3,8-triazaspiro[4.5]decan-4-one (1 eq, 2.16 mmol), previously dissolved in THF. The reaction was warmed to room temperature and stirred for 18 hours. After the reaction was complete, as indicated by TLC and mass (ESI), the solvent was removed under vacuum and the residue was redissolved in DCM. The organic layer was washed three times with water, dried over $Na_2SO_4$, filtered and concentrated in vacuum. The crude yellowish oil was purified by flash chromatography (9.5:0.5 AcOEt/petroleum ether) obtaining the compound **45** as a light brown solid (180 mg).

MS (ESI) $[M+H]^+$: 393,14

Yield: 36%

**$^1$H NMR** (400 MHz, DMSO-$d_6$) δ 11.77 (d, J = 2.2 Hz, 1H), 8.85 (s, 1H), 7.39 (ddd, J = 25.2, 9.4, 3.6 Hz, 2H), 7.27 –7.17 (m, 2H), 7.05 (td, J = 9.3, 2.6 Hz, 1H), 6.87 – 6.83 (m, 1H), 6.80 – 6.75 (m, 3H), 4.63 (s, 2H), 4.44 – 4.35 (m, 2H), 3.32 (s, 2H), 2.50-2.48 (m, 2H) 1.78 (d, J = 13.9 Hz, 2H).

**$^{13}$C NMR** (101 MHz DMSO-$d_6$) δ 175.76, 162.01, 158.26, 155.95, 143.12, 132.63, 131.81, 129.21, 127.01, 126.90, 118.08, 114.31, 113.26, 113.17, 111.96, 111.69, 105.62, 105.38, 103.64, 58.78, 58.57, 28.68.

**$^{19}$F NMR** (376 MHz DMSO-$d_6$) δ -123.88, -123.89.

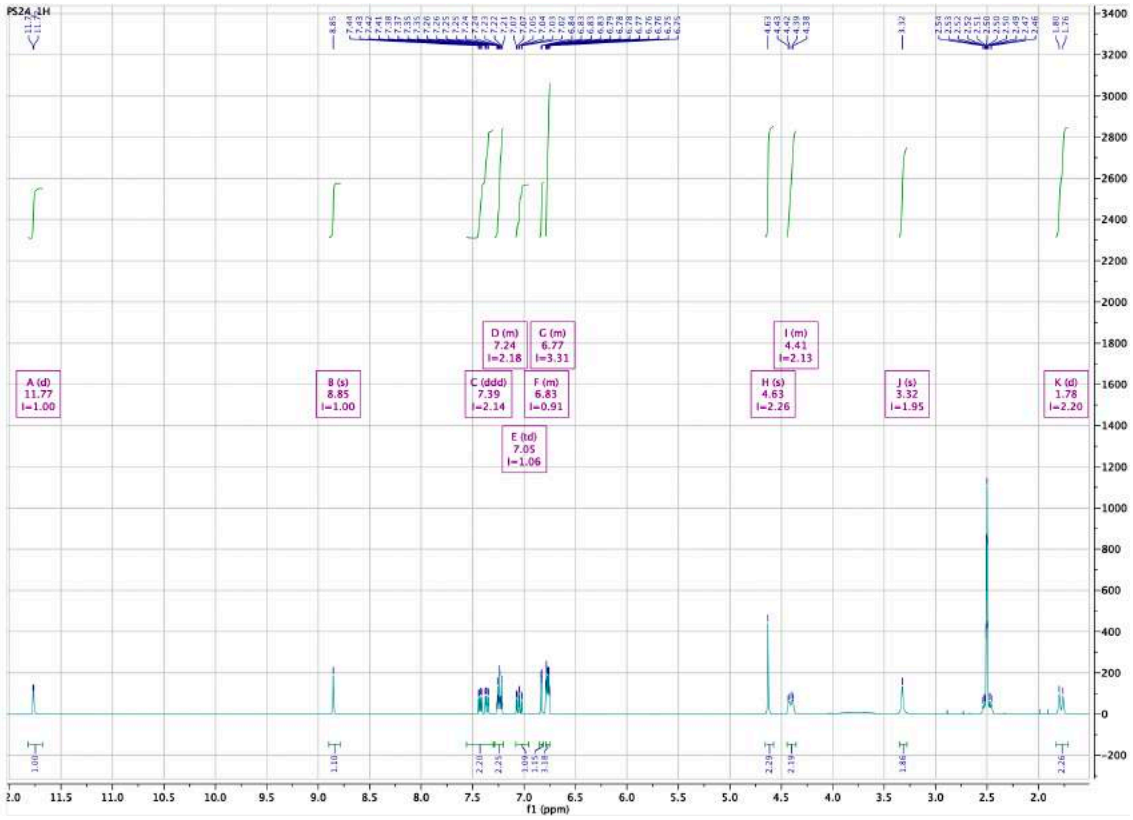


$^{1}$H NMR spectrum of compound **45**.

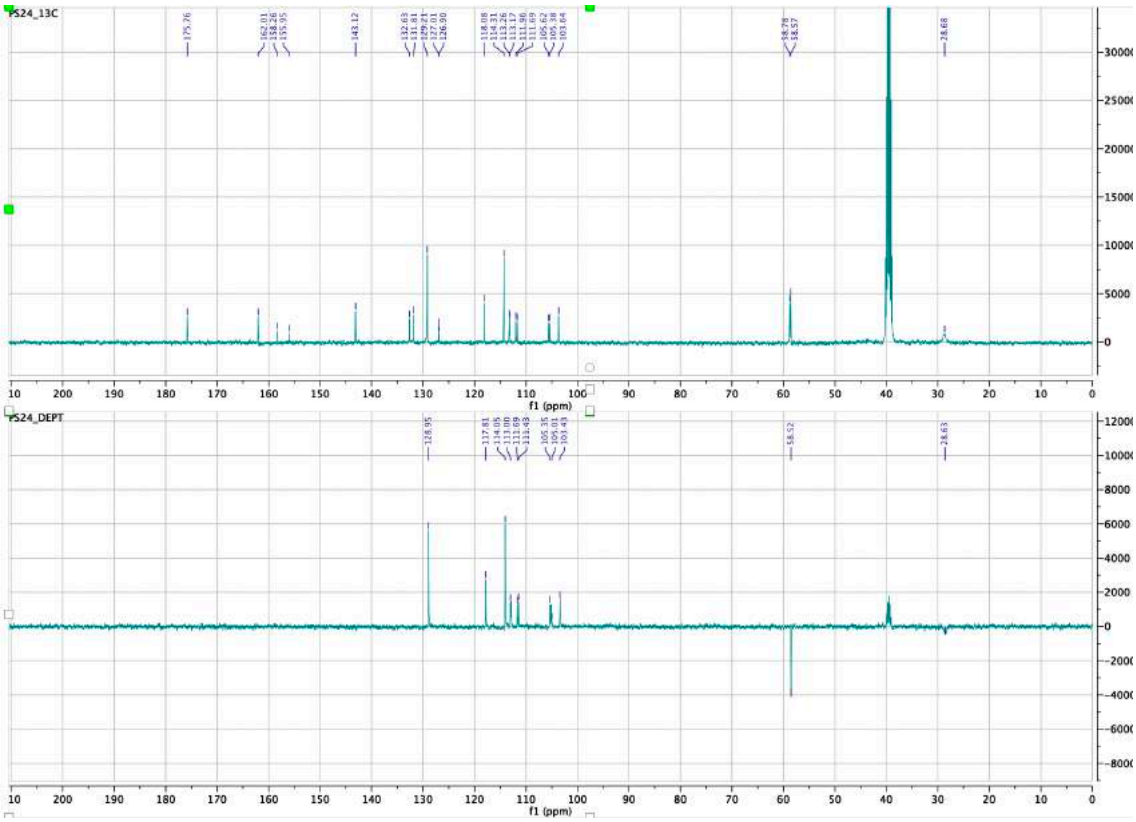


$^{13}$C NMR and DEPT spectra of compound **45**.

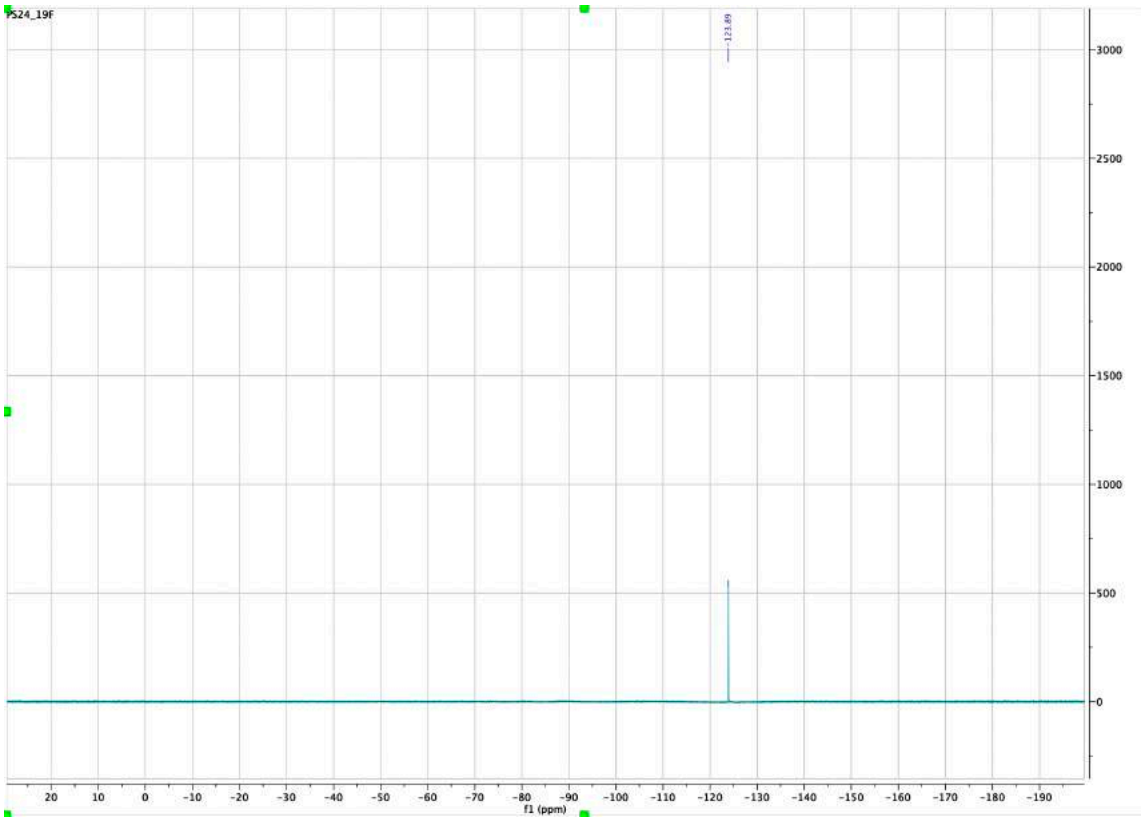


$^{19}F$ spectrum of compound **45**.

**Compound 46**. Synthesis of *8-(benzo[b]thiophen-2-ylmethyl)-1-phenyl-1,3,8-triazaspiro[4.5]decan-4-one*

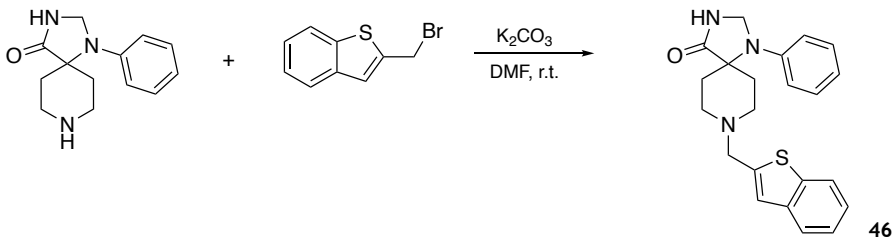


**46**

To a solution of 2-(bromomethyl)benzo[*b*]thiophene (1 eq, 2.16 mmol) in DMF, $K_2CO_3$ (1.2 eq, 2.6 mmol) was added, followed by a solution of the commercially available 1-phenyl-1,3,8-triazaspiro[4.5]decan-4-one (1 eq, 2.16 mmol), previously dissolved in DMF. The reaction was stirred for 4 hours. After the reaction was complete, as indicated by TLC and mass (ESI), the solvent was removed under vacuum and the residue was redissolved in DCM. The organic layer was washed three times with water, dried over $Na_2SO_4$, filtered and concentrated in vacuum. The crude yellowish oil was purified by flash chromatography (7:3 AcOEt/petroleum ether) obtaining the compound **46** as a white and crystalline solid (1.1 g).

MS (ESI) $[M+H]^+$: 378,25

Yield: 84%

**$^{1}$H NMR** (400 MHz, Chloroform-*d*) δ 7.85 – 7.78 (m, 1H), 7.70 (dd, J = 7.4, 1.6 Hz, 1H), 7.37 – 7.25 (m, 5H), 7.17 (s, 1H), 7.01 – 6.94 (m, 3H), 6.92 – 6.87 (m, 1H), 4.75 (s, 2H), 3.88 (s, 2H), 2.92 (s, 2H), 2.76 (s, 1H), 1.76 – 1.69 (m, 3H).

**$^{13}$C NMR** (101 MHz, Chloroform-*d*) δ 178.28, 144.91, 143.24, 140.16, 139.88, 129.74, 129.47, 124.18, 123.92, 123.20, 122.48, 121.83, 118.95, 115.23, 59.37, 59.27, 58.07, 49.94, 29.29.

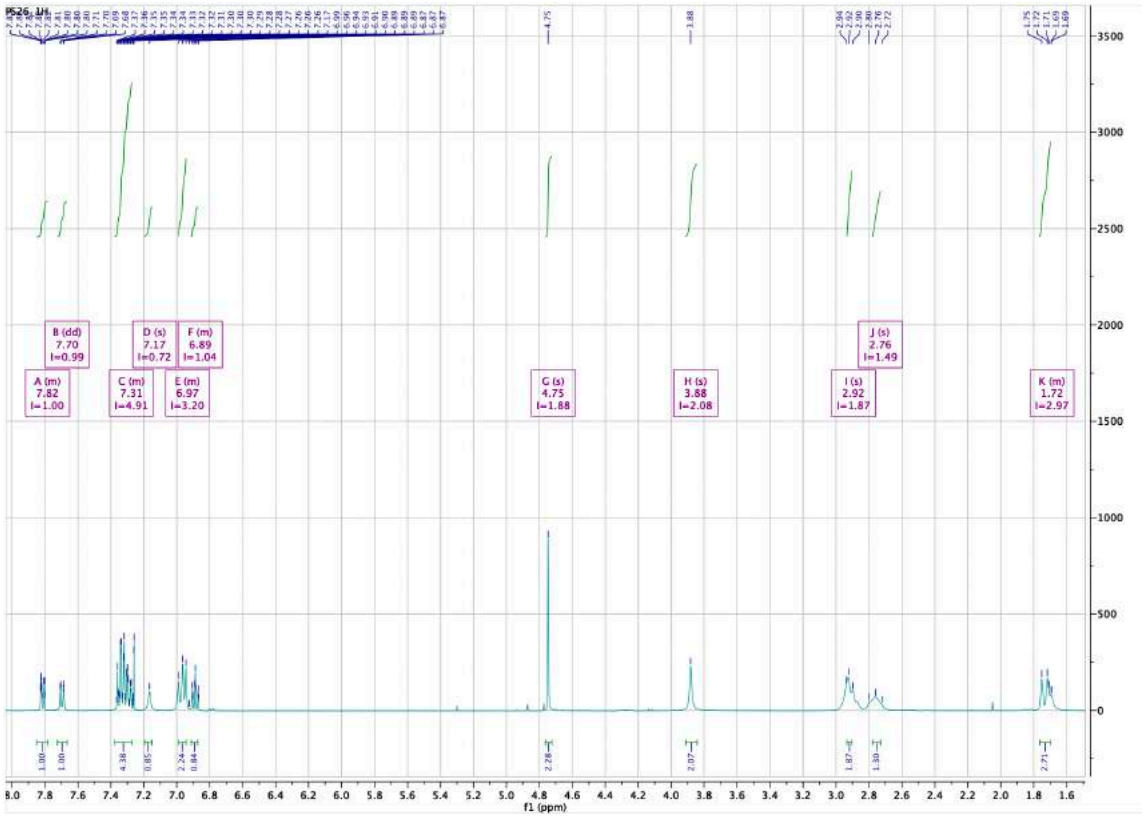


$^{1}$H NMR spectrum of compound **46**.

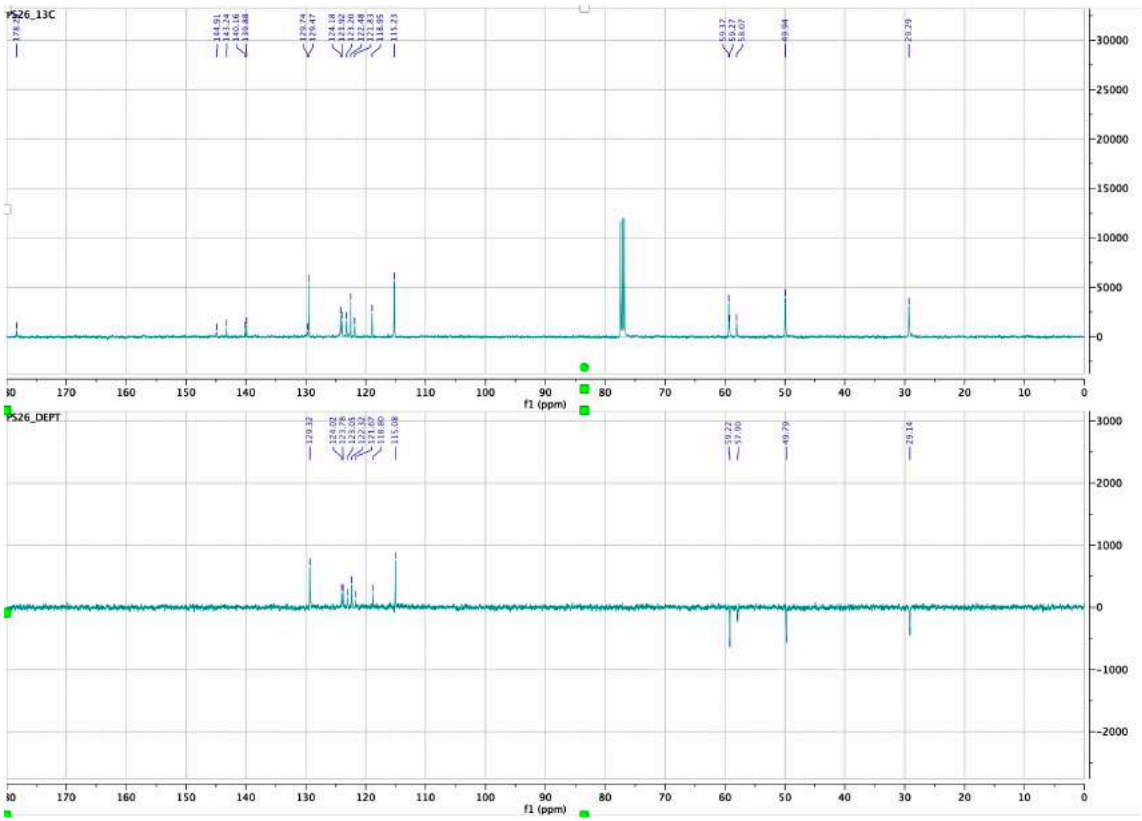


$^{13}$C NMR and DEPT spectra of compound **46**.

**Compound 47**. Synthesis of *2-(bromomethyl)benzo[b]thiophene*

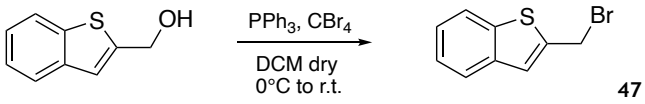


**47**

To a solution of benzo[*b*]thiophen-2-ylmethanol (1 eq, 6.09 mmol) in dry DCM, triphenylphosphine ($PPh_3$, 1.2 eq, 7.30 mmol) was added. Then, once $PPh_3$ was dissolved, the reaction was cooled to 0°C and carbon tetrabromide ($CBr_4$, 1.2 eq, 7.30 mmol) was added slowly and in small portion. The reaction was warmed to room temperature and monitored via TLC. After 3 hours, the solvent was evaporated under vacuum and the crude compound was purified by chromatographic column (1:9 AcOEt: petroleum ether). The purified compound was obtained as a white crystalline solid and it is not appreciable via MS-ESI analysis.

Yield: 70%

**$^1$H NMR** (400 MHz, Chloroform-*d*) δ 7.81 – 7.77 (m, 1H), 7.75 – 7.71 (m, 1H), 7.37 – 7.31 (m, 3H), 4.79 (d, J = 0.7 Hz, 2H).

**$^{13}$C NMR** (101 MHz, Chloroform-*d*) δ 141.23, 140.75, 139.36, 125.17, 124.78, 124.64, 124.00, 122.61, 27.41.

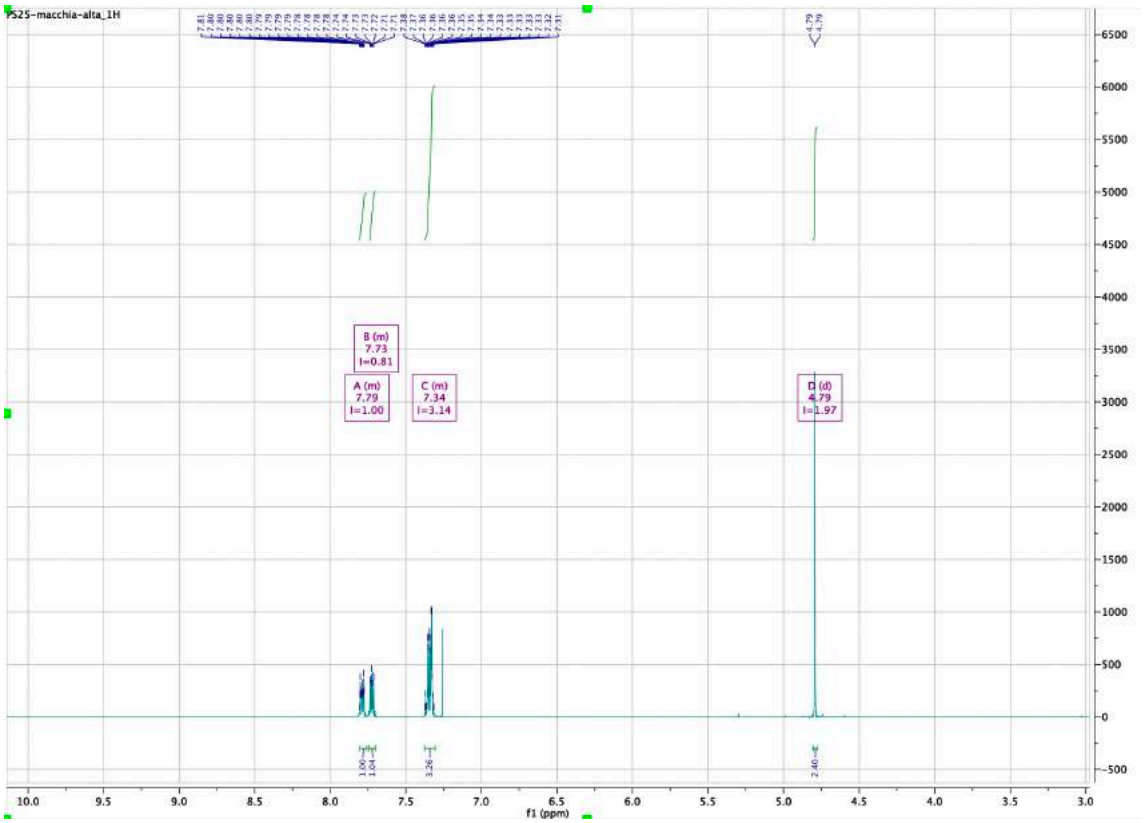


$^{1}$H NMR spectrum of compound **47**.

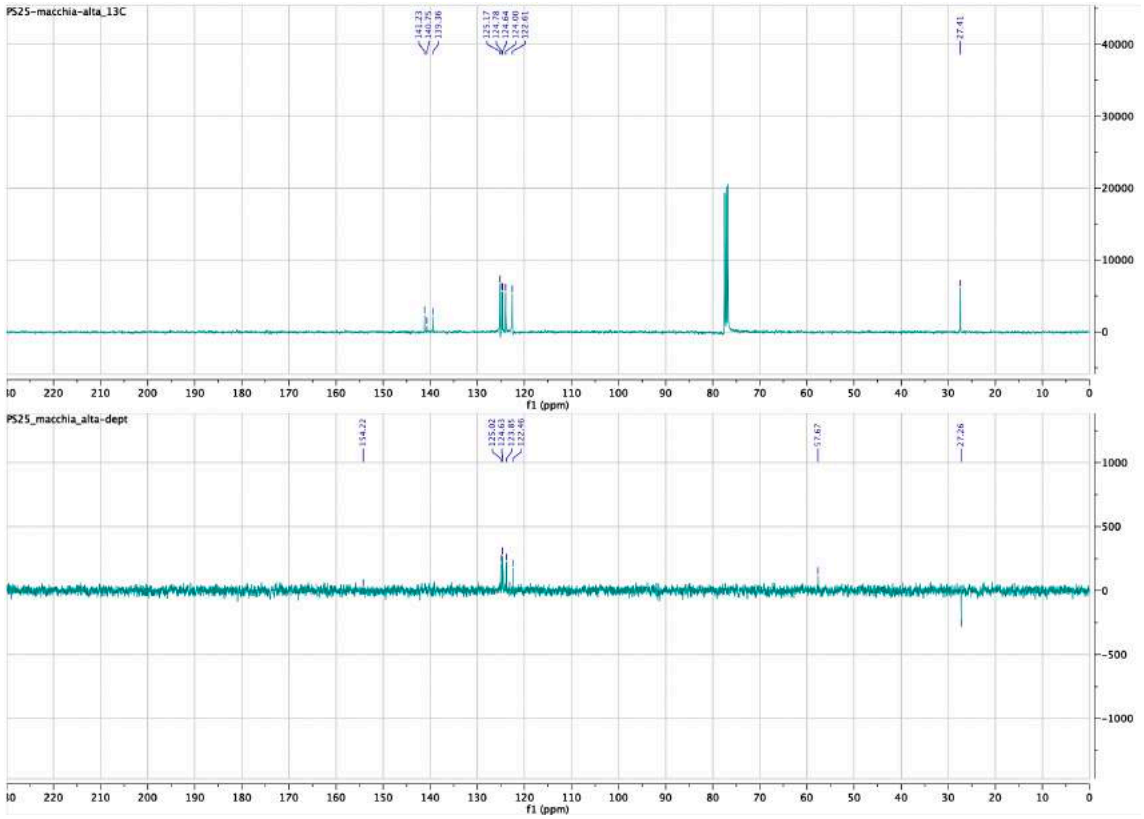


$^{13}$C NMR and DEPT spectra of compound **47**.

## 5.2.3 GENERAL PROCEDURE FOR THE SYNTHESIS OF MONOSPIRANIC COMPOUNDS **62-64.**

Intermediates **48-50**.

**Compound 48**. Synthesis of *1-benzoylpiperidin-4-one*

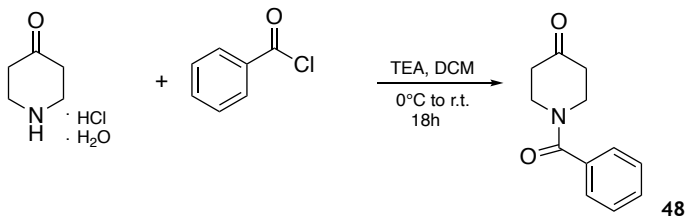


**48**

In a round bottomed flask, piperidin-4-one monohydrated monochloride (1eq, 6,51 mmol) is suspended in DCM and then TEA (3eq, 19,53 mmol) is added dropwise. After 1 hour, the reaction was cooled to 0°C and a solution of benzoyl chloride (3 eq, 19.53 mmol) previously dissolved in DCM was slowly added. The reaction was allowed to warm to room temperature and stirred for 18 hours. Once the reaction was completed, as indicated by TLC, the mixture was treated: the solvent was evaporated under vacuum and resuspended in DCM. The organic layer was extracted three times with water, dried over $Na_2SO_4$, filtered and concentrated in vacuum. The crude brown oil was purified by flash chromatography (3:7 AcOEt/petroleum ether) obtaining the compound **48** as a white solid (1.3 g).

MS (ESI) $[M+H]^+$: 204.38
Yield: 57%
**$^1$H NMR** (400 MHz, Chloroform-*d)* δ 7.59 – 7.29 (m, 5H), 3.87 (d, J = 64.0 Hz, 4H), 2.50 (s, 4H).
**$^{13}$C NMR** (101 MHz, Chloroform-*d*) δ 206.82, 171.08, 135.26, 130.39, 128.82, 127.09, 42.20, 41.64, 41.36, 40.86.

**Compound 49**. Synthesis of *1-(6-fluoropicolinoyl)piperidin-4-one*

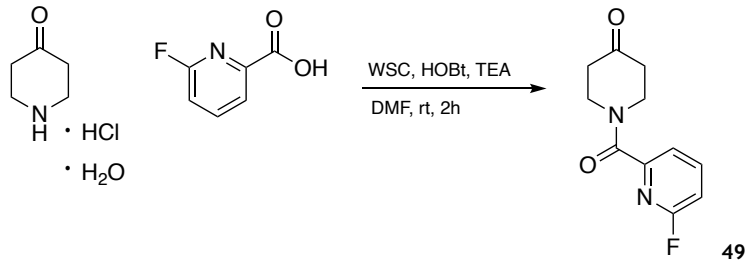


**49**

Suspend the solution of 4-piperidone hydrochloride monohydrate (1.1eq, 6.51mmol) in DMF (6ml) in a 100ml flask, then add TEA (1.5eq, 8.88mmol) and leave to react for 15 minutes. In another 100ml flask, place 6-fluoronicotinic acid (1eq, 5.92mmol), DMF (6ml), WSC (1.1eq, 6.51mmol) and allow to react for 5 minutes; next, add HOBt (1.1eq, 6.51mmol) and wait 10 minutes. Then, in this flask add piperidone mixture with TEA and leave to react at room temperature for 18 hours, monitoring the reaction by mass (ESI) and TLC (A8P2). Then evaporate DMF and extract successively: three times in AcOEt/citric acid and three times in saturated AcOEt/$NaHCO_3$. After drying and evaporating AcOEt, an orange oil is obtained, from which the product of

interest is isolated by column chromatography, using an eluent mixture of petroleum ether/AcOEt (2:8). Following evaporation of the organic solvent, a yellowish oil is obtained.

MS (ESI) [M+H+]: 223.29

Yield: 60%

**$^{1}$H NMR** (400 MHz, Chloroform-d) δ 7.94 (td, J = 8.1, 7.5 Hz, 1H), 7.67 (ddd, J = 7.4, 2.2, 0.8 Hz, 1H), 7.05 (ddd, J = 8.3, 2.7, 0.8 Hz, 1H), 4.04 (t, J = 6.4 Hz, 2H), 3.90 (t, J = 6.2 Hz, 2H), 2.61 (t, J = 6.4 Hz, 4H).

**$^{13}$C NMR** (101 MHz, Chloroform-d) δ 206.75, 165.94, 162.89, 160.47, 151.55, 151.43, 142.41, 142.34, 121.89, 121.85, 111.62, 111.26, 45.90, 42.08, 41.52, 40.83.

**Compound 50**. Synthesis of *1-((5-chlorothiophen-2-yl)sulfonyl)piperidin-4-one*

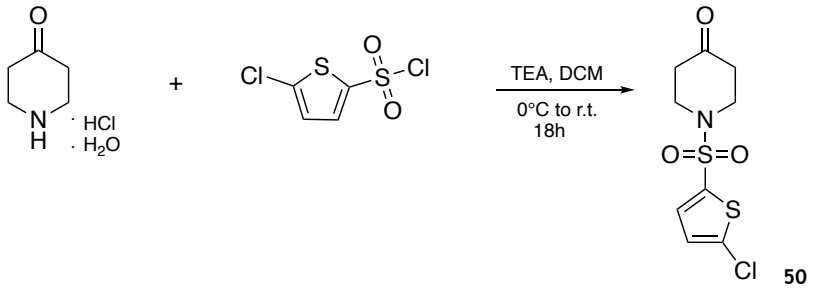

**50**

In a round bottomed flask, piperidin-4-one monohydrated monochloride (1eq, 6,51 mmol) is suspended in DCM and then TEA (3eq, 19,53 mmol) is added dropwise. After 15 minutes, the reaction was cooled to 0°C and a solution of 5-chlorothiophene-2-sulfonyl chloride previously dissolved in DCM was slowly added. The reaction was allowed to warm to room temperature and stirred for 18 hours. Once the reaction was completed, as indicated by TLC, the mixture was treated: the solvent was evaporated under vacuum and resuspended in DCM. The organic layer was extracted three times with water, dried over $Na_2SO_4$, filtered and concentrated in vacuum. The crude brown oil was purified by flash chromatography (3:7 AcOEt/petroleum ether) obtaining the compound **35** as a yellowish solid (1.3 g).

MS (ESI) $[M+H]^+$: 278,98

Yield: 95%

**$^{1}$H NMR** (400 MHz, Chloroform-*d*) δ 7.37 (d, J = 4.0 Hz, 1H), 6.99 (d, J = 4.0 Hz, 1H), 3.47 (d, J = 6.2 Hz, 4H), 2.57(d, J = 6.4 Hz, 4H).

**$^{13}$C NMR** (101 MHz, Chloroform-*d*) δ 205.10, 138.20, 134.79, 132.24, 127.37, 46.03, 40.55.

Intermediates **51-52**.

In an Argon environment, place the ketone **48-49** (1eq, 816mg, 4.02mmol) dissolved in distilled DCM. Next, add $InBr_3$ (10.1eq, 42.53mg, 0.40mmol) and wait for its complete dissolution for 5-10 minutes; then add TMSCN (2eq, 1.01ml, 8.04mmol) dropwise. Allow to react at room temperature for 18 hours, monitoring the reaction by TLC (A7P3) and mass spectrometry (ESI). Then evaporate the distilled DCM and extract in DCM/$H_2O$ deionized. After drying and evaporating the solvent, isolate the cyanohydrin **51-52** from its silyl derivative **51a-52a** by column chromatography, using a petroleum ether/AcOEt (3:7) eluent mixture.

Finally, deprotect the silyl derivative by acid hydrolysis: dilute in MeOH (10ml), place the flask in an ice bath and add HCl solution dropwise until pH-acid; then evaporate the organic solvent, extract with deionized water and AcOEt, dry and evaporate the organic solvent. The cyanohydrine derivatives **51-52** are obtained as white solid.

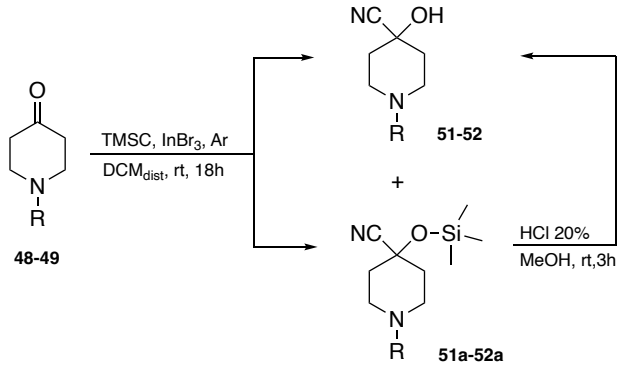


**Compound 51**. Synthesis of *1-benzoyl-4-hydroxypiperidine-4-carbonitrile*
MS (ESI) [M+H+]: 231.34
Yield: 78%
**$^{1}$H NMR** (401 MHz, Chloroform-d) δ 7.56 – 7.37 (m, 5H), 4.86 (s, 1H), 3.77 – 3.57 (m, 4H), 2.34 (t, J = 7.1 Hz, 4H).
**$^{13}$C NMR** (100 MHz, Chloroform-d) δ 170.36, 136.22, 130.67, 128.93, 127.63, 120.42, 66.15, 41.22, 39.00.

**Compound 52**. Synthesis of *1-(6-fluoropicolinoyl)-4-hydroxypiperidine-4-carbonitrile*
MS (ESI) [M+H+]: 322.18
Yield: 96%
**$^{1}$H NMR** (401 MHz, Chloroform-d) δ 7.83 – 7.77 (m, 1H), 7.77 – 7.71 (m, 1H), 7.25 – 7.17 (m, 1H), 4.84 (s, 1H), 3.82 – 3.66 (m, 4H), 2.40 – 2.24 (m, 4H).
**$^{13}$C NMR** (100 MHz, Chloroform-d) δ 164.60, 164.57, 162.37, 159.86, 148.08, 140.94, 120.42, 110.88, 66.56, 41.17, 38.45.

Intermediates **53-55**.

Dissolve the appropriate compound **51-52** in DCM (10ml) and add $InBr_3$ (0.1eq). Next, add benzylamine (1.5eq) dropwise. Allow to react at room temperature for 3 hours, keeping the reaction monitored by TLC and mass spectrometry (ESI). Upon completion, evaporate the DCM and extract with DCM and $NaHCO_{3sat}$ (3x30ml). After drying and evaporating the solvent, isolate the product of interest by column chromatography, using a petroleum ether/AcOEt (1:1) eluent mixture. Finally, evaporate the organic solvent, resulting in the desired aminonitrile derivative **53-54** as white solid.

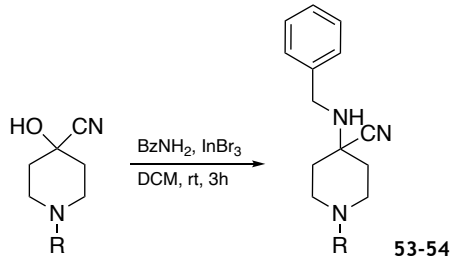

**53-54**

**Compound 53**. Synthesis of *1-benzoyl-4-(benzylamino)piperidine-4-carbonitrile*
MS (ESI) [M+H+]: 320.38
Yield: 81%
**$^{1}$H NMR** (400 MHz, Chloroform-d) δ 7.47 – 7.26 (m, 10H), 4.37 (s, 1H), 3.93 (s, 2H), 3.77 (s, 1H), 3.48 (p, J=5.8, 4.5 Hz, 2H), 2.19 – 2.09 (m, 1H), 2.00 (s, 1H), 1.88 (s, 1H)
**$^{13}$C NMR** (101 MHz, Chloroform-d) δ 170.41, 138.60, 135.37, 129.98, 128.63, 128.38, 127.70, 126.89, 120.74, 55.90, 48.91, 43.72.

**Compound 54**. Synthesis of *4-(benzylamino)-1-(6-fluoropicolinoyl)piperidine-4-carbonitrile*
MS (ESI) [M+H+]: 339.37
Yield:71%
**$^{1}$H NMR** (400 MHz, Chloroform-d) δ 7.97 – 7.87 (m, 1H), 7.59 (ddd, J = 7.4, 2.2, 0.8 Hz, 1H), 7.19 (dd, J = 8.1, 7.6 Hz, 1H), 7.03 (ddd, J = 8.3, 2.7, 0.8 Hz, 1H), 6.91 – 6.84 (m, 2H), 6.75 (ddd, J = 8.1, 2.6, 1.0 Hz, 1H), 4.30 (dt, J = 14.0, 4.9 Hz, 1H), 4.00 – 3.94 (m, 1H), 3.88 (d, J = 1.9 Hz, 2H), 3.59 – 3.49 (m, 2H), 2.20 – 2.09 (m, 2H), 1.91 (dp, J = 13.7, 5.1, 4.4 Hz, 2H).
**$^{13}$C NMR** (101 MHz, Chloroform-d) δ 165.83, 163.07, 160.66, 156.23, 151.72, 151.60, 142.52, 140.55, 129.94, 121.77, 120.89, 120.42, 115.22, 114.73, 111.51, 111.15, 55.76, 48.47, 43.27, 38.77, 35.69, 34.94.
**$^{19}$F NMR** (376 MHz, Chloroform-d) δ -66.46.

**Compound 55**. Synthesis of *4-(benzylamino)-1-((5-chlorothiophen-2-yl)sulfonyl)piperidine-4-carbonitrile*
This intermediate derives from compound **50** and follows the same procedure for the synthesis of compound **32** (see paragraph above).
MS (ESI) [M+H+]: 396.34
Yield: 84%
**$^{1}$H NMR** (400 MHz, Chloroform-d) δ 7.36 – 7.27 (m, 6H), 7.01 (d, J = 4.0 Hz, 1H), 3.89 (s, 2H), 3.62 – 3.53 (m, 2H), 2.98 (ddd, J = 12.5, 9.7, 3.1 Hz, 2H), 2.16 (dddd, J = 12.2, 6.0, 3.3, 1.6 Hz, 2H), 1.94 (ddd, J = 13.6, 9.7, 3.9 Hz, 2H).
**$^{13}$C NMR** (101 MHz, Chloroform-d) δ 138.51, 136.58, 134.39, 132.11, 128.84, 128.46, 127.90, 127.39, 120.48, 54.97, 48.72, 42.33, 34.69.

Intermediates **55-58**.

To a solution of intermediates **53-55** (1eq) in methanol (10ml), DMF/DMA (3eq) is added dropwise. The mixture is reacted at 55°C for 6/10 hours and is monitored by MS-ESI. At the completion of the reaction,

the solvent is evaporated and a yellow solid is obtained. The desired products **56-58**, checked by TLC and MS-ESI, are used as such for the next step.

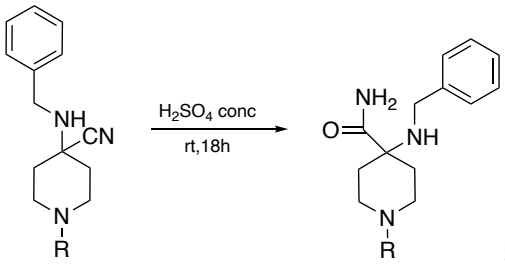


**56-58**

**Compound 56**. Syntehsis of 1-*benzoyl-4-(benzylamino)piperidine-4-carboxamide*
MS (ESI) [M+H+]: 338.18
Yield: 80%
**$^1$H NMR** (400 MHz, Acetone-d6) δ 7.82 – 6.86 (m, 9H), 6.45 (s, 1H), 3.98 (d, J = 59.3 Hz, 1H), 3.65 (s, 2H), 3.55 (d, J = 11.0 Hz, 2H), 1.78 (d, J = 38.7 Hz, 2H).
**$^{13}$C NMR** (101 MHz, Acetone-d6) δ 177.13, 169.25, 140.91, 137.04, 129.15, 128.25, 128.16, 126.87, 126.70, 59.97, 47.12, 43.52, 37.79, 33.02, 32.60.

**Compound 57**. Synthesis of *4-(benzylamino)-1-(6-fluoropicolinoyl)piperidine-4-carboxamide*
MS (ESI) [M+H+]: 357.37
Yield: 76%
**$^1$H NMR** (400 MHz, Chloroform-d) δ 7.94 – 7.87 (m, 1H), 7.54 (ddd, J = 7.4, 2.2, 0.8 Hz, 1H), 7.39 – 7.28 (m, 5H), 7.05 (s, 1H), 7.00 (ddd, J = 8.3, 2.7, 0.8 Hz, 1H), 5.55 (s, 1H), 4.06 (dd, J = 15.2, 5.8 Hz, 1H), 3.83 – 3.71 (m, 2H), 3.60 (ddd, J = 13.0, 8.3, 3.5 Hz, 1H), 2.25 – 2.19 (m, 2H), 1.85 – 1.75 (m, 3H).
**$^{13}$C NMR** (101 MHz, Chloroform-d) δ 177.68, 165.72, 163.10, 160.69, 152.41, 152.28, 142.17, 139.31, 128.70, 127.99, 127.49, 110.95, 110.59, 59.86, 43.60, 38.85, 33.41.

**Compound 58**. Synthesis of *4-(benzylamino)-1-((5-chlorothiophen-2-yl)sulfonyl)piperidine-4-carboxamide*
MS (ESI) [M+H+]: 414.32
Yield: 91%
**$^1$H NMR** (400 MHz, Chloroform-d) δ 7.38 – 7.21 (m, 6H), 6.98 (d, J = 4.0 Hz, 1H), 6.89 (s, 1H), 5.48 (s, 1H), 3.64 (s, 2H), 3.37 – 3.26 (m, 2H), 3.20 (ddd, J = 11.7, 7.7, 3.8 Hz, 2H), 2.26 (ddd, J = 12.3, 7.7, 3.9 Hz, 2H), 1.81 (ddd, J = 12.7, 7.5, 3.9 Hz, 2H).
**$^{13}$C NMR** (101 MHz, Chloroform-d) δ 177.40, 139.37, 137.56, 134.78, 131.86, 128.83, 128.01, 127.66, 127.26, 58.88, 47.24, 42.88, 33.15.

Intermediates **59-61**.

To a solution of intermediates **56-58** (1eq) in methanol (10ml), DMF/DMA (3eq) is added dropwise. The mixture is reacted at 55°C for 6/10 hours and is monitored by MS-ESI. At the completion of the reaction,

the solvent is evaporated and a yellow solid is obtained. The cyclized desired products **59-61**, checked by TLC and MS-ESI, are used as such for the next step.

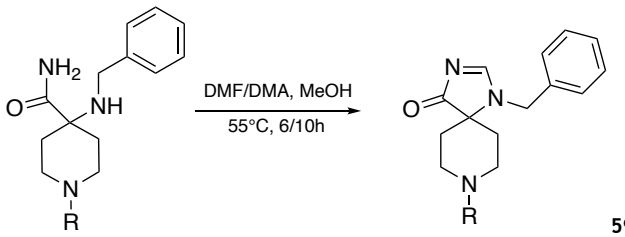


**59-61**

**Compound 59**. Synthesis of *8-benzoyl-1-benzyl-1,3,8-triazaspiro[4.5]dec-2-en-4-one*
MS (ESI) [M+H+]: 348.27
Yield: 93%
**$^{1}$H NMR** (400 MHz, Chloroform-d) δ 8.09 (s, 1H), 7.48 – 7.32 (m, 8H), 7.25 (dt, J = 7.3, 2.0 Hz, 2H), 4.66 (d, J = 13.1 Hz, 1H), 4.49 (d, J = 10.2 Hz, 2H), 4.03 (s, 1H), 3.75 (s, 1H), 3.66 – 3.58 (m, 1H), 2.02 (q, J = 14.5, 7.6 Hz, 2H), 1.72 (d, J = 16.9 Hz, 2H), 1.52 (s, 1H).
**$^{13}$C NMR** (101 MHz, Chloroform-d) δ 191.97, 170.73, 169.05, 135.53, 133.43, 130.01, 129.60, 129.30, 128.67, 128.35, 127.00, 63.36, 48.41, 41.68, 36.06, 31.01, 29.77.

**Compound 60**. Synthesis of *1-benzyl-8-(6-fluoropicolinoyl)-1,3,8-triazaspiro[4.5]dec-2-en-4-one*
MS (ESI) [M+H+]: 367.28
**$^{1}$H NMR** (401 MHz, Chloroform-d) δ 7.90 – 7.81 (m, 1H), 7.73 (dd, J = 8.2, 1.2 Hz, 1H), 7.62 (s, 1H), 7.36 – 7.21 (m, 5H), 7.11 (dd, J = 8.0, 1.2 Hz, 1H), 4.44 (d, J = 0.8 Hz, 2H), 3.82 – 3.69 (m, 4H), 2.30 (ddd, J = 15.5, 9.3, 6.5 Hz, 4H).

**Compound 61**. Synthesis of *1-benzyl-8-((5-chlorothiophen-2-yl)sulfonyl)-1,3,8-triazaspiro[4.5]dec-2-en-4-one*
MS (ESI) [M+H+]: 424.32
Yield:86%
**$^{1}$H NMR** (400 MHz, Chloroform-d) δ 8.10 (s, 1H), 7.46 – 7.39 (m, 3H), 7.32 (d, J = 4.1 Hz, 1H), 7.26 – 7.22 (m, 2H), 6.98 (dd, J = 4.0, 0.4 Hz, 1H), 4.49 (s, 2H), 3.70 (ddd, J = 11.8, 4.5, 2.3 Hz, 2H), 3.43 (td, J = 12.3, 2.6 Hz, 2H), 2.08 (td, J = 13.0, 5.0 Hz, 2H), 1.69 – 1.63 (m, 2H).
**$^{13}$C NMR** (101 MHz, Chloroform-d) δ 170.09, 137.92, 134.92, 133.71, 131.85, 129.68, 129.33, 128.15, 127.40, 76.98, 48.17, 40.35, 29.77.

Final compounds **62-64**.

The intermediates **59-61** (1eq) are suspended in methanol (10ml) and the mixture is cooled at 0°C with an ice bath. Then, $NaBH_4$ (1.2eq) is added slowly and bubbling is observed. The reaction is monitored with MS-ESI upon completion. Then, the reaction is quenched with deionized water, the methanol is evaporated and the resulting aqueous phase is extracted three times with DCM (3x30ml). The combined organic phases are dried and the solvent is evaporated. The resulting amorphous solid is titrated with $Et_2O$ to obtain the desired products **62-64** as white or yellow solid.

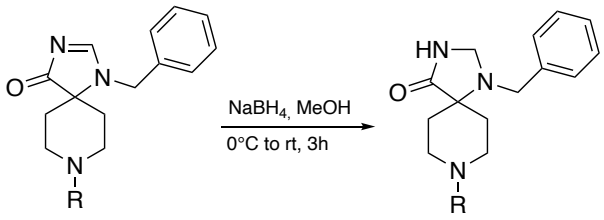


62-64

**Compound 62**. Synthesis of *8-benzoyl-1-benzyl-1,3,8-triazaspiro[4.5]decan-4-one*

MS (ESI) [M+H+]: 350.42

Yield: 88%

**$^{1}$H NMR** (400 MHz, DMSO-d6) δ 8.27 (s, 1H), 7.44 (dq, J = 2.6, 1.6 Hz, 5H), 7.33 (d, J = 4.4 Hz, 4H), 7.26 (ddd, J = 8.7, 5.1, 3.6 Hz, 1H), 4.38 (s, 1H), 3.81 (s, 2H), 3.77 – 3.61 (m, 3H), 1.81 (s, 3H), 1.66 (s, 1H).

**$^{13}$C NMR** (101 MHz, DMSO-d6) δ 176.82, 169.07, 138.59, 136.41, 129.26, 128.34, 128.29, 127.02, 126.66, 60.79, 59.02, 49.94, 43.49, 37.92, 29.51, 28.43.

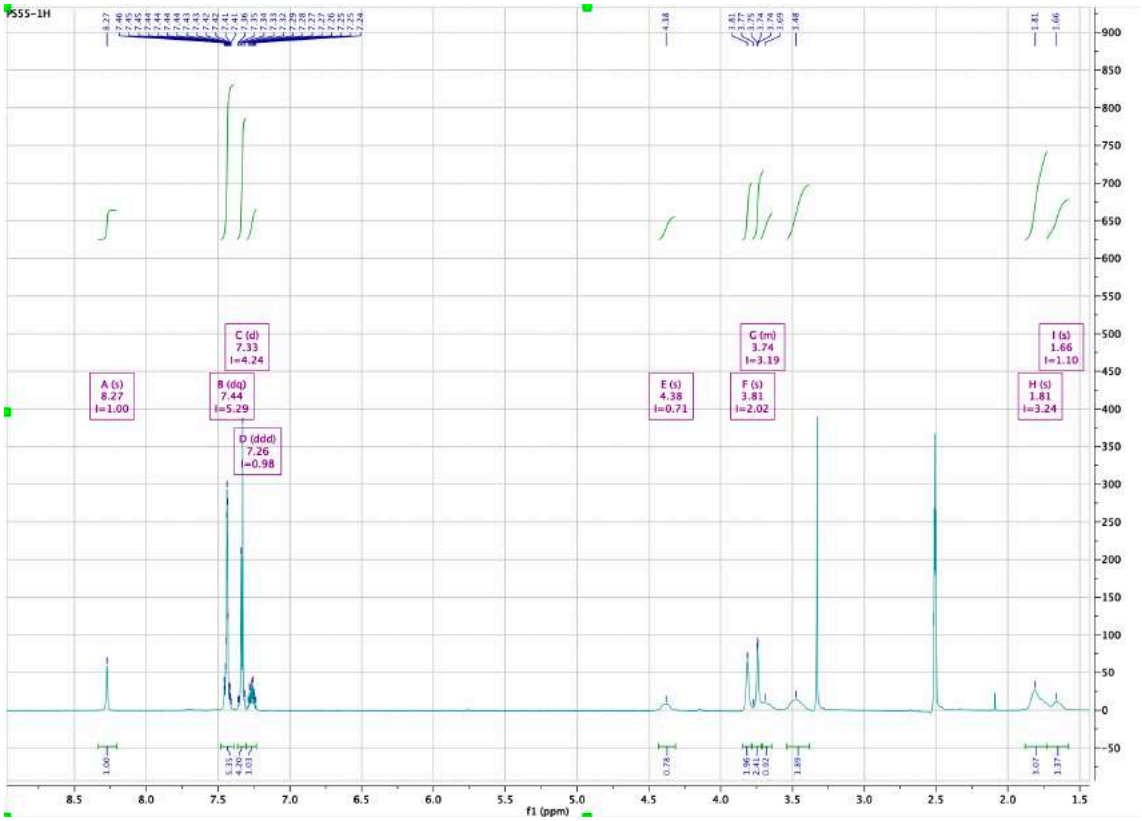


$^{1}$H NMR spectrum of compound **62**.

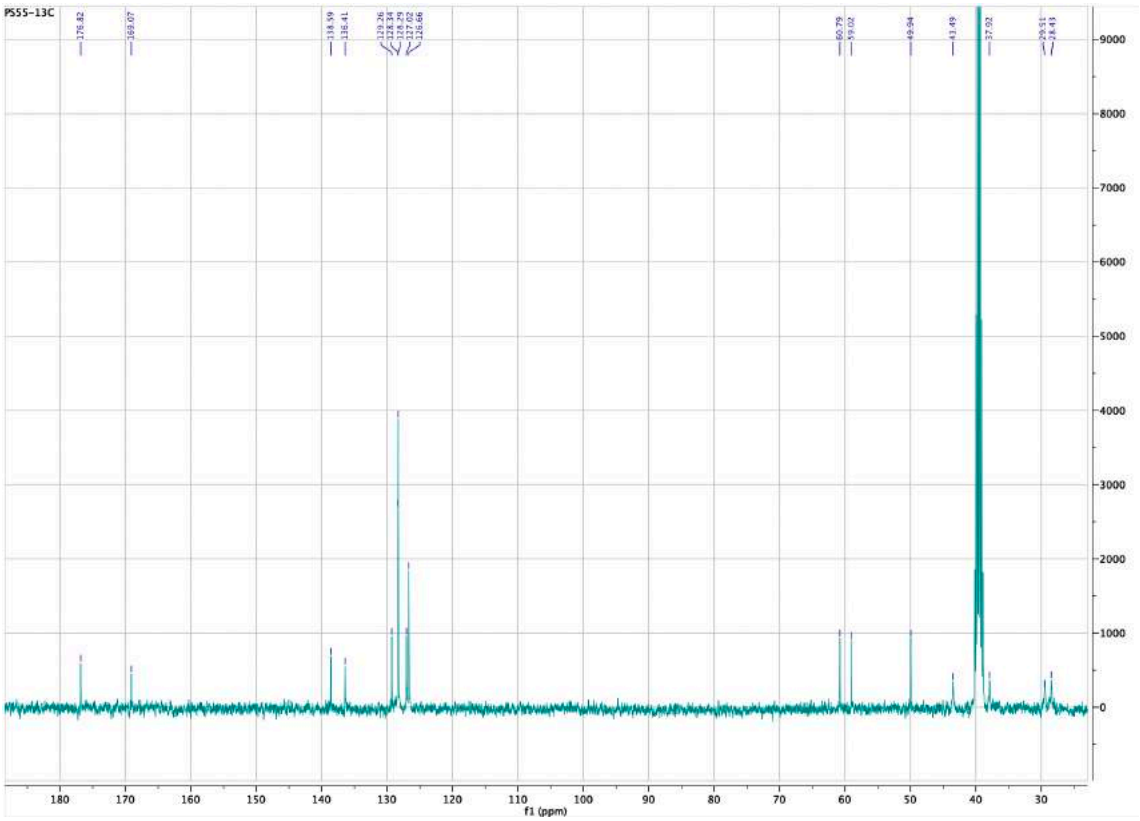


$^{13}$C NMR spectrum of compound **62**.

**Compound 63**. Synthesis of *1-benzyl-8-(6-fluoropicolinoyl)-1,3,8-triazaspiro[4.5]decan-4-one*

MS (ESI) [M+H+]: 369.37

Yield: 75%

**$^{1}$H NMR** (400 MHz, Chloroform-d) δ 7.94 (q, J = 7.8 Hz, 1H), 7.58 (dd, J = 7.4, 2.0 Hz, 1H), 7.46 (s, 1H), 7.35 (d, J = 4.1 Hz, 5H), 7.05 (dd, J = 8.2, 2.5 Hz, 1H), 4.67 (1H), 4.17 (s, 2H), 3.91 (dq, J = 28.2, 13.3 Hz, 4H), 3.64 – 3.54 (m, 1H), 2.16 – 1.96 (m, 4H).

**$^{13}$C NMR** (101 MHz, Chloroform-d) δ 166.42, 160.86, 159.92, 151.60, 151.47, 142.59, 142.52, 129.02, 128.91, 128.51, 121.71, 121.68, 111.69, 111.33, 61.60, 61.51, 50.96, 43.57, 39.24, 29.88, 28.62.

**$^{19}$F NMR** (376 MHz, Chloroform-d) δ -76.04.

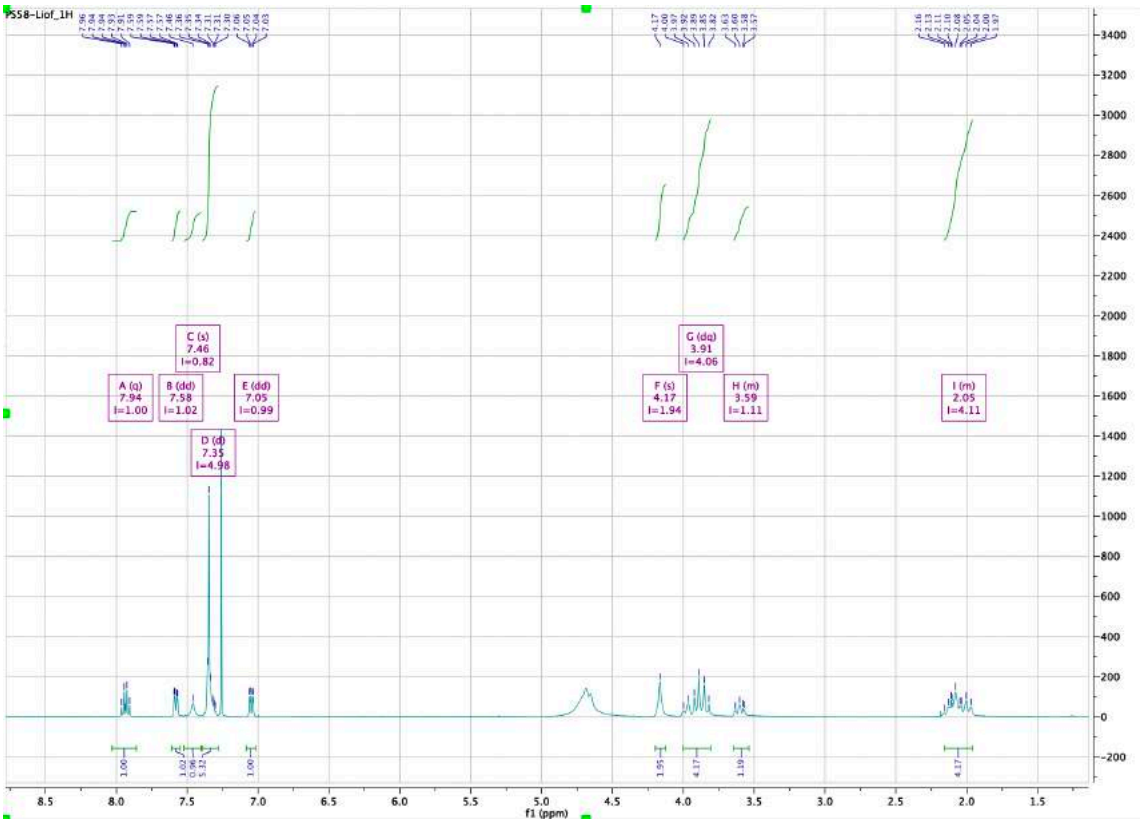


$^{1}$H NMR spectrum of compound **63**.

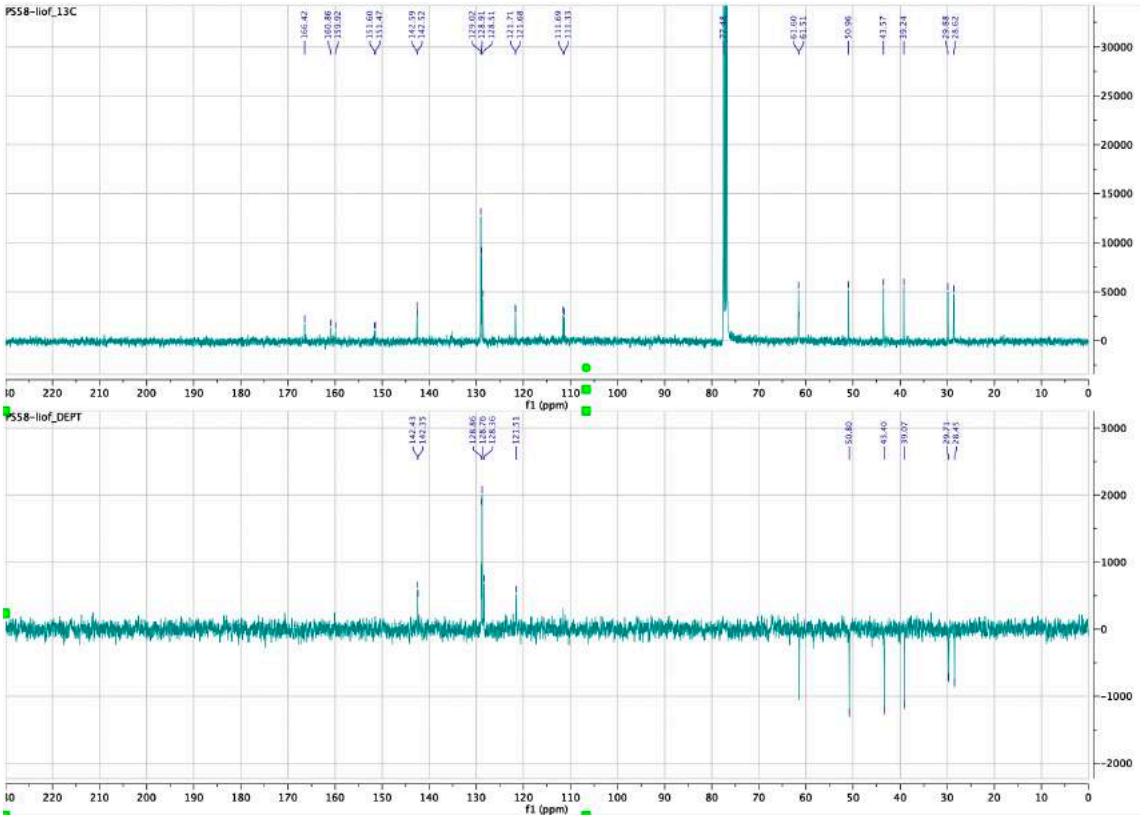


$^{13}$C NMR and DEPT spectra of compound **63**.

**Compound 64**. Synthesis of *1-benzyl-8-((5-chlorothiophen-2-yl)sulfonyl)-1,3,8-triazaspiro[4.5]decan-4-one*
MS (ESI) [M+H+]: 426.15
Yield: 90%
**$^{1}$H NMR** (400 MHz, DMSO-d6) δ 8.25 (s, 1H), 7.59 (d, J = 4.1 Hz, 1H), 7.40 (s, 1H), 7.33 – 7.26 (m, 5H), 3.79 – 3.77 (m, 2H), 3.67 (s, 2H), 3.54 (d, J = 11.4 Hz, 2H), 3.18 – 3.11 (m, 2H), 1.96 – 1.89 (m, 2H), 1.81 (d, J = 13.7 Hz, 2H).
**$^{13}$C NMR** (101 MHz, DMSO-d6) δ 224.41, 209.72, 203.19, 133.31, 129.19, 128.80, 128.75, 127.54, 61.20, 50.22, 43.16, 28.49.

$^{1}$H NMR spectrum of compound **64**.

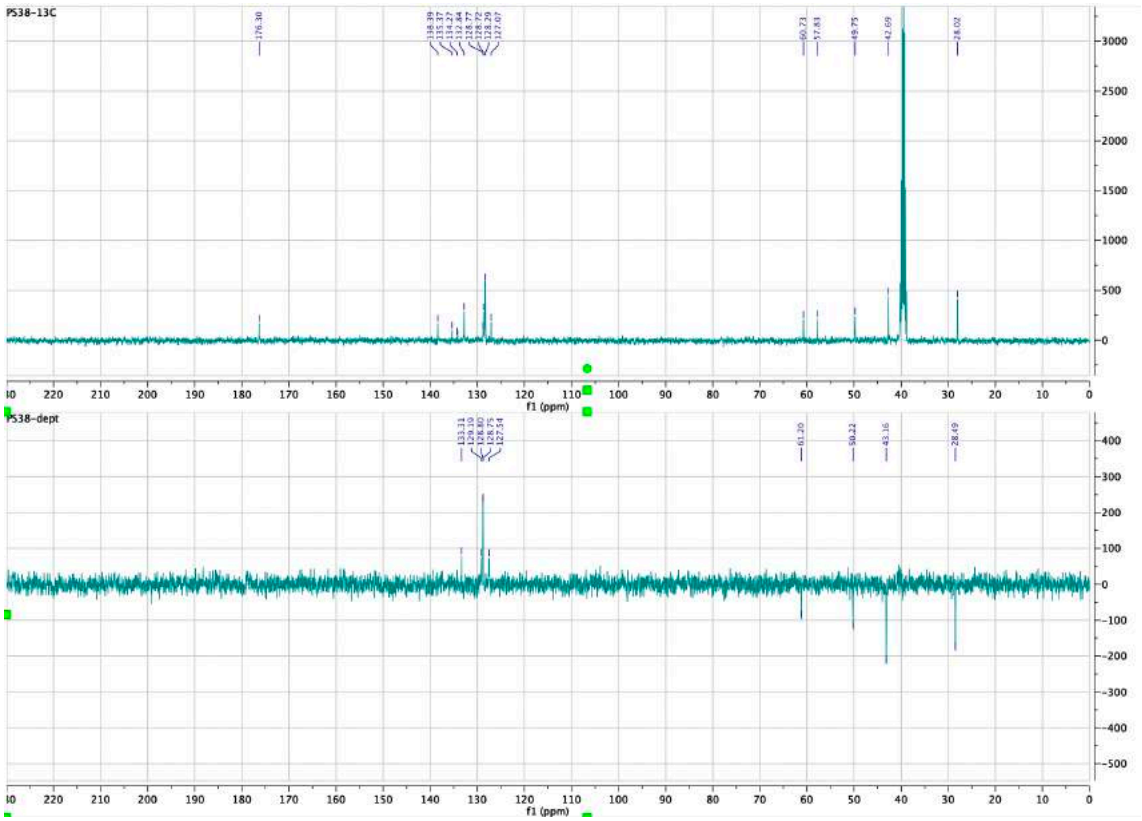


$^{13}$C NMR and DEPT spectra of compound **64**.

## 5.2.4 General procedure for the synthesis of monospiranic compounds **86-89.**

Functionalization of piperidone chlorhydrate monohydrate follow the procedures described above (see paragraphs 5.2.1. and 5.2.2), to obtain intermediates **31, 49, 50.** The para-fluoro benzoyl amide intermediate **65**, which follows the same route for the synthesis of compound **31,** using the appropriate acyl chloride as reagent.

**Compound 65**. Synthesis of 1-(4-fluorobenzoyl)piperidin-4-one

**$^1$H NMR** (400 MHz, Chloroform-d) δ 7.94 (td, J = 8.1, 7.5 Hz, 1H), 7.67 (ddd, J = 7.4, 2.2, 0.8 Hz, 1H), 7.05 (ddd, J = 8.3, 2.7, 0.8 Hz, 1H), 4.04 (t, J = 6.4 Hz, 2H), 3.90 (t, J = 6.2 Hz, 2H), 2.61 (t, J = 6.4 Hz, 4H).

Intermediates 66-69.

In a round bottomed flask, a solution of ammonium chloride ($NH_4Cl$, 1.3 eq, 3.08 mmol) in ammonium hydroxide ($NH_4OH$, 10 eq, 23.7 mmol) was added. Then, TMSCN (1.25 eq, 2.96 mmol) was dropped in. Immediately after, a solution of appropriately functionalized piperidone (respectively intermediates **31**, **49**, **50** and **65**, 1 eq, 2.37 mmol), previously dissolved in MeOH was added to the mixture. The reaction was stirred for 18 hours and monitored via TLC and MS (ESI). Upon the completion of the reaction, the solvent was evaporated and the residue was diluted with water; the aqueous phase was extracted three times with AcOEt, dried over $Na_2SO_4$ anhydrous, filtered and evaporated. The ammino-nitrile derivative was obtained as a white solid, without need of further purifications.

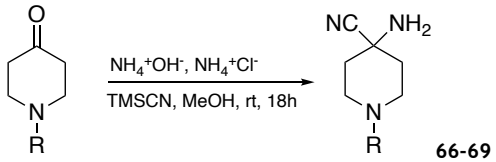

**66-69**

**Compound 66**. Synthesis of *4-amino-1-tosylpiperidine-4-carbonitrile*

MS (ESI) $[M+H]^+$: 279.10

Yield: 90%

**$^1$H NMR** (400 MHz, DMSO-$d_6$) δ 7.69 – 7.61 (m, 2H), 7.50 – 7.44 (m, 2H), 3.22 (ddd, *J* = 11.4, 5.5, 2.2 Hz, 2H), 2.75 (ddd, *J* = 11.9, 8.4, 3.3 Hz, 2H), 2.59 (s, 2H), 2.43 (s, 3H), 2.02 – 1.92 (m, 2H), 1.70 (ddd, *J* = 12.9, 8.5, 3.6 Hz, 2H).

**$^{13}$C NMR** (101 MHz, DMSO-$d_6$) δ 143.73, 132.21, 129.91, 127.49, 123.72, 48.05, 41.94, 35.22, 21.02.

**Compound 67**. Synthesis of *4-amino-1-(6-fluoropicolinoyl)piperidine-4-carbonitrile*

MS (ESI) $[M+H]^+$: 239.11

Yield:

**$^1$H NMR** (400 MHz, DMSO-$d_6$) δ 7.92 (td, *J* = 8.1, 7.4 Hz, 1H), 7.59 (ddd, *J* = 7.4, 2.2, 0.8 Hz, 1H), 7.02 (ddd, *J* = 8.2, 2.7, 0.8 Hz, 1H), 4.37 (dt, *J* = 13.2, 4.6 Hz, 1H), 4.00 (dq, *J* = 14.1, 4.1 Hz, 1H), 3.49 (ddt, *J* = 13.8, 10.0, 3.8 Hz, 2H), 2.18 – 2.02 (m, 2H), 1.83 (dtd, *J* = 13.9, 9.9, 3.9 Hz, 4H).

**Compound 68**. Synthesis of *4-amino-1-((5-chlorothiophen-2-yl)sulfonyl)piperidine-4-carbonitrile*

Yield: 91%

**$^1$H NMR** (400 MHz, DMSO-$d_6$) δ 7.60 (d, *J* = 4.1 Hz, 1H), 7.40 (d, *J* = 4.1 Hz, 1H), 3.26 (ddd, *J* = 11.5, 7.3, 3.8 Hz, 2H), 2.94 – 2.85 (m, 2H), 2.64 (s, 2H), 2.03 – 1.97 (m, 2H), 1.75 (ddd, *J* = 12.9, 8.2, 3.6 Hz, 2H).

**$^{13}$C NMR** (101 MHz, DMSO-$d_6$) δ 135.68, 133.56, 133.11, 128.86, 123.69, 47.85, 41.97, 35.02.

**Compound 69**. Synthesis of *4-amino-1-(4-fluorobenzoyl)piperidine-4-carbonitrile*

MS (ESI) $[M+H]^+$: 238.11

Yield: 71%

**$^1$H NMR** (400 MHz, DMSO-*d*6) δ 7.52 – 7.45 (m, 2H), 7.33 – 7.21 (m, 2H), 3.76 (d, *J* = 166.2 Hz, 2H), 3.25 (m, 2H), 2.69 (s, 2H), 1.95 (d, *J* = 14.3 Hz, 2H), 1.63 (s, 2H).

**$^{13}$C NMR** (101 MHz, DMSO-*d*6) δ 168.13, 163.74, 161.29, 132.28, 129.47, 129.39, 124.01, 115.48, 115.26, 49.26, 36.14, 36.05.

**$^{19}$F NMR** (376 MHz, DMSO-*d*6) δ -111.25.

Intermediates **70-73**.

Amino-nitrile derivatives (**66-69**) were dissolved in $H_2SO_4$ (96% w/w, 3 mL) and the mixture was stirred at room temperature for 18 h. After the reaction was complete, as indicated by MS (ESI), it was slowly basified (pH>10) by dropwise addition of a $NH_4OH$ solution (30% w/w) while maintaining the temperature between -10°C and 0°C, cooling the round bottomed flask with a mixture of water and salt. Then, at pH>10, the mixture was diluted with $CH_3OH$ and the ammonium salts were filtered away on a pad of Celite.

Subsequently, the filtrate was evaporated under vacuum and the resulting yellowish oil was extracted five times with $CH_2Cl_2$ (20 mL). The organic layer was washed with water (2x10 mL) and brine (1x10 mL). After drying over $Na_2SO_4$, the solvent was evaporated under reduced pressure to yield a solid residue, which was triturated with $Et_2O$ and filtered to isolate the carboxamide derivative as a pale-yellow solid. The final compound was used in the next step without further purification.

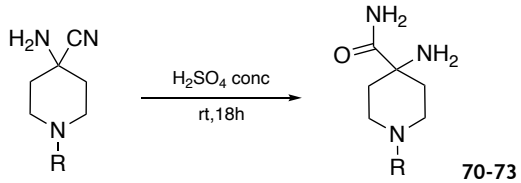


**70-73**

**Compound 70**. Synthesis of *4-amino-1-tosylpiperidine-4-carboxamide*

MS (ESI) $[M+H]^+$: 297.11

Yield: 88%

**$^1$H NMR** (400 MHz, DMSO-$d_6$) δ 7.69 – 7.53 (m, 2H), 7.48 – 7.41 (m, 2H), 7.35 (s, 1H), 6.94 (s, 1H), 3.27 (dt, *J* = 11.4, 4.1 Hz, 2H), 2.68 (td, *J* = 11.4, 2.9 Hz, 2H), 2.42 (s, 3H), 1.90 (ddd, *J* = 13.3, 11.3, 4.3 Hz, 2H), 1.69 (s, 2H), 1.41 (dd, *J* = 13.5, 3.6 Hz, 2H).

**$^{13}$C NMR** (101 MHz, DMSO-$d_6$) δ 179.24, 143.36, 132.66, 129.79, 127.47, 53.89, 41.82, 33.49, 21.01.

**Compound 71**. Synthesis of *4-amino-1-(6-fluoropicolinoyl)piperidine-4-carboxamide*

MS (ESI) $[M+H]^+$: 266.12

Yield: 88%

**$^1$H NMR** (400 MHz, DMSO-$d_6$) δ 7.90 (q, *J* = 7.9 Hz, 1H), 7.55 (ddd, *J* = 7.4, 2.2, 0.8 Hz, 1H), 7.31 (s, 1H), 7.00 (ddd, *J* = 8.3, 2.7, 0.8 Hz, 1H), 5.37 (s, 1H), 4.32 (q, *J* = 4.7, 4.2 Hz, 1H), 3.95 – 3.83 (m, 1H), 3.47 (q, *J* = 12.6, 11.4 Hz, 2H), 2.30 – 2.15 (m, 2H), 1.56 (d, *J* = 36.4 Hz, 4H).

**Compound 72**. Synthesis of *4-amino-1-((5-chlorothiophen-2-yl)sulfonyl)piperidine-4-carboxamide*

MS (ESI): $[M+H]^+$ = 323.02

Yield: 85%

**$^1$H NMR** (400 MHz, DMSO-$d_6$) δ 7.55 (d, *J* = 4.1 Hz, 1H), 7.39 (t, *J* = 4.8 Hz, 2H), 6.99 (s, 1H), 3.32 (d, *J* = 7.5 Hz, 2H WITH $D_2O$), 2.84 (td, *J* = 11.5, 2.9 Hz, 2H), 1.94 (ddd, *J* = 13.4, 11.5, 4.4 Hz, 2H), 1.81 (s, 2H), 1.49 – 1.42 (m, 2H).

**$^{13}$C NMR** (101 MHz, dmso) δ 179.11, 135.27, 134.09, 132.71, 128.68, 53.80, 41.88, 33.38

**Compound 73**. Synthesis of *4-amino-1-(4-fluorobenzoyl)piperidine-4-carboxamide*

MS (ESI): $[M+H]^+$ : 265.12

Yield: 66%

**$^1$H NMR** (400 MHz, DMSO-*d*6) δ 7.51 – 7.37 (m, 3H), 7.32 – 7.23 (m, 2H), 6.98 (s, 1H), 4.12 (s, 1H), 1.95 (s, 2H), 1.84 (s, 2H), 1.35 (d, *J* = 45.8 Hz, 2H).

**$^{13}$C NMR** (101 MHz, DMSO-*d*6) δ 179.27, 167.91, 163.62, 161.17, 132.73, 129.29, 129.21, 115.47, 115.25, 55.14, 43.36, 37.68, 34.72, 33.95.

**$^{19}$F NMR** (376 MHz, DMSO-*d*6) δ -111.52.

Intermediates **74-77**.

Amino-amidic derivatives **70-73** (1eq, 2.16 mmol) were dissolved in MeOH; then, dimethylformamide dimethylacetal (DMF/DMA, 3eq, 3.24 mmol) was added dropwise. The mixture was stirred at 55°C for 5 hours. The volatile fraction was evaporated under reduced pressure to yield a solid residue, which was crystallized with acetone to yield a pale-yellow solid. The obtained raw product was checked by MS-ESI and TLC and was used as such in the next step.


**74-77**

**Compound 74**. Synthesis of *8-tosyl-1,3,8-triazaspiro[4.5]dec-2-en-4-one*

MS (ESI): $[M+H]^+$ = 324.02

Yield: 85%;

**$^1$H NMR** (400 MHz, Chloroform-*d*) δ 7.75 (s, 1H), 7.68 – 7.61 (m, 2H), 7.34 – 7.29 (m, 2H), 3.73 (dt, *J* = 11.4, 4.0 Hz, 2H), 2.87 (td, *J* = 11.6, 2.8 Hz, 2H), 2.43 (s, 3H), 2.11 – 2.01 (m, 2H), 1.53 (d, *J* = 13.6 Hz, 2H).

**$^{13}$C NMR** (101 MHz, Chloroform-*d*) δ 185.31, 149.26, 143.77, 133.30, 129.89, 127.73, 67.03, 42.22, 32.12, 21.61.

**Compound 75**. Synthesis of *8-(6-fluoropicolinoyl)-1,3,8-triazaspiro[4.5]dec-2-en-4-one*

MS (ESI): $[M+H]^+$ = 276.10

Yield: 79%;

**$^1$H NMR** (400 MHz, Chloroform-*d*) δ 7.90 (q, *J* = 7.8 Hz, 1H), 7.78 (s, 1H), 7.57 – 7.50 (m, 1H), 6.99 (ddd, *J* = 8.3, 2.7, 0.8 Hz, 1H), 4.52 (dt, *J* = 13.5, 4.4 Hz, 1H), 3.95 (dt, *J* = 13.7, 4.3 Hz, 1H), 3.60 (ddd, *J* = 13.9, 11.0, 3.1 Hz, 1H), 3.47 (ddd, *J* = 13.7, 11.2, 3.2 Hz, 1H), 2.03 – 1.91 (m, 2H), 1.56 (dt, *J* = 13.6, 4.2 Hz, 1H), 1.45 (dd, *J* = 13.4, 4.2 Hz, 1H).

**Compound 76**. Synthesis of *8-((5-chlorothiophen-2-yl)sulfonyl)-1,3,8-triazaspiro[4.5]dec-2-en-4-one*

MS (ESI): $[M+H]^+$ = 333,10

Yield: 81%;

**$^1$H NMR** (400 MHz, DMSO-$d_6$) δ 7.96 (s, 1H), 7.60 (d, *J* = 4.0 Hz, 1H), 7.40 (d, *J* = 4.0 Hz, 1H), 3.56 (dd, *J* = 10.2, 5.9 Hz, 2H), 2.84 (dd, *J* = 11.5, 2.9 Hz, 2H), 1.77 (td, *J* = 12.5, 11.5, 4.2 Hz, 2H), 1.46 (d, *J* = 13.5 Hz, 2H).

**Compound 77**. Synthesis of *8-(4-fluorobenzoyl)-1,3,8-triazaspiro[4.5]dec-2-en-4-one*

MS (ESI): $[M+H]^+$ = 275.11;

**$^1$H NMR** (400 MHz, DMSO-$d_6$) δ 8.02 (s, 1H), 7.54 – 7.44 (m, 2H), 7.30 – 7.20 (m, 2H), 3.33 (s, 4H), 1.68 (s, 2H), 1.37 (s, 2H).

Intermediates **78-81**.

To a solution of the appropriate compound **74-77**, 1 eq, 2.14 mmol) in acetonitrile (DMF, 5ml) at 0°C, potassium carbonate ($K_2CO_3$, 1 eq, 2.14 mmol) was added. Then, (3-(bromomethyl)phenoxy)(*tert*-butyl)dimethylsilane (compound **92**, 0.9 eq, 1.93 mmol) previously dissolved in DMF was also dropped in. The mixture was allowed to warm to room temperature and stirred for 7 hours, monitoring the progress via TLC and MS (ESI). Upon the completion of the reaction, the solvent was evaporated and the crude compound was resuspended in water. The aqueous phase was extracted four times with DCM, dried over $Na_2SO_4$, filtered and evaporated. The residue was purified by flash chromatography (9:1 AcOEt/petroleum ether), obtaining the final product **78-81** as transparent amorphous.

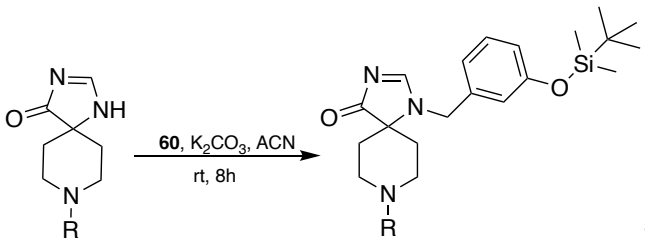


**78-81**

**Compound 78**. Synthesis of *1-(3-((tert-butyldimethylsilyl)oxy)benzyl)-8-tosyl-1,3,8-triazaspiro[4.5]dec-2-en-4-one*

MS (ESI): $[M+H]^+$ = 528.23

Yield: 50%

**$^1$H NMR** (400 MHz, DMSO-$d_6$) δ 8.05 (s, 1H), 7.65 (d, *J* = 7.9 Hz, 2H), 7.47 (d, *J* = 7.9 Hz, 2H), 7.21 (t, *J* = 7.8 Hz, 1H), 6.82 – 6.74 (m, 2H), 6.68 (s, 1H), 4.55 (s, 2H), 3.54 (d, *J* = 11.4 Hz, 2H), 2.67 (t, *J* = 11.2 Hz, 2H), 2.42 (s, 3H), 1.83 – 1.70 (m, 2H), 1.41 (d, *J* = 13.3 Hz, 2H), 0.96 – 0.88 (m, 9H), 0.15 (s, 6H).

**$^{13}$C NMR** (101 MHz, DMSO-$d_6$)) δ 183.16, 155.31, 153.81, 143.70, 138.32, 132.30, 129.98, 127.52, 120.20, 119.10, 118.60, 66.96, 43.33, 42.01, 31.57, 25.51, 21.02, 17.92, -4.58.

**Compound 79**. Synthesis of *1-(3-((tert-butyldimethylsilyl)oxy)benzyl)-8-(6-fluoropicolinoyl)-1,3,8-triazaspiro[4.5]dec-2-en-4-one*

MS (ESI): $[M+H]^+$ = 496.23

Yield:

**$^1$H NMR** (400 MHz, DMSO-$d_6$

**$^{13}$C NMR** (101 MHz, DMSO-$d_6$,

**Compound 80**. Synthesis of *1-(3-((tert-butyldimethylsilyl)oxy)benzyl)-8-((5-chlorothiophen-2-yl)sulfonyl)-1,3,8-triazaspiro[4.5]dec-2-en-4-one*

MS (ESI): $[M+H]^+$ = 554.13

Yield:

**$^1$H NMR** (400 MHz, DMSO-$d_6$, DEPROTECT AND PROTECT COMPOUNDS MIXTURE) δ 8.10 (s, 1H), 8.07 (s, 0H), 7.64 – 7.58 (m, 1H), 7.40 (d, *J* = 4.1 Hz, 1H), 7.22 (t, *J* = 7.9 Hz, 1H), 7.13 (t, *J* = 7.8 Hz, 0H), 6.85 – 6.69 (m, 3H), 6.68 – 6.56 (m, 1H), 4.58 (s, 2H), 4.54 (s, 0H), 3.57 (t, *J* = 6.1 Hz, 2H), 2.95 – 2.80 (m, 3H), 1.82 (td, *J* = 12.6, 10.9, 4.3 Hz, 3H), 1.48 (d, *J* = 13.4 Hz, 3H), 0.92 (s, 10H), 0.84 (s, 2H), 0.15 (s, 6H), -0.04 (s, 1H).
**$^{13}$C NMR** (101 MHz, DMSO-$d_6$, DEPROTECT AND PROTECT COMPOUNDS MIXTURE) δ 183.09, 155.33, 154.01, 138.31, 135.67, 133.70, 133.09, 129.99, 128.85, 120.22, 119.12, 118.64, 66.80, 43.39, 42.12, 31.43, 25.81, 25.52, 18.73, 17.92, -3.20, -4.56.

**Compound 81**. Synthesis of *1-(3-((tert-butyldimethylsilyl)oxy)benzyl)-8-(4-fluorobenzoyl)-1,3,8-triazaspiro[4.5]dec-2-en-4-one*
MS (ESI): $[M+H]^+$ = 495.24
Yield: 54%
**$^1$H NMR** (400 MHz, Acetone-*d*6) δ 8.01 (s, 1H), 7.59 – 7.53 (m, 2H), 7.27 – 7.21 (m, 2H), 6.95 – 6.91 (m, 1H), 6.85 – 6.81 (m, 2H), 4.69 – 4.65 (m, 2H), 3.49 (s, 2H), 1.92 – 1.82 (m, 2H), 1.43 (d, *J* = 7.6 Hz, 2H), 0.97 (s, 9H), 0.20 (s, 6H).
**$^{13}$C NMR** (101 MHz, Acetone-*d*6) δ 184.27, 169.68, 165.44, 162.97, 157.10, 154.05, 139.62, 131.00, 130.65, 130.56, 121.49, 120.49, 120.13, 116.32, 116.11, 44.71, 33.74, 33.39, 26.16, 18.93, -4.14.
**$^{19}$F NMR** (376 MHz, Acetone-*d*6) δ -111.25.

Intermediates **82-85**.

To a solution of the appropriate compound (**78-81**, 1eq, 0.61 mmol) in MeOH (5ml) at 0°C, $NaBH_4$ (1.3 eq, 0.78 mmol) was added in small portions. The reaction was allowed to warm to room temperature and stirred for 5 hours. After the completion of the reaction, as indicated by MS (ESI), solvent was evaporated and the residue was resuspended in water and then extracted four times with DCM. The combined organic layers were dried over $Na_2SO_4$ anhydrous, filtered and evaporated in vacuum. The crude compound was purified by flash chromatography (1.5:8.5 AcOEt/DCM) to obtain the reduced product as a transparent amorphous.

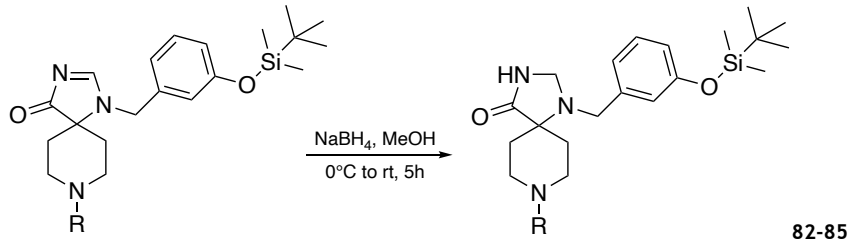

**82-85**

**Compound 82**. Synthesis of *1-(3-((tert-butyldimethylsilyl)oxy)benzyl)-8-tosyl-1,3,8-triazaspiro[4.5]decan-4-one*
MS (ESI): $[M+H]^+$ = 530.24
Yield: 89%

**$^1$H NMR** (400 MHz, DMSO-$d_6$) δ 7.67 – 7.60 (m, 2H), 7.49 – 7.42 (m, 2H), 7.20 (t, *J* = 7.8 Hz, 1H), 6.81 – 6.77 (m, 1H), 6.74 (ddd, *J* = 8.1, 2.5, 1.0 Hz, 1H), 6.67 (t, *J* = 2.0 Hz, 1H), 4.26 (s, 2H), 3.98 (d, *J* = 8.6 Hz, 2H), 3.48 (dd, *J* = 9.8, 5.8 Hz, 2H), 3.16 (t, *J* = 8.7 Hz, 1H), 2.46 (s, 1H), 2.41 (s, 3H), 1.71 (td, *J* = 13.1, 4.4 Hz, 2H), 1.50 (d, *J* = 13.3 Hz, 2H), 0.93 (s, 8H), 0.15 (s, 5H).
**$^{13}$C NMR** (101 MHz, DMSO-$d_6$) δ 129.84, 129.80, 127.51, 120.58, 118.96, 118.82, 60.40, 44.02, 42.08, 30.51, 21.01, -4.55.

**Compound 83**. Synthesis of 1-(3-((*tert*-butyldimethylsilyl)oxy)benzyl)-8-(6-fluoropicolinoyl)-1,3,8-triazaspiro[4.5]decan-4-one
MS (ESI): $[M+H]^+$ = 498.25
Yield: 89%
**$^1$H NMR** (400 MHz, DMSO-$d_6$)
**$^{13}$C NMR** (101 MHz, DMSO-$d_6$)

**Compound 84**. Synthesis of *1-(3-((tert-butyldimethylsilyl)oxy)benzyl)-8-((5-chlorothiophen-2-yl)sulfonyl)-1,3,8-triazaspiro[4.5]decan-4-one*
MS (ESI): $[M+H]^+$ = 556.14
Yield: 98%
**$^1$H NMR** (400 MHz, DMSO-$d_6$) δ 7.58 (d, *J* = 4.1 Hz, 1H), 7.38 (d, *J* = 4.1 Hz, 1H), 7.21 (t, *J* = 7.8 Hz, 1H), 6.85 – 6.79 (m, 1H), 6.69 (s, 1H), 4.29 (s, 2H), 4.03 (d, *J* = 8.5 Hz, 2H), 3.56 – 3.44 (m, 2H), 3.27 (d, *J* = 8.6 Hz, 2H), 2.73 – 2.59 (m, 2H), 1.76 (td, *J* = 12.7, 12.1, 4.3 Hz, 2H), 1.56 (d, *J* = 13.5 Hz, 3H), 0.93 (s, 10H), 0.16 (s, 6H).
**$^{13}$C NMR** (101 MHz, DMSO-$d_6$) δ 175.34, 157.61, 155.30, 138.40, 138.01, 135.51, 133.74, 132.97, 129.82, 129.60, 128.79, 120.59, 118.98, 118.85, 118.00, 114.37, 114.25, 60.45, 58.17, 44.21, 44.05, 42.22, 30.46, 25.81, 25.54, 17.93, -3.19, -4.53.

**Compound 85**. Synthesis of *1-(3-((tert-butyldimethylsilyl)oxy)benzyl)-8-(4-fluorobenzoyl)-1,3,8-triazaspiro[4.5]decan-4-one*
MS (ESI): $[M+H]^+$ = 497.25
Yield: 57%
**$^1$H NMR** (400 MHz, DMSO-*d*6) δ 7.53 – 7.45 (m, 2H), 7.34 – 7.25 (m, 2H), 7.15 – 7.09 (m, 1H), 6.70 – 6.59 (m, 3H), 4.27 (s, 2H), 4.10 (d, *J* = 8.3 Hz, 2H), 3.40 (t, *J* = 8.6 Hz, 1H), 1.65 (d, *J* = 14.2 Hz, 2H), 1.52 (s, 2H), 0.84 (s, 9H), -0.04 (d, *J* = 0.6 Hz, 5H).
**$^{13}$C NMR** (101 MHz, DMSO-*d*6) δ 175.53, 168.13, 161.24, 157.65, 138.05, 132.52, 129.58, 129.41, 129.33, 117.90, 115.48, 115.27, 114.32, 114.17, 60.59, 59.59, 44.19, 43.67, 31.52, 25.80, 25.53, 17.79, -3.20.

Final compounds **86-89**.

To a solution of the appropriate derivative (**82-85**) compound in MeOH (5ml) at 0°C, a solution of HCl (10% v/v) was dropped slowly until the pH is acidic. The reaction was then allowed to warm to room temperature and was stirred for 10 hours, monitoring via TLC and MS (ESI). Upon the completion of the reaction, the

mixture was basified (pH>9) at 0°C and the organic solvent was evaporated. The residue was extracted three times with DCM and the unprotected derivative (**86-89**) was obtained as a white solid.

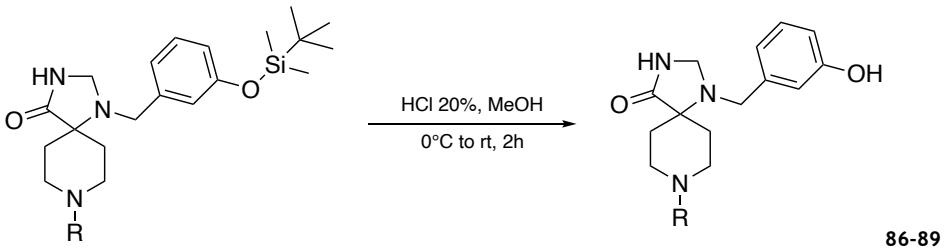


**86-89**

**Compound 86**. Synthesis of *1-(3-hydroxybenzyl)-8-tosyl-1,3,8-triazaspiro[4.5]decan-4-one*

MS (ESI): $[M+H]^+$ = 415.16

Yield: 40%

**$^1$H NMR** (400 MHz, DMSO-$d_6$) δ 9.45 (s, 1H), 7.67 – 7.60 (m, 2H), 7.49 – 7.41 (m, 2H), 7.14 – 7.07 (m, 1H), 6.64 (ddd, *J* = 8.1, 2.4, 1.1 Hz, 1H), 6.62 – 6.57 (m, 2H), 4.22 (s, 2H), 3.97 (d, *J* = 8.6 Hz, 2H), 3.50 (dt, *J* = 11.6, 3.8 Hz, 2H), 3.15 (t, *J* = 8.7 Hz, 1H), 2.46 (d, *J* = 2.8 Hz, 1H), 2.41 (s, 3H), 1.80 – 1.69 (m, 2H), 1.52 (d, *J* = 13.2 Hz, 2H).

**$^{13}$C NMR** (101 MHz, DMSO-$d_6$) δ 175.41, 157.60, 143.56, 138.02, 132.33, 129.84, 129.57, 127.50, 117.97, 114.34, 114.24, 60.40, 58.34, 44.19, 42.09, 30.52, 21.01.

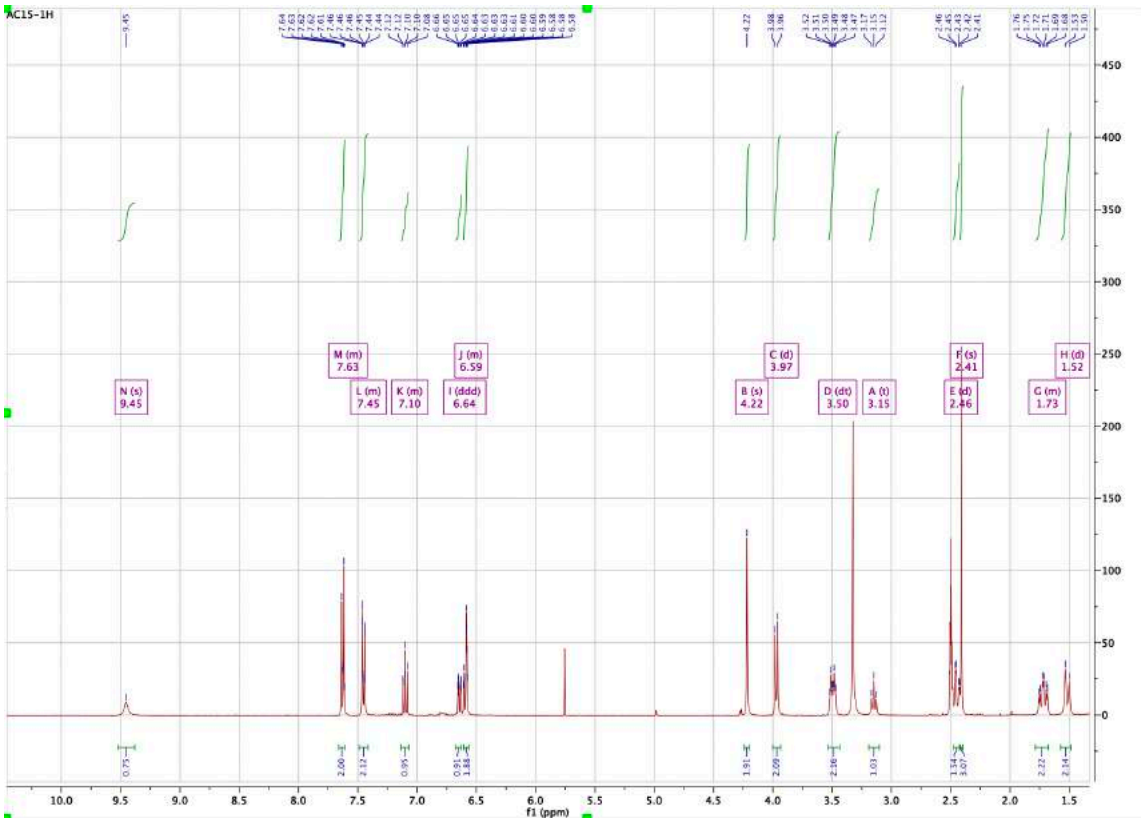


$^1$H NMR spectrum of compound **86**.

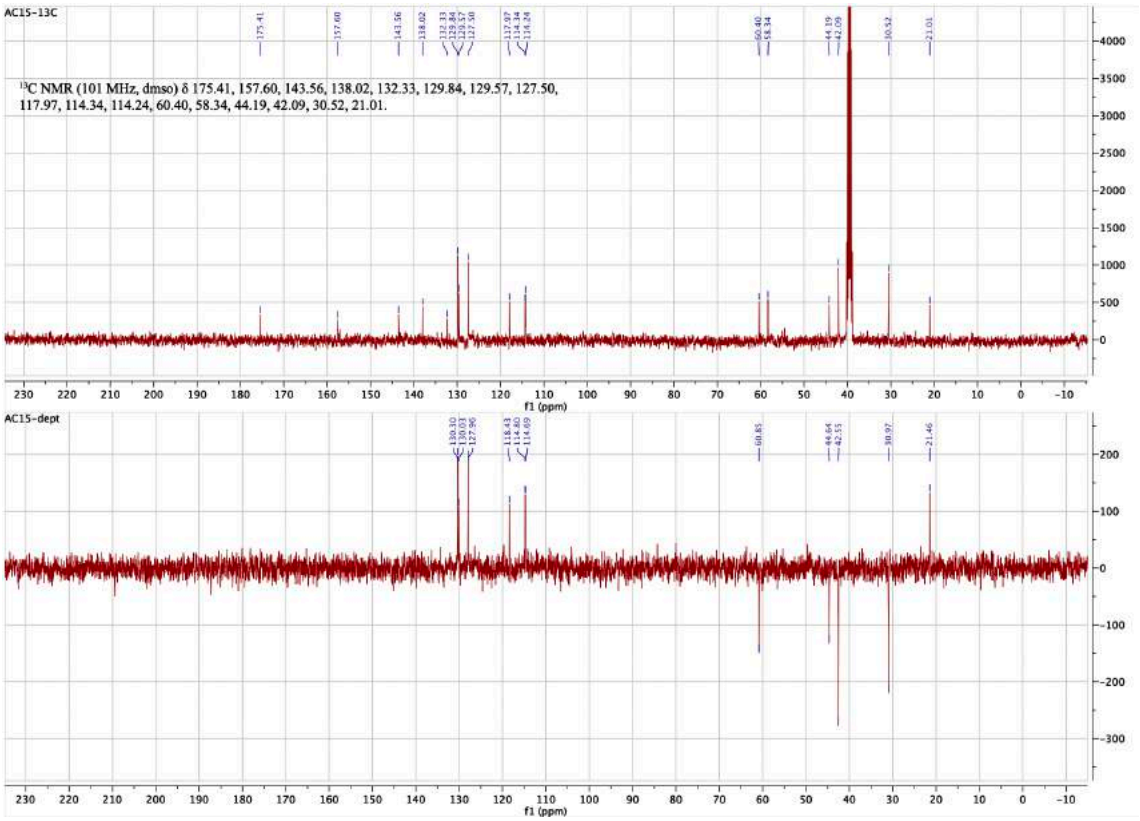


$^{13}$C NMR and DEPT spectra of compound **86**.

**Compound 87**. Synthesis of *8-(6-fluoropicolinoyl)-1-(3-hydroxybenzyl)-1,3,8-triazaspiro[4.5]decan-4-one*
MS (ESI): $[M+H]^+$ = 384.16
Yield: 50%
**$^1$H NMR** (400 MHz, Acetone-$d_6$) δ 8.12 (td, *J* = 8.2, 7.4 Hz, 1H), 7.58 (ddd, *J* = 7.4, 2.4, 0.8 Hz, 1H), 7.21 – 7.14 (m, 2H), 6.80 (ddd, *J* = 2.4, 1.8, 0.6 Hz, 1H), 6.78 – 6.74 (m, 2H), 4.54 (d, *J* = 6.2 Hz, 2H), 4.46 (s, 2H), 4.35 (dt, *J* = 13.6, 4.5 Hz, 1H), 3.90 (dq, *J* = 9.6, 4.7 Hz, 1H), 3.61 – 3.50 (m, 2H), 1.96 (dd, *J* = 8.4, 5.7 Hz, 1H), 1.91 – 1.85 (m, 1H).
**$^{13}$C NMR** (101 MHz, Acetone-$d_6$) δ 205.25, 172.59, 165.32, 163.20, 160.82, 157.76, 152.82, 152.69, 142.93, 142.85, 137.57, 129.77, 121.14, 118.70, 114.56, 114.34, 110.58, 110.22, 60.99, 58.80, 44.58, 42.69, 37.87, 31.28, 30.49.
**$^{19}$F NMR** (376 MHz, Acetone-$d_6$) δ -76.45.

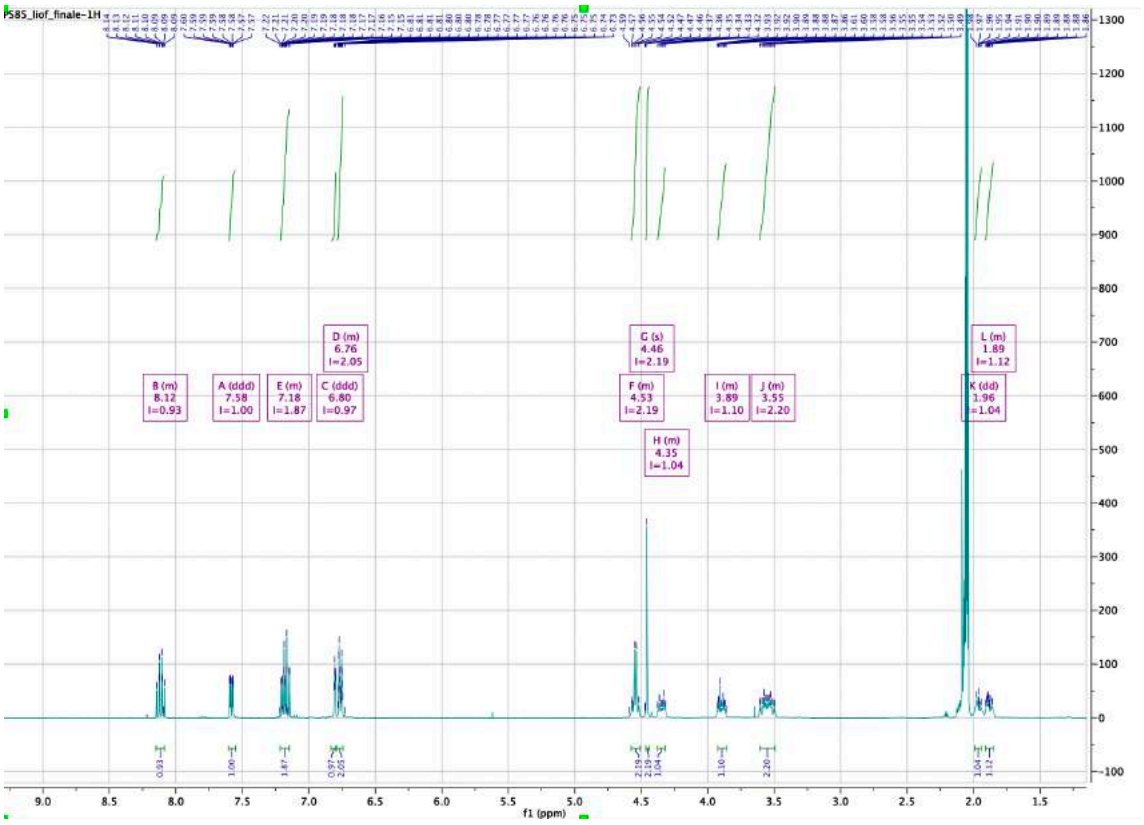


$^{1}$H NMR spectrum of compound **87**.

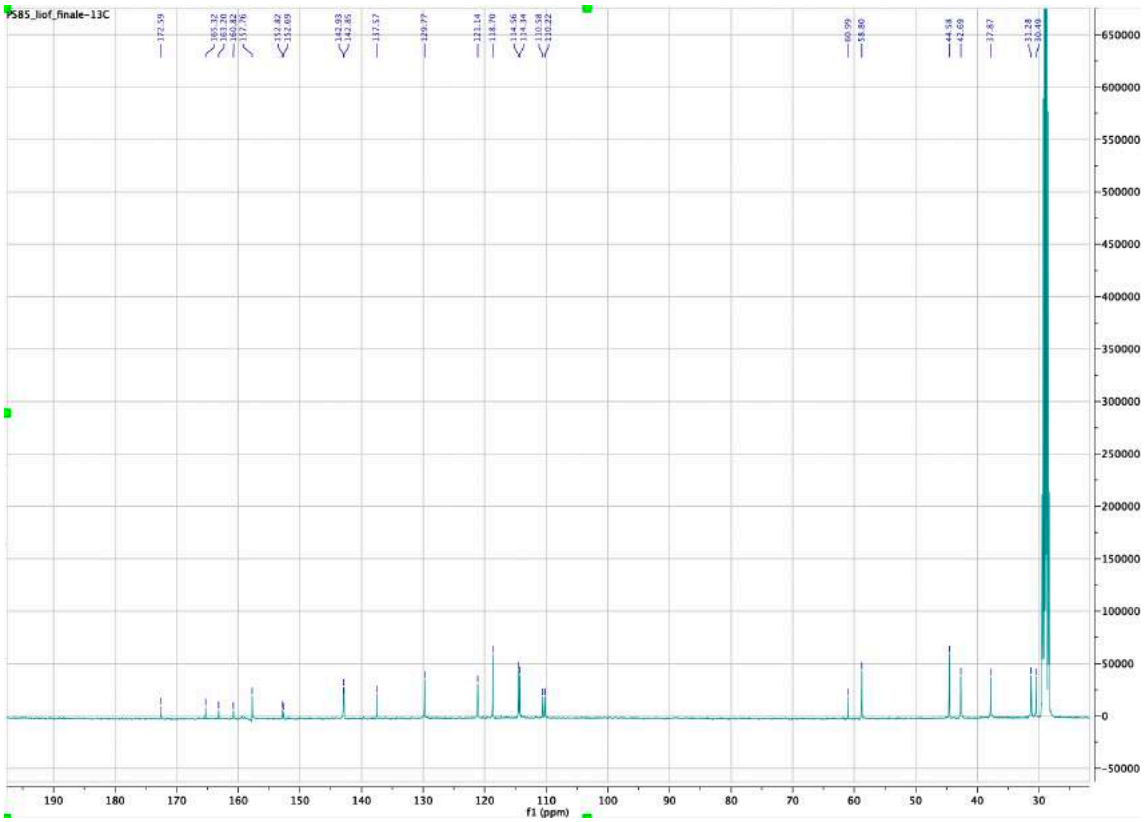


$^{13}$C NMR spectrum of compound **87**.

**Compound 88**. Synthesis of *8-((5-chlorothiophen-2-yl)sulfonyl)-1-(3-hydroxybenzyl)-1,3,8-triazaspiro[4.5]decan-4-one*

MS (ESI): $[M+H]^+$ = 442.06

Yield: 87%

**$^1$H NMR** (400 MHz, DMSO-$d_6$) δ 9.43 (s, 1H), 7.58 (d, *J* = 4.1 Hz, 1H), 7.40 (s, 1H), 7.12 (t, *J* = 7.8 Hz, 1H), 6.69 – 6.57 (m, 3H), 4.26 (s, 2H), 4.10 (s, 2H), 3.51 (dd, *J* = 10.0, 6.0 Hz, 2H), 2.74 (d, *J* = 11.7 Hz, 2H), 1.81 (t, *J* = 12.3 Hz, 2H), 1.67 (s, 2H).

**$^{13}$C NMR** (101 MHz, Chloroform-*d*) δ 156.85, 137.59, 137.24, 134.79, 131.90, 130.34, 127.32, 120.21, 115.54, 114.72, 60.76, 59.59, 45.51, 42.27, 31.37.

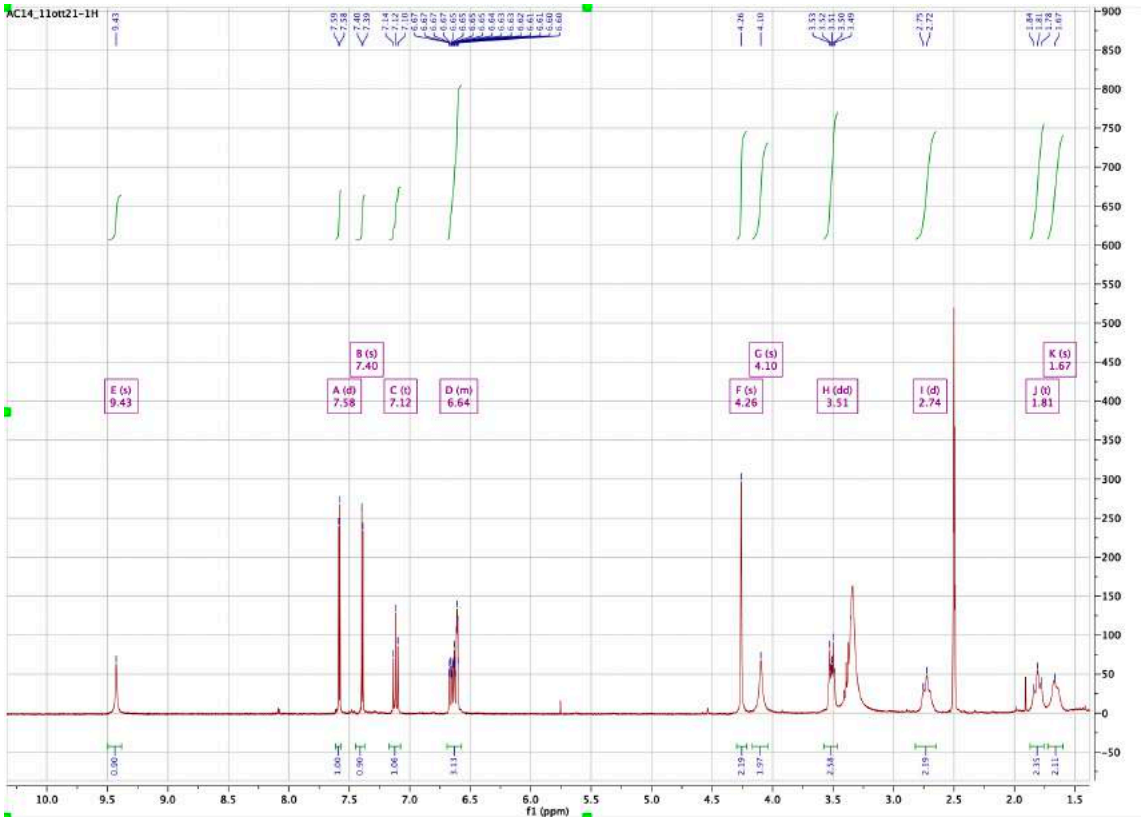


$^1$H NMR spectrum of compound **88.**

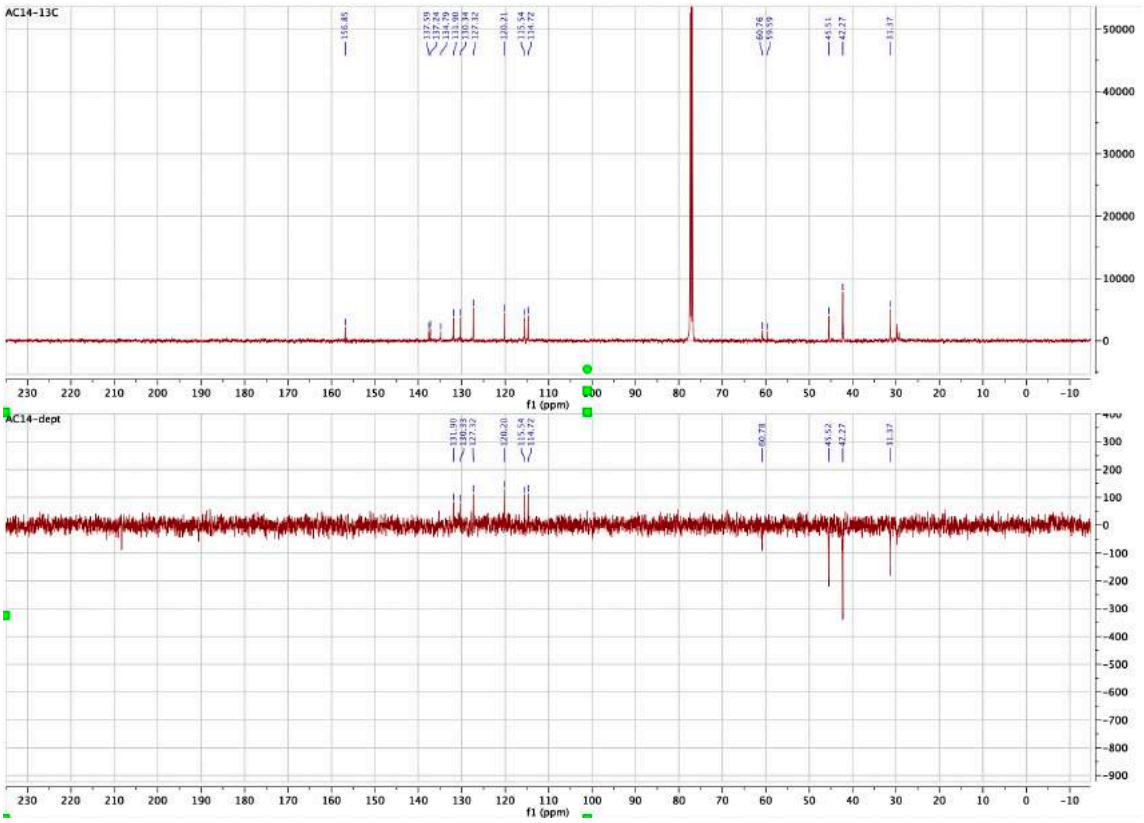


$^{13}$C NMR and DEPT spectra of compound **88**.

**Compound 89**. Synthesis of *8-(4-fluorobenzoyl)-1-(3-hydroxybenzyl)-1,3,8-triazaspiro[4.5]decan-4-one*

MS (ESI): $[M+H]^+$ = 383.16

Yield: 67%

**$^1$H NMR** (400 MHz, Acetone-*d*6) δ 8.37 (s, 1H), 7.56 – 7.49 (m, 2H), 7.27 – 7.19 (m, 2H), 7.17 – 7.11 (m, 1H), 6.77 – 6.70 (m, 3H), 4.36 (s, 2H), 4.23 (s, 2H), 3.71 (d, *J* = 30.4 Hz, 1H), 3.37 (d, *J* = 39.6 Hz, 2H), 2.99 (s, 1H), 1.86 (d, *J* = 21.7 Hz, 2H), 1.56 (s, 2H).

**$^{13}$C NMR** (101 MHz, Acetone-*d*6) δ 176.59, 169.38, 162.78, 158.66, 139.51, 134.03, 130.53, 130.43, 130.34, 119.59, 116.14, 115.92, 115.32, 115.29, 61.60, 60.85, 45.40, 32.63, 32.58.

**$^{19}$F NMR** (376 MHz, Acetone-*d*6) δ -113.08.

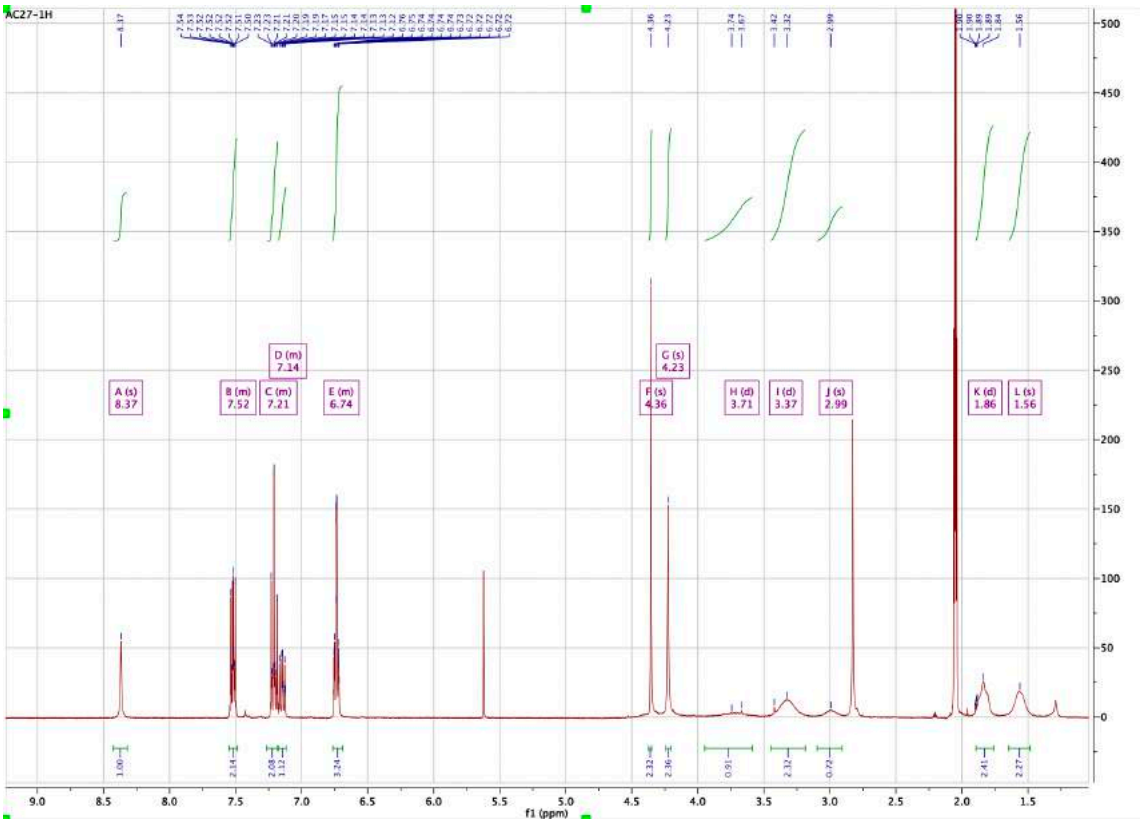


$^{1}$H NMR spectrum of compound **89.**

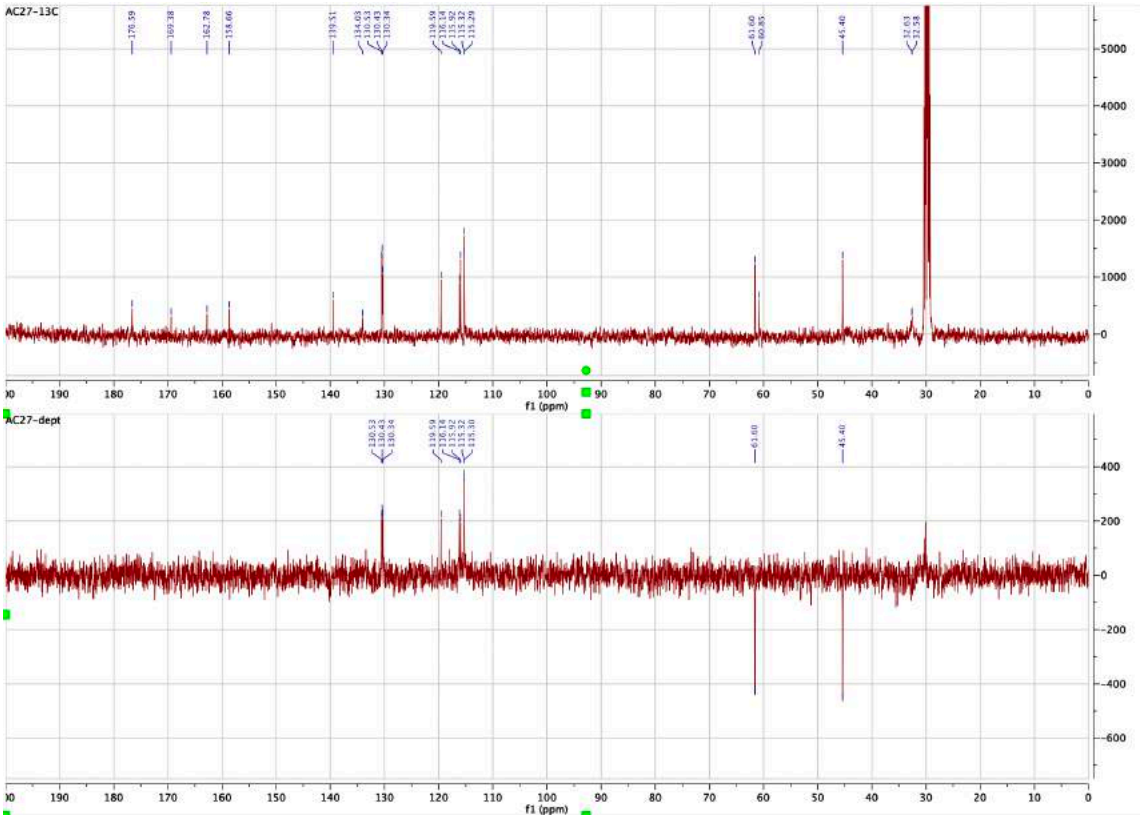


$^{13}$C NMR and DEPT spectra of compound **89**.

Intermediates **90-92**.

**Compound 90**. Synthesis of 3-*((tert-butyldimethylsilyl)oxy)benzaldehyde*

Dissolve imidazole (1.2eq, 9.83mmol) in DCM (6ml); next, add TBDMSCl (1.2eq, 9.83mmol) and 3-hydroxybenzaldehyde (1eq, 8.18mmol), previously dissolved in DCM (10ml). Allow to react at room temperature for 18 hours, monitored by TLC (A0.5P9.5). Afterwards, quench the reaction by adding deionized $H_2O$, evaporate the DCM and extract in DCM/$H_2O$. After drying and evaporating the solvent, the product of interest was iaolated by column chromatography using a petroleum ether/AcOEt (9.5:0.5) eluent mixture. Finally, evaporate the organic solvent, obtaining a transparent, slightly viscous oil.

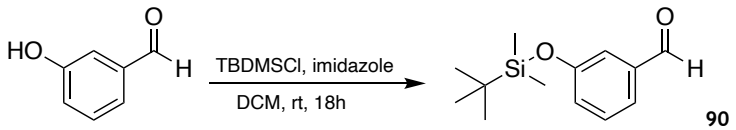

**90**

No molecular ion

Yield: 83%

**$^1$H NMR** (400 MHz, Chloroform-d) δ 9.95 (s, 1H), 7.47 (dt, J = 7.6, 1.4 Hz, 1H), 7.40 (ddd, J = 8.0, 7.6, 0.4 Hz, 1H), 7.34 – 7.31 (m, 1H), 7.10 (ddd, J = 8.0, 2.6, 1.2 Hz, 1H), 1.00 (s, 9H), 0.22 (s, 6H).

**Compound 91**. Synthesis of *(3-((tert-butyldimethylsilyl)oxy)phenyl)methanol*

Dissolve compound **90** (1eq, 4mmol) in MeOH (10ml) and cool it with an ice bath. Then, add $NaBH_4$ (1.5eq, 6mmol). Allow to react at room temperature for 3 hours and monitor via TLC (A0.5P9.5). Quench the reaction by adding deionized $H_2O$. Subsequently, evaporate MeOH, extract the aqueous phase with DCM, dry and evaporate the solvent. A colourless oil is obtained.

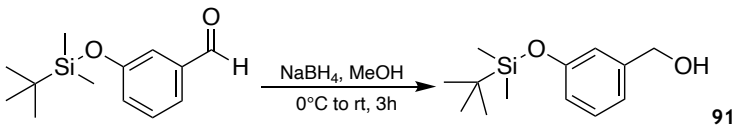

**91**

No molecular ion.

Yield: 92%.

**$^1$H NMR** (400 MHz, Chloroform-d) δ 7.20 (d, J = 7.8 Hz, 1H), 6.96 – 6.92 (m, 1H), 6.85 (d, J = 2.1 Hz, 1H), 6.76 (ddd, J = 8.0, 2.5, 1.0 Hz, 1H), 4.64 (s, 2H), 1.65 (s, 1H), 0.99 (d, J = 0.9 Hz, 9H), 0.20 (d, J = 0.9 Hz, 6H).

**Compound 92**. Synthesis of *(3-(bromomethyl)phenoxy)(tert-butyl)dimethylsilane*

Solubilize compound **91** (1eq, 3.64mmol) in anhydrous DCM (15ml) and add $PPh_3$ (1.2eq, 4.36mmol). Then add $CBr_4$ (1.2eq, 4.36mmol) in small portions at 0°C, remove the ice bath and allow to react at room temperature for 3 hours. Keep the reaction monitored by TLC (A0.5P9.5). Then evaporate the anhydrous

DCM to obtain an amorphous oil and isolate the product of interest by column chromatography using 100% petroleum ether as the solvent. Finally, evaporate the solvent, obtaining a colorless oil.

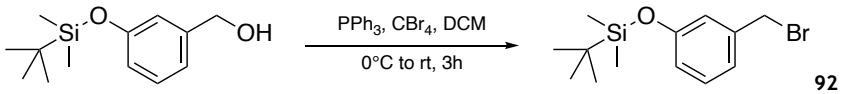


**92**

No molecular ion.

Yield: 65%

**$^1$H NMR** (400 MHz, Chloroform-d) δ 7.18 (t, J = 7.9 Hz, 1H), 6.97 (dt, J = 7.6, 1.4 Hz, 1H), 6.87 (s, 1H), 6.76 (ddd, J= 8.1, 2.4, 1.0 Hz, 1H), 4.43 (s, 2H), 0.98 (d, J = 0.9 Hz, 10H), 0.20 (s, 6H).

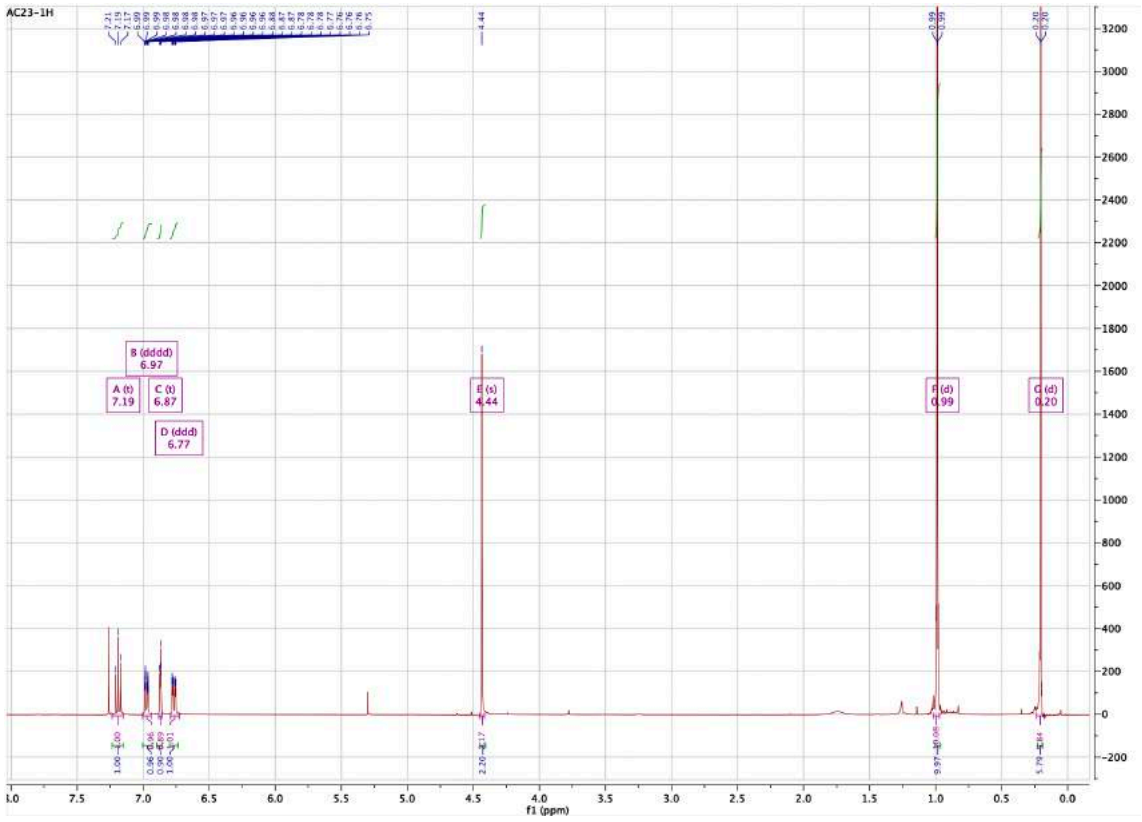


$^1$H NMR spectrum of compound **92.**

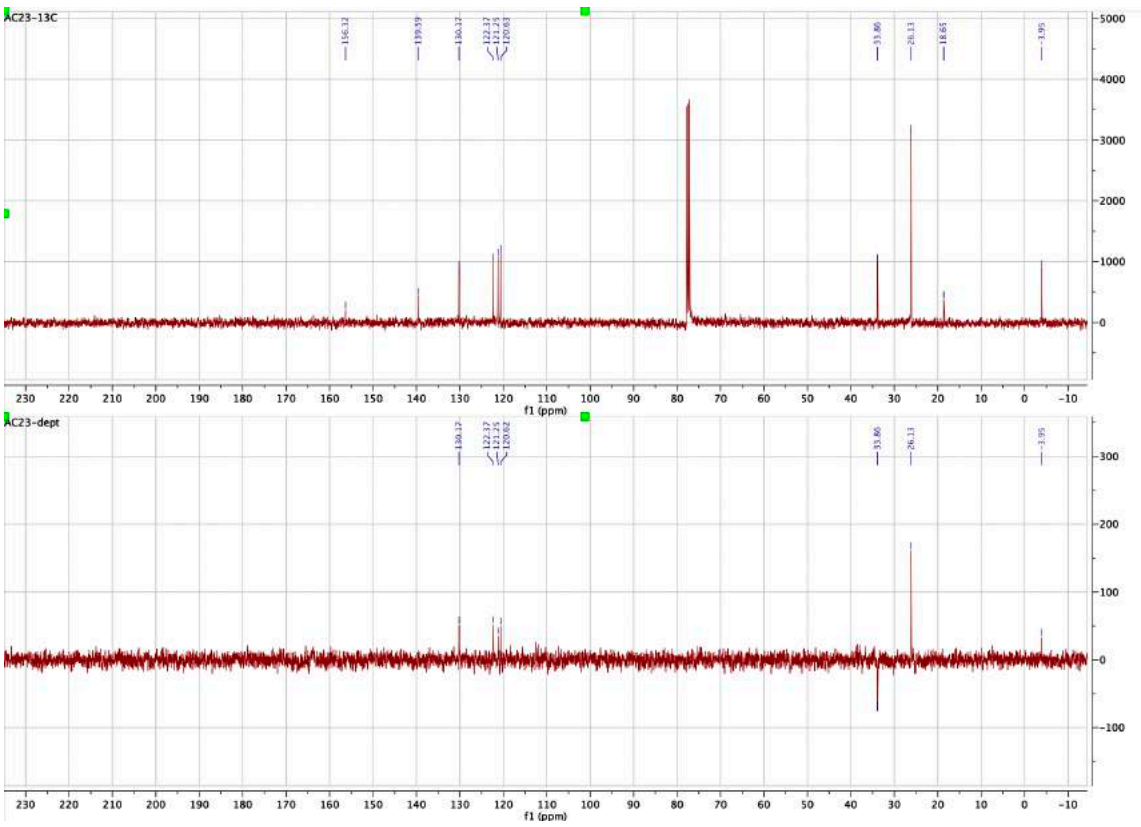


$^{13}C$ NMR and DEPT spectra of compound **92**.

## 5.3 PIPERIDINE SCAFFOLD-BASED DISPIRANIC COMPOUNDS.

### 5.3.1 GENERAL PROCEDURE FOR THE SYNTHESIS OF PIPERIDINE SCAFFOLD -BASED MONOSPIRANIC COMPOUNDS **98-102.**

Intermediates 93-97.

To a solution of the appropriate aldehyde (2 eq) in EtOH (10 ml), N-benzyl piperidone (1 eq) was added, followed by the NaOH solution (1 eq) dropwise. The reaction was stirred for 1-3 hours at room temperature and monitored by mass analysis. Once the reaction was completed, a yellowish precipitate was clearly visible: after filtration under pressure, the solid was isolated and analyzed as the desired product. These compounds were used without need of further purifications.

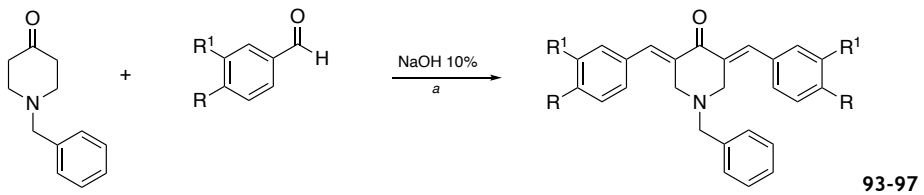


**93-97**

**Compound 93**. Synthesis of *(3E,5E)-1-benzyl-3,5-bis(4-cyanobenzylidene)piperidin-4-one*

MS (ESI): $[M+H]^+$ = 416,16;

Yield: 32%;

**$^{1}$H NMR** (400 MHz, Chloroform-*d*) δ 7.77 (s, 1H), 7.70 – 7.64 (m, 2H), 7.46 – 7.37 (m, 2H), 7.33 – 7.20 (m, 3H), 3.82 (d, *J* = 1.8 Hz, 2H), 3.72 (s, 1H).

**$^{13}$C NMR** (101 MHz, Chloroform-*d*) δ 187.00, 139.52, 136.82, 135.61, 134.77, 132.38, 130.60, 129.01, 128.78, 128.62, 127.84, 118.53, 112.46, 61.50, 54.16.

**Compound 94**. Synthesis of (*3E,5E)-1-benzyl-3,5-bis(benzylidene)piperidin-4-one*

MS (ESI): $[M+H]^+$ = 366,18;

Yield: 60%;

**$^{1}$H NMR** (400 MHz, Chloroform-*d*) δ 7.84 (s, 1H), 7.45 – 7.32 (m, 6H), 7.32 – 7.16 (m, 3H), 3.89 (s, 2H), 3.73 (s, 1H).

**$^{13}$C NMR** (101 MHz, Chloroform-*d*) δ 136.77, 135.32, 130.48, 130.44, 129.14, 129.10, 128.79, 128.66, 128.54, 128.47, 127.52, 61.47, 54.47

**Compound 95**. Synthesis of (*3E,5E)-1-benzyl-3,5-bis(4-fluorobenzylidene)piperidin-4-one*

MS (ESI): $[M+H]^+$ = 402,16;

Yield: 62%;

**$^{1}$H NMR** (400 MHz, Chloroform-*d*) δ 7.79 (s, 1H), 7.39 – 7.22 (m, 5H), 7.18 – 7.02 (m, 2H), 3.85 (d, *J* = 1.9 Hz, 2H), 3.73 (s, 1H).

**$^{13}$C NMR** (101 MHz, Chloroform-*d*) δ 187.55, 164.26, 161.76, 137.22, 135.66, 132.95, 132.44, 132.35, 131.43, 129.11, 128.53, 127.63, 115.97, 115.75, 61.50, 54.32.

**$^{19}$F NMR** (376 MHz, Chloroform-*d*) δ -110.89.

**Compound 96**. Synthesis of (*3E,5E)-1-benzyl-3,5-bis(4-chlorobenzylidene)piperidin-4-one*

MS (ESI): $[M+H]^+$ = 434,16;

Yield: 77%;

**$^{1}$H NMR** (400 MHz, Chloroform-*d*) δ 7.76 (s, 1H), 7.40 – 7.32 (m, 2H), 7.28 (d, *J* = 0.5 Hz, 1H), 3.87 – 3.80 (m, 2H), 3.73 (s, 1H).

**$^{13}$C NMR** (101 MHz, Chloroform-*d*) δ 135.50, 135.20, 133.66, 131.65, 129.09, 128.98, 128.57, 127.69, 61.53, 54.34.

**Compound 97**. Synthesis of (*3E,5E)-1-benzyl-3,5-bis(naphtylidene)piperidin-4-one*

MS (ESI): $[M+H]^+$ = 466,21;

Yield: 32%;

**$^{1}$H NMR** (400 MHz, Chloroform-*d*) δ 8.00 (t, *J* = 1.6 Hz, 1H), 7.91 – 7.80 (m, 4H), 7.61 – 7.42 (m, 3H), 7.35 – 7.11 (m, 3H), 4.01 (d, *J* = 1.8 Hz, 2H), 3.75 (s, 1H).

**$^{13}$C NMR** (101 MHz, Chloroform-*d*) δ 187.80, 137.34, 136.89, 133.68, 133.31, 133.19, 132.94, 130.62, 129.17, 128.63, 128.49, 128.28, 127.79, 127.55, 127.21, 126.67, 61.60, 54.66.

Final compounds **98-102.**

**Compound 98.** Synthesis of *4,4'-((1R,4R,5R,7S,8S,11S)-13-benzyl-4,11-dihydroxy-6-oxo-2,9-dithia-13-azadispiro[4.1.47.35]tetradecane-1,8-diyl)dibenzonitrile*

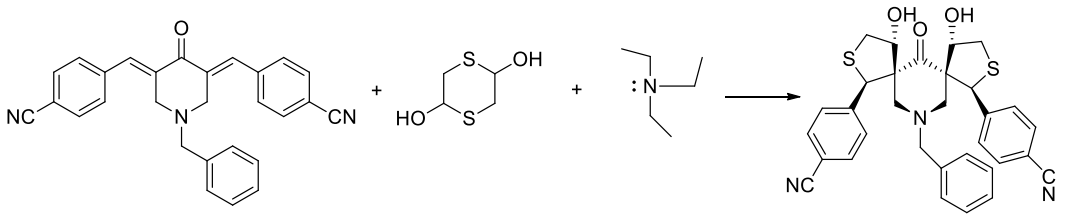


**1 eq** **MW = 415** | **2 eq** **MW = 152,23** | **2 eq** **MW = 101,19** | **MW = 567,25**

The appropriate intermediate (1 eq) and 1,4-dithiane-2,5-diol (2 eq) were solubilized in absolute ethanol (5ml). The reaction mixture was maintained at 0°C using an ice bath. Once the temperature was reached, TEA (2 eq) was added dropwise and the reaction was stirred at room temperature for 10 minutes. Then, it was set at 90°C for three hours and monitored by TLC (A1P4). Once the reaction was completed, the solvent was evaporated and the crude residue was purified by flash silica gel chromatography with an eluent mixture of ethyl acetate and petroleum ether (A1P4). After evaporation, a with white solid was obtained.

MS (ESI): $[M+H]^+$ = 568,25;
Yield: 79%;
**$^1$H NMR** (400 MHz, DMSO-$d_6$) δ 7.45 – 7.19 (m, 8H), 5.51 (s, 4H), 5.20 (t, *J* = 4.4 Hz, 2H), 5.09 (d, *J* = 4.1 Hz, 2H), 3.43 (s, 0H), 3.34 (s, 4H), 3.14 (dd, *J* = 12.1, 4.7 Hz, 2H), 2.72 (dd, *J* = 25.8, 12.1 Hz, 2H), 1.58 (d, *J* = 12.1 Hz, 2H).
**$^{13}$C NMR** (101 MHz, DMSO-$d_6$) δ 203.58, 138.47, 134.81, 131.94, 131.38, 128.79, 128.35, 127.77, 127.30, 79.21, 68.26, 60.85, 54.49, 50.85, 36.46.

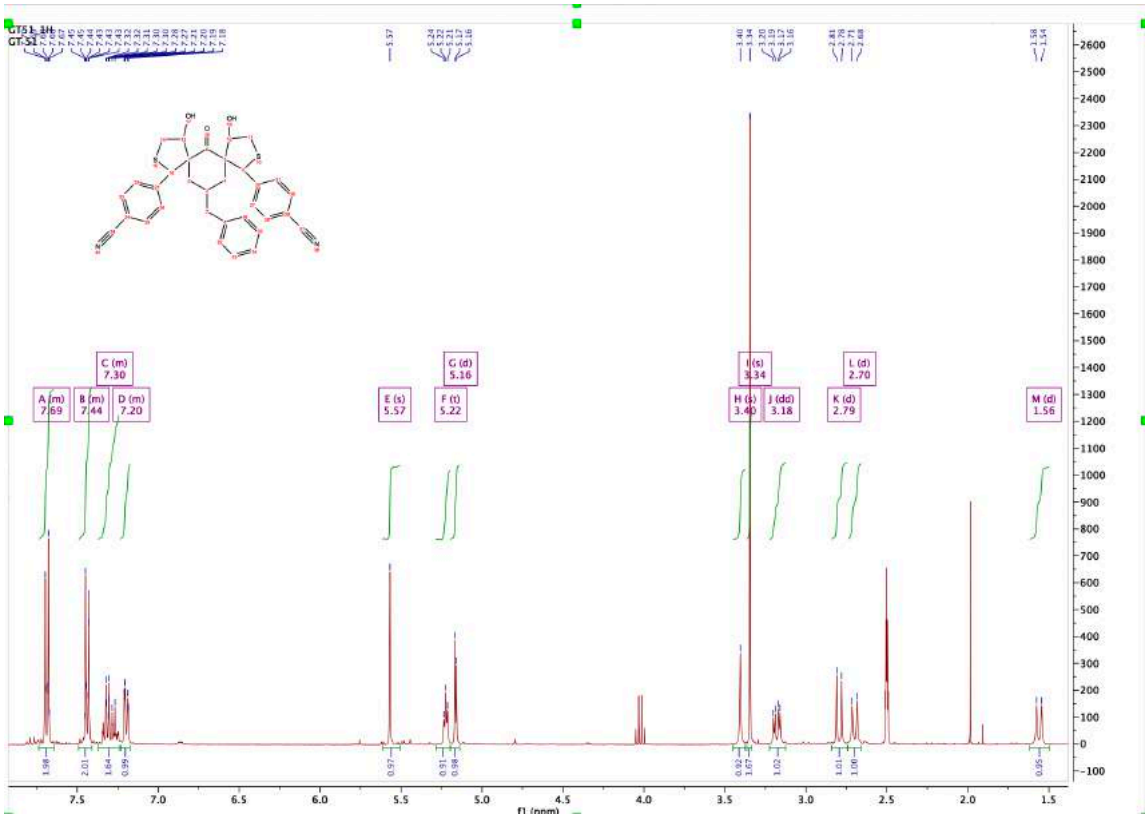

$^{1}$H NMR spectrum of compound **98.**

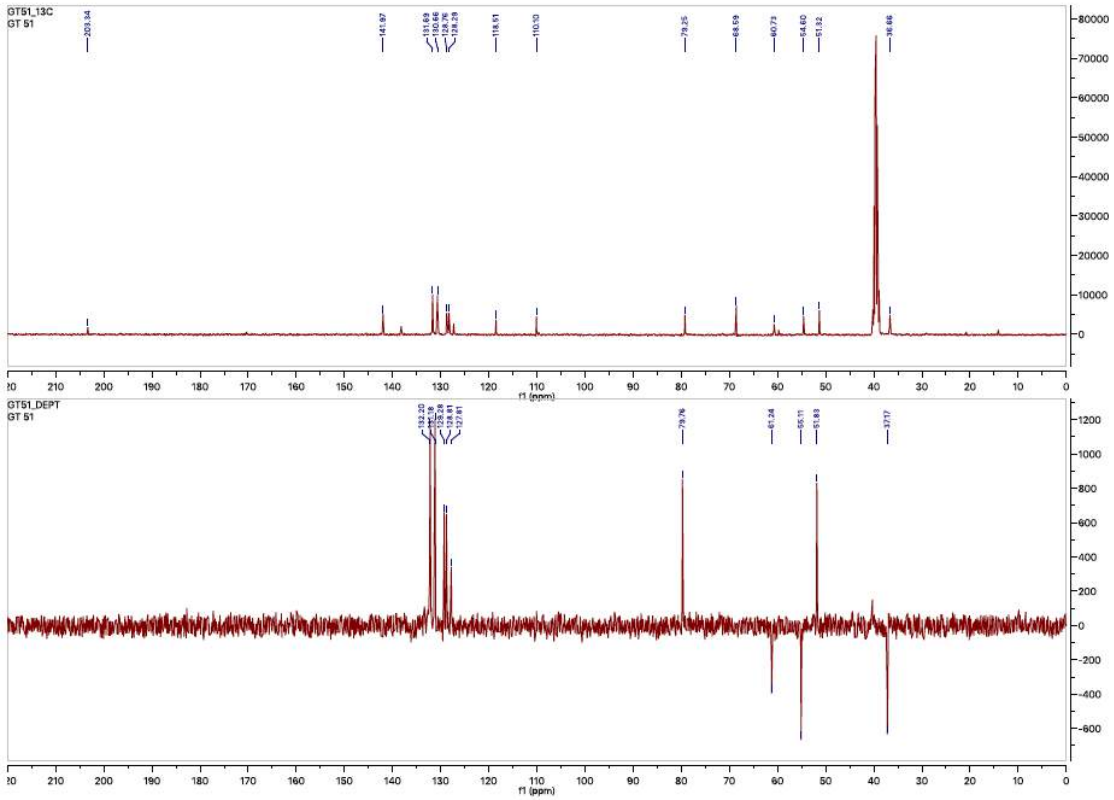

$^{13}$C NMR and DEPT spectra of compound **98**.

**Compound 99**. Synthesis of *(1R,4R,5R,7S,8S,11S)-13-benzyl-4,11-dihydroxy-1,8-diphenyl-2,9-dithia-13-azadispiro[4.1.47.35]tetradecan-6-one*

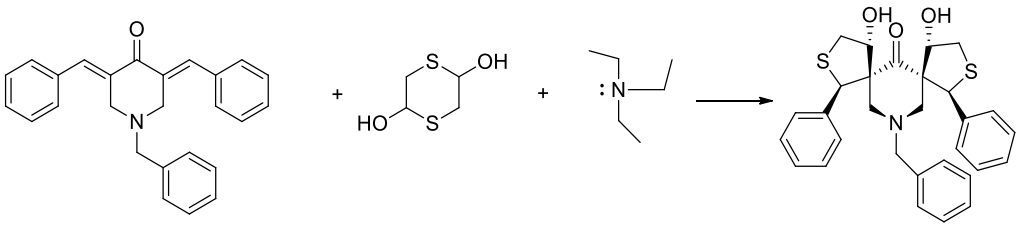


Compound **63** (1 eq) and 1,4-dithiane-2,5-diol (2 eq) were solubilized in absolute ethanol (5ml). The reaction mixture was maintained at 0°C using an ice bath. Once the temperature was reached, TEA (2 eq) was added dropwise and the reaction was stirred at room temperature for 10 minutes. Then, it was set at 90°C for three hours and monitored by TLC (A1P4). Once the reaction was completed, the solvent was evaporated and the crude residue was purified by flash silica gel chromatography with an eluent mixture of ethyl acetate and petroleum ether (A1P4). After evaporation, a with white solid was obtained.

MS (ESI): $[M+H]^+$ = 518,23;
Yield: 92%;
**$^1$H NMR** (400 MHz, DMSO-$d_6$) δ 7.75 – 7.59 (m, 8H), 7.47 – 7.39 (m, 4H), 7.40 – 7.26 (m, 2H), 7.26 – 7.14 (m, 2H), 5.57 (s, 2H), 5.22 (t, *J* = 4.4 Hz, 2H), 5.16 (d, *J* = 4.1 Hz, 2H), 3.40 (s, 1H), 3.34 (s, 4H), 3.18 (dd, *J* = 12.1, 4.5 Hz, 2H), 2.79 (d, *J* = 12.1 Hz, 2H), 2.70 (d, *J* = 12.1 Hz, 2H), 1.56 (d, *J* = 12.2 Hz, 2H).
**$^{13}$C NMR** (101 MHz, DMSO-$d_6$) δ 203.34, 141.97, 131.69, 130.66, 128.76, 128.29, 118.51, 110.10, 79.25, 68.59, 60.73, 54.60, 51.32, 36.66.

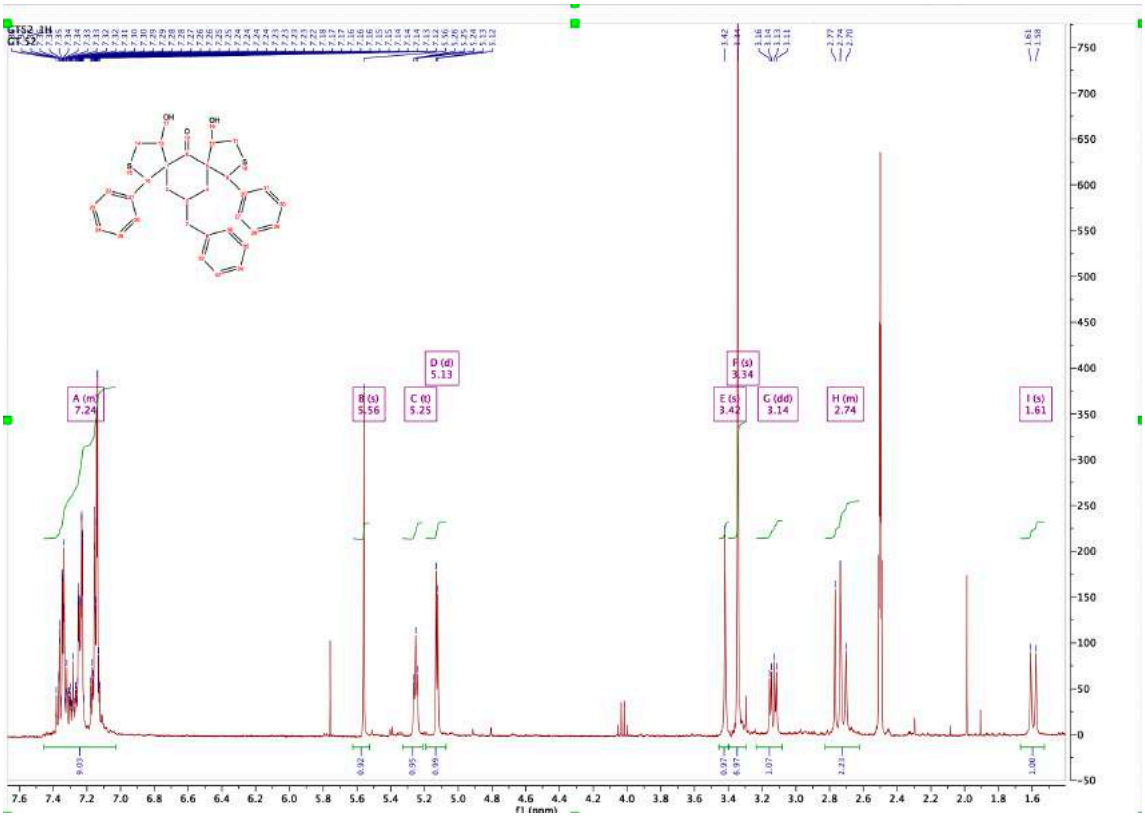


$^{1}$H NMR spectrum of compound **99.**

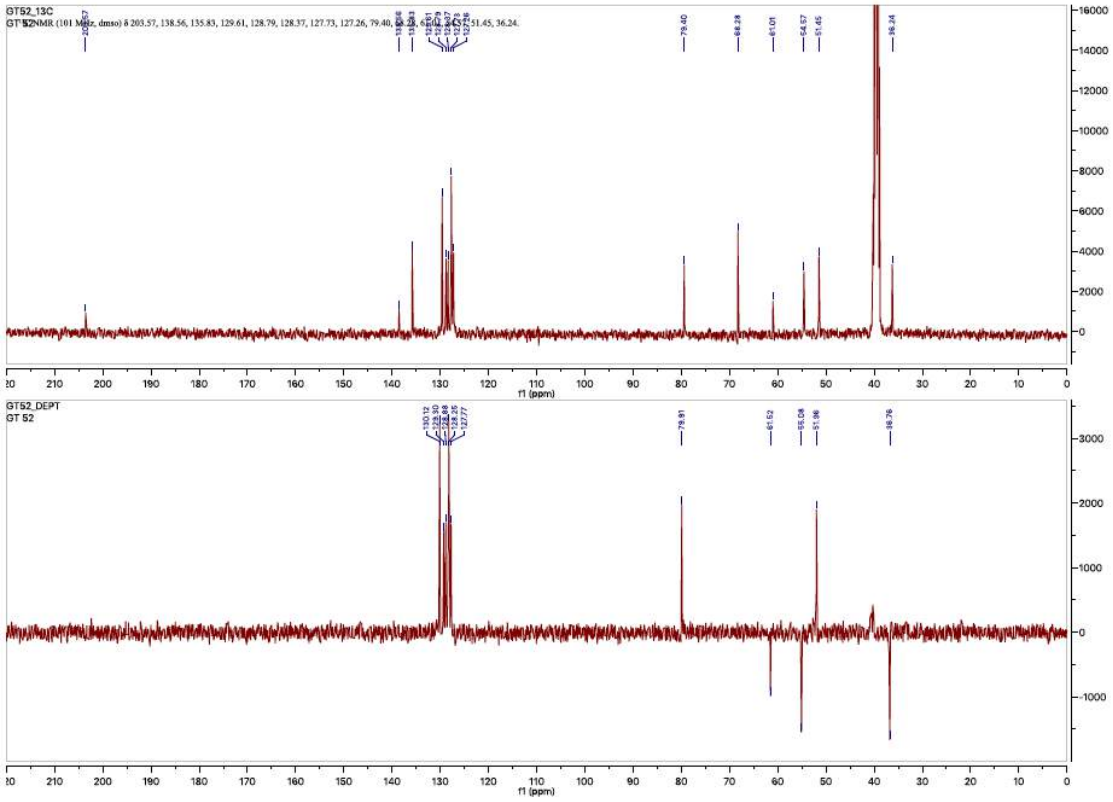


$^{13}$C NMR and DEPT spectra of compound **99.**

**Compound 100**. Synthesis of *(1R,4R,5R,7S,8S,11S)-13-benzyl-1,8-bis(4-fluorophenyl)-4,11-dihydroxy-2,9-dithia-13-azadispiro[4.1.47.35]tetradecan-6-one*

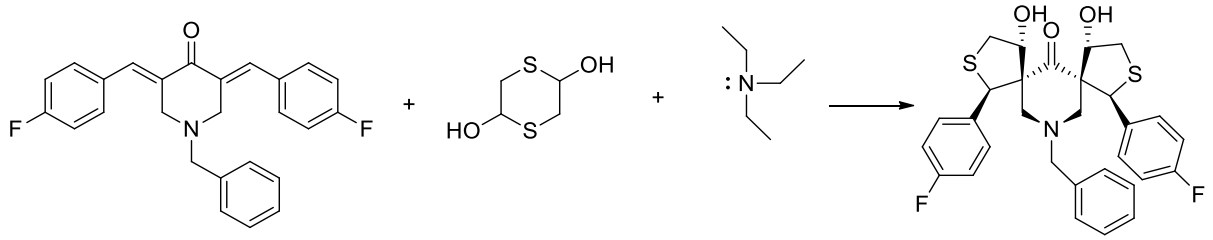


**1 eq** **MW = 401** | **2 eq** **MW = 152,23** | **2 eq** **MW = 101,19** | **MW = 553,16**

Compound **64** (1 eq) and 1,4-dithiane-2,5-diol (2 eq) were solubilized in absolute ethanol (5ml).The reaction mixture was maintained at 0°C using an ice bath. Once the temperature was reached, TEA (2 eq) was added dropwise and the reaction was stirred at room temperature for 10 minutes. Then, it was set at 90°C for three hours and monitored by TLC (A1P4). Once the reaction was completed, the solvent was evaporated and the crude residue was purified by flash silica gel chromatography with an eluent mixture of ethyl acetate and petroleum ether (A1P4). After evaporation, a with solid was obtained.

MS (ESI): $[M+H]^+$ = 554,16;
Yield: 32%;
**$^1$H NMR** (400 MHz, DMSO-$d_6$) δ 7.49 – 7.21 (m, 8H), 7.15 – 6.99 (m, 4H), 5.53 (s, 2H), 5.22 (d, *J* = 4.6 Hz, 2H), 3.44 (s, 4H), 3.14 (dd, *J* = 12.2, 4.8 Hz, 2H), 2.73 (dd, *J* = 14.8, 12.0 Hz, 2H), 1.56 (d, *J* = 12.1 Hz, 2H).
**$^{13}$C NMR** (101 MHz, DMSO-$d_6$) δ 203.59, 162.45, 160.02, 138.45, 131.82, 131.56, 131.48, 128.80, 128.35, 127.33, 114.61, 114.40, 79.14, 68.18, 60.95, 54.53, 50.70, 36.28.

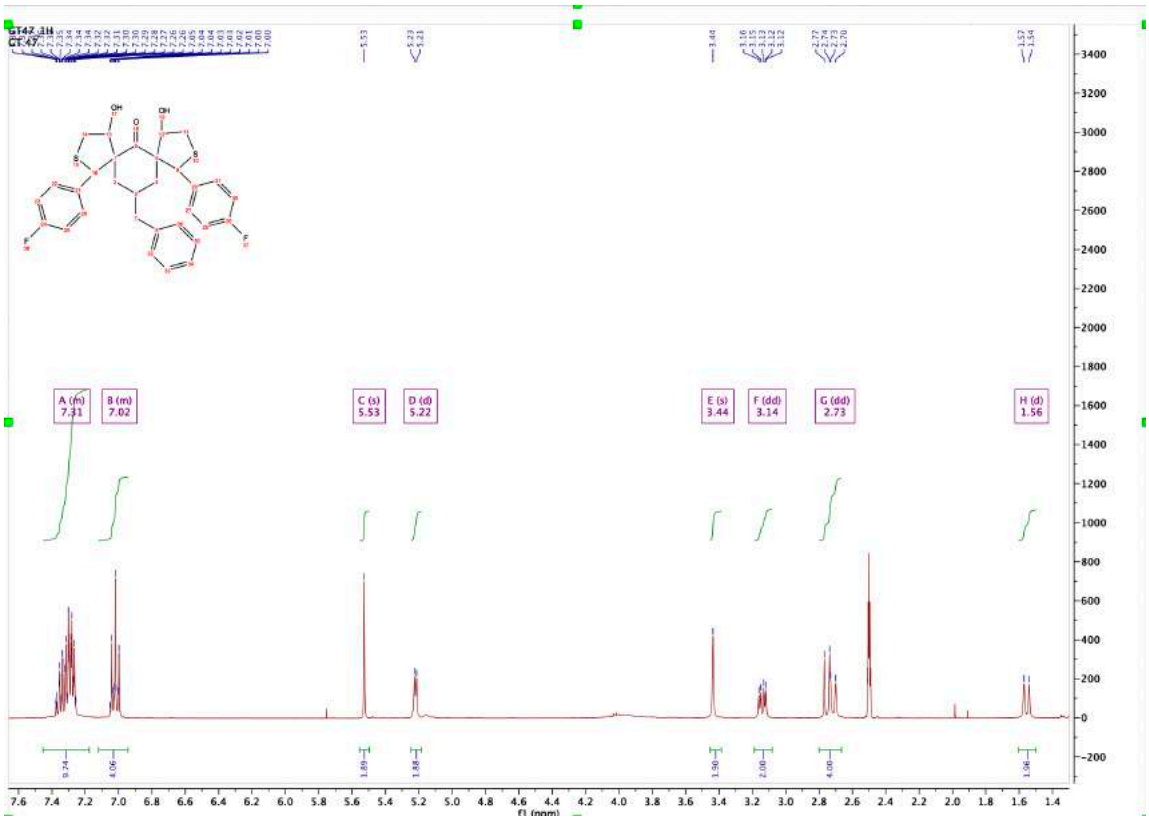


$^{1}$H NMR spectrum of compound **100.**

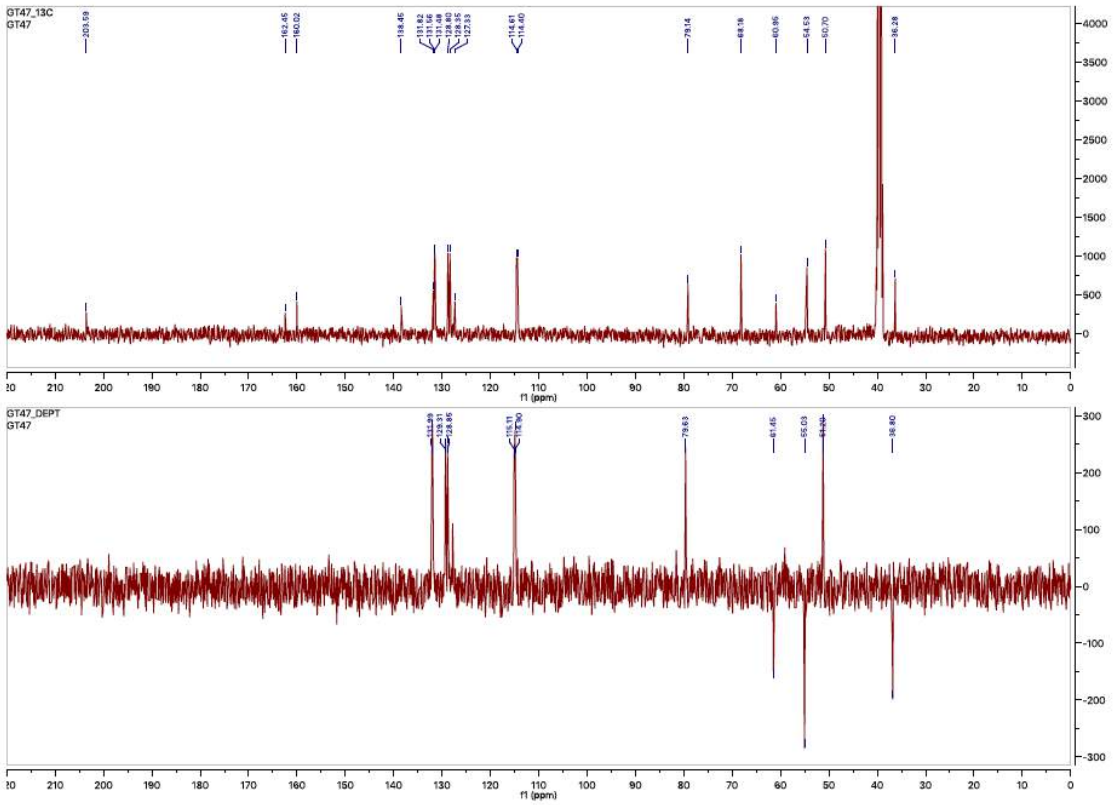


$^{13}$C NMR and DEPT spectra of compound **100**.

**Compound 101.** Synthesis of (*1R,4R,5R,7S,8S,11S)-13-benzyl-4,11-dihydroxy-1,8-bis(4-nitrophenyl)-2,9-dithia-13-azadispiro[4.1.47.35]tetradecan-6-one*

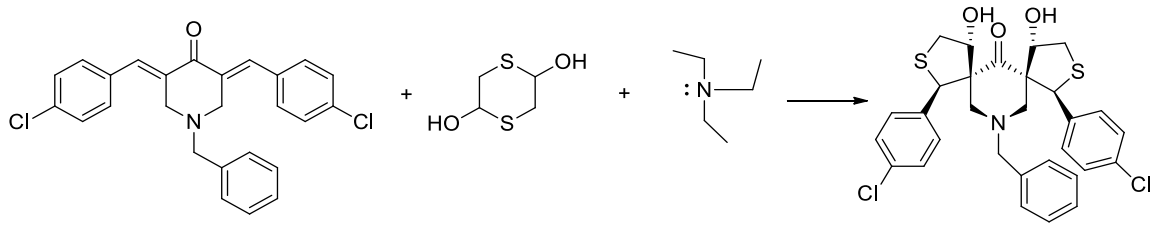


**1 eq** **MW = 433** | **2 eq** **MW = 152,23** | **2 eq** **MW = 101,19** | **MW = 586,98**

Compound **65** (1 eq) and 1,4-dithiane-2,5-diol (2 eq) were solubilized in absolute ethanol (5ml). The reaction mixture was maintained at 0°C using an ice bath. Once the temperature was reached, TEA (2 eq) was added dropwise and the reaction was stirred at room temperature for 10 minutes. Then, it was set at 90°C for three hours and monitored by TLC (A1P4). Once the reaction was completed, the solvent was evaporated and the crude residue was purified by flash silica gel chromatography with an eluent mixture of ethyl acetate and petroleum ether (A1P4). After evaporation, a with pale yellow solid was obtained.

MS (ESI): $[M+H]^+$ = 587,98;
Yield:90%
$^1$**H NMR** (400 MHz, DMSO-$d_6$) δ 7.49 – 7.21 (m, 8H), 7.15 – 6.99 (m, 4H), 5.53 (s, 2H), 5.22 (d, *J* = 4.6 Hz, 2H), 3.44 (s,4H), 3.14 (dd, *J* = 12.2, 4.8 Hz, 2H), 2.73 (dd, *J* = 14.8, 12.0 Hz, 2H), 1.56 (d, *J* = 12.1 Hz, 2H).
$^{13}$**C NMR** (101 MHz, DMSO-$d_6$) δ 203.59, 162.45, 160.02, 138.45, 131.82, 131.56, 131.48, 128.80, 128.35, 127.33, 114.61, 114.40, 79.14, 68.18, 60.95, 54.53, 50.70, 36.28.

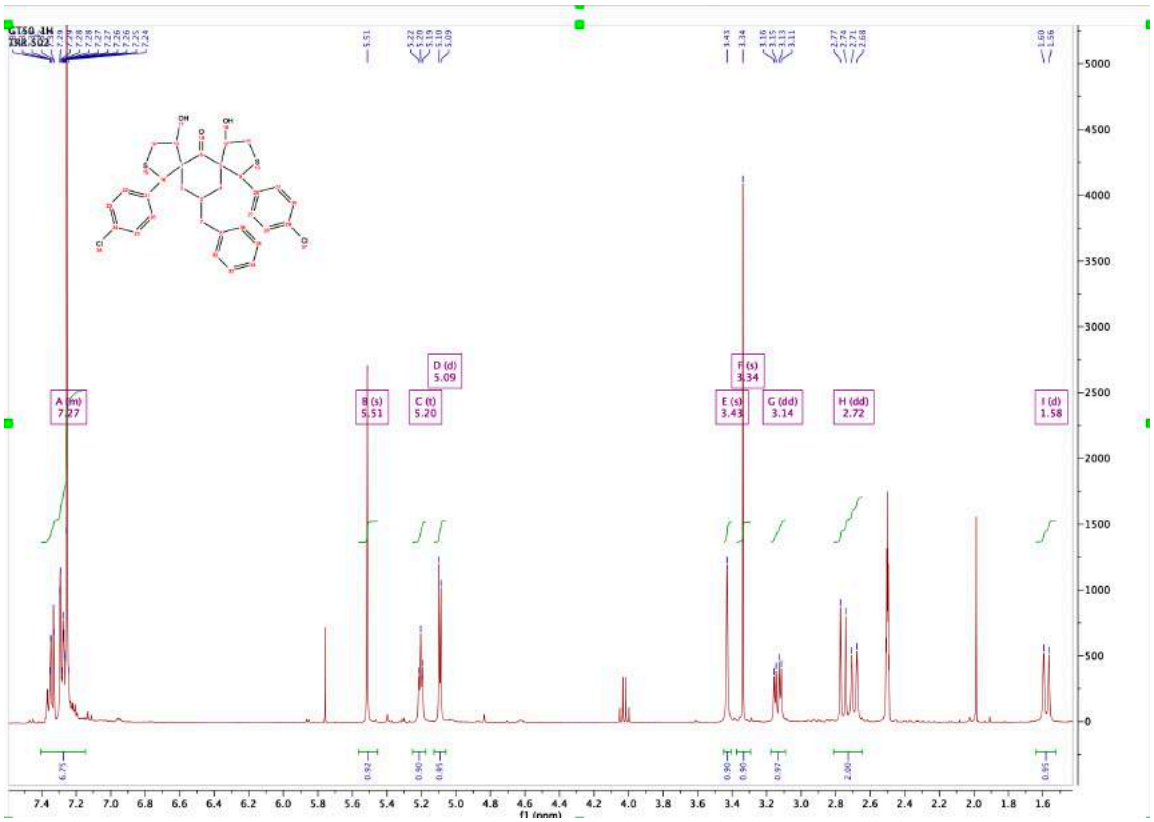


$^{1}$H NMR spectrum of compound **101.**

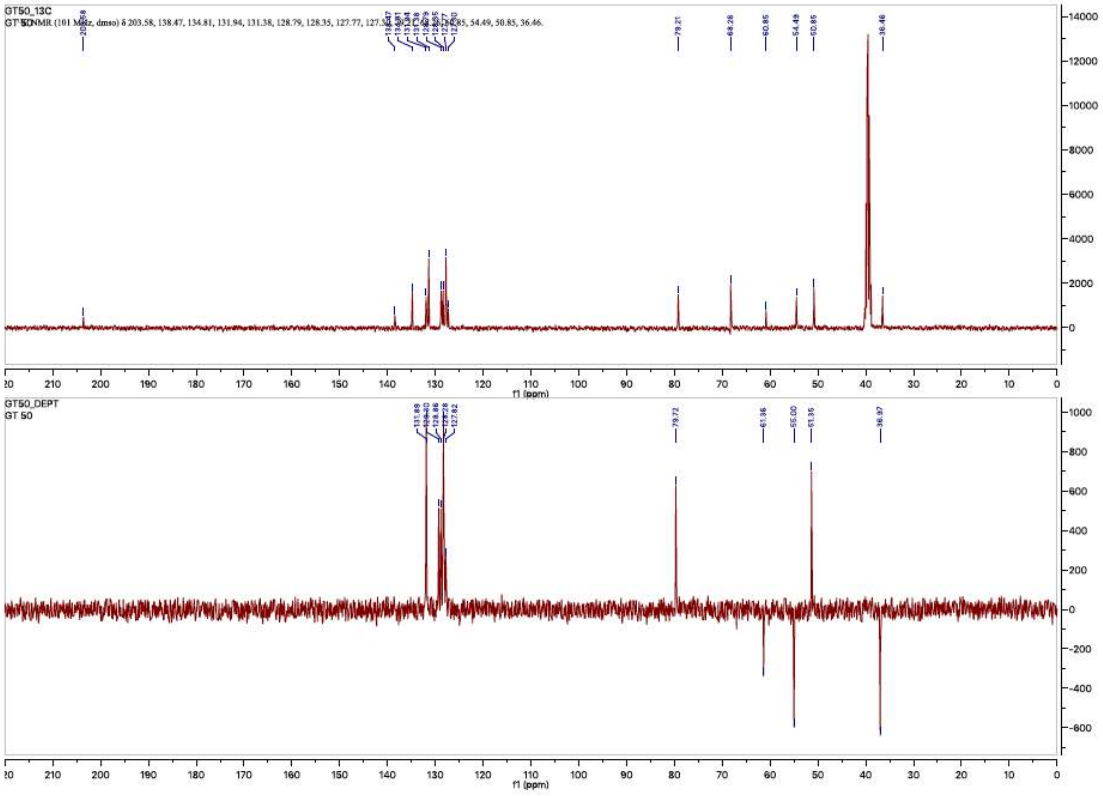


$^{13}$C NMR and DEPT spectra of compound **101.**

**Compound 102**. Synthesis of *(1R,4R,5R,7S,8S,11S)-13-benzyl-4,11-dihydroxy-1,8-di(naphthalen-2-yl)-2,9-dithia-13-azadispiro[4.1.47.35]tetradecan-6-one*

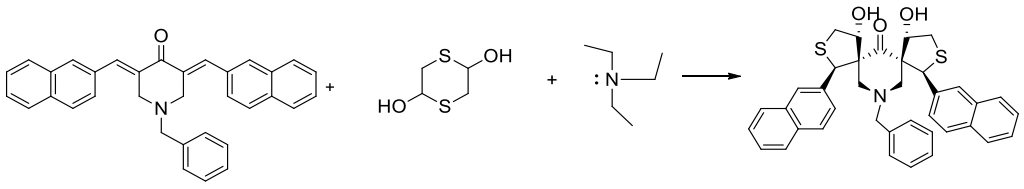

| 1 eq | 2 eq | 2 eq | |
|---|---|---|---|
| MW = 465 | MW = 152,23 | MW = 101,19 | MW = 617,21 |

Compound **66** (1 eq) and 1,4-dithiane-2,5-diol (2 eq) were solubilized in absolute ethanol (5ml). The reaction mixture was maintained at 0°C using an ice bath. Once the temperature was reached, TEA (2 eq) was added dropwise and the reaction was stirred at room temperature for 10 minutes. Then, it was set at 90°C for three hours and monitored by TLC (A1P4). Once the reaction was completed, the solvent was evaporated and the crude residue was purified by flash silica gel chromatography with an eluent mixture of ethyl acetate and petroleum ether (A1P4). After evaporation, a with white solid was obtained.

MS (ESI): $[M+H]^+$ = 618,18;
Yield: 57%;
**$^1$H NMR** (400 MHz, DMSO-$d_6$) δ 7.47 – 6.99 (m, 8H), 5.56 (s, 4H), 5.25 (t, *J* = 4.4 Hz, 2H), 5.13 (d, *J* = 4.0 Hz, 2H), 3.42 (s, 4H), 3.34 (s, 2H), 3.14 (dd, *J* = 12.1, 4.7 Hz, 2H), 2.83 – 2.67 (m, 2H), 1.61 (s, 2H).
**$^{13}$C NMR** (101 MHz, DMSO-$d_6$) δ 203.57, 138.56, 135.83, 129.61, 128.79, 128.37, 127.73, 127.26, 79.40, 68.28, 61.01, 54.57, 51.45, 36.24.

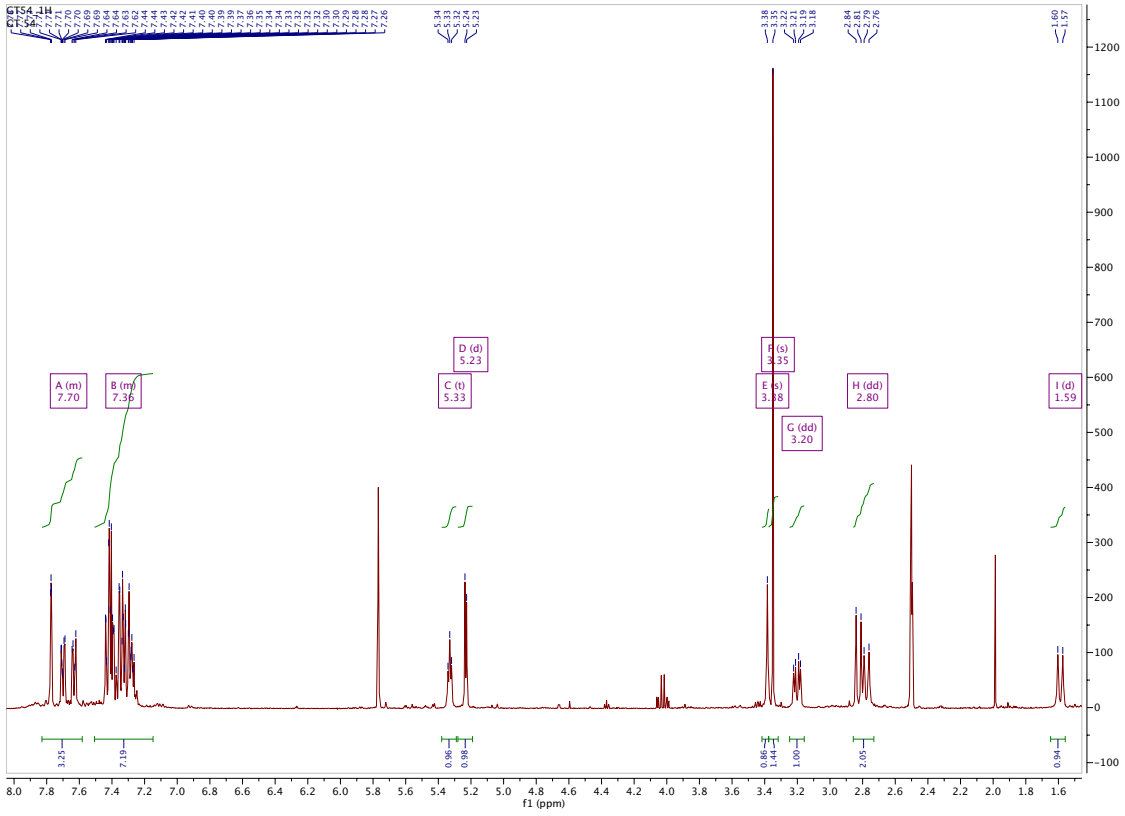


$^1$H NMR spectrum of compound **102.**

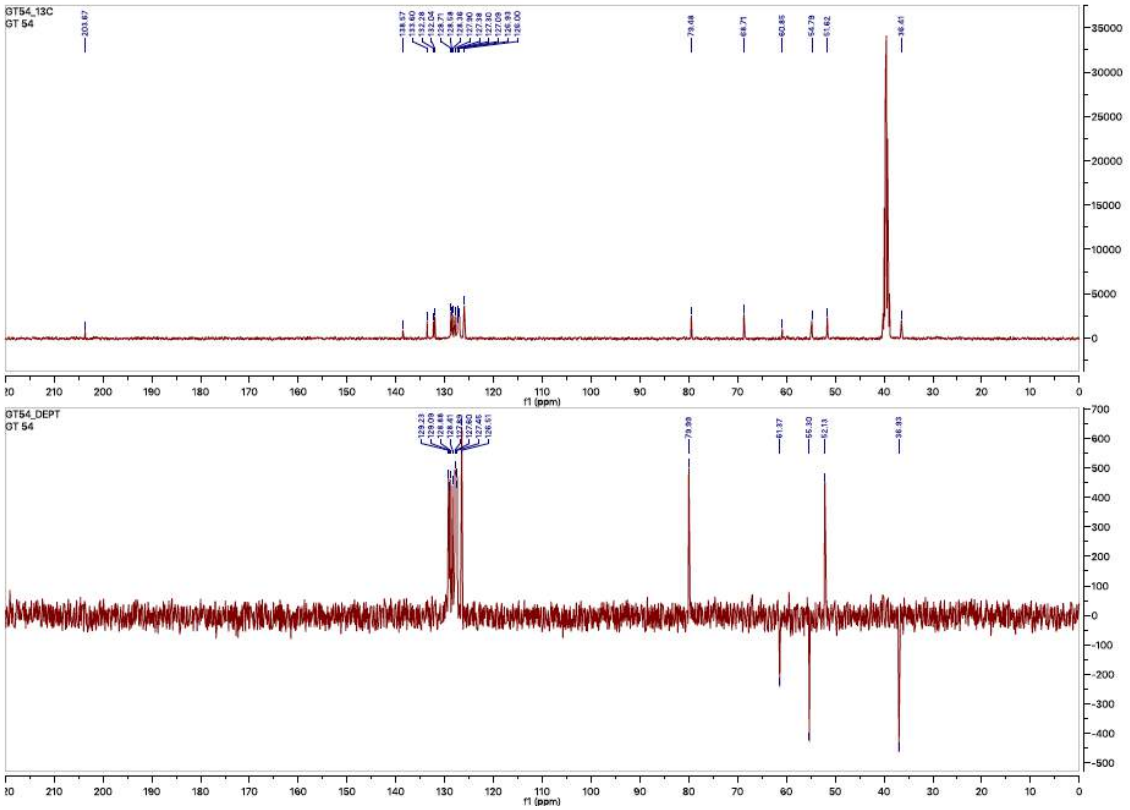


$^{13}C$ NMR and DEPT spectra of compound **102.**

## 5.4 PYRROLIDINE SCAFFOLD-BASED DISPIRANIC COMPOUNDS.

### 5.4.1 GENERAL PROCEDURE FOR THE SYNTHESIS OF PYRROLIDINE SCAFFOLD-BASED DISPIRANIC COMPOUNDS 103-111.

**Compound 103**. Synthesis of *1',5-dimethyldispiro[cyclohexane-1,3'-pyrrolidine-2',3''-indoline]-2,2''-dione*

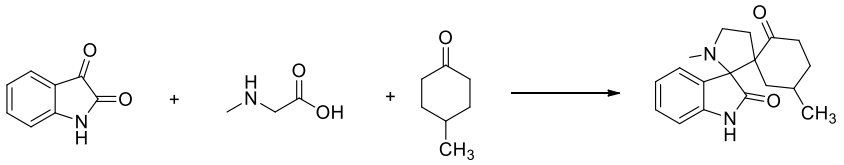

| 1eq | 1.5 eq | 1 eq | |
|---|---|---|---|
| MW = 147 | MW= 89 | MW = 112,17 | MW = 298,17 |

To a solution of isatin (1 eq, 3.4 mmol) in MeOH (15 ml), sarcosine (1.5 eq, 5.1 mmol) and 4-methylcyclohexan-1-one ( 1 eq, 3.4 mmol) were added. The reaction was stirred at 90°C under reflux for 10 hours. The reaction was monitored through MS analysis and TLC (A1P1). Upon completion of the reaction, this was quenched with NaHCO3 sat and deionized water. The organic solvent was evaporated and the aqueous phase was extracted three times with ethyl acetate (40 ml). The organic phases, taken together, after treatment with anhydrous sodium sulphate, were evaporated and an amorphous orange solid was obtained. The crude product was then purified by flash silica gel chromatography with eluent mixture of ethyl acetate and petroleum ether (A1P1). After evaporation of the solvent, a pale pink solid was obtained.

MS (ESI): $[M+H]^+$ = 299,17
mp: 110-112°C
Yield: 51%
**$^1$H NMR** (400 MHz, Chloroform-*d*) δ 9.01 (s, 1H), 7.29 – 7.09 (m, 1H), 7.05 – 6.75 (m, 3H), 3.29 – 3.13 (m, 2H), 2.83 – 2.69 (m, 1H), 2.60 (dt, *J* = 14.6, 3.1 Hz, 1H), 2.26 – 2.11 (m, 1H), 2.03 (s, 3H), 1.90 – 1.62 (m, 2H), 1.40 – 1.06 (m, 3H), 0.79 (d, *J* = 6.4 Hz, 3H).
**$^{13}$C NMR** (101 MHz, $CDCl_3$) δ 211.40, 179.40, 141.51, 129.51, 127.51, 126.93, 122.64, 110.30, 76.34, 62.84, 52.07, 45.37, 41.70, 35.71, 34.66, 34.54, 28.66, 21.86.

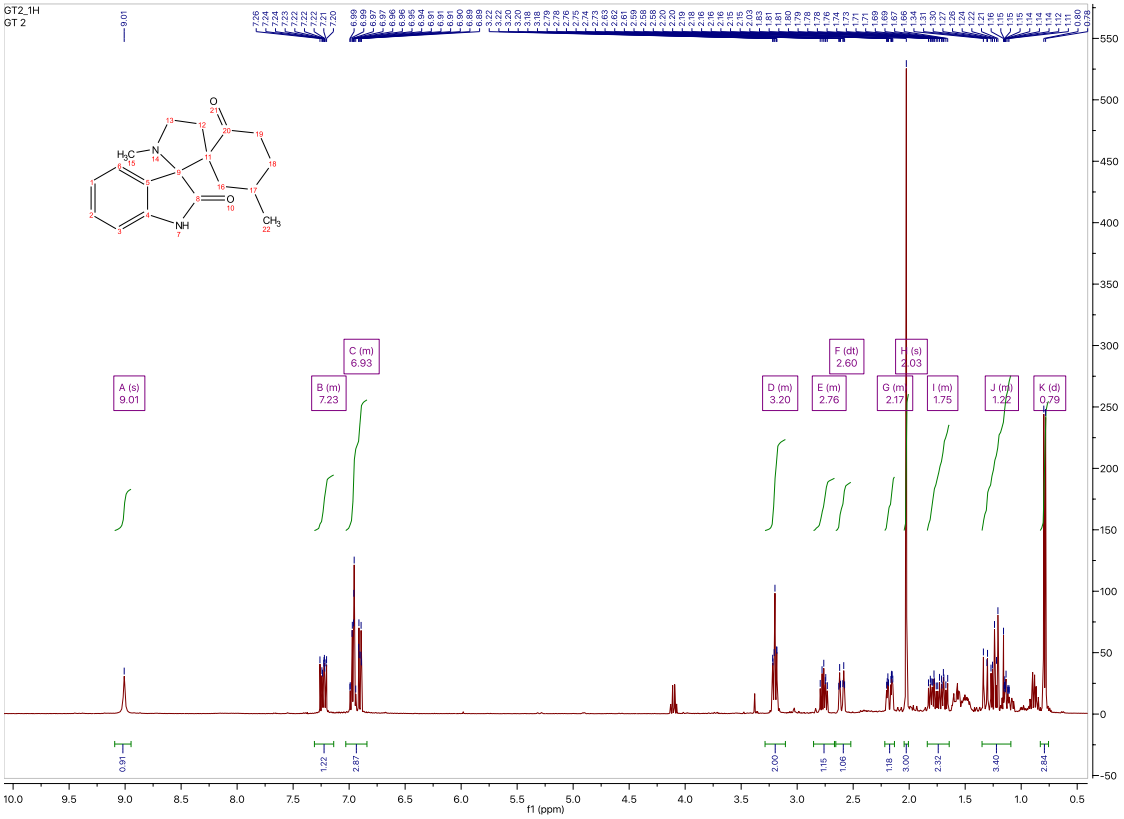


$^{1}$H NMR spectrum of compound **103.**

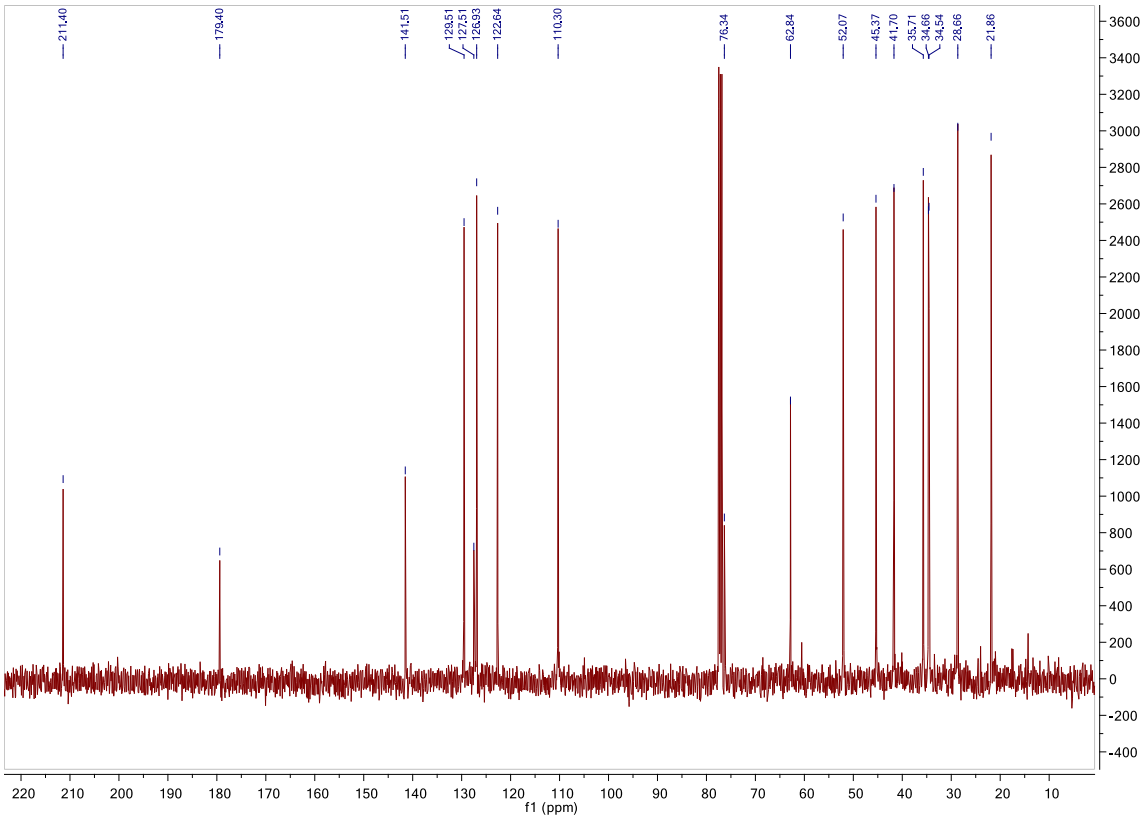


$^{13}$C NMR spectrum of compound **103**.

**Compound 104**. Synthesis of *1'-methyldispiro[cyclohexane-1,3'-pyrrolidine-2',3''-indoline]-2,2''-dione*

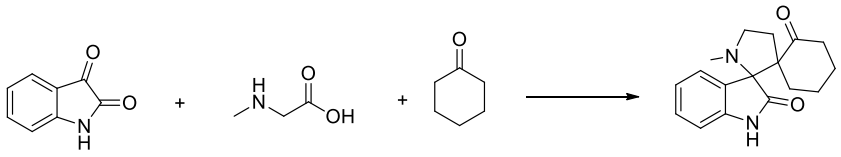

| 1eq | 1.5 eq | 1 eq | |
|---|---|---|---|
| MW = 147 | MW= 89 | MW = 98,15 | MW = 284,16 |

To a solution of isatin (1 eq, 3.4 mmol) in MeOH (15 ml), sarcosine (1.5 eq, 5.1 mmol) and cyclohexan-1-one ( 1 eq, 3.4 mmol) were added. The reaction was stirred at 90°C under reflux for 10 hours. The reaction was monitored through MS analysis and TLC (A1P1). Upon completion of the reaction, this was quenched with NaHCO3 sat and deionized water. The organic solvent was evaporated and the aqueous phase was extracted three times with ethyl acetate (40 ml). The organic phases, taken together, after treatment with anhydrous sodium sulphate, were evaporated and an amorphous orange solid was obtained. The crude product was then purified by flash silica gel chromatography with eluent mixture of ethyl acetate and petroleum ether (A1P1). After evaporation of the solvent, a pale pink solid was obtained.

MS (ESI): $[M+H]^+$ = 285,16;
Yield: 51%;
mp: 144-146 °C
**$^1$H NMR** (400 MHz, Chloroform-*d*) δ 8.86 (s, 1H), 7.32 – 7.09 (m, 1H), 7.09 – 6.93 (m, 2H), 6.90 (d, *J* = 7.8 Hz, 1H), 3.26 (h, *J* = 3.9, 3.4 Hz, 2H), 2.68 (ddd, *J* = 12.7, 7.5, 5.3 Hz, 1H), 2.44 (dt, *J* = 13.5, 3.9 Hz, 1H), 2.22 (dd, *J* = 14.6, 4.4 Hz, 1H), 2.08 (s, 3H), 2.03 – 1.91 (m, 1H), 1.77 (ddd, *J* = 14.9, 11.5, 7.0 Hz, 1H), 1.67 (ddd, *J* = 14.7, 10.9, 3.7 Hz, 2H), 1.59 – 1.45 (m, 2H), 1.43 – 1.32 (m, 1H).
**$^{13}$C NMR** (101 MHz, Chloroform-*d*) δ 212.01, 179.02, 141.71, 135.09, 129.55, 128.33, 127.09, 123.44, 122.75, 115.29, 110.23, 62.83, 52.14, 41.30, 35.85, 35.64, 34.10, 27.70, 25.44, 21.69.

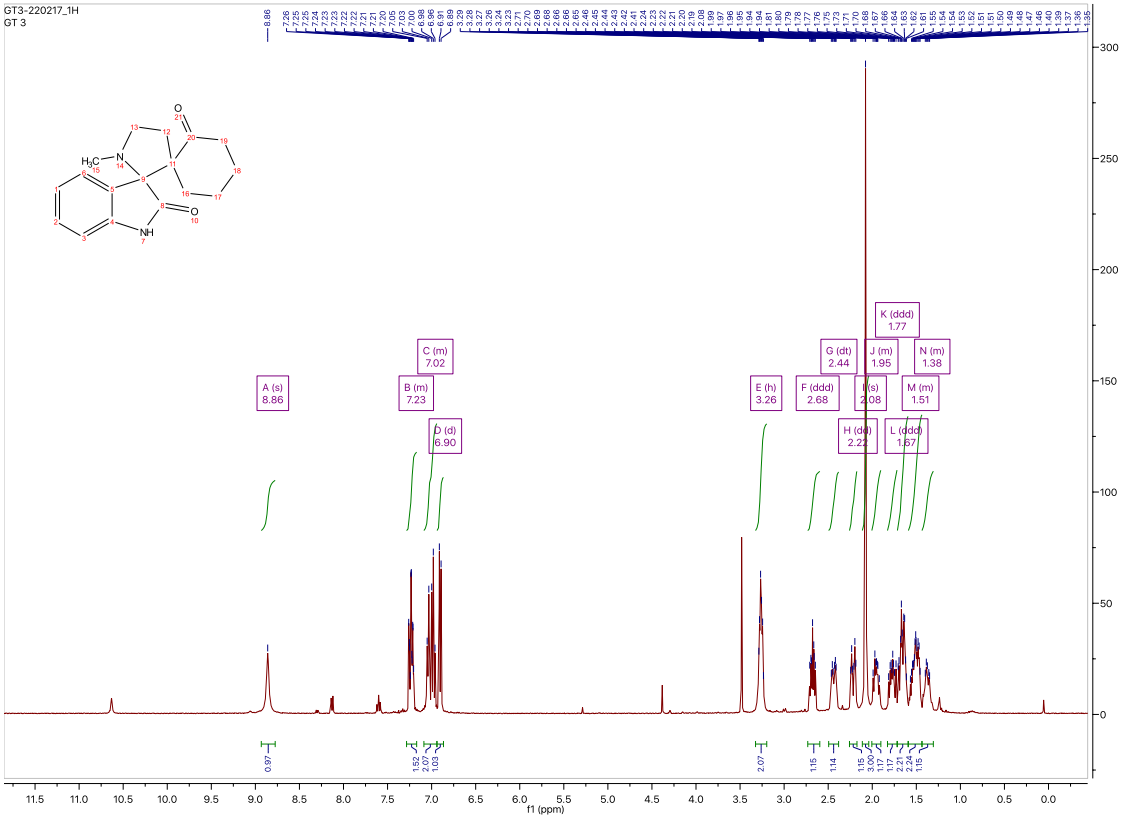


$^{1}$H NMR spectrum of compound **104.**

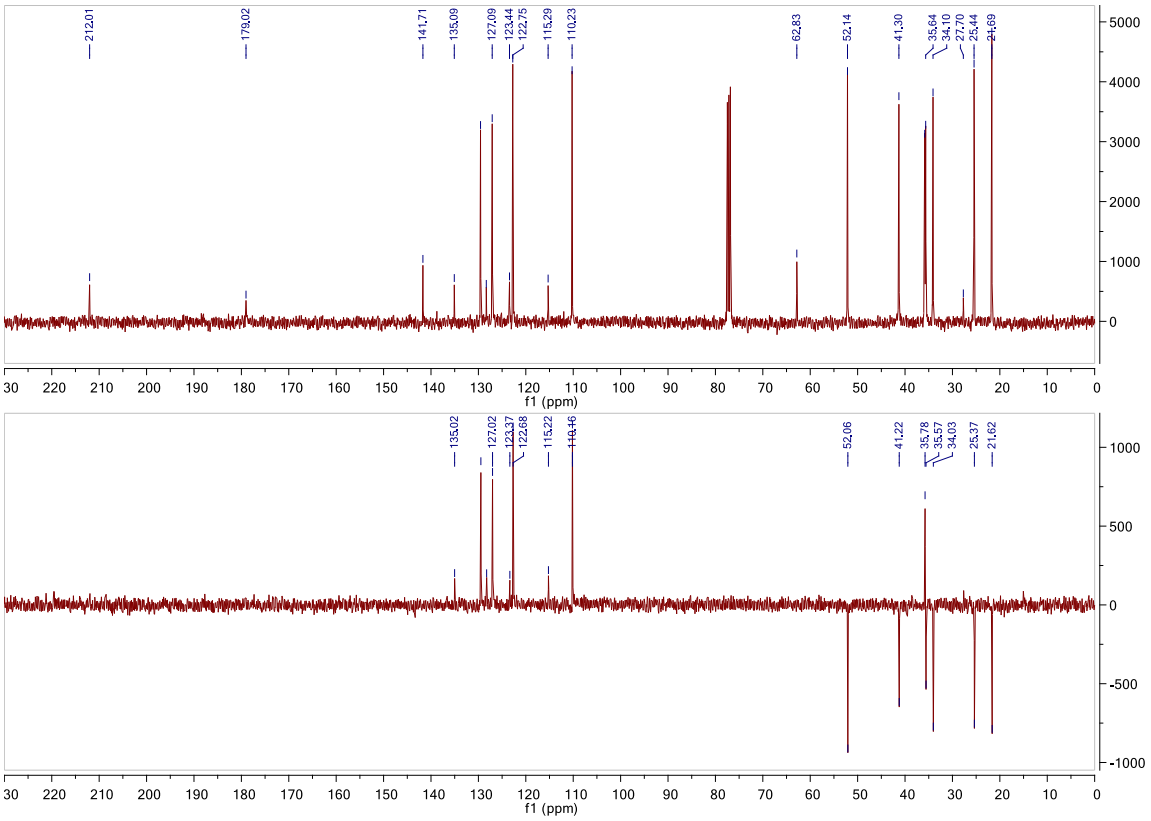


$^{13}$C NMR and DEPT spectra of compound **104**.

**Compound 105.** Synthesis of *1'-methyl-3",4"-dihydro-1"H-dispiro[indoline-3,2'-pyrrolidine-3',2"-naphthalene]-1",2-dione*

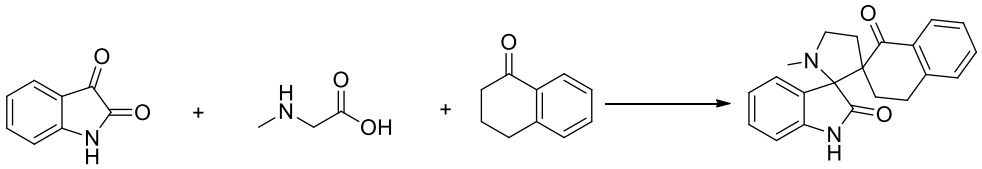

| 1eq | 1.5 eq | 1 eq | |
|---|---|---|---|
| MW = 147 | MW= 89 | MW = 146,19 | MW = 332,16 |

To a solution of isatin (1 eq, 3.4 mmol) in MeOH (15 ml), sarcosine (1.5 eq, 5.1 mmol) and 3,4-dihydronaphthalen-1(2*H*)-one ( 1 eq, 3.4 mmol) were added. The reaction was stirred at 90°C under reflux for 10 hours. The reaction was monitored through MS analysis and TLC (A1P1). Upon completion of the reaction, this was quenched with NaHCO3 sat and deionized water. The organic solvent was evaporated and the aqueous phase was extracted three times with ethyl acetate (40 ml). The organic phases, taken together, after treatment with anhydrous sodium sulphate, were evaporated and an amorphous orange solid was obtained. The crude product was then purified by flash silica gel chromatography with eluent mixture of ethyl acetate and petroleum ether (A1P1). After recrystallization with a mixture of ethyl ether/petroleum ether (3:7), a dark yellow solid was obtained.

MS (ESI): $[M+H]^+$ = 333,16;
Yield: 52%;
mp: 194-196 °C
**$^1$H NMR** (400 MHz, Chloroform-*d*) δ 10.20 (s, 1H), 8.35 – 8.01 (m, 4H), 7.62 (ddd, *J* = 8.6, 7.3, 1.5 Hz, 1H), 7.41 – 6.43 (m, 2H), 4.39 (s, 3H), 3.49 (s, 4H), 2.79 – 2.02 (m, 9H).
**$^{13}$C NMR** (101 MHz, $CDCl_3$) δ 210.13, 162.80, 152.08, 143.47, 138.59, 135.13, 133.27, 131.81, 128.45, 127.94, 126.87, 125.20, 123.52, 118.73, 115.15, 114.57, 109.84, 57.72, 51.38, 27.74, 26.04.

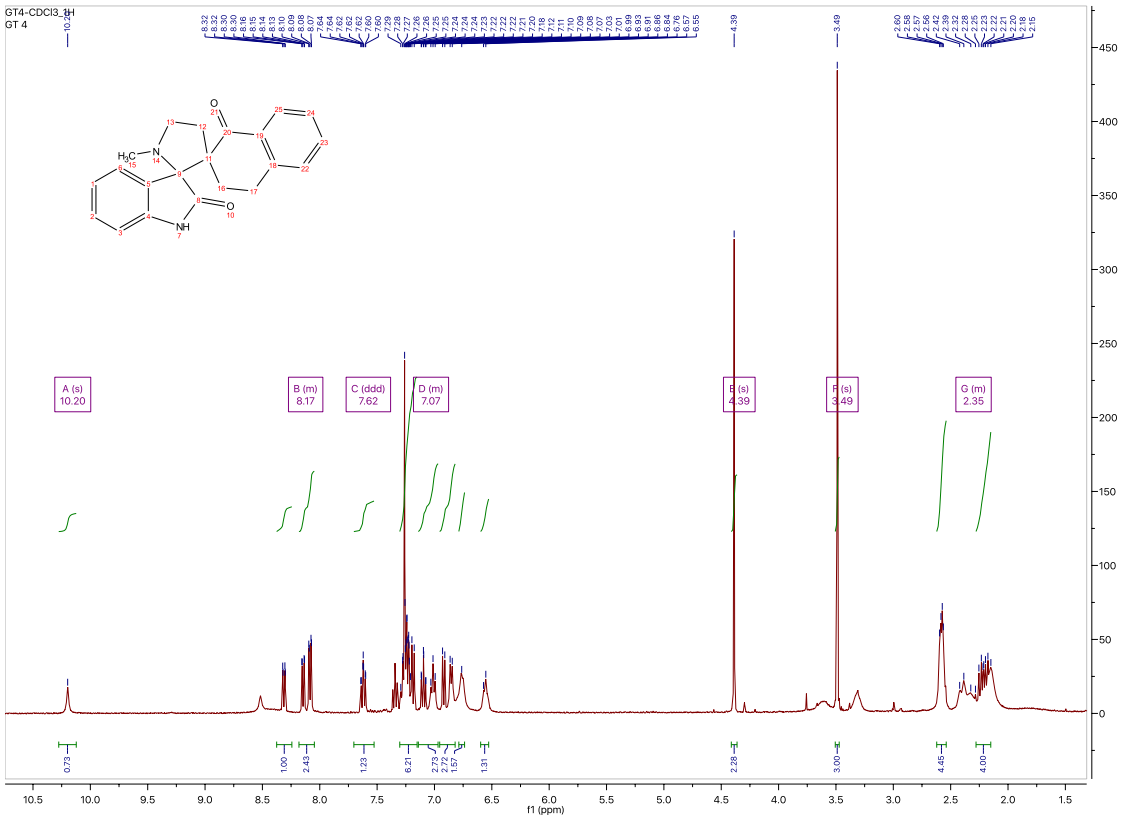


$^{1}$H NMR spectrum of compound **105.**

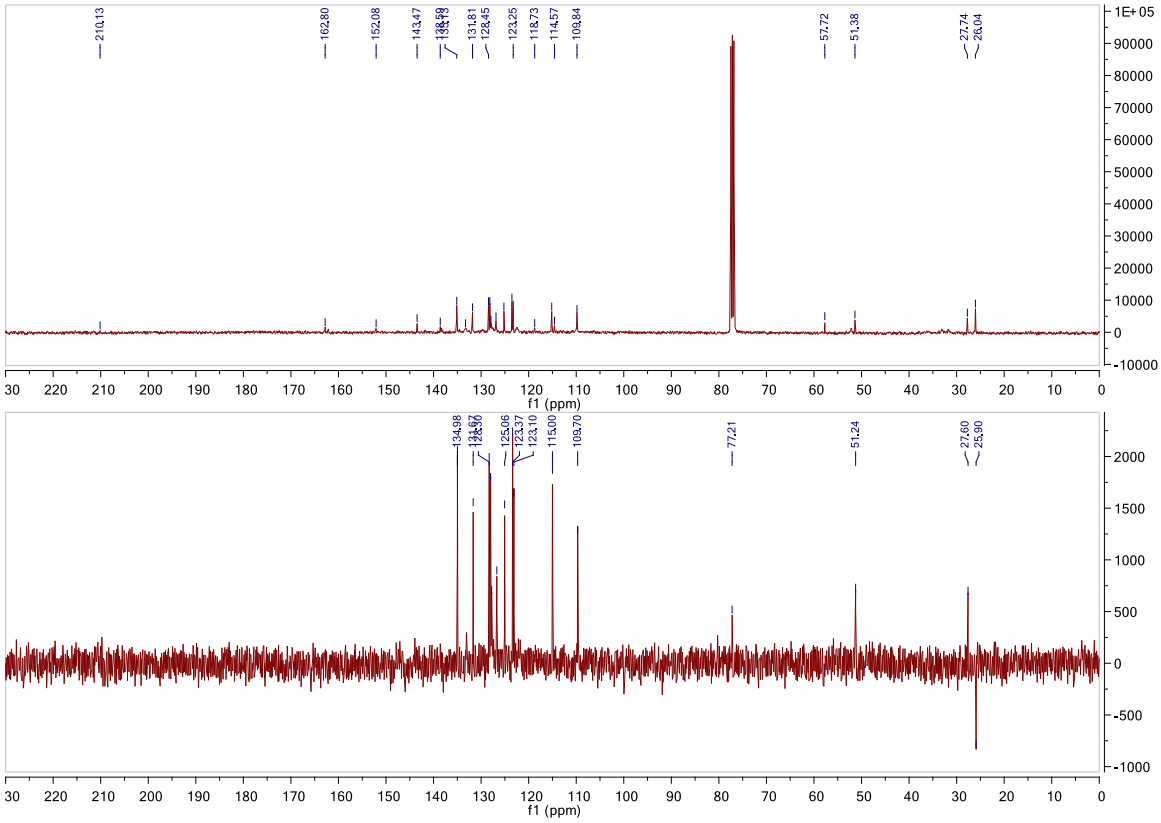


$^{13}$C NMR spectrum of compound **105**.

**Compound 106.** Synthesis of *1'-methyl-2H-dispiro[acenaphthylene-1,3'-pyrrolidine-2',3''-indoline]-2,2''-dione*

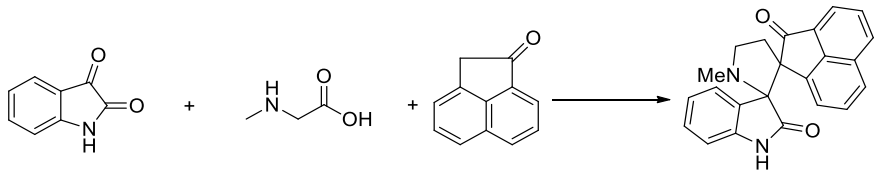


**1eq** **MW = 147** | **1.5 eq** **MW= 89** | **1 eq** **MW = 144,78** | **MW = 354,16**

To a solution of isatin (1 eq, 3.4 mmol) in MeOH (15 ml), sarcosine (1.5 eq, 5.1 mmol) and acenaphtenone ( 1 eq, 3.4 mmol) were added. The reaction was stirred at 90°C under reflux for 10 hours. The reaction was monitored through MS analysis and TLC (A1P1). Upon completion of the reaction, this was quenched with NaHCO3 sat and deionized water. The organic solvent was evaporated and the aqueous phase was extracted three times with ethyl acetate (40 ml). The organic phases, taken together, after treatment with anhydrous sodium sulphate, were evaporated and an amorphous orange solid was obtained. The crude product was then purified by flash silica gel chromatography with eluent mixture of ethyl acetate and petroleum ether (A1P1). After recrystallization with a mixture of ethyl ether/petroleum ether (3:7), an orangish solid was obtained.

MS (ESI): $[M+H]^+$ = 355,14
Yield: 15% to 30%
mp: 210-212 °C
**$^1$H NMR** (400 MHz, Chloroform-*d*) δ 7.90 (d, *J* = 8.1 Hz, 1H), 7.85 (d, *J* = 7.0 Hz, 1H), 7.70 (dd, *J* = 7.7, 5.8 Hz, 2H), 7.56 (dd, *J* = 8.1, 7.0 Hz, 1H), 7.47 (dd, *J* = 8.4, 7.0 Hz, 1H), 6.91 (td, *J* = 7.7, 1.3 Hz, 1H), 6.76 (td, *J* = 7.6, 1.1 Hz, 1H), 6.46 (d, *J* = 7.7 Hz, 1H), 3.84 (s, 1H), 3.64 (td, *J* = 9.5, 8.6, 4.1 Hz, 1H), 3.06 (td, *J* = 11.9, 5.1 Hz, 1H), 2.46 (ddd, *J* = 12.8, 8.5, 4.2 Hz, 1H), 2.30 (s, 4H).
**$^{13}$C NMR** (101 MHz, Chloroform-*d*) δ 204.87, 177.95 , 142.05 , 141.52 , 132.66 , 132.53 , 131.68 , 131.28 , 130.34 , 129.92 , 129.44 , 128.94 , 128.68 , 128.22 , 128.12 , 126.65 , 124.89 , 122.66 , 122.53 , 121.70 , 121.58 , 109.67 , 109.60 , 79.00 , 63.48 , 52.45 , 35.98 , 31.73 .

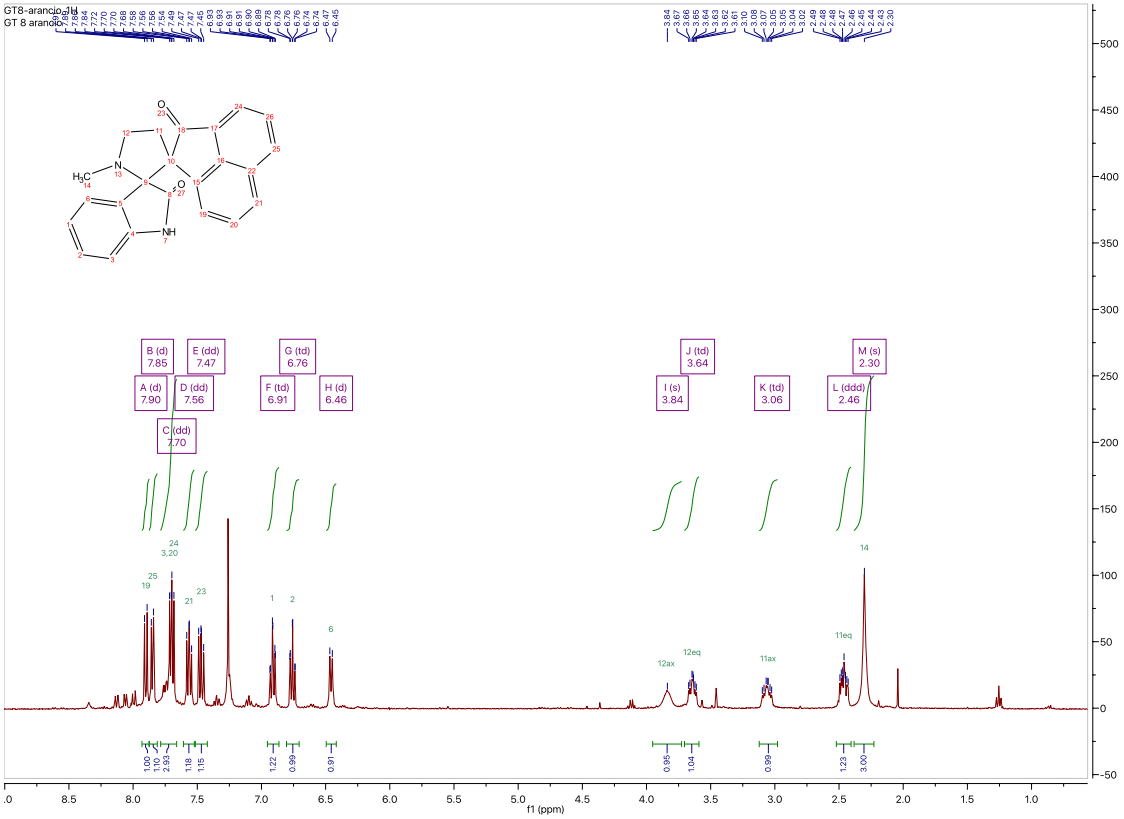


$^{1}$H NMR spectrum of compound **106.**

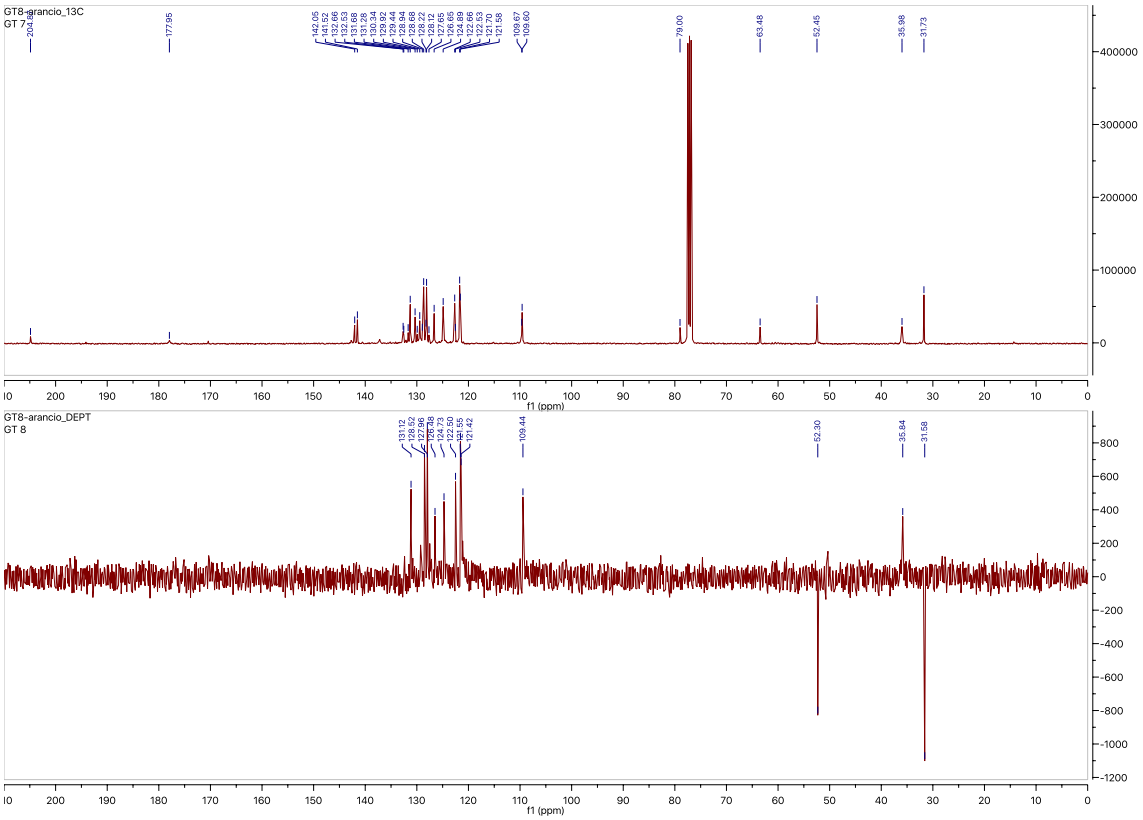


$^{13}$C NMR spectrum of compound **106.**

**Compound 107**. Synthesis of *1-benzyl-1'-methyl-3",4"-dihydro-1"H-dispiro[indoline-3,2'-pyrrolidine-3',2"-naphthalene]-1",2-dione*

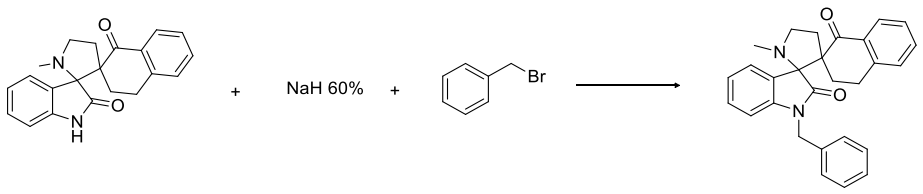


**1eq** **MW = 332,16** | **1 eq** **MW= 24** | **1 eq** **MW = 171,04** | **MW = 422,16**

In a two-necked flask with an anhydrous environment, the amide (1 eq) was dissolved in DMF (5 ml). Then, sequentially, NaH (1 eq) and benzyl bromide (1 eq) were added. A chromatographic change from yellow to purple to green was evident. The reaction was monitored by TLC (A1P1). After 30 min, the reaction was completed and the organic solvent was evaporated, followed by a treatment with diethyl ether (5 ml). The solid phase was then filtered on Gooch and the diethyl ether evaporated. Separation by chromatographic column with eluent mixture A1P1 was carried out. After evaporation of the organic solvent, a yellow solid was obtained.

MS (ESI): $[M+H]^+$ = 423,20;
Yield: 65%;
mp:150-152 °C;
**$^1$H NMR** (400 MHz, Chloroform-*d*) δ 8.07 (dd, *J* = 7.3, 2.1 Hz, 1H), 7.43 – 7.13 (m, 8H), 6.95 (t, *J* = 7.6 Hz, 1H), 6.86 – 6.72 (m, 2H), 6.62 (d, *J* = 7.8 Hz, 1H), 6.51 (t, *J* = 7.6 Hz, 1H), 4.99 (d, *J* = 15.3 Hz, 1H), 4.84 (d, *J* = 15.3 Hz, 1H), 3.58 (s, 1H), 3.40 – 3.20 (m, 1H), 2.57 (ddd, *J* = 12.6, 8.6, 4.2 Hz, 1H), 2.49 – 2.12 (m, 5H), 2.08 (s, 3H).
**$^{13}$C NMR** (101 MHz, Chloroform-*d*) δ 198.48, 142.95, 142.73, 135.37, 132.57, 132.20, 128.53, 128.28, 127.41, 127.30, 127.16, 127.07, 126.21, 126.02, 121.47, 107.98, 57.18, 51.30, 43.13, 35.01, 32.83, 31.37, 25.34.

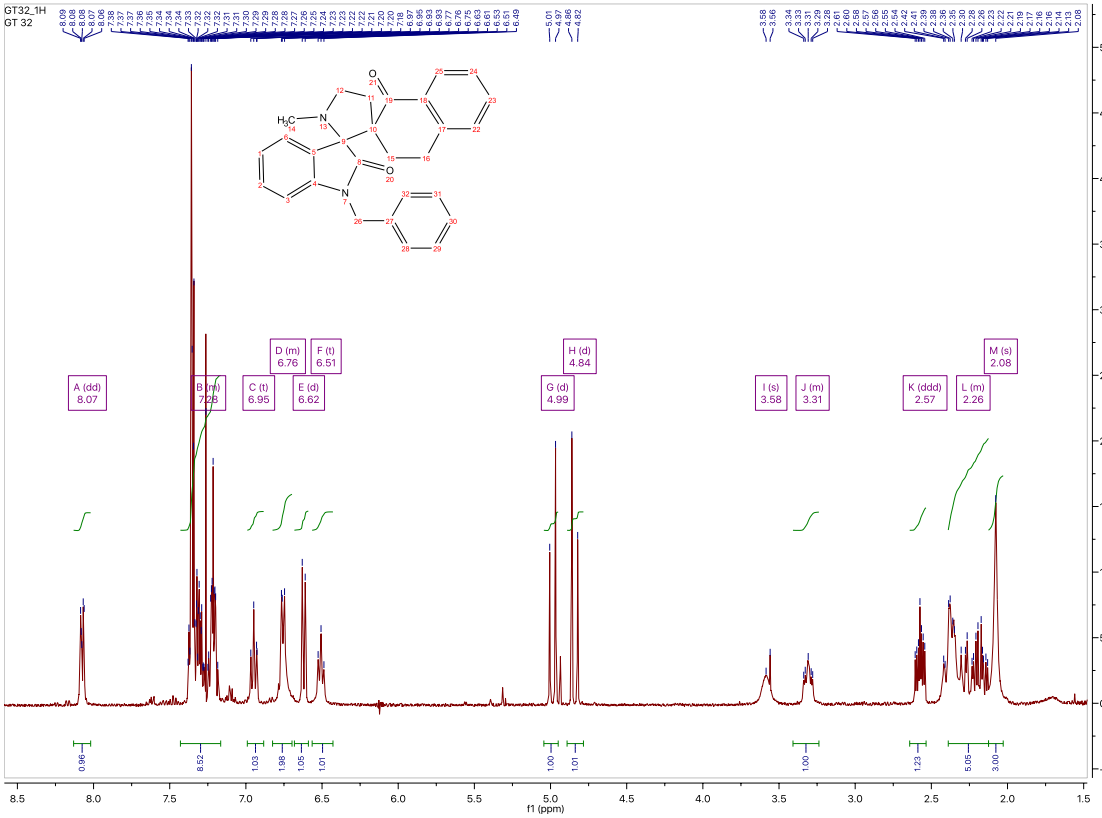


$^{1}$H NMR spectrum of compound **107.**

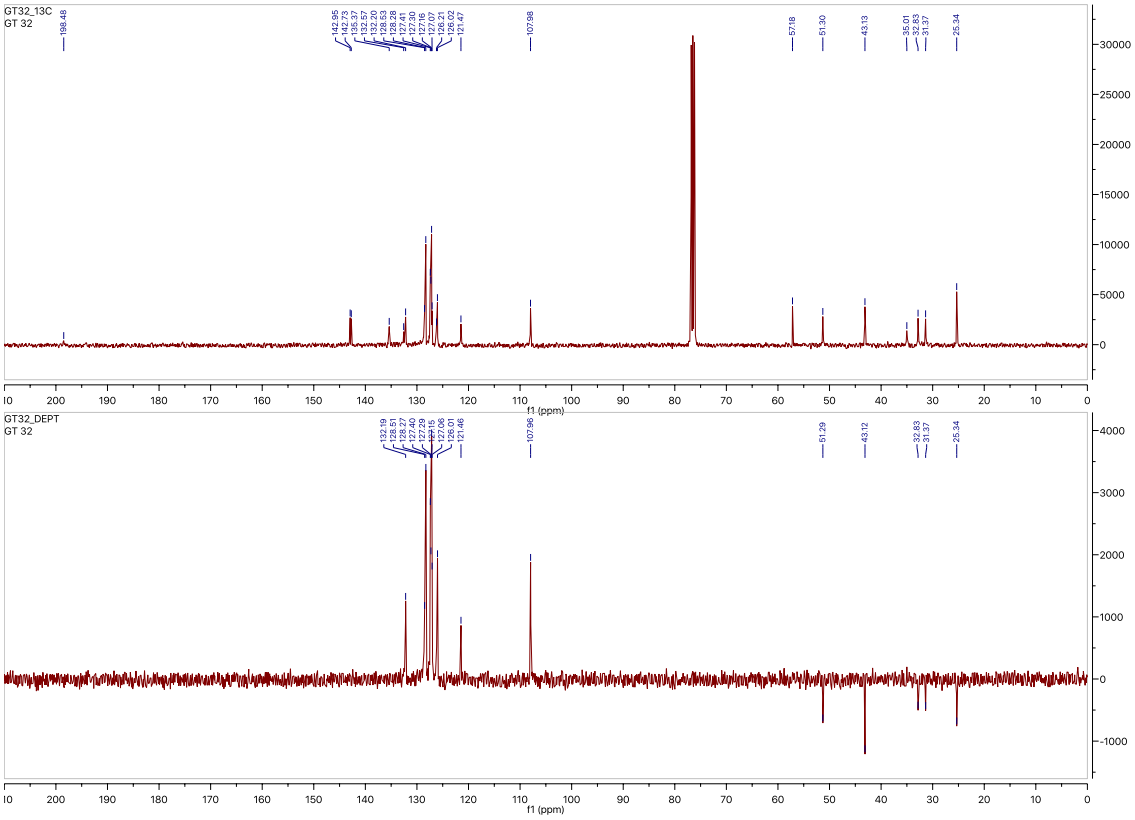


$^{13}$C NMR spectrum of compound **107.**

**Compound 108**. *Synthesis of 5''-fluoro-1'-methyldispiro[cyclohexane-1,3'-pyrrolidine-2',3''-indoline]-2,2''-dione*

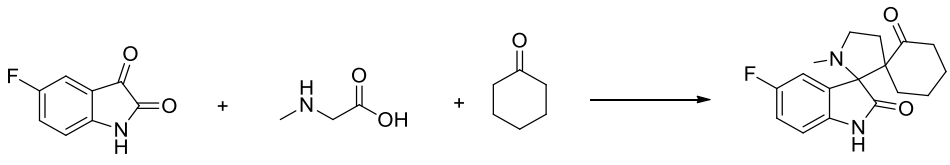

**1eq** **MW = 165,123** | **1.5 eq** **MW= 89** | **1 eq** **MW = 98,15** | **MW = 302,14**

To a solution of 5-Fluoro-isatine (1 eq, 3.03 mmol) in MeOH (15 ml), sarcosine (1.5 eq, 4.54 mmol) and cyclohexanone (1 eq, 3.03 mmol) were added sequentially. The reaction was then stirred at 90°C under reflux for 10 hours. The reaction was monitored by mass analysis and TLC (A1P1). Upon the completion of the reaction, this was quenched with NaHCO3 sat and deionized water. The organic solvent was evaporated and the aqueous phase was extracted three times with ethyl acetate (40 ml). The organic phases, taken together, after treatment with anhydrous sodium sulphate, were evaporated and an amorphous orange solid was obtained. The crude product was then purified by flash silica gel chromatography with eluent mixture of ethyl acetate and petroleum ether (A1P1), obtaining a white solid.

MS (ESI): $[M+H]^+$ = 303,15
Yield: 72%
mp: 153-155 °C;
**$^1$H NMR** (400 MHz, Chloroform-*d*) δ 8.56 (s, 1H), 6.95 (td, *J* = 8.7, 2.6 Hz, 1H), 6.89 – 6.76 (m, 2H), 3.33 – 3.12 (m, 2H), 2.62 (ddd, *J* = 12.8, 7.4, 5.7 Hz, 1H), 2.43 – 2.22 (m, 2H), 2.07 (s, 3H), 1.99 (ddd, *J* = 12.6, 8.4, 6.8 Hz, 1H), 1.83 (ddd, *J* = 15.0, 11.1, 7.0 Hz, 1H), 1.75 – 1.55 (m, 2H), 1.45 – 1.37 (m, 1H).
**$^{13}$C NMR** (101 MHz, Chloroform-*d*) δ 211.58, 179.03, 160.25, 157.86, 137.59, 116.13, 115.89, 115.21, 114.96, 110.65, 110.57, 62.95, 52.02, 41.19, 35.79, 35.36, 34.03, 25.34, 21.67.
**$^{19}$F NMR** (376 MHz, Chloroform-*d*) δ -119.61.

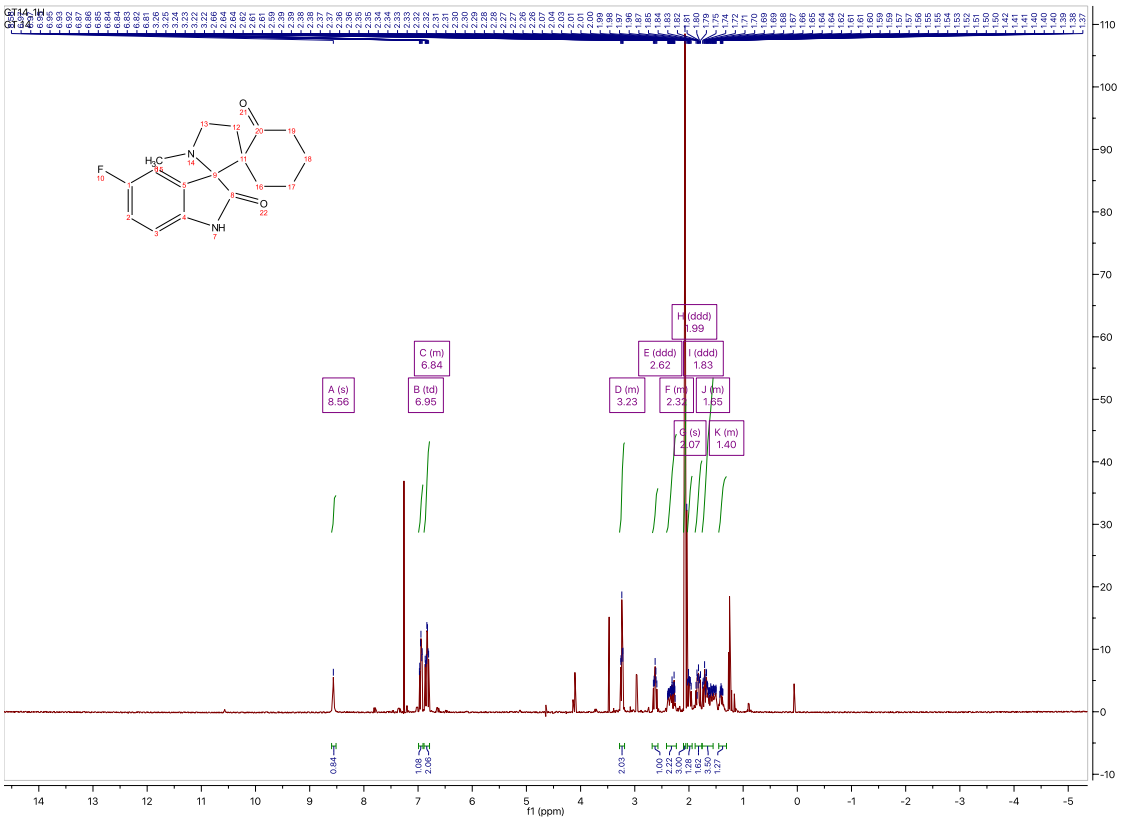


$^{1}$H NMR spectrum of compound **108.**

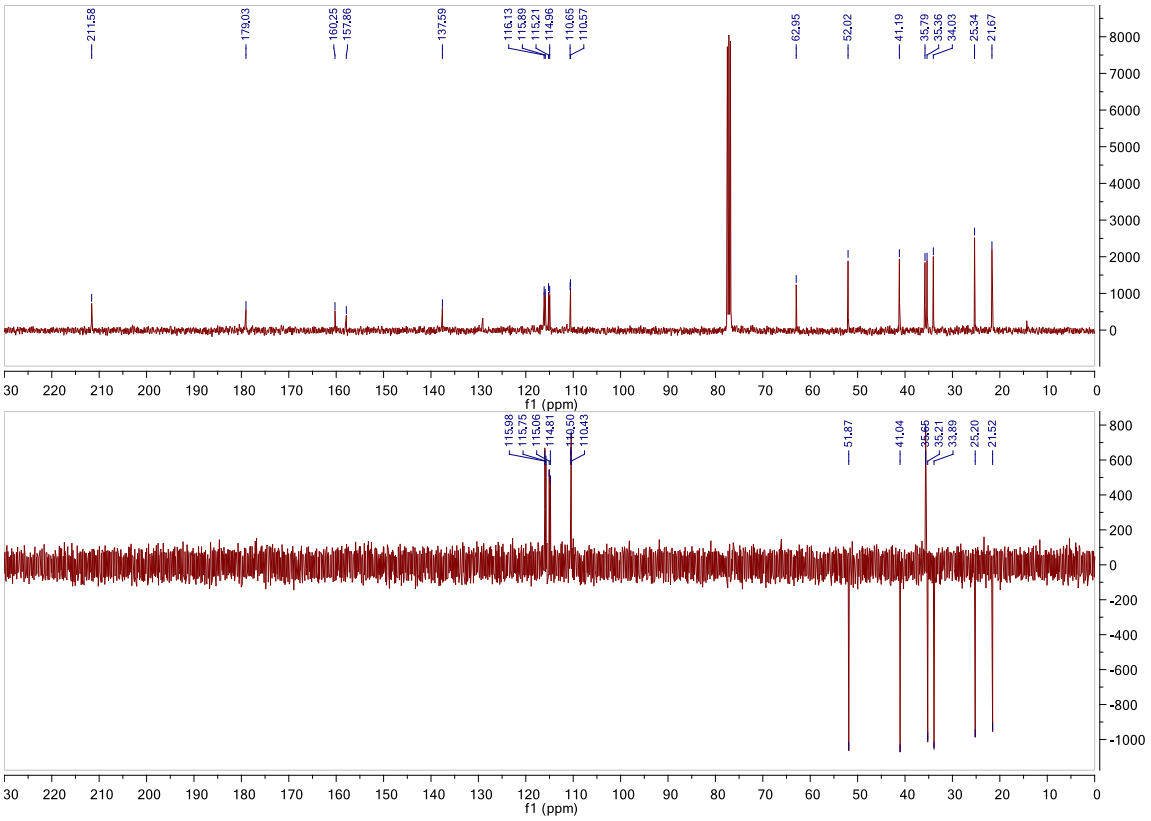


$^{13}$C NMR and DEPT spectra of compound **108**.

**Compound 109.** Synthesis of *5-fluoro-1'-methyl-3",4"-dihydro-1"H-dispiro[indoline-3,2'-pyrrolidine-3',2"-naphthalene]-1",2-dione*

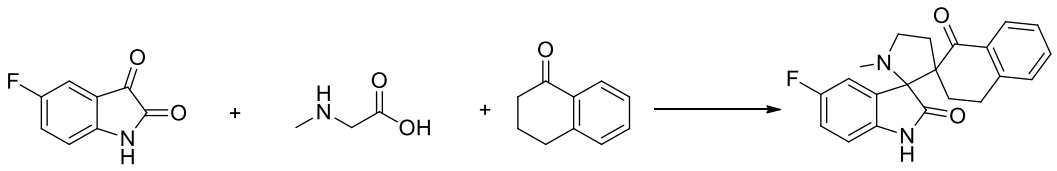

**1eq** **1.5 eq** **1 eq**

**MW = 165,123** **MW= 89** **MW = 146,19** **MW = 350,16**

To a solution of 5-Fluoro-isatine (1 eq, 3.03 mmol) in MeOH (15 ml), sarcosine (1.5 eq, 4.54 mmol) and 3,4-dihydronaphthalen-1(2*H*)-one (1 eq, 3.03 mmol) were added sequentially. The reaction was then stirred at 90°C under reflux for 10 hours. The reaction was monitored by mass analysis and TLC (A1P1). Upon the completion of the reaction, this was quenched with NaHCO3 sat and deionized water. The organic solvent was evaporated and the aqueous phase was extracted three times with ethyl acetate (40 ml). The organic phases, taken together, after treatment with anhydrous sodium sulphate, were evaporated and an amorphous orange solid was obtained. The crude product was then purified by flash silica gel chromatography with eluent mixture of ethyl acetate and petroleum ether (A1P1), obtaining an orange solid.

MS (ESI): $[M+H]^+$ = 351,15

Yield: 48%

**$^1$H NMR** (400 MHz, Chloroform-*d*) δ 8.29 (s, 1H), 8.09 (dd, *J* = 7.7, 1.7 Hz, 1H), 7.37 – 7.16 (m, 3H), 6.94 – 6.81 (m, 1H), 6.76 – 6.62 (m, 2H), 6.62 – 6.44 (m, 1H), 3.53 (q, *J* = 8.4 Hz, 1H), 3.25 (ddd, *J* = 10.6, 8.8, 4.3 Hz, 1H), 2.58 (ddd, *J* = 12.7, 9.1, 4.2 Hz, 3H), 2.42 (dt, *J* = 14.5, 4.1 Hz, 1H), 2.34 – 2.19 (m, 2H), 2.10 (s, 3H).

**$^{13}$C NMR** (101 MHz, Chloroform-*d*) δ 198.74, 159.86, 157.46, 143.25, 137.47, 137.45, 133.26, 133.03, 128.14, 127.85, 126.97, 115.82, 115.58, 110.06, 109.98, 57.97, 51.89, 35.57, 33.37, 31.96, 26.07.

**$^{19}$F NMR** (376 MHz, Chloroform-*d*) δ -120.56.

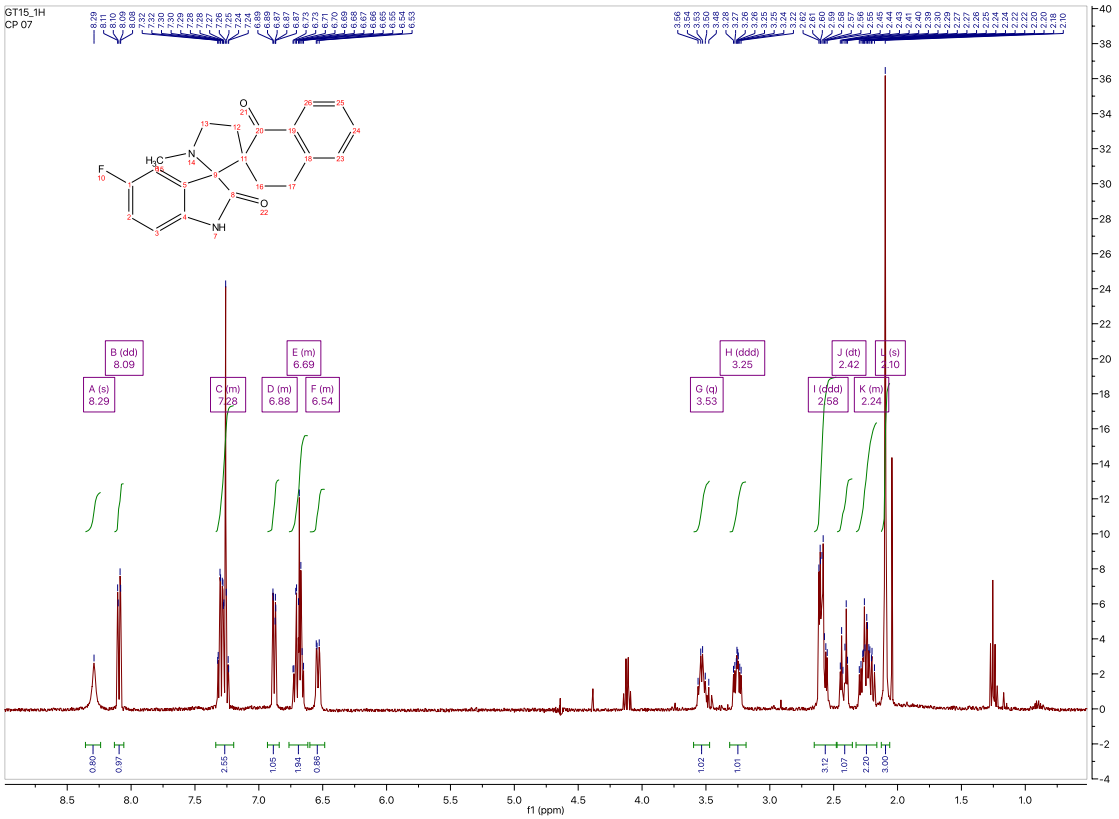


$^{1}$H NMR spectrum of compound **109.**

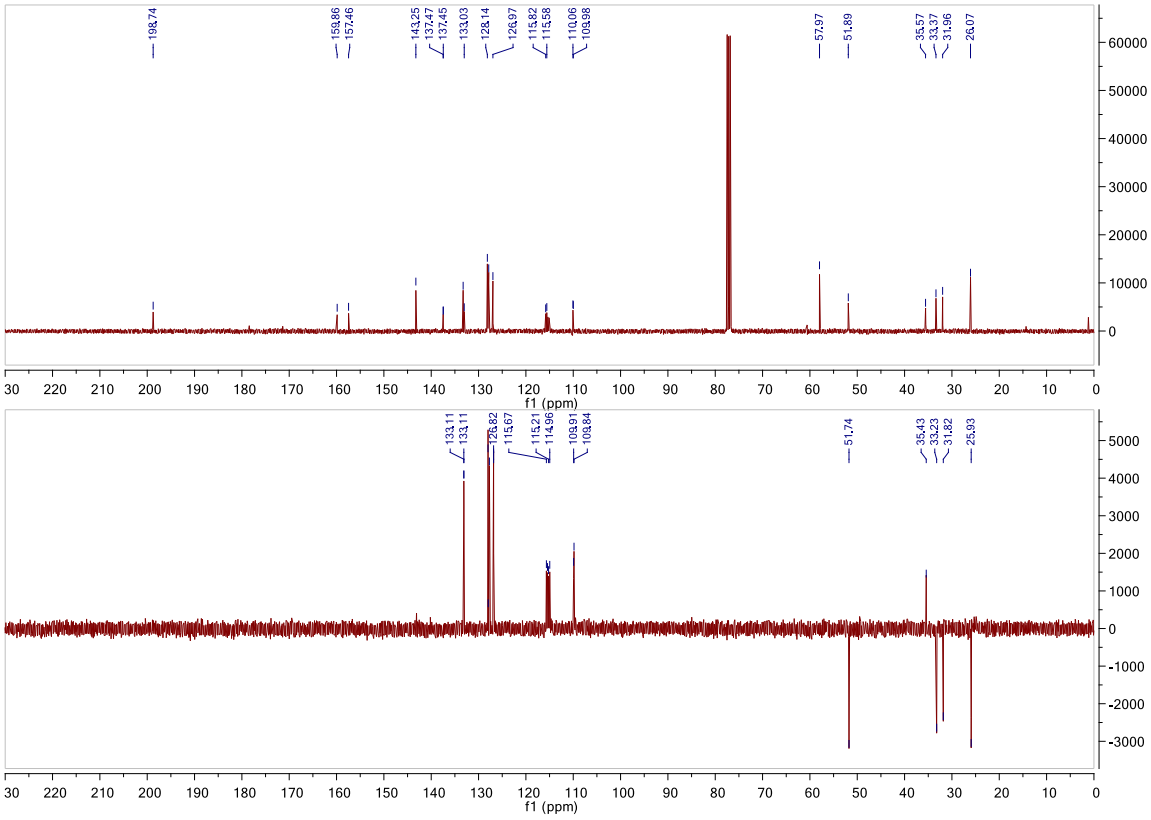


$^{13}$C NMR and DEPT spectra of compound **109**.

**Compound 110.** Synthesis of *5''-fluoro-1'-methyl-2H-dispiro[acenaphthylene-1,3'-pyrrolidine-2',3''-indoline]-2,2''-dione*

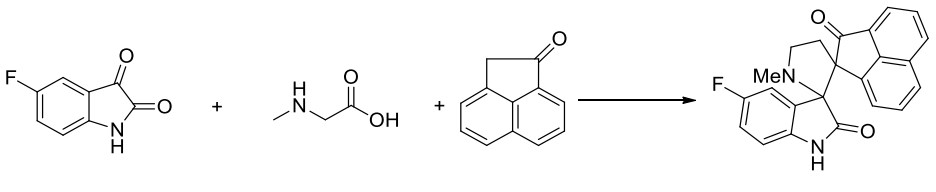


**1eq** **MW = 165,123** | **1.5 eq** **MW= 89** | **1 eq** **MW = 168,19** | **MW = 372,13**

To a solution of 5-Fluoro-isatine (1 eq, 3.03 mmol) in MeOH (15 ml), sarcosine (1.5 eq, 4.54 mmol) and acenaphtenone (1 eq, 3.03 mmol) were added sequentially. The reaction was then stirred at 90°C under reflux for 10 hours. The reaction was monitored by mass analysis and TLC (A1P1). Upon the completion of the reaction, this was quenched with NaHCO3 sat and deionized water. The organic solvent was evaporated and the aqueous phase was extracted three times with ethyl acetate (40 ml). The organic phases, taken together, after treatment with anhydrous sodium sulphate, were evaporated and an amorphous orange solid was obtained. The crude product was then purified by flash silica gel chromatography with eluent mixture of ethyl acetate and petroleum ether (A1P1), obtaining an amorphous solid. Re-crystallization with a mixture of diethyl ether and petroleum ether (3:7) gave the desired product as an orange solid.

MS (ESI): $[M+H]^+$ = 373,16;
Yield 40%;
mp: 207-209 °C;
**$^1$H NMR** (400 MHz, Chloroform-*d*) δ 7.98 – 7.87 (m, 1H), 7.77 – 7.66 (m, 1H), 7.60 (ddd, *J* = 8.1, 7.1, 5.5 Hz, 1H), 7.50 (dd, *J* = 8.3, 7.1 Hz, 2H), 7.02 (dd, *J* = 8.6, 2.6 Hz, 1H), 6.66 – 6.57 (m, 1H), 6.39 (dd, *J* = 8.4, 4.2 Hz, 2H), 3.87 – 3.78 (m, 1H), 3.61 (ddd, *J* = 10.7, 8.8, 4.1 Hz, 3H), 3.05 (ddd, *J* = 13.0, 10.7, 5.4 Hz, 2H).
**$^{13}$C NMR** (101 MHz, Chloroform-d) δ 204.60 , 160.14 , 157.74 , 142.01 , 132.47 , 132.00 , 131.43 , 130.35 , 128.70 , 128.28 , 128.06 , 125.01 , 122.59 , 121.83 , 121.77 , 116.04 , 115.81 , 114.67 , 114.41 , 110.15 , 110.07 , 63.59 , 52.43 , 35.89 , 31.78 .
**$^{19}$F NMR** (376 MHz, Chloroform-d) δ -120.60

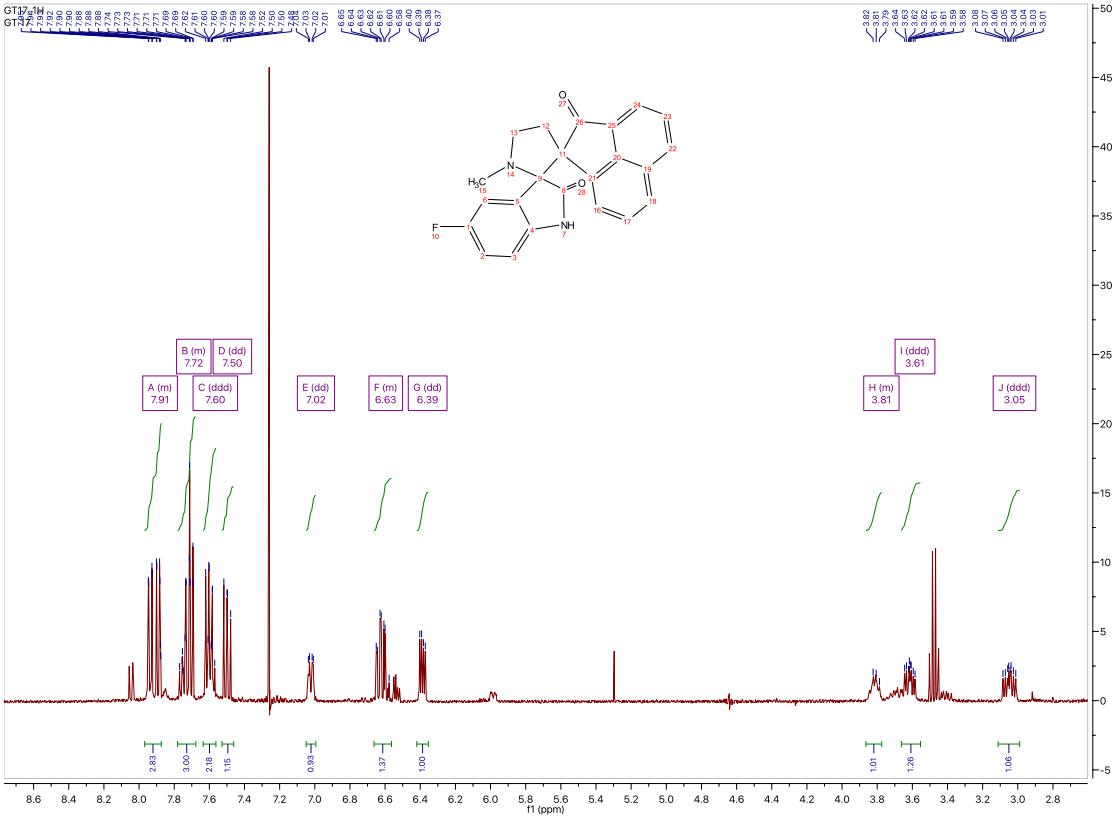


$^{1}$H NMR spectrum of compound **110.**

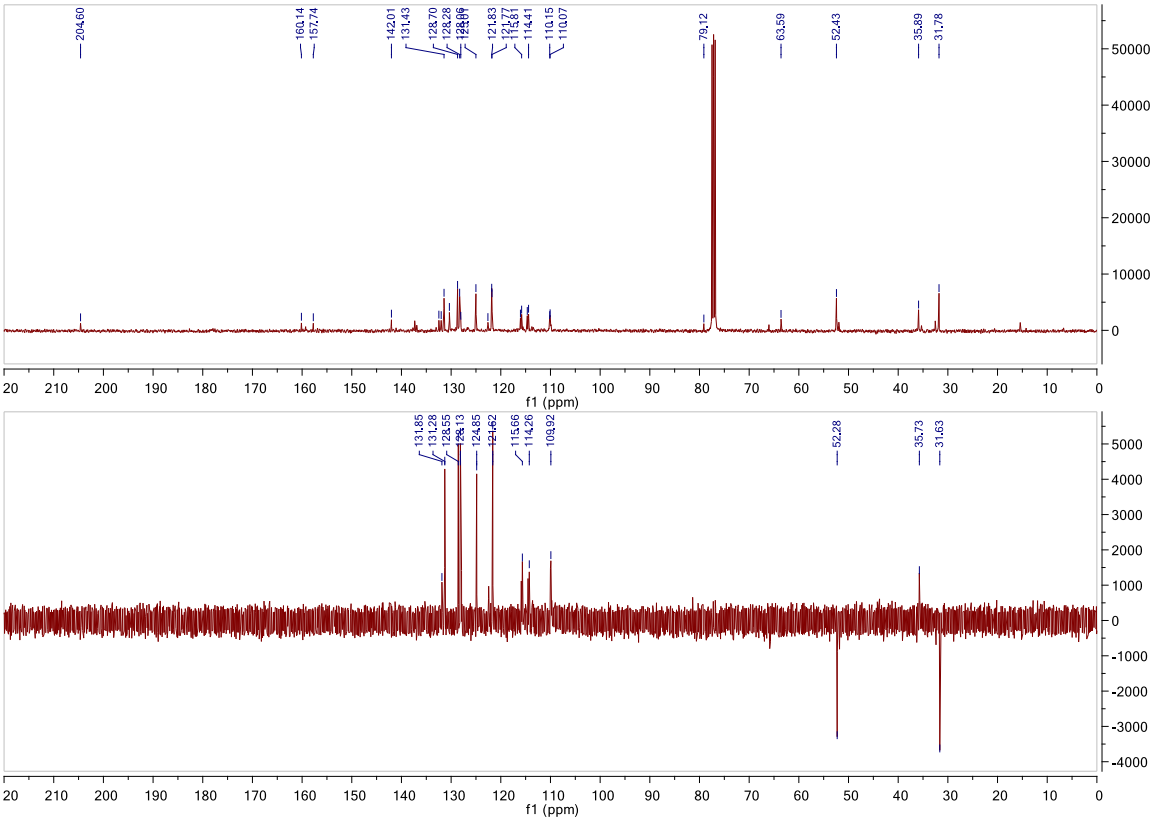


$^{13}$C NMR and DEPT spectra of compound **110.**

**Compound 111.** Synthesis of *1-benzyl-5-fluoro-1'-methyl-3",4"-dihydro-1"H-dispiro[indoline-3,2'-pyrrolidine-3',2"-naphthalene]-1",2-dione*

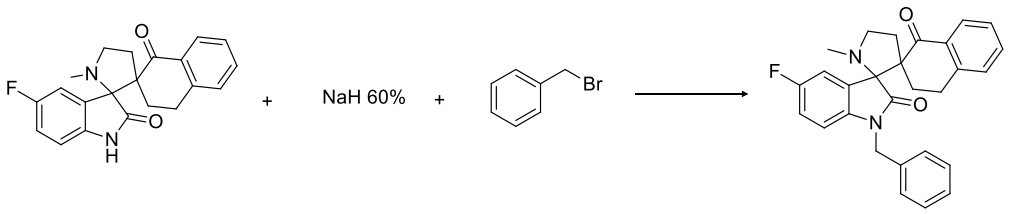


| 1eq | 1 eq | 1 eq | |
|---|---|---|---|
| MW = 351,16 | MW= 24 | MW = 171,04 | MW = 441,16 |

In a two-necked flask with an anhydrous environment, the amide (1 eq) was dissolved in DMF (5 ml). Then, sequentially, NaH (1 eq) and benzyl bromide (1 eq) were added. A chromatographic change from yellow to purple to green was evident. The reaction was monitored by TLC (A1P1). After 30 min, the reaction was completed and the organic solvent was evaporated, followed by a treatment with diethyl ether (5 ml). The solid phase was then filtered on Gooch and the diethyl ether evaporated. Separation by chromatographic column with eluent mixture A1P1 was carried out. After evaporation of the organic solvent, a yellow solid was obtained.

MS (ESI): [M+H]+ = 441,16
Yield: 98%;
mp: 152-154 °C;
**$^{1}$H NMR** (400 MHz, Chloroform-d) δ 8.09 (dd, J = 7.5, 1.9 Hz, 1H), 7.42 – 7.18 (m, 7H), 6.89 – 6.76 (m, 1H), 6.65 (dd, J = 8.6, 2.6 Hz, 1H), 6.51 (dd, J = 8.5, 4.2 Hz, 1H), 5.01 – 4.76 (m, 2H), 3.56 (s, 1H), 3.31 (td, J = 9.7, 8.6, 4.2 Hz, 1H), 2.58 (ddd, J = 12.7, 8.6, 4.2 Hz, 1H), 2.52 – 2.15 (m, 4H), 2.08 (s, 3H).
**$^{13}$C NMR** (101 MHz, Chloroform-d) δ 198.75, 159.99, 157.58, 143.11, 139.51, 135.70, 133.15, 129.02, 128.10, 127.84, 127.78, 126.96, 115.56, 115.32, 114.97, 109.16, 58.15, 52.00, 43.94, 35.67, 33.47, 31.91, 26.02.
**$^{19}$F NMR** (376 MHz, Chloroform-d) δ -125.90.

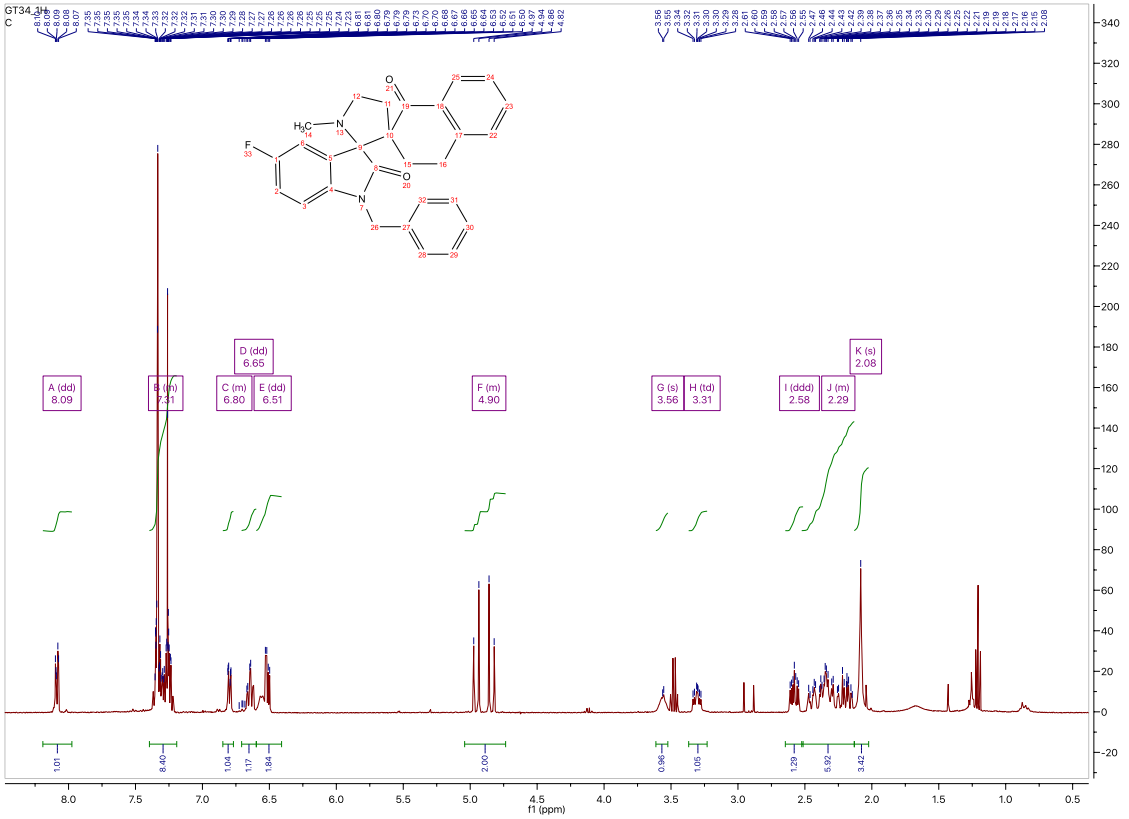


$^{1}$H NMR spectrum of compound **111.**

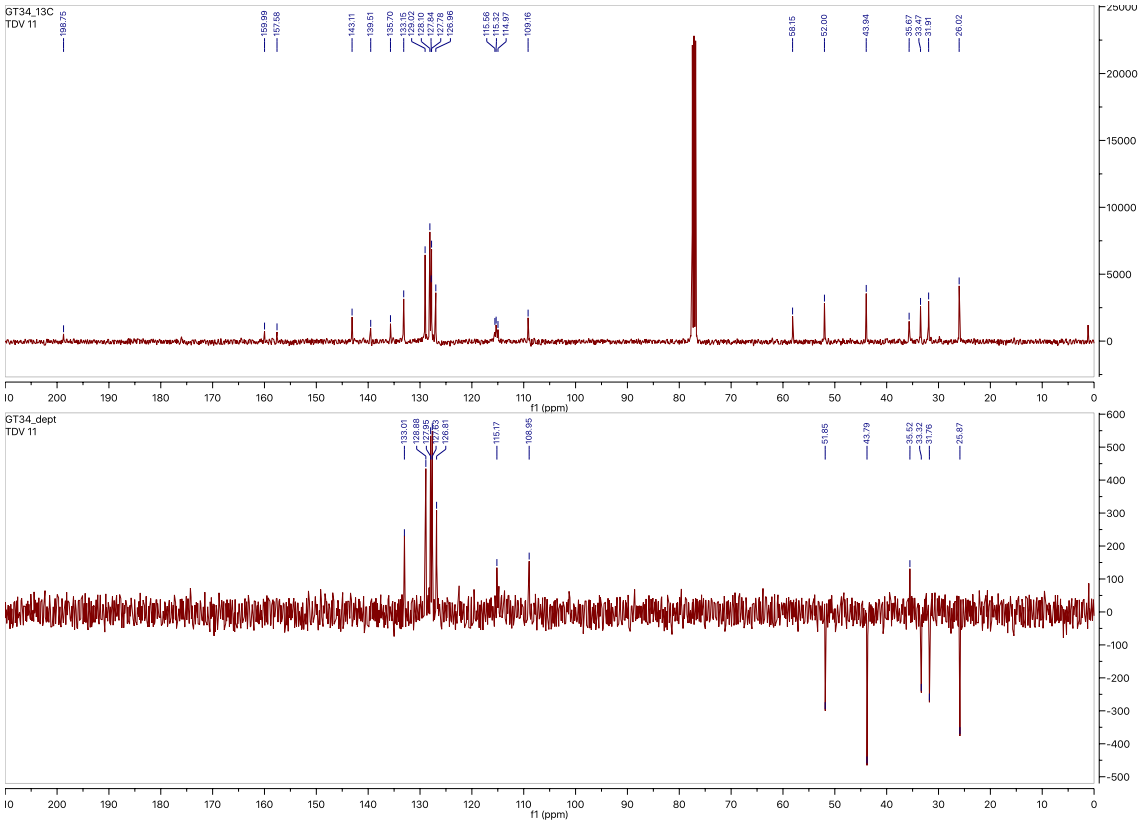


$^{13}$C NMR and DEPT spectra of compound **111.**

# 6. ABBREVIATIONS

Δp: potential difference

ACN: acetonitrile

AcOEt: Ethyl acetate

AcOH: Acetic acid

ADP Adenosine diphosphate

AMI: Acute myocardial infarction

ANT Adenine Nucleotide Translocase

Apaf-1: apoptotic protease activating factor-1

ATP Adenosine triphosphate

Bcl-2: B-cell lymphoma

$Ca^{2+}$: Calcium ion

CADD: Computer Aided Drug Design

$CBr_4$: carbon tetrabromide

$Cl^-$ Chloride ion

CsA Cyclosporin-A

CVD: cardiovascular disease

CypD Cyclophilin D

Cyt C: cytochrome C

Da: Dalton

DCC: dicyclohexylcarbodiimide

DCE: dichloroethane

DCM: dichloromethane

DCU: diclyclohexilurea

DISC: death-inducing signaling complex

DMF: Dimethylformamide

DMF: dimethylformamide

DMF/DMA: dimethylformamide/dimethylacetale

ER Endoplasmic reticulum

ETC: electron Transport Chain

EtOH: ethanol

$EtOH_{abs}$: absolute ethanol

FADD: FAS-associated death domain protein

$FADH_2$: flavin adenine dinucleotide

Glu: Glutamate

h: hours

$H^+$: Hydrogen ion

$H_2O$: water

$H_2SO_4$: sulfuric acid

HOBt: Hydroxybenzotriazole

HPLC: High Performance Liquid Chromatography

HTVS: High Throughput Virtual Screening

H/R: hypoxia / Reoxigenation

IHD: Ischemic heart disease

IMAC: inner mitochondrial anion channel

IMM: Inner mitochondrial membrane

IPC: Ischemic preconditioning

ipr-OH: isopropanol

IR: Ischemia reperfusion

IRI: Ischemia Reperfusion Injury

K: potassium

$K_2CO_3$: potassium carbonate

Kcal: kilocalories

kDa: kilodalton

KOH: potassium hydroxide

LV: Left ventricular

LVEDP: Left Ventricular Diastolic Pressure

MCU Mitochondrial calcium uniporter

MeOH: CH3OH, methanol

MI: Myocardial infarct

Mito-K: mitochondrial potassium channel

Mito-NCX: mitochondrial sodium/potassium exchanger

mPTP Mitochondrial permeability transition pore

MS-ESI: Electron Spray Ionization Mass Spectrometry

MS: mass spectroscopy

mtDNA mitochondrial DNA

mV: milliVolt

N: nitrogen atom

Na: sodium

$Na^+$: Sodium ion

$Na_2CO_3$: sodium carbonate

$NaBH_4$: sodium borohydride

NADH: nicotinamide adenine dinucleotide

NaOH: sodium hydroxide

$NH_4^+Cl^-$: ammonium chloride

$NH_4^+OH^-$: ammonium hydroxide

nM: nanoMolar

nM: nanoMolar

NMR: Nuclear Magnetic Resonance

NO Nitric oxide

ns: nanosecond

$O^{\bullet -}$: superoxide ion

$O_2$: molecular oxygen

OMM Outer mitochondrial membrane

OXPHOS: Oxidative Phosphorylation

p-TsCl: *para*-toluensulfonyl chloride

PCI: Percutaneous Coronary Intervention

PDB: Protein Data Bank

$P_i$: Inorganic phosphates

PiC: Mitochondrial phosphate carrier

$PPh_3$: triphenylphosphine

QSAR: Quantitative Structure Activity Realationship

r.t.: Room Temperature

RIP: Receptor Interacting Protein

ROS: Reactive Oxigen Species

rt: room temperature

SfA: Sanglifherin A

SPD: Standard Precision Docking

STEMI: ST-segment elevation myocardial infarction

TBDMSCl: tertbutyl dimethylsilyl chloride

TEA: triethylamine

THF: Tetrahydrofuran

TLC: Thin Layer Chromatography

TMSCN: trimethylsilanecarbonitrile

TMSCN: trimethylsilylcyanide

TNF: Tumor Necrosis Factor

TRAIL: TNF- related apoptosis -inducing ligand

WSC: Water Soluble Carbodiimide

μM: micromolar

# 7. REFERENCES


(1) Lehninger, A. L.; Nelson, D. L.; Cox, M. L. *I principi di biochimica di Lehninger*; Zanichelli: Bologna, 2010.

(2) Yang, K.-C.; Kyle, J. W.; Makielski, J. C.; Dudley, S. C. Mechanisms of Sudden Cardiac Death: Oxidants and Metabolism. *Circ. Res.* **2015**, *116* (12), 1937–1955. https://doi.org/10.1161/CIRCRESAHA.116.304691.

(3) Capaldi, R. A.; Aggeler, R. Mechanism of the F1F0-Type ATP Synthase, a Biological Rotary Motor. *Trends Biochem. Sci.* **2002**, *27* (3), 154–160. https://doi.org/10.1016/S0968-0004(01)02051-5.

(4) Zimmerman, J. J.; von Saint André-von Arnim, A.; McLaughlin, J. Cellular Respiration. In *Pediatric Critical Care*; Elsevier, 2011; pp 1058–1072. https://doi.org/10.1016/B978-0-323-07307-3.10074-6.

(5) Bonora, M.; Patergnani, S.; Rimessi, A.; De Marchi, E.; SPinton, P. ATP Synthesis and Storage. *Purinergic Signal.* **2012**, *8* (3), 343–357. https://doi.org/10.1007/s11302-012-9305-8.

(6) Neupane, P.; Bhuju, S.; Thapa, N.; Bhattarai, H. K. ATP Synthase: Structure, Function and Inhibition. *Biomol. Concepts* **2019**, *10* (1), 1–10. https://doi.org/10.1515/bmc-2019-0001.

(7) Bernardi, P.; Rasola, A.; Forte, M.; Lippe, G. The Mitochondrial Permeability Transition Pore: Channel Formation by F-ATP Synthase, Integration in Signal Transduction, and Role in Pathophysiology. *Physiol. Rev.* **2015**, *95* (4), 1111–1155. https://doi.org/10.1152/physrev.00001.2015.

(8) Nesci, S.; Trombetti, F.; Ventrella, V.; Pagliarani, A. The C-Ring of the F1FO-ATP Synthase: Facts and Perspectives. *J. Membr. Biol.* **2016**, *249* (1–2), 11–21. https://doi.org/10.1007/s00232-015-9860-3.

(9) Nesci, S.; Trombetti, F.; Ventrella, V.; Pagliarani, A. Opposite Rotation Directions in the Synthesis and Hydrolysis of ATP by the ATP Synthase: Hints from a Subunit Asymmetry. *J. Membr. Biol.* **2015**, *248* (2), 163–169. https://doi.org/10.1007/s00232-014-9760-y.

(10) Symersky, J.; Osowski, D.; Walters, D. E.; Mueller, D. M. Oligomycin Frames a Common Drug-Binding Site in the ATP Synthase. *Proc. Natl. Acad. Sci.* **2012**, *109* (35), 13961–13965. https://doi.org/10.1073/pnas.1207912109.

(11) Lawen, A. Apoptosis?An Introduction. *BioEssays* **2003**, *25* (9), 888–896. https://doi.org/10.1002/bies.10329.

(12) Jeong, S.-Y.; Seol, D.-W. The Role of Mitochondria in Apoptosis. *BMB Rep.* **2008**, *41* (1), 11–22. https://doi.org/10.5483/BMBRep.2008.41.1.011.

(13) Elmore, S. Apoptosis: A Review of Programmed Cell Death. *Toxicol. Pathol.* **2007**, *35* (4), 495–516. https://doi.org/10.1080/01926230701320337.

(14) Amodeo, G. F.; Solesio, M. E.; Pavlov, E. V. From ATP Synthase Dimers to C-Ring Conformational Changes: Unified Model of the Mitochondrial Permeability Transition Pore. *Cell Death Dis.* **2017**, *8* (12), 1. https://doi.org/10.1038/s41419-017-0042-3.

(15) Ong, S.-B.; Samangouei, P.; Kalkhoran, S. B.; Hausenloy, D. J. The Mitochondrial Permeability Transition Pore and Its Role in Myocardial Ischemia Reperfusion Injury. *J. Mol. Cell. Cardiol.* **2015**, *78*, 23–34. https://doi.org/10.1016/j.yjmcc.2014.11.005.

(16) Haworth, R. A.; Hunter, D. R. The Ca2+-Induced Membrane Transition in Mitochondria. *Arch. Biochem. Biophys.* **1979**, *195* (2), 460–467. https://doi.org/10.1016/0003-9861(79)90372-2.

(17) Morciano, G.; Giorgi, C.; Bonora, M.; Punzetti, S.; Pinton, P. Molecular Identity of the Mitochondrial Permeability Transition Pore and Its Role in Ischemia-Reperfusion Injury. *J. Mol. Cell. Cardiol.* **2015**, *78*, 142–153. https://doi.org/10.1016/j.yjmcc.2014.08.015.

(18) Halestrap, A. P. What Is the Mitochondrial Permeability Transition Pore? *J. Mol. Cell. Cardiol.* **2009**, *46* (6), 821–831. https://doi.org/10.1016/j.yjmcc.2009.02.021.

(19) Kokoszka, J. E.; Waymire, K. G.; Levy, S. E.; Sligh, J. E.; Wallace, D. C. The ADP/ATP Translocator Is Not Essential for the Mitochondrial Permeability Transition Pore. *Nature* **2004**, *427* (6973), 461–465.

https://doi.org/10.1038/nature02229.

(20) Crompton, M.; Ellinger, H.; Costi, A. Inhibition by Cyclosporin A of a Ca2+-Dependent Pore in Heart Mitochondria Activated by Inorganic Phosphate and Oxidative Stress. *Biochem. J.* **1988**, *255* (1), 357–360.

(21) Gutiérrez-Aguilar, M.; Pérez-Martínez, X.; Chávez, E.; Uribe-Carvajal, S. In Saccharomyces Cerevisiae, the Phosphate Carrier Is a Component of the Mitochondrial Unselective Channel. *Arch. Biochem. Biophys.* **2010**, *494* (2), 184–191. https://doi.org/10.1016/j.abb.2009.12.002.

(22) Gutiérrez-Aguilar, M.; Douglas, D. L.; Gibson, A. K.; Domeier, T. L.; Baines, C. P. Genetic Manipulation of the Cardiac Mitochondrial Phosphate Carrier Does Not Affect Permeability Transition. *J. Mol. Cell. Cardiol.* **2014**, *72*, 316–325. https://doi.org/10.1016/j.yjmcc.2014.04.008.

(23) Arnold, I. Yeast Mitochondrial F1F0-ATP Synthase Exists as a Dimer: Identification of Three Dimer-Specific Subunits. *EMBO J.* **1998**, *17* (24), 7170–7178. https://doi.org/10.1093/emboj/17.24.7170.

(24) Giorgio, V.; Bisetto, E.; Soriano, M. E.; Dabbeni-Sala, F.; BBernardi, P.; Lippe, G. Cyclophilin D Modulates Mitochondrial F0F1-ATP Synthase by Interacting with the Lateral Stalk of the Complex. *J. Biol. Chem.* **2009**, *284* (49), 33982–33988. https://doi.org/10.1074/jbc.M109.020115.

(25) Bonora, M.; Bononi, A.; De Marchi, E.; Giorgi, C.; Pinton, P. Role of the c Subunit of the FO ATP Synthase in Mitochondrial Permeability Transition. *Cell Cycle Georget. Tex* **2013**, *12* (4), 674–683. https://doi.org/10.4161/cc.23599.

(26) Giorgio, V.; von Stockum, S.; Antoniel, M.; Fabbro, A.; Zoratti, M.; Szabó, I.; Lippe, G.; Bernardi, P. Dimers of Mitochondrial ATP Synthase Form the Permeability Transition Pore. *Proc. Natl. Acad. Sci.* **2013**, *110* (15), 5887–5892. https://doi.org/10.1073/pnas.1217823110.

(27) Bonora, M.; Morganti, C.; Morciano, G.; Pedriali, G.; Pinton, P. Mitochondrial Permeability Transition Involves Dissociation of $F_1$ $F_O$ ATP Synthase Dimers and C-ring Conformation. *EMBO Rep.* **2017**, *18* (7), 1077–1089. https://doi.org/10.15252/embr.201643602.

(28) Alavian, K. N.; Beutner, G.; Lazrove, E.; Sacchetti, S.; Jonas, E. A. An Uncoupling Channel within the C-Subunit Ring of the $F_1$ $F_O$ ATP Synthase Is the Mitochondrial Permeability Transition Pore. *Proc. Natl. Acad. Sci.* **2014**, *111* (29), 10580–10585. https://doi.org/10.1073/pnas.1401591111.

(29) Pagliarani, A.; Nesci, S.; Ventrella, V. Novel Drugs Targeting the C-Ring of the $F_1F_O$-ATP Synthase. *Mini-Rev. Med. Chem.* **2016**, *16* (10), 815–824. https://doi.org/10.2174/1389557516666160211120955.

(30) Briston, T.; Selwood, D. L.; Szabadkai, G.; Duchen, M. R. Mitochondrial Permeability Transition: A Molecular Lesion with Multiple Drug Targets. *Trends Pharmacol. Sci.* **2019**, *40* (1), 50–70. https://doi.org/10.1016/j.tips.2018.11.004.

(31) Porter, G. A.; Beutner, G. Cyclophilin D, Somehow a Master Regulator of Mitochondrial Function. *Biomolecules* **2018**, *8* (4), 176. https://doi.org/10.3390/biom8040176.

(32) Morciano, G.; Preti, D.; Pedriali, G.; Aquila, G.; Ferrari, R.; Wieckowski, M. R.; Campo, G.; Giorgi, C.; Trapella, C.; Pinton, P. Discovery of Novel 1,3,8-Triazaspiro[4.5]Decane Derivatives That Target the c Subunit of $F_1$ /$F_O$ -Adenosine Triphosphate (ATP) Synthase for the Treatment of Reperfusion Damage in Myocardial Infarction. *J. Med. Chem.* **2018**, *61* (16), 7131–7143. https://doi.org/10.1021/acs.jmedchem.8b00278.

(33) Timmis, A.; Townsend, N.; Gale, C. P.; Torbica, A.; Boateng, D. European Society of Cardiology: Cardiovascular Disease Statistics 2019. *Eur. Heart J.* **2020**, *41* (1), 12–85. https://doi.org/10.1093/eurheartj/ehz859.

(34) Neri, M.; Riezzo, I.; Pascale, N.; Pomara, C.; Turillazzi, E. Ischemia/Reperfusion Injury Following Acute Myocardial Infarction: A Critical Issue for Clinicians and Forensic Pathologists. *Mediators Inflamm.* **2017**, *2017*, 1–14. https://doi.org/10.1155/2017/7018393.

(35) Morciano, G.; Bonora, M.; Campo, G.; Aquila, G.; Pinton, P. Mechanistic Role of MPTP in Ischemia-Reperfusion Injury. In *Mitochondrial Dynamics in Cardiovascular Medicine*; Santulli, G., Ed.; Advances in Experimental Medicine and Biology; Springer International Publishing: Cham, 2017; Vol. 982, pp 169–189. https://doi.org/10.1007/978-3-319-55330-6_9.

(36) Carden, D. L.; Granger, D. N. Pathophysiology of Ischaemia-Reperfusion Injury. *J. Pathol.* **2000**, *190* (3), 255–266. https://doi.org/10.1002/(SICI)1096-9896(200002)190:3<255::AID-PATH526>3.0.CO;2-6.

(37) Weiss, J. N.; Korge, P.; Honda, H. M.; Ping, P. Role of the Mitochondrial Permeability Transition in Myocardial Disease. *Circ. Res.* **2003**, *93* (4), 292–301. https://doi.org/10.1161/01.RES.0000087542.26971.D4.

(38) Griffiths, E. J.; Halestrap, A. P. Mitochondrial Non-Specific Pores Remain Closed during Cardiac Ischaemia, but Open upon Reperfusion. *Biochem. J.* **1995**, *307* (1), 93–98. https://doi.org/10.1042/bj3070093.

(39) Ponticelli, C. Ischaemia-Reperfusion Injury: A Major Protagonist in Kidney Transplantation. *Nephrol. Dial. Transplant.* **2014**, *29* (6), 1134–1140. https://doi.org/10.1093/ndt/gft488.

(40) Kosieradzki, M.; Rowiński, W. Ischemia/Reperfusion Injury in Kidney Transplantation: Mechanisms and Prevention. *Transplant. Proc.* **2008**, *40* (10), 3279–3288. https://doi.org/10.1016/j.transproceed.2008.10.004.

(41) Sebald, W.; Wachter, E.; Tzagoloff, A. Identification of Amino Acid Substitutions in the Dicyclohexylcarbodiimide-Binding Subunit of the Mitochondrial ATPase Complex from Oligomycin-Resistant Mutants of Saccharomyces Cerevisiae. *Eur. J. Biochem.* **1979**, *100* (2), 599–607. https://doi.org/10.1111/j.1432-1033.1979.tb04207.x.

(42) Fantinati, A.; Morciano, G.; Turrin, G.; Pedriali, G.; Trapella, C. Identification of Small-Molecule Urea Derivatives as PTPC Modulators Targeting the c Subunit of F1/Fo-ATP Synthase. *Bioorg. Med. Chem. Lett.* **2022**, *72*, 128822. https://doi.org/10.1016/j.bmcl.2022.128822.

(43) Symersky, J.; Pagadala, V.; Osowski, D.; Krah, A.; Mueller, D. M. Structure of the C10 Ring of the Yeast Mitochondrial ATP Synthase in the Open Conformation. *Nat. Struct. Mol. Biol.* **2012**, *19* (5), 485–491. https://doi.org/10.1038/nsmb.2284.

(44) Bonora, M.; Morganti, C.; Morciano, G.; Giorgi, C.; Pinton, P. Comprehensive Analysis of Mitochondrial Permeability Transition Pore Activity in Living Cells Using Fluorescence-Imaging-Based Techniques. *Nat. Protoc.* **2016**, *11* (6), 1067–1080. https://doi.org/10.1038/nprot.2016.064.

(45) Strecker, A. Ueber die künstliche Bildung der Milchsäure und einen neuen, dem Glycocoll homologen Körper; *Ann. Chem. Pharm.* **1850**, *75* (1), 27–45. https://doi.org/10.1002/jlac.18500750103.

(46) Benetti, S.; De Risi, C.; Pollini, G. P.; Zanirato, V. Synthetic Routes to Chiral Nonracemic and Racemic Dihydro- And Tetrahydrothiophenes. *Chem. Rev.* **2012**, *112* (4), 2129–2163. https://doi.org/10.1021/cr200298b.

(47) Bharkavi, C.; Kumar, S.; Perumal, S. A Facile Stereoselective Domino Approach for the Construction of Novel Bis(Spiropiperidone)–Tetrahydrothiophene Hybrid Heterocycles. *Synlett* **2015**, *26* (12), 1665–1670. https://doi.org/10.1055/s-0034-1380722.

(48) Kumar, R. S.; Rajesh, S. M.; Perumal, S.; Banerjee, D.; Sriram, D. Novel Three-Component Domino Reactions of Ketones, Isatin and Amino Acids: Synthesis and Discovery of Antimycobacterial Activity of Highly Functionalised Novel Dispiropyrrolidines. *Eur. J. Med. Chem.* **2010**, *45* (1), 411–422. https://doi.org/10.1016/j.ejmech.2009.09.044.

(49) Suresh Kumar, R.; Perumal, S. Novel Three-Component Tandem Reactions of Cyclic Mono Ketones, Isatin and Sarcosine: Formation of Dispiropyrrolidines. *Tetrahedron Lett.* **2007**, *48* (40), 7164–7168. https://doi.org/10.1016/j.tetlet.2007.07.197.

(50) Morciano, G.; Pedriali, G.; Bonora, M.; Pavasini, R.; Pinton, P. A Naturally Occurring Mutation in ATP Synthase Subunit c Is Associated with Increased Damage Following Hypoxia/Reoxygenation in STEMI Patients. *Cell Rep.* **2021**, *35* (2), 108983. https://doi.org/10.1016/j.celrep.2021.108983.

# 8. APPENDIX

Hindawi
Journal of Chemistry
Volume 2019, Article ID 8143739, 13 pages
https://doi.org/10.1155/2019/8143739

*Research Article*

# Conjugation of LasR Quorum-Sensing Inhibitors with Ciprofloxacin Decreases the Antibiotic Tolerance of *P. aeruginosa* Clinical Strains

**Daria Bortolotti**,[1] **Claudio Trapella**,[2] **Alessandra Bragonzi**,[3] **Paolo Marchetti**,[2] **Vinicio Zanirato**,[2] **Andrea Alogna**,[1,2] **Valentina Gentili**,[1,2] **Carlo Cervellati**,[4] **Giuseppe Valacchi**,[5,6] **Mariangela Sicolo**,[1] **Giulia Turrin**,[2] **Anna Fantinati**,[2] **Dario Di Luca**,[1] **and Roberta Rizzo**[1,7]

[1]*Department of Medical Sciences, Section of Microbiology and Medical Genetics, University of Ferrara, Via Luigi Borsari, 46-44121 Ferrara, Italy*
[2]*Department of Chemical and Pharmaceutical Sciences, University of Ferrara, Via Fossato di Mortara, 17, 44121 Ferrara, Italy*
[3]*Division of Immunology, Transplantation and Infectious Diseases, IRCCS San Raffaele Scientific Institute, Milano, Italy*
[4]*Department of Biomedical and Specialist Surgical Sciences, Section of Medical Biochemistry, Molecular Biology and Genetics, University of Ferrara, Via Luigi Borsari, 46-44121 Ferrara, Italy*
[5]*Department of Life Sciences and Biotechnology, Section of Biology and Evolution, University of Ferrara, Via Luigi Borsari, 46-44121 Ferrara, Italy*
[6]*NC State University, Plants for Human Health Institute, Animal Science Deptment, NC Research Campus, Kannapolis, NC, USA*
[7]*LTTA-Electron Microscopy Center, University of Ferrara, Ferrara, Italy*

Correspondence should be addressed to Daria Bortolotti; brtdra@unife.it

Received 9 November 2018; Revised 15 January 2019; Accepted 10 February 2019; Published 11 March 2019

Academic Editor: Ajaya Kumar Singh



*Pseudomonas aeruginosa* is a Gram-negative bacterium that commonly infects subjects with weakened immune system causing deadly infections above all at pulmonary level. During infection, *P. aeruginosa* produces a well-organized bacterial structure, called biofilm, activating the quorum-sensing (QS) signaling, a mechanism of gene regulation. In this work, we synthesized already known QS inhibitors (QSi) designed on the scaffold of the N-(3-oxododecanoyl) homoserine lactone (3O-C12-HSL) QS molecule and conjugated them with ciprofloxacin to inhibit *P. aeruginosa* biofilm formation and increase the antibiotic susceptibility of clinical strains. We identified, for the first time, a QSi conjugated with ciprofloxacin (**ET37**), that is able to reduce the formation of biofilm and the onset of tolerant clones in *P. aeruginosa* clinical strains. This compound could have a wide application in clinical setting. The possibility to affect biofilm formation in chronically infected patients, such as patients affected by cystic fibrosis, and to reduce the onset of ciprofloxacin resistance would improve patient healing and allow to decrease antibiotic drug dosage.

## 1. Introduction

Microbial infections can result in complications, such as bacteremia, kidney failure, and toxic shock syndrome. For this, the identification of the systems to counteract bacterial infection is one of the challenges of modern medicine. The absence of novel molecules that control complications due to bacterial infections suggests the defective comprehension of the mechanisms used by bacteria to control host immune response and resist treatment. During host infection, several bacteria organize a bacterial population, and *Pseudomonas aeruginosa* is one of the most commonly studied. *P. aeruginosa* is a Gram-negative bacterium that especially infects subjects with weakened immune system causing deadly

infections above all at pulmonary level. In fact, cystic fibrosis (CF) or HIV patients exhibit increased susceptibility to *P. aeruginosa* lung infections. Since *P. aeruginosa* is a ubiquitous bacterium, exposure to this pathogen in the hospital setting results to be frequent, making it one of the most problematic nosocomial infections.

The antibiotics used to treat *P. aeruginosa* infection include ciprofloxacin, tobramycin, ceftazidime, gentamicin, and imipenem. *P. aeruginosa* bacteria present a high degree of resistance to these antibiotics. Interestingly, the response to ciprofloxacin is very effective at the beginning of the treatment, but high-level resistance is rapidly acquired by *P. aeruginosa*, making the treatment ineffective in the 30% of strains obtained from clinical isolates [1].

The mechanisms that could increase *P. aeruginosa* antibiotic susceptibility still remain unclear [2–4].

*P. aeruginosa* is characterized by a low permeability of its cell wall that increases its resistance to antibiotics because of a lower drug uptake or higher efflux pumps expression that cause decreased intracellular drug concentrations [5]. Alterations in QRDR of the target sites *DNA gyrase* (*gyrA*) and *topoisomerase IV*, encoded by *parC* and *parE* subunits, are considered the main reason of bacterial resistance to quinolones [6, 7].

The acquisition of resistance to ciprofloxacin is a multistage process in *P. aeruginosa*: in stage I, the exposure to the drug kills the susceptible cells; in stage II, a small population survives antibiotic exposure without increasing the resistance and maintaining a slow growth; in stage III, a the population is reconstituted by a slow-growing population with an increased drug resistance [8]. The appearance of a drug-resistant population limits the possibility to use prolonged therapies with existing or newly developed antibiotic drugs. We suggest the possible use of the inhibitor of quorum-sensing (QS). One of the main defense mechanisms adopted by *P. aeruginosa* is represented by biofilm formation, which allows the bacteria to avoid both host immune system and antibiotics effects [9, 10]. QS is a mechanism of gene regulation sensitive to population density that enables host colonization contrasting the immune surveillance through biofilm formation and the expression of virulence factors [10] via the production of self-generated extracellular signal molecules [11–13]. *P. aeruginosa* is characterized by two QS systems, Las and Rhl, based on acylhomoserine lactone [14] molecules [15]. The las system is controlled by the transcriptional activator LasR and the autoinducer synthase enzyme LasI, which directs the synthesis of N-(3-oxododecanoyl) homoserine lactone (3O-C12-HSL). Similarly, the Rhl system is regulated by the transcriptional activator RhlR and the RhlI AI synthase that synthesizes N-butyryl homoserine lactone (C4-HSL). 3O-C12-HSL binds LasR and activates the LasR/3O-C12-HSL complex; the multimerization will promote the transcription of RhlR, RhlI, LasI genes, and other virulence genes that are connected to the regulon [16–18]. In a similar way, RhlR/C4-HSL complex dimerizes and activates the expression of its own regulon and RhlI [19]. LasR/3O-C12-HSL regulates the quinolone signal by inducing expression of PqsR, as well as PQS [20]. PQS, in turn, increases the transcription of RhlI and the production of C4-HSL [21]. Interestingly, PqsR expression is inhibited by RhlR/C4-HSL [21], suggesting that the ratio between 3O-C12-HSL and C4-HSL concentrations controls the Pqs signaling system.

Since QS molecules are important during infection, the interference on QS signaling represents a potential strategy to contrast bacterial virulence, decreasing antibiotics dosage and facilitating the natural bacterial clearance by host immune response. Brackman et al. have shown that QS inhibitors (QSi) increase the susceptibility of bacterial biofilms to different types of antibiotics [22]. We report the results of our work on the effect of different QSi compounds, designed on the scaffold of QS inducer 3O-C12-HSL, conjugated with ciprofloxacin. These results will set up the initial steps developing new strategies that may subvert the ciprofloxacin resistance of *P. aeruginosa*.

## 2. Materials and Methods

*2.1. Chemical Synthesis.* The compounds tested in this work are antagonists of LasR and are designed on 3O-C12-HSL scaffold [23]. Previous evaluations of these derivatives showed that S absolute configuration at the 3-position of the homoserine lactone was important for the activity of the compounds. On the contrary, the R derivative was not effective. For this reason, we synthetized all the compounds in the S absolute configuration. The chemical synthesis was performed as described in Geske et al. [23]. The compounds tested in this study derived from libraries of AHL mimics designed to be capable of intercepting the LasR and RhlR QS system which are specific for *P. aeruginosa*. The LasR antagonists interact with the N-terminal ligand-binding domain of LasR, blocking the binding site for QS molecules [23].

*2.2. Samples.* Ten sequential *P. aeruginosa* isolates from four patients with CF were chosen from the strains collection of the CF clinic in Hannover. We selected two strains from patients SG (SG1 and SG58, both LasR wild type (wt)), three strains from patients AA (AA2 and AA12 LasR wt and AA11 LasR mutant), three strains from patient TR (TR2 LasR wt and TR1 and TR66 LasR mutants), and two strains from patient KK (KK1 and KK72, both LasR mutants). These strains were characterized in previous work [24]. Patients were checked after the diagnosis of CF, and meanwhile, the respiratory specimens were sampled. The "early" isolates of *P. aeruginosa* strains were collected from the first positive cultures, whereas late isolates were collected 7 to 16 years after colonization or prior to death or lung transplantation. CF isolates behaviour was compared with the laboratory strain PAO1 for their phenotypic diversity [25, 26].

*2.3. Phenotypic Analysis for LasR Mutants.* Colony surface iridescence and metallic sheen were evaluated and considered as a phenotypic characteristic of LasR mutants [25, 26]. The DNA sequence confirmed the presence of LasR mutations (Table 1).

Table 1: Mutations in LasR in *P. aeruginosa* isolates.

| Patients | LasR[a] | *lasR*[b] | LasR[b] |
|---|---|---|---|
| SG1 | WT | WT | WT |
| SG58 | WT | WT | WT |
| AA2 | WT | WT | WT |
| AA12 | WT | WT | WT |
| AA11 | MUT | G217A | D73N |
| TR2 | WT | WT | WT |
| TR1 | MUT | C133T | Q45stop |
| TR66 | MUT | C147del | Frameshift |
| KK1 | MUT | T461C | L154P |
| KK72 | MUT | C646T | R216W |

[a]LasR status evaluated by phenotypic analysis. [b]Numbering is based on the sequence of LasR gene and LasR protein from PAO1.

*2.4. Biofilm Formation Inhibition and Cell Growth Evaluation.* *P.aeruginosa* PAO1 or clinical strains were grown in a static culture in M9 medium for liquid culture. Flat-bottomed polystyrene 96-well plates were used for biofilm formation experiments, and optical density measurements were performed in a plate reader at 600 nm. In order to screen compounds for QS inhibition, a microplate-based assay was used. Briefly, *P. aeruginosa* strains were seeded and grown in M9 for 24 hours at 37°C. The optical density (OD600) at inoculation was 0.04. The compounds were dissolved in DMSO added to planktonic cell cultures. Cell growth was evaluated by reading absorbance at 600 nm, while biofilm formation was analysed as previously described [27]. Briefly, after 24 hours of treatment, the planktonic cells were gently removed, and the wells were washed three times with PBS 1x. The plate was let at 60°C for 1 hour in order to dry the biofilm. The biofilm mass was measured by staining with crystal violet 1% w/v and then resuspended in 200 $\mu$l of 33% glacial acetic acid and read at 570 nm. 3O-C12-HSL and DMSO were used as positive and negative controls, respectively. Results are reported as mean ± SD and are obtained from three independent experiments.

*2.5. Syto9 Assay.* *P.aeruginosa* was cultured in 8-chamber slides and treated and left for 24 hours at 37°C. Planktonic cells were removed, and each chamber was washed with PBS 1x. 200 $\mu$l of Syto9 working solution prepared by diluting Syto9 stock solution (5 mM in DMSO, Invitrogen) 1 : 1200 was added and kept in dark for 30 minutes at RT. The chambers were then washed two times with PBS 1x, and the biofilm was visualized by fluorescent microscopy (ZOE Fluorescent Cell Imager, Biorad). Pictures of the biofilm were compared to the untreated control.

*2.6. Minimal Inhibitory Concentration.* The MIC for each strain was determined in triplicate using M.I.C. Evaluator (Oxoid, Basingstoke, Hants, UK) containing ciprofloxacin in final concentrations of 32, 16, 8, 4, 2, 1, 0.5, 0.25, 0.12, 0.06, 0.03, 0.015, 0.008, 0.004, 0.002, and 0 $\mu$g/ml. The M.I.C. was evaluated after 3 passages in antibiotic-free media [28]. The inoculum was Mueller-Hinton agar inoculated with a standard inoculum ($10^5$ to $10^6$ CFU/ml) according to the European Committee on Antimicrobial Susceptibility Testing guidelines [29].

*2.7. Time-Kill Studies.* Ciprofloxacin and **ET37** time-kill studies were performed at concentrations equal to the theoretical plasma peak (4 $\mu$g/mL), then at concentrations equal to 1/2, 2, 4, 8, X $MIC_{50}$ of the antibiotic used. Bacteria were cultured for 24 h at 37°C on Mueller-Hinton agar (MHB, BioMérieux, France) and used to prepare the exponential growth phase at standard inoculum ($10^6$ CFU/mL) in Mueller-Hinton broth. The inoculum of $10^6$ CFU/ml was supplemented with ciprofloxacin or **ET37** at the different concentrations and cultured for 24 h at 37°C. 100 ml of culture supernatants were collected at 2, 4, 6, and 24 h and plated on agar for colony counts.

*2.8. Pyocyanin and Elastase Assay.* *P. aeruginosa* strains were cultured overnight at 37°C with shaking. Cultures were back diluted 1 : 1,000 into fresh medium and grown for 18 h. The cells were pelleted by centrifugation, and the culture supernatants were filtered through 0.22 $\mu$m filters. The production of pyocyanin was reported as $A_{380}/A_{600}$ ratio [30]. The production of LasB elastase was assessed through the measurement of elastase activity using elastin-Congo red and reported as $A_{495}/A_{600}$ ratio [31].

*2.9. GyrA and ParC Amplification and DNA Sequencing.* QRDR amplification of gyrA and parC from resistant and intermediate isolates was carried out using specific primers: GyrA-1 (5′-GTGTGCTTTATGCCATGAG-3′) and GyrA-2 (5′-GGTTTCCTTTTCCAGGTC-3′) for the amplification of 287 bp of the fluoroquinolone resistance-determining region of the gyrA gene and ParC-1 (5′-CATCGTCTACGCCATGAG-3′) and ParC-2 (5′-AGCAGCACCTCGGAATAG-3′) were used to amplify 267 bp of the fluoroquinolone resistance-determining region of ParC as previously reported [14]. Amplified products were then separated using 1.5% agarose gels, and PCR products were sequenced, and the sequence of each of the sample was compared with *P. aeruginosa* PAO1 sequence. The sequences were multiple aligned by ClustalW2 (http://www.ebi.ac.uk/Tools/msa/clustalw) in order to detect mutations. Nucleotide sequences were translated by Expasy Bioinformatics Resource Portal (http://web.expasy.org/translate/) then compared with *P. aeruginosa* PAO1 protein sequence using ClustalW2 to find changes in amino acid sequences.

*2.10. Disk Diffusion Ciprofloxacin Susceptibility Testing.* The antibiotic susceptibility of bacterial isolates was determined using the disk diffusion method standardized according to the EUCAST (http://www.eucast.org/ast_of_bacteria/disk_diffusion_methodology/), with interpretation based on the EUCAST Clinical Breakpoint Tables v. 9.0, valid from 2019 to 01-01, the zone diameter breakpoint >26 for susceptible strains (*S*), and <26 for resistant strains (*R*). The bacterial strains were inoculated onto Mueller-Hinton agar. Antibiotic disks were placed on the

surface, and this was followed by incubation at 35 ± 1°C in air for 18 ± 2 h ours. Inhibition zone diameter values were read by a pair of calipers, in millimeters to one decimal place. Ciprofloxacin disks (5 $\mu$g) were obtained from Oxoid Ltd (Oxoid AB, Hampshire, UK).

*2.11. Determination of Minimum Biofilm Inhibitory Concentration (MBIC).* The MBICs of ciprofloxacin and **ET37** were determined in PAO1 strain, as previously reported [32]. The experiments were done in 96-well polystyrene microtiter plates with round bottoms. An overnight culture with a turbidity equivalent to that of a 0.5 McFarland standard, obtained with TSB, was aliquoted into the wells of microtiter plates. The plates were incubated for 24 h at 37°C. The wells were washed three times with phosphate-buffered saline (PBS) to remove unattached bacteria and dried in an inverted position. Volumes of 100 $\mu$L of appropriate two-fold dilutions of the ciprofloxacin or **ET37** in Mueller-Hinton broth were transferred into the dried wells with established biofilms. The microtiter plates were incubated for 18–20 hours at 37°C, and minimum biofilm inhibitory concentration (MBIC) was determined, which corresponds to the lowest concentration of antibiotic which inhibits growth of biofilm cells as indicated by absence of visible growth in the wells. A positive control and a negative control were included in all experiments. The experiment was repeated three times.

*2.12. Determination of Minimum Duration for Killing 99% of the Population ($MDK_{99}$).* $MDK_{99}$ was determined by measuring the time to kill 99% of the population [33]. MDK99 was tested in *P. aeruginosa* clinical strains with concentration 1x the MIC of ciprofloxacin or 1x the MIC **ET37** in *P. aeruginosa* wild-type and LasR mutant clinical strains.

## 3. Results

*3.1. Effect of LasR Antagonists on Biofilm Formation in P. aeruginosa PAO1 Laboratory Strain.* We selected 4 compounds reported to be active antagonists of LasR of *P. aeruginosa* and designed on 3-O-C12-HLS scaffold (Figure 1, # **1, 2, 3, 4**) [23]. The synthesis was performed as described in Geske et al. and references cited therein.

We evaluated the effect of the selected 4 LasR antagonists on cell growth and biofilm formation of *P. aeruginosa* PAO1 laboratory strain. We treated PAO1 immediately after seeding the planktonic bacteria with LasR antagonists at different concentrations (0.1, 1.0, 10.0, 25.0, and 50.0 $\mu$M) for 24 hrs. We evaluated cell growth by reading the optical density at 600 nm, and we observed no effect on this parameter (data not shown). Considering biofilm formation, the treatment with number **3** and number **4** compounds reduced the formation of biofilm of more than 50% (Figure 2(a)) ($p < 0.0001$; Student's $t$-test). In particular, in the concentration range of 1.0–10.0 $\mu$M, we observed the highest effect on biofilm inhibition for both number **3** and number **4** compounds. On the contrary, compounds number 1 and 2 failed to significantly inhibit biofilm formation, also increasing the time of exposure to 48–72 hrs (data not shown). On the basis of these results, we selected number **3** and number **4** compounds and the range of concentrations 1.0–10.0 $\mu$M for further investigations on clinical isolates.

*3.1.1. Effect of Number 3 and Number 4 Compounds on Biofilm Formation in Clinical Strains.* First, we evaluate the efficacy of QSi in acting as LasR antagonists in *P. aeruginosa* clinical strains. We selected two subgroups of *P. aeruginosa* clinical strains: (i) wild type for the expression of 3O-C12-HSL receptor (LasR); (ii) *P. aeruginosa* LasR mutant. LasR mutant clinical strains were phenotypically evidenced as producing iridescent and metallic colonies [34, 35]. We performed our analysis on 10 different isolates from four CF individuals (SG, AA, TR, and KK) wild type or mutant for LasR. In order to evaluate LasR functionality, we treated wild-type ($N = 5$) and LasR mutant ($N = 5$) clinical strains immediately after seeding the planktonic bacteria with LasR agonist (1.0, 5.0, 10.0, 25.0, and 50.0 $\mu$M) for 24 hours. We analysed cell growth by reading the optical density at 600 nm, and we observed no effect on this parameter (data not shown). Concerning biofilm formation in wild-type strains, we observed biofilm inhibition of 60% with the compound number **3** at the concentrations of 5.0–10.0 $\mu$M (Figure 2(b)) and compound number **4** reduced biofilm formation of the 30–40% (Figure 2(b)). We observed also a reduction in biofilm formation in LasR mutant clinical strains treated with the same two compounds (number **3** and **4**) at the concentrations of 5.0–10.0 $\mu$M, reporting a decrease of the 30% and 60–70%, when treated with LasR antagonist number **3** and **4**, respectively, (Figure 2(c)). To confirm the results obtained by crystal violet staining, we performed the Syto9 assay, based on fluorescence staining. We choose to use Syto9 staining to confirm our data and to overcome the variability of the results that could arise by crystal violet staining of *P. aeruginosa* biofilm [36]. Similarly, Syto9 assay showed a clear decrease of biofilm formation after the addition of the compounds number **3** and **4** in both wild-type and mutant strains (Figure 2(d)), with the highest effect observed at the concentration of 10.0 $\mu$M.

Since QS inhibition results in a reduced expression of the virulence factors pyocyanin and elastase and in an alteration of biofilm morphology/phenotype [37], the effect of compound numbers **3** and **4** was tested also on the expression of these genes. We observed that both compound numbers **3** and **4** were able to reduce the production of pyocyanin and elastase in wild-type and LasR mutant strains (Figure 3).

*3.1.2. ET37 Effect on PAO1 Strain Susceptibility to Ciprofloxacin.* Ciprofloxacin belongs to the group of fluoroquinolones, active against bacterial infections. It has demonstrated a high efficacy towards *P. aeruginosa* infection and experienced in clinical practice. Since both compounds **3** and **4** resulted efficient in decreasing biofilm formation, we selected both of them to associate with ciprofloxacin, on the basis of its chemical structure. The chimeric derivatives

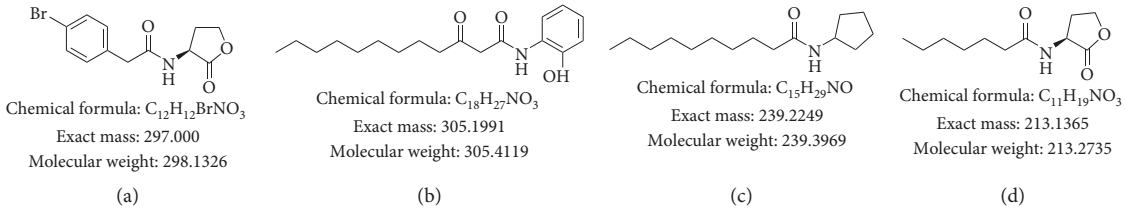


Figure 1: Molecular structure of *P. aeruginosa* QS antagonists (#**1, 2, 3, 4**) designed on 3-O-C12-HSL scaffold. (a) LasR antagonist #1. (b) LasR antagonist #2. (c) LasR antagonist #3. (d) LasR antagonist #4.

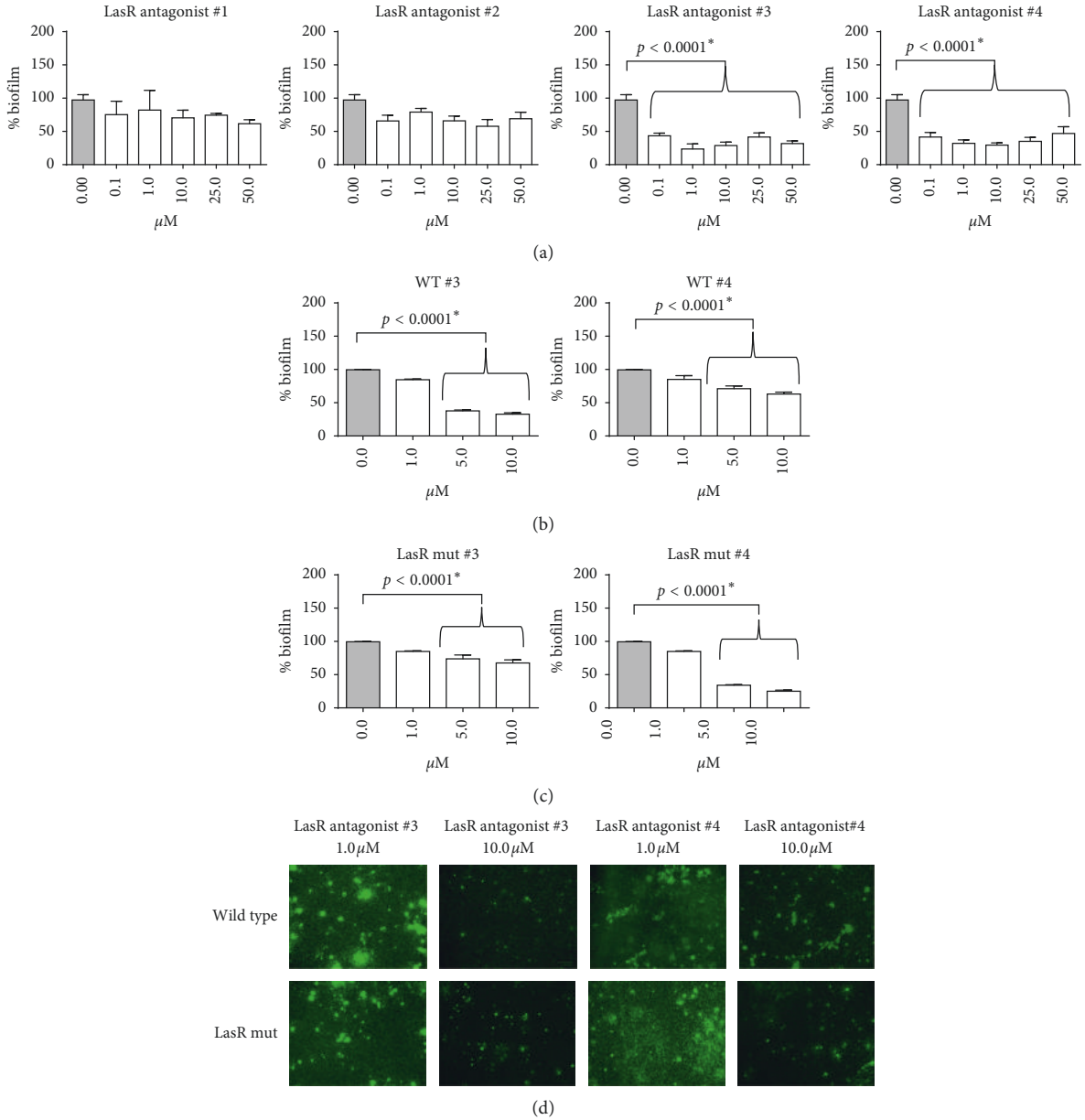


Figure 2: Evaluation of biofilm mass after LasR antagonists (#**1, 2, 3, 4**) treatment on (a) *P. aeruginosa* PAO1 strain and after treatment with number **3** and number **4** compounds on (b) wild-type and (c) LasR mutant clinical strains, using crystal violet assay. (d) Evaluation of biofilm mass after treatment with number **3** and number **4** compounds, using Syto9 assay in LasR wild-type (upper line) and mutant clinical (lower line) strains. *Student's *t*-test.

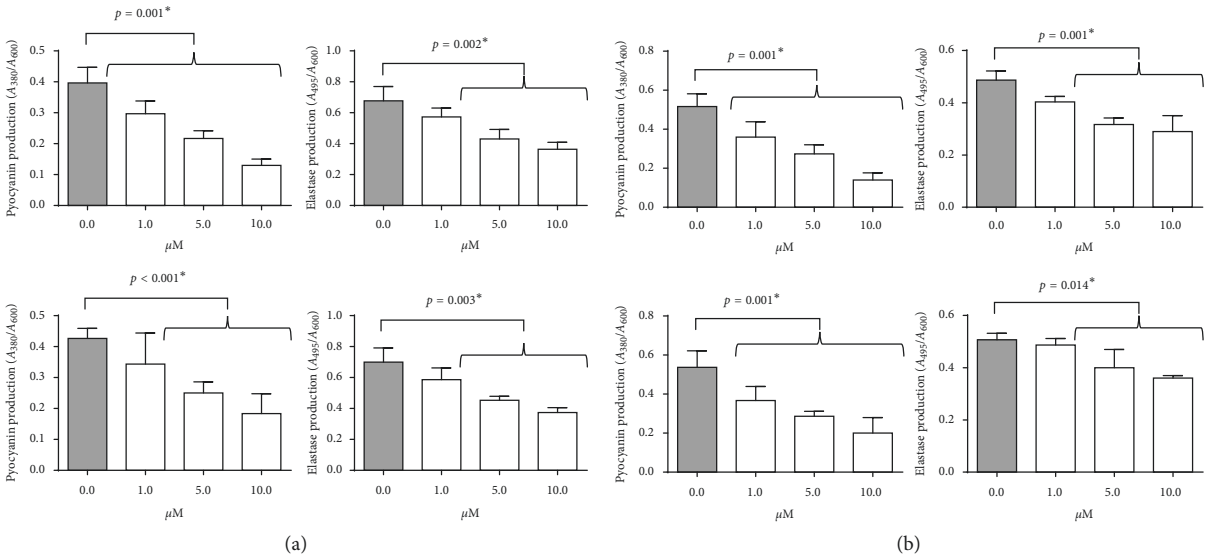


Figure 3: Evaluation of pyocyanin and elastin production after compound number **3** (upper panels) or compound number **4** (lower panels) treatment of (a) wild-type and (b) LasR mutant clinical strains. *Student's *t*-test.

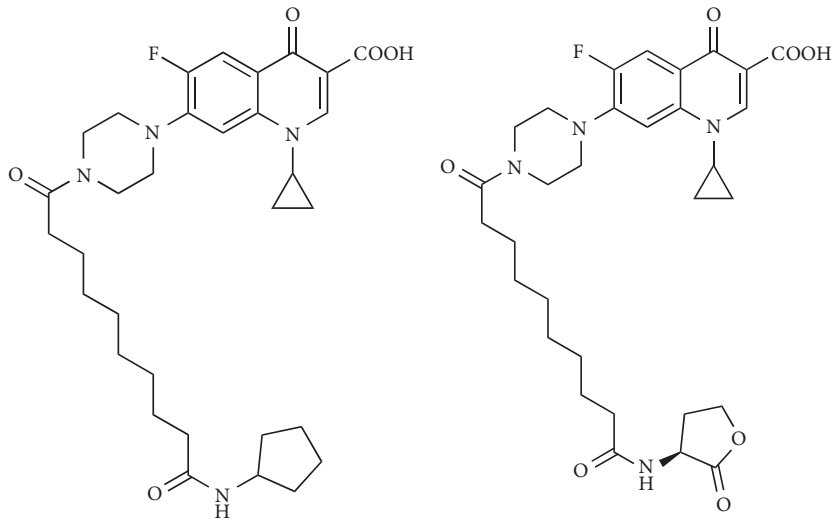


Figure 4: The chimeric derivatives between compounds **3** and **4** and ciprofloxacin. (a) ET-37. (b) ET-39.

between compounds **3** and **4** and ciprofloxacin are depicted in Figure 4.

The molecules **ET37** and **ET39** were synthesized as depicted in Figure 5; the decanedioic acid monoethylester **5** was condensed to the amine moiety of the piperazine ring present in the commercially available ciprofloxacin antibiotics to obtain compound **6** that was subjected to 2N NaOH saponification to achieve acid derivative **7** [38]. Finally, compound **7** was condensed to the cyclopentylamine and L-homoserine lactone using WSC/HOBt as activating agents to obtain, respectively, compound **ET37** and compound **ET39** that were fully characterized by NMR and exact mass spectrometry.

**ET37** and **ET39** were preliminarily tested on PAO1 and *P. aeruginosa* clinical strains. **ET37** maintained its ability to decrease biofilm formation in PAO1 (Figure 6(a)), wild-type (Figure 6(b)) and LasR mutant clinical strains (Figure 6(c)). On the contrary, **ET39** lost the efficacy of compound number **4** (Figure 6). Similarly, pyocyanin and elastin were reduced by **ET37** treatment in both wild-type (Figure 7(a)) and LasR mutant clinical strains (Figure 7(b)). Starting with PAO1 strain, we evaluated the minimal inhibitory ciprofloxacin concentration [28] using the Etest to establish a baseline. The $MIC_{50}$ was within the expected ranges, with the PAO1 $MIC_{50}$ at 0.5 $\mu$g/ml ciprofloxacin, corroborating previous research [39]

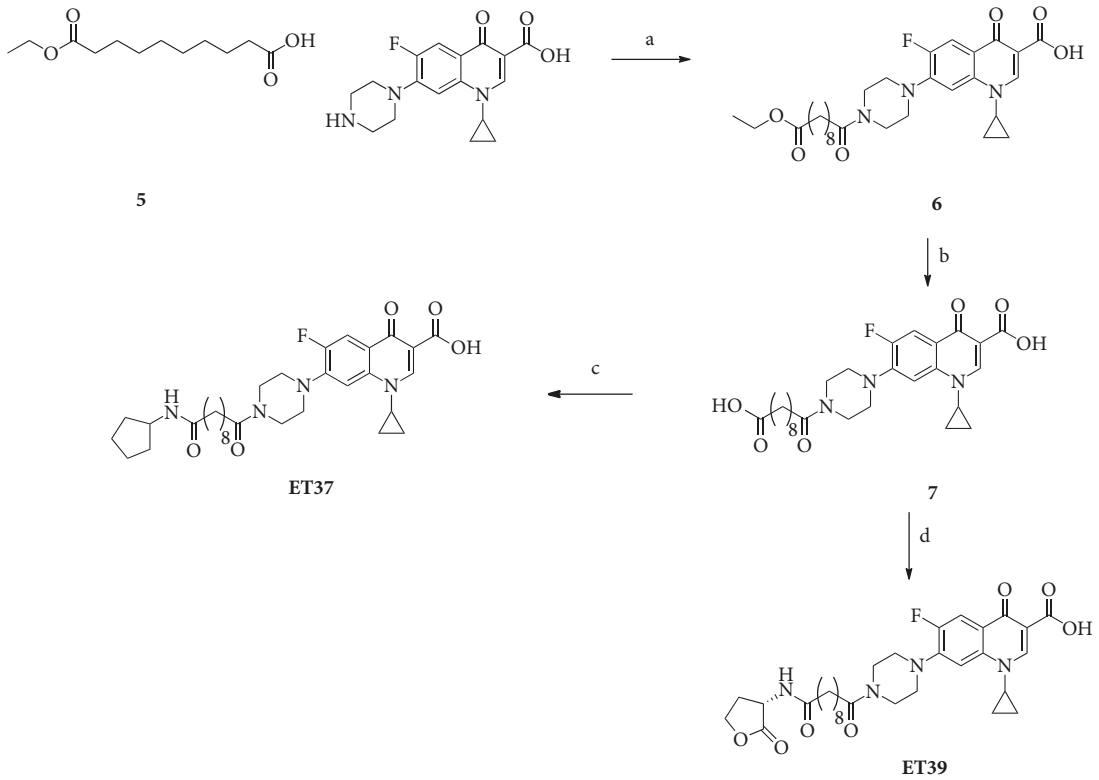


Figure 5: Schematic synthesis of **ET37** and **ET39** compounds. Conditions: (a) WSC/HOBt, DMF, 0°C, o.n., $Y = 88\%$. (b) NaOH 2N, EtOH, r.t. 4 h, $Y =$ quant. (c) WSC/HOBt, cyclopentylamine, DMF, 0°C, 12 h, $Y = 71\%$. (d) WSC/HOBt, L-homoserine, NMO, DMF, 12°h, $Y = 63\%$.

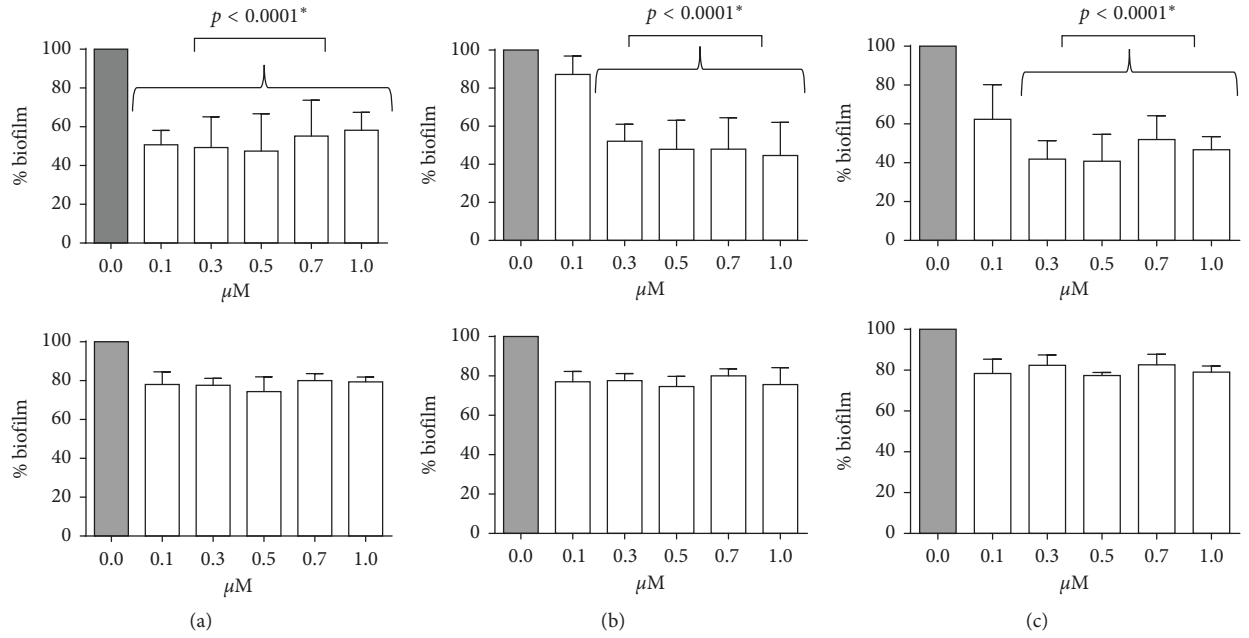


Figure 6: Evaluation of biofilm mass after **ET37** (upper panel) or **ET39** (lower panel) treatment on (a) *P. aeruginosa* PAO1, (b) wild-type, and (c) LasR mutant clinical strains, using crystal violet assay. *Student's *t*-test.

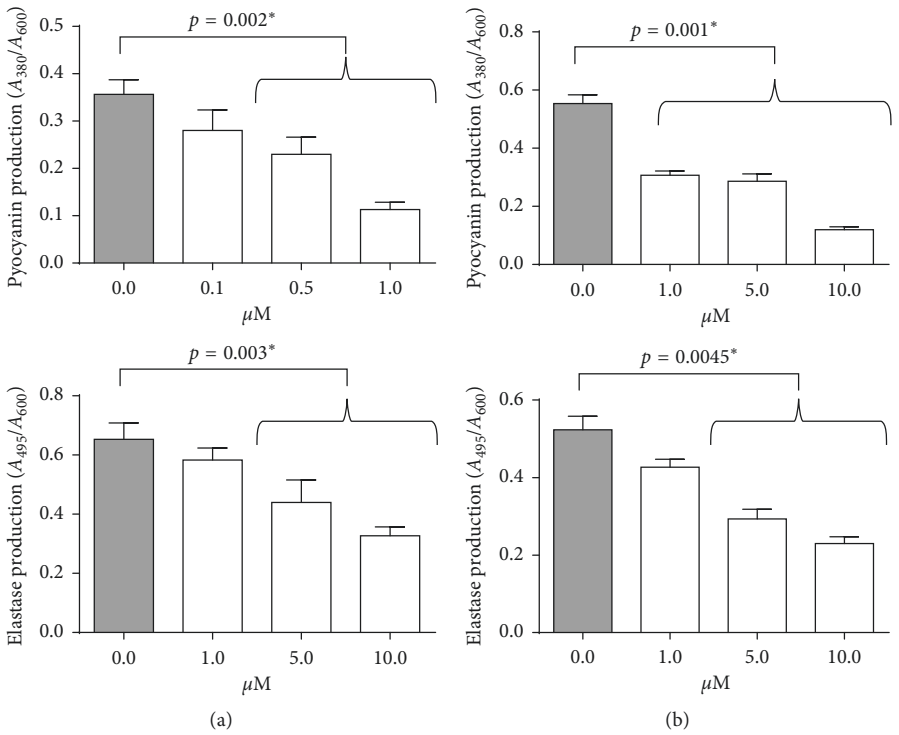


Figure 7: Evaluation of pyocyanin (upper panels) and elastin (lower panels) production after compound **ET37** treatment of (a) wild-type and (b) LasR mutant clinical strains. *Student's *t*-test.

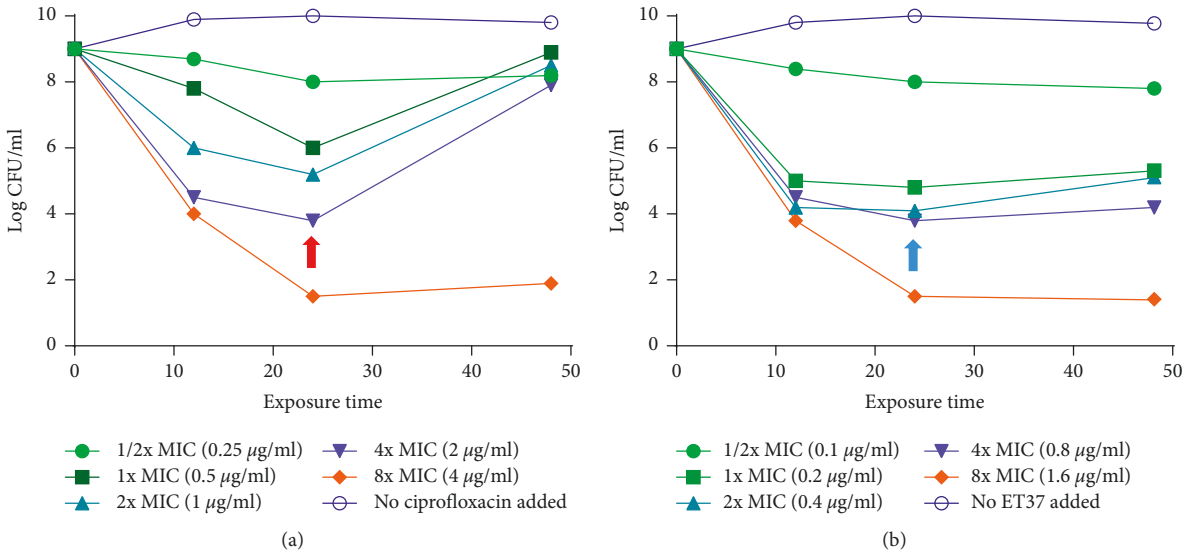


Figure 8: Time-kill studies with PAO1 with concentration ranging from 0.5 to 8x the MIC of (a) ciprofloxacin or (b) **ET37** treatment. Red arrow: "drug-tolerant" cells in ciprofloxacin-treated PAO1; blue arrow: "drug-tolerant" cells in **ET37**-treated PAO1.

and at 0.2 $\mu$g/ml ET37. The $MIC_{90}$ and modal MIC were $\geq$32 $\mu$g/ml.

We evaluate the population dynamics in response to ciprofloxacin unconjugated and conjugated to compound number **3** (**ET37**). The exposure was at concentrations ranging from 0.5 to 8x the MIC in PAO1 strain (Figure 8). After the treatment with ciprofloxacin, a large part of the bacteria was killed by the drug (Figure 8(a)), as the expected response to an antibiotic treatment with an efficacy of 24 h, as illustrated in Figure 5(a). At lower exposure levels, there was a surviving subpopulation of "drug-tolerant" cells, that survived after ciprofloxacin treatment (Figure 8(a), red

arrow). The "drug-tolerant" cell population was not present in **ET37** treated PAO1 cultures (Figure 8(b), blue arrow).

Previous data showed that ciprofloxacin reduced virulence factors and biofilm formation decreasing the production of QS signal molecules in *P. aeruginosa* [40]. We tested the minimal biofilm inhibitory concentration (MBIC) of both ciprofloxacin and **ET37** on PAO1. Results demonstrated that **ET37** MBIC was similar to $MIC_{50}$ (0.22 $\mu$g/ml) while ciprofloxacin MICB was eight times higher (4.0 $\mu$g/ml) than $MIC_{50}$ (0.5 $\mu$g/ml).

*3.1.3. ET37 Effect on P. aeruginosa Clinical Strains Susceptibility to Ciprofloxacin.* The efficacy of ciprofloxacin was then tested also on *P. aeruginosa* clinical strains. The resulting $MIC_{50}$ are reported in Table 2.

Three strains were resistant to ciprofloxacin (TR2, TR1, and KK72), three where intermediate (AA2, TR66, and KK1), and four were susceptible (SG1, SG58, AA12, and AA11). We evaluated the genetic background at the basis of ciprofloxacin resistance. QRDRs regions of GyrA and ParC, implicated in *P. aeruginosa* resistance to quinolone [6, 7], were amplified from resistant isolates and were sequenced for mutations involved in ciprofloxacin resistance. One strain resistant to ciprofloxacin (TR1) had a mutation in GyrA (Thr83⟶Ile) and a mutation in ParC (Ser87⟶ Leu or Trp). Two strains resistant to ciprofloxacin (TR2 and KK72) and three intermediate strains (AA2, TR66, and KK1) had a mutation in GyrA (Thr83⟶Ile).

When we evaluated the time-kill studies with the **ET37** concentration of 4 $\mu$g/ml, equal to the theoretical plasma peak [41], we observed 6-log decrease at 24 h for strain SG1, SG58, AA12, and AA11 (Figure 9), which are the most susceptible according to their MICs (Table 2). Interestingly, a bactericidal activity was observed with 3.0-log inoculum reduction at 12 h for strains AA2 and TR66, that were categorized as intermediate and TR2 and KK72, that were considered resistant to ciprofloxacin (Table 2) (Figure 9). A bacterial growth reoccurred at 24 h for strains TR1 and KK1 (Figure 9), the most resistant strains according to their MICs (Table 2).

*3.1.4. Time-Kill Studies on P. aeruginosa Clinical Strains.* Time-kill studies were performed in parallel, on *P. aeruginosa* clinical strains, with 1/2, 2, 4, 8, X $MIC_{50}$, for both ciprofloxacin and **ET37** (Table 2). Following 24 h treatment with ciprofloxacin, there was a surviving subpopulation of "drug-tolerant" cells only in low-dose ciprofloxacin-treated *P. aeruginosa* clinical strains (Figure 10(a)), while both wild-type and LasR mutant clinical strains did not change over 48 h treatment with **ET37** (Figure 10(b)).

The clinical strains were then tested for their tolerance to ciprofloxacin or ET37 treatment. The measured $MDK_{99}$ decreased in the **ET37**-treated strains in comparison with the ciprofloxacin-treated strains (Figure 11). Both *P. aeruginosa* wild-type and LasR mutant clinical strains showed a $MDK_{99}$ of 12 hours after treatment with **ET37** in comparison with the $MDK_{99}$ of 24 hours observed in the same strains without **ET37** treatment ($p < 0.1$).

Table 2: MIC ($\mu$g/ml) of the *P. aeruginosa* clinical strains.

| Clinical strain | LasR status | $MIC_{50}$ cipro | Diameter inhibitory zone (mm)* | Categorization |
|---|---|---|---|---|
| SG1 | WT | 0.12 | 32 | S |
| SG58 | WT | 0.25 | 33 | S |
| AA2 | WT | 1.0 | 27 | I |
| AA12 | WT | 0.008 | 36 | S |
| AA11 | MUT | 0.5 | 34 | S |
| TR2 | WT | 2.0 | 10 | R |
| TR1 | MUT | 2.0 | 13 | R |
| TR66 | MUT | 1.0 | 27 | I |
| KK1 | MUT | 1.0 | 27 | I |
| KK72 | MUT | 2.0 | 11 | R |

*According to the EUCAST Clinical Breakpoint Tables v. 9.0, valid from 2019 to 01-01, the zone diameter breakpoint >26 for susceptible strains (*S*) and <26 for resistant strains (*R*).

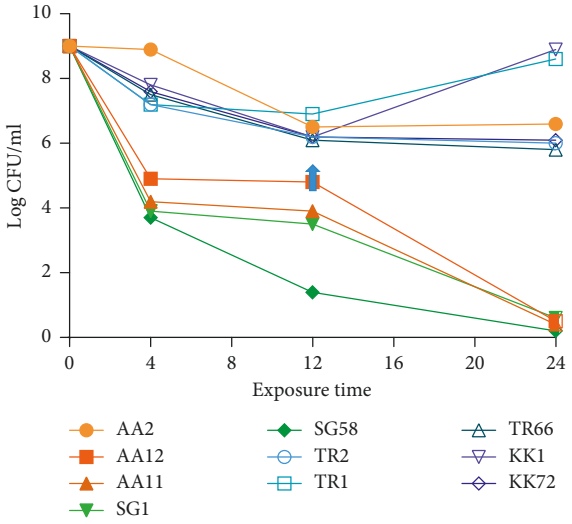


Figure 9: Time-kill studies with *P. aeruginosa* clinical strains with a concentration of **ET37** equal to the theoretical plasma peak (4 $\mu$g/ml). Blue arrow: "drug-tolerant" cells in **ET37** treated *P. aeruginosa* clinical strains.

## 4. Discussion

In this research, for the first time, we analysed the effect of selected LasR antagonists, on *P. aeruginosa* clinical strains, and we identified two compounds designed on 3O-C12-HSL scaffold, number **3** and number **4**, which exhibit an inhibitory effect on both LasR wild-type and mutant strains. These LasR antogonists interact with the N-terminal ligand-binding domain of LasR, blocking the binding site for QS molecules.

Since clinical *P. aeruginosa* strains are commonly LasR mutants, it is fundamental to obtain QSi with a demonstrated functionality also in LasR mutant clinical strains. Both number **3** and **4** compounds are able to counteract biofilm formation also in LasR mutant strains, possibly due to the shorter aliphatic chain that results in a lower steric hindrance that could facilitate the cross interaction with RhlR [17, 18]. In fact, it has been reported that LasR antagonist could be effective also on other QS receptors, as

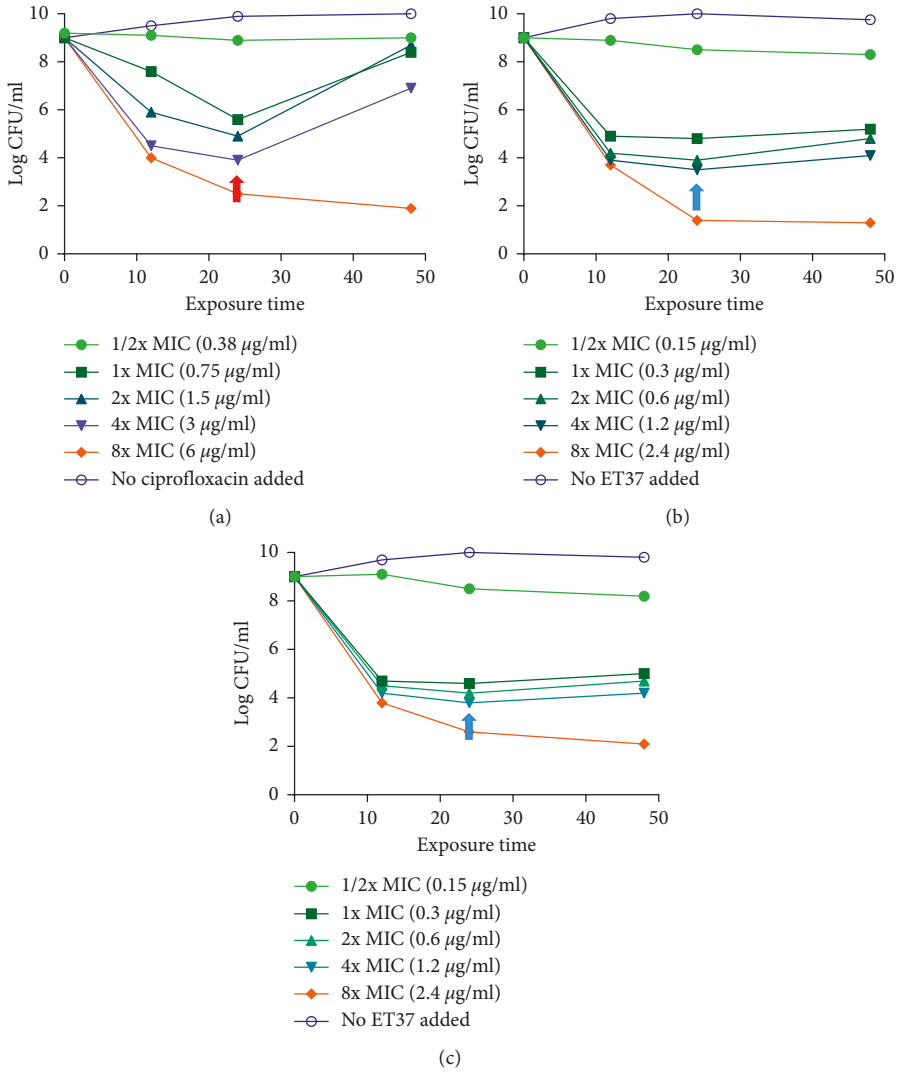


Figure 10: (a) Time-kill studies with *P. aeruginosa* clinical strains with concentration ranging from 0.5 to 8x the MIC of ciprofloxacin. (b) Time-kill studies with *P. aeruginosa* wild-type clinical strains with concentration ranging from 0.5 to 8x the MIC of **ET37** treatment. (c) Time-kill studies with *P. aeruginosa* LasR mutant clinical strains with concentration ranging from 0.5 to 8x the MIC of **ET37** treatment. Red arrow: "drug-tolerant" cells in ciprofloxacin-treated *P. aeruginosa* clinical strains; blue arrows: "drug-tolerant" cells in **ET37**-treated *P. aeruginosa* clinical strains.

RhlR [17, 19]. We speculate that, in the presence of LasR mutations, LasR antagonists numbers **3** and **4** could interact with other QS receptors that are still functional in LasR mutant strains. It has been described that some virulence factors, such as pyocyanin, are still produced in LasR mutants, confirming that QS system is still functional. This could be explained by the ability of *P. aeruginosa* to circumvent QS deficiency using rhl and Pqs systems [20]. Similarly, 3O-C12-HSL is known to bind not only its receptor LasR, but also other QS receptor, as RhlR and PqsR. This is in line with the results of Kalaiarasan and coauthors reporting the ability of two anti-QS compounds to decrease biofilm production in two *P. aeruginosa* clinical isolates, affecting both lasR and rhlR transcription [42].

The identification of new mechanisms to block the appearance of drug resistance in *P. aeruginosa* is important because it is characterized by a quick adaptation to resist to new drug compounds [1], causing chronic lung infection in individuals with CF [43] or chronic obstructive pulmonary disease (COPD) [44], and the 10% of hospital-acquired infections.

The antibiotics used to treat *P. aeruginosa* infection include ciprofloxacin, tobramycin, ceftazidime, gentamicin, and imipenem. *P. aeruginosa* bacteria present a high degree of resistance to these antibiotics. Interestingly, the response to ciprofloxacin is very effective at the beginning of the treatment, but high-level resistance is rapidly acquired by *P. aeruginosa*, making the treatment ineffective in the 30% of strains obtained from clinical isolates [1]. The mechanisms that could increase *P. aeruginosa* antibiotic susceptibility still remain unclear [2–4] and few studies tried to develop therapeutic strategies to decrease the insurgence of resistances.

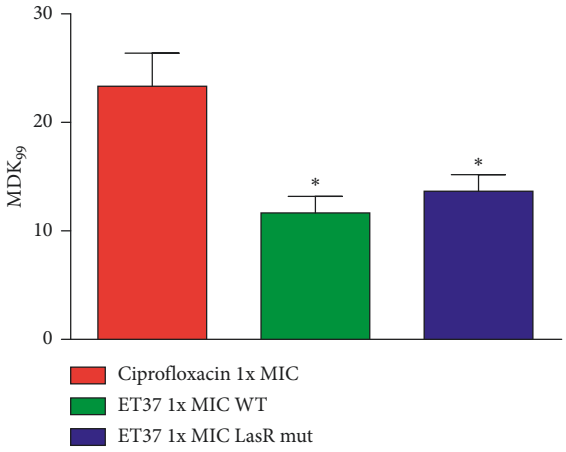


FIGURE 11: $MDK_{99}$ was determined by measuring the time to kill 99% of the population, in *P. aeruginosa* clinical strains with concentration 1x the MIC of ciprofloxacin (red histogram), *P. aeruginosa* wild-type clinical strains (green histogram, WT) and LasR mutant clinical strains (blue histogram, LasR mut) with 1x the MIC **ET37**. $^{*}p$ value $< 0.01$, obtained by Student's $t$-test. Data are presented as the mean ± SD.

The onset of resistant mutants seems to be connected with the use of antibiotic concentrations that can select mutants, that ranges between 0.5 and 8 $\mu g\,ml^{-1}$ [45], in line with the concentrations used in our work. As drug concentrations increased, we observed the selection of particular tolerant clones ("drug-tolerant"). The use of **ET37** reduced the formation of biofilm, the expression of virulence genes (e.g., pyocyanin and elastin), and the onset of tolerant clones. This was obtained also in those strains that presented a genetic mutation in GyrA and ParC, that are now known to play an integral role in quinolone resistance in *P. aeruginosa* [6, 7].

From the time-kill curves with ciprofloxacin and **ET37**, it seems that the pharmacodynamics of ciprofloxacin changes from concentration-/dose-dependent killing, as reported in Figure 8(a), to more time-dependent killing, as we observed similar time-killing curves at different **ET37** concentrations (1x, 2x, and 4x MICs), as reported in Figure 8(b). This is also evident in the time-kill curves of the clinical isolates presented in Figure 10. This might suggest that the mechanisms involved in ciprofloxacin tolerance is quorum-sensing related. In fact, when the clinical strains were tested for their tolerance to ciprofloxacin or **ET37** treatment, we observed a decrease in $MDK_{99}$ after **ET37** treatment in comparison with the ciprofloxacin (Figure 11). Both *P. aeruginosa* wild-type and LasR mutant clinical strains showed an $MDK_{99}$ of 12 hours after treatment with **ET37** in comparison with the $MDK_{99}$ of 24 hours observed in the same strains without **ET37** treatment. The reduced incidence of tolerant bacteria after **ET37** treatment could be associated with a modified gene expression [34]. In particular, ciprofloxacin treatment induces the production of hydroxyl radicals that might cause oxidation-mediated cell death [46]. The onset of drug-tolerant bacteria might be associated with the increase in the phosphorylation of two proteins, PA0265 (succinate-semialdehyde dehydrogenase (SSADH), encoded by GabD) and PA3570 (methylmalonate-semialdehyde dehydrogenase (MMSADH), encoded by MmsA) [8], that seems to induce the production of NADH as a reaction product. NADH is a reducing agent, induced in response to environmental stress [35] to prevent oxidative damage. Therefore, the upregulation of NADH by the phosphorylation of these two proteins might buffer oxidative stress induced by ciprofloxacin and facilitate the onset of tolerant bacteria. **ET37** compound could facilitate the accumulation of ciprofloxacin within the cell, increasing the intracellular superoxide anion ($O2^{-}$) concentration causing more oxidative stress that cannot be buffered by SSADH/MMSADH, than in *P. aeruginosa* strains treated with ciprofloxacin alone. The benefit of **ET37** in comparison with ciprofloxacin is its ability to reduce the formation of biofilm and consequently diminishing the physical barrier to ciprofloxacin penetration into bacterial cells. In fact, the MBIC of **ET37** was similar to $MIC_{50}$ (0.22 $\mu$g/ml), while ciprofloxacin MBIC was eight times higher (4.0 $\mu$g/ml) than $MIC_{50}$ (0.5 $\mu$g/ml). Moreover, the inhibition of QS could also affect the production of rhamnolipid. The production of rhamnolipid in *P. aeruginosa* is controlled by the transcriptional regulator RhlR of the QS system [47]. Even if the role of rhamnolipids in bacterial physiology is not clear, they seem to take part to the assimilation of insoluble substrates [36], to antimicrobial activities [48], to hemolytic activity [49], to the solubilization of the quinolone signal, and to the swarming motility [50]. Moreover, rhamnolipids seem to reduce the activation of host innate immunity, facilitating *P. aeruginosa* survival and colonization on compromised epithelia. The decrease in rhamnolipids production by QSi could facilitate the elimination of the infection by the host's immune system.

## 5. Conclusions

On the basis of our results, we reported, for the first time, the reduction of biofilm formation and ciprofloxacin tolerance in *P. aeruginosa* clinical strains treated with **ET37** compound. This molecule, generated by the conjugation of a QSi and ciprofloxacin, could have a wide application in clinical setting. The possibility to affect biofilm formation in chronically infected patients, such as CF and COPD patients, and to reduce the onset of ciprofloxacin tolerance would improve patient healing and allow to decrease antibiotic drug dosage.

## Data Availability

The data used to support the findings of this study are available from the corresponding author upon request.

## Disclosure

An earlier version of this study was presented as a poster in "Congresso Nazionale della Società Italiana di Microbiologia, 2018".

## Conflicts of Interest

The authors declare that there are no conflicts of interest regarding the publication of this paper.

## Authors' Contributions

Daria Bortolotti and Claudio Trapella equally contributed to the work.

## Acknowledgments

We thank Iva Pivanti for technical support and Linda M. Sartor for language revision of the manuscript. This work was supported by University of Ferrara FAR 2017 and 2018.

## Supplementary Materials

The experimental part of the synthesis of the chemical compounds and NMR data are reported in the Supplementary Material file. (*Supplementary Materials*)

## References

[1] G. Manno, M. Cruciani, L. Romano, S. Scapolan, M. Mentasti, and R. L. Lorini, "Antimicrobial use and *Pseudomonas aeruginosa* susceptibility profile in a cystic fibrosis centre," *International Journal of Antimicrobial Agents*, vol. 25, no. 3, pp. 193–197, 2005.

[2] D. C. Minicucci, "Mechanisms of action and resistance of older and newer fluoroquinolones," *Clinical Infectious Diseases*, vol. 31, no. 2, pp. 24–28, 2000.

[3] A. Kureishi, J. M. Diver, B. Beckthold, T. Schollaardt, and L. E. Bryan, "Cloning and nucleotide sequence of *Pseudomonas aeruginosa* DNA gyrase GyrA gene from strain PAO1 and quinolone-resistant clinical isolates," *Antimicrobial Agents and Chemotherapy*, vol. 38, no. 9, pp. 1944–1952, 1994.

[4] C. Walsh, "Molecular mechanisms that confer antibacterial drug resistance," *Nature*, vol. 406, no. 6797, pp. 775–781, 2000.

[5] R. E. W. Hancock and D. P. Speert, "Antibiotic resistance in *Pseudomonas aeruginosa*: mechanisms and impact on treatment," *Drug Resistance Updates*, vol. 3, no. 4, pp. 247–255, 2000.

[6] H. Y. Chenia, B. Pillay, and D. Pillay, "Analysis of the mechanisms of fluoroquinolone resistance in urinary tract pathogens," *Journal of Antimicrobial Chemotherapy*, vol. 58, no. 6, pp. 1274–1278, 2006.

[7] L. S. Redgrave, S. B. Sutton, M. A. Webber, and L. J. V. Piddock, "Fluoroquinolone resistance: mechanisms, impact on bacteria, and role in evolutionary success," *Trends in Microbiology*, vol. 22, no. 8, pp. 438–445, 2014.

[8] H.-C. Su, K. Ramkissoon, J. Doolittle et al., "The development of ciprofloxacin resistance in *Pseudomonas aeruginosa* involves multiple response stages and multiple proteins," *Antimicrobial Agents and Chemotherapy*, vol. 54, no. 11, pp. 4626–4635, 2010.

[9] M. J. Richards, J. R. Edwards, D. H. Culver, and R. P. Gaynes, "Nosocomial infections in medical intensive care units in the United States," *Critical Care Medicine*, vol. 27, no. 5, pp. 887–892, 1999.

[10] T. R. De Kievit, R. Gillis, S. Marx, C. Brown, and B. H. Iglewski, "Quorum-sensing genes in *Pseudomonas aeruginosa* biofilms: their role and expression patterns," *Applied and Environmental Microbiology*, vol. 67, no. 4, pp. 1865–1873, 2001.

[11] I. Joint, J. Allan Downie, and P. Williams, "Bacterial conversations: talking, listening and eavesdropping. An introduction," *Philosophical Transactions of the Royal Society B: Biological Sciences*, vol. 362, no. 1483, pp. 1115–1117, 2007.

[12] P. Williams, "Quorum sensing, communication and cross-kingdom signalling in the bacterial world," *Microbiology*, vol. 153, no. 12, pp. 3923–3938, 2007.

[13] S. B. von Bodman, J. M. Willey, and S. P. Diggle, "Cell-cell communication in bacteria: united we stand," *Journal of Bacteriology*, vol. 190, no. 13, pp. 4377–4391, 2008.

[14] N. Gorgani, S. Ahlbrand, A. Patterson, and N. Pourmand, "Detection of point mutations associated with antibiotic resistance in *Pseudomonas aeruginosa*," *International Journal of Antimicrobial Agents*, vol. 34, no. 5, pp. 414–418, 2009.

[15] J. Lee and L. Zhang, "The hierarchy quorum sensing network in *Pseudomonas aeruginosa*," *Protein & Cell*, vol. 6, no. 1, pp. 26–41, 2015.

[16] P. Kiratisin, K. D. Tucker, and L. Passador, "LasR, a transcriptional activator of *Pseudomonas aeruginosa* virulence genes, functions as a multimer," *Journal of Bacteriology*, vol. 184, no. 17, pp. 4912–4919, 2002.

[17] A. Latifi, M. Foglino, K. Tanaka, P. Williams, and A. Lazdunski, "A hierarchical quorum-sensing cascade in *Pseudomonas aeruginosa* links the transcriptional activators LasR and RhlR (VsmR) to expression of the stationary-phase sigma factor RpoS," *Molecular Microbiology*, vol. 21, no. 6, pp. 1137–1146, 1996.

[18] E. C. Pesci, J. P. Pearson, P. C. Seed, and B. H. Iglewski, "Regulation of las and Rhl quorum sensing in *Pseudomonas aeruginosa*," *Journal of Bacteriology*, vol. 179, no. 10, pp. 3127–3132, 1997.

[19] I. Ventre, F. Ledgham, V. Prima, A. Lazdunski, M. Foglino, and J. N. Sturgis, "Dimerization of the quorum sensing regulator RhlR: development of a method using EGFP fluorescence anisotropy," *Molecular Microbiology*, vol. 48, no. 1, pp. 187–198, 2003.

[20] G. Xiao, J. He, and L. G. Rahme, "Mutation analysis of the *Pseudomonas aeruginosa* mvfR and pqsABCDE gene promoters demonstrates complex quorum-sensing circuitry," *Microbiology*, vol. 152, no. 6, pp. 1679–1686, 2006.

[21] S. L. McKnight, B. H. Iglewski, and E. C. Pesci, "The Pseudomonas quinolone signal regulates Rhl quorum sensing in *Pseudomonas aeruginosa*," *Journal of Bacteriology*, vol. 182, no. 10, pp. 2702–2708, 2000.

[22] G. Brackman, P. Cos, L. Maes, H. J. Nelis, and T. Coenye, "Quorum sensing inhibitors increase the susceptibility of bacterial biofilms to antibiotics in vitro and in vivo," *Antimicrobial Agents and Chemotherapy*, vol. 55, no. 6, pp. 2655–2661, 2011.

[23] G. D. Geske, J. C. O'Neill, and H. E. Blackwell, "Expanding dialogues: from natural autoinducers to non-natural analogues that modulate quorum sensing in Gram-negative bacteria," *Chemical Society Reviews*, vol. 37, no. 7, pp. 1432–1447, 2008.

[24] A. Bragonzi, M. Paroni, A. Nonis et al., "Pseudomonas aeruginosa microevolution during cystic fibrosis lung infection establishes clones with adapted virulence," *American Journal of Respiratory and Critical Care Medicine*, vol. 180, no. 2, pp. 138–145, 2009.

[25] D. A. D'Argenio, M. Wu, L. R. Hoffman et al., "Growth phenotypes of *Pseudomonas aeruginosa* LasR mutants adapted to the airways of cystic fibrosis patients," *Molecular Microbiology*, vol. 64, no. 2, pp. 512–533, 2007.

[26] L. R. Hoffman, H. D. Kulasekara, J. Emerson et al., "*Pseudomonas aeruginosa* LasR mutants are associated with cystic

fibrosis lung disease progression," *Journal of Cystic Fibrosis*, vol. 8, no. 1, pp. 66–70, 2009.

[27] S. Chugani, B. S. Kim, S. Phattarasukol et al., "Strain-dependent diversity in the *Pseudomonas aeruginosa* quorum-sensing regulon," *Proceedings of the National Academy of Sciences*, vol. 109, no. 41, pp. 2823–2831, 2012.

[28] D. M. Michaelson, "APOE ε4: the most prevalent yet understudied risk factor for Alzheimer's disease," *Alzheimer's & Dementia*, vol. 10, no. 6, pp. 861–868, 2014.

[29] EUCAST, "Clinical breakpoints," May 2018, http://www.eucast.org/clinical_breakpoints/.

[30] T. Rasamiravaka, O. M. Vandeputte, L. Pottier et al., "*Pseudomonas aeruginosa* biofilm formation and persistence, along with the production of quorum sensing-dependent virulence factors, are disrupted by a triterpenoid coumarate ester isolated from dalbergia trichocarpa, a tropical legume," *PLoS One*, vol. 10, no. 7, Article ID e0132791, 2015.

[31] U. Muh, M. Schuster, R. Heim, A. Singh, E. R. Olson, and E. P. Greenberg, "Novel *Pseudomonas aeruginosa* quorum-sensing inhibitors identified in an ultra-high-throughput screen," *Antimicrobial Agents and Chemotherapy*, vol. 50, no. 11, pp. 3674–3679, 2006.

[32] L. Cernohorská and M. Votava, "Antibiotic synergy against biofilm-forming *Pseudomonas aeruginosa*," *Folia Microbiol (Praha)*, vol. 53, pp. 57–60, 2008.

[33] A. Brauner, N. Shoresh, O. Fridman, and N. Q. Balaban, "An experimental framework for quantifying bacterial tolerance," *Biophysical Journal*, vol. 112, no. 12, pp. 2664–2671, 2017.

[34] M. D. Brazas and R. E. W. Hancock, "Ciprofloxacin induction of a susceptibility determinant in *Pseudomonas aeruginosa*," *Antimicrobial Agents and Chemotherapy*, vol. 49, no. 8, pp. 3222–3227, 2005.

[35] R. A. Proctor and A. von Humboldt, "Bacterial energetics and antimicrobial resistance," *Drug Resistance Updates*, vol. 1, no. 4, pp. 227–235, 1998.

[36] R. A. Al-Tahhan, T. R. Sandrin, A. A. Bodour, and R. M. Maier, "Rhamnolipid-induced removal of lipopolysaccharide from *Pseudomonas aeruginosa*: effect on cell surface properties and interaction with hydrophobic substrates," *Applied and Environmental Microbiology*, vol. 66, no. 8, pp. 3262–3268, 2000.

[37] K. M. Smith, Y. Bu, and H. Suga, "Library screening for synthetic agonists and antagonists of a *Pseudomonas aeruginosa* autoinducer," *Chemistry & Biology*, vol. 10, no. 6, pp. 563–571, 2003.

[38] S.-J. Zhang and W.-X. Hu, "Synthesis, antiproliferation, and docking studies of N-phenyl-lipoamide and 8-mercapto-N-phenyloctanamide derivatives: effects of C6 position thiol moiety," *Medicinal Chemistry Research*, vol. 21, no. 10, pp. 3312–3320, 2012.

[39] J. M. Andrews, "Determination of minimum inhibitory concentrations," *Journal of Antimicrobial Chemotherapy*, vol. 48, no. 1, pp. 5–16, 2001.

[40] P. Gupta, S. Chhibber, and K. Harjai, "Subinhibitory concentration of ciprofloxacin targets quorum sensing system of *Pseudomonas aeruginosa* causing inhibition of biofilm formation & reduction of virulence," *Indian Journal of Medical Research*, vol. 143, no. 5, pp. 643–651, 2016.

[41] A. Grillon, F. Schramm, M. Kleinberg, and F. Jehl, "Comparative activity of ciprofloxacin, levofloxacin and moxifloxacin against *Klebsiella pneumoniae*, *Pseudomonas aeruginosa* and *stenotrophomonas maltophilia* assessed by minimum inhibitory concentrations and time-kill studies," *PLoS One*, vol. 11, no. 6, Article ID e0156690, 2016.

[42] E. Kalaiarasan, K. Thirumalaswamy, B. N. Harish, V. Gnanasambandam, V. K. Sali, and J. John, "Inhibition of quorum sensing-controlled biofilm formation in *Pseudomonas aeruginosa* by quorum-sensing inhibitors," *Microbial Pathogenesis*, vol. 111, pp. 99–107, 2017.

[43] J. A. Bosso, "Use of ciprofloxacin in cystic fibrosis patients," *American Journal of Medicine*, vol. 87, no. 5, pp. 123–127, 1989.

[44] D. Lieberman and D. Lieberman, "Pseudomonal infections in patients with COPD," *American Journal of Respiratory Medicine*, vol. 2, no. 6, pp. 459–468, 2003.

[45] G. T. Hansen, X. Zhao, K. Drlica, and J. M. Blondeau, "Mutant prevention concentration for ciprofloxacin and levofloxacin with *Pseudomonas aeruginosa*," *International Journal of Antimicrobial Agents*, vol. 27, no. 2, pp. 120–124, 2006.

[46] M. A. Kohanski, D. J. Dwyer, B. Hayete, C. A. Lawrence, and J. J. Collins, "A common mechanism of cellular death induced by bactericidal antibiotics," *Cell*, vol. 130, no. 5, pp. 797–810, 2007.

[47] V. Jensen, D. Lons, C. Zaoui et al., "RhlR expression in *Pseudomonas aeruginosa* is modulated by the *Pseudomonas quinolone* signal via PhoB-dependent and independent pathways," *Journal of Bacteriology*, vol. 188, no. 24, pp. 8601–8606, 2006.

[48] X. L. Wang, L. Y. Gong, S. K. Liang, X. R. Han, C. J. Zhu, and Y. B. Li, "Algicidal activity of rhamnolipid biosurfactants produced by *Pseudomonas aeruginosa*," *Harmful Algae*, vol. 4, no. 2, pp. 433–443, 2005.

[49] K. Fujita, T. Akino, and H. Yoshioka, "Characteristics of heat-stable extracellular hemolysin from *Pseudomonas aeruginosa*," *Infection and Immunity*, vol. 56, pp. 1385–1387, 1988.

[50] E. Deziel, F. Lepine, S. Milot, and R. Villemur, "RhlA is required for the production of a novel biosurfactant promoting swarming motility in *Pseudomonas aeruginosa*: 3-(3-hydroxyalkanoyloxy) alkanoic acids (HAAs), the precursors of rhamnolipids," *Microbiology*, vol. 149, no. 8, pp. 2005–2013, 2003.

PLOS ONE

RESEARCH ARTICLE

# HelixComplex snail mucus as a potential technology against $O_3$ induced skin damage

**Valentina Gentili[1☯], Daria Bortolotti[1☯], Mascia Benedusi[2], Andrea Alogna[1], Anna Fantinati[1], Anna Guiotto[2], Giulia Turrin[1], Carlo Cervellati[2], Claudio Trapella[1], Roberta Rizzo[1]*, Giuseppe Valacchi[2,3,4☯]***

**1** Department of Chemical and Pharmaceutical Sciences, University of Ferrara, Ferrara, Italy, **2** Department of Biomedical and Specialist Surgical Sciences, Section of Medical Biochemistry, Molecular Biology and Genetics, University of Ferrara, Ferrara, Italy, **3** Department of Animal Science, Plants for Human Health Institute, North Carolina Research Campus, Kannapolis, North Carolina, United States of America, **4** Department of Food and Nutrition; Kyung Hee University, Seoul, South Korea

☯ These authors contributed equally to this work.
* rbr@unife.it (RR); gvalacc@ncsu.edu (GV)



OPEN ACCESS

**Citation:** Gentili V, Bortolotti D, Benedusi M, Alogna A, Fantinati A, Guiotto A, et al. (2020) HelixComplex snail mucus as a potential technology against $O_3$ induced skin damage. PLoS ONE 15(2): e0229613. https://doi.org/10.1371/journal.pone.0229613

**Editor:** Ahmad Salimi, School of Pharmacy, Ardabil University of Medical Sciences, ISLAMIC REPUBLIC OF IRAN

**Received:** October 23, 2019

**Accepted:** February 10, 2020

**Published:** February 21, 2020



**Data Availability Statement:** All relevant data are within the paper and its Supporting Information files.

**Funding:** CT and RR are grateful to Italian Ministry of Education, University and Research (https://www.miur.gov.it/) (PNR 2015–2020 project n° ARS01_01163 Green Chemistry) and to Camera di Commercio di Ferrara (http://www.fe.camcom.it/) (2018 Grant; Activae Project) for financial support. The funders had no role in study design, data

## Abstract

Mucus form *H. aspersa muller* has been reported to have several therapeutic proprieties, such as antimicrobial activity, skin protection and wound repair. In this study, we have analyzed *H. aspersa* mucus (Helixcomplex) bio-adhesive efficacy and its defensive properties against the ozone ($O_3$) (0.5 ppm for 2 hours) exposure in human keratinocytes and reconstructed human epidermis models. Cytotoxicity, tissue morphology and cytokine levels were determined. We confirmed HelixComplex regenerative and bio-adhesive properties, the latter possibly via the characteristic mucopolysaccharide composition. In addition, HelixComplex was able to protect from $O_3$ exposure by preventing oxidative damage and the consequent pro-inflammatory response in both 2D and 3D models. Based on this study, it is possible to suggest HelixComplex as a potentially new protective technology against pollution induced skin damage.

## Introduction

Being the skin our first defense against the external world, this organ is continuously exposed to several stressors among which pollution has been shown to be among the most toxic [1–3]. Although the troposphere is characterized by the presence of multiple pollutants, $O_3$ has been shown to be one of the most toxic and recent evidences have supported the idea that $O_3$ is able to not only affect skin homeostasis but also play a role in the development of several skin conditions. Indeed, in the last decade several studies have shown the correlation between $O_3$ levels and ER visits for skin diseases [4–6]. Xu et al were able to link skin conditions such as eczema, urticaria, rash/eruption, contact dermatitis, and infection to high 8-hour concentrations of $O_3$ [6]. Medical examination for conjunctivitis and skin rash were associated with $O_3$ concentrations in a study from 22 cities in France [7]; and we have found positive associations of short-term $O_3$ concentrations with hospital admissions for skin conditions (such as cellulitis, dermatitis, urticaria) in multiple areas in Canada [8].

collection and analysis, decision to publish, or preparation of the manuscript.

**Competing interests:** The authors have declared that no competing interests exist.

Although it has been shown the ability of $O_3$ to induce oxidative damage, $O_3$ is not a radical per se and it is too reactive to penetrate the skin. It has now well documented that its ability to affect cutaneous tissues is mainly a consequence of its reaction with the skin lipids present in the stratum corneum leading to the formation of reactive biomolecules among which $H_2O_2$ and aldehydes are among the most reactive [9]. Several natural and synthetic compounds, have been analyzed in the cosmeceutical field to prevent the $O_3$ damage to skin [10]. Recently, a growing literature and interest has highlighted the ability of snail secretion (snail mucus), extracted from snails maintained in a laboratory setting. to improve skin conditions thanks to its emollient, moisturizing, lubricating and protective properties [11].

In particular, mucus form *H. aspersa muller* has already been reported to have different properties, such as antimicrobial activity [12] and wound repair [13, 14]. The biochemical analysis of *H. aspersa* mucus showed the presence of mucopolysaccharide that permits considerable hydrogen bonding with adjacent water molecules, which effectively leads to hydration of the surrounding tissue [13]. In addition, it stimulates endogenous hyaluronate synthesis, resulting in an increase in water-binding capacity and viscoelasticity of the skin [13, 14]. Moreover, the presence of mucopolysaccharide could improve the adhesion of the mucus to the skin and act as a barrier to prevent epithelial cell insults from pollution and the presence of polyphenols could give to the mucus the ability to prevent and counteract the pollution induced cutaneous oxidative damage.

In this study, we have investigated the protective effect of *H. aspersa* mucus (HelixComplex) in ozone induced skin damage by the use of both 2D and 3D skin models. Our study supports the topical usage of *H. aspersa* mucus (HelixComplex) as a new antipollution technology to prevent premature skin aging.

## Materials and methods

### HelixComplex collection and microbiological evaluation

The *Helix aspersa* snails were fostered in the private snail farming "Corte Frazza" (Via Frattina 22, 44049 Vigarano Mainarda, Ferrara, Italy) (geographical co-ordinates 44˚50'37.6"N 11˚ 28'01.3"E), certified for the snail fostering by the local health unit company (AUSL Ferrara) with the permission number 022FE022. *Helix aspersa* mucus (HelixComplex) was collected by HelixPharma industries (Ferrara, Italy), certified for the collection of snail mucus by the local health unit company (AUSL Ferrara) with the permission number ABP5076. The snail mucus was extracted for the purpose of this study using a patented extractor machine (Beatrix®; HelixPharma industries; Ferrara, Italy) (Patent N WO2013011371A1) that collects about 600 ml of crude extract from 500 snails (about 10 kg) after 45 minutes. The mucus was obtained using low concentrations of NaCl (3%) that was sprayed on snails. The stress caused by this solution induced the snails to produce mucus, that was collected in underlying canisters. Then the snails were rehydrated and re-entered the field. The process does not cause mortality to the snails, as confirmed by the permission obtained by the local health unit company (AUSL Ferrara) (N: ABP5076). Mucus was then sterilized with a peristaltic pump and a filtration device (0.2μm; Pall) (Patent N 10207000117547), specifically developed for mucus filtration and stored at 4˚C or -80˚C. The mucus is available by request to HelixPharma industries. The composition of HelixComplex is reported in Table 1 [13].

### Cell lines

Human keratinocyte cell line (HaCaT; AddexBio Ca, USA, Catalog N. T0020001) (Certificate of analysis in Supplementary material; S1 Fig) was cultured in DMEM medium (Gibco, Grand

**Table 1. Quali-quantitative chemical and microbiological composition of HelixComplex.**

| Specification | Values | Measure unit |
|---|---|---|
| Aspect | Clear | |
| Color | Yellow | |
| Smell | Odourless | |
| pH | 7.0 | |
| Density | 1.1 | |
| Dry residual | 3.2 | g/L |
| Yield% | 0.12 | |
| Minerals | 350 | mg/L |
| Heavy metals | Absent | |
| Proteins | 250 | mg/L |
| GAGs (sulfurated) | 90 | mg/L |
| GAGs (unsulfurated) | 80 | mg/L |
| Glycolic acid | <200 | mg/L |
| Allantoin | <20 | mg/L |
| Poliphenols | 80 | mg/L |
| Sugars | 0.027 | g/L |
| Collagen | 80 | mg/L |
| Gram + | 0 | CFU |
| Gram – | 0 | CFU |
| Fungi | 0 | CFU |

https://doi.org/10.1371/journal.pone.0229613.t001

Island, NY, USA), supplemented with 1% glutamine, 1% penicillin/streptomycin and 10% FBS. The cells were grown with the 5% CO2 at 37˚C as previously described [15].

## 3D skin tissue models

EpiDermTM Tissue Model (MatTek *In Vitro* Life Science Laboratories, Bratislava, Slovak Republic) were kept at 37˚C in a 95% humidified, 5% $CO_2$ atmosphere in a maintenance medium provided by manufacturers until the exposure. Prior to HelixComplex treatment, media was aspirated and fresh media was added. Reconstructed human epidermis (RHE) was topically treated with or without HelixComplex (ranging from 4 to 400 ug/ml) for 4 hours. Control tissue was exposed to the same doses of vehicle (medium). To avoid excess tissue moistening, a minimum suspension volume was used and tissues were kept at 37˚C in a humidified 5% $CO_2$ atmosphere in a maintenance medium for 4 hours. The control tissues (with or without HelixComplex treatment) were also exposed to filtered air [16].

## Cell viability and cytotoxicity assays

At different time points after treatment, cell viability was examined by Trypan blue dye exclusion and MTT (3-(4,5-dimethilthiazol-2yl)-2,5-diphenyl tetrazolium bromide) colorimetric assay (Roche Diagnostics Corporation, Indianapolis, IN) as previously described [13].

Cytotoxicity studies were performed after the different treatments by assessing LDH (lactate dehydrogenase) release in the culture media (EuroClone, Milan, Italy). In order to obtain a representative maximal LDH release (100% of toxicity) samples were lysed with 2% (V/V) Triton X-100 in culture media for 30 min at 37˚C [17].

## Bioadhesivity test

Bio-adhesivity is an important property of substances presenting the ability to get in close contact with biological structures, allowing a protracted retention period of active molecules. We used an easy and standardized lectin-based assay for evaluation of HelixComplex bioadhesive properties [18]. Lectin is known to be able to bind mucines expressed on mucosal surfaces. For this reason, this assay tested the ability of substances to bind the mucosa and consequently interfere with lectin-mucin interaction. Briefly, cells were seeded in a 8-chamber slide at the final concentration of 20.000/well. After 24 hours, the medium was removed and cells dried for 15 minutes. Cells were fixed with 100 μl of 1:1 methanol/acetone solution for 30 minutes at -20˚C and dry again at room temperature. Cells were finally rehydrated for 5 minutes by adding 500 μl of PBS 1x. 200 μl of HelixComplex were added to cells. 200 μl of PBS 1x were used as negative control while 200 μl of a bio-adhesive solution, containing 1g/10ml of Sucralfate gel, diluted 1:5 in sterile water and a solution of 0,8mg/ml of a natural molecular complex containing polysaccharides, natural mineral and Arabic gum were added as positive control. After 15 minutes at 37˚C, 200 μl of biotinylated lectin 10 μg/ml was added to each well and let 30 minutes at 37˚C. Then, each well was washed three times with 500 μl of 0.05% tween20-PBS 1X for 5 minutes in agitation. After washes, 200 μl of Streptavidine-HRP (2.5 μg/ml) 1:100 diluted, were added for 1 hour at 37˚C. Cells were then washed three times and 100 μl of TMB substrate were added in each well for 5 minutes. The reaction was stopped with 100 μl of HCl 1N and 100 μl of sample were transferred on a 96-well plate and read at 450 nm. The absorbance is inversely correlated with bio-adhesive properties of the substance tested.

## In vitro scratch wound assay

The healing properties of HelixComplex were tested on HaCaT cells by scratch assay. Briefly, keratinocytes were seeded at the final concentration of $1x10^6$ in a 6-well plate. After 24 hours, medium was removed and a linear scratch in the middle of the well was done using a p200 tip as previously described [19]. Then 400μl of HelixComplex or media (control) were added to each well. Scratch repair was monitored by optical microscopy.

## Ozone treatment

$O_3$ was generated from $O_2$ by electrical corona arc discharge ($ECO_3$ model CUV-01, Torino, Italy), as previously described [20]. The $O_2$–$O_3$ mixture (95% $O_2$, 5%$O_3$) was combined with ambient air and allowed to flow into a Teflon-lined exposure chamber, with the $O_3$ concentration in chamber adjusted to 0.5 ppm and continuously monitored by an $O_3$ detector. Temperature and humidity were monitored during exposures (37˚C and 45–55%, respectively). The control tissues (with or without HelixComplex treatment) were also exposed to filtered air in similar exposure chambers except that filtered airflow was released into the chamber at flow rates similar to the $O_3$ output. To assess the efficacy of HelixComplex to protect skin tissues, RHE were pre-treated with HelixComplex 400 μg/ml for 4 hours and then exposed to 0.5 ppm of ozone for 2 hrs (S2 Fig), after 24 the following analysis were performed: i) cell cytotoxicity (LDH assay); ii) tissue morphology by hematoxilin-eosin staining (H&E); iii) $H_2O_2$ levels; iv) 4HNE formation); v) cytokine expression and release.

## Histological analysis

RHE tissues, with or without HelixComplex treatment, exposed to $O_3$, were immersion-fixed in 10% NBF (neutral-buffered formalin) for 24 hours at room temperature, then dehydrated in alcohol gradients and embedded in paraffin. For histological observation, the sections (6 μm

thickness) were deparafinized in xylene and rehydrated in alcohol gradients (100%, 90%, 80% 70%). The sections were stained with hematoxylin for 3–5 minutes, washed in running tap water no more than 5 min, and then stained with Eosin Y for 2 min. The sections were washed in tap water for 1–5 min, dehydrated in increasing concentrations of alcohols and cleared in xylene. The sections were then mounted with a rapid non aqueous mounting medium, contains tolulene (Entellan, Merck KGaA, Darmstadt, Germany) and observed under Nikon Microphot FXA microscope (Nikon Instruments, Amsterdam, Netherlands) [21].

## RNA extraction

RNA was extracted from RHE using the RNeasy mini kit (Qiagen, Hilden, Germany). DNA contamination in RNA preparations was eliminated by digestion with DNase I RNase-free (Thermo Fisher Scientific, Waltham, MA, USA) and subsequent purification using the MinElute Cleanup Kit (Qiagen, Hilden, Germany). DNA elimination was assured by β-actin PCR amplification prior to reverse transcription, as previously described [22]. RNAs were reverse-transcribed using SuperScript II First-Strand Synthesis System according to the manufacturer's protocol (Invitrogen Carlsbad, CA, USA). cDNA aliquots corresponding to 200 ng RNA were used for human cytokines expression analysis.

## qPCR

cDNAs were amplified by specific oligonucleotide primers for: IL-1alpha, IL-1beta, IL-6, IL-8, IL-10 and TNF-alpha (Table 2), and RNaseP (Thermo Fisher Scientific, Waltham, MA, USA) was used as house-keeping control gene. qPCR reactions were carried out in triplicate on a QuantStudio3 PCR System using PowerUP SYBR Green Master Mix (Thermo Fisher Scientific, Waltham, MA, USA). Comparative ΔΔCt method was used to evaluate the relative expression of each gene. Fold changes in the expression of cytokines was calculated as $2^{-\Delta\Delta Ct}$.

## Hydrogen peroxide ($H_2O_2$) analysis

$H_2O_2$ level was measured by Amplex Red Hydrogen Peroxide/Peroxidase assay kit (Life Technologies) [23]. The quantity of $H_2O_2$ was determined by comparing its absorbance with that of a $H_2O_2$ standard curve according to the manufacturer's instructions. Resorfurin formation due to Amplex Red (25 μM) oxidation by HRP (0.5 U/ml) bound to $H_2O_2$, was measured in Synergy H1 Hybrid Multi-Mode Reader (BioTek Instruments, Inc., Winooski, VT, US) at 530 nm (excitation) and 590 nm (emission). After an initial stabilization period, 10 μl of maintenance medium were added to the reaction mixture. A calibration curve was performed using $H_2O_2$ solutions as standard and its production level was expressed in nM. Controls in the absence of sample or HRP indicate that nonspecific probe oxidation was minimum (< 1%). Results were expressed as nmol/min mg protein.

**Table 2. Sequences of forward and reverse primers used to amplify the cytokines.**

| TARGET | FORWARD PRIMER | REVERSE PRIMER |
|---|---|---|
| IL-1 alpha | GGAGCTTGTCACCCCAAACT | TCCGAAGTCAAGGGGCTAGA |
| IL-1 beta | CTGAGCTCGCCAGTGAAATG | TGTCCATGGCCACAACAACT |
| IL-6 | TAGGACTGGAGATGTCTGAGGCT | GACCGAAGGCGCTTGTGGA |
| IL-8 | GGTGCAGTTTTGCCAAGGAG | TTCCTTGGGGTCCAGACAGA |
| IL-10 | GCTGGAGGACTTTAAGGGTTAC | GATGTCTGGGTCTTGGTTCTC |
| TNF-alpha | TGGCGTCTGAGGGTTGTTTT | CACCAAGGAAGTTTTCCGCTG |

https://doi.org/10.1371/journal.pone.0229613.t002

### 4-hydroxynonenal (4-HNE) levels

RHE 4-hydroxynonenal (4-HNE) levels before and after $O_3$ exposure in presence or not of HelixComplex, were evaluated by commercially available kit (BioSource, Milan, Italy). The measured amount of 4-HNE protein adduct was normalized with protein concentration measured with the Bradford method. A calibration curve was performed using 4-HNE standard. Results are expressed as μg 4-HNE/mg protein.

### Cytokine analysis

The levels of IL-6 and IL-10 were tested in culture supernatants by ELISA assay (Mybiosource, CA, USA) in all the different samples combinations. The ranges of detection were 469pg/ml-300pg/ml and 7.813-500pg/ml for IL-6 and IL-10, respectively. The assay sensitivity was <0.3pg/ml for IL-6 and 4.688pg/ml for IL-10.

### Statistics

Results were expressed as mean value ± SEM and represent the mean of triplicate determinations obtained in 3 separate experiments. Mann Whitney U-test was used to determine statistical significance (p values $< 0.05$ were considered significant).

## Results

### Evaluation of HelixComplex cytotoxicity

The first step of our study was to evaluate the cytotoxicity of the HelixComplex in human keratinocytes. Cells were treated with a range of concentrations (4–400μg/ml) of HelixComplex, and both LDH release (24hr) and morphology were assessed. As shown in Fig 1A and 1B, the treatment with HelixComplex did not shown any toxic effect at the doses tested. DMSO 10% was used as a positive control. In addition, treated keratinocytes with 400μg/ml of HelixComplex showed a normal morphology (Fig 1C).

### HelixComplex improves "in vitro" wound repair

Beside the cell viability, other important markers of keratinocytes physiological responses are their migration and proliferation properties that can be tested by the scratch wound assay. As shown in Fig 2A, pre-treatment with HelixComplex was able to improve the "in vitro" wound healing process after 24 hours respect to the control, where only 50% of the wound area was recovered ($p = 0.0003$) (Fig 2B).

### HelixComplex presents bio-adhesive properties on human keratinocytes

The efficacy of a skin treatment might be improved by the compound bio-adhesive properties; therefore we assessed the bio-adhesive rate of HelixComplex on human keratinocytes. As showed in Fig 2C, HelixComplex at the concentration of 400 μg/ml significantly prevent lectin binding to the keratinocytes surface ($p = 0.0036$), with a bio-adhesive property of about 80%.

### Effect of HelixComplex pre-treatment in ozone induced tissue damage

Tissue damage was evaluated by LDH release and as expected, right after $O_3$ exposure (T0) there was an increase levels of LDH of circa 40% that further increased at the later time point to 67% (T24). On the other hand, pretreatment with HelixComplex significantly prevented LDH release from the tissue after $O_3$ at T0 and T24 (28% and 30% respectively). (Fig 3A) ($p = 0.012$).

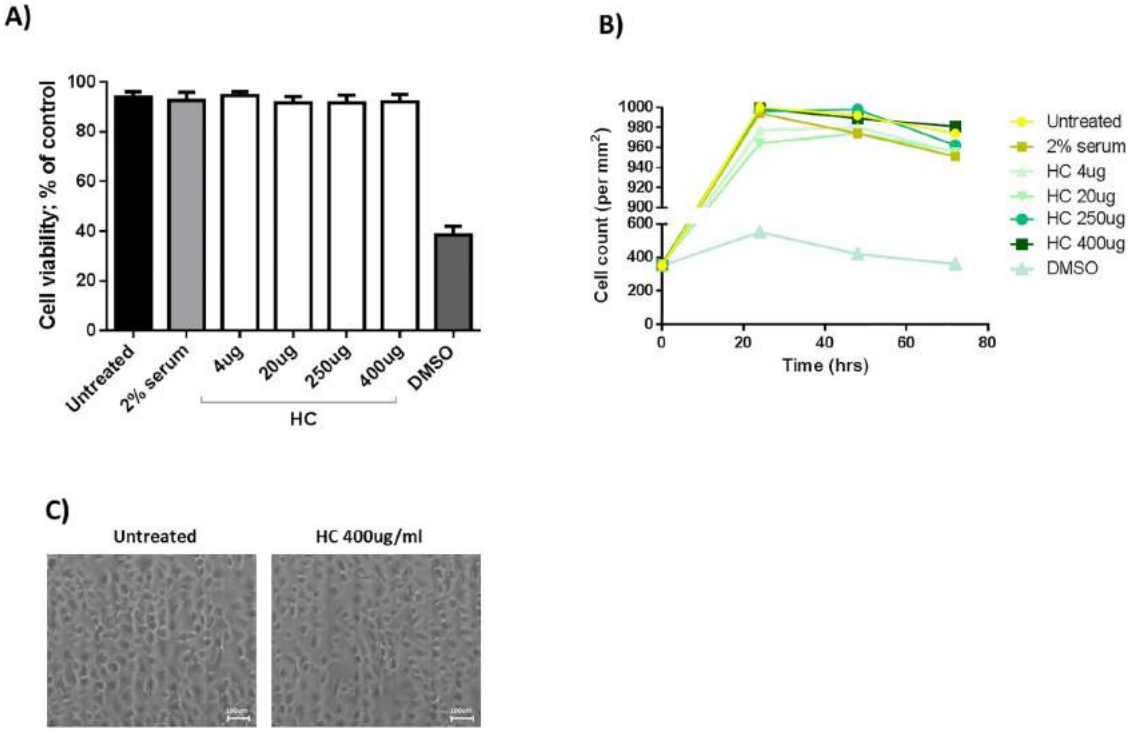


**Fig 1. Evaluation of HelixComplex cytotoxicity.** Keratinocytes were exposed to increasing doses of HelixComplex (HC) for up to 72 hours and cell viability was examined by MTT colorimetric assay. A) Cell viability was calculated at 24, 48 and 72 hours as percentage with respect to the control untreated cultures (set to 100% for each cell line). DMSO was used as positive control of cell death. B) Cell number was monitored over time by Trypan Blue staining. C) Representative images taken by light microscopy of monolayers of keratinocytes untreated or treated with HelixComplex at 48 hours. Magnification 100X.

https://doi.org/10.1371/journal.pone.0229613.g001

To evaluate the possible effects of HelixComplex on tissue morphology, H&E staining was performed on 3D skin tissues. As shown in Fig 3B, H&E histology reveals an intact structure of the epidermis where all the epidermis layers are clearly represented (basal, spinous, granulous and cornified epidermal layers). Respect to the control tissues, the HelixComplex treatment did not affect the RHE morphology over the experimental procedure. In particular, the stratum basale, containing mitotically active cells, was comparable in treated or non-treated tissues with a single layer of cuboidal-shaped cells. Concerning the stratum spinosum, the number of cell layers were similar in treated and non-treated samples and the characteristic stratum granulosum, with its grainy appearance and three to five layers of cells was analogues in all experimental conditions. Finally, the stratum corneum, the most superficial layer of the epidermis, did not show noticeable differences in the HelixComplex treated or non-treated tissues. As expected, while cytotoxicity was observed immediately after ozone exposure, the tissue morphology it has not been altered by a single pollutant insult.

## $H_2O_2$ and 4-HNE levels in RHE pretreated with HelixComplex

As mentioned previously, ozone damage is maily mediate by the formation of bioactive molecules among which $H_2O_2$ and 4-HNE. The Amplex Red-Horseradish Peroxidase (HRP) method confirmed that the exposure to ozone increased the levels of $H_2O_2$, while the pre-

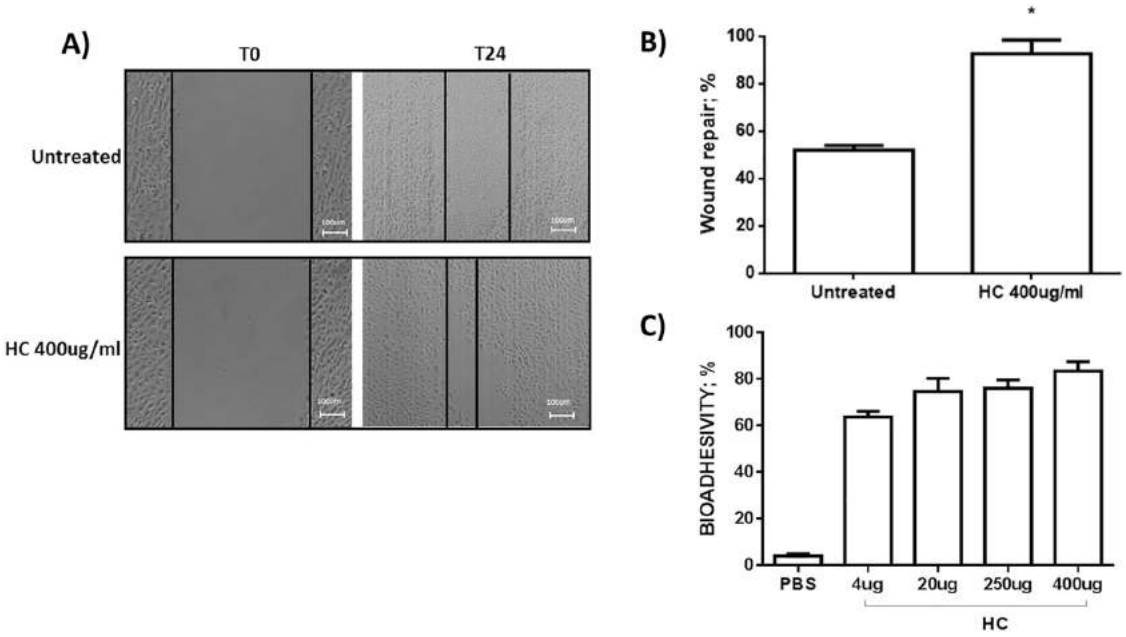


**Fig 2. Scratch-wound healing assay and bio-adhesivity. A**) scratch-wound healing assay, with representative images taken at the indicated time points post wounding; **B)** quantification of wound repair at 24 hours expressed as % of wound repair in comparison with the 0 hour time point ($^{*}p = 0.0003$); **C)** Bio-adhesivity of HelixComplex on human keratinocytes assessed by a lectin-based assay.

https://doi.org/10.1371/journal.pone.0229613.g002

treatment with 400 μg/ml of HelixComplex for 4 hours prevented is formation at both time points (T0 and T24) as depicted in Fig 3C.

Parallel with the $O_3$-induced increase in $H_2O_2$in the medium, we observed an increase in intracellular levels of 4-Hydroxynonenal (4-HNE). Also in this case the increased levels of 4HNE protein adducts (T24) were kept at the baseline levels by the pre-treatment with Helix-Complex (Fig 3D).

## HelixComplex prevents ozone induced tissue pro-inflammatory status

A well-documented connection of altered redox homeostasis is with the inflammatory process.

The induction of inflammation was evaluated by the analysis of Th1 (IL-1 beta; IL-6; IL-8) and Th2 (IL-10) cytokines. As shown in Fig 4, after 24hr of exposure, HelixComplex pre-treatment was able to prevent ozone induced increase of both IL-1beta and IL-8 mRNAs (Fig 4A and 4B). IL-6 mRNA was 6 times higher at T24 after $O_3$ exposure and the pre-treatment with HelixComplex partially prevented (50%) its expression (Fig 4C) at both mRNA (left panel) and protein (right panel) levels ($p = 0.01$; $p<0.001$, respectively). IL-10 mRNA expression was not significantly modified by $O_3$ treatment, although the pre-treatment with HelixComplex induced an increase of its expression at T24 (Fig 4D) at both mRNA (left panel) and protein (right panel) levels ($p<0.001$; $p = 0.012$, respectively, Student t test).

## Discussion

The recent report of the European Environmental Agency showed that up to 30% of the urban population in the EU is exposed to $O_3$ concentrations above the EU limit, and circa 98% to concentrations above the WHO recommendations [24]. This is a constant threat for living

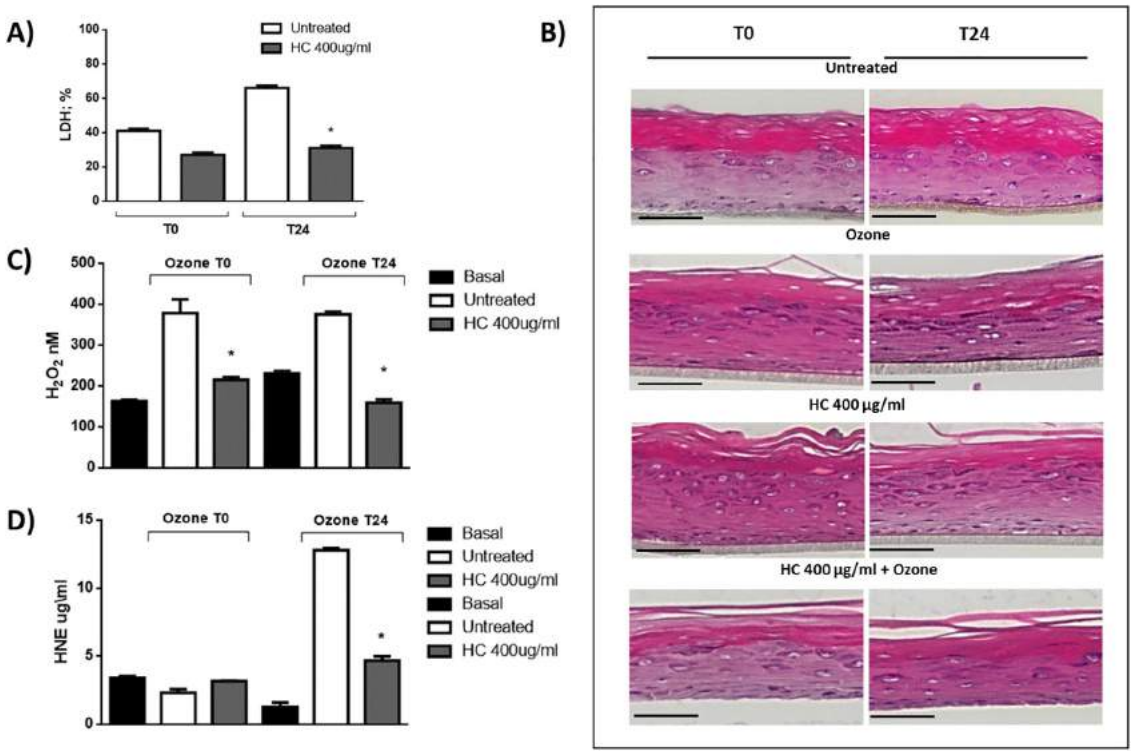


**Fig 3. Effect of HelixComplex pretreatment in ozone induce tissue damage.** A) Cytotoxicity evaluation was performed by LDH quantification. (*p = 0.012); B) Tissue morphology was evaluated by H&E staining. Basal, spinous, granulous and cornified epidermal layers are represented. Magnification 40X; Nikon Microphot FXA microscope (Nikon Instruments); C) The ability of $O_3$ to induce oxidative stress was evaluated by $H_2O_2$ levels in RHE exposed to $O_3$ and pre-treated with HelixComplex. (*T0 p = 0.02; T24 p = 0.0013); D) 4-Hydroxynonenal (4-HNE) levels (*T24 p = 0.001).

https://doi.org/10.1371/journal.pone.0229613.g003

organisms since $O_3$ is one of the most toxic compounds to which they are continuously exposed [25]. Therefore, the definition of new technologies to counteract the toxic effect of $O_3$ to skin would be of extreme help especially for the population living in polluted urban areas.

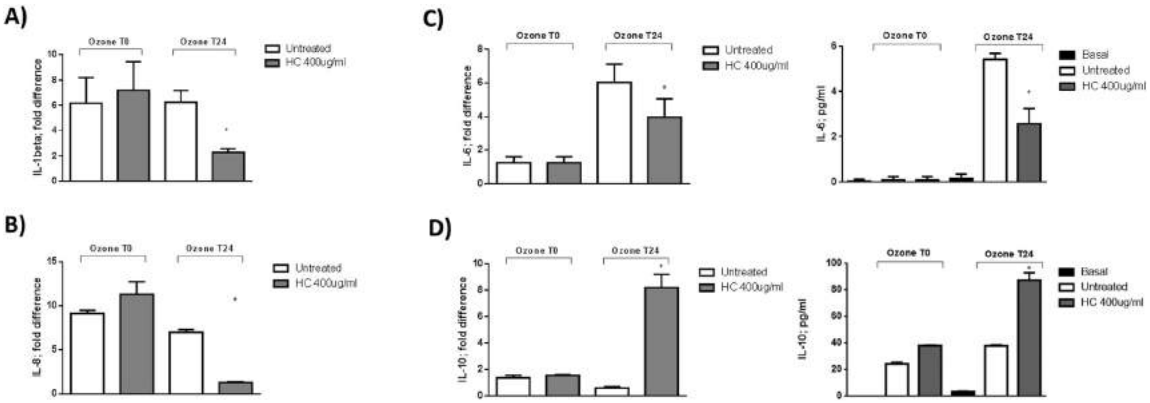


**Fig 4. Induction of molecular signals by HelixComplex treatment on RHE model.** A) IL-1beta mRNAs levels (*p = 0.0011), B) IL-8 (*p<0.001) mRNAs levels, C) IL-6 (*p = 0.0024) mRNAs (left panel) and protein (right panel) D) IL-10 (*p<0.0001) mRNAs (left panel) and protein (right panel). IL-6 (*p<0.001) and IL-10 (*p<0.0001) protein levels were determined by ELISA assay.

https://doi.org/10.1371/journal.pone.0229613.g004

In the present study we have tested the efficiency of HelixComplex, the purified mucus from *Helix aspersa muller*, as bio-adhesive, regenerative and protective agent against $O_3$ toxicity. Our study was able to demonstrate that HelixComplex treatment did not affect the morphology nor the cell viability of the models used in this study. On the other hand, our data suggest the ability of HelixComplex to improve "in vitro" wound healing, suggesting possible regenerative properties. These data confirm previous work where similar characteristics have been observed in skin fibroblasts. Because of the complex chemical composition of the HelixComplex [13], at this stage it is not possible to understand which one is the molecule more responsible for these beneficial properties. A recent study has compared the effect of HelixComplex with allantoin and glycolic acid which are among the main compounds present in HelixComplex. The results have shown that both allantoin and glycolic acid alone did not have any regenerative properties, suggesting that possibly the beneficial effect is a consequence not only of all the molecules present in the mixture but also of the specific ratio of which each component is present in the natural mucus. In addition, as reported previously, HelixComplex composition is also characterized by the presence of polyphenols that, although the exact type of polyphenols is not yet identified, it has been well recognized their ability to quench, either directly or indirectly, pro-oxidant molecules [26]. $O_3$ is a small molecule and has a strong oxidizing property that can act directly on the surface of the skin affecting the deeper layers of the cutaneous tissues via the generation of a cascade of bioactive compounds. Indeed, although it is not a radical species *per se*, $O_3$ is able to oxidize components of the cell membrane, mainly lipids, generating classical radical species such as hydroxyl radicals that, in turn, drive the production of cytotoxic, non-radical species including aldehydes [27]. It should be mentioned that $O_3$ is not able to penetrate the tissue and its action is completely consumed in the outmost layer of the skin, the stratum corneum (SC) which is rich in fatty acids, cholesterol and ceramide, all molecules easily prone to be oxidized. It has been shown that once $O_3$ interacts with the SC is able to generate the formation of secondary messengers able to trigger signaling cascades across the different layers of skin, leading to pro-oxidative and inflammatory processes [28]. For this reason, in our study we have used 3D skin model, to mimic the interaction that ozone has with cutaneous tissues. Indeed, this model is characterized by the presence of all the epidermis layers including the stratum corneum and is one of the most reliable model to study cutaneous toxicology [29]. Previous and recent works have shown that ozone exposure was able to increase levels of 4-HNE in human skin confirming the concept previously advanced by Pryor et al. [30–32] in relation to the respiratory tract. According to this hypothesis, the exposure of non-cellular constituents of surface epithelial cells to $O_3$ is capable of generating toxic peroxidation products among which 4-HNE and $H_2O_2$ seem to be the most responsible for ozone toxicity [33].

This led us determine the levels of both 4-HNE and $H_2O_2$ in our system and as expected $O_3$ exposure clearly increase both molecules. Of note is that pre-treatment with HelixComplex prevented the formation of 4-HNE and $H_2O_2$ suggesting either direct or indirect antioxidant property. It is possible that the presence of polyphenols could activate defensive mechanisms such as the NRF2 pathways and this can trigger an antioxidant response able to prevent or quench $O_3$-induced tissue redox imbalance [26]. For instance, in our previous work, the combination of different natural molecules such as Ferulic Acid, vitamin E and vitamin C were able to prevent ozone induced oxidative damage in keratinocytes, in RHE and also in human skin via NRF2 activation, suggesting that ozone noxious effect can be modulated by tissue antioxidant responses [10, 32].

Modification of redox homeostasis has been associated with a pro-inflammatory status [34], therefore in our work we have evaluated the cutaneous induction of pro- and anti-inflammatory cytokines upon ozone exposure. As observed in this study, ozone exposure clearly induced the levels of IL-8, IL-6 and IL-1beta, all cytokines associated to skin inflammatory

conditions. It should be mentioned that all those pro-inflammatory mediators have NFkB in their promoter, which is a well-known redox sensitive transcriptional factor. Several groups, including ours, were able to clearly show that ozone is able to induce NFkB activation, not only in skin but in other target tissues including lungs [35]. Therefore, it is possible that the formation of pro-oxidant molecules such as $H_2O_2$ lead to the activation of NFkB which then will transcribe for pro-inflammatory mediators that will contribute to an inflammatory skin condition [36]. Of note, pre-treatment with HelixComplex was able to significantly and clearly prevent the induction of pro-inflammatory cytokines while appeared to induce the anti-inflammatory mediator IL-10, suggesting a clear anti-inflammatory property.

## Conclusion

This study has further evidenced the ability of HelixComplex to counteract ozone-induced skin damage highlighting its future usage as a new anti-pollution topical technology. Whether its beneficial properties can be extended also to other pollutants is still under investigation and in addition, in vivo and human studies need to be performed to better confirm the HelixComplex antipollution properties.

## Supporting information

**S1 Fig. HaCaT cell line certificate of analysis.**
(PDF)

**S2 Fig. 3D models experimental procedure.**
(TIF)

## Acknowledgments

We thank HelixPharma s.r.l. to supply HelixComplex and Professor Stefano Manfredini (University of Ferrara) for fruitful discussions. We thank Iva Pivanti for the technical support. We also thank the medical writer P.P. for proofreading the manuscript.

## Author Contributions

**Conceptualization:** Carlo Cervellati, Claudio Trapella, Roberta Rizzo, Giuseppe Valacchi.

**Data curation:** Valentina Gentili, Daria Bortolotti, Roberta Rizzo.

**Formal analysis:** Valentina Gentili.

**Funding acquisition:** Claudio Trapella, Roberta Rizzo.

**Investigation:** Valentina Gentili, Daria Bortolotti, Mascia Benedusi, Andrea Alogna, Anna Guiotto.

**Methodology:** Valentina Gentili, Daria Bortolotti.

**Project administration:** Roberta Rizzo, Giuseppe Valacchi.

**Resources:** Anna Fantinati, Giulia Turrin.

**Supervision:** Giuseppe Valacchi.

**Visualization:** Valentina Gentili.

**Writing – original draft:** Carlo Cervellati, Roberta Rizzo, Giuseppe Valacchi.

**Writing – review & editing:** Valentina Gentili.

## References


1. McDaniel D, Farris P, Valacchi G. Atmospheric skin aging-Contributors and inhibitors. J Cosmet Dermatol. 2018; 17(2):124–137. https://doi.org/10.1111/jocd.12518 PMID: 29575554
2. Valacchi G, Sticozzi C, Pecorelli A, Cervellati F, Cervellati C, Maioli E. Cutaneous responses to environmental stressors. Ann N Y Acad Sci. 2012; 1271:75–81. https://doi.org/10.1111/j.1749-6632.2012.06724.x PMID: 23050967
3. Weber SU, Han N, Packer L. Ozone: an emerging oxidative stressor to skin. Curr Probl Dermatol. 2001; 29: 52–61. https://doi.org/10.1159/000060653 PMID: 11225201
4. Kousha T, Valacchi G. The air quality health index and emergency department visits for urticaria in Windsor, Canada. J Toxicol Environ Health A. 2015; 78(8): 524–33. https://doi.org/10.1080/15287394.2014.991053 PMID: 25849769
5. Valacchi G, Porada E, Rowe BH. Ambient ozone and bacterium Streptococcus: A link between cellulitis and pharyngitis. Int J Occup Med Environ Health. 2015; 28(4): 771–4. https://doi.org/10.13075/ijomeh.1896.00267 PMID: 26216315
6. Xu F, Yan S, Wu M, Li F, Xu X, Song W et al. Ambient ozone pollution as a risk factor for skin disorders. Br J Dermatol. 2011; 165: 224–225. https://doi.org/10.1111/j.1365-2133.2011.10349.x PMID: 21457212
7. Larrieu S, Lefranc A, Gault G, Chatignoux E, Couvy F, Jouves B et al. Are the short-term effects of air pollution restricted to cardiorespiratory diseases? Am J Epidemiol. 2009; 169: 1201–1208. https://doi.org/10.1093/aje/kwp032 PMID: 19342399
8. Kousha T, Valacchi G. The air quality health index and emergency department visits for urticaria in Windsor, Canada. J Toxicol Environ Health. 2015; 78: 524–533.
9. Pryor WA. Mechanisms of radical formation from reactions of ozone with target
10. Valacchi G, Sticozzi C, Belmonte G, Cervellati F, Demaude J, Chen N et al. Vitamin C Compound Mixtures Prevent Ozone-Induced Oxidative Damage in Human Keratinocytes as Initial Assessment of Pollution Protection. PLoS One 2015; 10(8):e0131097. https://doi.org/10.1371/journal.pone.0131097 PMID: 26270818
11. Newar J. & Ghatak A. Studies on the Adhesive Property of Snail Adhesive Mucus. Langmuir. 2015; 31: 12155–12160. https://doi.org/10.1021/acs.langmuir.5b03498 PMID: 26480243
12. Bortolotti D, Trapella C, Bernardi T, Rizzo R. Letter to the Editor: Antimicrobial properties of mucus from the brown garden snail Helix aspersa. Br J Biomed Sci. 2016; 73: 49–50. https://doi.org/10.1080/09674845.2016.1155377 PMID: 27182678
13. Trapella C, Rizzo R, Gallo S, Alogna A, Bortolotti D, Casciano F et al. HelixComplex snail mucus exhibits pro-survival, proliferative and pro-migration effects on mammalian fibroblasts. Sci Rep. 2018; 8 (1):17665. https://doi.org/10.1038/s41598-018-35816-3 PMID: 30518946
14. López Angulo DE, do Amaral Sobral PJ. Characterization of gelatin/chitosan scaffold blended with aloe vera and snail mucus for biomedical purpose. Int J Biol Macromol. 2016; 92: 645–653. https://doi.org/10.1016/j.ijbiomac.2016.07.029 PMID: 27453523
15. Sticozzi C, Pecorelli A, Belmonte G, Valacchi G. Cigarette smoke affects ABCAI expression via liver X receptor nuclear translocation in human keratinocytes. Int J Mol Sci. 2010; 11: 3375–3386. https://doi.org/10.3390/ijms11093375 PMID: 20957101
16. Magnani ND, Muresan XM, Belmonte G, Cervellati F, Sticozzi C, Pecorelli A et al. Skin Damage Mechanisms Related to Airborne Particulate Matter Exposure. Toxicol Sci. 2016; 149: 227–236. https://doi.org/10.1093/toxsci/kfv230 PMID: 26507108
17. Cervellati F, Muresan XM, Sticozzi C, Gambari R, Montagner G, Forman HJ et al. Comparative effects between electronic and cigarette smoke in human keratinocytes and epithelial lung cells. Toxicol In Vitro. 2014; 28: 999–1005. https://doi.org/10.1016/j.tiv.2014.04.012 PMID: 24809892
18. Lisowska E, Duk M, Wu AM. Preparation of Biotinylated Lectins and Application in Microtiter Plate Assays and Western Blotting. In: Meier T., Fahrenholz F. (eds) A Laboratory Guide to Biotin-Labeling in Biomolecule Analysis. BioMethods. Birkhäuser Basel; 1996. pp 115–129.
19. Valacchi G, Pecorelli A, Mencarelli M, Carbotti P, Fortino V, Muscettola M et al. Rottlerin: a multifaced regulator of keratinocyte cell cycle. Exp Dermatol. 2009; 18: 516–521. https://doi.org/10.1111/j.1600-0625.2008.00816.x PMID: 19492998
20. Lim Y, Phung AD, Corbacho AM, Aung HH, Maioli E, Reznick AZ et al. Modulation of cutaneous wound healing by ozone: differences between young and aged mice. Toxicol Lett. 2006; 160: 127–134. https://doi.org/10.1016/j.toxlet.2005.06.013 PMID: 16129572
21. Muresan XM, Narzt MS, Woodby B, Ferrara F, Gruber F, Valacchi G. Involvement of cutaneous SR-B1 in skin lipid homeostasis. Arch Biochem Biophys. 2019; 666: 1–7. https://doi.org/10.1016/j.abb.2019.03.005 PMID: 30876920

22. Bortolotti D, Gentili V, Rotola A, Cultrera R, Marci R, Di Luca D et al. HHV-6A infection of endometrial epithelial cells affects immune profile and trophoblast invasion. Am J Reprod Immunol. 2019; 82: e13174. https://doi.org/10.1111/aji.13174 PMID: 31338899

23. Sticozzi C, Belmonte G, Pecorelli A, Arezzini B, Gardi C, Maioli E et al. Cigarette smoke affects keratinocytes SRB1 expression and localization via $H_2O_2$ production and HNE protein adducts formation. PLoS One 2012; 7:e33592. https://doi.org/10.1371/journal.pone.0033592 PMID: 22442701

24. EEA. Air quality in Europe—2017 report; European Environment Agency, Kongens Nytorv 6, 1050 Copenhagen, Denmark. EEA Technical Report. 2017. 80 p. https://www.eea.europa.eu/publications/air-quality-in-europe-2017.

25. Cross CE, Valacchi G, Schock B, Wilson M, Weber S, Eiserich J et al. Environmental oxidant pollutant effects on biologic systems: a focus on micronutrient antioxidant-oxidant interactions. Am J Respir Crit Care Med. 2002; 166: S44–50. https://doi.org/10.1164/rccm.2206015 PMID: 12471088

26. Forman HJ, Davies KJ, Ursini F. How do nutritional antioxidants really work: nucleophilic tone and parahormesis versus free radical scavenging in vivo. Free Radic Biol Med. 2014; 66: 24–35. https://doi.org/10.1016/j.freeradbiomed.2013.05.045 PMID: 23747930

27. Pecorelli A, Woodby B, Prieux R, Valacchi G. Involvement of 4-hydroxy-2-nonenal in pollution-induced skin damage. Biofactors 2019; 45: 536–547. https://doi.org/10.1002/biof.1513 PMID: 31087730

28. Valacchi G, Fortino V, Bocci V. The dual action of ozone on the skin. Br J Dermatol. 2005; 153: 1096–1100. https://doi.org/10.1111/j.1365-2133.2005.06939.x PMID: 16307642

29. Dellambra E, Odorisio T, D'Arcangelo D, Failla CM, Facchiano A. Non-animal models in dermatological research. ALTEX 2019; 36: 177–202. https://doi.org/10.14573/altex.1808022 PMID: 30456412

30. Valacchi G,van der Vliet A, Schock BC, Okamoto T, Obermuller-Jevic U, Cross CE et al. Ozone exposure activates oxidative stress responses in murine skin. Toxicology. 2002; 179: 163–170. https://doi.org/10.1016/s0300-483x(02)00240-8 PMID: 12204552

31. Valacchi G, Weber SU, Luu C, Cross CE, Packer L. Ozone potentiates vitamin E depletion by ultraviolet radiation in the murine stratum corneum. FEBS Lett. 2000; 466: 165–168. https://doi.org/10.1016/s0014-5793(99)01787-1 PMID: 10648834

32. Valacchi G, Pecorelli A, Belmonte G, Pambianchi E, Cervellati F, Lynch S et al. Protective Effects of Topical Vitamin C Compound Mixtures against Ozone-Induced Damage in Human Skin. J Invest Dermatol. 2017; 137: 1373–1375. https://doi.org/10.1016/j.jid.2017.01.034 PMID: 28219661

33. Sticozzi C, Pecorelli A, Romani A, Belmonte G, Cervellati F, Maioli E, et al. Tropospheric ozone affects SRB1 levels via oxidative post-translational modifications in lung cells. Free Radic Biol Med. 2018; 126: 287–295. https://doi.org/10.1016/j.freeradbiomed.2018.07.007 PMID: 30059777

34. Lei Y, Wang K, Deng L, Chen Y, Nice EC, Huang C. Redox regulation of inflammation: old elements, a new story. Med Res Rev. 2015; 35: 306–340. https://doi.org/10.1002/med.21330 PMID: 25171147

35. Bromberg PA. Mechanisms of the acute effects of inhaled ozone in humans. Biochim Biophys Acta. 2016; 1860: 2771–2781. https://doi.org/10.1016/j.bbagen.2016.07.015 PMID: 27451958

36. Kabe Y, Ando K, Hirao S, Yoshida M, Handa H. Redox regulation of NF-kappaB activation: distinct redox regulation between the cytoplasm and the nucleus. Antioxid Redox Signal. 2005; 7: 395–403. https://doi.org/10.1089/ars.2005.7.395 PMID: 15706086

Journal of Inorganic Biochemistry 199 (2019) 110787

Contents lists available at ScienceDirect

Journal of Inorganic Biochemistry

journal homepage: www.elsevier.com/locate/jinorgbio

# A new amido-phosphine of dichloroacetic acid as an active ligand for metals of pharmaceutical interest. Synthesis, characterization and tests of antiproliferative and pro-apoptotic activity

Lorenza Marvelli[a], Valeria Ferretti[a], Valerio Bertolasi[a], Ilaria Lampronti[b], Roberto Gambari[b], Claudio Trapella[a], Giulia Turrin[a], Francesca Bonotto[a], Antonio Moriello[a], Paola Bergamini[a,*]

[a] Dipartimento di Scienze Chimiche e Farmaceutiche, Università degli Studi di Ferrara, via L. Borsari 46, 44121 Ferrara, Italy
[b] Dipartimento di Scienze della Vita e Biotecnologie, Sezione di Biochimica e Biologia Molecolare, Università degli Studi di Ferrara, via Fossato di Mortara 74, 44121 Ferrara, Italy

ARTICLE INFO

*Keywords:*
Inorganic drugs
Anticancer complexes
Dichloroacetic acid
Cell apoptosis
Antiproliferative activity

ABSTRACT

We herein describe the synthesis and characterization of the new amido-phosphinic ligand 3,7-bis(dichloroacetyl)-1,3,7-triaza-5-phosphabicyclo[3.3.1]nonane (DCP), a derivative of dichloroacetic acid (DCA), whose ability to reverse the suppressed mitochondrial apoptosis in cancer cells is known. DCP was obtained by a double N-acylation of PTA (1,3,5-triaza-7-phosphaadamantane) occurring with loss of $CH_2$, in appropriate conditions. Due to the hindered rotation around the amidic CN bonds, three rotameric forms of DCP were observed, whose ratio in solution was dependent on the solvent, while the X-ray crystal structure of DCP showed an opposite orientation of the two amidic carbonyl groups (*anti* rotamer). The lipophilic, air and thermally stable DCP was found able to act regiospecifically as a P-donor ligand toward soft metal ions. By ligand substitution on appropriate precursors, we obtained the complexes **1–9**, where proapoptotic DCA is associated with metal ions of known cytotoxic activity on cancer cells ($Pt^{2+}$, $Pd^{2+}$, $Ru^{2+}$, $Re^{+}$, $Au^{+}$). The antiproliferative activity of DCP and its complexes was tested in vitro, in comparison with cisplatin, on three human tumor cell lines: A2780 (ovarian cisplatin-sensitive), A2780*cis* (ovarian cisplatin-resistant) and K562 (erythroleukemic). The results showed that the simultaneous presence of DCP (containing two residues of proapoptotic DCA) and Pt(II) produces the best performances with respect to non-platinum complexes. Experiments of pro-apoptotic activity indicated that the antiproliferative activity of the most active DCP-Pt(II) complexes is associated with induction of apoptosis.

## 1. Introduction

The aliphatic phosphine PTA (1,3,5-triaza-7-phosphaadamantane) is a stable water soluble ligand widely used in metal complexes for many purposes, including catalysis [1–5], new materials [6–8], and metal-based therapeutics [9–12]. The basic structure can be modified at each position under appropriate conditions. We [13–17] and others [18–21] described several N-alkylation reactions, which occurred with complete regioselectivity on a single nitrogen producing cationic derivatives still able to give metal coordination through phosphorus donor (Fig. 1a). In 2004 and in 2007, two examples of PTA derivatives obtained by N-acylation were reported: 3,7-diacetyl-1,3,7-triaza-5-phosphabicyclo[3.3.1]nonane (DAPTA) and 3,7-diformyl-1,3,7-triaza-5-phosphabicyclo[3.3.1]nonane (DFPTA) (Fig. 1b) [22–23].

While the N-alkylation of PTA generates quaternary ammonium cations, the acylation involves two nitrogen atoms, with loss of a $CH_2$ bridge, producing neutral structures where the adamantane-like cage is open.

Inspired by these molecules, DAPTA and DFPTA, due to our interest in metal-based drugs, we designed the analogue 3,7-bis(dichloroacetyl)-1,3,7-triaza-5-phosphabicyclo[3.3.1]nonane (DCP), where PTA is functionalized with dichloroacetyl groups, (Fig. 2).

Dichloroacetic acid (DCA) is an orphan drug used for lactic acidosis, but recently it has attracted attention also as potential anticancer because of its ability to interfere selectively with the mechanism that makes cancer cells resistant to normal apoptotic processes. Several reports demonstrated that the DCA antitumor activity (also overcoming resistance to usual chemotherapy) is related to its ability to re-activate mitochondrial metabolism in tumor cells [24–25]. Nevertheless, its application is limited by the high concentrations needed for significant

* Corresponding author.
*E-mail address:* bgp@unife.it (P. Bergamini).

https://doi.org/10.1016/j.jinorgbio.2019.110787
Received 3 April 2019; Received in revised form 18 July 2019; Accepted 19 July 2019
Available online 22 July 2019

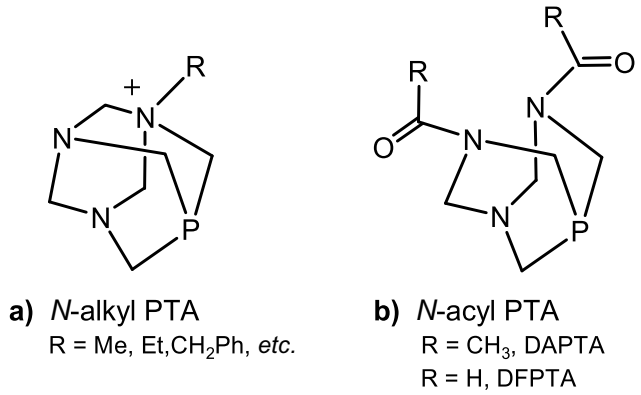


**Fig. 1.** General structures of *N*-alkyl PTA (**a**) and *N*-acyl PTA (**b**).

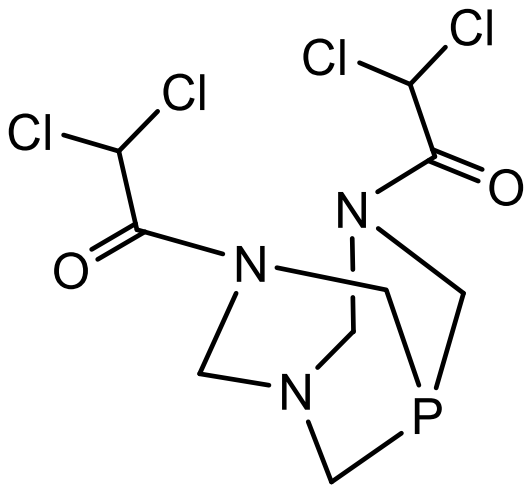

**Fig. 2.** DCP, 3,7-bis(dichloroacetyl)-1,3,7-triaza-5 phosphabicyclo[3.3.1] nonane.

therapeutic effect, producing detrimental side effects involving the nervous system [26]. For this reason there is a great interest in the development of DCA derivatives hopefully provided with a better therapeutic index. This aim has been previously pursued introducing DCA in large lipophilic molecules as an ester [27] or an amide [28].

In this work we propose the design and development of the new phosphino-amide DCP, potentially able to behave both as lipophilic carrier of DCA and as ligand for metal ions. DCP is the first reported example of phosphinic derivative of dichloroacetic acid. The chemical aims of the present work are to optimize its synthesis, to characterize it both in solution and in the solid state and to screen its ability to act as a ligand for a variety of metal ions. The metal complexes of DCP, combining dichloroacetic acid and an active metal ion (e.g. $Pt^{2+}$, $Pd^{2+}$, $Ru^{2+}$) in the same molecule, could act as anticancer drugs provided of dual therapeutic action, pro-apoptotic (mitochondria reactivator) and antiproliferative (DNA or essential proteins damaging agents) toward cancer cells. A series of biochemical experiments have been conducted in order to see if the presence of a dichloroacetic derivative boosts the effect of metal complexes.

## 2. Results and discussion

### 2.1. Synthesis and characterization of 3,7-bis (dichloroacetyl)-1,3,7-triaza-5-phosphabicyclo[3.3.1]nonane (DCP)

The reported N-acyl derivatives of PTA, DAPTA [22] and DFPTA [23], were obtained by treating PTA with an excess of acetyl anhydride and formyl anhydride respectively, in water. Following the same procedure with DCA anhydride, only PTA was recovered in its N-protonated form, as shown by the small shift in the $^{31}P$ signal (from −98 ppm of PTA to −91 ppm of $PTAH^+$) [29]. In fact the formation of DCP implies the releasing of two equivalents of dichloroacetic acid (Scheme 1), a much stronger acid than acetic and formic acid, released in the formation of DAPTA e DFPTA respectively. DCA is able to protonate PTA, reducing its nucleophilic power and therefore inhibiting its reaction with the anhydride.

We found that the basicity of the reaction medium is the crucial parameter in the synthesis of DCP. The yield increased from *ca* 10% obtained using $NaHCO_3$ (pH 8.35) to *ca* 74.5% with $Na_2CO_3$ (0.12 M, pH 11.7). The volume of the basic solution was modulated to have $Na_2CO_3$ in molar excess with respect to the DCA anhydride. In fact the chloroacetic acid, progressively formed by the reaction, reacts with part of sodium carbonate giving a $NaHCO_3/Na_2CO_3$ buffer solution (measured pH = 9.3), which prevents the protonation of PTA.

The new amido-phosphine DCP was characterized by several techniques. In HPLC-ESI MS, DCP presents a single peak at 368 (M + 1), but the NMR investigation in DMSO shows the presence of three rotamers due to the double bond character of the amidic N═C−O group (Fig. 3) [30].

Also for DAPTA [31] and DFPTA [23] several species were observed by NMR, whose number was depending on the solvent.

In the case of DCP, in DMSO, the $^{31}P$ NMR showed three single signals at $\delta$ −78.5, −68.8 e –68.4 ppm in a 1:7:1 estimated intensity ratio. The $^1H$ NMR spectrum in DMSO-$d_6$ showed four singlets for the $COCHCl_2$ group of DCA at 7.07, 7.18, 7.20 and 7.28 ppm, with an intensity ratio of 1:1:4:4, exactly reproducible in different preparations. We assigned the pair of intense signals at 7.20 and 7.28 ppm to the two nonequivalent $COCHCl_2$ groups of the *anti* rotamer. The 1:1:8 ratio was in fair agreement with that observed in $^{31}P$ NMR (1:1:7).

Trying to see if the rotational barrier could be overtaken, we tried high temperature NMR experiments in DMSO-$d_6$. In $^{31}P$ NMR, one signal was observed at 120 °C, but its accentuate broadening did not allow to conclude if it was effectively a single peak or if it contained other signals in its width [32].

In acetone, DCP is present as a single rotamer (*anti*). In $^{31}P$ NMR, a single peak was found at −69.2 ppm and the $^1H$ NMR spectrum showed two equally intense singlets, due to the inequivalent $CHCl_2$ groups of the *anti* rotamer at 6.82 and 6.90 ppm. Nine signals due to the ten cage protons were also observed between 3.5 and 5.7 ppm. We assigned them on the basis of a COSY experiment. In Table 1 the $^1H$ NMR data in acetone of the ten cage protons of DCP and their attributions are compared with the corresponding reported for DAPTA by Laguna et al. [31].

All the geminal diastereotopic protons of $CH_2$ (except Hc) gave distinct signals. This observation supports the identification of DCP in acetone as the *anti* rotamer, the only one where the P atom is a stereogenic center because the two N═$COCHCl_2$ groups have different geometries (Z and E) [33].

Concerning the solid state, DCP was re-crystallized by slow cooling of an acetone solution taken to 45 °C and the X-ray crystal structure was acquired.

The crystal structure of DCP confirms that the molecule is present as the *anti* rotamer, in view of the relative position of the $CHCl_2C$═O groups (Fig. 4). The C1 atom lies on the crystallographic twofold rotation axis, so that P1 and N1 atoms are interchangeable; the disorder has been modelled refining the two atoms on the same position and giving them a 50% occupancy. As a consequence, C1-P1/N1 distances have high estimated standard deviations and are respectively shorter/longer than the standard ones (Tables 2 and 3).

Although DCP and DAPTA have a similar structure, their solubility in water is remarkably different. The presence of four bulky hydrophobic chlorine atoms enormously decreases the solubility in water ($S_M$ of DCP < 2.7 μM) with respect to the non-chlorinated analogue

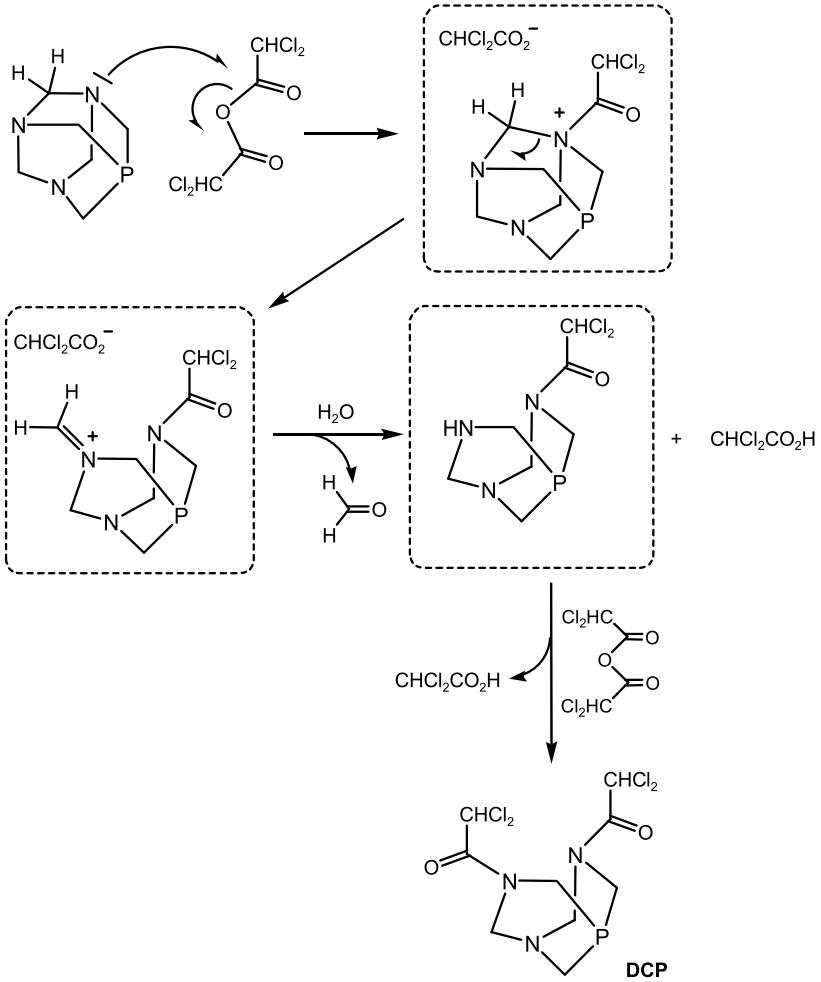


**Scheme 1.** Synthesis of 3,7-bis(dichloroacetyl)-1,3,7-triaza-5-phosphabicyclo[3.3.1]nonane (DCP).

DAPTA, reported as the most water soluble phosphine ($S_M$ = 7.4 M) [22]. DCP is soluble in a 10:1 DMSO/$H_2O$ mixture ($S_M = 2.5 \cdot 10^{-2}$ M), where is stable for at least 10 days at $^{31}$P NMR observation, and also in DMF, in acetone and in $CH_3CN$.

### 2.2. Coordination of 3,7-bis(dichloroacetyl)-1,3,7-triaza-5-phosphabicyclo [3.3.1]nonane (DCP) to metal ions

The acylation of PTA involves two nitrogen atoms, leaving the phosphorus atom available for coordination to metals, including $Pt^{2+}$, $Pd^{2+}$, $Ru^{2+}$, $Re^{+}$ and $Au^{+}$ which are exploited or under investigation for their anticancer activity.

We realized the coordination of DCP to these metals, obtaining products **1**–**9**, where the new ligand is introduced following the pattern of complexes whose cytotoxic activity has been reported.

#### 2.2.1. Pt(II) complexes of DCP: synthesis and characterization

We prepared a series of Pt(II) complexes (**1**–**4**) of the new ligand DCP, bearing an increasing number of DCA residues (Fig. 5).

Following the classical scheme of Pt anticancer drugs, two neutral ligands, two anionic ligands, *cis* disposition, we designed *cis*-[$PtCl_2(DCP)_2$] (**2**), which was obtained in good yield (79%) through the direct reaction of DCP with commercial $K_2PtCl_4$ (2:1 ratio) in $CH_3CN$.

The $^{31}$P NMR spectrum of *cis*-[$PtCl_2(DCP)_2$] appeared different in different solvents: in acetone it showed two singlets with satellites at −27.3 ($^1J_{PtP}$ = 3389 Hz) and –27.1 ($^1J_{PtP}$ = 3341 Hz) which we attributed to the two diastereomeric forms (*meso* and racemate), due to

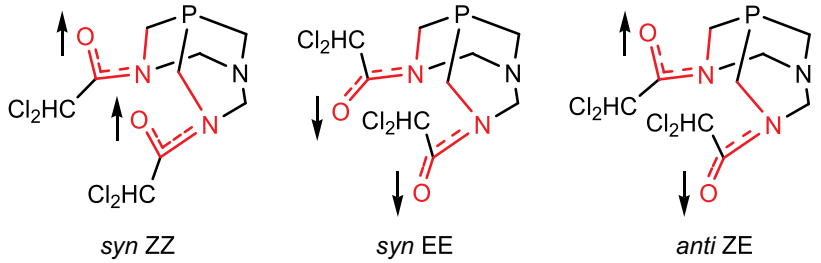


**Fig. 3.** Three rotameric forms of DCP. (For interpretation of the references to color in this figure, the reader is referred to the web version of this article.)

**Table 1**
$^1$H NMR data in acetone and attributions of the ten cage protons of DCP and DAPTA.

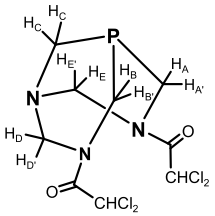


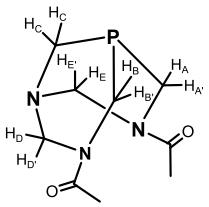


| | DCP<br>Acetone-$d_6$, δ (ppm); $J$(Hz) | DAPTA<br>$CDCl_3$, δ (ppm); $J$(Hz), [31] |
|---|---|---|
| $H_A$ | 3.60 dt, $^2J_{HH}$ = $^2J_{PH}$ 15.1, $^2J_{HH}$ 2.3 | 3.20 dt, $^2J_{HH}$ = $^2J_{PH}$ 15.2, $^4J_{HH}$ 2.5 |
| $H_C$ | 3.78 d, $^2J_{PH}$ 11.3 | 3.51 d, $^2J_{PH}$ 11.4 |
| $H_B$ | 4.15 dt, $^2J_{HH}$ = $^2J_{PH}$ 14.7, $^4J_{HH}$ 2.3 | 3.79 ddd, $^2J_{HH}$ 15.4, $^2J_{PH}$ 4.7, $^4J_{HH}$ 2.8 |
| $H_D$ | 4.32 d, $^2J_{HH}$ 13.7 | 3.95 d, $^2J_{HH}$ 14.0 |
| $H_B$ | 4.63 d, $^2J_{HH}$ 15.0 | 4.28 d, $^2J_{HH}$ 15.4 |
| $H_E$ | 4.78 d, $^2J_{HH}$ 13.9 | 4.53 d, $^2J_{HH}$ 13.8 |
| $H_A$ | 4.85 d, $^2J_{HH}$ 15.6 | 5.25 dd, $^2J_{HH}$ 15.2, $^2J_{PH}$ 2.0 |
| $H_E$ | 5.22 d, $^2J_{HH}$ 13.9 | 4.93 d, $^2J_{HH}$ 13.8 |
| $H_D$ | 5.62 d, $^2J_{HH}$ 13.7 | 5.79 d, $^2J_{HH}$ 14.0 |

the presence of two phosphorus atoms, stereogenic in the *anti* form of DCP.

In DMSO six $^{31}$P NMR signals of different intensity were observed at −28.0, −27.8, −27.7, −26.8, −26.6 and –26.5 ppm, with similar values of $^1J_{PtP}$ (ca. 3400 Hz). This pattern is reproducible for different preparations and it did not change at a daily observation for 15 days. The six signals are probably due to combinations of the three rotameric forms of the ligand DCP.

Crystals of complex **2** suitable for X-ray crystal structure determination were obtained from acetone and ether, (Fig. 6 and Tables 4 and 5).

The asymmetric unit is formed by a Pt complex and a co-crystallized water molecule. The complex presents a slightly distorted square-planar geometry, with the metal center bound through the phosphorous atom to two DCP (both in *anti* conformation) and two chlorine atoms in *cis* position; the distortion from the ideal geometry is mainly due to the steric encumbrance of the organic ligands. The Pt atom is located 0.016 Å above the least-squares plane formed by Cl1, Cl2, P1, P2 atoms. As for Pt—P and Pt—Cl distances, they are in good agreement with the mean values of 2.25(4) and 2.36(4) Å calculated for analogous complexes (1959 hits in the Cambridge Structural Database (CSD). Due to the lack of good hydrogen bonding donors, the crystal packing of the structure is characterized by the presence of a number of weak C—H…O interactions, listed in Table 5. The only exception is the Cl7…Cl9 interaction with an inter-halogen distance that is less than the sum of the van der Waals radii (Table 5). For this type of interactions there are two preferred geometries, according to the values assumed by $\theta_1$ (R1—X…X) and $\theta_2$ (X…X—R2) angles the first occurs when $\theta_1 = \theta_2$, while the second occurs when $\theta_1 \approx 180^\circ$ and $\theta_2 \approx 90^\circ$ [35]. In the present case the second arrangement has been found, the C16—Cl7…Cl9 and Cl7…Cl9—C18 angles measuring 172° and 100°, respectively. The co-crystallized water molecule is loosely bound, not being involved in any hydrogen bonding interaction.

In order to obtain the mixed phosphine complex *cis*-[$PtCl_2$(DCP)(PTA)] (**1**), bearing two dichloroacetic groups, we exploited the reaction of complex *cis*-[$PtCl_2(PTA)_2$] with one equivalents of DCP, a stronger nucleophile, in $CH_3CN$. The $^{31}$P NMR of **1** in acetone showed two broad signals at −28.0 ppm ($^1J_{PtP}$ ca. 3393 Hz) and –53.4 ppm ($^1J_{PtP}$ 3118 Hz) corresponding to coordinated DCP and coordinated PTA respectively.

The cationic complex **3**, containing three DCP ligands (corresponding to a total of six dichloroacetyl residues), was obtained by adding solid $K_2PtCl_4$ to a solution containing three eq. of DCP in $CH_3CN$, or alternatively by adding one eq. of DCP to complex **2**.

The identity of complex **3** was confirmed by ESI-MS giving a single peak corresponding to $M^+$ at 1332 *m/z*. The $^{31}$P NMR in DMSO showed a very broad signal centered at −27.6 ppm with $^1J_{PtP}$ = ca. 3362 Hz.

Complex **4**, containing two DCP ligands and two dichloroacetate ions as anionic ligands, carrying a total of six dichloroacetyl groups,

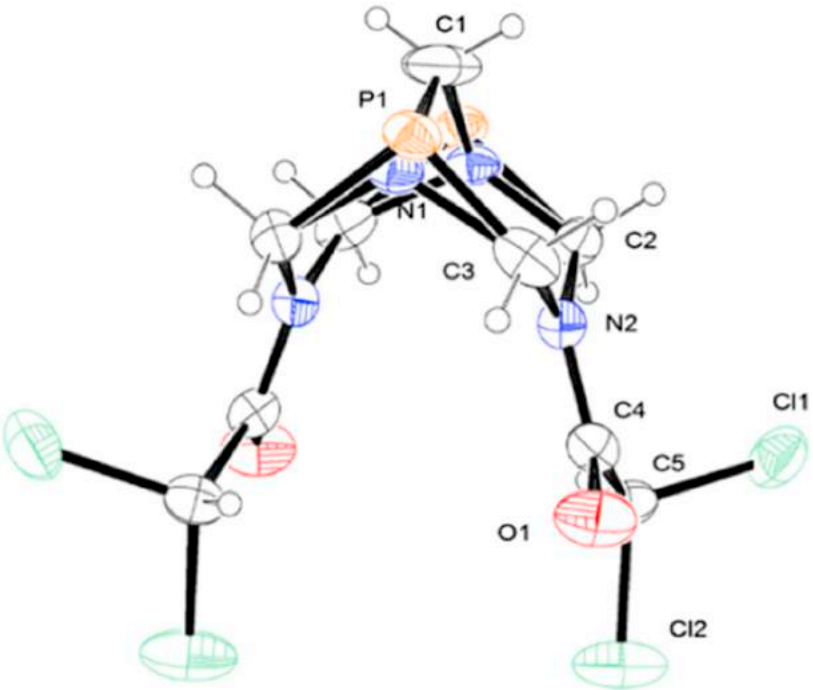


**Fig. 4.** ORTEP-III view and atom numbering scheme for DCP [34].
Thermal ellipsoids are drawn at the 40% probability level.

**Table 2**
Selected bond distances and angles (Å,°) for DCP.

| Bond distances | (Å) | Bond angles | (°) |
|---|---|---|---|
| C4−O1 | 1.225(4) | N2−C4−C5 | 117.5(3) |
| C5−Cl2 | 1.751(4) | C4−C5−Cl1 | 109.3(3) |
| C5−Cl1 | 1.781(4) | N2−C4−O1 | 123.4(3) |
| C1−P1 | 1.652(4) | C4−C5−Cl2 | 110.7(2) |
| C1−N1 | 1.633(9) | C5−C4−O1 | 119.0(3) |
| | | Cl1−C5−Cl2 | 109.8(2) |

**Table 3**
Structural parameters of hydrogen bonds (Å,°) for DCP.

| D−H…A | D−H | D…A | H…A | D−H…A |
|---|---|---|---|---|
| C2−H…O1$^{i}$ | 1.00(4) | 3.398(5) | 2.50(4) | 149(3) |
| C5−H…O1$^{i}$ | 0.87(5) | 3.128(5) | 2.27(5) | 173(4) |
| C3−H…O1$^{ii}$ | 0.90(4) | 3.431(5) | 2.58(4) | 157(4) |

Equivalent positions: (i) x,1-y, z + 1/2; (ii) 1-x,1-y,1-z.

was prepared in two steps from $[PtCO_3(DMSO)_2]$ (Scheme 2). The $^{31}P$ NMR of the carboxylate complex **4** showed two broad signals in DMSO (−36.1, $^{1}J_{PtP}$ = 3501 Hz and − 37.7, $^{1}J_{PtP}$ = 3467 Hz), and a single signal in acetone (−36.6 $^{1}J_{PtP}$ = 3577 Hz).

### 2.2.2. Coordination of DCP to Pd(II)

Although the use of Pd complexes in medicinal chemistry was largely less explored than Pt, some Pd complexes have revealed a promising cytotoxic action on several tumor cell lines [36]. For example, Pd(II) complexes containing PTA were reported, with IC50 values comparable to that of cisplatin on tumor cells A2780 (cisplatin-sensitive ovarian carcinoma), showing at the same time high cytotoxicity on the A2780*cis* line (cisplatin-resistant) [37–38].

The Pd complex *cis*-$[PdCl_2(DCP)_2]$ (**5**), (Fig. 7), analogue of the above described Pt complex **2**, was easily prepared in 88% yield by treating $PdCl_2$ with 2 eq. of DCP in $CH_2Cl_2$. The *cis* geometry is confirmed by the IR spectrum which showed the diagnostic pair of Pd−Cl stretching at 366 e 356 $cm^{-1}$. In ESI-MS a peak was observed at 935, corresponding to M + $Na^+$.

The cationic Pd complex **6**, (Fig. 7), was obtained from $PdCl_2$, treated in $CH_2Cl_2$ with 3 eq. of DCP. Although the $^{31}P$ and $^{1}H$ NMR are not very informative due to a diffuse signals broadening, the identity of **6** was unequivocally confirmed by ESI-MS where a single peak was observed, corresponding to $M^+$ at 1242 *m/z*.

### 2.2.3. Synthesis of $[RuCl_2(\eta^6$p-cymene)(DCP)] (7), a Ru(II) complex

Another metal ion belonging to Pt group metals, $Ru^{2+}$ has been studied for its peculiar properties in the anticancer action: it was reported that Ru(II) complexes with PTA, named "RAPTA" series, are provided of anti-metastatic activity [39–40]. Ru complexes of alkylPTA [41–43] and Ru(II) DAPTA complexes [44], provided of anti-proliferative activity, were also described.

We prepared $[RuCl_2(\eta^6$p-cymene)(DCP)], complex **7**, (Fig. 8), by treating the known chloro-bridged dimeric complex $[Ru_2Cl_4(\eta^6$p-cymene$)_2]$ with two equivalents of DCP in $CH_3CN$.

Alternatively complex **7** can be obtained also by acylation of Ru-coordinated PTA in $[RuCl_2(\eta^6$p-cymene)(PTA)], although with a low yield (30%). The $^{31}P$ NMR of complex **7** in DMSO showed three signals of the three rotamers at −13.0 ppm −7.8, −7.1 in about 1:9:3 ratio, the same found also in $^{1}H$ NMR, which displayed for the $CHCl_2$ group two close signals at 7.09 and 7.10 ppm due to the *anti*, major rotamer, a signal at 7.29 (*syn*), and finally another singlet at 7.42 ppm (*syn*). In acetone, where **7** is scarcely soluble, a single signal was observed in $^{31}P$ NMR at −8.1 ppm and in $^{1}H$ NMR only two signals belonging to the inequivalent $CHCl_2$ of the *anti* form were found at 6.82 and 6.90 ppm.

### 2.2.4. Synthesis of $[Re(CO)_3$(o-phen)DCP]$NO_3$ (8), a Re(I) complex

In a recent paper, a series of cationic complexes of Re(I) $[Re(CO)_3$(*o*-phen)$(PR_3)]^+$ (*o*-phen = 1,10-phenanthroline; $PR_3$ = PTA, THMP, DAPTA) have been considered for photoactivated anticancer activity in vitro [45]. The best performance was observed with $[Re(CO)_3$(*o*-phen)(DAPTA)$]^+$. We prepared the DCP analogue (**8**), (Fig. 9).

The precursor $[Re(CO)_3$(*o*-phen)Cl], prepared as described [46], was dissolved in $CH_3CN$ and converted in the solvento-complex $[Re(CO)_3$(*o*-phen)$(CH_3CN)]NO_3$ by adding $AgNO_3$. DCP was then added for replacing the Re coordinated $CH_3CN$. The final yellow solution contained complex **8**, $[Re(CO)_3$(*o*-phen)(DCP)$]NO_3$, which was recovered in high yield by precipitation with ether.

The ESI-MS of complex **8** showed the $M^+$ peak at 816 *m/z*. The NMR characterization confirmed the complex identity.

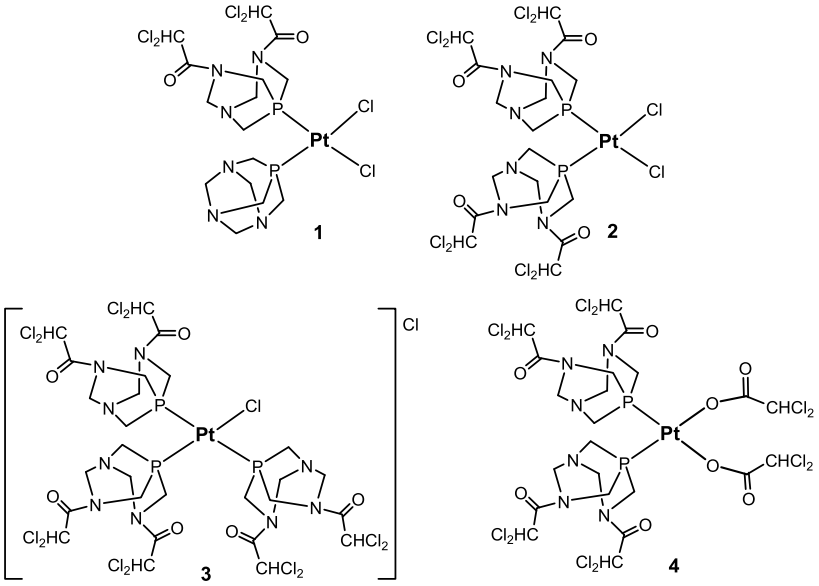


**Fig. 5.** Platinum complexes of DCP: *cis*-$[PtCl_2(DCP)(PTA)]$ (**1**), *cis*-$[PtCl_2(DCP)_2]$ (**2**), *cis*-$[PtCl(DCP)_3]Cl$ (**3**) and *cis*-$[Pt(DCA)_2(DCP)_2]$ (**4**).

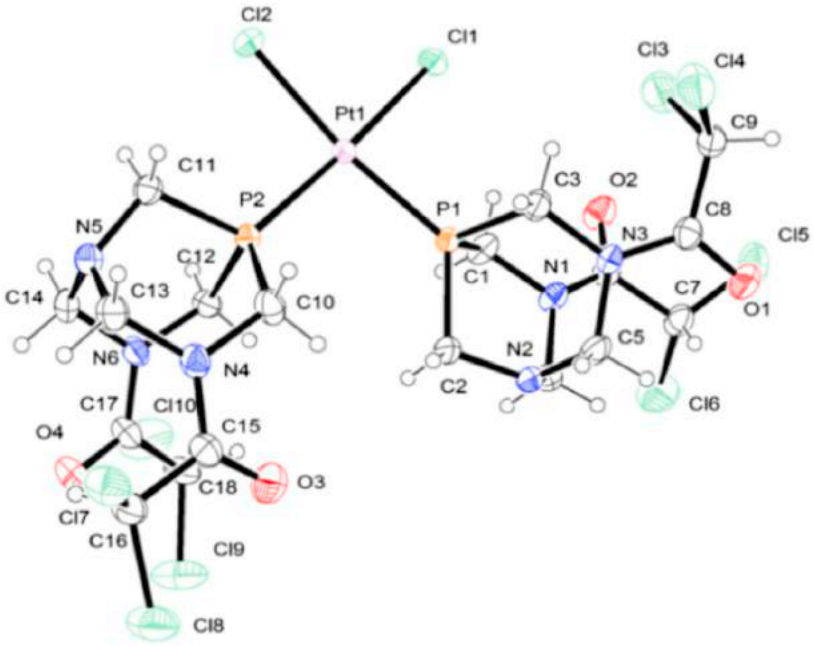


**Fig. 6.** ORTEP-III view and atom numbering scheme for complex **2** [34]. Thermal ellipsoids are drawn at the 40% probability level. The co-crystallized water molecule is not shown for clarity.

**Table 4**
Selected bond distances and angles (Å,°) for complex **2**.

| Bond distances | (Å) | Bond angles | (°) |
|---|---|---|---|
| Pt1−P1 | 2.231(1) | P1−Pt1−P2 | 98.36(5) |
| Pt1−P2 | 2.236(2) | P1−Pt1−Cl1 | 85.20(5) |
| Pt1−Cl1 | 2.357(2) | P2−Pt1−Cl2 | 89.55(5) |
| Pt1−Cl2 | 2.348(1) | P2−Pt1−Cl1 | 174.58(5) |
| | | P1−Pt1−Cl2 | 171.75(5) |
| | | Cl1−Pt1−Cl2 | 87.08(5) |

**Table 5**
Structural parameters of hydrogen bonds (Å, °) for **2**.

| D−H…A | D−H | D…A | H…A | D−H…A |
|---|---|---|---|---|
| C3−H…Cl3 | 0.97 | 3.325(7) | 2.57 | 134 |
| C2−H…O1W$^{i}$ | 0.97 | 3.524(9) | 2.61 | 156 |
| C18−H…O1W$^{i}$ | 0.98 | 3.238(9) | 2.41 | 142 |
| C5−H…O1$^{ii}$ | 0.97 | 3.494(6) | 2.59 | 155 |
| C4−H…O1$^{ii}$ | 0.97 | 3.482(6) | 2.58 | 154 |
| C7−H…O1$^{ii}$ | 0.98 | 3.263(7) | 2.38 | 148 |
| C9−H…O4$^{iii}$ | 0.98 | 3.053(8) | 2.21 | 143 |
| C12−H…O2$^{iv}$ | 0.97 | 3.134(6) | 2.31 | 141 |
| Short Cl…Cl contact: | | | | |
| Cl7…Cl9$^{v}$ | | 3.340(2) | | |

Equivalent positions: (i) -x, -y-1, -z; (ii) -x, -y-1, -z-1; (iii) x, y, z-1; (iv) -x, -y, -z; (v) x + 1, y, z.

### 2.2.5. Synthesis of [AuCl(DCP)] (9), a Au(I) complex

Several gold species provided with antiproliferative activity were reported, including phosphine complexes. Their mechanism of action, different from that of the platinum-based drugs, seems to be due to alterations of mitochondrial functions triggered by TxR (thioredoxin reductase) inhibition [47–50].

The complexes [AuCl(PTA)] [51] and [AuCl(DAPTA)] [31] were prepared by replacement of tetrahydrothiophene (tht) from [AuCl(tht)] with the appropriate phosphine. Analogously, the reaction of [AuCl(tht)] with DCP in $CH_2Cl_2$ gave complex [AuCl(DCP)], (**9**), in high yield, (Fig. 10). In DMSO the presence of the expected three rotamers was found, whose signals are well distinct in $^{31}$P NMR at −24.8, −19.3 and –18.4 ppm, in a 1:12.5:1 ratio, and partially overlapped in $^{1}$H and $^{13}$C NMR. In acetone a single form was detected ($^{31}$P NMR −19.2 ppm).

### 2.3. Anti-proliferative activity

The anti-proliferative activity of the new ligand DCP and of the complexes **1–9** was assayed on the A2780 (sensitive to cisplatin) and A2780*cis* (cisplatin resistant) ovarian cancer cell lines (both growing attached on the tissue culture flask and representative of solid tumors), and on the erythroleukemia K562 cell line (growing in suspension and representative of liquid tumors). The antineoplastic agent cisplatin was used as positive control in parallel cell cultures for each experiment. The obtained results are reported in Table 6.

Concerning the human ovarian cancer cell lines A2780 and A2780*cis*, while the known marked anti-proliferative activity of cisplatin ($IC_{50}$ = 0.4 ± 0.1 μM) on A2780 and the cisplatin-resistance of the A2780*cis* ($IC_{50}$ = 4.51 ± 0.7 μM) were both confirmed [52–54], all the here described new complexes demonstrated anti-proliferative activity on both cell lines, at different levels. When the results obtained using the A2780 cell line were comparatively analyzed, only complex **3** showed a relevant activity ($IC_{50}$ = 0.78 ± 0.1 μM), comparable with cisplatin and stronger than the uncoordinated ligand DCP. On the cisplatin-resistant A2780*cis* cells, the noteworthy activity of the ligand DCP ($IC_{50}$ = 0.94 ± 0.1 μM) was improved by Pt coordination in complexes **2**, **3** and **4** ($IC_{50}$ = 0.09 ± 0.01, 0.32 ± 0.04, 0.62 ± 0.06 μM, respectively).

On the K562 cells the anti-proliferative effects of the complexes, compared with cisplatin ($IC_{50}$ = 0.52 ± 0.1 M), were significantly different: **1**, **5**, **6**, **7** exhibited low activity ($IC_{50}$ = 15–20 μM); **2**, **3**, **8** and **9** revealed intermediate activity ($IC_{50}$ = 2–8 μM), whereas the complex **4** ($IC_{50}$ = 0.58 ± 0.1 μM) showed an efficacy very similar to the positive control cisplatin and better than the free ligand DCP (3.98 ± 0.7 μM). These results seem to indicate that the association of DCP with Pt(II) produces the best performances. The activity of Pt complexes **1**, **2** and **3** on cisplatin-resistant cells seems to indicate that they act through a different mechanism from that of classical Pt anticancer drugs.

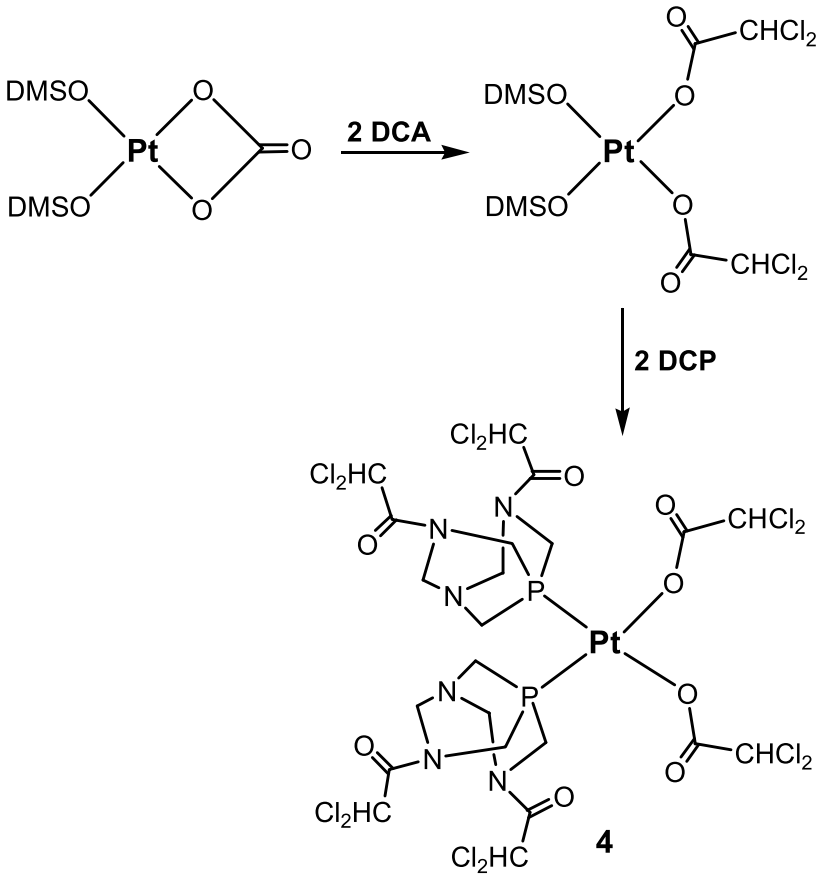


**Scheme 2.** Synthesis of *cis*-[Pt(DCA)$_2$(DCP)$_2$] (**4**).

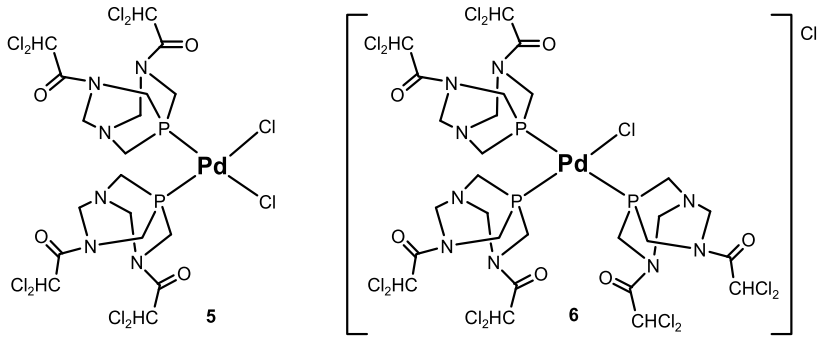


**Fig. 7.** Pd complexes of DCP: *cis*-[PdCl$_2$(DCP)$_2$] (**5**) and *cis*-[PdCl(DCP)$_3$]Cl (**6**).

The complexes containing DCP and non-platinum metal ions (**5–9**) were found not very active.

### 2.4. Pro-apoptotic effects

To attest whether the anti-proliferative activity of the complexes is associated to the activation of the apoptotic pathway, all the complexes were comparatively assayed, using the Annexin V test and a Muse™ Cell Analyzer [55–56]. All the MUSE-plots are reported in the Supplementary material, and the summary of the data obtained is shown in Table 7. Each derivative, with the exception of the compound **7** on A2780 cells and **8** on K562 cells, induced clearly appreciable pro-apoptotic effects on the employed cell lines. We have performed the assays using concentrations able to induce anti-proliferative effects, previously determined.

On the A2780 cell line at 5 μM, the Pt complexes **2**, **3** and **4** were identified as the best inducers of apoptosis (ca 50%), although less efficient than cisplatin, when used at the same concentration (77%). On the A2780*cis* cell line, cisplatin is not very active (as expected), while the Pt complexes **2**, **3** and **4** were found very active (51.60, 68.75 and 45.50 respectively) at the same dose (1 μM).

On K562 cells, the cisplatin proapoptotic activity is not very marked. Considering the values at 5 μM, all the Pt complexes (except **4**, that was among the most active when antiproliferative activity was considered, see Table 6) are more active than cisplatin. Surprisingly, the complexes containing Pd (**5** and **6**), Ru (**7**) and Au (**9**) showed a remarkable activity, while the Re complex (**8**) is nearly inactive. The free ligand DCP is less proapoptotic than its metal complexes on the three lines.

There is a good agreement between the antiproliferative activity

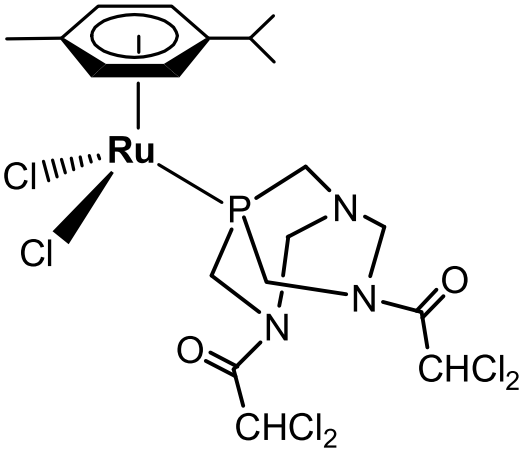


**Fig. 8.** Ruthenium complex of DCP, [$RuCl_2(\eta^6$*p*-cymene)(DCP)] (**7**).

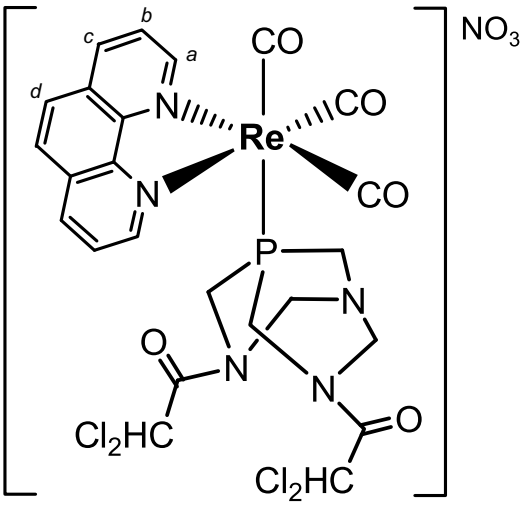


**Fig. 9.** Rhenium complex of DCP, [Re(*o*-phen)$(CO)_3$(DCP)]$NO_3$ (**8**).

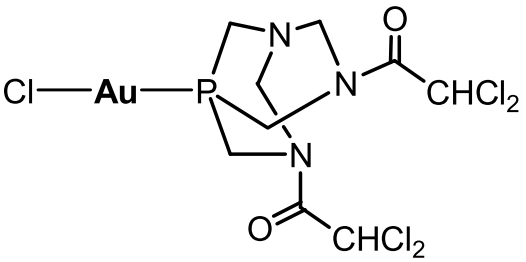


**Fig. 10.** Gold complex of DCP [AuCl(DCP)] (**9**).

(Table 6) and the proapoptotic effects (Table 7) on the ovarian cancer cell lines and Pt complexes **2**, **3** and **4** show the best activity when both tests are considered. Remarkably, the complex **4** (very active on inhibition of cell growth and induction of apoptosis when A2780 and A2780*cis* are employed) displayed, on K562 cells, a very high antiproliferative activity (0.58 ± 0.1 μM), associated with very poor proapoptotic effects.

The mixed PTA/DCP complex **1** shows negligible activity in both tests. Comparing the activity e.g. on A2780 of *cis*-[$PtCl_2(PTA)_2$] ($IC_{50}$ > 50 μM [57]) *cis*-[$PtCl_2$(PTA)(DCP)] (**1**, $IC_{50}$ = 7.99 ± 0.1 μM) and *cis*-[$PtCl_2(DCP)_2$] (**2**, $IC_{50}$ = 4.22 ± 0.3 μM), a positive trend is appreciable with the increasing of DCP.

The ability of inducing differentiation on the K562 cells was also tested, in comparison with cisplatin, whose activity was reported [58], but all the new species were found inactive (data not shown).

**Table 6**
Effects of the complexes on the proliferation of A2780, A2780*cis* and K562 cells. The inhibition of cell growth is represented as $IC_{50}$.

| Complex | $IC_{50}$(μM)A2780 | $IC_{50}$(μM)A2780*cis* | $IC_{50}$(μM)K562 |
|---|---|---|---|
| Cisplatin | 0.40 ± 0.1 | 4.51 ± 0.7 | 0.52 ± 0.1 |
| DCP | 4.74 ± 0.6 | 0.94 ± 0.1 | 3.98 ± 0.7 |
| **1** | 7.99 ± 0.1 | 6.39 ± 0.4 | 23.04 ± 0.9 |
| **2** | 4.22 ± 0.3 | 0.09 ± 0.01 | 1.88 ± 0.2 |
| **3** | 0.78 ± 0.1 | 0.32 ± 0.04 | 1.96 ± 0.4 |
| **4** | 3.26 ± 0.3 | 0.62 ± 0.06 | 0.58 ± 0.1 |
| **5** | 5.27 ± 0.9 | 4.83 ± 0.8 | 14.84 ± 0.7 |
| **6** | 4.49 ± 0.8 | 3.60 ± 0.2 | 15.33 ± 1.3 |
| **7** | 9.95 ± 0.9 | 6.82 ± 0.03 | 15.12 ± 1.4 |
| **8** | 2.42 ± 0.2 | 6.65 ± 0.5 | 8.45 ± 0.3 |
| **9** | 4.17 ± 0.2 | 6.78 ± 0.2 | 4.01 ± 0.2 |

**Table 7**
Pro-apoptotic effects of DCP and complexes **1–9** on human A2780, A2780*cis* and K562 cells.

| Sample | A2780 | | A2780*cis* | | K562 | |
|---|---|---|---|---|---|---|
| | Live cells (%) | Apoptotic cells (%) | Live cells (%) | Apoptotic cells (%) | Live cells (%) | Apoptotic cells (%) |
| C- | 91.90 | 7.85 | 89.50 | 8.80 | 96.30 | 3.70 |
| CisPt 0.5 μM | 81.30 | 18.10 | 89.75 | 9.60 | 95.05 | 4.15 |
| CisPt 1.0 μM | 59.30 | 40.20 | 85.55 | 11.80 | 79.45 | 19.90 |
| CisPt 5.0 μM | 22.00 | 77.25 | 72.40 | 28.20 | 66.37 | 32.13 |
| DCP 0.1 μM | | | 68.90 | 29.00 | | |
| DCP 0.5 μM | | | 83.75 | 15.15 | | |
| DCP 1.0 μM | 91.50 | 8.00 | 72.80 | 26.70 | 91.20 | 8.55 |
| DCP 5.0 μM | 59.60 | 39.55 | | | 56.72 | 35.40 |
| DCP 10 μM | 46.70 | 50.05 | | | 64.50 | 43.00 |
| **1** 1.0 μM | 91.85 | 7.50 | 82.87 | 13.29 | 79.15 | 20.65 |
| **1** 5.0 μM | 69.30 | 26.55 | 66.71 | 30.17 | 49.90 | 49.20 |
| **1** 10 μM | 76.65 | 21.20 | 60.63 | 36.31 | 16.30 | 83.70 |
| **2** 0.1 μM | | | 80.25 | 18.80 | | |
| **2** 0.5 μM | | | 58.25 | 41.15 | | |
| **2** 1.0 μM | 79.85 | 20.00 | 47.20 | 51.60 | 95.70 | 4.05 |
| **2** 5.0 μM | 43.80 | 52.90 | | | 57.40 | 41.75 |
| **2** 10 μM | 38.70 | 58.60 | | | 15.34 | 84.59 |
| **3** 0.05 μM | | | 88.05 | 11.05 | | |
| **3** 0.1 μM | | | 81.65 | 17.90 | | |
| **3** 0.5 μM | | | | | 74.71 | 24.89 |
| **3** 1.0 μM | 67.60 | 29.70 | 26.05 | 68.75 | 60.30 | 39.65 |
| **3** 5.0 μM | 29.55 | 66.20 | | | 40.45 | 59.40 |
| **3** 10 μM | 47.20 | 49.95 | | | | |
| **4** 0.1 μM | | | 69.85 | 28.25 | | |
| **4** 0.5 μM | | | 51.10 | 44.40 | | |
| **4** 1.0 μM | 88.15 | 11.35 | 53.55 | 45.50 | 95.20 | 4.45 |
| **4** 5.0 μM | 44.40 | 50.35 | | | 95.30 | 4.70 |
| **4** 10 μM | 39.95 | 49.95 | | | 81.75 | 18.25 |
| **5** 1.0 μM | 91.95 | 7.50 | 84.17 | 14.45 | 73.13 | 26.70 |
| **5** 5.0 μM | 69.50 | 28.05 | 57.79 | 40.58 | 25.70 | 74.30 |
| **5** 10 μM | 58.95 | 37.05 | 19.38 | 79.80 | 20.93 | 79.01 |
| **6** 1.0 μM | 91.85 | 7.05 | 82.05 | 16.50 | 65.89 | 33.54 |
| **6** 5.0 μM | 71.10 | 25.25 | 64.23 | 34.31 | 37.45 | 62.30 |
| **6** 10 μM | 66.99 | 31.50 | 37.68 | 60.67 | 31.45 | 68.15 |
| **7** 1.0 μM | 90.25 | 8.95 | 84.15 | 14.94 | 82.80 | 16.91 |
| **7** 5.0 μM | 82.90 | 16.20 | 60.49 | 34.53 | 52.70 | 45.85 |
| **7** 10 μM | 87.40 | 11.60 | 47.47 | 47.63 | 44.65 | 54.95 |
| **8** 1.0 μM | 87.55 | 10.85 | 81.45 | 17.31 | 89.93 | 8.97 |
| **8** 5.0 μM | 71.65 | 27.40 | 66.85 | 32.39 | 93.77 | 6.08 |
| **8** 10 μM | 37.40 | 61.45 | 52.54 | 47.10 | 89.43 | 10.09 |
| **9** 1.0 μM | 92.05 | 6.90 | 82.08 | 17.21 | 86.34 | 12.90 |
| **9** 5.0 μM | 63.05 | 33.15 | 48.72 | 43.44 | 44.14 | 54.92 |
| **9** 10 μM | 76.35 | 21.30 | 38.22 | 60.41 | 15.50 | 84.40 |

## 3. Experimental section

### 3.1. General procedures

All the manipulations were carried out in air unless otherwise noted. Commercial starting materials $K_2PtCl_4$, $PdCl_2$, $[Ru_2Cl_4(\eta^6p\text{-cymene})_2]$, $HAuCl_4$ and all the solvents and reagents were purchased and used without further purification. PTA [59], *cis*-$[PtCl_2(PTA)_2]$ [60], *cis*-$[Pt(DCA)_2(DMSO)_2]$ [57], $[RuCl_2(\eta^6p\text{-cymene})PTA]$ [41–43] $[Re(CO)_3(o\text{-phen})Cl]$ [46], [AuCl(tht)] [61] were prepared as described in the literature.

Elemental analyses were determined using a Carlo Erba instrument model EA1110. Mass spectra were recorded by an ESI single quadrupole mass spectrometer Waters ZQ 2000 (Waters instruments UK) and in each case the isotope pattern fitted the calculated (see Supplementary material). NMR spectra were recorded on a Varian Gemini 300 MHz spectrometer ($^1$H at 300 MHz, $^{13}$C at 75.43 MHz, $^{31}$P at 121.50 MHz) or a Varian Mercury Plus ($^1$H at 400 MHz, $^{13}$C at 100.58 MHz, $^{31}$P at 161.92 MHz). The $^{13}$C and $^{31}$P spectra were run with proton decoupling, $^{13}$C signals are reported in ppm relative to external tetramethylsilane (TMS), $^{31}$P signals are reported in ppm relative to an external 85% $H_3PO_4$ standard. The NMR spectra were recorded on fresh solutions (10–60 min) and the stability of the complexes in DMSO was routinely checked by the re-observation of $^{31}$P NMR spectra after 24 h.

### 3.2. Synthesis and characterization of DCP

PTA (500 mg, $3.18\cdot10^{-3}$ mol, MW 157.15 g/mol) was dissolved in a $Na_2CO_3$ solution (0.12 M, pH 11.7, 8 mL) and 10 mL of $CH_2Cl_2$ were added. The emulsion was then put under inert atmosphere and dichloroacetic anhydride (2.3 mL, $1.4\cdot10^{-2}$ mol, MW 239.9 g/mol, 4.4 eq.) was added dropwise under vigorous stirring, triggering the formation of a white precipitate at the interphase. The reaction mixture was kept under stirring at room temperature for an hour and then was filtered to recover the solid product which was carefully washed with water and ethanol to remove traces of sodium dichloroacetate, then dried under the vacuum on $P_2O_5$.

DCP was obtained as a white powder (872 mg, $2.38\,10^{-3}$ mol, MW 367.00 g/mol, yield 74.5%).

$^1$H NMR (DMSO-$d_6$)/COSY: $\delta$ = 3.53 ppm (dd, $^2J_{HH} = {}^2J_{PH}$ = 15.6 Hz, 1H, A), 3.59 ppm (d, $^2J_{PH}$ = 10.8 Hz, 2H, C), 3.93 ppm (dd, $^2J_{HH} = {}^2J_{PH}$ = 13.2 Hz, 1H, B), 4.18 ppm (d, $^2J$ = 13.4 Hz, 1H, D), 4.52 ppm (m, 2H, E, B′), 4.76 ppm (d, $^2J$ = 15.6 Hz, 1H, A′), 5.09 ppm (d, $^2J$ = 14.0 Hz, 1H, E′), 5.27 ppm (d, $^2J$ = 13.2 Hz, 1H, minor), 5.48 ppm (d, $^2J$ = 13.4 Hz, 1H, D′), 7.04 ppm (s, $CHCl_2$, 1H, major) and 7.15 ppm (s, $CHCl_2$, 1H, major), 7.18 ppm (s, $CHCl_2$ minor), 7.28 ppm (s, $CHCl_2$ minor). $^1$H NMR (DMSO-$d_6$): at 80 °C single broad peak for $CHCl_2$ at 7.12 ppm. General broadening of the other signals. $^{31}$P NMR (DMSO-$d_6$): $\delta$ = −78.5 ppm (s), −68.8 ppm (s), −68.4 ppm (s), estimated intensity ratio 1:7:1. At 120 °C ca −70 ppm (broad signal). $^{13}$C NMR/DEPT-HETCOR (DMSO-$d_6$) $\delta$ = 38.0 ppm (d, $CH_2P$, $^1J_{PC}$ = 28.4 Hz, major), 40.8 ppm (d, $CH_2P$, $^1J_{PC}$ = 29.2 Hz, minor), 41.6 ppm (d, $CH_2P$, $^1J_{PC}$ = 27.5 Hz, major), 44.7 ppm (d, $CH_2P$, $^1J_{PC}$ = 15.3 Hz, major), 62.8 ppm (s, $NCH_2N$, major), 63.6 ppm (s, $NCH_2N$, minor), 65.2 ppm e 65.4 ppm (s, $CHCl_2$, minor), 65.6 ppm (s, $CHCl_2$, major), 65.8 ppm (s, $NCH_2N$, major), 66.1 ppm (s, $CHCl_2$, major), 161.4 ppm (s, CO minor), 161.7 ppm (s, CO minor) 161.6 ppm and 162.0 (s, CO, major). $^1$H NMR (acetone-$d_6$)/COSY: $\delta$ = 3.60 ppm (dt, $^2J_{HH} = {}^2J_{PH}$ = 15.1 Hz, $^4J_{HH}$ = 2.3 Hz, 1H, A), 3.78 ppm (d, $^2J_{PH}$ = 11.3 Hz, 2H, C), 4.15 ppm (dt, $^2J_{HH} = {}^2J_{PH}$ = 14.7 Hz, $^4J_{HH}$ = 2.3 Hz, 1H, B), 4.32 ppm (d, $^2J_{HH}$ = 13.7 Hz, 1H, D), 4.63 ppm (d, $^2J_{HH}$ = 15.0 Hz, 1H, B′), 4.78 ppm (d, $J_{HH}$ = 13.9 Hz, 1H, E), 4.85 ppm (d, $J_{HH}$ = 15.6 Hz, 1H, A′), 5.22 ppm (d, $^2J_{HH}$ = 13.9 Hz, 1H, E′), 5.62 ppm (d, $^2J_{HH}$ = 13.7 Hz, 1H, D′), 6.85 ppm (s, $CHCl_2$, 1H), 6.88 ppm (s, $CHCl_2$, 1H). $^{31}$P NMR (acetone): −69.23 ppm. $^{31}$P NMR (acetonitrile): −68.6 ppm. $^{31}$P NMR (DMF): −77.4 ppm (s), −67.5 ppm (s), −67.1 ppm (s) estimated intensity ratio ca 1:7:1. ESI-MS: $m/z$ = 368 ($MH^+ = C_9H_{13}Cl_4N_3O_2P$). Anal. Calcd. for $C_9H_{12}Cl_4N_3O_2P$: C 29.45, H 3.30, N 11.45; found C 29.38, H 3.45, N 11.42. The crystallographic structure of **1** was determined on crystals grown in acetone (see Tables 2 and 3, Fig. 4).

### 3.3. Coordination of DCP to metal ions

#### 3.3.1. Synthesis of cis-$[PtCl_2(DCP)_2]$ (2)

Solid $K_2PtCl_4$ (100 mg, $2.41\cdot10^{-4}$ mol, MW 415.0 g/mol) was added to a solution of DCP (177 mg, $4.82\cdot10^{-4}$ mol, MW 367.0 g/mol, 2 eq.) in 60 mL of $CH_3CN$. The suspension was left under stirring for 18 h. The obtained colorless solution, taken to dryness by rotary evaporator left a white solid residue which was washed with water (to remove the side product KCl), filtered and dried under vacuum over $P_2O_5$ (190 mg, $1.9\cdot10^{-4}$ mol, MW 1000.0 g/mol, yield 79%).$^1$H NMR (DMSO-$d_6$): $\delta$ = 3.85–5.45 ppm (10H of DCP), 6.83 ppm and 6.97 ppm and 7.18 ppm (3 s, 2H, $CHCl_2$). $^{31}$P NMR (DMSO-$d_6$): −28.0 ppm ($^1J_{PtP}$ = ca 3400 Hz), −27.8 ppm ($^1J_{PtP}$ = ca 3400 Hz), −27.7 ppm ($^1J_{PtP}$ = ca 3400 Hz), −26.8 ppm ($^1J_{PtP}$ = ca 3454 Hz), −26.6 ppm ($^1J_{PtP}$ = ca 3454 Hz) and –26.5 ppm ($^1J_{PtP}$ = ca 3454 Hz). $^{31}$P NMR (acetone): $\delta$ = −27.3 ppm (s, $^1J_{PtP}$ = 3389 Hz) and –27.2 ppm (s, $^1J_{PtP}$ = 3341 Hz). $^{31}$P NMR (acetonitrile): $\delta$ = −28.1 (s, $^1J_{PtP}$ = 3395 Hz). Anal. Calcd. for $C_{18}H_{24}Cl_{10}N_6O_4P_2Pt$: C 21.61, H 2.42, N 8.40; found C 21.63, H 2.40, N 8.47. The crystallographic structure of **2** was determined on crystals grown in acetone and ether (see Tables 4 and 5, Fig. 6).

#### 3.3.2. Synthesis of cis-$[PtCl_2(PTA)(DCP)]$ (1)

DCP (127 mg, $3.45\cdot10^{-4}$ mol, MW 367.0 g/mol) was dissolved in 57 mL of $CH_3CN$ and added to a suspension of *cis*-$[PtCl_2(PTA)_2]$ (200 mg, $3.45\cdot10^{-4}$ mol, MW 579.9 g/mol) in 33 mL of $CH_3CN$ + 13 mL of $CH_3OH$. During 48 h stirring, the suspension turned to a clear colorless solution which was taken to dryness by rotary evaporator. The white solid residue was suspended in water, left under stirring for 18 h and finally filtered. It was then dried under vacuum over $P_2O_5$ (117 mg, $1.48\cdot10^{-4}$ mol, MW 790.1 g/mol, yield 43%).

$^1$H NMR (300 MHz, acetone-$d_6$): $\delta$ = 4.17 ppm (d, 2H, $^2J_{HH}$ = 18 Hz), 4.4–4.7 ppm (m, 11 H, DCP + PTA), 4.85 ppm (d, 2H, $^2J_{HH}$ = 18 Hz), 5.2–5.7 ppm (m, 7H, DCP), 6.78 and 6.83 (2s, 2H, $CHCl_2$). $^{31}$P NMR (acetone): $\delta$ = −53.4 ppm (bs, $^1J_{PtP}$ = 3118 Hz), −28.0 ppm (bs, $^1J_{PtP}$ = 3393 Hz). $^{31}$P NMR (DMSO): $\delta$ = −51.1 ppm (bs, $^1J_{PtP}$ = 3131 Hz), −27.4 ppm (bs, $^1J_{PtP}$ = 3400 Hz, major), −26.2 ppm (bs, $^1J_{PtP}$ = 3400 Hz, minor). IR nujol: 398 and 374 $cm^{-1}$ $\nu$ Pt-Cl *cis*, 446 and 435 $cm^{-1}$ $\nu$ Pt-P. Anal. Calcd. for $C_{15}H_{24}Cl_6N_6O_2P_2Pt$: C 22.79, H 3.06, N 10.64; found C 22.66, H 2.98, N 10.62.

#### 3.3.3. Synthesis of $[PtCl(DCP)_3]Cl$ (3)

DCP (100 mg, $2.72\cdot10^{-4}$ mol, MW 367.00 g/mol, 3 eq.) was dissolved in 30 mL of $CH_3CN$. Solid $K_2PtCl_4$ (38 mg, $9.15\cdot10^{-5}$ mol, MW 415.1 g/mol) was added to the solution and left under stirring at room temperature for 18 h. The suspension was taken to dryness by rotary evaporator. The white solid residue was washed with water, filtered and dried under vacuum over $P_2O_5$ (79 mg, $5.78\cdot10^{-5}$ mol, MW 1367.0 g/mol, yield 63%).

$^1$H NMR (DMSO-$d_6$): $\delta$ = 3.8–5.5 ppm (10H of DCP), 7.0 ppm and 7.15 ppm and 7.3 ppm (3s, 2H, $CHCl_2$). $^{31}$P NMR (DMSO-$d_6$): $\delta$ = −27.6 ppm (br) with $^1J_{PtP}$ = ca. 3362 Hz. ESI-MS: $m/z$ = 1332 ($M^+ = C_{27}H_{36}Cl_{13}N_9O_6P_3Pt$). Anal. Calcd. for $C_{27}H_{36}Cl_{14}N_9O_6P_3Pt$: C 23.71, H 2.65, N 9.22; found C 23.81, H 2.70, N 9.29.

#### 3.3.4. Synthesis and characterization of cis-$[Pt(DCA)_2(DCP)_2]$ (4)

*cis*-$[Pt(DCA)_2(DMSO)_2]$ (94 mg, $1.55\cdot10^{-4}$ mol, MW 607.2 g/mol) was suspended in 5 mL of acetone and DCP (114 mg, $3.1\cdot10^{-4}$ mol, 367.00 g/mol, 2 eq.) dissolved in 15 mL of $CH_3CN$ was added dropwise. After stirring for an hour and a half at room temperature, the volume of the solution was reduced, leaving a white precipitate which was

filtered, washed with small portions of ether and finally dried under vacuum over $P_2O_5$ (82 mg, $6.92 \cdot 10^{-5}$ mol, MW 1184.9 g/mol, yield 45%).

$^1$H NMR (300 MHz, DMSO-$d_6$): $\delta$ = 4.0–5.5 ppm (m, 20H), 5.9 and 6.15 ppm (bs, $CHCl_2$ of DCA, 2H), 6.92 ppm, 7.07 ppm and 7.3 ppm (3 s, 4H, $CHCl_2$). $^{31}$P NMR (DMSO): $\delta$ = −37.7 ppm (s, $^1J_{PtP}$ = 3467 Hz), −36.1 ppm (s, $^1J_{PtP}$ = 3501 Hz). $^1$H NMR (400 MHz, acetone-$d_6$): $\delta$ = 4.2–5.7 ppm (m, 20H), 6.18 ppm ($CHCl_2$ of DCA, 2H), 6.75 ppm and 6.90 ppm (2 s, 4H, $CHCl_2$). $^{31}$P NMR (acetone): $\delta$ = −36.6 ppm (s, $^1J_{PPt}$ = 3577 Hz). Anal. Calcd. for $C_{22}H_{26}Cl_{12}N_6O_8P_2Pt$: C 22.29, H 2.21, N 7.09; found C 21.31, H 2.20, N 6.99.

### 3.3.5. Synthesis and characterization of cis-[$PdCl_2$(DCP)$_2$] (5)

A DCP suspension (415 mg, $1.1310^{-3}$ mol, MW 367.0 g/mol, 2 eq.) in 10 mL of $CH_2Cl_2$ was added under nitrogen to $PdCl_2$ (100 mg, $5.64 \cdot 10^{-4}$ mol, MW 177.3 g/mol) suspended in 20 mL of $CH_2Cl_2$. The resulting brown/red solution was kept under stirring overnight. The yellow precipitate was then filtered and dried under vacuum over $P_2O_5$ (452 mg, $4.96 \cdot 10^{-4}$ mol, MW 911.3 g/mol, yield 88%).

$^1$H NMR (DMSO-$d_6$, 300 MHz) 4–5.5 ppm (10H of DCP), 6.87 ppm and 7.09 ppm and 7.27 ppm (3 s, 2H, $CHCl_2$). $^{31}$P NMR (DMSO): $\delta$ = −5.06, −5.29, −5.46, −5.93, −6.11, −6.34 ppm. $^{31}$P NMR (acetone, 300 MHz): $\delta$ = −8.4 ppm (s).$^{31}$P NMR ($CH_3CN$): $\delta$ = −8.2 ppm (s). IR nujol: 366 and 356 $cm^{-1}$ $\nu$ Pd-Cl *cis*, 442–426 $cm^{-1}$ $\nu$ Pd-P. ESI-MS: *m/z* = 935 ($M + Na^+ = C_{18}H_{24}Cl_{10}NaN_6O_4P_2Pd$). Anal. Calcd. for $C_{18}H_{24}Cl_{10}N_6O_4P_2Pd$: C 23.71, H 2.65, N 9.22; found C 23.86, H 2.60, N 9.21.

### 3.3.6. Synthesis and characterization of [$PdCl(DCP)_3$]Cl (6)

Solid $PdCl_2$ (16 mg, $9.02 \cdot 10^{-5}$ mol, MW 177.3 g/mol) was added to a solution of DCP (100 mg, $2.71 \cdot 10^{-4}$ mol, MW 367.0 g/mol, 3 eq.) in 30 mL of $CH_3CN$. After 15 min $PdCl_2$ was completely dissolved. The pale yellow solution was left under stirring at room temperature for 18 h and then taken to dryness. The yellow solid residue of **6** was dried under vacuum over $P_2O_5$ (116 mg, $9.02 \cdot 10^{-5}$ mol, MW 1278.3 g/mol, yield 100%). $^1$H NMR (DMSO-$d_6$, 400 MHz): $\delta$ = 3.83 ÷ 5.52 ppm (30H of DCP), 6.92 ppm (bs, 2H, $CHCl_2$), 7. 10 ppm (s, 2H, $CHCl_2$), 7.28 ppm (s, 2H, $CHCl_2$). $^{31}$P NMR (DMSO): br s –5.0 ÷ −7.0 ppm. ESI-MS: *m/z* = 1242 ($M^+ = C_{27}H_{36}Cl_{13}N_9O_6P_3Pd$). Anal. Calcd. for $C_{27}H_{36}Cl_{14}N_9O_6P_3Pd$: C 25.35, H 2.84, N 9.86; found C 25.59, H 2.79, N 10.06.

### 3.3.7. Synthesis of [$RuCl_2(\eta^6$*p*-cymene)(DCP)] (7)

Complex **7** can be obtained in two ways: a) reaction of [$Ru_2Cl_4(\eta^6$*p*-cymene)$_2$] with DCP or b) acylation of [$RuCl_2(\eta^6$*p*-cymene)(PTA)] with dichloroacetic anhydride.

a) from [$Ru_2Cl_4(\eta^6$*p*-cymene)$_2$]: a DCP suspension (120 mg, $3.26 \cdot 10^{-4}$ mol, MW 367.0 g/mol, 2 eq.) in 20 mL of $CH_3CN$ was added in small portions to a [$Ru_2Cl_4(\eta^6$*p*-cymene)$_2$] orange solution (100 mg, $1.63 \cdot 10^{-4}$ mol, MW 612.4 g/mol). After 18 h, an orange solid precipitated which was filtered, washed with $CH_3CN$ and dried under vacuum over $P_2O_5$ (54 mg, $1.5 \cdot 10^{-4}$ mol, MW 673.2 g/mol, yield 46%).

b) from [$RuCl_2(\eta^6$*p*-cymene)(PTA)]: [$RuCl_2(\eta^6$*p*-cymene)(PTA)][20c] (140 mg, $3.02 \cdot 10^{-4}$ mol, MW 463.3 g/mol) was dissolved in a $Na_2CO_3$ solution (2 M, 2 mL) and 5 mL of $CH_2Cl_2$ were added. Under inert atmosphere, 162 µL of dichloroacetic anhydride ($9.06 \cdot 10^{-4}$ mol, MW 239.9 g/mol, 3 eq.) were added dropwise under vigorous stirring, and a precipitate immediately formed at the interphase. The reaction mixture was kept under stirring at room temperature for 4 h. The orange precipitate was then filtered, washed with water and ethanol and then dried under the vacuum on $P_2O_5$. [$RuCl_2(\eta^6$*p*-cymene)(DCP)] (**7**) was obtained as an orange powder (61 mg, $9.02 \cdot 10^{-5}$ mol, MW 673.2 g/mol, yield 30%). $^1$H NMR/COSY (400 MHz, DMSO-$d_6$): $\delta$ = 1.11 and 1.12 ppm (2d, $^3J_{HH}$ = 6.83 Hz, 6H, isoprop), 1.93 ppm (s, 3H, p-$CH_3$), 2.59 ppm (ept, $^3J_{HH}$ = 6.83 Hz, 1H, isoprop), 3.9 ppm (m, 3H of $NCH_2P$ groups), 4.28 ppm (m, 2H, $NCH_2P$ and $NCH_2N$), 4.72 ppm (m, 2H, $NCH_2P$ and $NCH_2N$), 5.14 ppm (m, 2H, $NCH_2P$ and $NCH_2N$), 5.47 ppm (d, $^2J_{HH}$ = 13.5 Hz, 1H, $NCH_2N$), 5.87 ppm (m, 4H, aromatic), 7.09 ppm and 7.10 ppm (2 s, $CHCl_2$ of *anti* rotamer), 7.29 ppm and 7.42 ppm (2 s, $CHCl_2$ of *syn* rotamers *A* and *B*). $^{31}$P NMR (121.44 MHz, DMSO): $\delta$ = −13.0 ppm (s), −7.8 ppm (s), −7.1 ppm (s), estimated ratio 1:9:3. $^{13}$C NMR-DEPT-Hetcor (100.58 MHz, DMSO): some signals of 2 out of 3 rotamers are distinguishable $\delta$ = 18.3 ppm (p-$CH_3$), 22.0 ppm, 22.1 ppm and 22.2 ppm (3s, two belonging to the *anti* rotamer and the other to the *syn*, $CH_3$ of isoprop), 30.6 ppm (CH of isoprop), 41.2 ppm (d, $^1J_{PC}$ = 19 Hz, $PCH_2N$), 43.8 ppm (d, $^1J_{PC}$ = 19 Hz, $PCH_2N$), 46.9 ppm (d, $^1J_{PC}$ = 25 Hz, $PCH_2N$), 63.4–66.2 ppm (m, $NCH_2N$ and $CO\underline{C}HCl_2$), 85.6, 86.0, 86.1 ppm (3s, CH arom), 88.8, 89.0, 89.4 ppm (3s, CH arom), 97.0 (s, C-quat, *anti*), 97.2 (s, C-quat, *syn*), 106.3 (s, C-quat), 162.1 ppm (s $\underline{C}OCHCl_2$, *syn*), 162.3 ppm and 162.5 ppm (2 s, $\underline{C}OCHCl_2$, *anti*). $^1$H NMR (400 MHz, acetone-$d_6$): $\delta$ = 1.22 ppm (d, $^3J_{HH}$ = 6.8 Hz, 6H, $CH_3$ isop), below the solvent (p-$CH_3$), below the solvent (CH isoprop), 4.06 ppm (m, 3H of $NCH_2P$), 4.45 ppm (m, 2H, $NCH_2P$ and $NCH_2N$), 4.88 ppm (m, 2H, $NCH_2P$ and $NCH_2N$), 5.32 ppm (m, 2H, $NCH_2P$ and $NCH_2N$), 5.62 ppm (d, 1H, $^2J_{HH}$ = 14.1 Hz, $NCH_2N$), 5.85 ppm (m, 4H, aromatic), 6.82 ppm and 6.90 ppm (2s, 2H, $CHCl_2$ of *anti* rotamers). $^{31}$P NMR (acetone): $\delta$ = −8.1 ppm (s). Anal. Calcd. for $C_{19}H_{26}Cl_6N_3O_2PRu$: C 33.88, H 3.89, N 6.24; found C 33.86, H 3.74, N 5.95.

### 3.3.8. Synthesis and characterization of [Re(*o*-phen)$(CO)_3$DCP]$NO_3$ (8)

Solid $AgNO_3$ (19 mg, $1.14 \cdot 10^{-4}$ mol, MW 169.9 g/mol) was added to a solution of [ReCl(*o*-phen)$(CO)_3$] (50 mg, $1.09 \cdot 10^{-4}$ mol, MW 486.0 g/mol) in 5 mL of $CH_3CN$. The vial was placed in the microwave at 120 °C for 15 min. AgCl was eliminated by centrifugation and the ligand DCP (45 mg, $1.23 \cdot 10^{-4}$ mol, MW 367.0 g/mol 1.1 eq.) was added to the solution containing the solvento-complex [Re(*o*-phen)$(CO)_3(CH_3CN)]NO_3$. The mixture was placed again in the microwave at 120 °C for 15 min and a clear-yellow solution was obtained. The solution volume was reduced to a half and ether added (10 mL). The precipitate of [Re(*o*-phen)$(CO)_3$DCP]$NO_3$ was filtered and washed with ether (88 mg, $1.00 \cdot 10^{-4}$ mol, MW 879.4 g/mol, yield 92%). $^1$H NMR (300 MHz, DMSO-$d_6$): $\delta$ = 3.6–5.6 ppm (m, DCP, 10H), 6.95 ppm (s, $CHCl_2$, *anti*) and 7.07 ppm (s, $CHCl_2$, *anti*), 7.10 ppm (s, $CHCl_2$, *syn*), 7.14 ppm (s, $CHCl_2$, *syn*), 8.18 ppm (m, $2H_c$, *o*-phen), 8.40 ppm (m, 2 $H_d$, *o*-phen), 9.1 ppm (m, 2 $H_b$, *o*-phen), 9.5 ppm (m, 2 $H_a$, *o*-phen). $^{31}$P NMR (DMSO-$d_6$): $\delta$ = −57.8 ppm (s, *syn*), −47.9 ppm (s, *syn*), −42.3 ppm (s, *anti*, major). $^1$H NMR/COSY (acetone-$d_6$, 400 MHz): three rotamers, $\delta$ = 4–5.6 ppm (m, DCP, 10H, 3 rotamers), 6.60 ppm and 6.72 ppm (2 s, $CHCl_2$, *anti*), 6.87 ppm, 7.21 and 7.38 ppm (s, $CHCl_2$, 2 *syn rotamers*), 8.23 ppm (dd, $J_{HH}$ 8.6 Hz, $J_{HH}$ 5.1 Hz) + 8.31 ppm (dd) + 8.35 (dd) ($2H_c$, *o*-phen), 8.38 ppm (s) + 8.48 ppm (s) + 8.50 (s) ($2H_d$, *o*-phen), 9.05 ppm (dd, $J_{HH}$ 8.2 Hz, $J_{HH}$ 1.6 Hz) + 9.15 ppm (m) ($2H_b$, *o*-phen), 9.58 ppm (dd $J_{HH}$ 5.1 Hz, $J_{HH}$ 1.6 Hz) + 9.62 ppm (dd) + 9.58 (d, $J_{HH}$ 5.0 Hz) ($2H_a$, *o*-phen). $^{31}$P NMR (acetone-$d_6$): $\delta$ = −58.3 ppm (s, *syn*), −52.1 ppm (s, *syn*), −41.7 ppm (s, *anti*, major). $^{13}$C NMR (acetone-$d_6$): $\delta$ = 40–45 ppm ($NCH_2P$), 63–67 ppm ($NCH_2N$ and $CHCl_2$), 127–157 ppm (*o*-phen), 162.7 ppm, 162.9 ppm, 163.1 ppm and 163.9 ppm (4s, $COCHCl_2$), 187.7 ppm (d, ReCO *trans* to P, $^2J_{PC}$ 64 Hz), 197.0 ppm (s, ReCO), 194.6 ppm (s, ReCO), 197.9 ppm (s, ReCO). ESI-MS: *m/z* 816 ($M^+ = C_{24}H_{20}Cl_4N_5O_5PRe$). UV–Vis (DMSO/PBS = 0.1 mL: 10 mL, 150 µM): $\lambda_{max}$ = 275 nm ($\varepsilon$ = 14,300 $M^{-1}$ $cm^{-1}$), 370 nm (sh). Anal. Calcd. for $C_{24}H_{22}Cl_4N_6O_9PRe$: C 32.10, H 2.47, N 9.37; found C 31.92, H 2.39, N 9.13.

### 3.3.9. Synthesis and characterization of [AuCl(DCP)] (9)

The precursor [AuCl(tht)] (210 mg, $6.55 \cdot 10^{-4}$ mol, MW 320.6 g/mol) was dissolved in 30 mL of $CH_2Cl_2$. Solid DCP (240 mg, $6.55 \cdot 10^{-4}$ mol, MW 367.0 g/mol, 1 eq.) was added to the solution and the obtained suspension was left under stirring at room temperature for 2 h. The white precipitate was then filtered, washed with $CH_2Cl_2$ and dried under vacuum over $P_2O_5$ (335 mg, $5.59 \cdot 10^{-4}$ mol, MW 599.4 g/

mol, yield 85%).

$^{1}$H NMR (400 MHz, DMSO-$d_6$). *Anti* (major): 4.06 ppm (m, 3H), 4.32 ppm (d, $^{2}J_{HH}$ = 12.8 Hz, 1H), 4.46 ppm (d, $^{2}J_{HH}$ = 15.6 Hz,1H), 4.65 ppm (d, $^{2}J_{HH}$ = 14 Hz,1H), 4.97 ppm (m, 1H), 5.15 ppm (m, 2H), 5.47 ppm (d, $^{2}J_{HH}$ = 14 Hz,1H), 7.09 ppm (s, $CHCl_2$) and 7.18 ppm (s, $CHCl_2$); *syn-A* and *syn-B*: all the signals are overlapped to the *anti* signals except 7.20 ppm (s, $CHCl_2$), 7.25 ppm (s, $CHCl_2$). Estimated ratio: 12.8:1:1. $^{31}$P NMR (121.44 MHz, DMSO): $\delta = -24.8$ ppm (s, *syn*), −19.3 ppm (s, *anti*, major), −18.4 ppm (s, *syn*) (ratio 1:12.5:1). $^{13}$C NMR (100.58 MHz, DMSO-$d_6$). *Anti* (major): 44.0 ppm (d, $^{1}J_{PC}$ = 30.6 Hz, $PCH_2N$), 47.5 ppm (d, $^{1}J_{PC}$ = 29.2 Hz, $PCH_2N$), 63.3 ppm (d, $^{3}J_{PC}$ = 5.3 Hz, $NCH_2N$), 65.8 ppm (s, $CHCl_2$), 66.2 ppm (d, $^{3}J_{PC}$ = 5.3 Hz, $NCH_2N$), 66.4 ppm (s, $CHCl_2$), 162.4 ppm (s, CO), 162.7 ppm (s, CO). *syn-A* and *syn-B*: all the signals are overlapped to the *anti* signals except 65.3 ppm (s, $CHCl_2$), 65.6 ppm (s, $CHCl_2$).

$^{31}$P NMR (acetone-$d_6$): $\delta = -19.2$ ppm (s). Anal. Calcd. for $C_9H_{12}Cl_5N_3O_2PAu$:C 18.02, H 2.02, N 7.01; found C 17.91, H 1.86, N 6.96.

### 3.4. Single-crystal X-ray diffraction

Single-crystal diffraction data for DCP and complex **2** were collected at 295 K on a Nonius Kappa diffractometer equipped with a CCD detector with graphite-monochromated Mo Kα radiation (λ = 0.71069 Å). Intensities were corrected for Lorentz, polarization and absorption effects [62]. The structures were solved by direct methods with the SIR97 program and refinement were performed on $F^2$ by full matrix least-squares methods with all non-H atoms anisotropic. To model the disorder of DCP, the same crystallographic position has been assigned to P1 and N1 atoms, with a 50% occupancy [63].

In DCP, the hydrogen atoms were located in the difference-Fourier map and refined isotropically; in complex **2** the C-H hydrogens were included on calculated positions, riding on their carrier atoms, while it was impossible to locate the H atoms of the cocrystallized water molecule.

All calculations were performed using SHELXL2014/7 [64] implemented in the WinGX system of programs [65]. Experimental details are given in Table 8. A selection of bond distances and angles is reported in Tables 2, 4 and hydrogen bonding contacts parameters are reported in Tables 3 and 5. ORTEP-III [34] views of DCP and **2** are shown in Figs. 4 and 6, respectively.

CCDC 1859639-1859640 contain the supplementary crystallographic data for this paper. These data are provided free of charge by the Cambridge Crystallographic Data Centre.

### 3.5. Growth inhibition assays

The human ovarian cancer A2780 and A2780*cis* cell lines were obtained from ATCC (Manassas, VA) and maintained in RPMI 1640 medium (Lonza, Verviers, Belgium), supplemented with 10% fetal bovine serum (FBS; Biowest, Nuaillé, France), 50 units/mL penicillin (Lonza, Verviers, Belgium) and 50 µg/mL streptomycin (Lonza, Verviers, Belgium). To conserve the resistance, 1 µM cisplatin was routinely added to the A2780*cis* cells. The pH of the medium was 7.2 and the incubation was performed at 37 °C in a 5% $CO_2$ humidified atmosphere. The A2780 and A2780*cis* cells were detached from the tissue culture flasks as follows: after a gentle cleanup with 1X PBS, trypsin (100 µL/well) was added. After 3 min incubation at 37 °C, FBS (100 µL/well) and RPMI (800 µL/well) are added.

The human erythroleukemia K562 cells were isolated and characterized by Lozzio CB and Lozzio BB, from a patient with chronic myelogenous leukemia (CML) in blast crisis [66]. K562 cells were cultured in humidified atmosphere of 5% $CO_2$, in RPMI-1640 medium (Lonza, Verviers, Belgium) supplemented with 10% fetal bovine serum (FBS; Biowest, Nuaillé, France), 50 units/mL penicillin (Lonza, Verviers, Belgium) and 50 µg/mL streptomycin (Lonza, Verviers, Belgium) [67].

**Table 8**
Experimental details.

| | DCP | Complex **2** |
|---|---|---|
| Chemical formula | $C_9H_{12}Cl_4N_3O_2P$ | $C_{18}H_{24}Cl_{10}N_6O_4P_2Pt{\cdot}H_2O$ |
| $M_r$ | 366.99 | 1017.98 |
| Crystal system, space group | Monoclinic, *C*2/*c* | Triclinic, $P\bar{1}$ |
| *a*, *b*, *c* (Å) | 15.4455 (8), 9.6375 (6), 10.2555 (4) | 9.7176(3), 13.3124(4), 14.5640(4) |
| α, β, γ (°) | 90, 105.066 (3), 90 | 116.055(2), 94.649(2), 90.310(2) |
| *V* (Å$^3$) | 1474.12 (13) | 1685.25 (9) |
| *Z* | 4 | 2 |
| µ (mm$^{-1}$) | 0.91 | 5.09 |
| Crystal size (mm) | 0.48 × 0.24 × 0.19 | 0.15 × 0.10 × 0.06 |
| No. of measured, independent and observed [$I > 2s(I)$] reflections | 6589, 1750, 1492 | 28,836, 7350, 6563 |
| $R_{int}$ | 0.028 | 0.062 |
| $R[F^2 > 2s(F^2)]$, $wR(F^2)$, $S$ | 0.074, 0.206, 1.09 | 0.036, 0.093, 1.06 |
| No. of reflections/ parameters | 1750/121 | 7350/380 |
| $\Delta\rho_{max}$, $\Delta\rho_{min}$ (e Å$^{-3}$) | 0.87, −0.83 | 1.60, −1.65 |

The derivatives were added to cell cultures at serial dilutions and incubated for 72 h. For the stock mother solution, the compounds have been dissolved in DMSO at the final concentration of 50 mM. All the working solutions of the complexes were obtained following a further dilution using pure DMSO, in order to obtain 50 µM concentrations. Finally the compounds were diluted in the complete medium (RPMI and FBS) in order to obtain the final concentrations to be used on the cells (the DMSO concentration never exceeded 0.2% concentration). In any case control experiments demonstrated lack of biological effects of the DMSO vehicle. Cisplatin (diluted in $H_2O$) was employed as control for all the cell lines, A2780, A2780*cis* and K562. Untreated cells were placed in every plate as negative control. The vehicle DMSO was verified to be not able to induce antiproliferative activity. The cells were exposed to the compounds in 1000 µL total volume. Cells were finally suspended in physiological solution and counted with a Z2 Coulter Counter (Coulter Electronics, Hialeah, FL, USA). The cell number/mL was determined as $IC_{50}$ after 3 days of culture, when untreated cells are in log phase of growth [52–54].

### 3.6. Apoptosis assays

Annexin V and Dead Cell assays on A2780, A2780*cis* and K562 cells, untreated and treated for 72 h with different doses of analyzed derivatives, were performed with a Muse™ Cell Analyzer (Millipore, Billerica, MA, USA), according to the instructions supplied by the manufacturer [52,68–69]. This procedure is based on Annexin V to detect PS (PhosphatidylSerine) on the external membrane of apoptotic cells. Moreover, a dead cell marker was employed in the same kit as indicator of cell membrane structural integrity. Cells were diluted (1:1) with the one step addition of the Muse Annexin V & Dead Cell reagent. After 20 min of incubation between cell samples and kit at room temperature in the dark, samples were analyzed. Data were acquired and recorded utilizing the Annexin V and Dead Cell Software Module (Millipore, Billerica, MA, USA).

### 3.7. Cell differentiation evaluation

Erythroid differentiation was assayed on K562 cells treated with all the complexes in comparison with the known inducer cisplatin [58]. Cells were cultured for 7 days and the enzymatic-colorimetric benzidine

test was used to determine the possible effects after 5, 6 and 7 days culture of K562 cells incubated with different concentrations of derivatives.

## 4. Conclusions

The new ligand DCP, designed as a carrier of either proapoptotic dichloroacetic acid and a cytotoxic metal ion, was obtained in high yield under appropriate conditions (pH, solvent and reagents ratio). Its structural features, including the presence of rotameric forms due to the hindered rotation around the amidic CN bonds, were studied both in solution (NMR and ESI-MS) and in solid (X-ray crystal structure). The coordination of DCP acting as a P-donor to a variety of cytotoxic metal ions, ($Pt^{2+}$, $Pd^{2+}$, $Ru^{2+}$, $Re^{+}$, $Au^{+}$) gave nine new complexes, whose antiproliferative and proapoaptotic activity in human tumor cell lines have been tested.

The antiproliferative activity was tested in vitro on cisplatin-sensitive A2780, cisplatin-resistant A2780*cis* and K562 cell lines, in comparison with cisplatin, used as positive standard.

Platinum complexes **3** for A2780 cells, **2**, **3** and **4** for A2780*cis* cells and **4** for K562, displayed antiproliferative comparable to cisplatin and higher than the free ligand DCP showing that the simultaneous presence of DCP (containing two residues of proapoptotic DCA) and Pt(II) produces the best performances.

Moreover, it was observed that the anti-proliferative activity of the most active Pt(II) complexes is associated with induction of apoptosis.

On the contrary, the association of DCP with other active metal ions did not give good results, with the exception of the complexes containing Pd (**5** and **6**), Ru (**7**) and Au (**9**), that showed a remarkable proapoptotic activity on the erythroleukemic K562 cell line.

Although more specific tests are necessary for clarifying the target of the compounds here presented, the apoptosis mechanisms seem to be involved.

## Abbreviations

| | |
|---|---|
| DCP | 3,7-bis(dichloroacetyl)-1,3,7-triaza-5-phosphabicyclo[3.3.1] nonane |
| DCA | dichloroacetic acid/dichloroacetate |
| PTA | 1,3,5-triaza-7-phosphaadamantane |

## Funding

This work was supported by University of Ferrara (Grant FAR 2017 to IL) and CIRCMSB (Consorzio Interuniversitario di ricerca in chimica dei metalli nei sistemi biologici). R.G. is funded by AIRC (Associazione Italiana Ricerca sul Cancro) and by CIB (Consorzio Interuniversitario per le Biotecnologie).

## Declaration of Competing Interest

No potential conflicts of interest were disclosed.

## Acknowledgements

We thank E. Bianchini, P. Formaglio, T. Bernardi and D. Preti for technical assistance.

## Appendix A. Supplementary data

Supplementary data to this article can be found online at https://doi.org/10.1016/j.jinorgbio.2019.110787.

## References

[1] P. Barbaro, L. Gonsalvi, A. Guerriero, F. Liguori, Green Chem. 11 (2012) 3211–3219.
[2] S. Moret, P.J. Dyson, G. Laurenczy, Nature Comm 5 (2014) 4017–4023.
[3] M.A. Affan, P.G. Jessop, Inorg. Chem. 56 (2017) 7301–7305.
[4] F. Scalambra, N. Holzmann, L. Bernasconi, S. Imberti, A. Romerosa, ACS Catal. 8 (2018) 3812–3819.
[5] M. Serrano-Ruiz, P. Lorenzo-Luis, A. Romerosa, A. Mena-Cruz, Dalton Trans. 42 (2013) 7622–7630.
[6] S.W. Jaros, M.F.C. Guedes da Silva, J. Krol, M. Conceicao Oliveira, P. Smolenski, A.J.L. Pombeiro, A.M. Kirillov, Inorg. Chem. 55 (2016) 1486–1496.
[7] S.W. Jaros, M.F.C. Guedes da Silva, M. Florek, P. Smolenski, A.J.L. Pombeiro, A.M. Kirillov, Inorg. Chem. 55 (2016) 5886–5894.
[8] B. Sierra-Martin, M. Serrano-Ruiz, V. Garcia-Sakai, F. Scalambra, A. Romerosa and A. Fernandez-Barbero, Polymers 10 (2018) 528/1–528/12.
[9] F. Battistin, F. Scaletti, G. Balducci, S. Pillozzi, A. Arcangeli, L. Messori, E. Alessio, J. Inorg. Biochem. 160 (2016) 180–188.
[10] R. Pettinari, A. Petrini, F. Marchetti, C. Pettinari, T. Riedel, B. Therrien, P.J. Dyson, Eur. J. Inorg. Chem. (12) (2017) 1800–1806.
[11] R.H. Berndsen, A. Weiss, U.K. Abdul, T.J. Wong, P. Meraldi, A.W. Griffioen, P.J. Dyson, P. Nowak-Sliwinska, Sci. Rep. 7 (2017) 43005.
[12] B.S. Murray, M.V. Babak, C.G. Hartinger, P.J. Dyson, Coord. Chem. Rev. 306 (2016) 86–114.
[13] P. Bergamini, L. Marvelli, A. Marchi, F. Vassanelli, M. Fogagnolo, P. Formaglio, T. Bernardi, R. Gavioli, F. Sforza, Inorg. Chim. Acta 391 (2012) 162–170.
[14] R. Cortesi, P. Bergamini, L. Ravani, M.S. Drechsler, A. Costenaro, M. Pinotti, M. Campioni, L. Marvelli, E. Esposito, Int. J. Pharm. 431 (2012) 176–182.
[15] P. Bergamini, L. Marvelli, A. Marchi, V. Bertolasi, M. Fogagnolo, P. Formaglio, F. Sforza, Inorg. Chim. Acta 398 (2013) 11–18.
[16] V. Ferretti, M. Fogagnolo, A. Marchi, L. Marvelli, F. Sforza, P. Bergamini, Inorg. Chem. 53 (2014) 4881–4890.
[17] R. Cortesi, C. Damiani, L. Ravani, L. Marvelli, E. Esposito, M. Drechsler, A. Pagnoni, P. Mariani, F. Sforza, P. Bergamini, Int. J. Pharm. 492 (2015) 291–300.
[18] J.M. Forward, Z. Assefa, R.J. Staples, J.P. Fackler Jr., Inorg. Chem. 35 (1996) 16–22.
[19] A.M. Kirillov, P. Smolenski, M. Haukka, M.F.C. Guedes da Silva, A.J.L. Pombeiro, Organometallics 28 (2009) 1683–1687.
[20] E. Atrian-Blasco, S. Gascon, M.J. Rodriguez-Yoldi, M. Laguna, E. Cerrada, Eur. J. Inorg. Chem. (17) (2016) 2791–2803.
[21] A. Guerriero, M. Peruzzini, L. Gonsalvi, Coord. Chem. Rev. 355 (2018) 328–361.
[22] D.J. Darensbourg, C.G. Ortiz, J.W. Kamplain, Organometallics 23 (2004) 1747–1754.
[23] D.A. Krogstad, G.S. Ellis, A.K. Gunderson, A.J. Hammrich, J.W. Rudolf, J.A. Halfen, Polyhedron 26 (2007) 4093–4100.
[24] W. Liu, J. Jiang, Y. Xu, S. Hou, L. Sun, Q. Ye, L. Lou, J. Inorg. Biochem. 146 (2015) 14–18.
[25] X.X. Stander, B.A. Stander, A.M. Joubert, Cell. Physiol. Biochem. 35 (2015) 1499–1526.
[26] E. Babu, S. Ramachandran, V. Coothankandaswamy, S. Elangovan, P.D. Prasad, V. Ganapathy, M. Thangaraju, Oncogene 30 (2011) 4026–4037.
[27] R.K. Pathak, S. Marrache, D.A. Harn, S. Dhar, ACS Chem. Biol. 9 (2014) 1178–1187.
[28] C. Trapella, R. Voltan, E. Melloni, V. Tisato, C. Celeghini, S. Bianco, A. Fantinati, S. Salvadori, R. Guerrini, P. Secchiero, G. Zauli, J. Med. Chem. 59 (2016) 147–156.
[29] D.J. Darensbourg, J.B. Robertson, D.L. Larkins, J.H. Reibenspies, Inorg. Chem. 38 (1999) 2473–2481.
[30] E. Bisz, A. Piontek, B. Dziuk, R. Szostak, M. Szostak, J. Org. Chem. 83 (2018) 3159–3163.
[31] E. Vergara, S. Miranda, F. Mohr, E. Cerrada, E.R.T. Tiekink, P. Romero, A. Mendía, M. Laguna, Eur. J. Inorg. Chem. (2007) 2926–2933.
[32] K. Sungsoo, K. Jungyu, K. Jieun, W. Daeun, C. Suk-Kyu, C. Wansik, J. Keunhong, A. Sangdoo, K. Kyungwon, Molecule 23 (2018) 2294–2312.
[33] V. Prelog, G. Helmchen, Angew. Chemie 21 (1982) 567–583.
[34] M.N. Burnett, C.K. Johnson, ORTEP-III: oak ridge thermal ellipsoid plot program for crystal structure illustrations, Oak Ridge National Laboratory Report ORNL-6895, 1996.
[35] G. Cavallo, P. Metrangolo, R. Milani, T. Pilati, A. Primagi, G. Resnati, G. Terraneo, Chem. Rev. 116 (2016) 2478–2601.
[36] A.R. Kapdi, I.J.S. Fairlamb, Chem. Soc. Rev. 43 (2014) 4751–4777.
[37] E. Guerrero, S. Miranda, S. Lüttenberg, N. Fröhlich, J.-M. Koenen, F. Mohr, E. Cerrada, M. Laguna, A. Mendía, Inorg. Chem. 52 (2013) 6635–6647.
[38] M. Carreira, R. Calvo-Sanjuán, M. Sanaú, I. Marzo, M. Contel, Organometallics 31 (2012) 5772–5781.
[39] C.S. Allardyce, P.J. Dyson, D.J. Ellis, S.L. Heath, Chem. Comm. (2001) 1396–1397.
[40] C.S. Allardyce, A. Dorcier, C. Scolaro, P.J. Dyson, Appl. Organomet. Chem. 19 (2005) 1–10.
[41] A. Dorcier, P.J. Dyson, C. Gossens, U. Rothlisberger, R. Scopelliti, I. Tavernelli, Organometallics 24 (2005) 2114–2123.
[42] R. Pettinari, F. Condello, F. Marchetti, C. Pettinari, P. Smoleński, T. Riedel, R. Scopelliti, P.J. Dyson, Eur. J. Inorg. Chem. (22) (2017) 2905–2910.
[43] C. Scolaro, A. Bergamo, L. Brescacin, R. Delfino, M. Cocchietto, G. Laurenczy, T.J. Geldbach, G. Sava, P.J. Dyson, J. Med. Chem. 48 (2005) 4161–4171.
[44] P. Nowak-Sliwinska, J.R. van Beijnum, A. Casini, A.A. Nazarov, G. Wagnières, H. van den Bergh, P.J. Dyson, A.W. Griffioen, J. Med. Chem. 54 (2011) 3895–3902.
[45] S.C. Marker, S.N. MacMillan, W.R. Zipfel, Z. Li, P.C. Ford, J. Wilson, Inorg. Chem. 57 (2018) 1311–1331.
[46] P. Kurz, B. Probst, B. Spingler, R. Alberto, Eur. J. Inorg. Chem. (2006) 2966–2974.
[47] I. Ott, Coord. Chem. Rev. 253 (2009) 1670–1681.
[48] S. Jurgens, A. Casini, Chimia 71 (2017) 92–101.

[49] O. Karaca, V. Scalcon, S.M. Meier-Menches, R. Bonsignore, J.M.J.L. Brouwer, F. Tonolo, A. Folda, M.P. Rigobello, F.E. Kuehn, A. Casini, Inorg. Chem. 56 (2017) 14237–14250.
[50] B. Bertrand, A. Citta, I.L. Franken, M. Picquet, A. Folda, V. Scalcon, M.P. Rigobello, P. Le Gendre, A. Casini, E. Bodio, J. Biol. Inorg. Chem. 20 (2015) 1005–1020.
[51] Z. Assefa, B.G. McBurnett, R.J. Staples, J.P. Fackler Jr., B. Assmann, K. Angermaier, H. Schmidbaur, Inorg. Chem. 34 (1995) 75–83.
[52] T. Scattolin, I. Caligiuri, L. Canovese, N. Demitri, R. Gambari, I. Lampronti, F. Rizzolio, C. Santo, F. Visentin, Dalton Trans. 47 (2018) 13616–13630.
[53] T. Scattolin, L. Canovese, F. Visentin, S. Paganelli, P. Canton, N. Demitri, Appl. Organomet. Chem. 32 (2018) e4034.
[54] P. Bergamini, L. Marvelli, V. Ferretti, C. Gemmo, R. Gambari, Y. Hushcha, I. Lampronti, Dalton Trans. 45 (2016) 10752–10760.
[55] K.M. Henkels, J.J. Turchi, Cancer Res. 59 (1999) 3077–3083.
[56] S. Dasari, P.B. Tchounwou, Eur. J. Pharmacol. 740 (2014) 364–378.
[57] V. Ferretti, P. Bergamini, L. Marvelli, Y. Hushcha, C. Gemmo, R. Gambari, I. Lampronti, Inorg. Chim. Acta 470 (2018) 119–127.
[58] I. Lampronti, N. Bianchi, C. Zuccato, A. Medici, P. Bergamini, R. Gambari, Bioorg. Med. Chem. 14 (2006) 5204–5210.
[59] D.J. Daigle, Inorg. Synth. 32 (1998) 40–45.
[60] S. Otto, A. Roodt, W. Purcell, Inorg. Chem. Commun. 1 (1998) 415–417.
[61] R. Usón, A. Laguna, M. Laguna, Inorg. Synth. 26 (1989) 85–91.
[62] R.H. Blessing, Acta Crystallogr. A 51 (1995) 33–38.
[63] A. Altomare, M.C. Burla, M. Camalli, G. Cascarano, C. Giacovazzo, A. Guagliardi, A.G. Moliterni, G. Polidori, R. Spagna, J. Appl. Crystallogr. 32 (1999) 115–119.
[64] G.M. Sheldrick, Acta Crystallogr. C 71 (2015) 3–8.
[65] L.J. Farrugia, J. Appl. Crystallogr. 45 (2012) 849–854.
[66] C.B. Lozzio, B.B. Lozzio, Blood 45 (1975) 321–334.
[67] I. Lampronti, M.T. Khan, M. Borgatti, N. Bianchi, R. Gambari, eCAM. 5 (2008) 303–312.
[68] A. Baldisserotto, S. Vertuani, A. Bino, D. De Lucia, I. Lampronti, R. Milani, R. Gambari, S. Manfredini, Bioorg. Med. Chem. 23 (2015) 264–271.
[69] R. Milani, E. Brognara, E. Fabbri, A. Finotti, M. Borgatti, I. Lampronti, G. Marzaro, A. Chilin, K.K. Lee, S.H. Kok, C.H. Chui, R. Gambari, Oncol. Res. 26 (2018) 1307–1315.

Bioorganic Chemistry 119 (2022) 105518

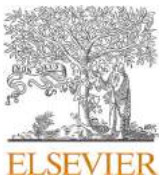

Contents lists available at ScienceDirect

Bioorganic Chemistry

journal homepage: www.elsevier.com/locate/bioorg

# Synthesis and biological evaluation of novel rhodanine-based structures with antiviral activity towards HHV-6 virus

Valentina Gentili [1], Giulia Turrin [1], Paolo Marchetti, Sabrina Rizzo, Giovanna Schiuma, Silvia Beltrami, Virginia Cristofori, Davide Illuminati, Greta Compagnin, Claudio Trapella [*], Roberta Rizzo [*], Daria Bortolotti [1], Anna Fantinati [1]

*University of Ferrara, Department of Chemical, Pharmaceutical and Agricultural Sciences, Via Fossato di Mortara, 17, 44121 Ferrara, Italy*

A B S T R A C T

An increased awareness of diseases associated with Human herpesvirus 6 (HHV-6) infection or reactivation has resulted in a growing interest in the evaluation of the best treatment options available for the clinical management of HHV-6 disease. However, no compound has yet been approved exclusively for HHV-6 infection treatment. For this reason, the identification of anti-HHV6 compounds provides a valuable opportunity for developing efficient antiviral therapies. A possible target for antiviral drugs is the virus-cell fusion step. In this study, we synthetized potential fusion intermediates inhibitors based on the rhodanine structure. The obtained derivatives were tested for cytotoxicity and for antiviral activity in human cells infected with HHV6. Level of infection was monitored by viral DNA quantification at different time points up to 7 days post infection. Among the synthetized derivatives, **9e** showed a significative inhibitory effect on viral replication that lasted over 7 days, probably attributable to the particular combination of hydrophilic and hydrophobic substituents to the rhodanine moiety. Our results support the use of these amphipathic fusion inhibitors for the treatment of HHV-6 infections.

## 1. Introduction

Most of available antiviral drugs are design to target specific viral proteins [1,2]. However, this therapeutic approach determines a selection for resistance [3], and also display a limited spectrum of action. In view of this, novel antivirals are therefore needed.

In the last years, several studies were focused on the identification of new antiviral targets based on the interference with viral fusion on cell membrane [4]. In fact, fusion of enveloped virus with the host cell is crucial in viral infectivity. Viral fusion is a process driven by specialized protein expressed on viral envelope that, after conformational modifications due to their binding to specific cellular receptors, leads to envelope-cell membrane fusion and the consequent release of the nucleocapsid into the cytoplasm.

The steps of the viral fusion process evidenced two possible moments on which fusion inhibitors could be effective: *i.* pre-fusion step, which involved the engagement of the cellular receptor during the viral adsorption and *ii.* fusion intermediates step, in which a physical fusion occurs between the lipid bilayers of both envelope and cytoplasmic membrane [5].

Various molecules are proposed in literature as membrane fusion inhibitors that affect the viral attachment through cell receptor, disturbing the viral adsorption phase [5]. Essentially, these molecules exert their function by blocking the cognate virus-receptor interaction via competition for the entry receptors, representing the classical inhibitors of virus entry [5]. The use of this strategy is exemplified by Maraviroc (Selzentry; Pfizer), a competitive molecule for the virus co-receptor CC-chemokine receptor 5 (CCR5) that inhibits HIV-1 entry [6]. However, despite the potential efficacy of these competitors as antivirals, the development of receptor-specific entry inhibitors for the great majority of viral pathogens is limited by the identification of the actual receptors. In this view, the design of new antivirals, capable of inhibiting cell entry of enveloped viruses by blocking the formation of fusion intermediates seems to represent the most convenient approach. In fact, these molecules could act independently from the cellular receptor involved during viral entry, thus no specific receptor structure is required.

Fusion intermediates inhibitors work mainly by modifying the lipidic structure of both virus and host cell membrane, in order to avoid the release of the nucleocapsid inside the cells. Among antiviral mechanisms of action against the entry of enveloped viruses, the most studied include the induction of cholesterol depletion [7] and the alteration of membrane components that modify membrane fluidity [8] or cause virolysis.

* Corresponding authors at: University of Ferrara, Department of Chemical, Pharmaceutical and Agricultural Sciences, Via Luigi Borsari 46, 44121 Ferrara, Italy (R. Rizzo). University of Ferrara, Department of Chemical, Pharmaceuticaland Agricultural Sciences, Via Fossato di Mortara, 17 44121 Ferrara, Italy (C. Trapella).

*E-mail addresses:* trap@unife.it (C. Trapella), rbr@unife.it (R. Rizzo).

[1] These authors contributed equally to the research.

https://doi.org/10.1016/j.bioorg.2021.105518

Received 3 June 2021; Received in revised form 4 October 2021; Accepted 23 November 2021

Available online 26 November 2021

This, for instance, is observed in treatment with rigid amphipathic fusion inhibitors (RAFIs) [9-12].

Other molecules displaying a broad-spectrum of antiviral activity through a selective action on enveloped viruses are rhodanine and thiobarbituric derivatives. Their activity is due to lipid oxidation ability, which affects the fluidity of the lipid bilayer and interferes with virus-cell fusion. Recently, polyrhodanine nanostructure has been reported as antiviral, anticancer and bacteriostatic [13]

Fusion intermediate inhibitors are promising antiviral drugs since they exert their function in the early phase of infection, namely before damages have occurred to cells [14,15]. The advantage of using this kind of antivirals includes the broad spectrum of enveloped viruses that could be inhibited without the risk of developing resistance. Some of these antivirals have been described to be effective on different human viruses, such as the respiratory syncytial virus (RSV) [16], Hepatitis B (HBV) [17] and C (HCV) viruses [18,19].

Considering enveloped viruses associated to different human pathological conditions, herpesviruses are among the most studied. In particular, these viruses are characterized by the ability to develop a latency phase after the primary infection, causing as a consequence the onset of symptoms throughout the life span.

The Herpesiviridae family includes nine components that infect humans and can be divided into three subfamilies: alpha-, beta- and gamma-herpesvirus according to their different cell tropism and symptomatology.

Human Herpes Virus-6 (HHV-6) is a beta-herpesvirus with a worldwide distribution that exists in two different species characterized by peculiar biological differences [20]: HHV-6A and HHV-6B. HHV-6B is the etiologic agent of roseola (*exanthema subitum*), while the disease associated with HHV-6A infection is still not clearly identified. These differences could be attributed to a different engagement of cell receptors by the two viruses. In fact, while HHV-6B recognizes CD134, expressed on *T*-cells, HHV-6A uses CD46, expressed on all nucleated cells [21], subtending its ability to infect a wide range of tissues, as confirmed by the recent association of HHV-6A infection with several diseases, including Multiple Sclerosis (MS) [22], Alzehimer's Disease (AD) [23,24] and infertility [25,26]. Importantly, to date, the treatment for HHV-6 infection consists only in antivirals that are already used to treat other herpetic infections and that target specific viral protein in order to inhibit viral replication and gene expression [27,28]. Moreover, HHV-6 establishes a latent infection in the target tissues and it could be reactivated several times during life, thus it requires several treatments with antivirals which can increase the risk of resistances [29,30]. In light of this, the use of fusion intermediates inhibitors to threat HHV-6 infection may represent an efficient strategy to improve infection control and decrease resistance onset.

The data available in literature on the use of fusion inhibitors to control herpetic infections report mainly the effect of some compounds in affecting the pre-fusion phase, by interfering with glycoprotein B interaction and cellular-membrane lipid rafts formation [31-33]. On the other hand, concerning the inhibition of the fusion intermediate formation, Cagno et al. described the antiviral activity of rhodanine derivatives on enveloped viruses including HSV-2 acyclovir resistant strain [34] and Boresnstein et al. recently reported the effect of ginkgolic acid on several herpes viruses, including EBV, HSV-1 and HCMV [35].

Conversely, no data are available on the use of fusion intermediates inhibitors for this particular type of infection.

In this study, we have synthesized ten potential fusion intermediates inhibitors based on rhodanine structure, potentially active on HHV-6 infection. We tested the compounds on human cell lines, to determine their toxicity and effectiveness in controlling the HHV-6 infection, in order to identify the most safe and active compound.

## 2. Results and discussion

### 2.1. Chemistry

Recently different works has been published on the synthesis of antiviral molecule based on rhodanine heterocycle [34], acting as disrupting molecules for the enveloped viruses such as HSV-2, Influenza A virus, Zika.

Referring to the work of Cagno et al. [34] we chose the rhodanine-based compound **1** as reference compound to develop a SAR study focused on the modification of its hydrophilic head and lipophilic chain (Fig. 1). Different specific modifications have been made, considering RAFIs and their mechanism of action as starting point for this study [36].

The synthesis of the rhodanine scaffold was focused on the introduction of several aromatic rings, starting from different primary chiral and achiral amines, in order to build a small library of compounds bearing a series of substituents attached to the nitrogen atom (Scheme 1).

The synthesis of rhodanine derivatives has been achieved in a one-pot reaction between bromo-acetyl bromide (**2**) and the corresponding primary amine **3a-f** in carbon disulfide, to obtain in moderate to good yield the rhodanine core **4a-f.** Then, as shown in Scheme 2, to insert structural modifications of the polar head of the compound **1** (Fig. 1), we used a palladium catalyzed Suzuki reaction as a key step for the formation of the carbon–carbon bond between the iodo derivatives **5a-e** and the five-membered heterocycles, **6a-b** (furane or thiophene). Due to the instability of the rhodanine scaffold in basic conditions [37], we decided to work with the corresponding methyl ester derivatives **5a-e** to obtain the aldehydic compounds **7a-e** with higher yields. Then, we removed the ester function in the next step through lithium hydroxide hydrolysis, to afford compounds **8a-d**.

Once obtained the derivatives **8a-d**, we could bind them with the rhodanine scaffold trough a Knowenagel condensation [38], to obtain the desired products **9a**. Starting from **9a** we conceptualized new compounds with different lipophilic tails (**9b-f)** or different hydrophilic heads (**10a-d)** as depicted in Scheme 3.

### 2.2. Biological evaluation

#### 2.2.1. Evaluation of cytotoxicity of *9a* and derivate compounds with different lipophilic tails

**9a-f** cytotoxicity was assayed in human lymphocytic cell lines by MTT assay, after 24 h treatment at 100 μM, 10 μM and 1 μM. As shown in Fig. 2, all the compounds did not affect cell viability at the concentrations of 1μM and 10 μM, while the concentration of 100 μM showed a high cytotoxic effect ($p < 0.0001$, Student T test). The anti-viral efficacy was evaluated for the concentrations of 1 and 10 μM, that are hundred-ten times lower than the cytotoxic concentration and ensure a safe use as

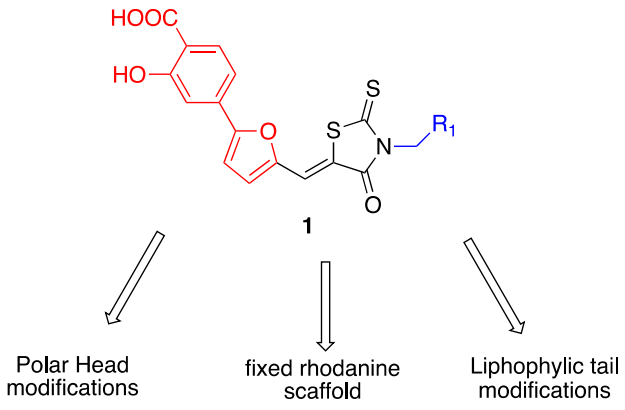


**Fig. 1.** Structure of the rhodamine-based reference compound.

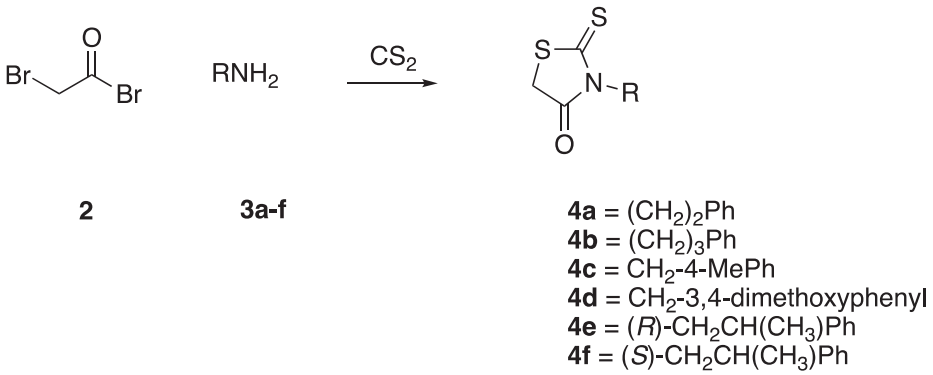


**Scheme 1.** Synthesis of rhodanine derivatives with modifications at lipophilic tail.

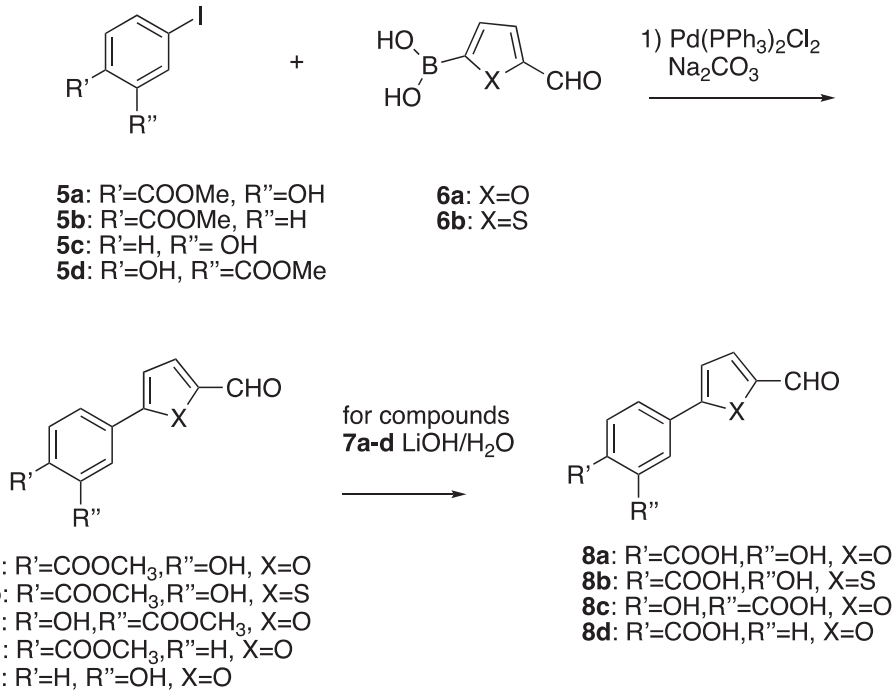


**Scheme 2.** Synthesis of polar head bearing the aldehyde moiety.

a drug. The absence of cytotoxicity in the 1 and 10 μM range of concentration could be explained by the fact that cellular membranes are metabolically active and are characterized by a regenerative activity, that is absent in viromes.

*2.2.2. Anti-HHV-6 activity of **9a** and derivate compounds with different lipophilic tails*

The antiviral activity of **9a-f** compounds was tested on HHV-6A infected J-Jhan cells and HHV-6B SupT1 infected cells. The compounds were added to infected cell cultures at the concentration of 1 and 10μM and pellet cell samples were collected at 24, 48, 72 h (hpi) and 7 days post infection (dpi) for HHV-6 DNA quantification by real time PCR. Results are reported as percentage compared to untreated infected control.

**9a-9d** molecules did not affect viral replication when used at the concentration of 1 μM (Fig. 3a, b), while **9e** and **9f** molecules were able to decrease viral replication in a significant level ($p < 0.0001$, Student T test) (Fig. 3a, b).

The treatment at 10μM was more effective in reducing HHV-6A and HHV-6B replication (Fig. 3c, d). In particular, the highest antiviral effect was observed in presence of **9a, 9e** and **9f** treatment, which significantly decreased viral replication at all the time points considered, showing a decrease of 90–75% of viral load already after 24 hpi compared to untreated control ($p < 0.01$, Student T test), followed by a complete drop of the viral infection till 7 dpi for **9a** and **9e** ($p < 0.0001$, Student T test) (Fig. 3c, d). On the contrary, in presence of **9b**, **9c** and **9d** treatment we observed no effect on viral load at 24 hpi, while there was a drop in both HHV-6A and HHV-6B replication at 48 hpi that is maintained until 7dpi ($p < 0.0001$, Student T test) (Fig. 3c, d).

*2.2.3. Evaluation of cytotoxicity and antiviral activity of **9a** derivatives with modified hydrophilic head*

MTT assay was performed to assess the **10a**, **10b** and **10c** derivatives cytotoxicity on human lymphocyte cell lines after treatment for 24 h at the concentration of 1 and 10μM. The results showed that **10a**, **10b** and **10d** did not affect cell viability, while **10c** resulted in a significant cytotoxic effect (Fig. 4, $p < 0.05$ Student T test). We hypothesize that the toxicity of compound 10c might be due to the lack of the phenol OH that is involved in the hydrogen bond with the carboxylic moiety. In fact, both 10b and 10d are not toxic, where the OH group of 10b makes a

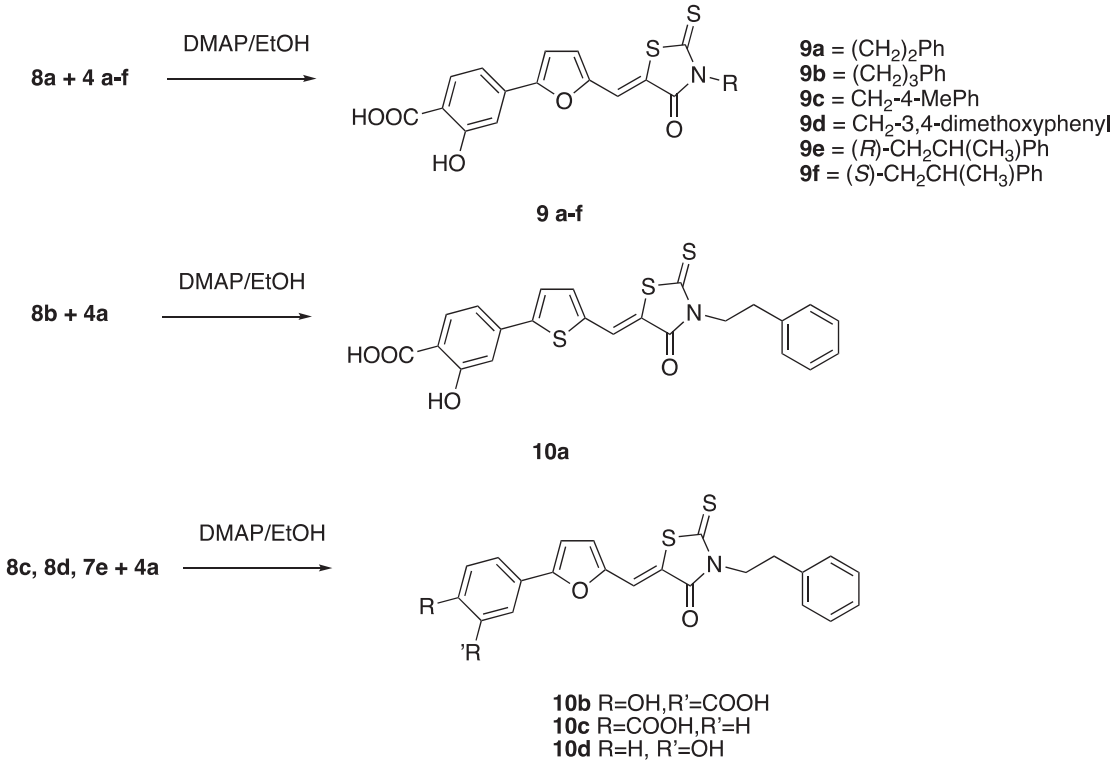


**Scheme 3.** Synthesis of the final rhodanine scaffold bearing different polar heads and lipophylic tails.

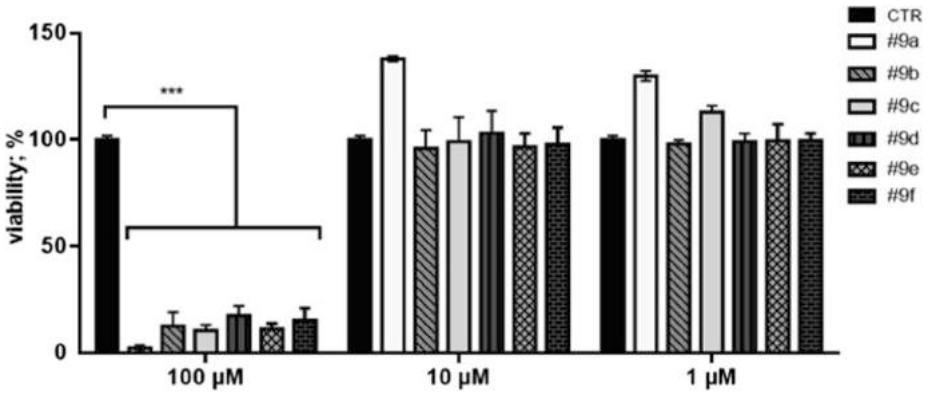


**Fig. 2.** Cell viability analysis by MTT assay in human lymphocyte cell lines after 24 h treatment with #**9a-9f** at the concentrations of 1, 10 and 100 µM. Values are reported as mean ± SD of 3 independent experiments.

hydrogen bond with the carboxylic moiety, 10d lacks the COOH function, supporting that the toxicity of 10c might be related to this acidic function when it's not involved in the hydrogen bond due to the lack of hydroxyl group. Basing on this result, **10c** was not considered for further analysis.

Antiviral activity of **10a, 10b and 10d** compounds was evaluated. As shown in Fig. 5, the HHV-6A and HHV-6B viral load was reduced of 52 and 54% ($p = 0.0016$, Student T test) and 90 and 89% ($p = 0.0002$, Student T test), respectively, after 72hpi and 7dpi after treatment with **10b**. **10a** treatment reduced the viral load of 52% ($p = 0.0046$, Student T test) and 49% ($p = 0.0044$, Student T test), at 48hpi and 72hpi, respectively, but the anti-HHV-6A and HHV-6B effect was lost after 7dpi (Fig. 5). **10d** treatment reduced the viral load of 90% ($p < 0.0001$, Student T test) at 24hpi and 48hpi, but the anti-HHV-6A and HHV-6B effect was lost after 72hpi (Fig. 5).

This data confirmed that the modification of **9a** polarity obtained in these derivatives does not improve its inhibition of the viral replication, suggesting that this moiety participates only partially at the antiviral effect.

## 3. Conclusion

Despite the increasing evidence reporting HHV-6A and HHV-6B association with different diseases [22-26], there are no specific antiviral drugs available acting against this specific virus. The present study explores the antiviral effects of rhodanine-based fusion intermediate inhibitors on HHV-6 infection in human cells. Since HHV-6 is an enveloped virus, we synthesized potential fusion intermediate inhibitors [14,15], characterized by the presence of a rhodanine scaffold, with the aim of blocking the virion-cell fusion. We obtained different derivatives by substitution and bioisosteric replacements of hydrophilic head and lipophilic tail of the molecules tested for their cytotoxicity and antiviral

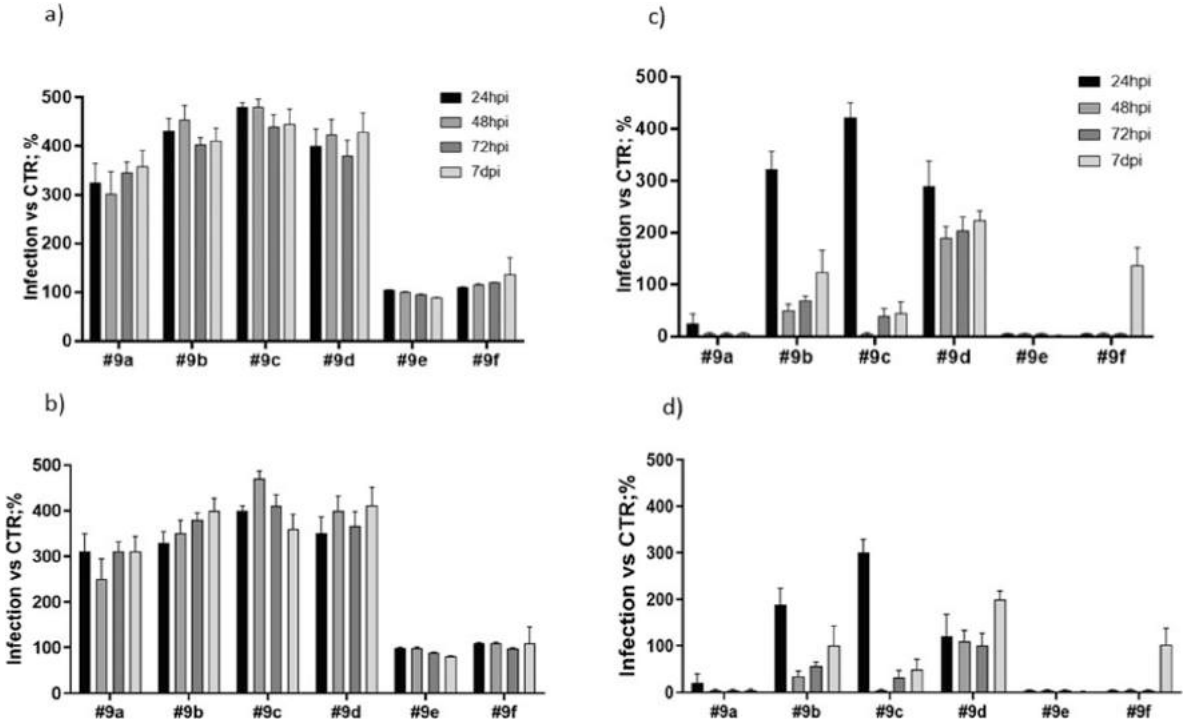


**Fig. 3.** Infection percentage compared to the untreated infected control (CTR) after treatment at 1 μM (a, b) and 10 μM (c, d) with #**9a-9f** compounds 24, 48 and 72 h and 7 days post infection with HHV-6A (a, c) and HHV-6B (b, d). HHV-6 genomes were quantified by real time-PCR and normalized for housekeeping RNaseP gene. Data were reported as mean percentage ± SD obtained from 3 independent experiments compared to untreated infected cells.

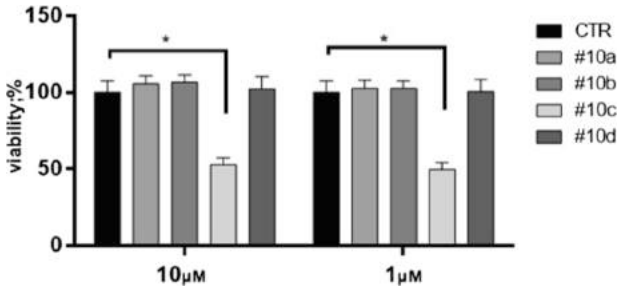


**Fig. 4.** Cell viability analysis by MTT assay in human lymphocyte cell lines after 24 h treatment with #**10a**, #**10b**, #**10c** and #**10d** at the concentration of 1 and 10 μM, compared to untreated control (CTR). Values are reported as mean ± SD of 3 independent experiments. *$p < 0.05$ Student T test.

effect on HHV-6A and HHV-6B replication. Experimental results identified the **9a** derivative as the lead compound, showing a complete reduction of HHV-6 viral load 48 h after infection, when used at 10uM, without showing any cytotoxicity. In order to improve the antiviral effect of the lead compound **9a**, we worked on the modification of the hydrophilic head or the lipophilic tail to increase the amphipacity of the molecule, obtaining different derivatives. Among these, compound **9e** at the concentration of 10uM, showed the highest antiviral activity, with a complete abatement of the viral load after 24 h and no cytotoxicity. The improved efficacy of compound **9e** could be attributed to its peculiar combination of hydrophilic and hydrophobic substituents to the rhodanine moiety, that possibly allowed a better interaction with the viral envelope. The insertion into the viral envelop might induce envelope structure destabilization and virolysis that inhibit virion fusion and infection of the target cell. These results support the use of amphipathic fusion intermediate inhibitors based on rhodanine structure to treat HHV-6A and HHV-6B infection. Despite the two viruses engage different cellular receptors, we observed a comparable inhibitory effect by treating with inhibitors based on rhodanine structure. This could be ascribable to the amphipathic nature of the compounds, which disorganize the viral envelope structure, avoiding the viral fusion with the host cell membranes, without engaging specific viral structures. In fact, enveloped viruses as HHV-6, gain their external membrane during virions release directly from cell surface. Anyway, while cell membranes are metabolically active, viral envelopes are not. In this way, rhodanine derivatives could induce virolysis and interfere with envelope-cell fusion process by intercalating in the viral outer phospholipidic bilayer without inducing critical cell membrane alteration, as proved by the absence of cytotoxicity observed after treating cells with antiviral concentrations.

This characteristic might avoid the onset of resistance in the new viral progeny, that usually observed with repeated treatments with common antiviral drugs.

## 4. Experimental section

### 4.1. Chemistry

Reagents were purchased from commercial suppliers and used without further purification. $^{1}H$ and $^{13}C$ NMR spectra were recorded, in deuterated DMSO or $CDCl_3$ solution, respectively, at 400 and 100 MHz on a Varian Mercury Plus 400, and peak positions are given in parts per million and were referenced to residual $^{1}H$ signals of the deuterated solvents respectively ($\delta^{1}H$ 7.26 for $CDCl_3$, $\delta$ $^{1}H$ 2.50 for DMSO-$d_6$). J values are expressed in Hertz. Positive-ion electrospray ionization (ESI) mass spectra were recorded on ESI Micromass ZQ 2000 instrument. Thin layer chromatography (TLC) was carried out using Merck precoated silica gel F-254 plates. Flash chromatography was done using Merck silica gel 60 (0.063–0.200 mm). Solvents were dried according to standard procedures, and reactions requiring anhydrous conditions were performed under argon. Solutions containing the final products were dried with $Na_2SO_4$, filtered, and concentrated under reduced

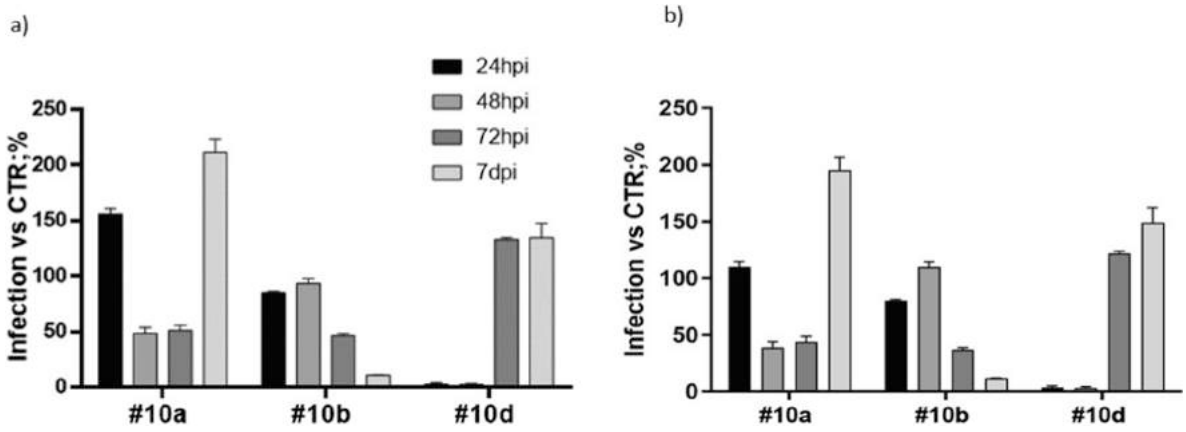


**Fig. 5.** Infection percentage compared to the untreated infected control after treatment with 10 μM **10a**, **10b** and **10d** compounds 24, 48 and 72 h and 7 days post infection with HHV-6A (a) and HHV-6B (b) . HHV-6 genomes were quantified by real time-PCR and normalized for housekeeping RNaseP gene. Data were reported as mean percentage ± SD obtained from 3 independent experiments compared to untreated infected cells.

pressure using a rotatory evaporator. The purity of the tested compounds was determined by combustion elemental analyses conducted by the Microanalytical Laboratory of the Chemistry Department of the University of Ferrara, Italy, with a Yanagimoto MT-5 CHN recorder elemental analyzer. All tested compounds yielded data consistent with a purity of at least 95% compared with the theoretical values. Melting points were determined on a Reichert-Kofler apparatus and are uncorrected.

*4.1.1. General procedure for the synthesis of rhodanines **4a-f***

Bromoacetyl bromide (1 mmol) was added, drop by drop, to a mixture of the pertinent amine (1 mmol) in $CS_2$ (5 mL) at 0–2 °C. The reaction mixture was allowed to warm up to room temperature and then heated at 100 °C for 3 h. After this time, AcOEt (25 mL) was added and the mixture was washed with $H_2O$ (3 × 7 mL). After evaporation of the solvent the resulting crude product (brown–red oil) was purified by column chromatography using as eluent mixtures of solvents in the proportions indicated for each compound.

*4.1.2. General procedure for the synthesis of compounds **7a-e***

Methyl-4-iodosalycilate **5a-e** (1.00 mmol) and 5-formyl-2-furan boronic acid **6a, b** (1.30 mmol) were dissolved in EtOH (10 mL) and DMF (5 mL) mL. The reaction mixture was stirred for 10 min under Argon at room temperature, then $Pd(PPh_3)_2Cl_2$ (0.1 mmol) and a 2 M solution of $Na_2CO_3$ (4 mL) were added. After 1 h, to the resultant orange suspension was added $H_2O$ (20 mL) and 2 N HCl till pH = 4–5 and then extracted with EtOAc (3 × 20 mL). When necessary, the mixture was stirred until organic and aqueous layers become clear. The combined organic layers were washed with brine (2 × 10 mL), dried over $Na_2SO_4$, filtered, and evaporated to give a crude product that was purified by flash chromatography with the opportune eluent to yield the desired product **7a-e** as brown-orange solids.

*4.1.3. General procedure for the synthesis of compounds **8a-d***

LiOH (10 mmol) was added to a solution of compounds **7a-e** (1 mmol) in $CH_3OH$ (10 mL) and $H_2O$ (5 mL). The reaction mixture was refluxed till ester disappeared in TLC (~1h), acidified with HCl 2 N till pH 4–5 and extracted with AcOEt (3 × 25 mL). The combined organic layers were washed with a $NaHCO_3$ saturated solution (2 × 20 mL) and brine (2 × 20 mL). The desired products **8a-e** were obtained as brown–red solid after evaporation of the solvent.

*4.1.4. General procedure for the synthesis of final compounds **9a-f, 10** and **10a-c***

A solution of compounds **8a-8d** (1 mmol), **4a-f** (1 mmol) and DMAP (0.2 mmol) in EtOH (10 mL) was refluxed overnight. The resulting suspension was filtered and the filtrate washed with cooled isopropanol to give the product as an orange-red solid that was purified by column chromatography using as eluent mixtures of solvents in the proportions indicated for each compound.

*4.1.5. **(4a)** 3-(2-phenylethyl)-2-thioxo-1,3-thiazolidin-4-one*

Oil, Yield 59%. $^1$H NMR ($CDCl_3$) d: 2.92–2.96 (m, 2H), 3.92 (s, 2H), 4.18–4.22 (m, 2H), 7.25–7.31 (m, 5H). $^{13}$C NMR ($CDCl_3$) d: 35.7, 35.3, 45.7, 126.8, 128.6, 128.9, 137.4, 173.5, 200.9. M.p.: 106–8 °C. $R_f$ AcOEt/P 1/4: 0.51.

*4.1.6. **(4b)** 3-(3-phenylpropyl)-2-thioxo-1,3-thiazolidin-4-one*

Oil, Yield 55%. $^1$H NMR ($CDCl_3$) d: 1.98–2.04 (m, 2H), 2.69 (t, 2H, J = 10.2), 3.74 (s, 2H), 4.01–4.06 (m, 2H), 7.18–7.27 (m, 5H) 126.4, 128.5, 128.7, 141.0, 174.1, 200.6. $^{13}$C NMR ($CDCl_3$) d: $R_f$ AcOEt/P 1/6: 0.46.

*4.1.7. **(4c)** 3-(4′-methylphenylmethyl)-2-thioxo-1,3-thiazolidin-4-one*

Solid, Yield 65 %. $^1$H NMR ($CDCl_3$) d: 2.33 (s, 3H), 3.98 (s, 2H), 5.16 (s, 2H), 7.13 (d, 2H, J = 8), 7.35 (d, 2H, J = 8). $^{13}$C NMR ($CDCl_3$) d: 21.4, 35.5, 47.5, 129.2, 129.3, 131.8, 138.1, 173.9, 201.1. M.p.: 71–2 °C. $R_f$ AcOEt/P 1/10: 0.25.

*4.1.8. **(4d)** 3-(3′,4′-dimethoxyphenylmethyl)-2-thioxo-1,3-thiazolidin-4-one*

Oil, Yield 53 %. $^1$H NMR (DMSO) d: 3.71 (s, 3H), 3.72 (s, 3H), 4.33 (s, 2H), 5.00 (s, 2H), 6.80–6.86 (m, 1H), 6.87 (d, 1H J = 8), 6.95 (d, 1H, J = 2). $^{13}$C NMR (DMSO) d: 35.8, 46.6, 55.3, 55.4, 111.5, 112.0, 120.2, 127.3, 148.2, 148.4, 174.4, 203.1. $R_f$ AcOEt/P 1/1: 0.523.

*4.1.9. **[(R)-4e]** (R)-3-(2-phenylpropyl)-2-thioxo-1,3-thiazolidin-4-one*

Oil, Yield 62%. $^1$H NMR ($CDCl_3$) d: 1.31 (d, 3H, J = 7.2), 3.47–3.57 (m, 1H), 3.79 (d, 1H, J = 22), 3.88 (d, 1H, J = 22), 4.10–4.17 (m, 2H) 7.24–7.33 (m, 5H). $^{13}$C NMR ($CDCl_3$) d: 17.6, 34.5, 36.1, 50.4, 126.4, 126.8, 127.9, 142.0, 173.1, 200.8. $R_f$ AcOEt/P 1/6: 0.3.

*4.1.10. **[(S)-4f]** (S)-3-(2-phenylpropyl)-2-thioxo-1,3-thiazolidin-4-one*

Oil, Yield 56%. $^1$H NMR ($CDCl_3$) d: 1.31 (d, 3H, J = 7.2), 3.47–3.57 (m, 1H), 3.79 (d, 1H, J = 22), 3.88 (d, 1H, J = 22), 4.10–4.17 (m, 2H) 7.24–7.33 (m, 5H). $^{13}$C NMR ($CDCl_3$) d: 17.6, 34.5, 36.1, 50.4, 126.4, 126.8, 127.9, 142.0, 173.1, 200.8. $R_f$ AcOEt/P 1/6: 0.3.

*4.1.11. **(7a)** 4-(5-formylfuran-2-yl)-2-hydroxybenzoate methyl ester*

Solid, Yield: 65% $^1$H NMR (DMSO) d 3.90 (s, 3H), 7.45–7.47 (m, 3H),

7.67 (d, 1H, J = 3.6), 7.88 (d, 1H, J = 8), 9.65 (s, 1H), 10.6 (s, 1H). $^{13}$C NMR (CDMSO) d: 52.4, 111.1, 113.0, 113.8, 115.7, 124.7, 131.0, 134.4, 152.1, 156.1, 159.9, 168.3, 178.2. $[M + H]^+$: 247.4. M.p.: 155–7 °C $R_f$ AcOet/Pet 1/2: 0.43.

*4.1.12. **(7b)** 4-(5-formylthiophen-2-yl)-2-hydroxybenzoate methyl ester*

Solid, Yield: 70 %. $^1$H NMR ($CDCl_3$) d:3.98 (s, 3H), 7.17–7.19 (m, 1H), 7.29 (d, 1H, J = 2), 7.48 (d, 1H, J = 4), 7.75 (d, 1H, J = 4), 7.87–7.89 (m, 1H), 9.9 (s, 1H), 10.8 (s, 1H), $^{13}$C NMR ($CDCl_3$) d: 52.5, 112.8, 114.9, 117.2, 125.6, 130.8, 137.0, 139.7, 143.7, 152.1, 161.8, 170.0, 182.8. $[M + H]^+$: 263.8. M.p.: 123–25 °C. $R_f$ AcOEt/Pet 1/2: 0.5

*4.1.13. **(7c)** 3-(5-formylfuran-2-yl)-4-hydroxybenzoate methyl ester*

Colorless solid, Yield: 72%. $^1$H NMR ($CDCl_3$) d 4.00 (s, 3H), 6.75 (d, 1H, J = 3.6), 7.06 (d, 1H, J = 8.8), 7.31 (d, 1H, J = 3.6), 7.88 (m, 1H), 8.32 (d, 1H, J = 2.4), 9.6 (s, 1H), 11.0 (s, 1H). $^{13}$C NMR ($CDCl_3$) d: 52.6, 106.7, 112.8, 118.5, 120.7, 127.1, 132.5, 151.8, 158.6, 162.6, 170.1, 176.9. $[M + H]^+$: 247.3. M.p.: 130–2 °C. $R_f$ AcOet/Pet 1/2: 0.2.

*4.1.14. **(7d)** 4-(5-formylfuran-2-yl)benzoate methyl ester*

Colorless solid, Yield: 83%. $^1$H NMR ($CDCl_3$) d: 3–96 (s, 3H), 6.97 (d, 1H, J = 3.6), 7.35 (d, 1H, J = 3.6), 7.89 (m, 1H), 8.12 (m, 1H), 9.70 (s, 1H). $^{13}$C NMR ($CDCl_3$) d: 52.4, 109.4, 123.1, 125.1, 130.3, 130.8, 132.9, 152.6, 158.0, 166.5, 177.6. $[M + H]^+$: 231.3. M.p.: 143–5 °C. $R_f$ AcOet/Pet 1/2: 0.4.

*4.1.15. **(7e)** 5-(3-hydroxyphenyl)furan-2-carboxaldehyde*

Colorless solid, Yield: 90%. $^1$H NMR ($CDCl_3$) d: 6.82 (d, 1H, J = 3.6), 6.92 (m, 1H), 7.26–7.38 (m, 4H), 9.61 (s, 1H). $^{13}$C NMR ($CDCl_3$) d: 108.1, 112.1, 117.1, 117.8, 130.2, 130.3, 151.8, 156.4, 159.5, 177.4. $[M + H]^+$: 189.2. M.p.: 128–30 °C. $R_f$ AcOet/Pet 1/2: 0.3.

*4.1.16. **(8a)** 4-(5-formylfuran-2-yl)-2-hydroxybenzoic acid*

Solid. Yield: 95%. $^1$H NMR (DMSO) d 7.39–7.45 (m, 3H), 7.65 (d, 1H, J = 3.6), 7.86–7.89 (m, 1H), 9.63 (s, 1H).$^{13}$C NMR (DMSO) d: 111.6, 112.9, 114.2, 116.1, 124.9, 131.0, 135.1, 152.7, 157.0, 162.0, 171.4, 178.8. $[M + H]^+$: 243.2. M.p.: 230 °C (Dec.). $R_f$ $CH_2Cl_2$/MeOH 4/1: 0.3.

*4.1.17. **(8b)** 4-(5-formylthiophen-2-yl)-2-hydroxybenzoic acid*

Solid, Yield: 89%. $^1$H NMR (DMSO) d: 7.04–7.07 (m, 2H), 7.71 (d, 1H, J = 4), 7.77 (d, 1H, J = 8), 8.02 (d, 1H, J = 4), 9.89 (s, 1H), 11.5 (br. s., 1H). $^{13}$C NMR (DMSO) d: 113.4, 114.0, 117, 127, 131.3, 138.7, 138.8, 143.0, 150.3, 161.3, 171.2, 184.2. $[M + H]^+$: 259.7. M.p.: 203–5 °C (Dec.). $R_f$ $CH_2Cl_2$/MeOH 3/1: 0.35.

*4.1.18. **(8c)** 3-(5-formylfuran-2-yl)-4-hydroxybenzoic acid*

Solid, Yield: 91%. $^1$H NMR (DMSO) d: 6.94 (d, 1H, J = 12), 7.12 (d, 1H, J = 4), 7.55–7.60 (m, 2H), 7.86 (m, 1H), 8.20 (d, 1H, J = 2.4), 9.5 (s, 1H). $^{13}$C NMR (DMSO) d: 107.3, 116.7, 118.4, 119.1, 127.3, 131.5, 151.6, 159.0, 164.0, 171.4, 177.6, 206.9. $[M + H]^+$: 243.5. M.p.: 213–15 °C. $R_f$ $CH_2Cl_2$/MeOH 4/1: 0.3.

*4.1.19. **(8d)** 4-(5-formylfuran-2-yl)benzoic acid*

Solid, Yield: 96%. $^1$H NMR ($CDCl_3$) d 7.43 (d, 1H, J = 3.6), 7.67 (d, 1H, J = 3.6), 7.66–8.04 (m, 4H), 9.64 (s, 1H), 13.18 (br s, 1H). $^{13}$C NMR ($CDCl_3$) d: 111.0, 125.4, 130.6, 131.7, 132.8, 152.6, 157.3, 167.1, 178.7, 206.9. $[M + H]^+$: 217.8. M.p.: 130–2 °C. $R_f$ $CH_2Cl_2$/MeOH 4/1: 0.4.

*4.1.20. **(9a)** 2-Hydroxy-4-{5-[4-oxo-3-phenethyl-2-thioxothiazolidin-5-ylidenemethyl]furan-2-yl}benzoic acid*

Orange solid, Yield 78%. $^1$H NMR ($CDCl_3$) d 2.95–2.99 (m, 2H), 4.11–4.14 (m, 2H), 7.17–7.38 (m, 9H), 7.61 (s, 1H), 7.82 (d, 1H, J = 8.2). $^{13}$C NMR ($CDCl_3$) d: 32.6, 45.7, 111.7, 112.1, 113.8, 118.7, 119.1, 123.5, 127.1, 129.0, 129.1, 131.5, 132.6, 138.1, 149.8, 158.1, 163.2, 166.7, 171.8, 194.1. $[M + H]^+$: 452.4. M.p.: 118–20 °C. $R_f$ $CH_2Cl_2$/MeOH 8/1: 0.33

*4.1.21. **(9b)** 2-Hydroxy-4-{5-[4-oxo-3-phenylpropyl-2-thioxothiazolidin-5-ylidenemethyl]furan-2-yl}benzoic acid*

Orange solid, Yield 81%. $^1$H NMR (DMSO) d 1.94–1.98 (m, 2H), 2.65 (t, 2H, J = 7.6), 4.05 (t, 2H, J = 7.6), 6.90 (d, 1H, J = 8.4), 7.14–736 (m, 7H), 7.65 (s, 1H), 7.83 (d, 1H, J = 8.2), 8.21 (d, 1H, J = 8.4). $^{13}$C NMR (DMSO) d: 27.7, 32.2, 43.9, 106.7, 110.6, 111.4, 112.5, 118.1, 118.5, 122.9, 125.8, 128.1, 128.2, 130.8, 131.3, 140.7, 149.1, 158.0, 163.2, 166.5, 171.0, 193.8. $[M + H]^+$: 466.6. M.p.: 188–190 °C. $R_f$ $CH_2Cl_2$/MeOH 10/1: 0.3.

*4.1.22. **(9c)** 2-Hydroxy-4-{5-[4-oxo-3-(4′methylphenylmethyl)-2-thioxothiazolidin-5-ylidenemethyl]furan-2-yl}benzoic acid*

Orange solid, Yield 82%. $^1$H NMR (DMSO) d 2.24, (s, 3H), 5.18 (s, 2H), 7.12 (d, 2H, J = 8), 7.19–7.23 (m, 4H), 7.36 (s, 2H), 7.69 (s, 1H), 7.85 (d, 1H, J = 8). $^{13}$C NMR (DMSO) d: 20.6, 46.7, 111.4, 111.6, 113.4, 118.5, 123.2, 127.6, 129.0, 131.0, 131.9, 136.8, 149.4, 157.6, 162.5, 166.5, 171.2, 193.7. $[M + H]^+$: 452.3. M.p.: 267 °C (Dec.). $R_f$ $CH_2Cl_2$/MeOH 8/1: 0.28.

*4.1.23. **(9d)** 2-Hydroxy-4-{5-[4-oxo-3-(3′,4′-dimethoxyphenyl)methyl]-2-thioxothiazolidin-5-ylidenemethyl]furan-2-yl}benzoic acid*

Orange solid, Yield 75%. $^1$H NMR (DMSO) d 3.00 (s, 3H), 3.69 (s, 3H), 4.10–4.12 (m, 2H), 5.16 (s, 1H), 6.70 (d, 1H J = 7.6), 6.84–6.87 (m, 1H), 7.10–7.13 (m 1H), 7.28–7.34 (m, 1H), 7.66–7.68 (m, 2H), 7.78 (d, 1H, J = 8), 8.12 (d, 1 h, J = 6.8). $^{13}$C NMR (DMSO) d: 55.8, 67.8, 107.2, 111.2, 112.1, 112.4, 112.9, 119.1, 120.6, 123.8, 129.1, 132.0, 132.1, 146.0, 148.8, 149.0, 167.4, 171.3, 194.4. $[M + H]^+$: 498.0. M.p.: 226–28 °C. $R_f$ $CH_2Cl_2$/MeOH/Tol 17/2/1: 0.22.

*4.1.24. **(9e)** (R)-2-Hydroxy-4-{5-[4-oxo-3-(2-phenylpropyl)methyl]-2-thioxothiazolidin-5-ylidenemethyl]furan-2-yl}benzoic acid*

Orange solid, Yield 91%. $^1$H NMR (DMSO) d 1.23 (d, 1H, J = 7.2), 3.40–3.45 (m, 1H), 4.14 (d, 2H, J = 7.6), 7.13–7.31 (m, 9H), 7.58 (s, 1H), 7.82 (d, 1H, J = 8.4). $^{13}$C NMR (DMSO) d: 18.7, 37.0, 51.0, 111.3, 112.0, 113.2, 118.6, 118.8, 121.0, 123.6, 127.2, 127.6, 128.9, 131.4, 131.9, 143.2, 149.6, 158.6, 163.7, 167.0, 171.7, 194.5. $[M + H]^+$: 466.8. M.p.: 227–30 °C. $R_f$ $CH_2Cl_2$/MeOH 6/1: 0.25.

*4.1.25. **(9f)** (S)-2-Hydroxy-4-{5-[4-oxo-3-(2-phenylpropyl)methyl]-2-thioxothiazolidin-5-ylidenemethyl]furan-2-yl}benzoic acid*

Orange solid, Yield 88%. $^1$H NMR (DMSO) d 1.23 (d, 1H, J = 7.2), 3.40–3.45 (m, 1H), 4.14 (d, 2H, J = 7.6), 7.13–7.31 (m, 9H), 7.58 (s, 1H), 7.82 (d, 1H, J = 8.4). $^{13}$C NMR (DMSO) d: 18.7, 37.0, 51.0, 111.3, 112.0, 113.2, 118.6, 118.8, 121.0, 123.6, 127.2, 127.6, 128.9, 131.4, 131.9, 143.2, 149.6, 158.6, 163.7, 167.0, 171.7, 194.5. $[M + H]^+$: 466.8. M.p.: 227–30 °C. $R_f$ $CH_2Cl_2$/MeOH 6/1: 0.25.

*4.1.26. **(10a)** 2-Hydroxy-4-{5-[4-oxo-3-phenethyl-2-thioxothiazolidin-5-ylidenemethyl]tiophen-2-yl}benzoic acid*

Orange solid, Yield 65%. $^1$H NMR (DMSO) d 2.92–2.96 (m, 2H), 4.19–4.23 (m, 2H), 7.04 7.08 (m, 2H), 7.20–7.31 (m, 5H), 7.71–7.75 (m, 3H), 8.03 (s, 1H). $^{13}$C NMR (DMSO) d: 32.6, 46.0, 11.4, 113.8, 119.8, 126.6, 127.1, 129.0, 129.1, 131.4, 136.0, 137.0, 138.3, 138.1, 152.3, 163.8, 166.8, 171.4, 192.4. $[M + H]^+$: 468.7. M.p.: 190–192 °C (dec.). $R_f$ $CH_2Cl_2$/MeOH 4/1: 0.32.

*4.1.27. **(10b)** 2-Hydroxy-5-{5-[4-oxo-3-phenethyl-2-thioxothiazolidin-5-ylidenemethyl]furan-2-yl}benzoic acid*

Orange solid, Yield 79%. 1H NMR (DMSO) d 3.93–397 (m, 2H), 4.02–4.24 (m, 2H), 6.81 (d, 1H, J = 8.4), 7.05 (d, 1H, J = 4), 7.58 (s, 1H), 7.67–7.70 (m, 1H), 8.18–8.20 (m, 1H). $^{13}$C NMR (DMSO) d: 32.0, 45.1, 106.8, 107.3, 115.6, 116.0, 117.5, 118.4, 120.1, 124.4, 126.5, 126.7, 128.4, 128.6, 137.6, 140.0, 147.8, 156.5, 160.1, 166.2, 170.3, 193.4. $[M + H]^+$: 452.2. M.p.: 230–2 (dec.) °C. $R_f$ $CH_2Cl_2$/MeOH 8/1:

0.2.

#### 4.1.28. (**10c**) 4-{5-[4-oxo-3-phenethyl-2-thioxothiazolidin-5-ylidenemethyl]furan-2-yl}benzoic acid

Yellow-orange solid, Yield 65%. $^{1}$H NMR (DMSO) d 2.94–2.98 (m, 2H), 4.21–4.25 (m, 2H), 7.64 (s, 1H), 7.23–7.46 (m, 7H), 7.92–7.94 (m, 2H), 8.07–8.09 (m, 2H), 13.19 (br s, 1H). $^{13}$C NMR (DMSO) d: 32.0, 45.1, 112.0, 118.0, 119.2, 122.9, 124.2, 126.5, 128.4, 128.6, 130.2, 131.9, 137.5, 149.9, 159.7, 166.1, 166.7, 193.5. $[M + H]^+$: 436.5. M.p.: 270 °C (dec.). $R_f$ $CH_2Cl_2$/MeOH 2/1: 0.7.

#### 4.1.29. (**10d**) 5-[[5-(4-hydroxyphenyl)-2-furanyl]methylene]-2-thioxo-3-phenethyl-4-thiazolidinone,

Orange solid, Yield 66%. $^{1}$H NMR (DMSO) d 3.00–3.04 (m, 2H), 4.33–4.37 (m, 2H), 5.20 (br s, 1H), 6.84 (d, 1H, J = 3.6), 6.85–6.92 (m, 1H), 6.93 (d, 1H, J = 3.6), 7.26–7.36 (m, 8H), 7.44 (s, 1H). $^{13}$C NMR (DMSO) d: 33.0, 45.7, 109.3, 111.3, 116.5, 117.4, 117.9, 119.8, 121.4, 126.7, 128.6, 129.0, 130.3, 130.5, 137.6, 149.4, 156.1, 158.5, 167.3, 194.2. $[M + H]^+$: 408.4. M.p.: 194–6 °C. AcOet/Pet 1/3: 0.2.

### 4.2. Biological evaluation

#### 4.2.1. Cell culture and treatment

The human T cell line J-Jhan and Sup-T1 were cultured in RPMI-1640 (Gibco BRL, Invitrogen Corporation, Carlsbad, CA, USA) with 10% FCS supplemented with 100 U/ml each of penicillin and streptomycin and maintained at 37 °C in humidified atmosphere of 5% $CO_2$. J-Jhan and Sup-T1 have been selected since are known to represent cell lines of choice which allow HHV-6A and HHV-6B replication, respectively. Both cell lines were seeded into 24-well plate at the cell density of $0.5 \times 10^6$ /ml and treated with synthetized HHV-6 inhibitors at concentration of 1, 10 and 100 μM, for 24 h.

#### 4.2.2. Cell viability analysis by MTT assay

Cell viability was determined by MTT test (3-(4,5-dimethilthiazol-2yl)-2,5-diphenyl tetrazolium bromide) colorimetric assay (Roche Diagnostics Corporation, Indianapolis, IN, USA) following the manufacturer's instructions as previously described [39]. Cell viability was determined by treating human lymphocyte cell lines with different concentration of HHV-6 inhibitors, 10-fold serially diluted from 0 to 100 μM, for 24 h. Afterwards, MTT assay was performed, and absorbance was read at 570 nm.

#### 4.2.3. HHV-6 infection

J-Jhan cells were infected with a HHV-6A (U1102 strain) cell-free inoculum and Sup T1 cells were infected with a HHV-6B (Z29 strain) cell-free inoculum as previously described [24] at a 100:1 multiplicity of infection (MOI, virus genomes:cell ratio). Virus adsorption was carried out in a 1% FBS medium for 3 h, then the excess virus was eliminated by centrifugation and washing in PBS, and cells were finally seeded at $0.5 \times 10^6$ cells/ml in complete medium with high FBS concentration. Control cells were treated with the same procedure but uninfected. At 1, 2, 3, and 7 days post-infection (d.p.i.) cell samples were collected by centrifugation at 1000 × g for 5 min at 4 °C. Cell pellets were then washed in PBS, and analyzed for viral DNA presence by Real Time PCR.

#### 4.2.4. Analysis of HHV-6 replication inhibition

The inhibitory effect on HHV-6 replication was determined by analyzing viral DNA from J-Jhan HHV-6A infected cells and Sup T1 HHV-6B infected cells. Total DNA was extracted from cell pellets collected from both infected or uninfected cell lines by a commercial kit (Exgene Cell SV kit, GeneAll, Seoul, Korea), and quantified by spectrophotometric reading at 260 and 280 nm. 100 ng of total extracted DNA was analyzed by specific qPCR targeting U42 gene of HHV-6 in duplicate, as previously described [40]. Briefly, a standard curve ranging from $10^7$ to 10 copies of U42 gene was used to quantify the infection by interpolation and normalized to the human RNaseP housekeeping gene (TaqMan™ Copy Number Reference Assay, human, RNase P, ThermoFisher Scientific, USA) used as a control.

#### 4.2.5. Statistical analysis

Results obtained ad mean ± SD from 3 independent experiments were evaluated for statistical significance by Student T test using GraphPad Prism9 software.

## Declaration of Competing Interest

The authors declare that they have no known competing financial interests or personal relationships that could have appeared to influence the work reported in this paper.

## Acknowledgement

We thank Dr. Erika Marzola for HPLC analysis, Dr. Alberto Casolari for the acquisition of proton and carbon NMR spectra and Dr Ercolina Bianchini for the elemental analysis. We thank Iva Pivanti and Dr Mercedes Fernandez for technical support and Alessandro Sofia for statistical analysis. This study was supported by HHV-6 foundation grant and FISM – Fondazione Italiana Sclerosi Multipla – cod. 2019/R-Single/004 and financed or co-financed with the '5 per mille' public funding.

## Appendix A. Supplementary material

Supplementary data to this article can be found online at https://doi.org/10.1016/j.bioorg.2021.105518.

## References

[1] E. De Clercq, A. Brancale, A.V. Hodge, H.J. Field, Antiviral chemistry and chemotherapy's current antiviral agents Fact File 2006 (1st edition), Antivir. Chem. Chemother. 17 (2006) 113–166, https://doi.org/10.1177/095632020601700302.
[2] E. De Clercq, Three decades of antiviral drugs, Nat. Rev. Drug Discov. 6 (2007) 941, https://doi.org/10.1038/nrd2485.
[3] D. Pillay, The priorities for antiviral drug resistance surveillance and research, J. Antimicrob. Chemother. 60 (Suppl 1) (2007) i57–i58, https://doi.org/10.1093/jac/dkm159.
[4] G.P. Pattnaik, H. Chakraborty, Entry Inhibitors: Efficient Means to Block Viral Infection, J. Membr. Biol. 253 (5) (2020) 425–444, https://doi.org/10.1007/s00232-020-00136-z.
[5] F. Vigant, N.C. Santos, B. Lee, Broad-spectrum antivirals against viral fusion, Nat. Rev. Microbiol. 13 (7) (2015) 426–437, https://doi.org/10.1038/nrmicro3475.
[6] T.J. Henrich, D.R. Kuritzkes, HIV-1 entry inhibitors: recent development and clinical use, Curr. Opin. Virol. 3 (1) (2013) 51–57, https://doi.org/10.1016/j.coviro.2012.12.002.
[7] S. Pollock, N.B. Nichita, A. Böhmer, C. Radulescu, R.A. Dwek, N. Zitzmann, Polyunsaturated liposomes are antiviral against hepatitis B and C viruses and HIV by decreasing cholesterol levels in infected cells, PNAS 107 (40) (2010) 17176–17181, https://doi.org/10.1073/pnas.1009445107.
[8] F. Vigant, A. Hollmann, J. Lee, N.C. Santos, M.E. Jung, B. Lee, The rigid amphipathic fusion inhibitor dUY11 acts through photosensitization of viruses, J. Virol. 88 (3) (2014) 1849–1853, https://doi.org/10.1128/JVI.02907-13.
[9] H. Badani, R.F. Garry, W.C. Wimley, Peptide entry inhibitors of enveloped viruses: the importance of interfacial hydrophobicity, BBA 1838 (9) (2014) 2180–2197, https://doi.org/10.1016/j.bbamem.2014.04.015.
[10] H. Jenssen, P. Hamill, R.E.W. Hancock, Peptide antimicrobial agents, Clin. Microbiol. Rev. 19 (3) (2006) 491–511, https://doi.org/10.1128/CMR.00056-05.
[11] G. Cheng, A. Montero, P. Gastaminza, C. Whitten-Bauer, S.F. Wieland, M. Isogawa, B. Fredericksen, S. Selvarajah, P.A. Gallay, M.R. Ghadiri, F.V. Chisari, A virocidal amphipathic α-helical peptide that inhibits hepatitis C virus infection in vitro, PNAS 105 (2008) 3088–3093, https://doi.org/10.1073/pnas.0712380105.
[12] C.J. Sample, K.E. Hudak, B.E. Barefoot, M.D. Koci, M.S. Wanyonyi, S. Abraham, H. F. Staats, E.A. Ramsburg, A mastoparan-derived peptide has broad-spectrum antiviral activity against enveloped viruses, Peptides 48 (2013) 96–105, https://doi.org/10.1016/j.peptides.2013.07.014.
[13] S.M. Mousavi, M. Zarei, S.A. Hashemi, A. Babapoor, A.M. Amani, A conceptual review of rhodanine: current applications of antiviral drugs, anticancer and antimicrobial activities, Artif. Cells Nanomed. Biotechnol. 47 (1) (2019) 1132–1148, https://doi.org/10.1080/21691401.2019.1573824.
[14] N.A. Meanwell, Hepatitis C virus entry: an intriguing challenge for drug discovery, Curr. Opin. Invest. Drugs 7 (2006) 727–732.

[15] J.P. Yang, D. Zhou, F. Wong-Staal, Screening of small-molecule compounds as inhibitors of HCV entry, Methods Mol. Biol. 510 (2009) 295–304, https://doi.org/10.1007/978-1-59745-394-3_22.
[16] M.J. Brooks, J.J. Sasadeusz, G.A. Tannock, Antiviral chemotherapeutic agents against respiratory viruses: where are we now and what's in the pipeline? Curr. Opin. Pulm. Med. 10 (3) (2004) 197–203, https://doi.org/10.1097/00063198-200405000-00009.
[17] Y.S. Boriskin, I.A. Leneva, E.I. Pecheur, S.J. Polyak, Arbidol: a broadspectrum antiviral compound that blocks viral fusion, Curr. Med. Chem. 15 (2008) 997–1005, https://doi.org/10.2174/092986708784049658.
[18] C.C. Colpitts, A.V. Ustinov, R.F. Epand, R.M. Epand, V.A. Korshun, L.M. Schang, 5-(Perylen-3-yl)ethynyl-arabino-uridine (aUY11), an arabino-based rigid amphipathic fusion inhibitor, targets virion envelope lipids to inhibit fusion of influenza virus, hepatitis C virus, and other enveloped viruses, J. Virol. 87 (7) (2013) 3640–3654, https://doi.org/10.1128/JVI.02882-12. Epub 2013 Jan 2.
[19] Y.S. Boriskin, E.-I. Pécheur, S.J. Polyak, Arbidol: a broad-spectrum antiviral that inhibits acute and chronic HCV infection, Virol J 3 (1) (2006), https://doi.org/10.1186/1743-422X-3-56.
[20] R. Rizzo, D. Di Luca, Human herpesvirus 6A and 6B and NK cells, Acta Microbiol. Immunol. Hung. 65 (2) (2018) 119–125, https://doi.org/10.1556/030.65.2018.010. Epub 2018 Mar 7.
[21] E. Caselli, M. D'Accolti, F. Caccuri, I. Soffritti, V. Gentili, D. Bortolotti, A. Rotola, E. Cassai, S. Fiorentini, A. Zani, A. Caruso, R. Rizzo, D. Di Luca, The U94 Gene of Human Herpesvirus 6: A Narrative Review of Its Role and Potential Functions, Cells 9 (12) (2020) 2608, https://doi.org/10.3390/cells9122608.
[22] R. Rizzo, V. Gentili, I. Casetta, E. Caselli, R. De Gennaro, E. Granieri, E. Cassai, D. Di Luca, A. Rotola, Altered natural killer cells' response to herpes virus infection in multiple sclerosis involves KIR2DL2 expression, J. Neuroimmunol. 251 (1–2) (2012) 55–64, https://doi.org/10.1016/j.jneuroim.2012.07.004. Epub 2012 Aug 5.
[23] R. Rizzo, D. Bortolotti, V. Gentili, A. Rotola, S. Bolzani, E. Caselli, M.R. Tola, D. Di Luca, T. Fülöp, KIR2DS2/KIR2DL2/HLA-C1 Haplotype Is Associated with Alzheimer's Disease: Implication for the Role of Herpesvirus Infections, J. Alzheimers Dis. 67 (4) (2019) 1379–1389, https://doi.org/10.3233/JAD-180777.
[24] D. Bortolotti, V. Gentili, A. Rotola, E. Caselli, R. Rizzo, HHV-6A infection induces amyloid-beta expression and activation of microglial cells, Alzheimers Res. Ther. 11 (1) (2019), https://doi.org/10.1186/s13195-019-0552-6.
[25] R. Marci, V. Gentili, D. Bortolotti, G. Lo Monte, E. Caselli, S. Bolzani, A. Rotola, D. Di Luca, R. Rizzo, Presence of HHV-6A in Endometrial Epithelial Cells from Women with Primary Unexplained Infertility, PLoS One 11 (7) (2016) e0158304, https://doi.org/10.1371/journal.pone.0158304, eCollection 2016.
[26] D. Bortolotti, V. Gentili, A. Rotola, R. Cultrera, R. Marci, D. Di Luca, R. Rizzo, HHV-6A infection of endometrial epithelial cells affects immune profile and trophoblast invasion, Am. J. Reprod. Immunol. 82 (4) (2019) e13174, https://doi.org/10.1111/aji.13174. Epub 2019 Aug 17.
[27] S.H. James, N.B. Price, C.B. Hartline, E.R. Lanier, M.N. Prichard, Selection and recombinant phenotyping of a novel CMX001 and cidofovir resistance mutation in human cytomegalovirus, Antimicrob. Agents Chemother. 57 (7) (2013) 3321–3325, https://doi.org/10.1128/AAC.00062-13. Epub 2013 May 6.
[28] E. De Clercq, L. Naesens, In search of effective anti-HHV-6 agents, Rev. J. Clin. Virol. 37 (Suppl 1) (2006) S82–S86, https://doi.org/10.1016/S1386-6532(06)70017-8.
[29] P. Bonnafous, L. Naesens, S. Petrella, A. Gautheret-Dejean, D. Boutolleau, W. Sougakoff, H. Agut, Different mutations in the HHV-6 DNA polymerase gene accounting for resistance to foscarnet, Antivir. Ther. 12 (6) (2007) 877–888.
[30] Y. Isegawa, C. Matsumoto, K. Nishinaka, K. Nakano, T. Tanaka, N. Sugimoto, A. Ohshima, PCR with quenching probes enables the rapid detection and identification of ganciclovir-resistance-causing U69 gene mutations in human herpesvirus 6, Mol. Cell. Probes 24 (4) (2010) 167–177, https://doi.org/10.1016/j.mcp.2010.01.002. Epub 2010 Jan 18.
[31] N. Maeda, A. Furukawa, K. Kakita, M. Anada, S. Hashimoto, S. Matsunaga, K. Kuroki, T. Ose, A. Kato, J. Arii, Y. Kawaguchi, H. Arase, K. Maenaka, Rapid Screening by Cell-Based Fusion Assay for Identifying Novel Antivirals of Glycoprotein B-Mediated Herpes Simplex Virus Type 1 Infection, Biol. Pharm. Bull. 39 (11) (2016) 1897–1902, https://doi.org/10.1248/bpb.b16-00533.
[32] G.A. Wudiri, S.M. Schneider, A.V. Nicola, Herpes Simplex Virus 1 Envelope Cholesterol Facilitates Membrane Fusion, Front. Microbiol. 8 (2017) 2383, https://doi.org/10.3389/fmicb.2017.02383.
[33] H. Tang, A. Kawabata, M. Takemoto, K. Yamanishi, Y. Mori, Human herpesvirus-6 infection induces the reorganization of membrane microdomains in target cells, which are required for virus entry, Virology 378 (2) (2008) 265–271, https://doi.org/10.1016/j.virol.2008.05.028.
[34] V. Cagno, C. Tintori, A. Civra, R. Cavalli, M. Tiberi, L. Botta, A. Brai, G. Poli, C. Tapparel, D. Lembo, M. Botta, Novel broad spectrum virucidal molecules against enveloped viruses, PLoS One 13 (12) (2018) e0208333, https://doi.org/10.1371/journal.pone.0208333, eCollection 2018.
[35] R. Borenstein, B.A. Hanson, R.M. Markosyan, E.S. Gallo, S.D. Narasipura, M. Bhutta, O. Shechter, N.S. Lurain, F.S. Cohen, L. Al-Harthi, D.A. Nicholson, Ginkgolic acid inhibits fusion of enveloped viruses, Sci. Rep. 10 (1) (2020) 4746, https://doi.org/10.1038/s41598-020-61700-0.
[36] S. Speerstra, A.A. Chistov, G.V. Proskurin, A.V. Aralov, E.A. Ulashchik, P. P. Streshnev, V.V. Shmanai, V.A. Korshun, L.M. Schang, Antivirals acting on viral envelopes via biophysical mechanism of actions, Antiviral Res. 149 (2018) 164–173, https://doi.org/10.1016/j.antiviral.2017.11.018.
[37] D. Kaminskyy, D. Khyluk, O. Vasylenko, R. Lesyk, An efficient method for the transformation of 5-ylideneRhodanines into 2,3,5-trisubstituted-4-thiazolidinones, Tetrahedron Lett. 53 (5) (2012) 557–559, https://doi.org/10.1016/j.tetlet.2011.11.095.
[38] A.R. Katritzky, S.R. Tala, H. Lu, A.V. Vakulenko, Q.-Y. Chen, J. Sivapackiam, K. Pandya, S. Jiang, A.K. Debnath, Design, Synthesis, and Structure−Activity Relationship of a Novel Series of 2-Aryl 5-(4-Oxo-3-phenethyl-2-thioxothiazolidinylidenemethyl)furans as HIV-1 Entry Inhibitors, J. Med. Chem. 52 (23) (2009) 7631–7639, https://doi.org/10.1021/jm900450n.
[39] D. Bortolotti, J. LeMaoult, C. Trapella, D. Di Luca, E.D. Carosella, R. Rizzo, Pseudomonas aeruginosa Quorum Sensing Molecule N-(3-Oxododecanoyl)-l-Homoserine-Lactone Induces HLA-G Expression in Human Immune Cells, Infect. Immun. 83 (2015) 3918–3925, https://doi.org/10.1128/IAI.00803-15.
[40] R. Rizzo, I. Soffritti, M. D'Accolti, D. Bortolotti, D. Di Luca, E. Caselli, HHV-6A/6B infection of NK cells modulates the expression of miRNAs and transcription factors potentially associated to impaired NK activity, Front. Microbiol. 8 (2017) 2143, https://doi.org/10.3389/fmicb.2017.02143.

Bioorg. Med. Chem. Lett. 72 (2022) 128822

Contents lists available at ScienceDirect

Bioorganic & Medicinal Chemistry Letters

journal homepage: www.elsevier.com/locate/bmcl

# Identification of small-molecule urea derivatives as PTPC modulators targeting the c subunit of $F_1/F_o$-ATP synthase

Anna Fantinati [d,1], Giampaolo Morciano [b,c,1], Giulia Turrin [a], Gaia Pedriali [b], Salvatore Pacifico [a], Delia Preti [a], Valentina Albanese [d], Davide Illuminati [a], Virginia Cristofori [a], Carlotta Giorgi [c], Elena Tremoli [b], Paolo Pinton [b,c,*], Claudio Trapella [a,c,*]

[a] Department of Chemical, Pharmaceutical and Agricultural Sciences, University of Ferrara, 44121 Ferrara, Italy
[b] Maria Cecilia Hospital, GVM Care&Research, 48033, Cotignola, RA
[c] Laboratory for Technologies of Advanced Therapies (LTTA), Section of Experimental Medicine, Department of Medical Sciences, University of Ferrara, 44121 Ferrara, Italy
[d] Department of Enviromental and Prevention Sciences, University of Ferrara, 44121 Ferrara, Italy

ARTICLE INFO

*Keywords:*
Urea derivatives
PTPC
Mitochondria
Cardiovascular diseases

ABSTRACT

Maintaining a high percentage of living and functional cells in those pathologies in which excessive cell death occurs, such as neurodegenerative disorders and cardiovascular diseases, is one of the most intriguing challenges in the field of biochemical research for drug discovery. Here, mitochondrial permeability transition-driven regulated cell death is the main mechanism of mitochondrial impairment and cell fate; this pathway is still lacking of satisfying pharmacological treatments to counteract its becoming; for this reason, it needs continuous and intense research to find new compounds as modulator of the permeability transition pore complex (PTPC) activity. In this study, we report the identification of small-molecule urea derivatives able to inhibit PTPC opening following calcium overload and selected for future use in cytoprotection.

All cells of our body, sooner or later die, either naturally following a precise physiological program or upon pathological and accidental events. From this observation, it follows that different cell death types exist and each of them can be distinguished by quantifiable biochemical parameters[1]. Regulated cell death (RCD) is a pathway shared by both human physiology and in case of failing of adaptive responses to dangerous external stimuli. In the last years, one of the most studied RCD is that one driven by the mitochondrial permeability transition (mPT), because (but not exclusively related to this) it still lacks satisfying pharmacological approaches and genetic treatments to counteract its progression[2]. mPT consists in the irreversible permeabilization of the inner mitochondrial membrane (IMM) to solutes with a molecular weight of up to 1500 Da (as reviewed in[3]). Inducers of mPT like calcium overload, reactive oxygen species (ROS) production, but also increased phosphates concentration and a reduction in the adenine nucleotide intracellular pool, trigger the opening of the mitochondrial permeability transition pore complex (PTPC), that is responsible for mPT. This promotes severe and prolonged mitochondrial perturbation and the impairment of essential functions, seriously compromising cell life[4,5]. Indeed, in these conditions, failure of the mitochondrial electron transport chain (ETC) and the related break of ATP production occur. PTPC is a proteinaceous complex composed by an undefined number of proteins allocated at the crosstalk of inner and outer mitochondrial membranes (OMM)[6]. It is reported that mPT-driven RCD develops in neurodegeneration[7] and ischemia–reperfusion diseases like infarction[8–10]. Here, the maintenance of a balanced mitochondrial homeostasis and the "right" number of living cells allow minimizing the inauspicious phenotype arising with disease. Thus, pharmacological targeting of its modulators or pore-forming proteins would be beneficial against these deleterious effects of PTPC opening. Unfortunately, PTPC is still an evolving entity with cyclophilin D (CypD) as the only genetically confirmed modulator. But, from 2012, increasing evidences ascribed to the C subunit of $F_O$ ATP synthase (Csub) a key role as regulator of the PTPC[11–15]. In our previous paper we have confirmed its usefulness as cardioprotective strategy following ischemia/reperfusion injury (IRI) by the selective targeting of the protein with small-molecule

* Corresponding authors.
*E-mail addresses:* paolo.pinton@unife.it (P. Pinton), claudio.trapella@unife.it (C. Trapella).
[1] equally contributed.

https://doi.org/10.1016/j.bmcl.2022.128822
Received 22 March 2022; Received in revised form 19 May 2022; Accepted 23 May 2022
Available online 27 May 2022

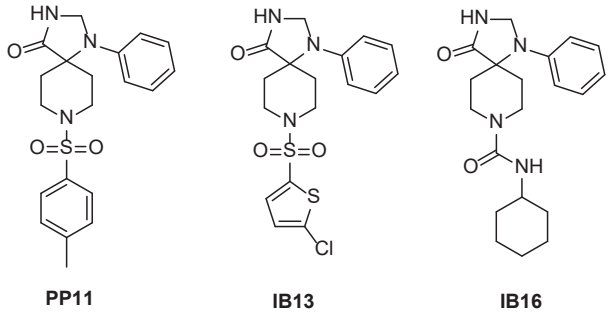


**Figure 1.** Structure of known PTPC inhibitors targeting the c subunit of $F_1/F_o$-ATP Synthase[16].

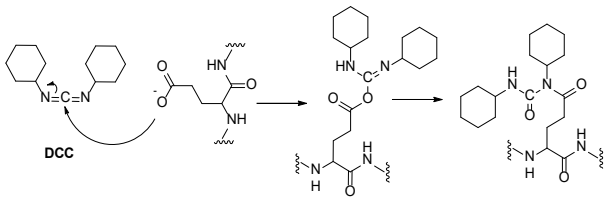


**Figure 2.** Interactions between DCC and Glu[59] of Csub.

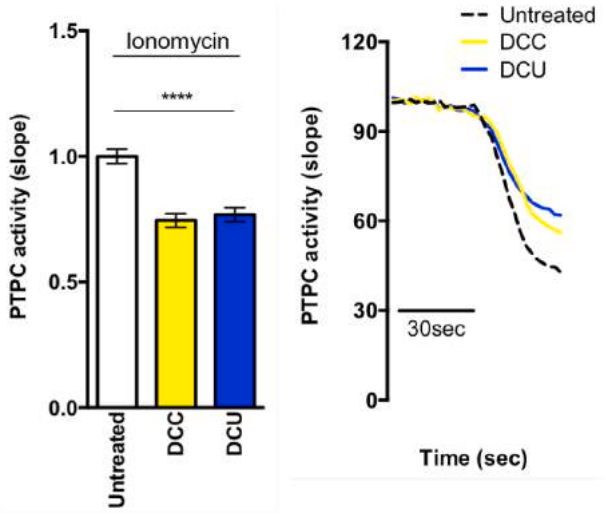


**Figure 3.** calcein-cobalt assay in AC16 cell line comparing PTPC inhibition between 15 μM DCC and 1 μM DCU.

inhibitors (see representative compounds in Figure 1)[16,17]. To the best of our knowledge, these triazaspiro[4.5]decane derivatives remain the only example of PTPC opening inhibitors with such mechanism of action reported thus far.

Given the difficulty for a functional compound to become a drug, intense efforts are needed in understanding chemical moieties that are involved in the modulation of the multiproteic components of PTPC. Also, a hyper-activation of this channel is useful in therapies, such as in cancers, where cells easily evade apoptosis.

In this manuscript we studied the chemistry of urea compounds for their ability to inhibit (but also to activate) PTPC opening as read out of putative mPT-driven RCD blockers.

Dicyclohexylcarbodiimide (DCC) has been considered as a starting point for the design of new PTPC inhibitors because of its known capability of binding Csub to Glu[59] (Figure 2)[18].

In particular, DCC induces an irreversible inhibition according to the formation of a dicyclohexyl-*N*-acylisourea (DCNU)-modified c-monomer. Despite this recognized mechanism we considered that DCC in aqueous solution is partially hydrated to the corresponding dicyclohexylurea (DCU) that was tested for its activity as PTPC opening inhibitor.

According to the calcein-cobalt assay[19] performed in human ventricular cardiomyocytes (AC16) and under conditions of mitochondrial calcium overload, DCU itself showed a higher activity by working at a 15-fold lower concentration (1 μM) than DCC (15 μM) to exert the same extend of PTPC inhibition (specifically 28% for DCU, Figure 3, Table 2). Of note, 15 μM DCC has been already tested by us[13] for PTPC inhibition and beneficial effects under IRI conditions. Even more important for the present project, DCU is not supposed to bind covalently the investigated target protein, thus, being devoid of the potential side effects typical of covalent ligands. In addition, covalent inhibitors of PTPC are not functional to our purpose because after the first block of its activity in IRI, cardiomyocytes will be able to start the ATP synthesis as in the physiological way. As described by Simersky and co-workers[20] the DCC interacts with the Glu[59] trough a covalent bond (Figure 2) with the cyclohexyl groups fitting into a hydrophobic pocket that was previously occupied by Phe[64] of the c -ring.

To directly monitor target engagement inside cells, we performed a cellular thermal shift assay (CETSA)[21,22] using a protocol based on ligand-induced thermal stabilization of the target protein, the c subunit of $F_O$-ATP synthase. We were able to detect DCU binding with the Csub between 53 °C and 65 °C. Despite the low sensitivity of the assay and an inability to perform any molecular docking assays, Figure 4 clearly shows that the Csub protein was thermally stabilized by DCU pretreatment (C subunit expression in Western Blot image and blue line of the linked quantification) and that this effect was absent in other mitochondrial proteins of the same complex, such as ATP5A (ATP5A expression in Western Blot image and brown lines of the linked quantification).

In light of this, DCU has been chosen as a promising hit compound suitable for structure–activity optimization. Except for very few examples (see compound IB16 in Figure 1), there are no previous evidences for Csub inhibition by urea derivatives, thus compounds **1**–**14** (Table 1) have been synthesized in order to obtain useful information about the relevance of different parts of these molecules for interactions within the protein. It is interesting to note that IB16 is an asymmetric cyclohexylurea derivative. In this work, punctual modifications have been introduced either to the urea moiety or to the N/N' substitutions. In addition, some of the most interesting modifications have been combined in a single compound. The general structure of these derivatives is depicted in Table 1.

Following this approach, five classes of DCU derivatives have been synthesized. Firstly, the intact urea moiety has been maintained and a number of symmetric (compounds **1**–**7**) or asymmetric (**8**–**9**) N/N' modifications were introduced by combination of different alkyl/cycloalkyl/(substituted)aryl/benzyl groups. Secondly, the urea function has been substituted with a thiourea group so to evaluate the effect of the removal of a potential hydrogen bond acceptor. Even in this case, symmetric (**10, 11**) and asymmetric (**12**) compounds have been prepared. Lastly, two carbamates derivatives were synthesized (**13**–**14**), in order to understand how a hydrogen bond acceptor instead of a donor

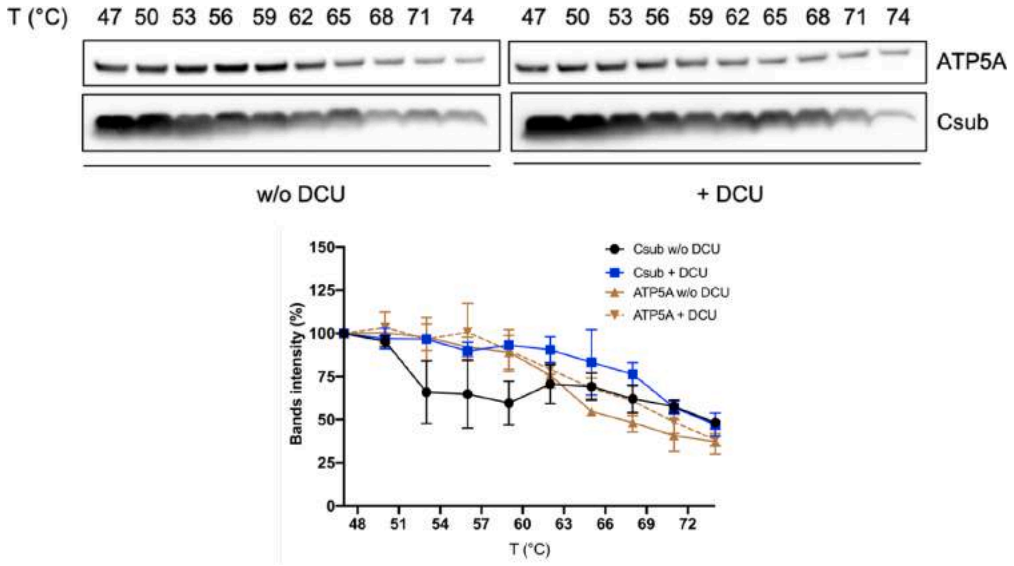


**Figure 4.** Cellular thermal shift assay which supports the engagement of Csub by DCU.

**Table 1**
DCU and its derivatives.

SYMMETRIC UREAS

DCU

1

2

3

4

5

6

7

ASYMMETRIC UREAS

8

9

ASYMMETRIC THIOUREAS

12

ASYMMETRIC CARBAMATES

13

14

SYMMETRIC THIOUREAS

10

11

one influences the activity.

The synthesis of DCU derivatives have been carried out following different straightforward approaches, through which the target molecules were easily produced, purified and almost all of the reactions led to high yields.

Symmetric ureas **1 – 7** have been prepared by the typical reaction between carbonyldiimidazole (CDI) and two equivalents of aromatic or aliphatic primary amines (see Scheme 1 and supporting information).

Since the reaction between CDI and primary amines rearranges into an isocyanate intermediate, this approach can conceivably be used for the synthesis of asymmetric ureas, by adding a different amine. However, because of its rather high reactivity, the isocyanate intermediate is not easy to isolate for the further reaction with amines. For this reason, asymmetric ureas, as well as thioureas (**8**–**12**) have been prepared by the direct reaction between aromatic or aliphatic primary amines and commercially available isocyanates or isothiocyanates.

Carbamates **13** and **14** were prepared by reacting either aryl- or cyclohexyl-amine with ditertbutyl-dicarbonate.

In producing urea derivatives, five classes of structural modifications have been introduced (Table 1), in order to investigate which parts of DCU are involved in the PTPC inhibition, to figure out which improvements can be undertaken for the biological activity optimization.

To test the biological activity of urea derivatives, AC16 has been chosen as cell model to study PTPC inhibition under mitochondrial calcium overload conditions induced by the ionophore ionomycin (see supporting information for details). The method used is a well-established approach[16] to evaluate if compounds may drive PTPC inhibition and thus potential beneficial effects against cell death.

Among symmetric urea derivatives, we observed that aliphatic cyclic substituents with less than six carbon atoms demonstrated to have less inhibition potency if compared to DCU.

Moreover, in the case of N,*N*-diphenyl substitution, the presence of electron-withdrawing groups showed to be detrimental for the inhibitory activity contrarily to the electron-donor ones that, inducing the enolic or thioenolic form, lose the inhibition function in favor of an activation of PTPC.

In particular, regarding the first statement of our supposed ratio, we observed that the inhibition activity of the compounds **1** and **2**, that have five and three ring carbon members respectively, decreases in a relevant way correlated with the steric hindrance (- 16,4% compound **1**, −3,9% compound **2**) (Table 2).

**Table 2**
Nomenclature, scheme and biological activity of urea-derivatives.

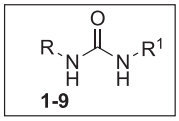


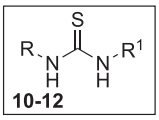


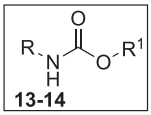


| Compound | R | R' | PTPC activity (% at 1 μM) |
|---|---|---|---|
| DCU |  |  | −28% |
| 1 |  |  | −16,4% |
| 2 |  |  | −3,87% |
| 3 |  |  | −28,11% |
| 4 | 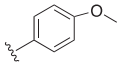 | 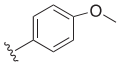 | +53,61% |
| 5 | 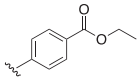 | 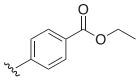 | −9,75% |
| 6 | 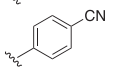 | 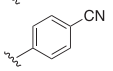 | −25,43% |
| 7 | 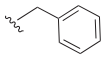 | 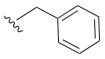 | +30,39% |
| 8 |  |  | −43,17% |
| 9 |  | 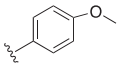 | −4,6% |
| 10 |  |  | +32,43% |
| 11 | 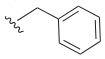 | 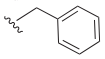 | +37,18% |
| 12 |  |  | +3% |
| 13 |  |  | +42,54% |
| 14 |  |  | +60,82% |

Considering the binding site interaction of the known PTPC inhibitor Oligomycin with Glu[59] residue through a hydrogen bond with a molecule of water,[18] we speculated that the –NH group of the DCU is the one binding the oxygen of the water. The hydrogen of the water is able to interact with the carboxylate of Glu[59] residue through another H-bond. (Scheme 2).

This mechanism is evident in some derivatives namely compounds **3**, **5**, **6**, **8**, **9**; in particular, we noticed that compound **8** is more efficient than the others (see the dose–response curves of compound **8** and DCU in Figures S43 and S44, supporting information), not only because of these reasons but also due to the steric hindrance of the *tert*-butyl group: in fact, here we observed a synergistic combination that affects positively the inhibitory activity of the PTPC opening.

In the case for example of the compound **6**, we assumed that having an electron-withdrawing as substituent doesn't change much on the inhibition activity.

On the other side, to see the activator functionality we supposed that electron-donor groups as substituents promote the enolic or thioenolic form, subtracting the molecule of water from the interaction with Glu[59] (Scheme 2).

It is worth noting that compounds **4**, **7**, **10**, **11**, **12**, **13**, **14** showed a consistent behavior with the mechanism we support (Table 2). In fact, compounds with electron-donor substituents, such as methoxy group (compound **4**) or benzyl group (that as a protecting group can decrease the reactivity of the nitrogen: compounds **7** and **11**) as well as aliphatic substituents without any lone pair available (compounds **10**) favor the enolic (compound **7**) or the thioenolic form of the thiourea over the thioketonic form because of the weak stability of the latter.

Also, the compounds **13** and **14** were observed to be stronger activators of PTPC opening than the ones cited above. This could be due to the presence of a carbamate functionality which displays an -O- atom instead of a –NH- moiety. Here, the oxygen atom acts as H-bond acceptor with a molecule of water, which could prevent the water molecule from interacting through a hydrogen bond with Glu[59] residue (Scheme 2).

On the bottom part of the scheme, three different interactions between DCU-derivatives and the amino acid residue are shown:

a) Interaction between urea derivatives and Glu[59] through interposition of a water molecule which behaves as a "bridge-molecule" thanks to the capability of the urea –NH group and the carboxylate of glutamate to form H-bonds: this translates in an inhibitory potential;
b) In the case of thiourea derivatives, the more stable thioenolic form subtracts the water molecule from the interaction with the carboxylate. This could be translated in an activating behavior as observed.
c) In the case of carbamate derivatives, both the two oxygen atoms work as H-bond acceptors with water, which in turn is not able to prevent carboxylate of the glutamate from proceeding in the physiological way: also in this case, an activator potency is observed.

In conclusion in this work we have firstly demonstrated that part of the PTPC inhibition activity of DCC is due to its behavior as a prodrug, in fact the corresponding urea is a more potent inhibitor respect to DCC. Shading light to this mechanism we investigated the importance of steric hindrance and stereo-electronic effects on the ability of urea-based compounds to interact with the PTPC. Despite the chemical simplicity of the molecules in this study, the fine regulation of the electronic effects on the urea or thiourea carbonyl allowed us to hypothesize the different mechanism of action between inhibitors and activators of PTP multiproteic complex. Further studies will be necessary to confirm these hypotheses, also with the aid of molecular modeling or new experimental evidence with different classes of molecules.

## Declaration of Competing Interest

The authors declare that they have no known competing financial interests or personal relationships that could have appeared to influence the work reported in this paper.

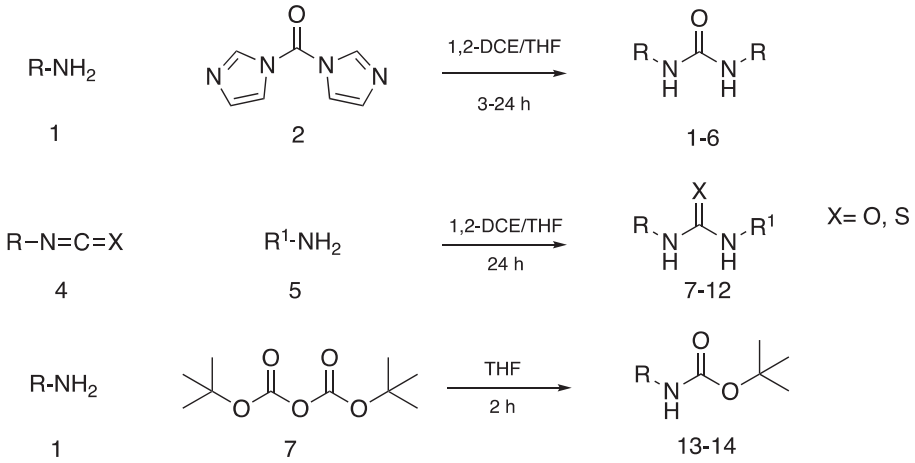


**Scheme 1.** reactions conditions.

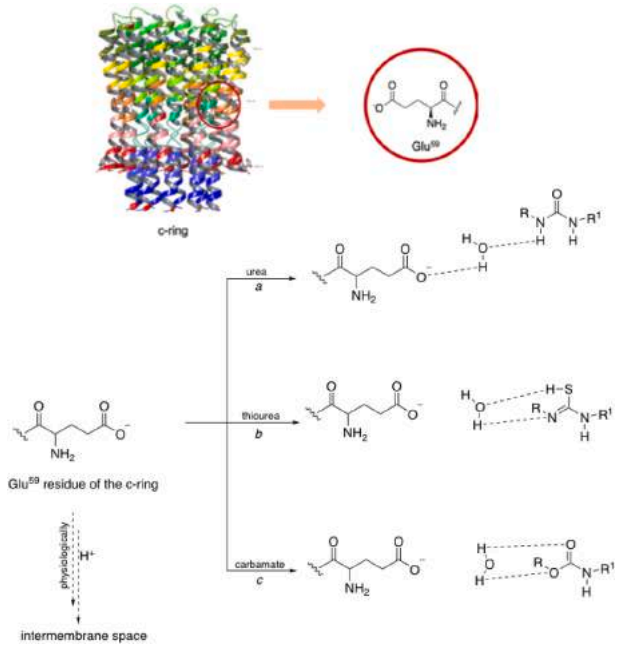


**Scheme 2.** Supposed interaction mechanism of urea or thiourea compounds with Glu[59]. The c-ring crystal (PDB 4F4S,[17]) is shown on the top of the Scheme and some amino acid residues, involved in the proton translocation, are put in evidence. In particular, as mentioned above, residue Glu[59] (circled in red) plays a crucial role in the mechanism.

## Acknowledgments

The authors would like to thank Dr. Giorgia Macedonio for the acquisition of the NMR spectra, Dr. Erika Marzola for her help in acquiring the HPLC chromatograms and Dr. Ercolina Bianchini for the elemental analysis. C.T. is supported by the fund FAR-2021 (Fondo di Ateneo per la Ricerca) of the University of Ferrara. P.P. is supported by the Italian Association for Cancer Research (AIRC: IG-23670), A-ROSE and Progetti di Rilevante Interesse Nazionale (PRIN2017E5 L5P3). C.G. is supported by Italian Association for Cancer Research (AIRC: IG-19803), A-ROSE, Progetti di Rilevante Interesse Nazionale (PRIN20177E9EPY), the Italian Ministry of Health (GR-2013-02356747) and the European Research Council (ERC; 853057-InflaPML). G.M. is supported by the Italian Ministry of Health (GR-2018-12367114 and GR-2019-12369862). P.P. is grateful to Camilla degli Scrovegni for continuous support.

## Appendix A. Supplementary data

Supplementary data to this article can be found online at https://doi.org/10.1016/j.bmcl.2022.128822.

## References

1 Galluzzi L, Bravo-San Pedro JM, Vitale I, et al. Essential versus accessory aspects of cell death: recommendations of the NCCD 2015. *Cell Death Differ*. 2015;22:58–73.
2 Bonora M, Giorgi C, Pinton P. Molecular mechanisms and consequences of mitochondrial permeability transition. *Nat. Rev. Mol Cell. Biol.*. 2021 https://doi.org/10.1038/s41580-021-00433-y.
3 Morciano G, Giorgi C, Bonora M, et al. Molecular identity of the mitochondrial permeability transition pore and its role in ischemia-reperfusion injury. *J Mol Cell Cardiol*. 2015;78:142–153.
4 Bonora M, Wieckowski MR, Sinclair DA, Kroemer G, Pinton P, Galluzzi L. Targeting mitochondria for cardiovascular disorders: therapeutic potential and obstacles. *Nat Rev Cardiol*. 2019;16:33–55.
5 Giorgi C, Marchi S, Pinton P. The machineries, regulation and cellular functions of mitochondrial calcium. *Nat Rev Mol Cell Biol*. 2018;19:713–730.
6 Morciano G, Naumova N, Koprowski P, et al. The Mitocondrial permeability transition pore: an involving concept critical for cell life and death. *Biol. Rev. Camb. Philos. Soc*. 2021;96:2489–2521.
7 Warne J, Pryce G, Hill JM, et al. Selective Inhibition of the Mitochondrial Permeability Transition Pore Protects against Neurodegeneration in Experimental Multiple Sclerosis. *J Biol Chem*. 2016;291:4356–4373.
8 Ferrari R, Balla C, Malagu M, et al. Reperfusion Damage- A Story of Success, Failure, and Hope. *Circ J*. 2017;81:131–141.
9 Tonet E, Bernucci D, Morciano G, Campo G. Pharmacological protection of reperfusion injury in ST-segment elevation myocardial infarction. Gone with the wind? *Postepy Kardiol Interwencyjnej*. 2018;14:5–8.
10 Morciano G, Patergnani S, Bonora M, et al. Mitophagy in Cardiovascular Diseases. *J Clin Med*. 2020;9.
11 Alavian KN, Beutner G, Lazrove E, et al. An uncoupling channel within the c-subunit ring of the F1FO ATP synthase is the mitochondrial permeability transition pore. *Proc Natl Acad Sci U S A*. 2014;111:10580–10585.
12 Bonora M, Bononi A, De Marchi E, et al. Role of the c subunit of the FO ATP synthase in mitochondrial permeability transition. *Cell Cycle*. 2013;12:674–683.
13 Bonora M, Morganti C, Morciano G, et al. Mitochondrial permeability transition involves dissociation of $F_1F_O$ ATP synthase dimers and C-ring conformation. *EMBO Rep*. 2017;18:1077–1089.
14 Campo G, Morciano G, Pavasini R, et al. Fo ATP synthase C subunit serum levels in patients with ST-segment Elevation Myocardial Infarction: Preliminary findings. *Int J Cardiol*. 2016;221:993–997.
15 Neginskaya MA, Solesio ME, Berezhnaya EV, et al. ATP Synthase C-Subunit-Deficient Mitochondria Have a Small Cyclosporine A-Sensitive Channel, but Lack the Permeability Transition Pore. *Cell Rep*. 2019;26:11–17 e12.
16 Morciano G, Preti D, Pedriali G, et al. Discovery of Novel 1,3,8-Triazaspiro[4.5] decane Derivatives That Target the c Subunit of F1/FO-Adenosine Triphosphate (ATP) Synthase for the Treatment of Reperfusion Damage in Myocardial Infarction. *J Med Chem*. 2018;61:7131–7143.

17 Morciano G, Pedriali G, Bonora M, et al. A naturally occuring muthation in ATP synthase subunit C is associated with increased damage following hypoxia/reoxygenation in STEMI patients. *Cell. Rep.* 2021;35, 108983.
18 Sebald W, Wachter E, Tzagoloff A. Identification of amino acid substitutions in the dicyclohexylcarbodiimide-binding subunit of the mitochondrial ATPase complex from oligomycin-resistant mutants of Saccharomyces cerevisiae. *Eur J Biochem*. 1979; 100:599–607.
19 Bonora M, Morganti C, Morciano G, Giorgi C, Wieckowski MR, Pinton P. Comprehensive analysis of mitochondrial permeability transition pore activity in living cells using fluorescence-imaging-based techniques. *Nat Protoc*. 2016;11: 1067–1080.
20 J. Symersky, V. Pagadala, D. Osowski, A. Krah, T. Meier, J.D. Faraldo-Gomez, D.M. Mueller, Structure of the c(10) ring of the yeast mitochondrial ATP synthase in the open conformation, Nat Struct Mol Biol, 19 (2012) 485-491, S481.
21 Jafari R, Almqvist H, Axelsson H, et al. The cellular thermal shift assay for evaluating drug target interactions in cells. *Nat. Protoc.* 2014;9:2100–2122.
22 Martinez Molina D, Jafari R, Ignatushchenko M, et al. Monitoring drug target engagement in cells and tissues using the cellular thermal shift assay. *Science*. 2013: 84–87.

International Journal of
*Molecular Sciences*

MDPI

*Article*

# Synthesis and NLRP3-Inflammasome Inhibitory Activity of the Naturally Occurring Velutone F and of Its Non-Natural Regioisomeric Chalconoids

**Tiziano De Ventura [1,†], Mariasole Perrone [2,3,†], Sonia Missiroli [2,3], Paolo Pinton [2,3,4], Paolo Marchetti [1], Giovanni Strazzabosco [1], Giulia Turrin [1], Davide Illuminati [1], Virginia Cristofori [1], Anna Fantinati [5], Martina Fabbri [1], Carlotta Giorgi [2,3,*], Claudio Trapella [1,3,*] and Vinicio Zanirato [1]**

[1] Department of Chemistry, Pharmaceutical and Agricultural Sciences, University of Ferrara, Via Luigi Borsari 46, 44121 Ferrara, Italy
[2] Department of Medical Sciences, Section of Experimental Medicine, University of Ferrara, Via Fossato di Mortara, 64/b, 44121 Ferrara, Italy
[3] Laboratory for Technologies of Advanced Therapies (LTTA), Via Fossato di Mortara, 70, 44121 Ferrara, Italy
[4] Maria Cecilia Hospital, GVM Care & Research, 48033 Cotignola, Italy
[5] Department of Environmental and Prevention Sciences, University of Ferrara, Via Fossato di Mortara 17, 44121 Ferrara, Italy
* Correspondence: carlotta.giorgi@unife.it (C.G.); trap@unife.it (C.T.); Tel.: +39-0532-455802 (C.G.); +39-0532-455924 (C.T.)
† These authors contributed equally to this work.

**Abstract:** Plant-derived remedies rich in chalcone-based compounds have been known for centuries in the treatment of specific diseases, and nowadays, the fascinating chalcone framework is considered a useful and, above all, abundant natural chemotype. Velutone F, a new chalconoid from *Millettia velutina*, exhibits a potent effect as an NLRP3-inflammasome inhibitor; the search for new natural/non-natural lead compounds as NLRP3 inhibitors is a current topical subject in medicinal chemistry. The details of our work toward the synthesis of velutone F and the unknown non-natural regioisomers are herein reported. We used different synthetic strategies both for the construction of the distinctive benzofuran nucleus (**BF**) and for the key phenylpropenone system (**PhP**). Importantly, we have disclosed a facile entry to the velutone F via synthetic routes that can also be useful for preparing non-natural analogs, a prerequisite for extensive SAR studies on the new flavonoid class of NLRP3-inhibitors.

**Keywords:** flavonoid; chalcone-based compounds; NLRP3-inflammasome inhibitors



**Citation:** De Ventura, T.; Perrone, M.; Missiroli, S.; Pinton, P.; Marchetti, P.; Strazzabosco, G.; Turrin, G.; Illuminati, D.; Cristofori, V.; Fantinati, A.; et al. Synthesis and NLRP3-Inflammasome Inhibitory Activity of the Naturally Occurring Velutone F and of Its Non-Natural Regioisomeric Chalconoids. *Int. J. Mol. Sci.* **2022**, *23*, 8957. https://doi.org/10.3390/ijms23168957

Academic Editor: Atsushi Matsuzawa

Received: 13 July 2022
Accepted: 9 August 2022
Published: 11 August 2022



## 1. Introduction

Chalcone-based compounds can act as photoinitiators of polymerization under visible light with an excellent profile for (i) free radical polymerization, (ii) cationic polymerization, (iii) synthesis of interpenetrating polymer networks (IPNs), and (iv) thiol-ene reactions [1]. Additionally, fluorescent chalcone derivatives have been used for the development of a mouse embryonic stem cell probe [2]. On the other hand, in-depth pharmacological studies concluded that natural extracts containing chalcone-based compounds exhibit an impressive array of biological activities, including anti-inflammatory/anticancer effects [3–5]. Actually, chalcones may inhibit specific enzymes such as different kinases [6–8], the aldose reductase [9,10], cyclooxygenases [11,12], and inducible nitric oxide synthase [13,14]. Moreover, it has been shown that both synthetic and natural chalconoids play a healthy role in several diseases by inhibiting the NLRP3-inflammasome formation [15–19]. The NLRP3 inflammasome is a large protein complex controlling the production of caspase-1 and ultimately of pro-inflammatory cytokines (IL-1 and IL-18). In this context, it was reported that velutone F (**1**) (Figure 1), a retrochalcone [20–22] recently identified in the ethanolic extract of the

leguminous plant *Millettia velutina* [23,24], inhibits the formation of the NLRP3 active complex. Among the eight new flavonoids identified in the lipophilic crude residue derived from 10 kg of dry vine stems of *Millettia velutina*, compound **1** exhibited the most potent inhibitory effect against nigericin-induced IL-1 release in THP-1 cells. Velutone F, featuring the 1-phenyl-2-propen-1-one moiety (**PhP**) and a substituted benzofuran core (**BF**), can be classified as a hybrid chalcone. The development of hybrid molecules incorporating different pharmacophores, each with its own molecular target, is an important area of research in medicinal chemistry [25]. Actually, both natural and synthetic benzofuran-derived compounds have potential therapeutic interests ranging from antibacterial, antifungal, anti-inflammatory, analgesic, antidepressant, anticonvulsant, anticancer, anti-HIV, antidiabetic, antituberculosis, and antioxidant [26–29].

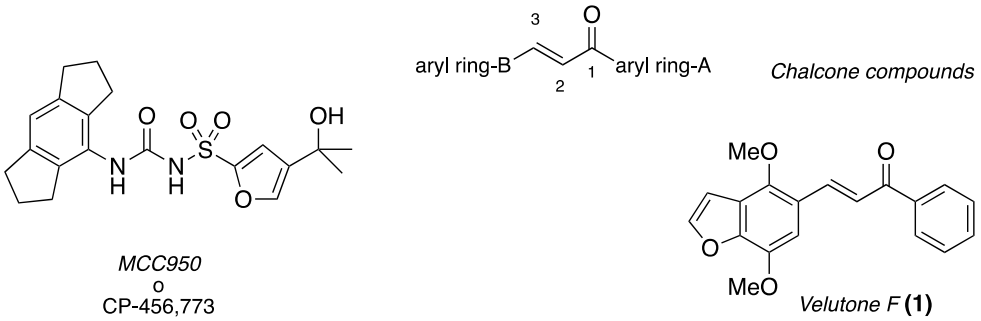


**Figure 1.** Natural and non-natural inhibitors of the NLRP3 inflammasome activation.

We are currently involved in a multidisciplinary study aimed at identifying new anti-inflammatory/anticancer compounds that mimic the MCC950 molecular structure (Figure 1). It has been demonstrated that the diarylsulfonylurea MCC950 powerfully inhibits the NLRP3 activation selectively [30,31]. In detail, MCC950 would seem to reversibly bind the NLRP3 multi-protein complex making it unable to generate the active complex, namely the NLRP3-inflammasome [32,33]. Because of the profoundly different chemical structures of the synthetic MCC950 compared to the one of velutone F (**1**), it is reasonable to assume that they can block the activation of the NLRP3-inflammasome by interfering with different bio-chemical targets. We were intrigued by the possibility of disposing of multi-milligrams amount of the natural substance **1** for the purpose of undertaking pharmacochemical investigations and mostly to shed some light on the mechanism by which compound **1** inhibits the nigericin-induced IL-1 release. Actually, when we started the search, the chemical identity of **1** was ascertained by spectroscopic means exclusively, primarily 2D NMR [23]. However, very recently [24], the same research teams got proof of the chalconoid structure of compound **1** by its semi-synthesis from Khellin.

The reasons mentioned above prompted us to design/develop synthetic routes for preparing both the natural substance originally extracted from the tropical plant *Millettia velutina* and analogs to be studied by the biologist team as promising anti-inflammatory agents.

## 2. Results and Discussion

A host of synthetic strategies has been developed to create the trans-carbon-carbon double bond of the 1,3-diaryl-2-propen-1-one moiety featuring chalcone compounds, including Claisen-Schmidt's condensations, Wittig, and Julia-Kocienski olefinations. Instead, palladium-catalyzed reactions, namely Heck, Sonogashira, and Suzuki-Miyaura cross couplings, have been used to establish the 1,3-diaryl-enone framework through A-ring/C-1 and/or C1/C2 bond formation [34].

Initially, we planned a synthetic strategy to compound **1** based on the introduction of the required alkene by Wittig olefination of 5-formyl-4,7-dimethoxy benzofuran **7** (**5-FBF**) with the 1-phenyl-2-(triphenylphosphoranylidene)ethanone counterpart **8** [35]. To this end we elaborated two synthetic approaches for the preparation of the key intermediate

**5-FBF** differing in the way the benzofuran core (**BF**) could be formed via annellation of the carbocyclic ring system onto a preformed furan, synthetic pathway A (Scheme 1), or alternatively, by creating the furan ring by intramolecular cyclization on a preexistent carbocyclic, synthetic pathway B (Scheme 2).

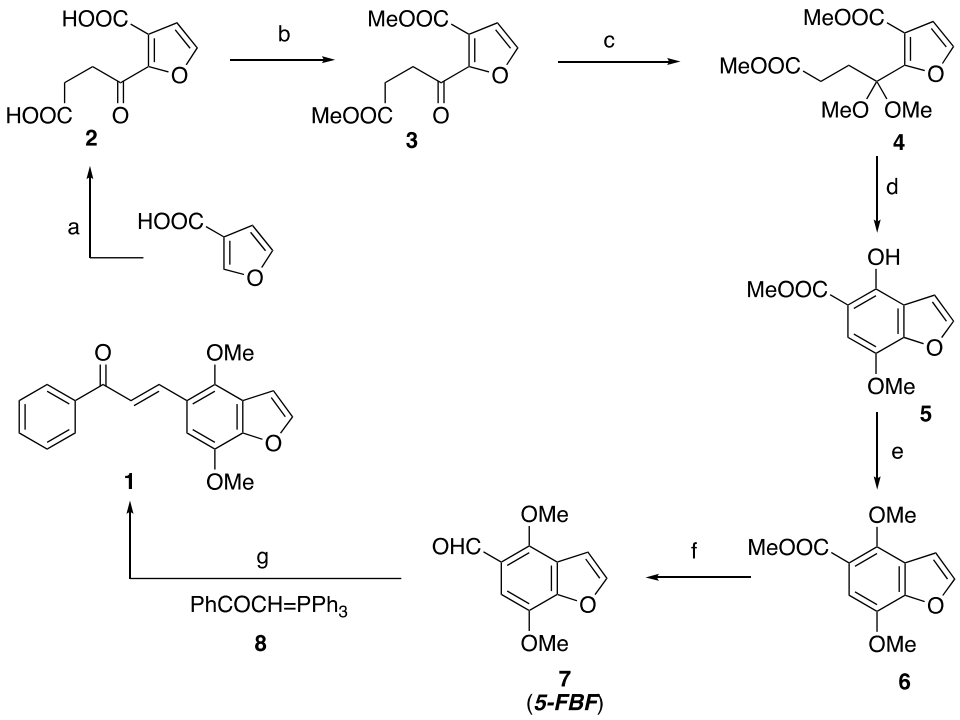


**Scheme 1.** Synthetic pathway A for target compound **1**. Reagents and conditions: (**a**) i: LDA, THF, −78 °C, succinic anhydride; ii: dil.HCl; 35%; (**b**) MeOH, $H_2SO_4$, 90%; (**c**) $HC(OMe)_3$, p-TsOH, MeOH reflux, 36 h, 90%; (**d**) i: t-BuOK, THF, −78 °C; ii: dil.HCl, 62%; (**e**) MeI, $Cs_2CO_3$, DMF, rt, 16 h, 96%; (**f**) i: $LiAlH_4$, $Et_2O$, 12 h; ii: PCC, $CH_2Cl_2$, rt, 1.5 h, 60% two steps; (**g**) MeCN, MW, 135 °C, 1.5 h, 70%.

### *2.1. Synthetic Pathway A for Target Compound* **1**

The first route starts by treating the 3-furoic acid with excess LDA to produce the corresponding C-2 lithiated carboxylate lithium salt, which, by reacting with succinic anhydride, gave the dicarboxylic acid **2**. The desired acyl derivative **3** could be isolated in a modest yield after esterification of **2** [36,37]. The subsequent carbonyl group protection as dimethyl ketal **4** opened the way to the creation of the annellated six-membered carbocyclic ring. Thus, the Dieckmann cyclization, performed with potassium tert-butoxide at −78 °C, occurred with simultaneous elimination of MeOH from the dimethyl ketal group yielding the aromatic derivative **5**, which was taken to the benzofuran derivative **6** by etherification. Subsequently, the methoxycarbonyl group was converted to the required formyl group by a two-step process entailing reduction with $LiAlH_4$ and oxidation of the resulting primary alcohol with pyridinium chlorochromate (PCC). The resulting **5-FBF** was eventually reacted with the stabilized phosphorous ylide **8**, in turn, prepared according to the literature [35]. The Wittig olefination under microwave irradiation provided velutone F (**1**) in 70% yield after chromatographic purification. As expected, NMR spectroscopic data for the synthesized velutone F were superimposable to the ones originally reported for the retrochalcone isolated from *Millettia velutina*.

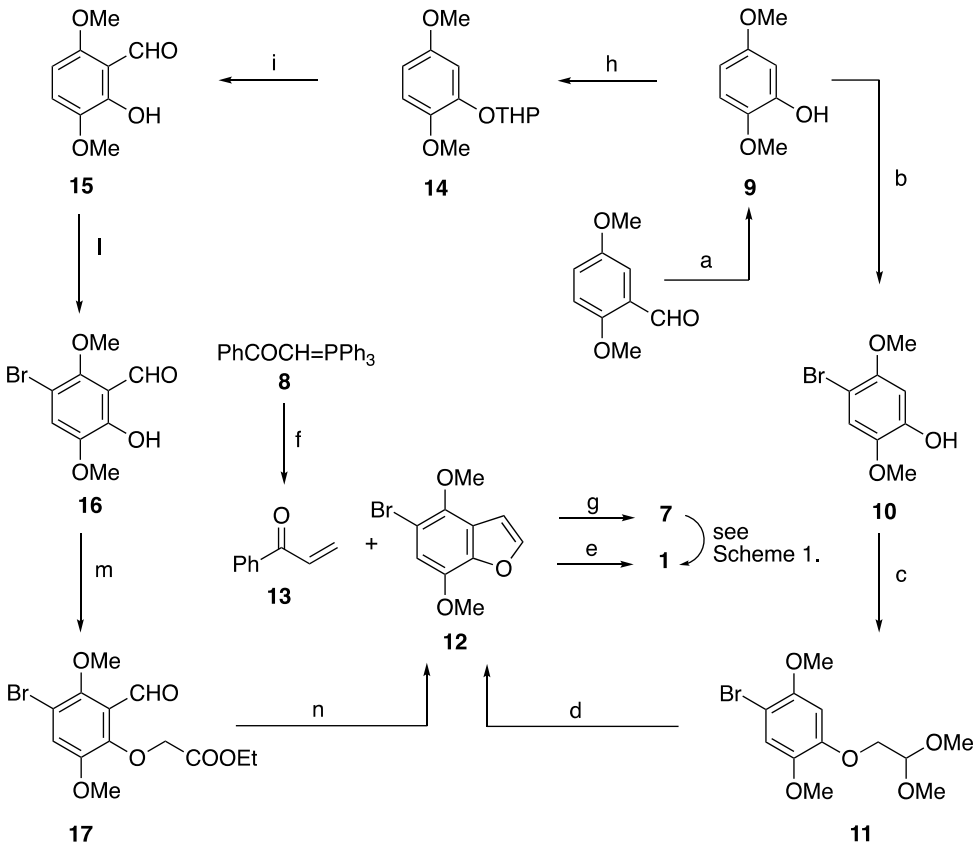


**Scheme 2.** Synthetic pathway B for target compound **1**. Reagents and conditions: (**a**) i: $H_2O_2$, t-BuOH, cat.$SeO_2$, rt, 12 h; ii: MeOH, $K_2CO_3$, 90% two steps; (**b**) NBS, MeCN, 0 °C, 30 min, 97%; (**c**) $BrCH_2CH(OMe)_2$, KOH, DMA, 140 °C, 1.5 h, 83%; (**d**) PPA, PhCl, reflux, 30 min, 50%; (**e**) $Pd(OAc)_2$, Tri(o-tolyl)phosphine, DIPEA:DMF (1:1), 32%; (**f**) $CH_2Cl_2$-formalin, reflux, 12 h, 80%; (**g**) i: BuLi, THF, −78 °C; ii: DMF, 50%; (**h**) DHP, PPTS, $CH_2Cl_2$, rt, 12 h, 91%; (**i**) i: BuLi, $Et_2O$, 0 °C, 2 h; ii: DMF, −78 to rt, 2 h; iii: HCl 6M, 80% overall; (**l**) $Br_2$-AcOH, AcONa, rt, 30 min, 80%; (**m**) $BrCH_2COOEt$, DMF, $Cs_2CO_3$, rt, 1 h, 85%; (**n**) i: LiOH, THF-$H_2O$, rt, 12 h; ii: AcONa, $Ac_2O$, 130 °C, 2 h; iii: EtOH, 60 °C, 2 h, 57%.

### *2.2. Synthetic Pathway B for Target Compound* **1**

The starting move of the alternative synthetic approach to **7** entailing the creation of the furan ring by intramolecular cyclization of the bromobenzene derivative **11** (Scheme 2) was the Dakin-like oxidation of the cheap 2,5-dimethoxybenzaldehyde by using the $H_2O_2$/cat. $SeO_2$ system in *tert*-BuOH [38]. Methanolysis of the resulting arylformate promptly furnished the 2,5-dimethoxyphenol **9**, which underwent regioselective bromination with NBS affording **10**. The exclusive C-4 bromination accounted for the marked para orienting effect of the phenolic hydroxyl group [39].

At this stage, with the aim of creating the annellated 2,3-unsubstituted furan ring, we needed to introduce an O-tethered functionalized two carbon fragment. Thus, compound **10** was easily converted to the aryl ether **11** by treatment with bromoacetaldehyde dimethyl acetal and KOH in dimethylacetamide (DMA) [40]. The anticipated intramolecular electrophilic aromatic substitution was carried out with polyphosphoric acid (PPA), providing the benzofuran derivative **12** in a 50% yield. Transformation of the 5-bromo benzofuran derivative **12** into 5-formyl-4,7-dimethoxy benzofuran **7** (**5-FBF**) was achieved through halogen-metal exchange with BuLi followed by reaction with DMF [41].

In order to make the critical furan ring annellation step more efficient, we turned our attention to a recently reported protocol for the synthesis of 6-hydroxybenzofuran based

on an unusual cycloaddition-cycloreversion sequence [42]. To this end, we prepared the penta-substituted benzene derivative **16** starting from the tri-substituted phenol derivative **9** (Scheme 2), exploiting the well-known ability of the OTHP as an ortho-directing group for the metalation [43]. Accordingly, compound **9** was promptly transformed into the corresponding tetrahydropyranyl ether **14** that was at first ortho-lithiated by treatment with BuLi and later reacted with DMF to give the tetra-substituted phenyl derivative **15**. The subsequent bromination para to the phenol group [44] afforded the desired penta-substituted benzene **16**, to which the O-ethoxycarbonylmethylene fragment was easily inserted by standard etherification reaction. In previous saponification, compound **17** was treated with the $Ac_2O$-AcONa system with heating to give the required 5-bromo benzofuran derivative **12** in an appreciable 57% yield. The mechanism proposed for the interesting cyclization reaction entails dehydration of the carboxyl group to give an unstable ketene intermediate that is trapped intramolecularly by the formyl group. The thermal [2 + 2] heterocycloaddition reaction is followed by a cycloreversion with the expulsion of $CO_2$ and production of the 2,3-unsubstituted benzofuran derivative **12** [42].

Having the suitably derivatized aryl ring-B moiety in hand, we conceived preparing compound **1** by exploiting the Mizoroki-Heck cross-coupling reaction between **12** and 1-phenyl-2-propen-1-one **13**. The latter reagent was, in turn, easily prepared by reacting phosphorous ylide **8** and formaldehyde according to a known Wittig protocol [45] (Scheme 2). Disappointingly, the Pd(0)-catalyzed reaction provided the retrochalcone **1** with a modest 32% yield [46].

### *2.3. Synthetic Pathways Providing the Non-Natural Regioisomers of Velutone F*

With the aim of learning about stereo-electronic properties of the hybrid benzofuran-retrochalcone scaffold, we decided to prepare the non-natural compounds **22**, **23,** and **28** featuring the **PhP** moiety attached, respectively, at C-2, C-6, and C-3 of the 4,7-dimethoxy benzofuran core (**BF**). The non-natural regioisomers of velutone F are previously unknown compounds.

#### 2.3.1. Synthetic Pathways to the Isomers 22 and 23

The direct formylation of electron-rich arenes can be conveniently accomplished via the Vilsmeier–Haack (V–H) reaction. Indeed, the benzo[b]furan nucleus is reported to yield the 2-formyl derivative by reaction with the V–H electrophilic species [47]. We anticipated that the regioselectivity of the V–H reaction could change if electron-donating groups were present on the phenyl ring of the benzo-fused system. In line with our hypothesis, we decided exploring the behavior of 4,7-dimethoxy benzo[b]furan **19** under V-H reaction conditions (Scheme 3). We planned to build the substituted benzo[b]furan **19** from **9** by creating the annellated 2,3-unsubstituted furan ring according to our previously sound synthetic pathway B for target compound **1** (Scheme 2). Thus, once etherified the phenolic group of **9** with the functionalized two carbon fragment, the resulting compound **18** was cyclized to **19** under the action of PPA (Sn-β zeolite also showed to efficiently promote this transformation [48]). As expected, we found the subsequent electrophilic aromatic substitution reaction was poorly regioselective: all but one of the regioisomeric formyl benzofuran derivatives **2-FBF**, **5-FBF**, and **6-FBF** were formed. In detail, chromatographic purification of the residue from the V-H reaction led us to isolate compounds **20** (**2-FBF**) together with **7** (**5-FBF**) in 37% yield ($^1$H NMR and HPLC analysis showed the isomers were in a 3.5:6.5 ratio), and compound **21** (**6-FBF**) in 30% yield. At this stage, we submitted the separated fractions to the Wittig olefination with the stabilized phosphorous ylide **8**. We obtained chalcone **23** from **6-FBF**, while in the same manner, the inseparable mixture of **2-FBF** and **5-FBF** furnished chalcones **22** and **1**, which, gratifyingly, could be easily separated by column chromatography.

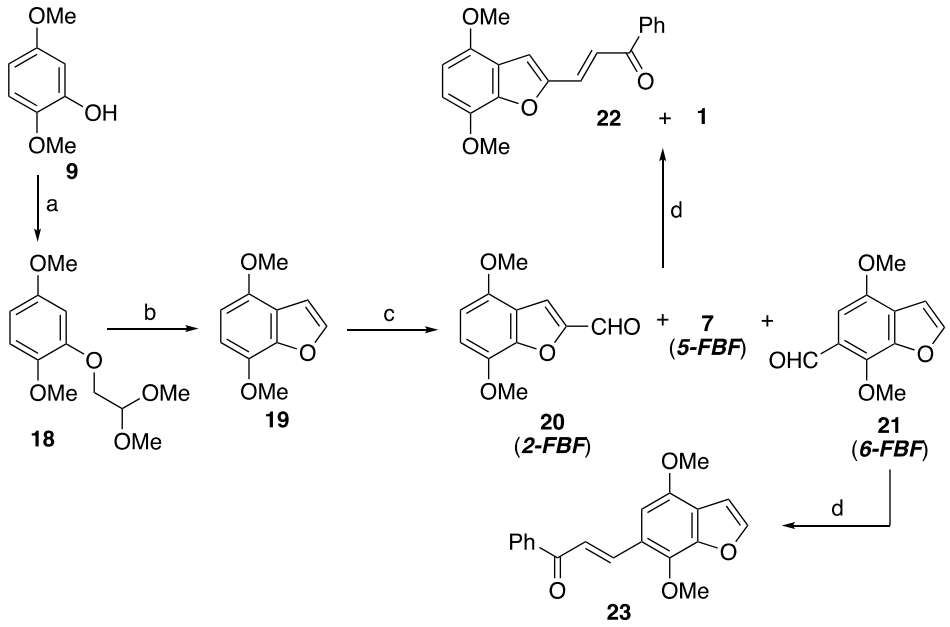


**Scheme 3.** Synthetic pathways to regioisomers **22** and **23**. Reagents and conditions: (**a**) KOH, DMAC, $BrCH_2CH(OMe)_2$, 140 °C, 2 h, 70%; (**b**) Sn-β zeolite, PhCl, 105 °C, 5 h, 62%; (**c**) $POCl_3$, DMF, 80 °C, 12 h, (**20**, 24%), (**7**, 13%), (**21**, 30%); (**d**) **8**, toluene, reflux, 12 h 50%.

2.3.2. Synthetic Pathway to the Isomer **28**

We envisaged setting up the **PhP** moiety of **28** by reaction of 3-formyl benzofuran derivative **27** (**3-FBF**) with the ylide **8** according to the previously tested protocol entailing a classical Wittig olefination. About **3-FBF** preparation, we selected compound **25** as the direct precursor having in mind a controlled oxidation of its C-3 methyl substituent in order to derive the pivotal electrophilic functional group [49,50] (Scheme 4). Thus, we devised preparing compound **25** in two steps from phenol **9**, namely: etherification with bromoacetone followed by acid-promoted cyclization of the resulting aryloxy acetone derivative **24**. The planned $SeO_2$-oxidation of the C-3 methyl residue of compound **25** furnished a 1:1 mixture of the primary alcohol **26** and the aldehyde **27**, which were separable by chromatography. However, we found it very easy to carry out the oxidation of **26** to **3-FBF** by using the Corey–Suggs reagent (PCC). Eventually, the microwave-promoted Wittig reaction between the aryl aldehyde **27** (**3-FBF**) and the phosphorous ylide **8** provided the aimed chalconoid **28** in good yield.

2.3.3. Inhibition of IL-1β Release In Vitro and In Vivo

Among the inflammasomes, NLRP3 is the most studied and characterized due to its implication in the pathogenesis of different human diseases [51]. The activation of NLRP3 inflammasomes consists of caspase-1 activation, which in turn induces secretion of the inflammatory cytokine IL-1β. Hence, IL-1β release is the most used read-out for NLRP3 inflammasome activation. In this study, IL-1β release was determined by ELISA assay to assess the inhibitory effects of synthesized compounds on NLRP3 inflammasome activation both in mouse bone marrow-derived macrophages (BMDMs) and in human PMA-differentiated lipopolysaccharide (LPS)-primed THP-1 macrophages (Figure 2). Velutone F (**1**) and the non-natural compounds **22**, **23**, and **28** demonstrated a high inhibitory capacity on the release of IL-1β.

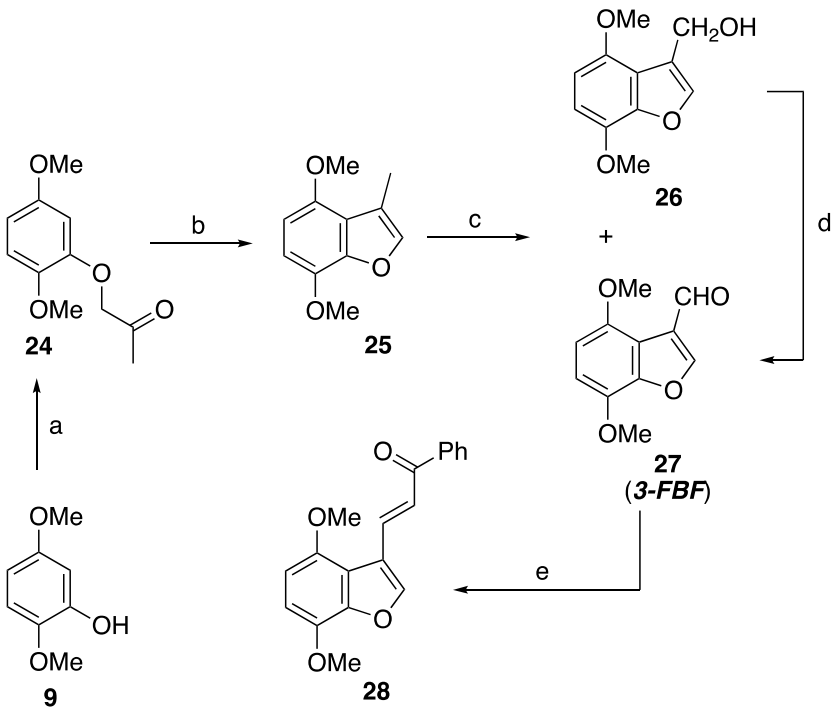


**Scheme 4.** Synthetic pathway to regioisomer **28**. Reagents and conditions: (**a**) $BrCH_2COCH_3$, $Cs_2CO_3$, DMF, rt, 12 h, 63%; (**b**) PPA, PhCl, 110 °C, 20 min, 50%; (**c**) $SeO_2$, dioxane, 75 °C, 96 h, 80%; (**d**) PCC, $CH_2Cl_2$, rt, 12 h, 95%; (**e**) **8**, MeCN, MW, 135 °C, 2 h, 65%.

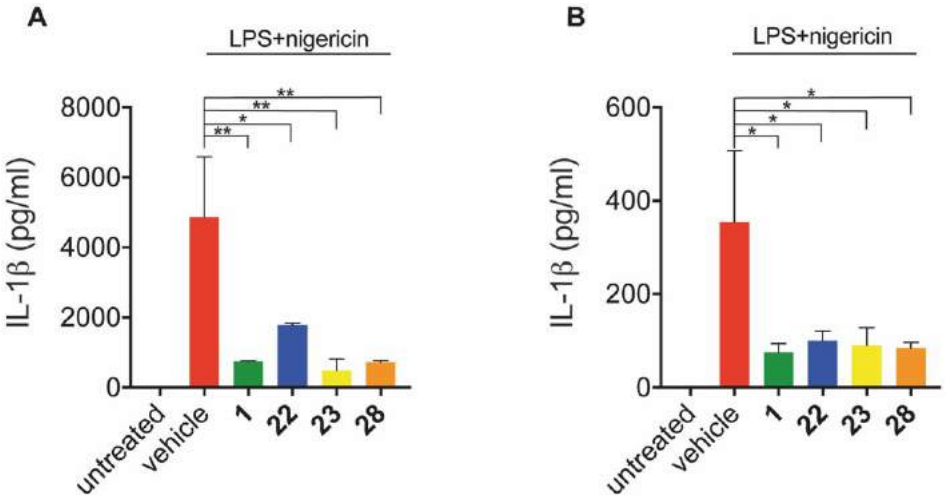


**Figure 2.** In vitro inhibition of IL-1β release. (**A**) BMDMs were stimulated with LPS (1 μg/mL) for 2 h, then treated with compounds for 30 min, and then activated with nigericin (10 μM) for 1 h. (**B**) LPS-primed PMA-differentiated THP-1 cells were stimulated with LPS (1 μg/mL) for 3 h, then treated with compounds for 30 min, and then activated with nigericin (10 μM) for 1 h. Cell supernatants were analyzed with ELISA test for the evaluation of IL-1β release (n = 3, mean ± SEM). Statistics differences were analyzed using one-way ANOVA: ** $p < 0.01$, * $p < 0.05$.

To confirm the anti-inflammatory activity of these compounds in vivo, we used an LPS-induced inflammation treatment. Mice were intraperitoneally (IP) pre-injected with velutone F (**1**) and the non-natural isomers **22**, **23**, and **28** or vehicle at 25 mg/kg and then were IP injected with LPS (1 mg/kg). After 4 h, plasma and peritoneal exudate were collected from mice and analyzed for evaluation of IL-1β release. The mice that received

pre-treatment with our compounds displayed a dramatic reduction in IL-1 production both in peritoneal exudate and blood samples (Figure 3).

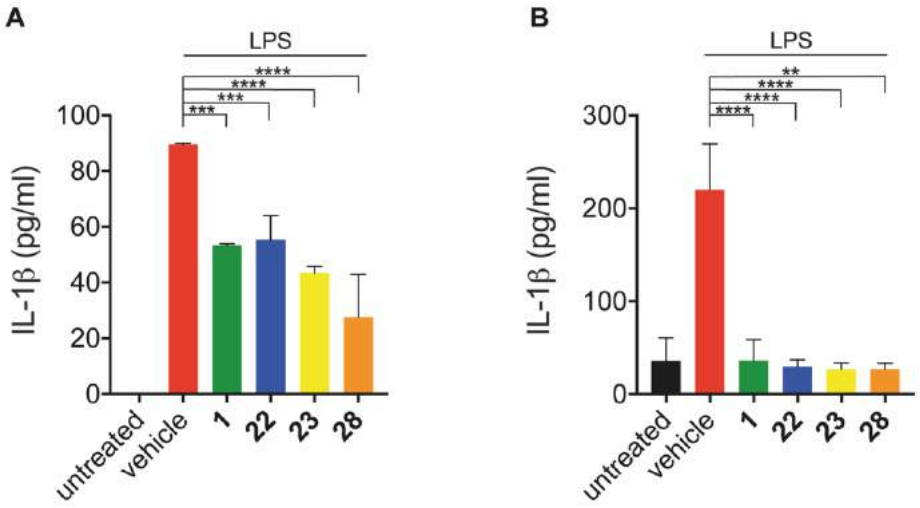


**Figure 3.** In vivo inhibition of IL-1β release. (**A**) Exudate and (**B**) plasma levels of IL-1β from C57BL/6 mice pretreated with compounds or vehicle control as determined by ELISA 4 h after intraperitoneally IP LPS (1 mg/kg) injection, n = 6/group. Data are shown as mean ± SEM. Statistical differences were analyzed using one-way ANOVA: **** $p < 0.0001$, *** $p < 0.001$, ** $p < 0.01$.

Taken together, these results revealed that synthesized velutone F (**1**), as well as its regioisomers 22, 23, and 28, exerted a strong inhibition on the NLRP3 inflammasome activation both in vitro and in vivo.

## 3. Materials and Methods

### *3.1. Chemistry: Materials and General*

All reagents and solvents that were commercially purchased were directly used without prior treatment. Reaction temperatures were recorded using a regular thermometer without correction. Melting points were determined on the Reichert Termovar apparatus and are uncorrected. Reactions were monitored by analytical thin-layer chromatography (TLC) on silica gel F254 glass plates (Merck, Darmstad, Germany) and visualized under UV light 254 nm and $KMnO_4$. Mobile phases abbreviations: A = Ethyl acetate, P = petroleum ether, DCM = dichloromethane. $^1$H NMR spectra were recorded with a Mercury Place Varian 400 MHz NMR spectrometer (Varian Palo Alto, CA, USA) at room temperature. Chemical shifts (in ppm) were recorded as parts per million (ppm) downfield to tetramethylsilane (TMS). The following abbreviations are used for a multiplicity of NMR signals: s, singlet; d, doublet; t, triplet; q, quartet; m, multiplet; dd, double doublet; dt, double triplet; ddd, doublet of doublet of doublets; dtd, doublet of triplet of doublets. MS was carried out using electrospray ionization (ESI MICROMASS ZQ 2000, Waters, Milford, MA, USA). HRMS was acquired by CIGS University of Modena e Reggio Emilia (Modena, Italy) using a Q-Exactive Hybrid Quadrupole Orbitrap (Thermo Scientific, Waltham, MA, USA). IR spectra were taken on a Perkin-Elmer FT-IR spectrum 100 spectrometer (Foster City, CA, USA). Analytical HPLC was performed with Beckman System Gold 168 (Milan, Italy) using a C18 100 A Phenomenex Kinetex (150 × 4.6 mm) and UV-DAD detection. [A]: 0.1% TFA in water and [B]: 0.1% TFA in acetonitrile was used as a binary mobile phase at a flow rate of 0.7 mL/min. Gradient: from 0% to 100% [B] in 25 min. Microwave reactions were performed in a Biotage Initiator Plus reactor (Biotage, Sweden) using 2–5 mL glass vials with a rubber cap. For all experimental spectra see Supplementary Materials.

3.1.1. Methyl 3-(4-Methoxy-4-oxobutanoyl)furan-2-carboxylate (**3**)

A solution of 3-Furoic acid (1 g, 8.92 mmol, 1 equiv.) in anhydrous THF (6 mL) was added dropwise, under argon atmosphere, to a cooled (−78 °C) solution of LDA, which was previously prepared from *n*-BuLi (12.5 mL, 1.6 M in hexane, 19.96 mmol, 2.2 equiv.) and *i*-$Pr_2NH$ (2.9 mL, 19.96 mmol, 2.2 equiv.) in THF (25 mL). The reaction mixture was stirred at −78 °C for 2 h, then a solution of succinic anhydride (1 g, 9.99 mmol, 1.1 equiv.) in anhydrous THF (8 mL) was added to the reaction flask. The cooling bath was removed, and aqueous 2 M HCl (30 mL) was added at room temperature. The mixture was extracted with chloroform, the organic phase was dried over $Na_2SO_4$, and solvent was evaporated. The solid residue was dissolved in MeOH (50 mL), cooled at 0 °C, and $H_2SO_4$ (0.45 mL, 95%) was added dropwise. The mixture was stirred at room temperature for 24 h, then a saturated $NaHCO_3$ solution was added, and the mixture was extracted with AcOEt. The organic phase, dried over $Na_2SO_4$, was evaporated under reduced pressure to give a crude that was purified by silica gel column chromatography with A/P 1:9, *v*/*v* as a solvent system. Title compound (**3**) was isolated as a colorless oil. Yield 32% over two steps. $^1$H NMR (400 MHz, Chloroform-*d*) δ 7.51 (d, *J* = 1.7 Hz, 1H), 6.81 (d, *J* = 1.7 Hz, 1H), 3.89 (s, 3H), 3.68 (s, 3H), 3.31 (t, *J* = 6.7 Hz, 2H), 2.73 (t, *J* = 6.6 Hz, 2H). $^{13}$C NMR (101 MHz, Chloroform-*d*) δ 187.72, 172.96, 162.89, 150.83, 144.36, 122.29, 113.62, 52.46, 51.83, 34.92, 27.47 [36,37].

3.1.2. Methyl 3-(1,1,4-Trimethoxy-4-oxobutyl)furan-2-carboxylate (**4**)

A solution of compound **3** (0.9 gr, 3.75 mmol, 1 equiv.), $HC(OMe)_3$ (2.1 mL, 19.48 mmol, 5.2 equiv.), and *p*-TsOH (0.05 gr) in MeOH (8 mL) was refluxed for 48 h. The reaction mixture was cooled to room temperature, pyridine (0.18 mL) was added, and the solvent evaporated.The residue was purified by silica gel column chromatography with A/P 1:4, *v*/*v* as a solvent system. Title compound **4** was obtained as a transparent oil. Yield 90%. $^1$H NMR (400 MHz, Chloroform-*d*) δ 7.36 (d, *J* = 1.7 Hz, 1H), 6.66 (d, *J* = 1.7 Hz, 1H), 3.81 (s, 3H), 3.58 (s, 3H), 3.20 (s, 6H), 2.47 (t, *J* = 6.7 Hz, 2H), 2.16 (t, *J* = 6.6 Hz, 2H). $^{13}$C NMR (101 MHz, Chloroform-*d*) δ 173.51, 163.81, 154.87, 141.84, 117.12, 112.38, 111.59, 101.72, 52.18, 51.97, 49.51, 30.35, 28.92 [36,37].

3.1.3. Methyl 4-Hydroxy-7-methoxybenzofuran-5-carboxylate (**5**)

*tert*-BuOK (0.61 g, 5.45 mmol, 2.2 equiv.) was poured into anhydrous THF (65 mL) under an argon atmosphere, and the suspension was cooled to −78 °C. A solution of compound **4** (0.71 g, 2.48 mmol, 1 equiv.) in anhydrous THF (2 mL) was added dropwise, and the mixture turned orange. After 1.5 h of stirring at −78 °C, anhydrous HCl (4 M in 1,4-dioxane) was added. The resulting transparent yellow reaction mixture was allowed to room temperature and stirred for 1 h. The precipitate was filtered through a Gooch filter, and the solvent was evaporated under reduced pressure. Chromatographic purification of the residue with A/P 1:9 *v*/*v* as the eluent phase provided title compound **5** as a white solid. Melting point: 125–127 °C. Yield 62%. $^1$H NMR (400 MHz, Chloroform-*d*) δ 11.14 (s, 1H), 7.60 (dd, *J* = 2.1 Hz, 1H), 7.17 (s, 1H), 6.98 (d, *J* = 2.1 Hz, 1H), 3.97 (d, *J* = 1.6 Hz, 6H). $^{13}$C NMR (101 MHz, Chloroform-*d*) δ 171.09, 152.43, 149.52, 144.76, 139.19, 118.90, 105.66, 105.38, 105.02, 56.51, 52.29 [36,37].

3.1.4. Methyl 4,7-Dimethoxybenzofuran-5-carboxylate (**6**)

A mixture of compound **5** (0.21 g, 0.95 mmol, 1 equiv.), $Cs_2CO_3$ (1.55 g, 5.75 mmol, 5 equiv.), and $CH_3I$ (0.29 mL, 4.75 mmol, 5 equiv.) in anhydrous DMF (6 mL) was stirred at room temperature for 16 h under an argon atmosphere. After complete conversion of starting material (checked by TLC A/P9 1:9), the reaction was partitioned between HCl 2 M and AcOEt; the organic phase was washed with HCl 2 M (×2) and brine, dried over $Na_2SO_4$, and the solvent was evaporated to dryness. Purification of the crude by column chromatography with A/P 1:4 as the eluent phase afforded title compound **6** as a colorless oil. Yield 96%. $^1$H NMR (300 MHz, Chloroform-*d*) δ 7.63–7.61 (m, 1H), 7.26 (s, 1H), 6.95–6.94

(m, 1H), 4.00 (d, *J* = 0.8 Hz, 6H), 3.94 (d, *J* = 0.8 Hz, 3H). $^{13}$C NMR (75 MHz, Chloroform-*d*) δ 167.04, 149.35, 148.04, 145.57, 141.84, 123.31, 117.58, 108.69, 105.80, 62.46, 56.77, 52.52.

3.1.5. 4,7-Dimethoxybenzofuran-5-carbaldehyde (**7**)

A solution of compound **6** (0.2 g, 0.84 mmol, 1 equiv.) in dry $Et_2O$ (4 mL) was added dropwise to a stirred to a cooled (0 °C) suspension of $LiAlH_4$ (0.08 g, 2.1 mmol, 2.5 equiv.) in anhydrous $Et_2O$ (5 mL) under argon atmosphere. The reaction mixture was stirred at room temperature overnight, then it was cooled to 0 °C, and aqueous NaOH solution (5 mL, 2 M) was added. After 30 min, the mixture was filtered on a celite pad, and the phases were separated. The aqueous phase was extracted with $Et_2O$. The combined organics were dried over $Na_2SO_4$, and the solvent was evaporated to give (4,7-dimethoxybenzofuran-5-yl)methanol as a white crystalline solid, which was used in the next oxidative step without further purification.

A solution of the primary alcohol (0.14 g, 1.29 mmol, 1 equiv.) in anhydrous DCM (5 mL) was added to a suspension of PCC (0.42 g, 1.93 mmol, 1.5 equiv.) in DCM (5 mL). The dark brown reaction mixture was magnetically stirred at room temperature for 1.5 h then $Et_2O$ was added. The supernatant was decanted from the black insoluble residue, which was further washed with $Et_2O$ (×3). The combined organic phases were filtered through a pad of silica, and the solvent was evaporated. Purification of the crude by column chromatography with A/P 1:4 *v*/*v* as a solvent system furnished title compound **7** as a white crystalline solid. Melting point: 142–145 °C. Yield 50%.$^1$H NMR (400 MHz, Chloroform-*d*) δ 10.46 (s, 1H), 7.67 (dd, *J* = 2.3, 0.4 Hz, 1H), 7.25 (s, 1H), 7.02 (d, *J* = 2.3 Hz, 1H), 4.15 (s, 3H), 4.00 (s, 3H). $^{13}$C NMR (101 MHz, Chloroform-*d*) δ 189.09, 149.92, 145.30, 142.04, 122.24, 120.30, 105.88, 103.45, 61.74, 56.29.

3.1.6. 2,5-Dimethoxyphenol (**9**)

$H_2O_2$ (2.4 mL, 30% *w*/*w*, 78.21 mmol, 5.4 equiv.) was added dropwise to a magnetically stirred mixture of 2,5-dimethoxybenzaldehyde (2.42 g, 14.56 mmol, 1 equiv.), $SeO_2$ (0.038 g, 0.342 mmol, 0.023 equiv.) in *tert*-BuOH (6 mL). The reaction mixture was stirred overnight at room temperature then $Et_2O$ (20 mL) was added. The resulting mixture was washed with brine (×3), the organic phase was dried over $Na_2SO_4$, and the solvent was evaporated to dryness. The residue was dissolved in MeOH (10 mL), and a solution of $K_2CO_3$ (2 g) in $H_2O$ (10 mL) was added to the solution. After 1 h, HCl 6M was added to reach pH 1, and the reaction mixture was extracted with DMC (20 mL ×3). The combined organic phases were dried over anhydrous $Na_2SO_4$, and the solvent was evaporated to dryness. Purification was carried out by silica gel column chromatography with A/P 1.5:8.5 *v*/*v* to obtain compound **9** as a transparent oil. Yield 90%. $^1$H NMR (400 MHz, Chloroform-*d*) δ 6.77 (d, *J* = 8.8 Hz, 1H), 6.56 (d, *J* = 2.9 Hz, 1H), 6.38 (dd, *J* = 8.8, 2.9 Hz, 1H), 5.66 (s, 1H), 3.84 (s, 3H), 3.75 (s, 3H). $^{13}$C NMR (101 MHz, Chloroform-*d*) δ 154.56, 146.44, 140.96, 111.45, 104.23, 101.73, 56.58, 55.66 [38].

3.1.7. 4-Bromo-2,5-dimethoxyphenol (**10**)

NBS (1.16 g, 6.55 mmol, 1 equiv.) was added to a cooled (0 °C) solution of **9** (1.0 g, 6.55 mmol, 1 equiv.) in acetonitrile (130 mL). Stirring at 0 °C was continued for 30 min. Then, $Na_2S_2O_3$ saturated solution was added, and the mixture was extracted with AcOEt (×3). The combined organic phases were washed with brine, dried over $Na_2SO_4$, and the solvent was evaporated. Purification of the residue by column chromatography by eluting with A/P 1:4 *v*/*v* gave **10** as a transparent oil. Yield 97%. $^1$H NMR (400 MHz, Chloroform-*d*) δ 7.02 (s, 1H), 6.61 (s, 1H), 5.65 (s, 1H), 3.83 (s, 3H), 3.81 (s, 3H). $^{13}$C NMR (101 MHz, Chloroform-*d*) δ 150.66, 145.71, 140.94, 115.77, 100.51, 99.81, 56.77, 56.74.

3.1.8. 1-Bromo-4-(2,2-dimethoxyethoxy)-2,5-dimethoxybenzene (**11**)

$BrCH_2CH(OMe)_2$ (1.0 mL, 8.82 mmol, 1.5 equiv.) was added dropwise to a stirred solution of **10** (1.37 g, 5.88 mmol, 1 equiv.) and KOH (0.66 g, 11.756 mmol, 2 equiv.) in

DMAC (12 mL). The reaction mixture was stirred at 140 °C for 1.5 h and then cooled to room temperature. $H_2O$ (20 mL) was added, and the resulting mixture was extracted with $Et_2O$ (40 mL ×3). The combined organic phases were washed with aqueous NaOH (30 mL, 5%) and $H_2O$ (30 mL), dried over $Na_2SO_4$, and the solvent was evaporated to dryness. Purification of the residue by column chromatography with A/P 1:4 *v*/*v* as the eluent furnished **11** as a white crystalline solid. Melting point: 57–60 °C. Yield 83%. $^1$H NMR (400 MHz, Chloroform-*d*) δ 7.05 (s, 1H), 6.63 (s, 1H), 4.72 (t, *J* = 5.2 Hz, 1H), 4.04 (d, *J* = 5.2 Hz, 0H), 3.83 (s, 3H), 3.80 (s, 3H), 3.46 (s, 6H). $^{13}$C NMR (101 MHz, Chloroform-*d*) δ 150.30, 148.22, 144.66, 117.47, 102.52, 102.07, 69.94, 57.10, 56.87, 54.51.

3.1.9. 5-Bromo-4,7-dimethoxybenzofuran (**12**) by Cyclization of (**11**)

A solution of compound **11** (0.37 g, 1.55 mmol, 1 equiv.) in chlorobenzene (3 mL) was added dropwise to a heated (120 °C) mixture of polyphosphoric acid (0.5 g) in chlorobenzene (15 mL). After 30 min, the reaction mixture was cooled to room temperature, diluted with $Et_2O$, and washed with $H_2O$. The removal of volatiles under reduced pressure gave a residue that was purified by column chromatography with A/P 0.5:9.5 *v*/*v*. Compound **12** was isolated as a white crystalline solid. Melting point: 63–65 °C. Yield 50%. $^1$H NMR (400 MHz, Chloroform-*d*) δ 7.59 (dd, *J* = 2.2, 0.5 Hz, 1H), 6.92 (s, 1H), 6.87 (dd, *J* = 2.1, 0.4 Hz, 1H), 3.97 (d, *J* = 1.7 Hz, 6H). $^{13}$C NMR (101 MHz, Chloroform-*d*) δ 145.11, 144.54, 143.95, 142.09, 122.44, 110.55, 107.66, 104.60, 61.06, 56.57.

3.1.10. 4,7-Dimethoxybenzofuran-5-carbaldehyde (**7**) via Halogen-Metal Exchange

*n*-BuLi (1.32 mL, 1.6 M in hexane, 2.1 equiv.) was added to a cooled (−78 °C) solution of compound **12** (0.26 g, 1.0 mmol, 1.0 equiv) in dry THF (5 mL) under argon atmosphere. The reaction mixture was stirred at −78 °C for 20 min. Then, DMF (0.25 mL, 3.25 equiv.) was added, and the cooling bath was removed. After 12 h, AcOEt (10 mL) was added, and the reaction was quenched with $NH_4Cl$ saturated aqueous solution. The organic layer was separated, washed with brine, dried over $Na_2SO_4$, and the solvent was evaporated to dryness. Chromatographic purification of the residue with A/P 1:4 *v*/*v* afforded the aldehyde **7** as a white crystalline solid. Melting point: 142–145 °C. Yield 50%. $^1$H NMR (400 MHz, Chloroform-*d*) δ 10.46 (s, 1H), 7.67 (dd, *J* = 2.3, 0.4 Hz, 1H), 7.25 (s, 1H), 7.02 (d, *J* = 2.3 Hz, 1H), 4.15 (s, 3H), 4.00 (s, 3H). $^{13}$C NMR (101 MHz, Chloroform-*d*) δ 189.09, 149.92, 145.30, 142.04, 122.24, 120.30, 105.88, 103.45, 61.74, 56.29.

3.1.11. 1-Phenylprop-2-en-1-one (**13**)

Formalin (0.8 mL, 37%, 10 mmol, 5 equiv.) was added to a solution of the ylide **8** (0.76 g, 2 mmol, 1 equiv.) in DCM (8 mL), and the mixture was heated at reflux overnight. After washing with brine, the organic phase was dried over anhydrous $Na_2SO_4$ and evaporated to dryness. Purification of the residue by column chromatography with A/P 1:4 *v*/*v* as the eluent phase furnished compound **13** as a clear oil. Yield 80%. $^1$H NMR (400 MHz, Chloroform-*d*) δ 7.97–7.93 (m, 2H), 7.58–7.55 (m, 1H), 7.51–7.45 (m, 2H), 7.16 (ddd, *J* = 17.2, 10.6, 0.6 Hz, 1H), 6.44 (dd, *J* = 17.2, 1.7 Hz, 1H), 5.95–5.91 (m, 1H). $^{13}$C NMR (101 MHz, Chloroform-*d*) δ 191.14, 137.35, 133.06, 132.47, 130.26, 129.00, 128.77, 128.70, 128.07 [45].

3.1.12. 2-(2,5-Dimethoxyphenoxy) tetrahydro-2H-pyran (**14**)

DHP (4.16 mL, 46 mmol, 10 equiv.) was added to a solution of compound **9** (0.71 g, 4.6 mmol, 1 equiv.) and PPTS (0.115 g, 0.46 mmol, 0.1 equiv.) in DCM (10 mL). The reaction mixture was stirred at room temperature overnight, then it was diluted with DCM and washed with NaOH solution and brine. The organic phase was dried over $Na_2SO_4$ and evaporated. Purification was performed by column chromatography using A/P 1:9 *v*/*v* as the eluent phase. Compound **14** was isolated as a clear oil. Yield 91%. $^1$H NMR (400 MHz, DMSO-$d_6$) δ 6.89 (d, *J* = 8.8 Hz, 1H), 6.68 (d, *J* = 2.9 Hz, 1H), 6.50 (dd, *J* = 8.9, 2.9 Hz, 1H), 5.39 (t, *J* = 3.3 Hz, 1H), 3.82 (ddd, *J* = 11.1, 8.9, 3.8 Hz, 1H), 3.71 (s, 3H), 3.67 (s, 3H), 3.53 (dtd, *J* = 11.5, 4.3, 1.2 Hz, 1H), 1.94–1.38 (m, 7H) [44].

3.1.13. 2-Hydroxy-3,6-dimethoxybenzaldehyde (**15**)

*n*-BuLi (4 mL, 1.6 M in hexane, 6.37 mmol, 1.1 equiv.) was added dropwise to a cooled (0 °C) solution of compound **14** (1.38 g, 5.79 mmol, 1 equiv.) in anhydrous $Et_2O$ (60 mL) under argon atmosphere. The reaction mixture turned purple, then yellow, and stirring was continued at room temperature for 2 h. The reaction flask was cooled to −78 °C, and anhydrous DMF (1.78 mL, 23.16 mmol, 4 equiv.) was added. The reaction mixture was stirred at room temperature for 2 h, quenched with HCl (5 mL, 6 N), and stirred at room temperature for 1 h. The aqueous phase was extracted with AcOEt (×3), the combined organics were dried over $Na_2SO_4$, and the solvent was evaporated. Purification of the residue was performed by column chromatography with A/P 1:4 *v*/*v* as the eluent phase. Compound 15 was isolated as bright yellow solid. Melting point: 67–69 °C. Yield 80%. $^1$H NMR (400 MHz, Chloroform-*d*) δ 12.17 (s, 1H), 10.31 (s, 1H), 7.02 (d, *J* = 8.9 Hz, 1H), 6.27 (d, *J* = 8.9 Hz, 1H), 3.84 (d, *J* = 0.8 Hz, 6H). $^{13}$C NMR (101 MHz, Chloroform-*d*) δ 194.91, 155.87, 153.58, 142.08, 120.27, 111.09, 99.36, 56.90, 55.78 [44].

3.1.14. 3-Bromo-6-hydroxy-2,5-dimethoxybenzaldehyde (**16**)

AcONa (0.091 gr, 1.1 mmol, 1.1 equiv.) and then $Br_2$ (0.056 mL, 1.1 mmol, 1.1 equiv.) was added to a cooled (0 °C) solution of compound **15** (0.182 g, 1 mmol, 1 eq) in acetic acid (3 mL). The reaction mixture was stirred at room temperature for 30 min. Then, $H_2O$ (10 mL) was added, and the mixture was extracted with DCM (10 mL × 3). The combined organic phases were washed with $H_2O$ (10 mL), dried over $Na_2SO_4$, and evaporated. Purification of the residue by column chromatography with A/P 1:4 *v*/*v* as the eluent phase furnished compound **16** as a light-yellow solid. Melting point: 92–95 °C. Yield 80%. $^1$H NMR (400 MHz, Chloroform-*d*) δ 11.89 (s, 1H), 10.21 (s, 1H), 7.19 (s, 1H), 3.92 (s, 3H), 3.87 (s, 3H). $^{13}$C NMR (101 MHz, Chloroform-*d*) δ 194.91, 152.63, 152.47, 145.51, 122.50, 115.15, 104.06, 63.41, 56.67 [44].

3.1.15. Ethyl 2-(4-bromo-2-formyl-3,6-dimethoxyphenoxy)acetate (**17**)

$Cs_2CO_3$ (0.36 g, 1.1 mmol, 1.1 equiv.) and $BrCH_2COOEt$ (0.12 mL, 1.1 mmol, 1.1 equiv.) were added to a solution of compound **16** (0.261 g, 1 mmol, 1 equiv.) in DMF (5 mL). The reaction mixture was stirred at room temperature for 1 h. $H_2O$ (10 mL) was added, and the mixture was extracted with AcOEt (20 mL × 3). The combined organic phases were washed with $H_2O$ (20 mL), dried over $Na_2SO_4$, and the solvent was evaporated. Compound **17** was isolated as a white grainy solid after trituration with petroleum ether. Melting point: 85–86 °C. Yield 85%. $^1$H NMR (400 MHz, Chloroform-*d*) δ 10.49 (s, 1H), 7.27 (s, 1H), 4.76 (s, 2H), 4.23 (q, *J* = 7.1 Hz, 2H), 3.85 (d, *J* = 2.1 Hz, 6H), 1.28 (t, *J* = 7.1 Hz, 3H). $^{13}$C NMR (101 MHz, Chloroform-*d*) δ 189.32, 168.96, 150.74, 148.89, 148.75, 121.27, 112.82, 69.75, 62.64, 61.36, 56.66, 14.24.

3.1.16. 5-Bromo-4,7-dimethoxybenzofuran (**12**) via Cyclization of (**17**)

$LiOH{\cdot}H_2O$ (0.032 g, 0.78 mmol, 3 equiv.) was added to a magnetically stirred solution of compound **17** (0.09 g, 0.26 mmol, 1 equiv.) in a 3:1 THF/$H_2O$ (4 mL) mixture. After stirring at room temperature overnight, the reaction mixture was acidified with 1 M HCl and extracted with AcOEt (10 mL × 3). The combined organics were washed with brine, dried over anhydrous $Na_2SO_4$, and evaporated to dryness. The white solid residue was dissolved in $Ac_2O$ (3 mL), AcONa (0.085 g, 1.035 mmol, 1.5 equiv.) was added, and the mixture was heated at 130 °C for 2 h. Successively, the temperature was lowered to 60 °C, and EtOH (3 mL) was added dropwise to consume acetic anhydride. The stirring was continued at 60 °C for 2 h. then, the reaction mixture was cooled to room temperature. $H_2O$ (3 mL) was added, and the mixture was extracted with AcOEt (10 mL). The organic phase was washed with NaOH (5 mL 2 N) and with $H_2O$ (5 mL), dried over $Na_2SO_4$, and evaporated. Chromatographic purification of the residue with A/P 0.5:9.5 provided compound 12 as a white crystalline solid. Melting point: 63–65 °C. Yield 57%.$^1$H NMR (400 MHz, Chloroform-*d*) δ 7.59 (dd, *J* = 2.2, 0.5 Hz, 1H), 6.92 (s, 1H), 6.87 (dd, *J* = 2.1, 0.4 Hz,

1H), 3.97 (d, *J* = 1.7 Hz, 6H).$^{13}$C NMR (101 MHz, Chloroform-*d*) δ 145.11, 144.54, 143.95, 142.09, 122.44, 110.55, 107.66, 104.60, 61.06, 56.57.

3.1.17. Synthesis of (**1**) from (**12**) via Mizoroki-Heck

A reaction flask containing DMF (1 mL) and DIPEA (1 mL) was charged with phenylpropenone **13** (0.165 g, 1.25 mmol, 1.25 equiv.), aryl bromide **12** (0.257 g, 1 mmol, 1 equiv.), $P(o\text{-tol})_3$ (0.121 gr, 0.4 mmol), and $Pd(OAc)_2$ (0.011 g, 0.05 mmol, 0.05 equiv.). The reaction mixture was stirred under an argon atmosphere at 110 °C for 5 h. Then, AcOEt (10 mL) and $H_2O$ (10 mL) were added to the residue after solvent evaporation. The insoluble solid was filtered on celite, and the organic phase was washed with brine and dried over $Na_2SO_4$. The solvent was evaporated, and Chromatographic purification of the residue with A/P 1:4 *v*/*v* provided compound **1** [10] as a yellow crystalline solid. Melting point: 98–103 °C. Yield 32%. $^1$H NMR (400 MHz, Chloroform-*d*) δ 8.22 (d, J = 15.8 Hz, 1H), 8.05–8.01 (m, 2H), 7.62 (d, *J* = 2.2 Hz, 1H), 7.59–7.48 (m, 4H), 7.05 (s, 1H), 6.95 (dd, *J* = 2.2, 0.6 Hz, 1H), 4.05 (s, 3H), 4.04 (s, 3H). $^{13}$C NMR (101 MHz, Chloroform-*d*) δ 191.00, 148.07, 144.97, 141.96, 140.32, 138.60, 132.53, 128.54, 128.50, 121.68, 121.47, 120.74, 105.34, 104.97, 61.51, 56.50. HPLC r.t. = 23,233 min. ESI = 309,2086 $[M + H]^+$. HRMS *m*/z: $[M + H]^+$ calc for $C_{19}H_{16}O_4$ 309.11214, found 309.1121; $[M + Na]^+$ calc 331.09408 found 331.0937. I.R. (neat) $cm^{-1}$ = 3126, 1654, 1598, 1586, 1572, 1480, 1440, 1354, 1287, 1231, 1202, 1185, 1159, 1072, 1013, 995, 935, 875, 853, 771, 738, 718, 704, 685, 662.

3.1.18. Synthesis of (**1**) from (**7**) via Wittig

A microwave vial was charged with aldehyde **7** (0.065 g, 0.3 mmol, 1 equiv.), ylide **8** (0.125 g, 0.33 mmol, 1.1 equiv.), and acetonitrile (3 mL); microwave was set at 135 °C for 1.5 h. The solvent was evaporated and the residue chromatographed by eluting with A/P 1:4 *v*/*v*. Yield 70%.

3.1.19. (E)-3-(4,7-Dimethoxybenzofuran-2-yl)-1-phenylprop-2-en-1-one (**22**)

A microwave vial was charged with aldehyde (**20**, in mixture ratio 65:35 with 7) (0.08 g, 0.38 mmol, 1 equiv.), ylide **8** (0.144 g, 0.38 mmol, 1 equiv.), and acetonitrile (3 mL); microwave was set at 135 °C for 1.5 h. The solvent was evaporated and the residue chromatographed by eluting with A/P 1:4 *v*/*v*. Yield 70%. Melting Point: 155–160 °C. $^1$H NMR (400 MHz, Chloroform-*d*) δ 8.12–8.06 (m, 2H), 7.71 (d, *J* = 4.9 Hz, 2H), 7.59 (ddt, *J* = 8.3, 6.6, 1.4 Hz, 1H), 7.55–7.47 (m, 2H), 7.13 (s, 1H), 6.80 (d, *J* = 8.6 Hz, 1H), 6.54 (d, *J* = 8.6 Hz, 1H), 4.01 (s, 3H), 3.91 (s, 3H). $^{13}$C NMR (101 MHz, Chloroform-*d*) δ 189.04, 151.81, 147.38, 145.17, 139.38, 137.41, 132.41, 130.13, 128.09, 128.05, 121.06, 120.40, 110.05, 108.56, 102.49, 56.09, 55.25. HPLC r.t. = 22,617 min. ESI = 3,092,086 [M + 1]. HRMS *m*/z: $[M + H]^+$ calc for $C_{19}H_{16}O_4$ 309.11214, found 309.1122; $[M + Na]^+$ calc 331.09408 found 331.094.

3.1.20. Synthesis of (**22** and **1**) from (**20** and **7**) via Wittig by Convectional Heating

A round bottom flask vial was charged with aldehydes (**20**, in mixture ratio 65:35 with **7**) (0.08 g, 0.38 mmol, 1 equiv.), ylide 8 (0.144 g, 0.38 mmol, 1 equiv.), and toluene (3 mL); the mixture was refluxed overnight. After complete conversion of the starting material, the solvent was evaporated and the residue chromatographed by eluting with A/P 1:4 *v*/*v*. Yield 70%.

3.1.21. (E)-3-(4,7-Dimethoxybenzofuran-6-yl)-1-phenylprop-2-en-1-one (**23**)

A microwave vial was charged with aldehyde **21** (0,08 mg, 0.38 mmol, 1 equiv.), ylide **8** (144 mg, 0.38 mmol, 1 equiv.), and acetonitrile (3 mL); the microwave was set at 135 °C for 1.5 h. The solvent was evaporated and the residue chromatographed by eluting with A/P 1:4 *v*/*v*. Yield 70%. Melting Point 138–141 °C $^1$H NMR (400 MHz, Chloroform-*d*) δ 8.23 (d, *J* = 15.9 Hz, 1H), 8.05–8.02 (m, 2H), 7.62 (d, *J* = 2.1 Hz, 1H), 7.61–7.49 (m, 4H), 6.89 (d, *J* = 2.1 Hz, 1H), 6.87 (s, 1H), 4.17 (s, 3H), 3.97 (s, 3H).$^{13}$C NMR (101 MHz, Chloroform-*d*) δ 191.16, 148.59, 147.46, 145.45, 140.43, 138.72, 132.61, 128.64, 128.61, 122.92, 122.26, 122.11,

105.07, 101.56, 61.41, 55.92.HPLC r.t. = 24,183 min. ESI = 3,092,086 [M + 1]. HRMS *m*/z: $[M + H]^+$ calc for $C_{19}H_{16}O_4$ 309.11214, found 309.1121; $[M + Na]^+$ calc 331.09408 found 331.0937.

3.1.22. 2-(Dimethoxymethoxy)-1,4-dimethoxybenzene (**18**)

Bromoacetaldehyde dimethyl acetale (1.14 mL, 9.73 mmol, 1.5 equiv.) was added dropwise to a solution of **9** (1 g, 6.49 mmol, 1 equiv.), KOH (727 mg, 13 mmol, 2 equiv.) in DMAC (13 mL) at room temperature. The mixture was heated at 140 °C and stirred for 2 h until the starting material was no longer detected by TLC (A/P 1:4). It was allowed to cool down to room temperature and quenched with $H_2O$ (20 mL). The crude was extracted with $Et_2O$ (40 mL × 3), and combined organic phases were washed with an aqueous solution of 5% NaOH (30 mL) and $H_2O$ (30 mL). After drying over anhydrous $Na_2SO_4$, the ether extraction phase was evaporated in vacuo. The residue was purified by silica gel column chromatography (elution system A/P 1:4 *v*/*v*) to obtain **18** as a white crystalline solid. Yield 70%. $^1$H NMR (400 MHz, Chloroform-*d*) δ 6.80 (d, *J* = 8.8 Hz, 1H), 6.56 (d, *J* = 2.9 Hz, 1H), 6.44 (dd, *J* = 8.8, 2.8 Hz, 1H), 4.77 (t, *J* = 5.2 Hz, 1H), 4.03 (d, *J* = 5.2 Hz, 2H), 3.78 (d, *J* = 21.9 Hz, 6H), 3.46 (s, 6H). $^{13}$C NMR (101 MHz, Chloroform-*d*) δ 154.26, 149.08, 144.18, 113.21, 104.69, 102.73, 102.37, 69.16, 56.84, 55.73, 54.35.

3.1.23. 4,7-Dimethoxybenzofuran (**19**)

Compound **18** (1 g, 4.12 mmol, 1 equiv.) and Sn-β zeolite (4.12 g) (kindly prepared by the analytical chemistry division of the University of Ferrara, Prof. Pasti Luisa) were poured in chlorobenzene (42 mL). The heterogeneous mixture was stirred at 105 °C. After 5 h, it was allowed to cool down to room temperature, filtered through a Gooch filter, and evaporated under reduced pressure. The residue was purified by silica gel column chromatography (elution system A/P 1:9 *v*/*v*) to obtain a white crystalline solid. Yield 62%. $^1$H NMR (400 MHz, Chloroform-*d*) δ 7.56 (d, *J* = 2.1 Hz, 1H), 6.86 (d, *J* = 2.1 Hz, 1H), 6.70 (d, *J* = 8.5 Hz, 1H), 6.54 (d, *J* = 8.5 Hz, 1H), 3.97 (s, 3H), 3.90 (s, 3H). $^{13}$C NMR (101 MHz, Chloroform-*d*) δ 147.60, 143.90, 140.38, 119.45, 106.43, 104.43, 102.72, 56.53, 55.80.

3.1.24. 1-(2,5-Dimethoxyphenoxy)propan-2-one (**24**)

Compound **9** (560 mg, 4.21 mmol, 1 equiv.) was dissolved in DMF (0.2 M), then $Cs_2CO_3$ (1.5 g, 4.631 mmol, 1.1 equiv.) and bromoacetone (0.63 gr, 4.63 mmol, 1.1 equiv.) were added. The mixture was stirred overnight at room temperature and quenched with brine and $H_2O$. The mixture was extracted with AcOEt, dried over $Na_2SO_4$, and the solvent was evaporated. The residue was purified by silica gel column chromatography (elution system A/P 1:4 *v*/*v*) to obtain 24 as a yellowish oil. Yield 63%.$^1$H NMR (400 MHz, Chloroform-*d*) δ 6.83 (d, *J* = 8.8 Hz, 1H), 6.47 (dd, *J* = 8.8, 2.8 Hz, 1H), 6.39 (d, *J* = 2.8 Hz, 1H), 4.57 (s, 2H), 3.84 (s, 3H), 3.74 (s, 3H), 2.28 (s, 3H).$^{13}$C NMR (101 MHz, Chloroform-*d*) δ 206.07, 154.22, 148.22, 144.00, 113.22, 105.29, 102.74, 74.46, 56.73, 55.77, 26.56.

3.1.25. 4,7-Dimethoxy-3-methylbenzofuran (**25**)

A mixture of polyphosphoric acid (0.52 g) in chlorobenzene (15 mL) was heated at 120 °C, and a solution of 24 (370 mg, 1.55 mmol, 1 equiv.) in chlorobenzene (3 mL) was added. The mixture turned black, and after 20 min, it was allowed to cool at room temperature. The chlorobenzene phase was decanted, and the residue was rinsed three times with 20 mL of $Et_2O$. The ether was evaporated, and cyclized product 25 was purified on silica gel column chromatography by eluting with A/P 0.2:9.8, *v*/*v*, to obtain a yellowish solid. Yield 50%. $^1$H NMR (400 MHz, Chloroform-*d*) δ 7.28 (d, *J* = 1.4 Hz, 1H), 6.66 (d, *J* = 8.5 Hz, 1H), 6.49 (d, *J* = 8.5 Hz, 1H), 3.95 (s, 3H), 3.86 (s, 3H), 2.35 (d, *J* = 1.3 Hz, 3H). $^{13}$C NMR (101 MHz, Chloroform-*d*) δ 149.34, 145.93, 140.50, 140.36, 120.11, 116.40, 106.33, 102.40, 56.58, 55.80, 29.78.

3.1.26. (4,7-Dimethoxybenzofuran-3-yl)methanol (**26**), 4,7-Dimethoxybenzofuran-3-carbaldehyde (**27**)

Compound **25** (109 mg, 0.57 mmol, 1 equiv.) and $SeO_2$ (125 mg, 1.134 mmol, 2 equiv.) in 1,4-dioxane were stirred at 75 °C for 96 h. The cooled mixture was filtered through Gooch, and the solvent evaporated under reduced pressure. Chromatographic purification of the residue using A/P 3:7 *v*/*v* as the eluent phase provided title compounds **26** and **27** in 1:1 ratio as brown and red solid, respectively. Yield 80%. $^1$H NMR (400 MHz, Chloroform-*d*) δ 7.47 (d, *J* = 1.0 Hz, 1H), 6.71 (d, *J* = 8.6 Hz, 1H), 6.56 (d, *J* = 8.6 Hz, 1H), 4.73 (d, *J* = 0.9 Hz, 2H), 3.95 (s, 3H), 3.94 (s, 3H), 2.85 (s, 1H). $^{13}$C NMR (101 MHz, Chloroform-*d*) δ 147.06, 146.03, 140.71, 140.55, 120.85, 118.54, 106.82, 102.70, 56.55, 55.94.

3.1.27. 4,7-Dimethoxybenzofuran-3-carbaldehyde (**27**)

A solution of **26** (50 mg, 0,24 mmol, 1 equiv.) in anhydrous DCM (5 mL) was added to a suspension of PCC (129 mg, 0.6 mmol, 2.5 equiv.) in anhydrous DCM (5 mL). The red mixture turned dark brown and was stirred at room temperature overnight. The insoluble cake was rinsed three times with anhydrous $Et_2O$. The ether portions were combined, filtered through a pad of Florisil, and evaporated. Compound **27** was afforded by chromatographic purification using A/P 3:7 *v*/*v* as the eluent phase. Yield 95%. $^1$H NMR (400 MHz, Chloroform-*d*) δ 10.41–10.41 (m, 1H), 8.21–8.18 (m, 1H), 6.77 (d, *J* = 8.6 Hz, 1H), 6.65 (d, *J* = 8.6 Hz, 1H), 3.96 (s, 3H), 3.92 (s, 3H). $^{13}$C NMR (101 MHz, Chloroform-*d*) δ 187.31, 148.52, 148.25, 145.99, 140.31, 123.46, 107.68, 104.36, 56.57, 55.82.

3.1.28. (E)-3-(4,7-Dimethoxybenzofuran-3-yl)-1-phenylprop-2-en-1-one (**28**)

A microwave vial was charged with aldehyde **27** (65 mg, 0.3 mmol, 1 equiv.), ylide **8** (125 mg, 0.33 mmol, 1.1 equiv.), and acetonitrile (3 mL); the microwave was set at 135 °C for 2 h. The solvent was evaporated, and the residue was purified on silica gel chromatography eluting with A/P 1:4 v/v to obtain the desired product **28** as a yellow-ocher solid. Yield 65%. $^1$H NMR (400 MHz, Chloroform-*d*) δ 8.08–8.02 (m, 3H), 7.97–7.84 (m, 2H), 7.61–7.48 (m, 3H), 6.78 (d, *J* = 8.6 Hz, 1H), 6.65 (d, *J* = 8.7 Hz, 1H), 3.98 (s, 3H), 3.96 (s, 3H). $^{13}$C NMR (101 MHz, Chloroform-*d*) δ 190.58, 148.41, 146.56, 145.78, 140.38, 138.38, 134.75, 132.62, 128.56, 128.46, 124.00, 119.85, 116.75, 107.53, 104.04, 56.56, 55.96. HPLC r.t. = 23,017 min. ESI = 3,092,086 [M + 1]. HRMS *m*/z: $[M + H]^+$ calc for $C_{19}H_{16}O_4$ 309.11214, found 309.1121; $[M + Na]^+$ calc 331.09408 found 331.0937.

3.1.29. Cell Cultures and Stimulation

Bone marrow-derived macrophages (BMDMs) were isolated from C57BL/6 mice as described [52] and differentiated for 7 days in Iscove's Modified Dulbecco's Medium supplemented with 15% fetal bovine serum (FBS, Gibco), 1% penicillin/streptomycin (P/S) and 10 ng/mL M-CSF. THP-1 cells were grown in RPMI medium supplemented with 10% FBS, 100 U/mL penicillin, and 100 mg/mL streptomycin. THP-1 cells were stimulated by 100 ng/mL PMA overnight to differentiate into macrophages. All cells were grown in a 5% $CO_2$ incubator at 37 °C. BMDMs were seeded at $5 \times 10^5$ in 24 well plates. After 12 h, the medium was removed, and cells were treated with LPS from *Escherichia coli* 055:B5 (1 μg/mL) in fresh Iscove's Modified Dulbecco's Medium for 2 h. After that, the medium was removed and replaced with a serum-free medium containing DMSO or compounds (10 μM) for 30 min. Cells were then stimulated with Nigericin (10 μM) for 1 h. Human THP-1 cells were seeded at $3 \times 10^5$ cells per well in 24 well plates. The following day, the overnight medium was replaced, and cells were stimulated with LPS (1 μg/mL) for 3 h. The medium was removed and replaced with a serum-free medium containing DMSO or compounds (10 μM) for 30 min. Cells were then stimulated with Nigericin (10 μM) for 1 h.

3.1.30. In Vivo LPS Challenge

C57BL/6 mice were IP injected with compounds (25 mg/kg) or vehicle control (DMSO) 30 min before IP injection of LPS 1 mg/kg (4 h) and then were euthanized, and blood and

peritoneal exudate were isolated. Mouse plasma was collected after blood centrifugation (1000× *g*, 15 min at 4 °C). ELISA for IL-1β was performed according to the manufacturer's instructions (R&D Systems).

#### 3.1.31. ELISA

Supernatants from BMDMs and THP-1 cell culture were assayed for mouse or human IL-1β, respectively, by ELISA according to the manufacturer's instructions (R&D Systems).

## 4. Conclusions

We succeeded in synthesizing the bioactive compound velutone F (**1**), the chalconoid contained in *Millettia velutina* stem, together with other 21 flavonoids. Our chemical total synthesis of velutone F is advantageous compare to the recently reported [24] seven steps semi-synthesis requiring the naturally occurring furanochromone derivative Khellin as the costly starting material (25 G > 800 USD). We could develop synthetic routes A and B; the first one establishes the benzofuran nucleus by creating the annellated carbocyclic ring onto a furan ring, while the second one proceeds exactly the other way. Instead, the Wittig olefination and the Heck coupling reaction are the featuring steps allowing for the assemblage of the 1,3-diaryl enone scaffold. Both the multi-step synthetic routes A and B establish the enone moiety at position C-5 of the 4,7-dimethoxybenzofuran thus, slightly modified synthetic approaches were designed in order to achieve the non-natural chalconoids **22**, **23**, and **28**, which formally are the C-2, C-3, and C-6 regioisomers of velutone F (**1**). The anti-inflammatory effects of the newly synthesized compounds are also reported.

**Supplementary Materials:** The following supporting information can be downloaded at: https://www.mdpi.com/article/10.3390/ijms23168957/s1.

**Author Contributions:** Conceptualization, C.T., V.Z. and C.G.; methodology, T.D.V., M.P. and S.M.; validation, P.P., C.G. and V.Z.; synthesis of calchonoids, T.D.V., D.I., P.M., G.T., V.C., G.S. and M.F.; writing—original draft preparation, V.Z., A.F., C.T., S.M. and C.G.; writing—review and editing, A.F., C.T. and T.D.V.; supervision, P.P., C.G. and C.T.; funding acquisition, C.T., P.P. and C.G. All authors have read and agreed to the published version of the manuscript.

**Funding:** The authors are greatly thankful to the University of Ferrara for the support. The Signal Transduction Laboratory is supported by the Italian Association for Cancer Research (IG-23670 to P.P., IG-19803 to C.G.), A-ROSE, Progetti di Rilevante Interesse Nazionale (PRIN2017E5L5P3 to P.P and PRIN20177E9EPY to C.G.), the Italian Ministry of Health (GR-2019-12369646 to S.M.), the European Research Council (853057-InflaPML to C.G.) and local funds from the University of Ferrara to C.G., P.P., V.Z. and C.T. M.P. is supported by AIRC research fellowship (ID: 26665). P.P. is grateful to C. Degli Scrovegni for her continuous support.

**Institutional Review Board Statement:** Procedures involving animals and their care were in conformity with institutional guidelines, and Animal Ethics Committee approved all experimental protocols (Authorization N° 481/2017-PR and CBCC2.N.BH4 approved by Italian Ministry of Health).

**Acknowledgments:** The authors thank Giorgia Macedonio for NMR analysis and Erika Marzola for HPLC analysis.

**Conflicts of Interest:** The authors declare no conflict of interest.

## References

1. Tehfe, M.-A.; Dumur, F.; Xiao, P.; Delgove, M.; Graff, B.; Fouassier, J.-P.; Gigmes, D.; Lalevée, J. Chalcone Derivatives as Highly Versatile Photoinitiators for Radical, Cationic, Thiol-ene and IPN Polymerization Reactions Upon Visible Lights. *Polym. Chem.* **2014**, *5*, 382–390. [CrossRef]
2. Lee, S.-C.; Kang, N.-Y.; Park, S.-J.; Yun, S.-W.; Chandran, Y.; Chang, Y.-T. Development of a fluorescent chalcone library and its application in the discovery of a mouse embryonic stem cell probe. *Chem. Commun.* **2012**, *48*, 6681–6683. [CrossRef]
3. Nowakowska, Z. A review of anti-infective and anti-inflammatory chalcones. *Eur. J. Med. Chem.* **2007**, *42*, 125–137. [CrossRef] [PubMed]

4. Zhou, B.; Xing, C. Diverse Molecular Targets for Chalcones with Varied Bioactivities. *Med. Chem.* **2015**, *5*, 388–404. [CrossRef] [PubMed]
5. Zhuang, C.; Zhang, W.; Sheng, C.; Zhang, W.; Xing, C.; Miao, Z. Chalcone: A Privileged Structure in Medicinal Chemistry. *Chem. Rev.* **2017**, *117*, 7762–7810. [CrossRef]
6. Funakoshi-Tago, M.; Tanabe, S.; Tago, K.; Itoh, H.; Mashino, T.; Sonoda, Y.; Kasahara, T. Licochalcone A Potently Inhibits Tumor Necrosis Factor α-Induced Nuclear Factor-*k*B Activation through the Direct Inhibition of I*k*B Kinase Complex Activation. *Mol. Pharmacol.* **2009**, *76*, 745–753. [CrossRef]
7. Pandey, M.K.; Sandur, S.K.; Sung, B.; Sethi, G.; Kunnumakkara, A.B.; Aggarwal, B.B. Butein, a Tetrahydroxychalcone, Inhibits Nuclear Factor (NF)-*k*B and NF-*k*B-regulated Gene Expression through Direct Inhibition of I*k*Bα Kinase β on Cysteine 179 Residue. *J. Biol. Chem.* **2007**, *282*, 17340–17350. [CrossRef]
8. Wang, J.P.; Tsao, L.T.; Raung, S.L.; Lin, C.N. Investigation of the inhibitory effect of broussochalcone A on respiratory burst in neutrophils. *Eur. J. Pharmacol.* **1997**, *320*, 201–208. [CrossRef]
9. Maccari, R.; Ottana, R. Targeting Aldose Reductase for the Treatment of Diabetes Complications and Inflammatory Diseases: New Insights and Future Directions. *J. Med. Chem.* **2015**, *58*, 2047–2067. [CrossRef]
10. Aida, K.; Tawata, M.; Shindo, H.; Onaya, T.; Sasaki, H.; Yamaguchi, T.; Chin, M.; Mitsuhashi, H. Isoliquiritigenin: A New Aldose Reductase Inhibitor from Glycyrrhizae Radix. *Planta Med.* **1990**, *56*, 254–258. [CrossRef]
11. Song, N.R.; Kim, J.E.; Park, J.S.; Kim, J.R.; Kang, H.; Lee, E.; Kang, Y.G.; Son, J.E.; Seo, S.G.; Heo, Y.S.; et al. Licochalcone A, a Polyphenol Present in Licorice, Suppresses UV-Induced COX-2 Expression by Targeting PI3K, MEK1, and B-Raf. *Int. J. Mol. Sci.* **2015**, *16*, 4453–4470. [CrossRef] [PubMed]
12. Nyandoro, S.S.; Nkunya, M.H.H.; Josepha, C.C.; Odalo, J.O.; Sattler, I. New Glucopyranosylglyceryl-N-Octenyl Adipate and Bioactivity of Retro and Condensed Chalcones from *Toussaintia orientalis*. *Tanz. J. Sci.* **2012**, *38*, 108–126, eISSN: 2507–7961. Print ISSN 0856-1761.
13. Lee, M.H.; Kim, J.Y.; Ryu, J.-H. Prenylflavones from *Psoralea corylifolia* Inhibit Nitric Oxide Synthase Expression through the Inhibition of I-*k*B-α Degradation in Activated Microglial Cells. *Biol. Pharm. Bull.* **2005**, *28*, 2253–2257. [CrossRef]
14. Daikonya, A.; Katsuki, S.; Kitanaka, S. Antiallergic Agents from Natural Sources 9. Inhibition of Nitric Oxide Production by Novel Chalcone Derivatives from *Mallotus philippinensis* (Euphorbiaceae). *Chem. Pharm. Bull.* **2004**, *52*, 1326–1329. [CrossRef]
15. Chen, H.; Chen, X.; Sun, P.; Wu, D.; Yue, H.; Pan, J.; Li, X.; Zhang, C.; Wu, X.; Hua, L.; et al. Discovery of dronedarone and its analogues as NLRP3 inflammasome inhibitors with potent anti-inflammation activity. *Bioorg. Med. Chem. Lett.* **2021**, *46*, 128160. [CrossRef]
16. Zhang, C.; Yue, H.; Sun, P.; Hua, L.; Liang, S.; Ou, Y.; Wu, D.; Wu, X.; Chen, H.; Hao, Y.; et al. Discovery of chalcone analogues as novel NLRP3 inflammasome inhibitors with potent anti-inflammation activities. *Eur. J. Med. Chem.* **2021**, *219*, 113417. [CrossRef] [PubMed]
17. Choi, H.R.; Lim, H.; Lee, J.H.; Park, H.; Kim, H.P. Interruption of *Helicobacter pylori*-Induced NLRP3 Inflammasome Activation by Chalcone Derivatives. *Biomol. Ther.* **2021**, *29*, 410–418. [CrossRef]
18. Swanson, K.V.; Deng, M.; Ting, J.P.Y. The NLRP3 inflammasome: Molecular activation and regulation to therapeutics. *Nat. Rev. Immunol.* **2019**, *19*, 477–489. [CrossRef] [PubMed]
19. Wang, Z.; Xu, G.; Gao, Y.; Zhan, X.; Qin, N.; Fu, S.; Li, R.; Niu, M.; Wang, J.; Liu, Y.; et al. Cardamonin from a medicinal herb protects against LPS-induced septic shock by suppressing NLRP3 inflammasome. *Acta Pharm. Sin. B* **2019**, *9*, 734–744. [CrossRef]
20. Aybe, S.I.; Furuya, T. Studies on Plant Tissue Cultures. Part 36. Biosynthesis of a Retrochalcone, Echinatin, and Other Flavonoids in the Cultured Cells of *Glycyrrhiza echinate*. A New Route to a Chalcone with Transposed A- and B-Rings. *J. Chem. Soc. Perkin Trans.* **1982**, *1*, 2725–2734. [CrossRef]
21. Aybe, S.I.; Furuya, T. Biosynthesis of a Retrochalcone, Echinatin: A Feeding Study with Advanced Precursors. *Tetrahedron Lett.* **1981**, *22*, 2097–2098. [CrossRef]
22. Ayabe, S.I.; Yoshikawa, T.; Kobayashi, M.; Furuya, T. Biosynthesis of a Retrochalcone, Echinatin: Involvement of *O*-Methyl Transferase to Licodione. *Phytochemistry* **1980**, *19*, 2331–2336. [CrossRef]
23. Ma, X.; Zhao, M.; Tang, M.-H.; Xue, L.-L.; Zhang, R.-J.; Liu, L.; Ni, H.-F.; Cai, X.-Y.; Kuang, S.; Hong, F.; et al. Flavonoids with Inhibitory Effects on NLRP3 Inflammasome Activation from *Millettia velutina*. *J. Nat. Prod.* **2020**, *83*, 2950–2959. [CrossRef] [PubMed]
24. Zhang, R.; Hong, F.; Zhao, M.; Cai, X.; Jiang, X.; Ye, N.; Su, K.; Li, N.; Tang, M.; Ma, X.; et al. New Highly Potent NLRP3 Inhibitors: Furanochalcone Velutone F Analogues. *ACS Med. Chem. Lett.* **2022**, *13*, 560–569. [CrossRef]
25. Mishra, S.; Singh, P. Hybrid molecules: The privileged scaffolds for various pharmaceuticals. *Eur. J. Med. Chem.* **2016**, *124*, 500–536. [CrossRef]
26. Miao, Y.H.; Hu, Y.H.; Yang, J.; Liu, T.; Sun, J.; Wang, X.J. Natural source, bioactivity and synthesis of benzofuran derivatives. *RSC Adv.* **2019**, *9*, 27510–27540. [CrossRef]
27. Chand, K.; Hiremathad, A.; Singh, M.; Santos, M.A.; Keri, R.S. A review on antioxidant potential of bioactive heterocycle benzofuran: Natural and synthetic derivatives. *Pharm. Rep.* **2017**, *69*, 281–295. [CrossRef]
28. Radadiya, A.; Shah, A. Bioactive benzofuran derivatives: An insight on lead developments, radioligands and advances of the last decade. *Eur. J. Med. Chem.* **2015**, *97*, 356–376. [CrossRef]
29. Khanam, H. Bioactive Benzofuran derivatives: A review. *Eur. J. Med. Chem.* **2015**, *97*, 483–504. [CrossRef]

30. Schwaid, A.G.; Spencer, K.B. Strategies for Targeting the NLRP3 Inflammasome in the Clinical and Preclinical Space. *J. Med. Chem.* **2021**, *64*, 101–122. [CrossRef]
31. Zhang, X.; Xu, A.; Lv, J.; Zhang, Q.; Ran, Y.; Wei, C.; Wu, J. Development of small molecule inhibitors targeting NLRP3 inflammasome pathway for inflammatory diseases. *Eur. J. Med. Chem.* **2020**, *185*, 1118222. [CrossRef]
32. Coll, R.C.; Hill, J.R.; Day, C.J.; Zamoshnikova, A.; Boucher, D.; Massey, N.L.; Chitty, J.L.; Fraser, J.A.; Jennings, M.P.; Robertson, A.A.; et al. MCC950 directly targets the NLRP3 ATP-hydrolysis motif for inflammasome inhibition. *Nat. Chem. Biol.* **2019**, *15*, 556–559. [CrossRef]
33. Tapia-Abellán, A.; Angosto-Bazarra, D.; Martínez-Banaclocha, H.; de Torre-Minguela, C.; Cerón-Carrasco, J.P.; Pérez-Sánchez, H.; Arostegui, J.I.; Pelegrin, P. MCC950 closes the active conformation of NLRP3 to an inactive state. *Nat. Chem. Biol.* **2019**, *15*, 560–564. [CrossRef]
34. Goyal, K.; Kaur, R.; Goyal, A.; Awasthi, R. Chalcones: A review on synthesis and pharmacological activities. *J. Appl. Pharm. Sci.* **2021**, *11* (Suppl. S1), 1–14. [CrossRef]
35. Chen, Z.; Hu, F.; Huang, S.; Zhao, Z.; Mao, H.; Qin, W. Organocatalytic Enantioselective Selenosulfonylation of a C−C Double Bond to Form Two Stereogenic Centers in an Aqueous Medium. *J. Org. Chem.* **2019**, *84*, 8100–8111. [CrossRef]
36. Gammill, R.B. Synthetic Routes to Benzofurans and Benzothiophenes and Intermediates Therefor. U.S. Patent 4,609,739, 2 September 1986.
37. Gammill, R.B. Preparing 4,7-Dialkoxybenzofurans, and Intermediates Used Therein. European Patent 95,835, 7 December 1983.
38. Guzman, J.A.; Mendoza, V.; Garcia, E.; Garibay, C.F.; Olivares, L.Z.; Maldonado, L.A. Baeyer-Villiger Oxidation of *β*-Aryl Substituted Unsaturated Carbonyl Compounds with Hydrogen Peroxide and Catalytic Selenium Dioxide. *Synth. Commun.* **1995**, *25*, 2121–2133. [CrossRef]
39. Pang, Y.; An, B.; Lou, L.; Zhang, J.; Yan, J.; Huang, L.; Li, X.; Yin, S. Design, Synthesis, and Biological Evaluation of Novel Selenium- Containing Isocombretastatins and Phenstatins as Antitumor Agents. *J. Med. Chem.* **2017**, *60*, 7300–7314. [CrossRef]
40. Ma, W.; Huang, J.; Huang, X.; Meng, S.; Yang, Z.; Li, C.; Wang, Y.; Qi, T.; Li, B. Direct construction of 2,3-unsubstituted benzofurans and benzothiophenes via a metal-free catalyzed intramolecular Friedel-Crafts reaction. *Org. Chem. Front.* **2019**, *6*, 493–497. [CrossRef]
41. Liu, H.; Ge, L.; Wang, D.; Chen, N.; Feng, C. Photoredox-Coupled F-Nucleophilic Addition: Allylation of *gem*-Difluoroalkenes, *Angew. Chem. Int. Ed.* **2019**, *58*, 3918–3922. [CrossRef]
42. Song, S.-Y.; Lu, H.-L.; Wang, G.-F.; Yang, Y.-Q.; Huang, Y.-S. An improved and scale-up synthesis of 6-hydroxybenzofuran. *Res. Chem. Intermed.* **2016**, *42*, 4433–4442. [CrossRef]
43. Bunce, R.A.; Moore, J.D. Tetrahydropyranyloxy-Directed *ortho* Lithiation of Aromatic Systems. Synthesis of *o*-Hydroxycinnamate Esters from Phenols. *Org. Prep. Proc. Int.* **1997**, *29*, 293–299. [CrossRef]
44. Wriede, U.; Fernandez, M.; West, K.F.; Harcour, D.; Moore, H.W. Synthesis of Halodimethoxy-1,2-benzoquinones. *J. Org. Chem.* **1987**, *52*, 4485–4489. [CrossRef]
45. Ma, T.; Fu, X.; Kee, C.W.; Zong, L.; Pan, Y.; Huang, K.-W.; Tan, C.-H. Pentanidium-Catalyzed Enantioselective Phase-Transfer Conjugate Addition Reactions. *J. Am. Chem. Soc.* **2011**, *133*, 2828–2831. [CrossRef]
46. Mikami, S.; Kitamura, S.; Negoro, N.; Sasaki, S.; Suzuki, M.; Tsujihata, Y.; Miyazaki, T.; Ito, R.; Suzuki, N.; Miyazaki, J.; et al. Discovery of Phenylpropanoic Acid Derivatives Containing Polar Functionalities as Potent and Orally Bioavailable G Protein-Coupled Receptor 40 Agonists for the Treatment of Type 2 Diabetes. *J. Med. Chem.* **2012**, *53*, 3756–3776. [CrossRef]
47. Sayson, L.V.; Custodio, R.J.P.; Ortiz, D.M.; Lee, H.J.; Kim, M.; Jeong, Y.; Lee, Y.S.; Kim, H.J.; Cheong, J.H. The potential rewarding and reinforcing effects of the substituted benzofurans 2-EAPB and 5-EAPB in rodents. *Eur. J. Pharmacol.* **2020**, *885*, 173527. [CrossRef]
48. Sun, N.; Huang, P.; Wang, Y.; Mo, W.; Hu, B.; Shen, Z.; Hu, X. Zeolite-catalyzed synthesis of 2,3-unsubstituted benzo[b]furans via the intramolecular cyclization of 2-aryloxyacetaldehyde acetals. *Tetrahedron* **2015**, *71*, 4835–4841. [CrossRef]
49. Zaidlewicz, M.; Chechlowska, A.; Prewysz-Kwinto, A. Enantioselective Synthesis of 2- and 3-benzofuryl β-amino alcohols. *Heterocycles* **2001**, *55*, 569–577. [CrossRef]
50. Ando, K.; Kawamura, Y.; Akai, Y.; Kunitomo, J.I.; Yokomizo, T.; Yamashita, M.; Ohta, S.; Ohishi, T.; Ohishi, Y. Preparation of 2-, 3-, 4- and 7-(2-alkylcarbamoyl-1-alkylvinyl)benzo[*b*]furans and their BLT1 and/or BLT2 inhibitory activities. *Org. Biomol. Chem.* **2008**, *6*, 296–307. [CrossRef]
51. Missiroli, S.; Perrone, M.; Boncompagni, C.; Borghi, C.; Campagnaro, A.; Marchetti, F.; Anania, G.; Greco, P.; Fiorica, F.; Pinton, P.; et al. Targeting the NLRP3 inflamasome as a new therapeutic option for overcoming cancer. *Cancers* **2021**, *13*, 2297. [CrossRef]
52. Ying, W.; Cheruku, P.S.; Bazer, F.W.; Safe, S.H.; Zhou, B. Investigation of macrophage polarization using bone marrow derived macrophages. *J. Vis. Exp.* **2013**, *76*, 50323. [CrossRef]

International Journal of Molecular Sciences

MDPI

*Article*

# 1,3,8-Triazaspiro[4.5]decane derivatives avoid the binding with Glu$^{119}$ of Fo-ATP synthase c subunit to exert permeability transition pore inhibition safer than Oligomycin A

**Gaia Pedriali [1,#], Daniela Ramaccini [1,#], Esmaa Bouhamida [1], Alessio Branchini [2], Giulia Turrin [3], Elisabetta Tonet [4], Antonella Scala [4], Simone Patergnani [5], Mirko Pinotti [2], Claudio Trapella [3], Carlotta Giorgi [5], Elena Tremoli [1], Gianluca Campo [4,*], Giampaolo Morciano [1,5], Paolo Pinton [1,5,*]**

[1] Maria Cecilia Hospital, GVM Care and Research, Cotignola (RA), Italy.
[2] Department of Life Sciences and Biotechnology, University of Ferrara, Ferrara, Italy.
[3] Department of Chemical, Pharmaceutical and Agricultural Sciences, University of Ferrara, Ferrara, Italy.
[4] Cardiology Unit, Azienda Ospedaliero Universitaria di Ferrara, Cona (FE), Italy.
[5] Department of Medical Sciences, University of Ferrara, Ferrara, Italy.

[#] These authors equally contributed
[*] These authors share senior correspondence: paolo.pinton@unife.it; gianluca.campo@unife.it; Tel: 0532/455802

**Abstract:** Permeability transition pore (PTP) molecular composition and activity modulation have been subjects matter of research for several years, especially due to their importance in ischemia reperfusion injury (IRI). Of note, c subunit of ATP synthase (Csub) has been pointed out as one of the PTP-forming proteins and target for cardioprotection. Oligomycin A is a well-known Csub interactor that has been in depth chemically modified to propose new pharmacological approaches against cardiac reperfusion injury. Indeed, taking advantage from its scaffold and thanks to focused chemical improvements, innovative Csub-dependent PTP inhibitors (1,3,8-Triazaspiro[4.5]decane) have been synthetized. Interestingly, four critical amino acids have been found to be involved in Oligomycin A-Csub binding in yeast. However, their position on the human sequence was unknown, like their function in PTP inhibition. The aim of this study was to i) understand whether the amino acids involved in Oligomycin A-Csub binding play roles in PTP inhibition; ii) provide direct proofs about the interaction of 1,3,8-Triazaspiro[4.5]decane derivatives with human Csub, iii) understand the differences of binding of both Oligomycin A and 1,3,8-Triazaspiro[4.5]decane with Csub that might explain different cardioprotective properties. In summary, we identified the amino acids involved in the binding Oligomycin A-Csub complex on the human sequence, we demonstrated their role in Oligomycin A-dependent PTP inhibition and we identified Glu$^{119}$ as one of the critical amino acids by which 1,3,8-Triazaspiro[4.5]decane derivatives exert PTP modulation safer than Oligomycin A.

**Keywords:** Permeability transition pore; Oligomycin A; c subunit of Fo-ATP synthase; small-molecules; cardioprotection.

**Citation:** To be added by editorial staff during production.

Academic Editor: Firstname Lastname

Received: date
Revised: date
Accepted: date
Published: date



## 1. Introduction

The mitochondrial permeability transition (mPT) is an altered permeabilization of the inner mitochondrial membrane (IMM) to low-molecular weight solutes, which leads to mitochondrial swelling, failure of mitochondrial functions and cell death [1,2]. High intracellular calcium ($Ca^{2+}$) concentrations, oxidative stress and a dyshomeostasis of phosphates, adenine nucleotides and many other substances in the mitochondrial matrix [3], all together concur to this pathological condition. The mPT is an evolutionarily conserved

event from yeast to mammals and is caused by the opening of multiple channels in the IMM, called permeability transition pores (PTP), but that also involves the cooperation of the outer mitochondrial membrane (OMM) [4] and, likely, additional modulatory proteins [5]. Although the PTP flickering is recognized to be important in physiology [6–8], the PTP opening is currently considered a cellular catastrophe representing one critical pathway of cell death in multiple pathologies.

The most studied phenomenon in which PTP opening triggers extensive cell death and tissue function loss is the ischemia reperfusion injury (IRI) [9–12]. In ischemic environments, the PTP is blocked due to the high concentration of protons, or by the cellular acidification induced from glycolytic pathways being activated in the absence of oxygen [13]; otherwise, during reperfusion PTP opening is prompted by reactive oxygen species (ROS) generation, pH recovery and mitochondrial $Ca^{2+}$ accumulation.

Several efforts in the understanding this channel have shown many analogies between the regulation of the PTP opening process and some ATP synthase catalytic peculiarities [14–17]. In 2013, these functional similarities were confirmed also in an overlapping structural composition of both machineries. Indeed, c subunit of ATP synthase (Csub) has been identified as one of the proteins forming the pore of the PTP [18–20] and the dimers of ATP synthase, under pathological conditions previously described, might disassembly in monomers facilitating the formation of the pores [21].

Of note, Csub expression has been identified as strongly correlated to several endpoints of reperfusion damage in patients affected by ST-segment elevation myocardial infarction (STEMI) [22]. In addition, mutations in the genes encoding Csub have been found associated to worse clinical outcomes [23] and the absence of Csub would protect cells from PTP opening and cell death [24].

As consequence of these findings, Csub protein has been proposed as target for new pharmacological approaches against IRI [25–27]. To achieve this goal, one of the known Csub interactors named Oligomycin A [28–30], has been taken into consideration for further studies to develop new Csub-dependent PTP inhibitors. The studies led to a *de novo* synthesis of small-molecules inhibitors of Csub through multiple modifications of the Oligomycin A chemical structure. In detail, these compounds retained part of the Oligomycin A scaffold considered to be essential in ensuring Csub binding, and were capable to improve PTP inhibition with beneficial effects on the cardiac performance after IRI, but without known side effects that hampered the use of this macrolide for therapeutic purposes [25].

Although, multiple experimental evidences have been collected about the binding of these small-molecules with the target protein, the proofs provided were indirect [25,26]. In consideration of the fact that it is necessary to better understand at which extent Oligomycin A and Csub-derived inhibitors are able to interact with the protein for further modifications and therapeutic purposes in PTP inhibition, in this study we provide key insights into the binding between two derivatives of the 1,3,8-Triazaspiro[4.5]decane scaffold (named as PP11 and compound 10) and Csub, including protein variants bearing substitutions at residues predicted to be crucial for compound binding.

## 2. Results

### *2.1. Identification of human Csub residues crucial for Oligomycin A binding*

In 2012, the establishment of a high-resolution crystal structure of the Oligomycin A – Csub complex allowed the researchers to understand which amino acids are critical for Oligomycin A binding on yeast Csub protein (PDB: 4F4S, [31]) (Figure 1A). Among these amino acids, three ($Leu^{57}$, $Leu^{63}$ and $Phe^{64}$) resulted to have a great impact on direct interactions with Oligomycin A (Figure 1B) and a fourth amino acid ($Glu^{59}$) is involved in indirect but essential binding. Indeed, $Glu^{59}$ residue binds the macrolide through a hydrogen bond and to a molecule of water which also entails the binding with the carbonyl

group of Leu[57] [32,33] (Figure 1B). Moreover, these residues, when mutated, conferred resistance to Oligomycin A [31].

Despite the current knowledge, the aminoacidic sites forming interactions with Oligomycin A on the human Csub sequence are currently unknown. It is suggested that the amino acid residues that form the Oligomycin A binding site are 100% conserved between human and yeast [31], but yeast and human Csub sequences display a low similarity degree and a different total length (76 aa for yeast and 136 aa for human). Thus, it is necessary to identify the different positions that conserved Leu[57], Glu[59], Leu[63] and Phe[64] amino acids hold on the human sequence.

To this aim, yeast (PDB: 3UD0, residues 1 to 76) and human Csub protein sequences have been aligned by BLAST algorithm from ncbi [34]. Analysis of the alignment (Figure 1C) revealed a 63% degree of similarity, with the key residues in yeast (Leu[57], Glu[59], Leu[63] and Phe[64]) identified as Leu[117], Glu[119], Leu[123] and Phe[124] in the human sequence.

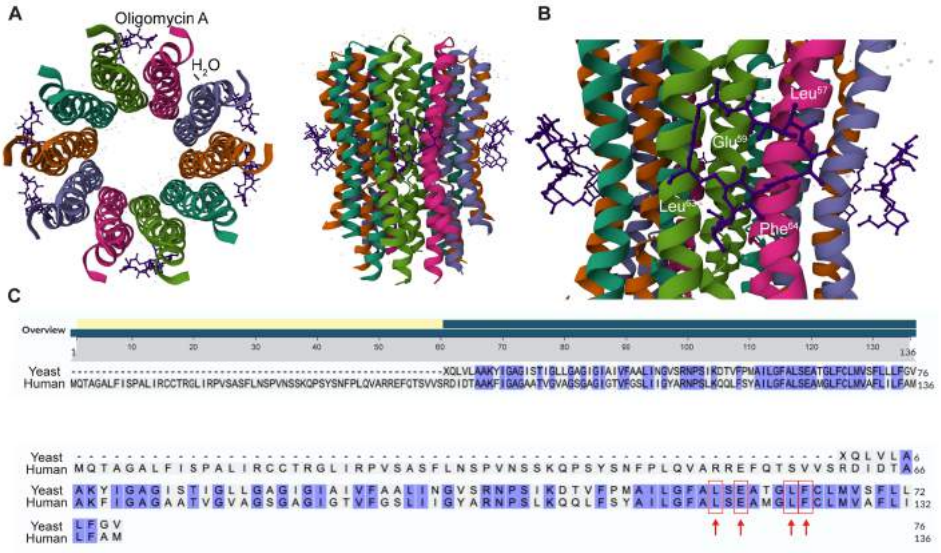


**Figure 1. Identification of conserved amino acids involved in Oligomycin A – Csub binding in human.** (**A**) High resolution crystal structure of Oligomycin A – C sub binding site in yeast (PDB: 4F4S); a top view on the left, a side view on the right. Molecules of Oligomycin A have been depicted in purple, $H_2O$ molecules in orange, Csub chains are colored with the "Chain Id" mode; (**B**) View of the Oligomycin A binding site on Csub of yeast. The residues involved in the binding are highlighted in white: Leu[57], Glu[59], Leu[63], Phe[64]; (**C**) Alignment of yeast Csub protein sequence with the human counterpart. All conserved amino acids were highlighted in blue, red arrows identified positive correspondence between the amino acids of interest and are found in human in the following positions: Leu[117], Glu[119], Leu[123] and Phe[124].

### *2.2. In vitro validation of the amino acids involved in Oligomycin A – Csub binding in Oligomycin A – mediated PTP inhibition.*

Besides a strong Fo-ATP synthase interactor, Oligomycin A is a known PTP inhibitor [35]. To assess the importance of Oligomycin A binding with Csub in PTP inhibition, we took advantage of an alanine scanning approach to mutate either the single Leu[117], Glu[119], Leu[123] and Phe[124] amino acids or all together to generate the mutant ATP5G1$^{4ALA}$, which are critical for the establishment of this binding.

First of all, we evaluated their expression and proper localization once transfected in human cardiac fibroblasts (HCF) cells. In Figure 2A, we show immunofluorescence of HCF transfected with the empty vector (pCMV6), the wild-type protein (ATP5G1$^{WT}$) or ATP5G1$^{L117A}$, ATP5G1$^{E119A}$, ATP5G1$^{L123A}$, ATP5G1$^{F124A}$ and ATP5G1$^{4ALA}$ mutants. In order to confirm their presence at mitochondrial level, we detected the signal of the mitochondrial marker ATP5A (in red) and the signal expressed by the FLAG-tag (in green), which

is present in all plasmids with exception of pCMV6. These data show that all single mutants are expressed in HCF cells and localized at mitochondrial level.

Then, in each of these experimental conditions, we evaluated PTP opening in living HCF to understand whether mutant overexpression can differently impact on PTP activity when compared to ATP5G1$^{WT}$ after 1 μM Ionomycin administration (Figure 2B). The Calcein-Cobalt quenching assay detected an increased opening of the PTP when ATP5G1$^{WT}$ is overexpressed and compared to pCMV6 ($p < 0.0001$). Moreover, the overexpression of each mutant, included ATP5G1$^{4ALA}$, impacts on PTP opening in a manner comparable to ATP5G1$^{WT}$, with no significant difference among conditions. These findings are in agreement with previous observations on increased PTP opening following ATP5G1$^{WT}$ overexpression, and also suggest that each mutation does not change the function of the wild-type form in terms of PTP activity (Figure 2B).

In order to understand whether Oligomycin A retains its inhibitory activities against PTP when Csub is mutated in the crucial binding pocket, the Calcein-Cobalt quenching assay has been performed in HCF expressing ATP5G1$^{WT}$, ATP5G1$^{L117A}$, ATP5G1$^{E119A}$, ATP5G1$^{L123A}$ and ATP5G1$^{F124A}$. Experimental conditions were subdivided in either vehicle or 30 min 10 μM Oligomycin A pre-treatment and the kinetics of the PTP evaluated. Firstly, we observed that Oligomycin A pre-treatment is able to inhibit PTP opening both in basal condition ($p < 0.0001$, Figure S1A) and upon ATP5G1$^{WT}$ overexpression ($p < 0.001$, Figure 2C). Interestingly, Oligomycin A failed to exert PTP inhibition when each Csub mutant is expressed. Indeed, we found no statistical differences between PTP activity in cells overexpressing mutants with or without Oligomycin A pre-treatment. All together these findings confirm the key role of these amino acids in Csub-dependent PTP inhibition exerted by the macrolide. ATP5G14$^{ALA}$ expressing cells have not been tested at this stage, for Oligomycin A efficiency, due to results expected to be overlapping to those obtained with single mutants.

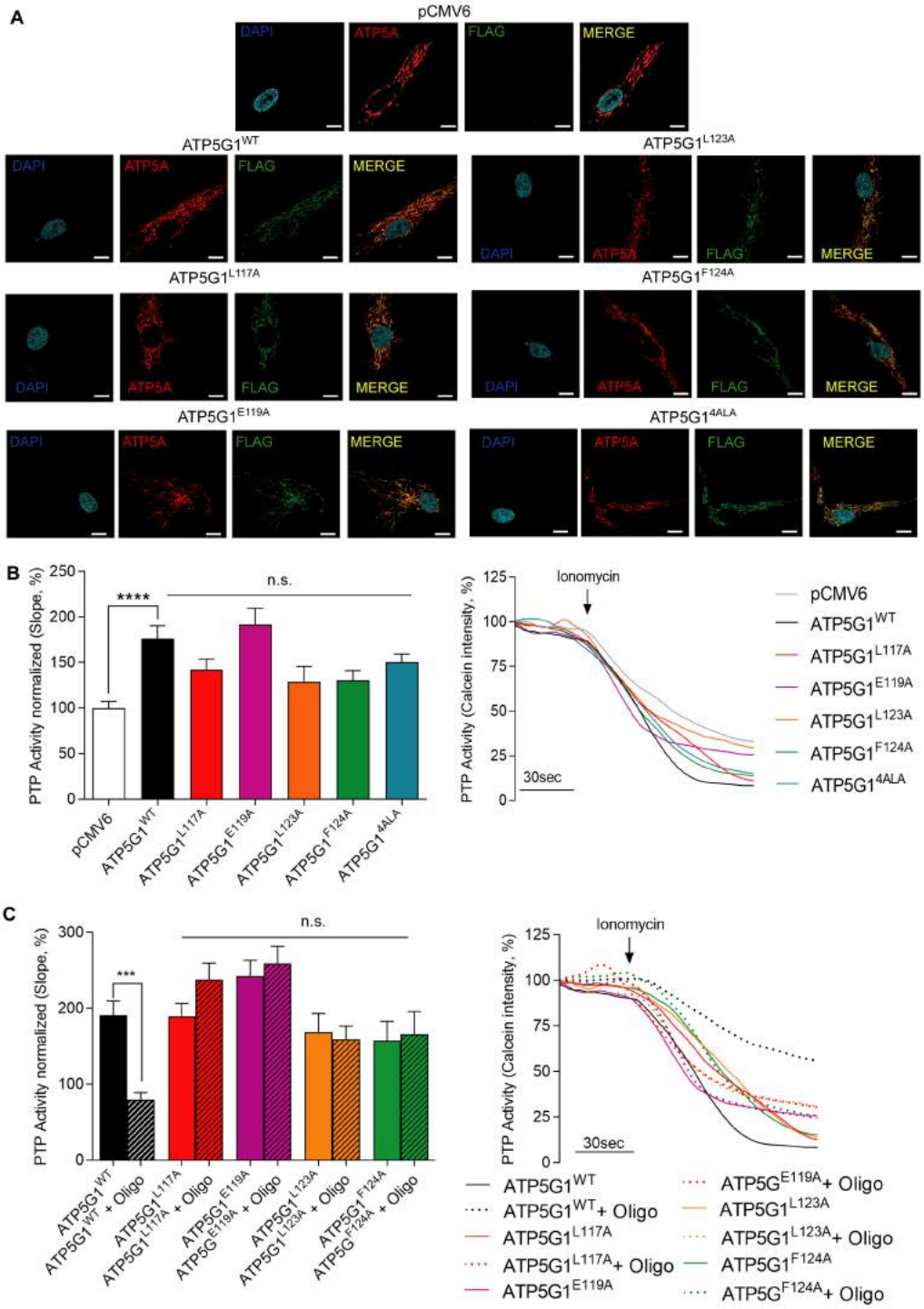


**Figure 2. Functional analysis of Oligomycin A-Csub binding in PTP inhibition in primary human cardiac fibroblasts**. (**A**) Immunofluorescence assay for mitochondrial localization of mutants. FLAG-tag (green), ATP5A as mitochondrial marker (red), nuclei (blue, DAPI), Scale bar in white 10 μm; (**B**) PTP activity measurement when mutants are expressed in HCF and compared to pCMV6 and ATP5G1$^{WT}$. On the left, statistic of PTP activity; on the right, representative kinetics; (**C**) PTP activity measurement when mutants are expressed in HCF with or without Oligomycin A pre-treatment (10 μM, 30 min). On the left, statistic of PTP activity; on the right, representative kinetics. Graphs show mean ± SEM. Statistics differences were analyzed using one-way ANOVA: **** $p < 0.0001$, *** $p < 0.001$.

*2.3. Leu$^{117}$ and Leu$^{123}$ residues are essential for the binding of PP11 to Csub.*

In order to understand whether 1,3,8-Triazaspiro[4.5]decane – based small-molecules, as Oligomycin A derivatives, inhibit PTP opening taking advantage of the same Oligomycin A chemical core, we firstly investigated the functional impact of PP11 in cells expressing each mutant. Thus, HCF cells were transfected with ATP5G1$^{WT}$, ATP5G1$^{L117A}$, ATP5G1$^{E119A}$, ATP5G1$^{L123A}$ or ATP5G1$^{F124A}$ constructs and pre-treated either with the vehicle or with 5 μM PP11 compound. Through the Calcein-Cobalt quenching assay, we firstly confirmed that PP11 inhibits PTP opening in basal condition ($p < 0.01$, Figure S1B) and after ATP5G1$^{WT}$ overexpression (Figure 3A). Interestingly, when ATP5G1$^{L117A}$ and ATP5G1$^{L123A}$ are the main isoforms expressed in cells, PP11 failed to inhibit PTP opening, suggesting that these amino acids, in their conserved form, are essential for the binding of PP11 and for PTP inhibition. These data are in agreement with those obtained with Oligomycin A. Despite not statistically significant, we found a decreasing trend in PTP activity after the use of PP11 in cells expressing ATP5G1$^{L117A}$, indicating that the inhibitory effect of this compound was not completely suppressed and that this amino acid might be less important for Csub binding compared to Leu$^{123}$ (Figure 3A).

Of interest, and differently from Oligomycin A, PP11 in HCF expressing ATP5G1$^{E119A}$ continues to exert PTP inhibition. This finding suggests that Glu$^{119}$ is not essential for PP11 binding to Csub and PTP inhibition.

The different data obtained with PP11 molecule pre-treatment suggest that probably the aromatic moiety in position 1 of the spirocyclic structure could interact with Leu$^{123}$ and the toluyl portion of the sulphonyl amide in position 8 could interact with Leu$^{117}$. Furthermore, this arrangement in the space permits to the sulfoxide moiety to disrupt the water molecule binding to Glu$^{119}$, avoiding the blockage of this amino acid that plays a key role in proton translocation, and so in the ATP synthase activity. This evidence may also explain the fact that, as previously proven by our team, treatment with Oligomycin A appears to irreversibly block ATP synthase activity and is therefore toxic to cells, unlike our newly designed compounds.

On the contrary, when ATP5G1$^{F124A}$ is expressed, PP11 pre-treatment triggered an abrupt increase in PTP opening, suggesting a side effect of the expression of this mutation only in the presence of the compound (Figure 3A). The possibility to install a binding between the hydrogen of the lactame ring in position 3 with the py elecrons of Phe$^{124}$ stabilize the conformational structure of the 1,3,8-Triazaspiro[4.5]decane scaffold. However, once the Phe is replaced by Ala, this interaction will be lost and probably the entire structure will change its shape, causing the activation of PTP.

*2.4. Leu$^{117}$, Leu$^{123}$ and Phe$^{124}$ amino acids are essential for the binding of compound 10 to Csub.*

In a similar way, the behavior of C.10 has been evaluated in Figure 3B. Firstly, we confirmed that 5 μM C.10 pre-treatment in HCF inhibited PTP opening both in resting conditions, as expected ($p < 0.0001$, Figure S1C), and in cells overexpressing ATP5G1$^{WT}$, ($p < 0.001$, Figure 3B). Cells overexpressing ATP5G1$^{L117A}$, ATP5G1$^{L123A}$ and ATP5G1$^{F124A}$ are not susceptible to the inhibition exerted by C.10, suggesting a key role of these amino acids for C.10-Csub binding complex in PTP modulation. Nevertheless, C.10 pre-treatment on ATP5G1$^{F124A}$ mutation induced a decrease in PTP activity by 36% compared to the untreated condition. Even if this effect was not statistically significant, we might envision that Phe$^{124}$ is less essential than ATP5G1$^{L117A}$ and ATP5G1$^{L123A}$.

Moreover, unlike Oligomycin A but in line with PP11 results, pre-treatment with C.10 in cells expressing ATP5G1$^{E119A}$ as main isoform, significantly inhibited PTP opening when compared to untreated cells ($p < 0.0001$). This finding suggests that, probably, Glu$^{119}$ is not involved in C.10 binding as well as PP11 (Figure 3B).

In support of these data, in a condition in which all four single residues were mutated and localized to mitochondria (Figure 2A), C.10 and PP11 pre-treatment are inefficient in the inhibition of PTP (Figure 3C).

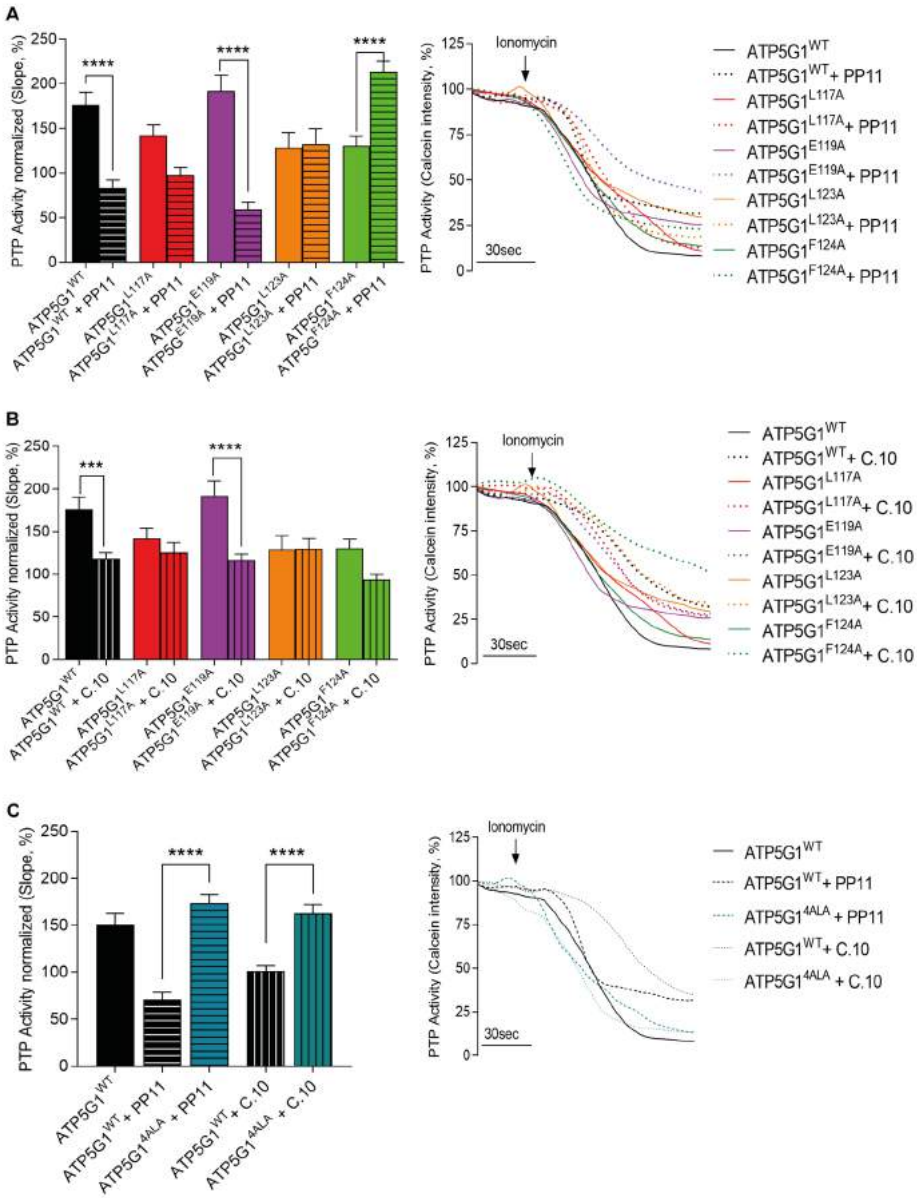


**Figure 3. Test of small-molecules Csub inhibitors binding of amino acids of interest.** (**a**) PTP activity measurement in condition of mutants overexpression with PP11 pre-treatment (5 μM, 15 min). On the left, PTP activity; on the right, representative traces of PTP activity; (**b**) PTP activity measurement in condition of mutants overexpression with C.10 pre-treatment (5 μM, 15 min). On the left, PTP activity; on the right, representative traces of PTP activity; (**c**) PTP activity measurement in condition of ATP5G1$^{4ALA}$ mutant overexpression pre-treated with both PP11 and C.10 and compared with ATP5G1$^{WT}$. On the left, PTP activity; on the right, representative traces of PTP activity. Graphs show mean ± SEM. Statistics differences were analyzed using one-way ANOVA: **** $p < 0.0001$, *** $p < 0.001$, ** $p < 0.01$.

## 3. Discussion

The complex interaction between Fo-ATP synthase and Oligomycin A has attracted considerable interest in multiple fields of research worldwide: as antiproliferative agent in cancer [36–38], as potent antimicrobial in infectious diseases [39], in the investigation of mitochondrial features and metabolomics studies, lately as PTP inhibitor to counteract cell death in cardiovascular diseases [28–30]. Thus, the scaffold of Oligomycin A, and how

it interacts with the target, is of great interest in pharmacology [39,40]. However, because of its side effects on healthy cells, the use in therapy in its native form was always postponed.

There are about ten different and 100% conserved amino acids involved in the binding between Csub and the macrolide [31]; among these, three resulted to have key roles on direct interactions established with Oligomycin A ($Leu^{57}$, $Leu^{63}$ and $Phe^{64}$) and a fourth amino acid, Glu59, would form an indirect but essential binding through a hydrogen bond of a molecule of water acting as a bridge [33]. Of note, when mutated they conferred resistance against Oligomycin A action.

For these reasons and given our interest in human cardiac diseases, we chose to mutagenize in alanine those residues matching with the human sequence of Csub (i.e., $Leu^{117}$, $Glu^{119}$, $Leu^{123}$ and $Phe^{124}$), to understand whether they can be also involved in Oligomycin A – dependent PTP inhibition. The choice of cardiac fibroblasts as cell model allows us to investigate this topic in a cardiac environment [41,42], but with a minimal contribution of endogenous Csub expression. Indeed, being fibroblasts a non-contractile tissue, thus requiring less ATP production compared to cardiomyocytes, they express lower levels of Csub (Figure S1D). Moreover, they also express lower levels of Csub compared to other tissues representing the cardiac district (Figure S1D).

In this context, the overexpression of the single $ATP5G1^{L117A}$, $ATP5G1^{E119A}$, $ATP5G1^{L123A}$ or $ATP5G1^{F124A}$ mutants in HCF cells allowed us to monitor a clear functional effect on PTP activity, which was not different from $ATP5G1^{WT}$ – induced PTP sensibilization but crucial for Oligomycin A binding. Indeed, Oligomycin A was able to inhibit PTP opening in cells overexpressing $ATP5G1^{WT}$, but it loses the modulatory effect when each site become mutated. This is a key finding further supporting the key role of Csub in the structure of the PTP.

A second investigation was aimed to provide more direct evidence on the suggested binding between new cardioprotective small-molecules PTP inhibitors and Csub [25,26]. In 2018, we have conceived and synthetized several classes of PTP inhibitors taking advantage from the minimal chemical structure of Oligomycin A required for the binding with Csub. This constituted another important point for the rationale about Csub mutagenesis. Small-molecules were further modified in order to propose new therapeutic strategies against reperfusion damage, targeting Csub without Oligomycin A side effects like ATP depletion [25]. We showed the exclusive localization of PP11 and C.10 at mitochondrial level or the putative site of action, the thermal stabilization of Csub protein at increasing concentrations of the inhibitors and the great potential in PTP inhibition and recovery from reperfusion damage [25].

In this study we provided evidence for a similar binding of both PP11 and C.10 compared to Oligomycin A which mainly involves three out of four amino acids: $Leu^{117}$, $Leu^{123}$ and $Phe^{124}$, even if the last one at a lesser extent. This finding was almost expected being Oligomycin A their derivative. However, we also expected to see some differences in that binding which could in part explain the absence of toxic effects of PP11 and C.10 on main mitochondrial and cellular parameters when compared to Oligomycin A [25]. Based on the data of this study, the answer could be found in the glutamic acid at position 119 which would not be essential for PTP inhibition for PP11 and C.10. Indeed, when mutated, both compounds continue to inhibit PTP opening through the putative binding with the other non-mutated essential residues. This observation has great repercussion as the absence of a crucial functional binding with $Glu^{119}$, an amino acid postulated to be involved directly in the movement of protons during ATP synthesis and that can interfere with this pathway during $F_O$ targeting, can avoid the side effects that are instead associated with Oligomycin A.

## 4. Materials and Methods

### *4.1. Cell culture*

Human cardiac fibroblasts (HCF) were provided by Innoprot (P10452) and used according to the manufacturer's instructions, cultured in Fibroblast Medium-2 containing fetal bovine serum, fibroblast growth supplement-2, and penicillin and streptomycin (Innoprot, P60108-2). All the experiments were performed at the same passages (p3-p8).

### *4.2. Transfection*

HCF were transfected with Lipofectamine™ LTX Reagent with PLUS™ Reagent (Thermo Fisher Scientific, A12621) according to the manufacturer's instructions.

Expression vectors were created by site-directed mutagenesis [43] of the human ATP5G1 coding sequence, cloned into the pCMV6-Entry plasmid, by using the QuickChange II Site-Directed Mutagenesis Kit (Agilent Technologies, USA). The forward oligonucleotides CTTGGCTTTGCC*GC*GTCTGAGGCCATG (ATP5G1$^{L117A}$), CTTTGCCCTGTCTG*C*GGCCATGGGGCTTTTC (ATP5G1$^{E119A}$), GAGGCCATGGGG*GCT*TTC TGTTTGATG (ATP5G1$^{L123A}$), and GCCATGGGGCTT*GC*CTGTTTGATGGTC (ATP5G1$^{F119A}$) were used to introduce substitutions to alanine and obtain single or double mutants. The modified nucleotides (underlined) and missense triplets (italics) are indicated. Reverse oligonucleotides were complementary to the forward ones. All plasmids have been validated by sequencing.

### *4.3. Immunofluorescence*

HCF were transfected with the empty vector (pCMV6), wild-type Csub (ATP5G1$^{WT}$) or the Csub mutants according the previous protocol. Then, cells were fixed with 4% paraformaldehyde (PFA) in phosphate-buffered saline (PBS), 15min at room temperature and permeabilized with 0.1% Triton in PBS for 15 min. After blocking with 2% bovine serum albumin (BSA) in PBS-Triton for 1 h, cells were incubated with primary antibody of appropriate dilutions for 1 h at +4°C. The primary antibody used were Anti-ATP5A antibody [15H4C4] (Abcam, ab14748) for mitochondria and ANTI-Flag® (F7425, Merck) for c-subunit mutants. After washing 2 times with PBS-Triton, cells were stained with corresponding secondary antibody in BSA 2% at dark. The secondary antibody used were Goat anti-Mouse IgG (H+L) Highly Cross-Adsorbed Secondary Antibody, Alexa Fluor 647 (Thermo Fisher Scientific, A-21236) and Goat anti-Rabbit IgG (H+L) Cross-Adsorbed Secondary Antibody, Alexa Fluor 488 (Thermo Fisher Scientific, A-11008). Cells were again washed 3 times with PBS-Triton before been mounted with the mounting buffer with 4,6-diamidino-2-phenylindole (DAPI) (Sigma-Aldrich, DUO82040).

High-resolution images of cells were recorded by using FV3000 Olympus confocal laser scanning microscopy, 60x objective lens (Plan-Fluor 60x/Oil, Zeiss, image size: 1024 × 1024). Acquired images were then analyzed by using open-source software ImageJ https://imagej.nih.gov/ij.

### *4.4. Western blot*

For immunoblotting, cells were lysed in RIPA Lysis and Extraction Buffer (Thermo Fisher Scientific, 89900), then quantified by the Lowry method and 10 μg of proteins were loaded on a 4–20% precast gel. After electrophoretic separation, proteins were transferred onto nitrocellulose membranes that were incubated overnight with primary antibodies as Anti-β-Actin (1:5000, Sigma-Aldrich, A1978) and ANTI-Csub (1:1000, ab181243, Abcam). The revelation was assessed by specific HRP-labelled secondary antibodies, followed by detection by chemiluminescence using ChemiDoc™ Touch Gel Imaging System. Western blots shown in figures are representative of at least three different independent experiments.

For cardiac cell lines lysates: Human Aortic Endothelial Cells (HAEC) were provided by Thermo-Fisher (C0065C) and cultured according to the manufacturer's instructions; AC16 Human Cardiomyocyte Cell Line were provided by Merck (SCC109) and cultured

according to the manifacturer's instructions; Human Cardiac Myocytes (HCM) were provided by Promocell (FB60C12810) and cultured according to the manufacturer's instructions.

### *4.5. Calcein–Cobalt Assay*

HCF cells were pretreated with Ethanol (vehicle) or 10 μM of Oligomycin A (Sigma-Aldrich, O4876) for 30 minutes, or with DMSO (vehicle), 5 μM of PP11 or 5 μM of IB13 for 15 minutes and then loaded with calcein acetoxymethyl ester and Co2+ as previously described [44]. Staining solution was added to the cells for 15 min at 37 °C in a 5% CO2 atmosphere. Image acquisitions were performed with a motorized Nikon AX R confocal microscope with a 40X/0.6 PlanApo objective and laser LU-N4S 405/488/561/640. Ionomycin (1 μM) was administered 30 sec after the beginning of the experiment to induce PTP opening. Each graphs shows the PTP activity expressed as percentage of the slope of each condition, normalized on the slope of control cells (pCMV6 transfected). Data are representative of at least three independent experiments. Graphs show mean ± SEM.

### *4.6. Statistical Analysis.*

One-way ANOVA with multiple comparisons has been performed by GraphPad Prism for all experiments. P values are reported in the figure legends.

**Supplementary Materials:** Figure S1. C-subunit protein levels and PTP activity inhibition with different compounds.

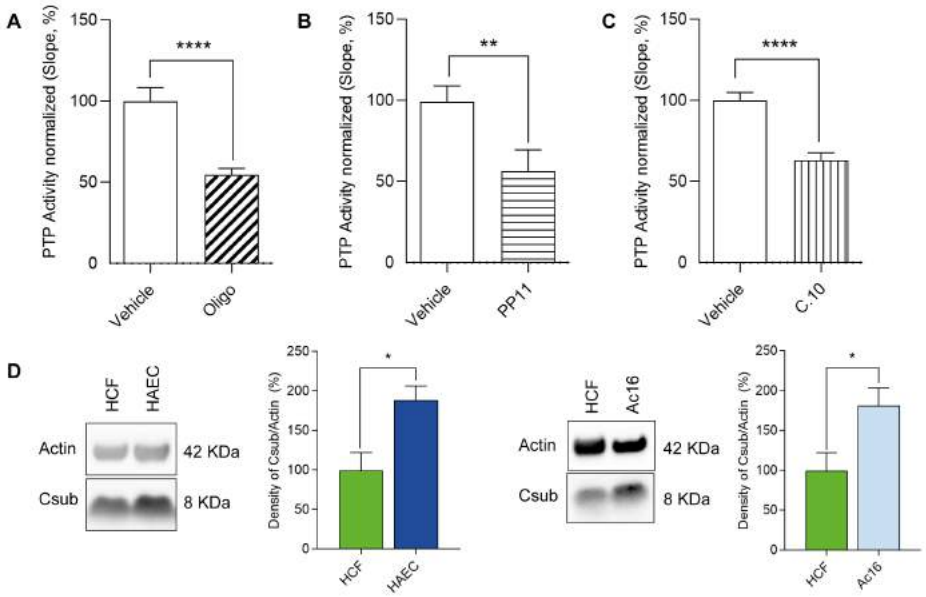


**Figure S1.** C-subunit protein levels and test of PTP activity inhibition with different compounds. (A) PTP activity measurement in non-transfected HCF with vehicle or Oligomycin pre-treatment (10 μM, 30 min). (B) PTP activity measurement in non-transfected HCF with vehicle or PP11 pre-treatment (5 μM, 15 min). (C) PTP activity measurement in non-transfected HCF with vehicle or C.10 pre-treatment (5 μM, 15 min). (D) Representative images of western blot showing Csub protein levels in different cardiac cell lines (HAEC on the left and Ac16 on the right) compared to HCF. Each graph shows the measurement of the signal emitted by Csub protein band normalized on Actin signal in each cardiac cell line. The data are expressed as percentage compared to the Csub/Actin signal of HCF. Statistics differences were analyzed using unpaired t test: **** $p < 0.0001$, ** $p < 0.01$, * $p < 0.05$. Data are representative of at least three independent experiments. Graphs show mean ± SEM.

**Author Contributions:** Conceptualization, G.M., P.P.; validation, P.P., G.M., C.T., G.T.; investigation, G.P., D.R., E.B., A.B.; writing—original draft preparation, G.M., G.P., D.R.; writing—review and editing, G.M., G.P., D.R., P.P, C.G., C.T.; supervision, G.M., P.P., C.G., G.C., M.P., E.T.; funding acquisition, P.P., C.G., G.M. All authors have read and agreed to the published version of the manuscript.

**Funding:** The Signal Transduction Laboratory is supported by the Italian Association for Cancer Research grants IG-23670 (to P.P.) and IG-19803 (to C.G.), A-ROSE (Associazione Ricerca Oncologica Sperimentale Estense); Progetti di Rilevante Interesse Nazionale grants PRIN2017E5L5P3 (to P.P.) and PRIN20177E9EPY (to C.G.); Italian Ministry of Health grants GR-2018-12367114 (to G.C. and G.M.) and GR-2019-12369862 (to G.M.); European Research Council grant 853057-InflaPML (to C.G.); local funds from the University of Ferrara (to P.P. and C.G.).

**Acknowledgments:** P.P. is grateful to Camilla degli Scrovegni for continuous support

**Conflicts of Interest:** The authors declare no conflict of interest.

## References

1. Morciano, G.; Naumova, N.; Koprowski, P.; Valente, S.; Sardão, V.A.; Potes, Y.; Rimessi, A.; Wieckowski, M.R.; Oliveira, P.J. The mitochondrial permeability transition pore: an evolving concept critical for cell life and death. *Biol. Rev. Camb. Philos. Soc.* **2021**, *96*, 2489–2521, doi:10.1111/brv.12764.
2. Bonora, M.; Giorgi, C.; Pinton, P. Molecular mechanisms and consequences of mitochondrial permeability transition. *Nat. Rev. Mol. Cell Biol.* **2022**, *23*, 266–285, doi:10.1038/s41580-021-00433-y.
3. Halestrap, A.P. What is the mitochondrial permeability transition pore? *J. Mol. Cell. Cardiol.* **2009**, *46*, 821–31, doi:10.1016/j.yjmcc.2009.02.021.
4. Crompton, M.; Costi, A.; Hayat, L. Evidence for the presence of a reversible Ca2+-dependent pore activated by oxidative stress in heart mitochondria. *Biochem. J.* **1987**, *245*, 915–8, doi:10.1042/bj2450915.
5. Elrod, J.W.; Molkentin, J.D. Physiologic functions of cyclophilin D and the mitochondrial permeability transition pore. *Circ. J.* **2013**, *77*, 1111–22, doi:10.1253/circj.cj-13-0321.
6. Korge, P.; Yang, L.; Yang, J.-H.; Wang, Y.; Qu, Z.; Weiss, J.N. Protective role of transient pore openings in calcium handling by cardiac mitochondria. *J. Biol. Chem.* **2011**, *286*, 34851–7, doi:10.1074/jbc.M111.239921.
7. Mnatsakanyan, N.; Beutner, G.; Porter, G.A.; Alavian, K.N.; Jonas, E.A. Physiological roles of the mitochondrial permeability transition pore. *J. Bioenerg. Biomembr.* **2017**, *49*, 13–25, doi:10.1007/s10863-016-9652-1.
8. Hom, J.R.; Quintanilla, R.A.; Hoffman, D.L.; de Mesy Bentley, K.L.; Molkentin, J.D.; Sheu, S.-S.; Porter, G.A. The permeability transition pore controls cardiac mitochondrial maturation and myocyte differentiation. *Dev. Cell* **2011**, *21*, 469–78, doi:10.1016/j.devcel.2011.08.008.
9. Morciano, G.; Giorgi, C.; Bonora, M.; Punzetti, S.; Pavasini, R.; Wieckowski, M.R.; Campo, G.; Pinton, P. Molecular identity of the mitochondrial permeability transition pore and its role in ischemia-reperfusion injury. *J. Mol. Cell. Cardiol.* **2015**, *78*, 142–53, doi:10.1016/j.yjmcc.2014.08.015.
10. Di Lisa, F.; Menabò, R.; Canton, M.; Barile, M.; Bernardi, P. Opening of the mitochondrial permeability transition pore causes depletion of mitochondrial and cytosolic NAD+ and is a causative event in the death of myocytes in postischemic reperfusion of the heart. *J. Biol. Chem.* **2001**, *276*, 2571–5, doi:10.1074/jbc.M006825200.
11. González-Montero, J.; Brito, R.; Gajardo, A.I.; Rodrigo, R. Myocardial reperfusion injury and oxidative stress: Therapeutic opportunities. *World J. Cardiol.* **2018**, *10*, 74–86, doi:10.4330/wjc.v10.i9.74.
12. Pedriali, G.; Ramaccini, D.; Bouhamida, E.; Wieckowski, M.R.; Giorgi, C.; Tremoli, E.; Pinton, P. Perspectives on mitochondrial relevance in cardiac ischemia/reperfusion injury. *Front. cell Dev. Biol.* **2022**, *10*, 1082095, doi:10.3389/fcell.2022.1082095.
13. Ong, S.-B.; Samangouei, P.; Kalkhoran, S.B.; Hausenloy, D.J. The mitochondrial permeability transition pore and its role in

myocardial ischemia reperfusion injury. *J. Mol. Cell. Cardiol.* **2015**, *78*, 23–34, doi:10.1016/j.yjmcc.2014.11.005.

14. Feniouk, B.A.; Suzuki, T.; Yoshida, M. The role of subunit epsilon in the catalysis and regulation of FOF1-ATP synthase. *Biochim. Biophys. Acta* **2006**, *1757*, 326–38, doi:10.1016/j.bbabio.2006.03.022.
15. Ko, Y.H.; Delannoy, M.; Hullihen, J.; Chiu, W.; Pedersen, P.L. Mitochondrial ATP synthasome. Cristae-enriched membranes and a multiwell detergent screening assay yield dispersed single complexes containing the ATP synthase and carriers for Pi and ADP/ATP. *J. Biol. Chem.* **2003**, *278*, 12305–9, doi:10.1074/jbc.C200703200.
16. Giorgio, V.; Bisetto, E.; Soriano, M.E.; Dabbeni-Sala, F.; Basso, E.; Petronilli, V.; Forte, M.A.; Bernardi, P.; Lippe, G. Cyclophilin D modulates mitochondrial F0F1-ATP synthase by interacting with the lateral stalk of the complex. *J. Biol. Chem.* **2009**, *284*, 33982–8, doi:10.1074/jbc.M109.020115.
17. Carraro, M.; Jones, K.; Sartori, G.; Schiavone, M.; Antonucci, S.; Kucharczyk, R.; di Rago, J.-P.; Franchin, C.; Arrigoni, G.; Forte, M.; et al. The Unique Cysteine of F-ATP Synthase OSCP Subunit Participates in Modulation of the Permeability Transition Pore. *Cell Rep.* **2020**, *32*, 108095, doi:10.1016/j.celrep.2020.108095.
18. Bonora, M.; Bononi, A.; De Marchi, E.; Giorgi, C.; Lebiedzinska, M.; Marchi, S.; Patergnani, S.; Rimessi, A.; Suski, J.M.; Wojtala, A.; et al. Role of the c subunit of the FO ATP synthase in mitochondrial permeability transition. *Cell Cycle* **2013**, *12*, 674–83, doi:10.4161/cc.23599.
19. Alavian, K.N.; Beutner, G.; Lazrove, E.; Sacchetti, S.; Park, H.-A.; Licznerski, P.; Li, H.; Nabili, P.; Hockensmith, K.; Graham, M.; et al. An uncoupling channel within the c-subunit ring of the F1FO ATP synthase is the mitochondrial permeability transition pore. *Proc. Natl. Acad. Sci. U. S. A.* **2014**, *111*, 10580–5, doi:10.1073/pnas.1401591111.
20. Elustondo, P.A.; Nichols, M.; Negoda, A.; Thirumaran, A.; Zakharian, E.; Robertson, G.S.; Pavlov, E. V Mitochondrial permeability transition pore induction is linked to formation of the complex of ATPase C-subunit, polyhydroxybutyrate and inorganic polyphosphate. *Cell death Discov.* **2016**, *2*, 16070, doi:10.1038/cddiscovery.2016.70.
21. Bonora, M.; Morganti, C.; Morciano, G.; Pedriali, G.; Lebiedzinska-Arciszewska, M.; Aquila, G.; Giorgi, C.; Rizzo, P.; Campo, G.; Ferrari, R.; et al. Mitochondrial permeability transition involves dissociation of F 1 F O ATP synthase dimers and C-ring conformation. *EMBO Rep.* **2017**, *18*, 1077–1089, doi:10.15252/embr.201643602.
22. Campo, G.; Morciano, G.; Pavasini, R.; Bonora, M.; Sbano, L.; Biscaglia, S.; Bovolenta, M.; Pinotti, M.; Punzetti, S.; Rizzo, P.; et al. Fo ATP synthase C subunit serum levels in patients with ST-segment Elevation Myocardial Infarction: Preliminary findings. *Int. J. Cardiol.* **2016**, *221*, 993–7, doi:10.1016/j.ijcard.2016.07.125.
23. Morciano, G.; Pedriali, G.; Bonora, M.; Pavasini, R.; Mikus, E.; Calvi, S.; Bovolenta, M.; Lebiedzinska-Arciszewska, M.; Pinotti, M.; Albertini, A.; et al. A naturally occurring mutation in ATP synthase subunit c is associated with increased damage following hypoxia/reoxygenation in STEMI patients. *Cell Rep.* **2021**, *35*, 108983, doi:10.1016/j.celrep.2021.108983.
24. Neginskaya, M.A.; Solesio, M.E.; Berezhnaya, E. V; Amodeo, G.F.; Mnatsakanyan, N.; Jonas, E.A.; Pavlov, E. V ATP Synthase C-Subunit-Deficient Mitochondria Have a Small Cyclosporine A-Sensitive Channel, but Lack the Permeability Transition Pore. *Cell Rep.* **2019**, *26*, 11-17.e2, doi:10.1016/j.celrep.2018.12.033.
25. Morciano, G.; Preti, D.; Pedriali, G.; Aquila, G.; Missiroli, S.; Fantinati, A.; Caroccia, N.; Pacifico, S.; Bonora, M.; Talarico, A.; et al. Discovery of Novel 1,3,8-Triazaspiro[4.5]decane Derivatives That Target the c Subunit of F1/FO-Adenosine Triphosphate (ATP) Synthase for the Treatment of Reperfusion Damage in Myocardial Infarction. *J. Med. Chem.* **2018**, *61*, 7131–7143, doi:10.1021/acs.jmedchem.8b00278.
26. Fantinati, A.; Morciano, G.; Turrin, G.; Pedriali, G.; Pacifico, S.; Preti, D.; Albanese, V.; Illuminati, D.; Cristofori, V.; Giorgi, C.; et al. Identification of small-molecule urea derivatives as PTPC modulators targeting the c subunit of F1/Fo-ATP synthase. *Bioorg. Med. Chem. Lett.* **2022**, *72*, 128822, doi:10.1016/j.bmcl.2022.128822.
27. Nesci, S.; Trombetti, F.; Ventrella, V.; Pagliarani, A. The c-Ring of the F1FO-ATP Synthase: Facts and Perspectives. *J. Membr. Biol.* **2016**, *249*, 11–21, doi:10.1007/s00232-015-9860-3.

28. LARDY, H.A.; JOHNSON, D.; McMURRAY, W.C. Antibiotics as tools for metabolic studies. I. A survey of toxic antibiotics in respiratory, phosphorylative and glycolytic systems. *Arch. Biochem. Biophys.* **1958**, *78*, 587–97, doi:10.1016/0003-9861(58)90383-7.
29. Zhu, Y.; Xu, H.; Huang, K. Mitochondrial permeability transition and cytochrome c release induced by selenite. *J. Inorg. Biochem.* **2002**, *90*, 43–50, doi:10.1016/s0162-0134(02)00407-5.
30. Chávez, E.; Rodríguez, J.S.; García, G.; García, N.; Correa, F. Oligomycin strengthens the effect of cyclosporin A on mitochondrial permeability transition by inducing phosphate uptake. *Cell Biol. Int.* **2005**, *29*, 551–8, doi:10.1016/j.cellbi.2005.03.009.
31. Symersky, J.; Osowski, D.; Walters, D.E.; Mueller, D.M. Oligomycin frames a common drug-binding site in the ATP synthase. *Proc. Natl. Acad. Sci. U. S. A.* **2012**, *109*, 13961–5, doi:10.1073/pnas.1207912109.
32. Sebald, W.; Wachter, E.; Tzagoloff, A. Identification of amino acid substitutions in the dicyclohexylcarbodiimide-binding subunit of the mitochondrial ATPase complex from oligomycin-resistant mutants of Saccharomyces cerevisiae. *Eur. J. Biochem.* **1979**, *100*, 599–607, doi:10.1111/j.1432-1033.1979.tb04207.x.
33. Symersky, J.; Pagadala, V.; Osowski, D.; Krah, A.; Meier, T.; Faraldo-Gómez, J.D.; Mueller, D.M. Structure of the c(10) ring of the yeast mitochondrial ATP synthase in the open conformation. *Nat. Struct. Mol. Biol.* **2012**, *19*, 485–91, S1, doi:10.1038/nsmb.2284.
34. Altschul, S.F.; Wootton, J.C.; Gertz, E.M.; Agarwala, R.; Morgulis, A.; Schäffer, A.A.; Yu, Y.-K. Protein database searches using compositionally adjusted substitution matrices. *FEBS J.* **2005**, *272*, 5101–9, doi:10.1111/j.1742-4658.2005.04945.x.
35. Mnatsakanyan, N.; Llaguno, M.C.; Yang, Y.; Yan, Y.; Weber, J.; Sigworth, F.J.; Jonas, E.A. A mitochondrial megachannel resides in monomeric F1FO ATP synthase. *Nat. Commun.* **2019**, *10*, 5823, doi:10.1038/s41467-019-13766-2.
36. Salomon, A.R.; Voehringer, D.W.; Herzenberg, L.A.; Khosla, C. Apoptolidin, a selective cytotoxic agent, is an inhibitor of F0F1-ATPase. *Chem. Biol.* **2001**, *8*, 71–80, doi:10.1016/s1074-5521(00)00057-0.
37. Lamb, R.; Harrison, H.; Hulit, J.; Smith, D.L.; Lisanti, M.P.; Sotgia, F. Mitochondria as new therapeutic targets for eradicating cancer stem cells: Quantitative proteomics and functional validation via MCT1/2 inhibition. *Oncotarget* **2014**, *5*, 11029–37, doi:10.18632/oncotarget.2789.
38. Zahreddine, H.A.; Culjkovic-Kraljacic, B.; Gasiorek, J.; Duchaine, J.; Borden, K.L.B. GLI1-Inducible Glucuronidation Targets a Broad Spectrum of Drugs. *ACS Chem. Biol.* **2019**, *14*, 348–355, doi:10.1021/acschembio.8b01118.
39. Hong, S.; Pedersen, P.L. ATP synthase and the actions of inhibitors utilized to study its roles in human health, disease, and other scientific areas. *Microbiol. Mol. Biol. Rev.* **2008**, *72*, 590–641, Table of Contents, doi:10.1128/MMBR.00016-08.
40. Nesci, S. The mitochondrial permeability transition pore in cell death: A promising drug binding bioarchitecture. *Med. Res. Rev.* **2020**, *40*, 811–817, doi:10.1002/med.21635.
41. Abrial, M.; Da Silva, C.C.; Pillot, B.; Augeul, L.; Ivanes, F.; Teixeira, G.; Cartier, R.; Angoulvant, D.; Ovize, M.; Ferrera, R. Cardiac fibroblasts protect cardiomyocytes against lethal ischemia-reperfusion injury. *J. Mol. Cell. Cardiol.* **2014**, *68*, 56–65, doi:10.1016/j.yjmcc.2014.01.005.
42. Liu, N.; Xie, L.; Xiao, P.; Chen, X.; Kong, W.; Lou, Q.; Chen, F.; Lu, X. Cardiac fibroblasts secrete exosome microRNA to suppress cardiomyocyte pyroptosis in myocardial ischemia/reperfusion injury. *Mol. Cell. Biochem.* **2022**, *477*, 1249–1260, doi:10.1007/s11010-021-04343-7.
43. Branchini, A.; Baroni, M.; Burini, F.; Puzzo, F.; Nicolosi, F.; Mari, R.; Gemmati, D.; Bernardi, F.; Pinotti, M. The carboxyl-terminal region is NOT essential for secreted and functional levels of coagulation factor X. *J. Thromb. Haemost.* **2015**, *13*, 1468–74, doi:10.1111/jth.13034.
44. Bonora, M.; Morganti, C.; Morciano, G.; Giorgi, C.; Wieckowski, M.R.; Pinton, P. Comprehensive analysis of mitochondrial permeability transition pore activity in living cells using fluorescence-imaging-based techniques. *Nat. Protoc.* **2016**, *11*, 1067–

80, doi:10.1038/nprot.2016.064. 494

495

Titolo: "**Derivatizzazione di nanoparticelle come sistema diagnostico per virus**"

Inventori **ANNA FANTINATI, ROBERTA RIZZO, ANDREA ALOGNA, VALENTINA GENTILI, DAVIDE ILLUMINATI, GIULIA TURRIN, REMO GUERRINI, ERIKA MARZOLA CLAUDIO TRAPELLA…..**

residenti in:

1 Via Giacomo Brodolini, 11, 45011 Adria (RO)

2 Via Arginone, 166/a 44124 Ferrara (FE)

3 Via G. Ungaretti, 12/A, 44124, Ferrara (FE)

4 Via dell'Albicocco, 30 44123, Ferrara (FE)

5 Via Munara,1 Tezze sul Brenta, 36056 Vicenza (VI)

6 Via Placido Fabris, 28b, 32016 Alpago-Pieve (BL)

7 Via Darsena n° 80; 44121 Ferrara (FE)

8 Via L. Passega, 105 44122, Ferrara (FE)

9 Via G. Ungaretti, 9 44124, Ferrara (FE)

## CAMPO DELL'INVENZIONE

La presente invenzione riguarda la derivatizzazione di nanoparticelle d'oro (GNP's) utilizzando peptidi bioattivi per il riconoscimento delle porzioni virali quali le proteine esterne del capside. Le nanoparticelle d'oro dal diametro compreso tra 20nm e 800nm possono essere derivatizzate con peptidi bioattivi di diversa lunghezza in dipendenza dalla specificità di riconoscimento delle proteine virali. Nello specifico l'invenzione fornisce delle GNP's selettive per il riconoscimento molecolare del virus SARS-CoV-2 responsabile del COVID-19. La possibilità di legare alle GNP's sequenze peptidiche in grado di riconoscere il capside virale presuppone che la tecnica sviluppata possa facilmente adattarsi a diverse tipologie virali anche ad oggi sconosciute.

## STATO DELLA TECNICA

Il nuovo, ed altamente patogeno, coronavirus SARS-CoV-2 che ha causato la pandemia da COVID-19 partendo dalla provincia di Hubei in Cina e ad oggi è presente in tutto il mondo è un virus della classe dei betacoronavirus che presenta sulla sua superfice una struttura proteica chiamata spike in grado di riconoscere attraverso il dominio RBD una specifica parte del recettore ACE-2 umano (J. Lan et.al.

*Nature* **2020**, 581, 215-228.). Lo studio del receptor binding domain (RBD) a livello cristallografico ci ha permesso di definire una porsione della proteina ACE-2 umana composta da 19 amminoacidi in grado di legare selettivamente la spike di SARS-CoV-2.

La sintesi in fase solida di peptidi naturali è una tecnica ben conosciuta ed altamente riproducibile che ci ha permesso di produrre diverse sequenze amminoacidiche che si sovrappongono alla porzione proteica interessata dal legamne con la protina virale ( Chemistry of Peptide Synthesis N.L. Benoiton, CRC press; ISBN 9781574444544). I peptidi prodotti in fase solida ed analizzati tramite HPLC-massa sono stati preparati inserendo in posizione C-terminale un residuo di cisteina che presenta un gruppo tiolico in catena laterale indispensabile per il legame con le GNP's. (C.F.W. Becker et.al. *ChemBioChem*, **2007**, 8, 32-36).

Le GNP's possono esser eprodotte direttamente per reazione di riduzione dell'acido aurico, oppure per riduzione dei corrispondente tiolati di oro I (Corbierre M. K. Et.al., *Chem Mater*, **2005**, 17, 5691-5696), in questo caso le dimensioni delle nanoparticelle non sono costanti e quindi richiedono una successiva purificazione. In alternativa le GNP's possono essere acquistate da diversi fornitori che ne certificano le dimensioni (https://www.sigmaaldrich.com/catalog/search?term=gold+nanoparticles&interface=All&N=0&mode=match%20partialmax&lang=it&region=IT&focus=product) rendendo le successive sintesi e modificazioni più agevoli.

Le dimensioni delle GNP's sono critiche in quanto il sistema di rilevazione del virus prevede il passaggio della nanoparticella d'oro derivatizzata e legata al virus in un sistema nanofluidico dedicato con pori di dimensioni stabilite (R. Whei et.al., *Nature nanotechnology*, **2012**, 7, 257-263.)

Il sistema di fluidica e nanoporo associato è caratteristico per dimensionalità con le GNP's che possono però essere derivatizzate con il sistema tiolico su qualunque dimensione.

SOMMARIO DELL'INVENZIONE

La presente invenzione riguarda l'identificazione di nanoparticelle d'oro derivatizzate con peptidi tramite legame tra la funzionalità tiolica di una cisteina o di un derivato tiolico legato al peptide e l'oro della nanoparticella di dimensioni note. Il peptide utilizzato per la funzionalizzazione delle GNP's è un peptide sintetico formato da amminoacidi della lunghezza variabile da 5 a 30 residui amminoacidici contenente nella porzione c terminale una cisteina con funzionalità SH libera per la formazione del legame tio-aurico. (I)

H-$AA_1$-$AA_2$-----$AA_{29}$-Cys-OH

(I)

In cui:

$AA_1$, $AA_2$, $AA_{29}$ possono essere amminoacidi naturali in configurazione L o D quali: Alanina, Asparagina, arginina, acido aspartico, acido glutammico, cisteina, glicina, glutammina, istidina, isoleucina, leucina, lisina, metionina, fenilalanina, prolina, serina, treonina, triptofano, tirosina e valina. La sequenza amminoacidica è strettamente funzionale al riconoscimento del patogeno, gli amminoacidi in configurazione D possono essere inseriti per favorire la stabilità metabolica del peptide stesso legato alla nanoparticella.

L'invenzione ha quindi fornito un composto di formula (I) come sistema di roconoscimento di patogeni quali virus o batteri alla nanoparticella in modo da fornire selettività verso il patogeno desiderato per il suo riconoscimento come legame alla nanoparticella.

Nella presente invenzione, quando si impiegano le seguenti definizioni:

-Amminoacido: si intende alfa amminoacidi della serie L o D;

-nanoparticella: si intende nanoparticelle d'oro o di polistirene sferiche dalle dimensioni definite comprese tra 20 e 500nm.

Sotto un altro aspetto l'invenzione concerne una composizione comprendente un composto di formula (I) o suo sale farmaceuticamente accettabile per l'uso come medicamento e/o diagnostico e additivi farmaceuticamente accettabili.

DESCRIZIONE DELLE FIGURE

La Figura 1 riporta lo schema di preparazione dei composti di formula (I) per l'uso come medicamenti e/o diagnostici. La sintesi dei derivati peptidici viene effettuata utilizzando la chimica Fmoc/$^t$Bu con un sintetizzatore di peptidi multiplo Syro XP (Biotage Sweden), come supporto solido è stata utilizzata la resina Rink amide MBHA (loading 0,51mmol/g). (Guerrini R. et.al., *Bioorg. Med Chem*, **2015**, 23, 1515-1520).

La figura 2 riporta lo schema di derivatizzazione delle nano particelle d'oro con i peptidi antigenici e l'utilizzo di sulfobetaina come sistema antiaggregante (Wang Y. Et.al., *Langmuir* **2019**, 35, 1652-1661).

DESCRIZIONE DETTAGLIATA DELL'INVENZIONE

L'invenzione pertanto concerne un peptide derivato dalla sequenza dell'ACE-2 umana (J.Lan et.al., Nature, 581, 2020, 215-221.) (I):

Sequenza peptide ACE-2: H-Gln-Ala-Lys-Thr-Phe-Asp-Lys-Phe-Asn-His-Glu-Ala-Glu-Asp-Leu-Phe-Tyr-Gln-Cys-$NH_2$.

(I)

In cui:

la sequenza peptidica sopraindicata è legata in modo covalente ad una nanoparticella d'oro dal diametro compreso tra 20 e 500nm con un legame tio-aurico tra gli atomi di oro della nanoparticella e il gruppo tiolico della cisteina carbossi terminale ammide. (II)

(nella figura bisogna mettere ammide in C-term)

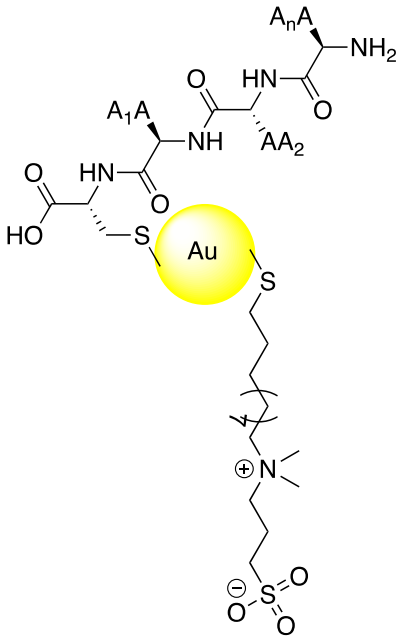


II

L'invenzione include altresì un composto di Formula (I) e Formula (II) marcato con almeno un radioisotopo quale per esempio trizio ($^{3}H$), carbonio ($^{14}C$), iodio ($^{125}I$) o con sonde fluorescenti, PET (Positron Emission Tomography) o SPECT (Single Photon Emission Tomography).

In un ulteriore aspetto l'invenzione concerne un composto di Formula (I) e Formula (II) per l'uso come medicamento e eccipienti farmacologicamente accettabili.

A scopi applicativi terapeutici i composti ivi descritti pertanto possono essere opportunamente formulati ai fini della somministrazione a mammiferi (in particolare a soggetto umano), come tali o associati in opportuna composizione farmaceutica con uno o più eccipienti e/o veicoli farmaceuticamente accettabili. Le composizioni dell'invenzione comprendono quelle destinate alla somministrazione orale, nasale, sublinguale e, in particolar modo, parenterale (sottocutanea,

intramuscolare, intravenosa e intradermica) in forma di preparazioni iniettabili sterili (soluzioni o sospensioni) acquose e non acquose.

In considerazione del profilo di attività biologica mostrato dai composti di Formula (I) e Formula (II) della presente invenzione, le composizioni farmaceutiche comprendenti gli stessi possono essere utilizzate come sistema diagnostico in vitro per la determinazione della presenza di virus Sars-Cov-2 sia in fluidi biologici. Tale metodica di identificazione rientra nel gruppo di test di screening antigenici, che si avvalgono della velocità di esecuzione e della specificità di riconoscimento.

L'invenzione verrà ora esemplificata in riferimento ad esempi di preparazione dei composti di Formula (I) dell'invenzione e di valutazione degli effetti terapeutici/medicali dei composti a titolo esemplificativo e non limitativo.

PARTE SPERIMENTALE

I composti dell'invenzione sono stati preparati secondo lo schema riportato nella Figura 1 ed in figura 2.

I diversi peptidi sono stati sintetizzati in fase solida utilizzando la chimica Fmoc/$^{t}$Bu utilizzando una resina ammidica Rink amide MBHA (loading 0,51mmol/g) come supporto solido. I reagenti, solventi ed agenti di coupling sono stati utilizzati al massimo grado di purezza presente in commercio.

A titolo esemplificativo si riporta la descrizione della sintesi del peptide ACE-2 di maggiore interesse.

Il composto I è stato ottenuto mediante sintesi in fase solida con chimica Fmoc/tBu usando un sintetizzatore automatico Syro XP. Come supporto solido è stata utilizzata una resina polistirenica funzionalizzata con linker Rink Ammide AmphiSpheres 20 RAM (con grado di derivatizzazione 0.55 mmol/g 75-150 µm). Gli amminoacidi naturali, non naturali sono stati solubilizzati in DMF ad una concentrazione 0.5M; N,N'-diisopropylcarbodiimide (DIC), idrossibenzotriazolo (HOBt), anidride acetica ($Ac_2O$) e N-metilmorfolina (NMM) sono stati sciolti nello stesso solvente a concentrazioni rispettivamente 1.09 M, 0.78 M, 0.5 M e 0.25 M. Il successivo trattamento con acido trifluoroacetico (TFA) al 95%, acqua ($H_2O$) al 2.5% e trietilsilano ($Et_3SiH$) al 2.5% portava al derivato I, che sarà poi utilizzato nella sintesi del composto II anch'esso parte della presente invenzione.

I tempi di ritenzione ($t_R$) riportati per i composti dell'invenzione sono stati ottenuti mediante analisi HPLC analitico Beckman System Gold 168 con colonna Kinetex® C8 (150 x 4.6 mm, 100 Å, 5µm) e rivelatore UV a lunghezza d'onda variabile, settata a 220nm. Il mezzo di eluizione è un sistema binario costituito dai componenti A (100% $H_2O$ + 0,1% TFA) e B (100% $CH_3CN$ + 0,1% TFA), le analisi hanno una durata di 30 minuti con un flusso di 0.7 mL/minuto con un gradiente lineare dal 100% di A al 100% del componente B in 25 minuti. Tutti i composti dell'invenzione sono stati purificati in

HPLC semi-preparativo Waters 600 Multisolvent Delivery System con una colonna RP (reversed phase) Phenomenex Jupiter® C18 (250 x 30mm, 300 Å, 15µm) avente come mezzo di eluizione una fase mobile binaria in cui i solventi A (100% $H_2O$ + 0,1% TFA) e B (60% $CH_3CN$, 40% $H_2O$ + 0,1% TFA) sono stati utilizzati in proporzioni variabili a seconda della composizione del residuo grezzo da purificare.

Esempio 1: Preparazione del composto **I**

Una sospensione della resina polistirenica (200 mg, 0.11 mmol) in DMF (2 mL) era lasciata in agitazione 5 min, successivamente il solvente veniva filtrato ed il supporto solido Fmoc-deprotetto (Piperidina al 40 % in DMF, 2 x 2mL). La reazione procedeva con la funzionalizzazione del C-terminale con il primo residuo amminoacidico Fmoc-L-Cys(Trt)-OH (4 eq) mediante coupling ammidico via DIC (4 eq) e HOBt (4 eq) in DMF (2 mL) a dare la resina derivatizzata con il primo amminoacido della sequenza. Trascorsi 30 min, la miscela di reazione veniva filtrata e si procedeva con capping via NMM (4 eq) e $Ac_2O$ (4 eq), Fmoc-deprotezione del primo amminoacido e successiva reazione di coupling ammidico con il secondo amminoacido Fmoc-L-Gln(Trt)-OH (2 eq) della durata di 1 ora. I cicli di deprotezione e coupling ammidico si ripetevano sino all'ottenimento della catena pseudopeptidica finale. Il composto **I** è stato fornito dal trattamento del supporto solido così funzionalizzato mediante sospensione in una miscela TFA/$H_2O$/$Et_3SiH$ per 3 ore. La miscela di sblocco veniva filtrata, concentrata ed il residuo grezzo così ottenuto veniva purificato via HPLC semi-preparativo. Il composto **I** veniva liofilizzato e successivamente purificato attraverso HPLC preparativo (Waters Delta Prep 3000) utilizzando il seguente gradiente: $A_0$ 95%, $A_{25}$ 40%, $A_{35}$ 15%, $A_{40}$ 0%, riequilibratura $A_{45}$95%, solvente A=$H_2O$/0.1% TFA, solvente B= $H_2O$/ACN/TFA 40%/60%/0.1%).

Il peptide a sequenza H-Gln-Ala-Lys-Thr-Phe-Asp-Lys-Phe-Asn-His-Glu-Ala-Glu-Asp-Leu-Phe-Tyr-Gln-Cys-$NH_2$ presenta un peso molecolare di 2446,7Da, in figura 3 è rappresentato lo spettro di massa ESI singolo quadrupolo del peptide purificato ed il suo HPLC analitico: MS (ESI): $[M+2H]^{2+}$ = 1224.31; $t_R$ (HPLC) = 14.80 min.

Sintesi delle nanoparticelle d'oro.

Le nanoparticelle d'oro derivatizzate sono state sintetizzate a partire dal peptide I e dalla sulfobetaina, nello specifico a titolo esemplificativo si riporta una sintesi modello.

6mL di una sospensione di nanoparticelle d'oro dal diametro di 300nm (Sigma Aldrich Italia) vengono sospese in una soluzione di soda 0.1N (6 mL) e successivamente dalla sospensione viene

rimosso l'ossigeno disciolto per insufflazione di argon anidro per 15 minuti. Terminata l'insufflazione di argon e mantenendo l'atmosfera inerte si aggiungono 3,48mg di peptide I e 300 microlitri di una soluzione di sulfobetaina 2N in soda 0.1N e si lasciano reagire a temperatura ambiente per 48 ore. Terminata la reazione si procede con la centrifugazione delle nanoparticelle (2200 rpm per 13 minuti a 4°C) ed il successivo lavaggio con 1mL di acqua per 5 volte consecutive. Dopo l'ultimo lavaggio le GNP's si risospendono in 1 mL di PBS per ottenere una concentrazione finale di circa $2E^9$ GNP's/mL di sospensione.

Una porzione di 50microlitri di GNP's viene trattata con la spike1 del virus SARS-Cov-2. L'interazione tra la sequenza selezionata di ACE2 e la proteina Spike1 virale è stata dimostrata dal riconoscimento in vitro tramite immunofluorescenza. Le biglie sono state cimentate per 10 minuti a temperatura ambiente con il frammento RBD della Spike1 di SARS-CoV-2, lavate con soluzione fisiologica, e successivamente marcate con anticorpo fluorescente contro la porzione RBD della Spike1 di SARS-CoV-2 (NovusBiotech). La visualizzazione al microscopio a fluorescenza ha consentito di identificare biglie fluorescenti, dimostrazione dell'interazione tra la biglia e la porzione RBD di Spike1 (Figura 5).

L'interazione tra la sequenza peptidica selezionata di ACE2 ed il virus SARS-CoV-2 è stata dimostrata dal riconoscimento in vitro tramite microscopia TEM. Le biglie sono state cimentate per 10 minuti a 37°C con il virus SARS-CoV-2, lavate con soluzione fisiologica, e successivamente fissate in glutaraldeide al 2.5%. La visualizzazione al microscopio TEM ha consentito di identificare biglie con legate particelle virali (Figura 6).

**RIVENDICAZIONI**

1. Un peptide di formula (I) e corrispondente alla sequenza aminoacidica H-Gln-Ala-Lys-Thr-Phe-Asp-Lys-Phe-Asn-His-Glu-Ala-Glu-Asp-Leu-Phe-Tyr-Gln-Cys-$NH_2$
2. Il sistema nanoparticellare di formula II:

In cui: la sequenza del peptide in grado di legare SARS-Cov-2 è: H-Gln-Ala-Lys-Thr-Phe-Asp-Lys-Phe-Asn-His-Glu-Ala-Glu-Asp-Leu-Phe-Tyr-Gln-Cys-$NH_2$,

3. L’utilizzo di nanoparticelle di formula (II) in sistemi di rilevazione della particella virale basati sulla modulazione della lettura della conduttanza o della deviazione della luce

4. La preparazione di nanoparticelle d’oro funzionalizzate con sulfobetaina e con sequenze peptidiche caratterizzate da una funzione tiolica.

**RIASSUNTO**

La presente invenzione è relativa a un sistema diagnostico per SArs-Cov-2 basato sulla tecnologia delle nanoparticelle d’oro derivatizzate con un peptide (composto I) in grado di riconoscere selettivamente le proteine spike del capside virale attraverso un lettore di corrente a nanopori brevettato dalla ditta Elements di Cesena. Il sistema di riconoscimento si basa sulla selettività proteina/recettore e sulle dimensioni relative del Virus e delle nanaoparticelle che andranno a transitare attraverso il sensore (foro nanometrico) del dispositivo di rilevazione, generando modulazioni nella corrente elettrica rilevata, caratteristici delle dimensioni dell’aggregato nanoparticella+virus. (qui inserire i riferimenti al brevetto flowcell, nota per Barzano).

**FIGURA 1**

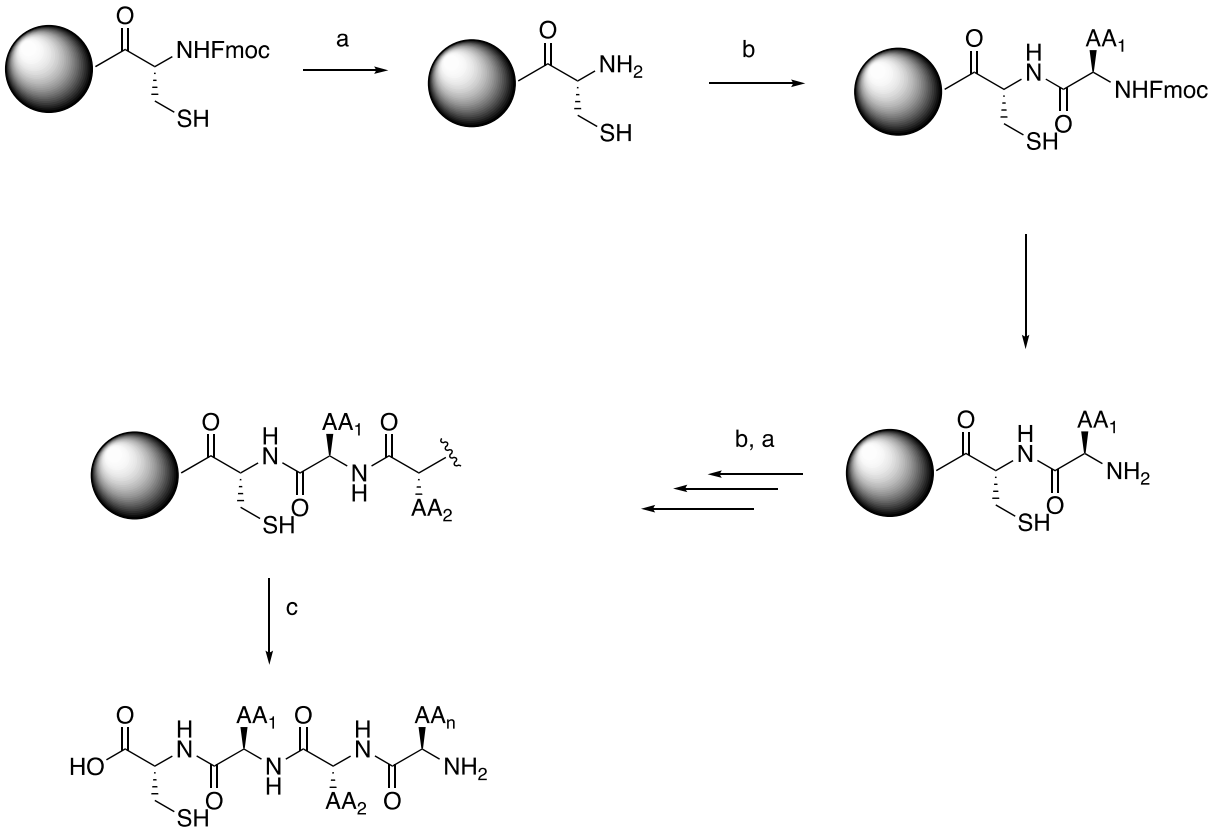


Condizioni: a) Piperidina 20%/DMF; b)Fmoc-$AA_1$-OH, WSC, HOBt, NMM, DMF; c) TFA/$Et_3Si/H_2O$.

Figura 2

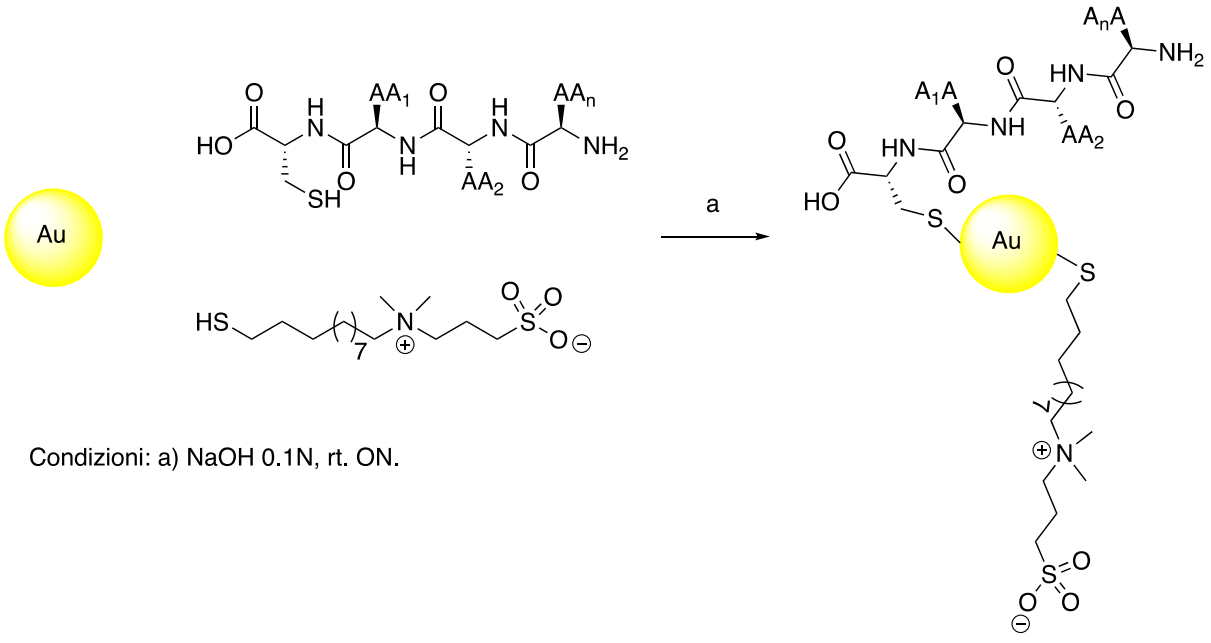


Condizioni: a) NaOH 0.1N, rt. ON.

Figura 3 Spettro massa ESI positive composto I

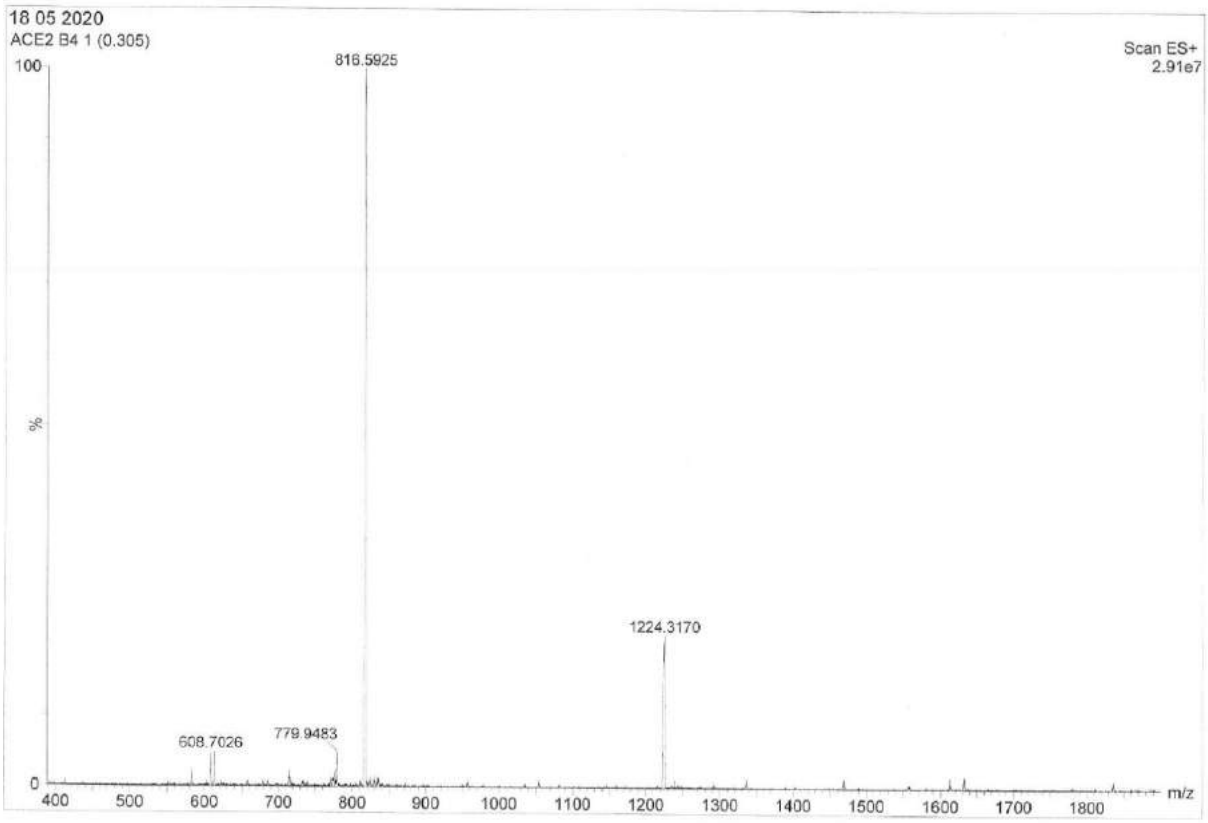


Figura 4 HPLC analitico composto I

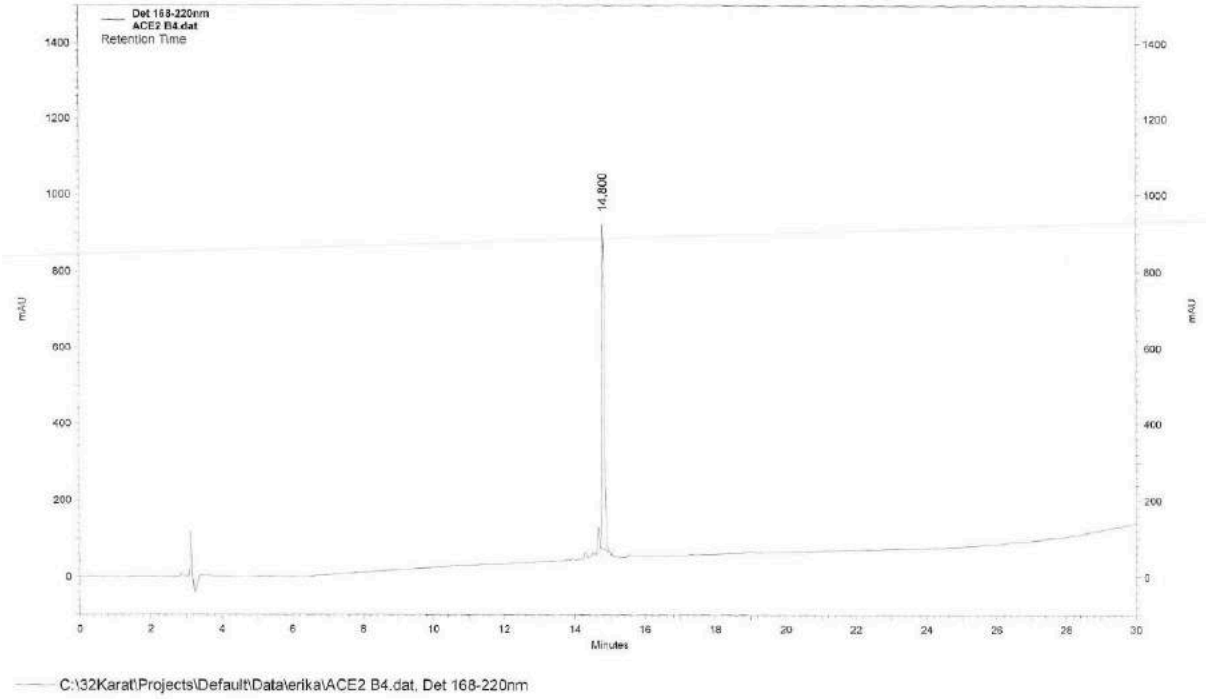

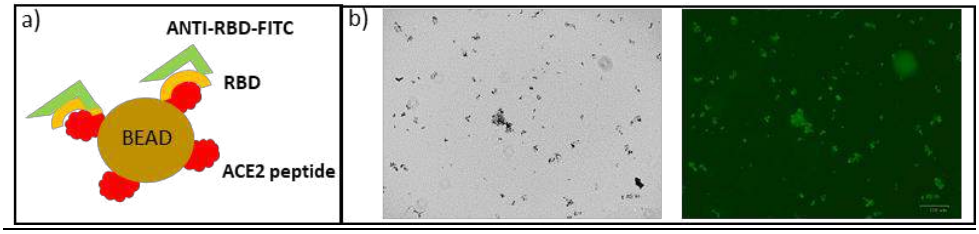


Figura 5. a) Schematizzazione dell'interazione tra biglie rivestite di peptide ACE2 e la porzione RBD della proteina Spike1 di SARS-CoV-2. B) Visualizzazione al microscopio a fluorescenza in campo chiaro (pannello sinistro) e in fluorescenza (pannello destro).

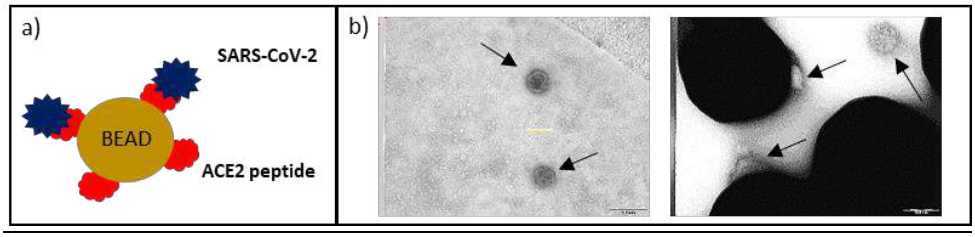


Figura 6. a) Schematizzazione dell'interazione tra biglie rivestite di peptide ACE2 e SARS-CoV-2. B) Visualizzazione al microscopio TEM del virus SARS-CoV-2 (pannello sinistro) e in presenza delle biglie (pannello destro). La freccia nera indica il virione di SARS-CoV-2.